Tales of a Lepidopterist:

Using Amine Polyalcohol Ligands in the Development of Novel Heterometallic Single-Molecule Magnets

R. B. C. Martin

Ph.D. 2023

Tales of a Lepidopterist:

Using Amine Polyalcohol Ligands in the Development of Novel Heterometallic Single-Molecule Magnets

ROBERT CHRISTOPHER MARTIN

A thesis submitted in partial fulfilment of the requirements of Manchester Metropolitan University for the degree of Doctor of Philosophy

Department of Natural Sciences
Manchester Metropolitan University

2023

Declaration and Consent

I declare that the thesis submitted is my own work and I have maintained professional integrity during all aspects of my research degree, and I have complied with the Institutional Code of Practice and the Regulations for Postgraduate Research Degrees.

No material contained in the thesis has been used in any other submission for another academic award. Any material which has been used for any other award or qualification is detailed. This includes any published material submitted by any other student of Manchester Metropolitan University or any other institution.

I permit the Faculty Research Degrees Administrator to automatically re-enrol my registration with the University between submission of my thesis and completion of the award, if this is not undertaken by myself.

I confirm that an e-copy of my thesis has been submitted to the Faculty Research Degrees Administrator for submission to Turnitin.

Acknowledgements

The author would like to thank his research group and director of studies, Dr S. K. Langley for their energy and enthusiasm over the last seven years.

Additionally, special mentions go to the four summer students who worked with the Langley group from 2016-23: Mr A. T. M. Wilcock, Mr L. Skilander, Mr A. Embleton and Mr J. J. Russell.

The author's personal gratitude is offered to all the academic and technical staff at MMU and other cooperating institution, without whom analysis would have proved infeasible, if not impossible. Additional thanks are offered to Dr G. Miller, Dr S. Gulzar and Dr M Hernandez-Guzman, alongside the analytical teams at the University of Southampton, Diamond Light Source, the Australian synchrotron MX1 beam-line and Nottingham Trent University.

The author recognises the support of four individuals within the department without whom this project would have seemed unreachable: Dr T. B. R. Robertson, Mr D. Dixon, Mr S. Elson and Mr J. J. Russell.

The author also wishes to thank his external examiners: Dr I. Gass and Dr L. F. Jones for their advice, approach and attitude during the viva voce and in clarifying communications since.

Finally, the author recognises the two people without whom his life would be incalculably different and infinitely worse: his long-suffering parents, may this thesis prove an item of pride in the days and years to come, or as kindling. Whichever is more pertinent at the time…

Table of Contents

List of Figures

List of Schemes

List of Tables

Abstract

The synthesis and characterisation of a series of thirty complexes is reported, based upon the binding of symmetric or asymmetric amine polyalcohol ligands to a predicted $\{TM_2\text{-}Ln_2\}$ core. All reactions proceeded *via* serendipitous self-assembly and thereby exhibit both designed and unexpected topologies. These topologies range from trimetallic partial butterflies to icosidyometallic propeller-like complexes. Magnetic susceptibility measurements were carried out on thirteen of the thirty complexes to assess their value as potential single-molecule magnets (SMMs).

Fourteen complexes were synthesised using N,N-bis(2-hydroxyethyl)-3-amino-2-hydroxypropanesulfonic acid ([**DIPSO**]H_4) as the primary structural ligand. Single crystal X-ray diffraction (SC-XRD) data is provided for each of these structures, thirteen of which are novel. Six of these compounds form as the intended {3d-4f} butterfly motif, whilst the remaining eight exhibit various other topologies. Magnetic data was collected for four of the samples, however no out-of-phase χ" signals were observed down to 2 K.

The attempted syntheses of the seven asymmetric amine polyalcohol ligands, 3-[(2-hydroxyethyl)(methyl)amino] propan-1-ol, [**HMAP**]H_2, 3-[(2-hydroxyethyl)(ethyl)amino] propan-1-ol, [**HEAP**]H_2, 3-[(2-hydroxyethyl)(iso-propyl)amino] propan-1-ol, [**H^{i}PrAP**]H_2, 3-[(2-hydroxyethyl)(phenyl)amino] propan-1-ol, [**HPhAP**]H_2, 3-[(2-hydroxyethyl)(tert-butyl)amino] propan-1-ol, [**H^{t}BuAP**]H_2, 3-[(2-hydroxyethyl)(adamantyl)amino] propan-1-ol, [**HAdAP**]H_2, 2,2'-[(3-hydroxypropyl)imino] bis-ethanol, [**^{n}Pr'DEA**]H_3, are described. Additionally, the syntheses of precursor molecules and their symmetric variants are also described, for a total of twenty-one precursor or pro-ligand molecules. Four of the seven target ligands are fully characterised, whilst the final three remain partially characterised. Syntheses proceeded by stepwise amine alkylations in non-polar media as to prevent reaction cascades common in conventional non-catalysed amine alkylation reactions.

Six reactions utilising synthesised asymmetric polyalcohol ligands with a {3d} metal source and {4f} metal source proceeded by serendipitous self-assembly to produce five novel complexes and one toroidal complex. Two of these complexes inhabit the traditional {3d-4f} butterfly motif, two exhibit a $\{TM_2Ln_2\}$ buckled core akin to the butterfly motif, one monomeric and one in a chain form. The final novel complex exhibits a square-in square type topology. Magnetic data was collected for three of the samples, of which two complexes, $[Cr^{III}_2Dy^{III}_2(OMe)_2(Benz)_4(HMAP)_2(NO_3)_2]$ and $[Cr^{III}_2Dy^{III}_2(OMe)_2(Benz)_4(HEAP)_2(NO_3)_2]$, exhibited open hysteresis loops up to 3.5 K, with maximum coercive fields of 2.5 T and 2.98 T at their lowest measured temperatures, respectively.

Similarly, nine reactions utilising synthesised symmetric and asymmetric ligands with a {4d} metal source and a {4f} metal source were performed to produce one known butterfly, seven novel butterflies and one $\{Ru_2Dy_4\}$ extended butterfly. A novel {5p-4f} complex was also synthesised forming an unusual propeller-like motif of formula $[In^{III}_{16}Dy^{III}_6(O)_6(OH)_{12}(OMe)_3(Benz)_{22}(HMAP)_6(NO_3)_5]$. Magnetic data was collected for six of the samples, two of which, $[Ru^{III}_2Dy^{III}_2(OMe)_2(Benz)_4(MDEA)_2(NO_3)_2]$ and $[Ru^{III}_2Dy^{III}_2(OMe)_2(2\text{-Cl-}4,5\text{-F-Benz})_4(MDEA)_2(NO_3)_2]$, revealed clear frequency and temperature dependant maxima in their out-of-phase components, indicative of SMM behaviour.

Keywords: Coordination Chemistry, Single-Molecule Magnets (SMMs), Butterfly Complexes, Hysteresis, Tertiary Amine Polyalcohols, Lepidoptery.

Abbreviations

^{13}C NMR	Carbon-13 Nuclear Magnetic Resonance spectroscopy
^{1}H NMR	Proton Nuclear Magnetic Resonance spectroscopy
2,3,4,5-tet-F-Benz	2,3,4,5-tetrafluorobenzoic acid
2,6-Cl-Benz	2,6-dichlorobenzoic acid
2Br-Benz	2-bromobenzoic acid
2-Cl-4,5-F-Benz	2-chloro-4,5-fluorobenzoic acid
2Cl-benz	2-chlorobenzoic Acid
2-ClEtOH	2-chloroethan-1-ol
2-ClPrOH	3-chloropropan-1-ol
2-F_3C-Benz	2-(trifluoromethyl)benzoic acid
2I-benz	2-iodobenzoic acid
ac	Alternating current
[Acac]H	Acetylacetone
[**AdAE**]H	2-(adamantylamino)ethan-1-ol
[**AdAPr**]H	3-(adamantylamino)propan-1-ol
[**AdDEA**]H_2	N-adamantyldiethanol amine
B	Magnetic field
Benz	Benzoic acid
$CDCl_3$	Deuterated chloroform
COSY	Correlated spectroscopy
D	Axial anisotropy parameter
dc	Direct current
[**DIPSO**]H_4	N,N-bis(2-hydroxyethyl)-3-amino-2-hydroxypropanesulfonic acid
[**EAE**]H	2-(ethylamino)ethan-1-ol
[**EDEA**]H_2	N-ethyldiethanolamine
ESI	Electrospray ionisation
FT-IR	Fourier transform infra-red
[**HAdAP**]H_2	Hydroxyethyl adamantylaminopropanol
[**HEAP**]H_2	Hydroxyethyl ethylaminopropanol

[Hfac]H	Hexafluoroacetlyacetone
[**H^{i}PrAP**]H_2	3-[2-(hydroxyethyl)(iso-propyl)amino]propan-1-ol
[**HMAP**]H_2	3-[2-(hydroxyethyl)(methyl)amino]propan-1-ol
HMQC	Heteronuclear Quantum Coherence
[**HPhAP**]H_2	3-[2-(hydroxyethyl)(phenyl)amino]propan-1-ol
HRMS	High Resolution Mass Spectrometry
[**H^{t}BuAP**]H_2	3-[2-(hydroxyethyl)(tert-butyl)amino]propan-1-ol
[^{i}**PrAE**]H	2-(isopropylamino)ethan-1-ol
[^{i}**PrDEA**]H_2	N-isopropyldiethanolamine
J	Total angular Momentum Quantum Number
k_B	Boltzmann Constant
k_BT	Boltzmann Energy
L	Azimuthal Quantum Number
Ln	Lanthanide
Ln SMMs	Lanthanide Single-Molecule Magnets
$Ln(NO_3)_x{\cdot}yH_2O$	Lanthanide Nitrate Hydrate
[MAE]H	2-(methylamino)ethan-1-ol
Mbar	Millibar
[**MDEA**]H_2	N-methyldiethanolamine
MeO^-	Methoxy-ion
MS	Mass Spectrometry
M_{sat}	Magnetic Saturation
N_a	Avogadro's Constant
[^{n}**BuDEA**]H_2	N-n-butyldiethanolamine
NEt_3	Triethylamine
NMR	Nuclear Magnetic Resonance
[^{n}**Pr'DEA**]H_3	2,2'-[(3-hydroxypropyl)imino]bis-ethanol
o-Tol	ortho-toluic acid
[**PhAE**]H	2-(phenylamino)ethan-1-ol
[**PhDEA**]H_2	N-phenyldiethanolamine
Piv	Pivalic acid
pm	Picometer

ppm	Parts per million
p-tol	para-toluic acid
QSAR	Quantitative Structure-Activity Relationship
QTM	Quantum Tunnelling of Magnetisation
Q-tof LC/MS	Quadrupole time-of-flight Liquid Chromatography Mass Spectrometry
[**RDEA**]H_2	R-diethanolamine, R = Me, Et, ^{i}Pr, etc
S	Spin Quantum Number
SATP	Standard Atmospheric Temperature and Pressure
SCM	Single-Chain Magnets
SC-XRD	Single Crystal X-Ray Diffraction
SMMs	Single-Molecule Magnets
SQUID	Superconducting QUantum Interference Device
TA-QTM	Thermally Assisted Quantum Tunnelling of Magnetisation
T_B	Blocking Temperature
Tbit	Terabit
[^{t}**BuAE**]H	2-(tertbutylamino)ethan-1-ol
[^{t}**BuAPr**]H	3-(tertbutylamino)propan-1-ol
[^{t}**BuDEA**]H_2	N-tertbutyldiethanolamine
T_C	Curie temperature
[**TEA**]H_3	Triethanolamine
T_{fN}	Ferrimagnetic Néel temperature
TM	Transition Metal
TM SMMs	Transition Metal Single-Molecule Magnets
$TM(NO_3)_x{\cdot}yH_2O$	Transition Metal Nitrate Hydrate
T_N	Néel temperature
Z	Atomic number
μ_B	Bohr Magneton
Θ	Weiss constant
μ_0	Permeability of a vacuum
χ	Magnetic susceptibility

1 Introduction

1.1 Magnetochemistry

Magnetochemistry, as defined by Selwood in 1943, is the "*application of magnetic susceptibilities and of closely related quantities to the solution of chemical problems*".[1] Nowadays the field and its applications have broadened significantly. In its simplest terms magnetochemistry is concerned with the magnetic properties of chemical compounds.[2] The study of magnetochemistry develops the understanding of the relationship between molecular arrangement and magnetic phenomena.[3] As the magnetic properties of chemical structures are broadly derived from the spin and orbital angular momentum of the electrons within said structures, they prove, to an extent, to be predictable and exploitable for analytical and material-based purposes, respectively.[4, 5] As the field has developed this has come to encompass many new practical techniques and redefined the standards by which chemistry is reported, thanks to the invent, growth and development of magnetic resonance techniques, amongst others.[6]

1.2 Magnetism and Magnetic Susceptibility

Magnetism, within magnetochemistry, is a complex topic, inherently linked to quantum mechanical roots, and is of great practical and technological import due to its diverse applications.[7-9] Magnetism is defined as a materials response to an external magnetic field.[10] Furthermore, as a physical phenomenon, magnetism is derived from the motion of electrons, that results in the exhibition of attractive and repulsive interactions between magnetic materials. Fundamentally, the presence of an unpaired electron is required for a material to be considered classically magnetic.[11] More precisely, rather than the electron itself, the intrinsic spin and orbital angular momentum of said electron generates a magnetic moment (μ), which defines a species as magnetic.[12]

The magnetic moment is comprised of two components, both derived from the motion of electrons. Electrons move in two ways – spinning on their axis, represented by the

quantum number S, and orbiting the nucleus, represented by the quantum number L – with the total angular momentum defined as the quantum number J.[13]

$$\textbf{Eq}^{\textbf{n}}\ \textbf{1}\text{:}\ J = S + L$$

The magnetic moment can then be calculated as a function of the total angular momentum, J, where g is a dimensionless quantity, or g-factor, which essentially acts as a proportionality constant, using the Hund-Landé Equation.[14]

$$\textbf{Eq}^{\textbf{n}}\ \textbf{2}\text{:}\ \mu = g\sqrt{J(J+1)}$$

$$\text{Where } g_J = 1 + \frac{S(S+1)-L(L+1)+J(J+1)}{2J(J+1)} = \frac{3}{2} + \frac{S(S+1)-(L(L+1)}{2J(J+1)}$$

In many cases the orbital moment is quenched, so the magnetic moment can be described by only accounting for the spin of the molecule's unpaired electrons.[15, 16] Whilst this method proves applicable to first row transition metals in most cases, it fails to account for the Russell-Saunders coupling[17] exhibited by any ion in which the orbital moment is not fully quenched.[18] This assumption becomes more egregious as the metal becomes more massive, proving to be a good first assumption in first row transition metals, but a poor fit to the behaviour of lanthanide ions.[19] This approximation of the magnetic moment is referred to as the spin-only magnetic moment (μ_{SO}).

$$\textbf{Eq}^{\textbf{n}}\ \textbf{3}\text{:}\ \mu_{SO} = \sqrt{n(n+2)} = \sqrt{4S(S+1)}$$

Where n is the number of unpaired electrons and S is the total spin quantum number.

As magnetism is the response of a material to an applied field, a value must be associated to a material which defines how disposed it is to the effect of said external field.[20] This value is termed the magnetic susceptibility (χ). Magnetic susceptibility should be considered the summation of two components, one diamagnetic and negative (χ^D), the other paramagnetic and positive (χ^P).

Eq^{n} 4: $\chi = \chi^D + \chi^P$

In perhaps its simplest terms, that of atomic magnetism, we can define the two classes of interactions between an isolated atom and an external field as either diamagnetic or paramagnetic. This is the result of each electron within the species acting akin to a tiny bar magnet and responding to any applied magnetic field. In the case of paramagnetic species, they will attract or align to the applied field due to the presence of an (or several) unpaired spin(s) (Total Spin, S≠0). Conversely, a diamagnetic species will instead repel or align against the external field, as any spin contribution is eliminated due to all electrons remaining paired within their orbitals (Total Spin, *S*=0). In this case, the interaction is instead a result of the angular orbital momentum.[21] All species can be said to act diamagnetically, but paramagnetic species have a dominant, opposing effect orders of magnitude stronger.[22, 23] The diamagnetic component can therefore be considered negligible for most elements prior to the fifth row, in the main case.[24]

The Curie law [25] describes the simplest behaviour of paramagnetic species, such that the magnetic susceptibility (χ_m) is inversely proportional to the temperature, T, related by a material specific Curie constant, C. Although it best models the colliding and tumbling of paramagnetic molecules in a fluid substance,[26] it can also be applied to solids containing open shelled metal ions[27] such as Mn(II) or Gd(III), as detailed later.

Eq^{n} 5: $\chi_m = C/T$

Magnetic susceptibility can be used to relate the strength of an external field (H) to the magnetisation (M) induced within a material that feels its effect.[28] Logically, placing a material within a stronger external field will exert a greater effect upon it, inducing a higher magnetisation.

Eq^{n} 6: $M = \chi_m . H$

The magnetisation of a material can also be expressed as a function of its total magnetic moment (μ_{Total}) and volume (V), more simply put, as a density of net magnetic dipole

moment within a material. It should be noted that magnetisation, as a vector quantity, should be considered directional.[29]

Eq^{n} 7: $M = \mu_{Total}/V$

In such a situation then the total magnetic field (B) can be related to the magnetisation by the values μ_0 and B_0, the magnetic permeability of space and externally applied magnetic field,[30] respectively.

Eq^{n} 8: $B = B_o + \mu_o M$

In heavier elements, such as the lanthanides, this formula becomes particularly useful. The accuracy of resultant values can be skewed by a lack of consideration for a materials diamagnetic component, which only becomes a more important contribution as the atomic number (Z) increases.[24]

The magnetic moment can be defined directly from a materials magnetic susceptibility by consideration alongside an array of physical constants: Boltzmann's Constant (k_B), Avogadro's number (N_A) and the Bohr magneton (μ_B), as shown below.

Eq^{n} 9: $\mu = \sqrt{\frac{3k_b}{N_A\,(\mu_B)^2}}.\sqrt{\chi T}$

Magnetic fields cause magnetic moments to align, whilst the variation of the spin state within an energy level defines the nature of the alignment. Each energy level can be split into several spin states defined by the spin multiplicity (2S+1) ranging from m_s=-S to m_s=S in integer increments. The energy of each spin state, E_{ms}, can be calculated within a field of known strength, as the degeneracy of the states is lifted by the presence of the magnetic field.

Eq^{n} 10: $E_{ms} = \mu_B g_J m_s B$

Therefore $\Delta_Z = \mu_B g_J B$, for immediately successive spin states.

The orientations of the electrons within a field are defined in relation to the field direction, such that the spin state m_s=-S, the lowest in energy, aligns parallel to the field whilst the spin state m_s=S, the highest in energy, aligns antiparallel to the field.[31] Should an m_s=0 spin state exist, this will align perpendicular to the direction of the field, effectively acting in a non-magnetic fashion. As the magnetic field increases, degenerate spin states will diverge proportionally, as shown in **Figure 1**, thereby increasing the probability of finding an electron within the lower energy spin states. This separation in energy of degenerate spin states with the application of an external field is referred to as the Zeeman effect.[32, 33]

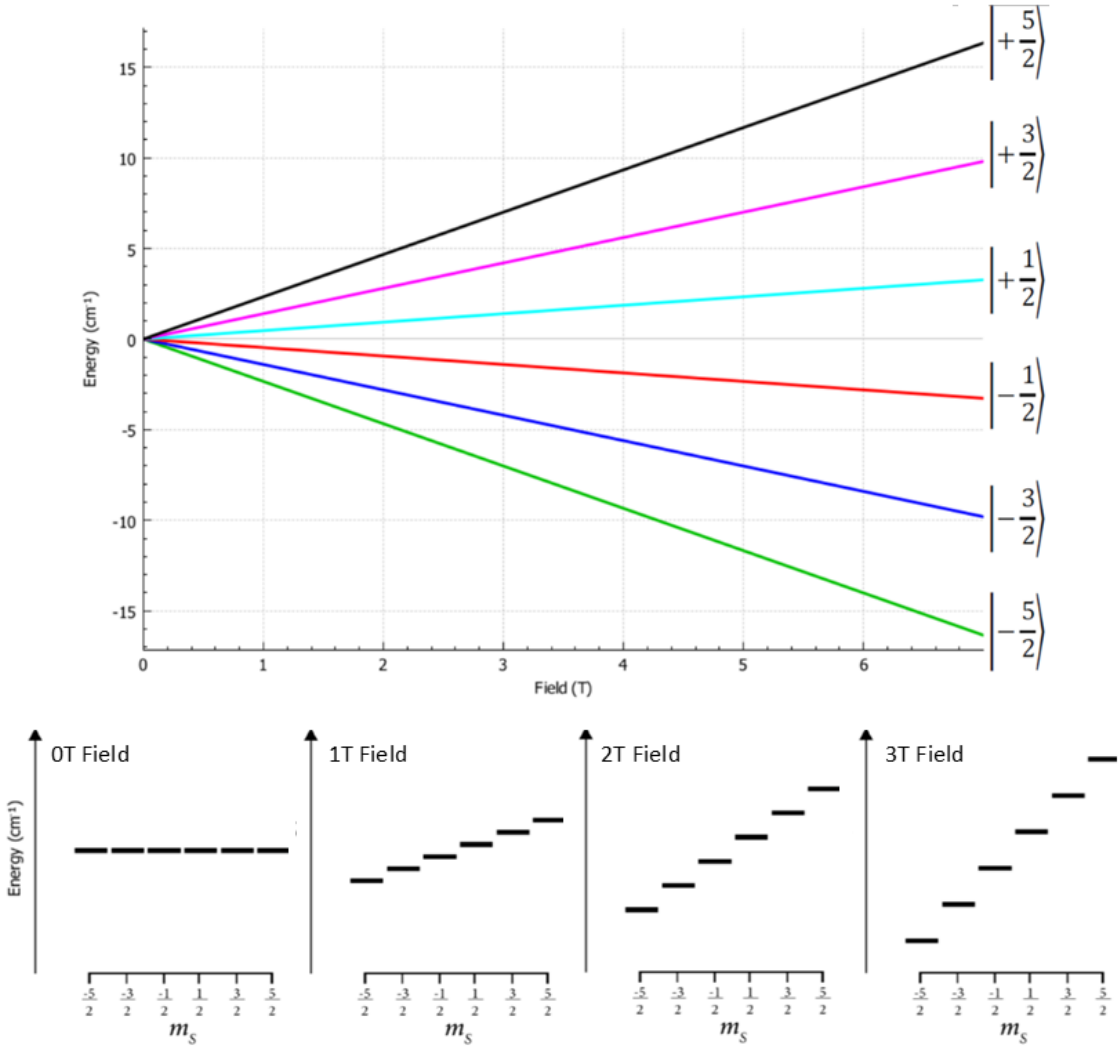

Figure 1- Zeeman splitting diagram exhibiting the divergence of degenerate m_s states in an external magnetic field of varying strength for a hypothetical S = 5/2 ion.

Further to Zeeman splitting, the degeneracy of spin states within an energy level can break down as the result of inter-electron repulsions in the absence of any field. The degree of separation in such cases is dictated by the symmetry of the system that the splitting acts in but is responsible in part for many of the properties thought of in classical magnetism. This form of spin state separation is intuitively referred to as zero-field splitting,[34] ZFS, as shown in **Figure 2**.

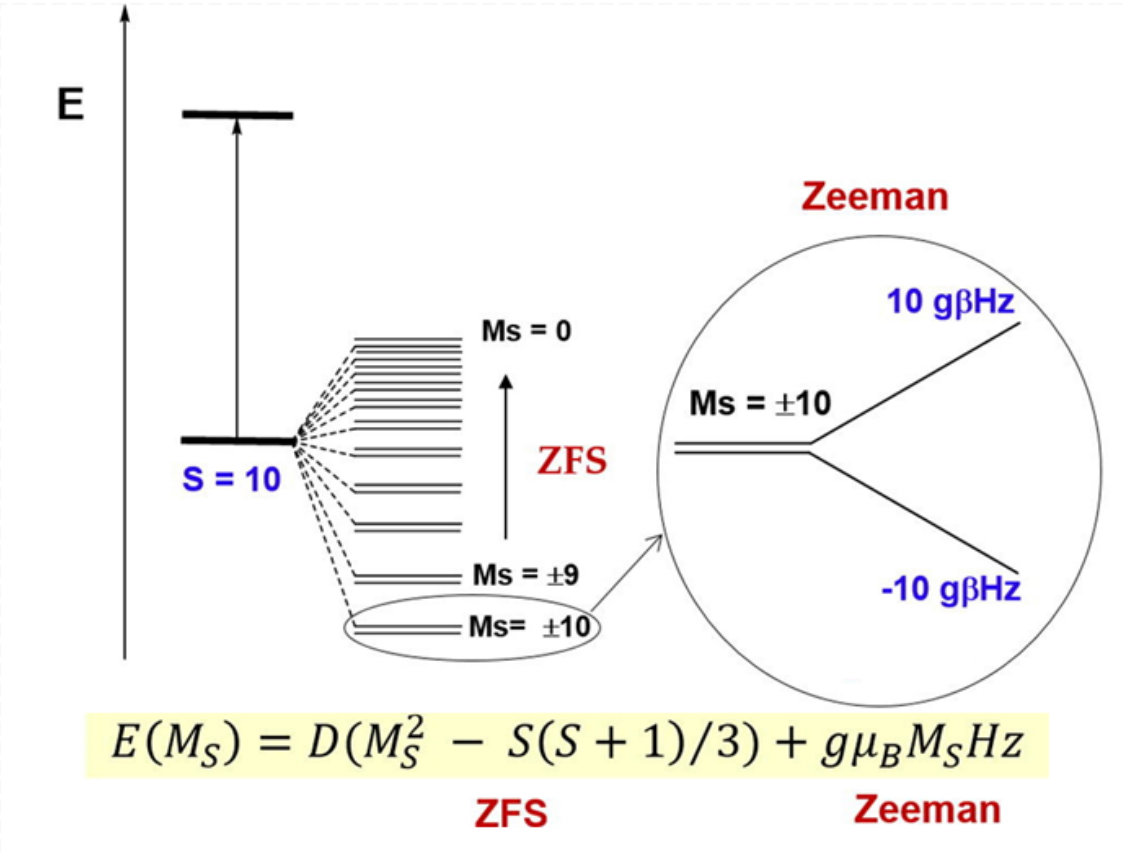

Figure 2- Simplified qualitative energy diagram of the zero-field splitting of Mn12-ac, the prototype SMM, with a modelled ground spin state S = 10. Inset: Zeeman splitting of the ground state doublet M_s = ±10.

Bulk magnetic properties are definable as a function of the arrangement of spins within a larger domain[35] – the most common of which are antiferromagnetism, ferromagnetism and ferrimagnetism, all of which shall be further discussed later in this chapter. A summary of the distinct properties and relative molar susceptibilities of various types of magnetic materials can be found, below, in **Table 1**.

Table 1- Characteristics of the molar susceptibility, χ_{mol}, for the major forms of bulk magnetism as observed at ordinary temperatures.[30]

Type of Behaviour	Magnitude*	Dependence on	
		Temperature	Applied Field
Diamagnetism	-10^{-3} Z	Y	N
Paramagnetism	1	Y	N†
Antiferromagnetism	≤ 0.1	Y	Y
Ferromagnetism	10^{7}	Y	Y
Ferrimagnetism	10^{6}	Y	Y
Pauli Paramagnetism	$\geq 10^{-2}$	N	N

*Referring to a typical paramagnetic susceptibility of 10^{-8} m^3 mol^{-1} at 300 K.
†Unless B/T is extremely large.

In the case of most forms of bulk and atomic magnetism discussed hereafter, except for diamagnetism, then the susceptibility of the material is a property of the ensemble rather than an inherent molecular characteristic. The various forms of bulk magnetism, other than ferrimagnetism and super-paramagnetism, are all exhibited by elemental materials at standard ambient temperature and pressure (SATP). The molar susceptibility of elements at SATP, as shown in **Figure 3**, exhibits distinct periodicity, groupings and transition steps as the atomic number, Z, increases. Simple, strong Curie paramagnetism is exhibited by elemental oxygen, as O_2,[36] although more complex paramagnetism is found amongst most of the lanthanide metals and later actinides.

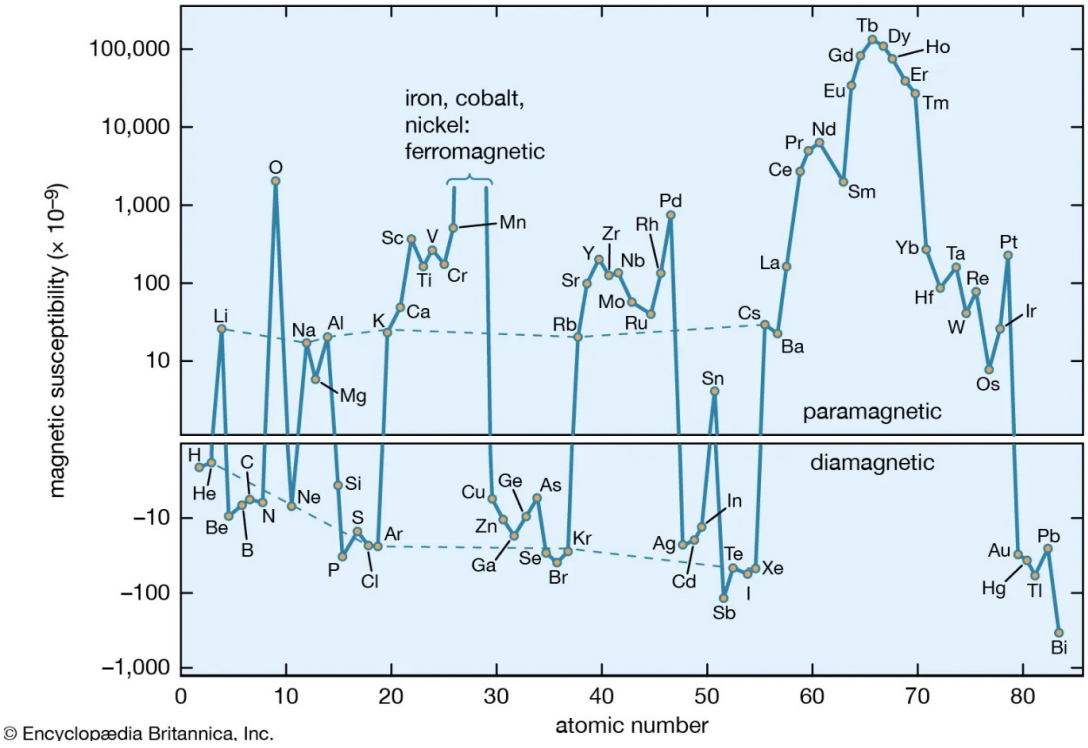

Figure 3- Atomic magnetic susceptibility of elements at SATP.[37]

1.2.1 Diamagnetism

Diamagnetism is a universal effect exhibited by all materials, whether atomic, ionic, or even in more complex arrangements such as molecules or lattices.[38] As such, the term is generally thought of to refer to something being non-magnetic, but this is a misconception in the presence of an applied field, as shown in **Figure 4**.

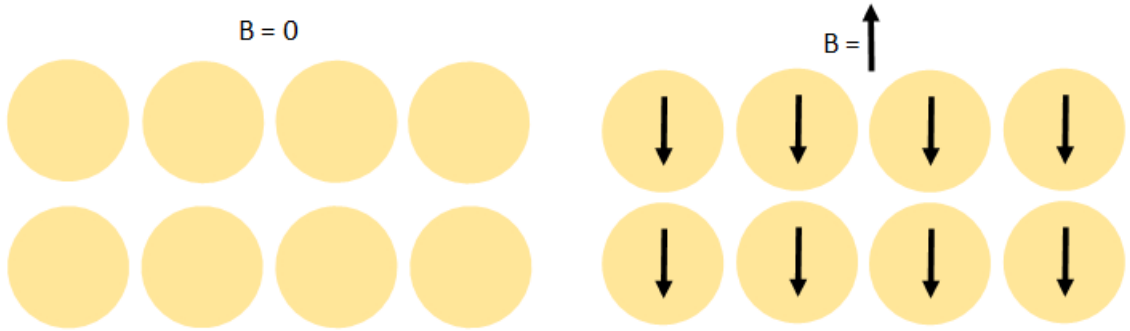

Figure 4- Alignment of diamagnetic centres in a zero field, left, and an applied field, right.

Diamagnetism is derived from what could be considered a distortion to the electronic orbital currents[38] - an induction due to small currents caused by the precession of electron orbits around an applied external magnetic field axis.[39] As such a small

magnetic moment density is generated which will be directed antiparallel, or against, the applied field, as shown in **Figure 4**. This requires the denotation of both the magnetisation (M) and susceptibility (χ_m) to be negative, such that the magnetic field within the diamagnetic material is reduced when compared to the external field. As such the magnetic permeability of a diamagnetic species would therefore be less than the permeability of a vacuum (μ_0). Crucially, diamagnetism is non-permanent, as it is a response to the materials exposure to an external field.[40]

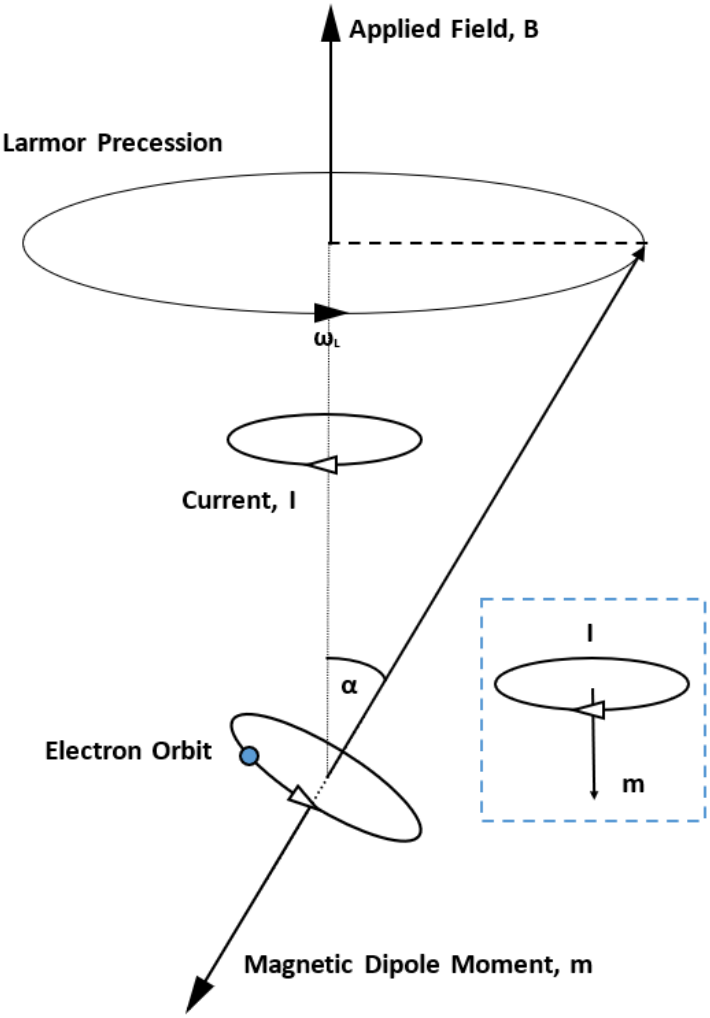

Figure 5- An application of Lenz's Law in the Larmor precession of electron orbitals for diamagnetic species. Inset: the simplified origin of the diamagnetic moment in an applied field following the right-hand screw rule.

Lenz's law of electromagnetic induction can be used to explain the observation of a diamagnetic species opposing the applied field.[41] The orbit of the electron is canted within the external magnetic field, see **Figure 5**, and so will experience a changing

magnetic flux as it precesses. This will cause the electron to feel an electromotive force. According to Lenz's law, the direction of the resultant current will be such that it opposes the change in magnetic flux that it causes. As such the induced circulation will produce a field in direct opposition to the applied field.

Diamagnetic species are defined by the lack of any unpaired electrons within their structures. Both open shell or closed shell atoms and ions can feasibly exhibit diamagnetism depending on the electronic structure of species being considered. The same does not apply to paramagnetic species which can only be found in open shell species. Typically, the molar susceptibility (χ_{mol}) of simple atomic diamagnetic materials can be found to be in the order of -10^{-11} Z m^3 mol^{-1}, where Z is the atomic number, see **Table 1**. Diamagnetism is a comparably minor effect, typically being significantly lower in intensity than the positive effects shown in open shell species with unpaired electrons. It should be noted that in rare cases, such as with bulk gold, the paramagnetic effect can be overcome by diamagnetic effects,[42] should the material's paramagnetism be sufficiently small. The magnetic susceptibility of purely diamagnetic species can usually be considered independent of temperature and the strength of the external field,[43] once more in direct opposition to that found in paramagnetic species. Superconductors can be considered perfect diamagnets as they can expel all magnetic fields as described by the Meissner effect.[44]

1.2.2 Paramagnetism

Paramagnetism is the simplest form of magnetisation and is only observed in open shell species, those which contain fewer than the maximum number of electrons within a shell permitted by the Pauli exclusion principle.[45] Closed shell atoms and ions cannot exhibit paramagnetism in their ground state regardless of their electronic structure or crystal field. As such, each individual atom, molecule or ion of a paramagnetic species has its own permanent magnetic dipole moment. This can be attributed to an (or several) unpaired electron(s) perturbing the species overall spin from net zero. Unlike with diamagnetic species, these spins will align parallel to an external field, as shown in **Figure 6**.

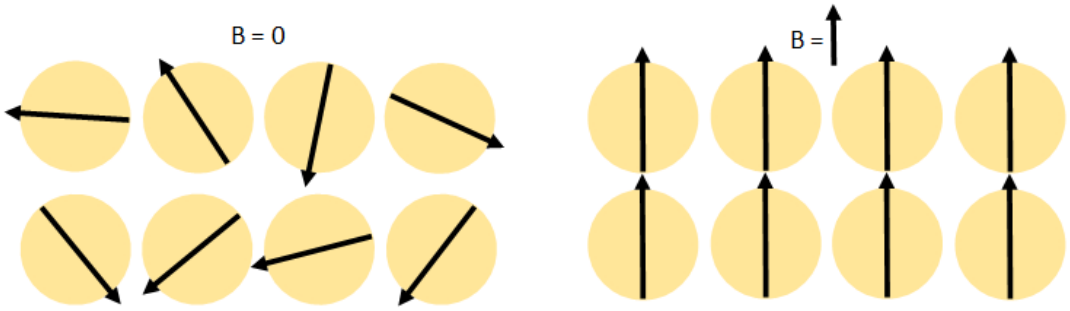

Figure 6- Alignment of paramagnetic centres in a zero field, left, and applied field, right. Domains are ignored in the zero field, assuming random thermal distribution.

When in the presence of an external field the equivalent ground states for the unpaired spin(s) separate with the parallel spin state favoured to the antiparallel spin state which encounters an energetic penalty,[46] as shown in **Figure 7**. As one state is energetically preferable in the presence of an external field, the population will skew in its favour. If the external field is then removed, the paramagnet will retain its orientation in proportion with the external field strength;[47] should certain conditions be met. This alignment effect is greatly impeded by thermal randomisation. Thermal energy within the system can be enough to disturb or counteract this skew. As such the energy imparted to a system by its environment can be enough to disturb the memorised alignment after the field is removed and return the population to a natural spin state equivalency. Thermal energy imparts chaos upon a system of aligned paramagnetic species as the orientation of molecular dipoles randomise, resulting in magnetisation that varies with temperature.[48]

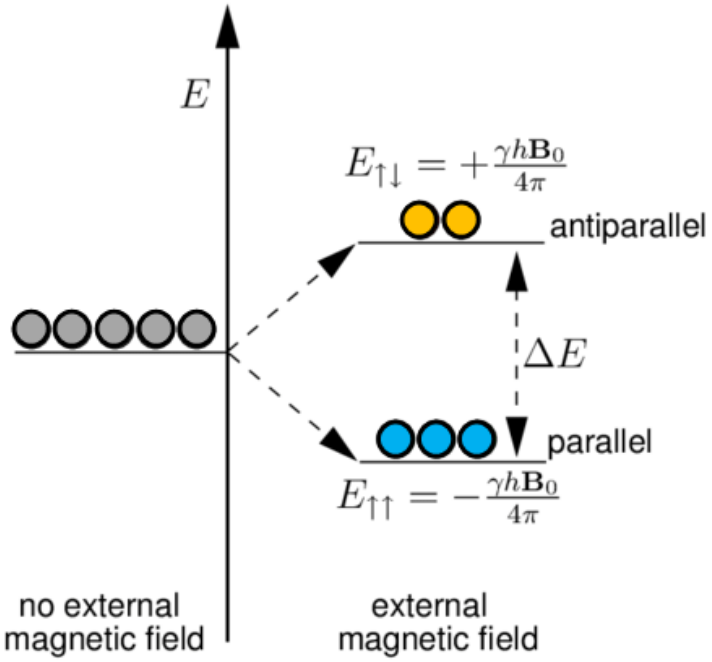

Figure 7- Ground states splitting in an external field resulting in the separation of parallel and antiparallel spin states. Note the skew in occupation.

Typically, the molar susceptibility (χ_{mol}) of simple atomic paramagnetic materials is usually ≥ -10^{-8} m^3 mol^{-1}, which is typically some two to three orders of magnitude greater than that seen for the molar diamagnetic susceptibility in absolute terms, see **Table 1**. This magnitude of magnetic susceptibility is typically enough to obscure any underlying diamagnetism but remains a reasonably small effect at ambient temperatures, hence its definition as 1 for comparative purposes in **Table 1**.

A secondary, weaker, form of paramagnetism – Pauli paramagnetism – is also known to exist. It deals with the presence of monatomic solid chemical bonding, such as that found in pure metallic materials, which generates a relatively free-flowing electron cloud which can itself be oriented by an applied field.[49] These electrons are found within the valence band, or for metallics, the conduction band. In simple, pre-transition metals, it is fair to assume that the valence electrons will be delocalised from ion cores, whilst in d and f-block metals, some of the valence electrons remain partially localised to the comparatively massive cores. In the absence of a magnetic field the conduction band contains perfectly paired electron spins, whilst the random motion of the electron cloud leads to an overall orbital momentum which tends towards net-zero. Application of a field leads to a small positive magnetisation because of an induced spin polarisation on

the Fermi surface of the electron gas.[50] In contrast to Curie paramagnetism where the unpaired electrons remain localised to an atomic or ionic centre, Pauli paramagnetism is essentially independent of temperature.[51]

The presence of individual atoms, ions or molecules with inherent, permanent magnetic dipole moments can then be transposed onto the example of bulk material. In the case of a purely paramagnetic material, should the magnetic centres be spaced far enough apart the short-ranged interactions between them can be ignored and are therefore magnetically dilute. However, as proximity between magnetic centres increases (*i.e.,* inter-centre distance decreases) and the short-range interactions become more applicable, spontaneous magnetic ordering can occur. This effect is analogous to a dipole in a polar liquid influencing the polarity of the molecules around it in solution. However, at ambient temperatures the Boltzmann energy, k_BT, is large compared to the energy of the interaction between paramagnetic species, causing extended bulk ordering to break down.

1.2.3 Antiferromagnetism

Assuming a through-space interaction, the most common form of magnetic ordering in solids is antiferromagnetism.[52] It involves the antiparallel coupling of neighbour magnetic dipoles, resulting in a relative reduction in the magnetic susceptibility when compared to the sum of the combined paramagnetic components. A simple two-dimensional schematic of the magnetic ordering in an antiferromagnetic solid is shown in **Figure 8**.

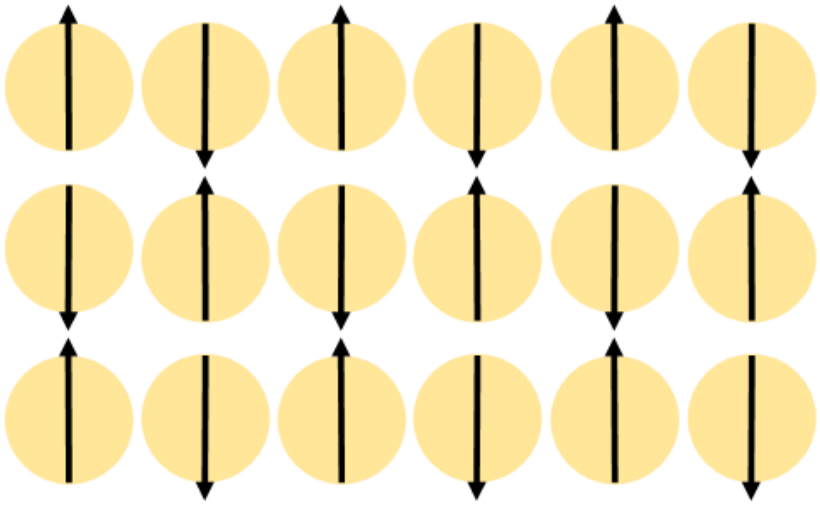

Figure 8- Magnetic ordering of centres in an antiferromagnetic lattice.

In a case where the magnetic centres being crystallographically equivalent, then as the temperature tends towards absolute zero then the magnetisation eventually vanishes. This is instigated as the coupling between the antiparallel sets exceeds the interaction of any individual dipole with the applied field, should the temperature be low enough for thermal chaos to subside and spontaneous magnetic ordering to dominate.[53] However, as the temperature of the system increases, and thermal fluctuations intensify, the alignment breaks down leading to an increase in the materials susceptibility. Eventually the susceptibility will then decline sharply again as antiferromagnetic ordering gives way to paramagnetism. This transition temperature is characteristic of the material and is known as the Néel temperature (T_N).[54] The variation of the magnetic susceptibility with temperature, alongside the transition from paramagnetism to an antiferromagnetic ordered phase is shown in **Figure 9**.

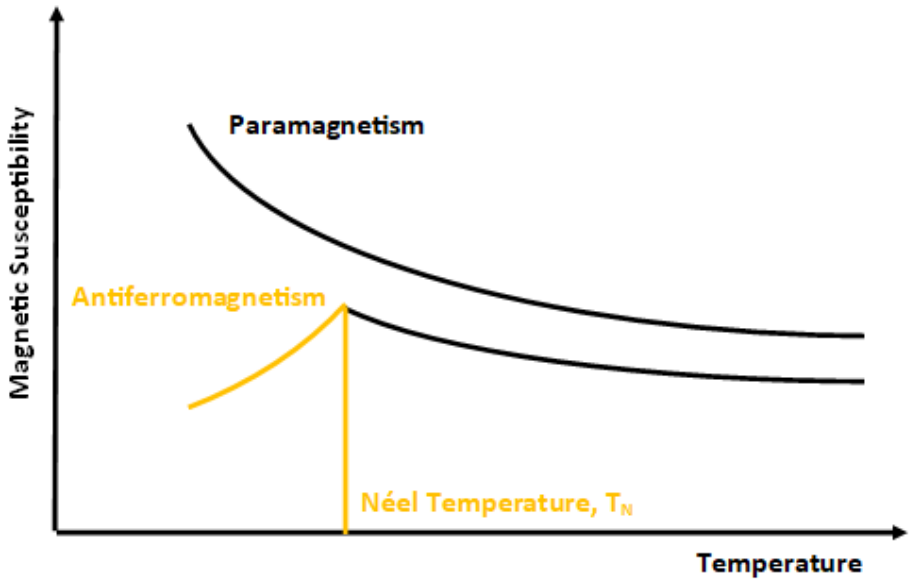

Figure 9- Transition between paramagnetic and antiferromagnetic behaviours.

Magnetic susceptibility of an antiferromagnet decreases inverse to temperature below T_N and increases inversely above it as the temperature is lowered. The general Curie-Weiss Law describes the relation between magnetic susceptibility and temperature as a function of two constants, C and θ, the Curie constant and Weiss constant respectively. The Weiss constant can be used to describe both antiferro- and ferromagnetic arrangements, exhibiting negative and positive values respectively.[55]

$$\textbf{Eq}^{\textbf{n}}\ \textbf{11}: \ \chi = \frac{C}{T-\theta}$$

As antiferromagnetism is dependent on both the temperature and applied field, it is difficult to apply a standard value for such a materials magnetic susceptibility. Typically, the resultant value is positive and of course lower than typical paramagnetic susceptibility for the same material. Materials such as transition metal compounds of chromium and manganese are known for exhibiting antiferromagnetic ordering.[56, 57]

1.2.4 Ferromagnetism

A rarer form of magnetic ordering, although better known, is where contiguous dipoles on an atomic level couple in parallel: ferromagnetism, so called because of the phenomenon originally being observed in metallic iron. The ordered phase of a

ferromagnetic material is characterised by huge magnetisations due to the concerted, long-range coalignment. A simple two-dimensional schematic of the magnetic ordering in a ferromagnetic solid is shown in **Figure 10**.

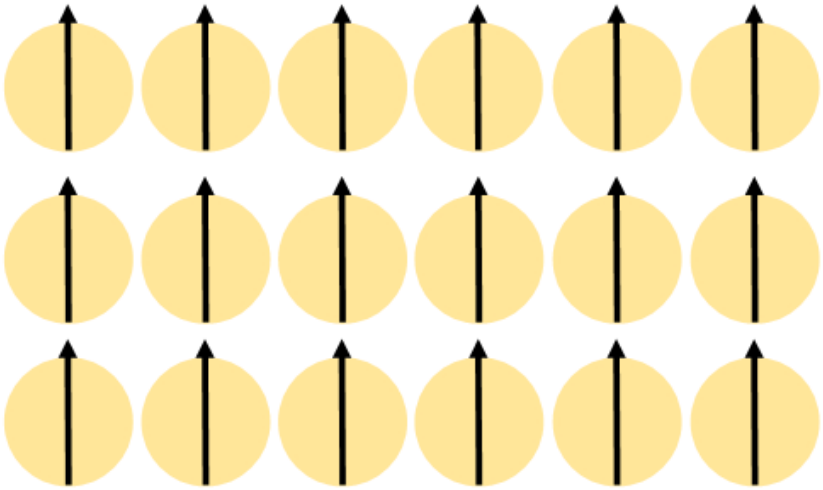

Figure 10- Magnetic ordering of centres in a ferromagnetic lattice.

The temperature at which paramagnetic behaviour gives way to ferromagnetic ordering is called the Curie temperature (T_C),[58] and although distinct in nature, fulfils a similar function to the antiferromagnetic Néel temperature, as shown in **Figure 11**.

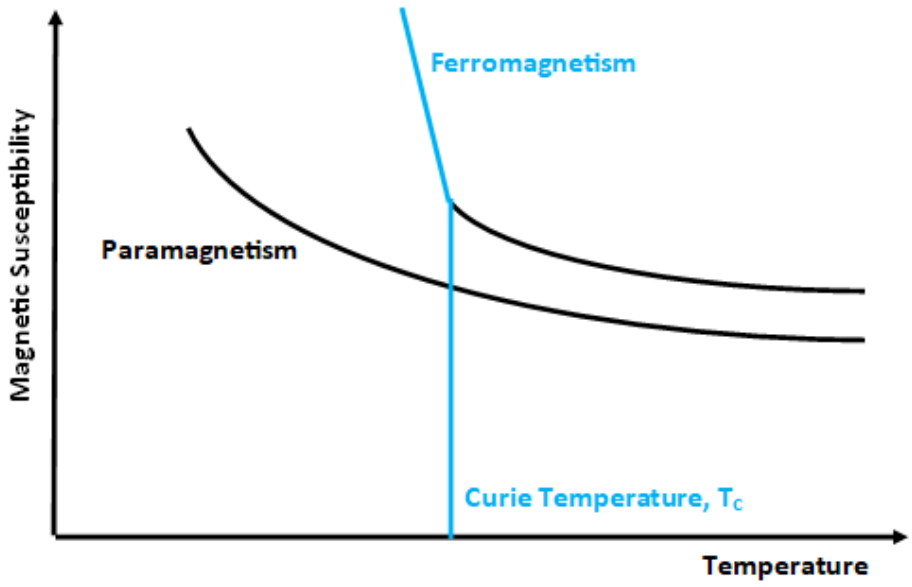

Figure 11- Transition between paramagnetic and ferromagnetic behaviours.

Thermal agitation can, once again, cause the breakdown of ferromagnetic ordering, but unlike with antiferromagnetism, where an increasing applied field strength can disturb the cooperative magnetism, then even at somewhat higher temperatures a sufficiently

intense applied field can reinforce the ferromagnetic ordering.[59] Below the Curie temperature the magnetisation increases exponentially until approaching its saturation value, M_{Sat}, at near absolute zero. By raising a ferromagnetic material above its Curie temperature, it is possible to essentially demagnetise the sample. The Curie temperature of compounds can vary significantly and in very rare cases, for example chromium (IV) oxide, can even be at or above ambient temperatures,[60] in this case T_c = 393 K. Curie temperatures of metals can range even further, with pure (soft) iron exhibiting an extremely high value of T_c = 1043 K.[61] The Curie temperature is a function of the strength of the magnetic exchange interactions and number of unpaired electrons per atom of a species. Paramagnetic species show very weak coupling in comparison to ferromagnetic compounds. The Curie-Weiss law, specific to ferro- and ferrimagnetic materials, describes the behaviour of a species above its critical temperature, T_c, resorting back to typical paramagnetic function.

Eq^n 12: $\chi = \frac{C}{T - T_C}$

Ferromagnetism can be further categorised into two classes of material – soft ferromagnets and hard ferromagnets, which exist upon a continuum. A perfect soft ferromagnet would exhibit proportionality between the magnetisation of the material and the application (or removal) of an external field.[62] As such, the magnetisation would reach zero as the applied field is reduced to zero. In hard ferromagnets, this is not the case. Instead, a hard ferromagnet exhibits highly coercive hysteresis,[63, 64] where there is a retention of magnetisation, or remanence, upon the removal of the field. It is remanence which allows for the construction and application of permanent magnets and shall be discussed further in later sections.

Cooling a potentially ferromagnetic material alone will not result in the material developing bulk ferromagnetism, the application of a field is required. The spontaneous ordering defining ferromagnetism is somewhat finite in the absence of an over-arching directing field, instead leading to the formation of micro regions, or domains of ferromagnetically coupled molecules,[65] each of which still exhibits a random magnetisation direction. Upon application of an external field the local magnetisation

vectors of each domain will align with the field, and hence each other, with this effect persisting upon removal of the field for hard ferromagnets, in the absence of any perturbing factors, should the temperature remain below the Curie temperature for the material.

Even though the ferromagnetic arrangement is once more temperature and applied field dependent,[66, 67] the additive effect on the magnetic susceptibility is distinct, with the values being some seven to eight orders of magnitude higher than that of a typical paramagnetic material at ordinary temperatures – with the volume susceptibility reaching as high as 10^5, in extreme cases. Materials such as transition metal compounds of iron, cobalt and nickel[68-70] are known for exhibiting ferromagnetic ordering, alongside rare earth metal species such as samarium or gadolinium.[71, 72]

1.2.5 Ferrimagnetism

Another form of cooperative magnetism is ferrimagnetism. It shows superficial similarities to both antiferromagnetism and ferromagnetism. In ferrimagnetic materials the dipolar coupling is typically antiparallel (akin to antiferromagnetism), but as the crystal structure contains different metal ions in non-equivalent sub lattices, a nonzero net magnetisation results (akin to ferromagnetism), parallel to that of the more intense or populous sub-lattice. A simple two-dimensional schematic of the magnetic ordering in a ferrimagnetic solid is shown in **Figure 12**.

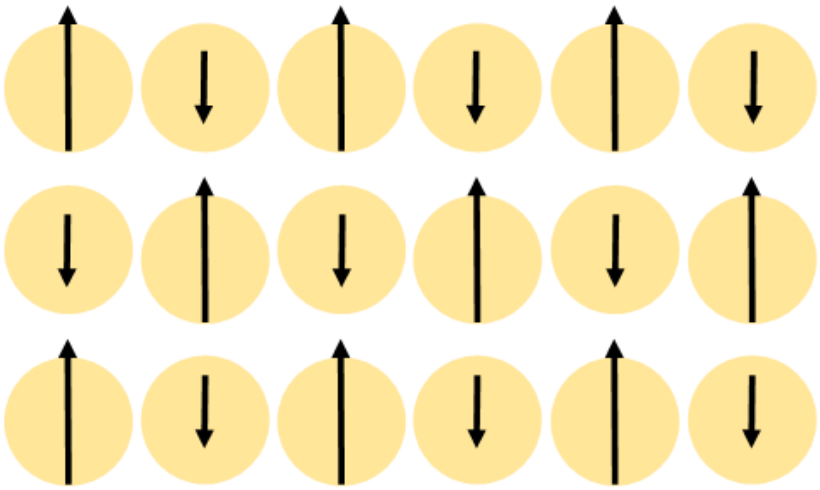

Figure 12- Magnetic ordering of centres in a ferrimagnetic lattice.

The antiparallel dipolar coupling between distinct ions from different sub-lattices in neighbouring positions is stronger than the respective interactions for either sub-lattice on its own, leading to what is best described as oppositely magnetised ionic arrays.[73] The outcome is a sub lattice of type X ions, with a magnetisation M_X, and a separate sub lattice of type Y ions with a magnetisation M_Y. As both lattices are inequivalent, the overall net magnetisation can be defined as M_X-M_Y in the direction of M_X (M_X-M_Y would be zero for equivalent sub lattices, and hence antiferromagnetic in nature). Interestingly as the two sub-lattices are invariably coupled antiparallel, the ordering within each sub lattice can effectively be considered ferromagnetic in nature.[74] The temperature below which ferrimagnetic ordering becomes dominant is referred to as the ferrimagnetic Néel temperature (T_{fN}). At higher temperatures the system cannot maintain spontaneous magnetisation and therefore acts as a paramagnet.

Ferrimagnetic susceptibilities can be exceedingly intense, as is seen in ferromagnetic materials, due to the long-distance additive effect of parallel spins. This depends on the comparative values of M_X and M_Y, but ferrimagnets typically exhibit lower magnetic susceptibilities than similar ferromagnetic counterparts. Ferrimagnetism is typically exhibited by iron oxides, or ferrites, the name from which the term is derived.[75]

1.2.6 Metamagnetism

In the case of metamagnetism, the definition is far more sweeping and indistinct. A sudden change to the magnetic behaviour of a metamagnetic material is observed as a physical change is imposed to the material or its environment, which drives the transition. This could be a first order phase transition, a continuous phase transition at a critical point, or even crossovers that involves no phase transition at all. As a result of these wide-spread physical explanations for often-dramatic changes in magnetic properties, metamagnetism is akin to a catch-all term comprised of many mechanisms and routes.

As a specific example, focus shall be drawn upon transitions promoted by a change to an applied field. Such transitions can be seen in materials that are comprised of components exhibiting both ferromagnetic and antiferromagnetic interactions. Iron (II)

chloride has a crystal lattice which adopts a layer structure. The coupling within layers is ferromagnetic, whilst the interactions between the planar layers are instead weakly antiferromagnetic. By applying an intensifying field to the material, whilst it is in its ordered phase, a point is eventually reached where the antiferromagnetic coupling is inverted by the field effects.[76] As such the concerted dipoles within a layer and between layers will orient with the field at low temperatures and/or high field strengths,[77] thereafter, exhibiting purely ferromagnetic behaviour. In so doing, the material exhibits a sudden surge in magnetisation as the field strength is increased due to the inversion of the antiferromagnetic component.

1.3 Molecular Magnetism

Classical magnetism is based upon the behaviour of metallic materials (including Fe, Co, Ni), or their oxides, and relies upon the unpaired spins of a bulk array of ions within a delocalised electron cloud. This collective behaviour response is not exhibited by molecular magnets, whose discreet forms and finite size provide the pinnacle of theoretically achievable spin-captured information storage and processing.[78, 79] Constraints on the current hardware represent a terminal asymptote for the growth of areal density, the unit of information storage per unit area, beyond which new methods must be utilised to condense information into even smaller areas. This field represents the maximum amount of storage achievable by materials-based science.

Traditional magnetic disk hard storage has seen massive increases in areal density over the course of its existence moving from 2000 bit in^{-2} in 1956,[80] the first hard disk drive presented by IBM, to 1.5 Tbit in^{-2} in a modern hard drive developed by Seagate between 2010 and 2015.[81] This progression is in line with growth predicted by Moore's Law.[82] In molecular magnetics-based systems, a single bit of information could be stored as a fixed spin of an individual paramagnetic species. An up spin could be seen to represent a 1 whilst a down spin represents a 0, essentially producing a crude binary system of information storage over the smallest area possible.[83] A simple model of areal density where the molecular bits pack perfectly in a single layer with no wasted space could represent a maximum areal density of 5000 Tbit in^{-2} for an isolated lanthanide of radius

200 pm. A more realistic prediction of an areal density of 50 Tbit in^{-2} could be reached for a molecule in which the entirety of the theoretical complex, including all its ligands, were encompassed within a radius of 2000 pm using this same simple model.

Molecular magnets also display a wide variety of other useful properties due to their combinatorial construction. Tuneable solubility, lightness, transparency and optical properties are feasible that were previously unavailable to purely metallic systems.[84-86] This is a result of the physical properties of a molecular magnet being traceable back to the electronic and crystallographic structure of its combined building blocks, alongside the interactions between said building blocks. It is theoretically possible to design, with rational decision making, a synergistic combination of chosen building blocks towards a discrete architecture exhibiting target properties by self-assembly principles. This designable element of the physicochemical properties at a synthetic level is a major advantage when compared to classical magnetic materials.[87-89]

Magnetic dipoles show an analogous coupling effect to electric dipoles: a direct through-space interaction.[90, 91] However, this coupling is too weak to describe the interactions exhibited by classical metallic and molecular magnets. In a solid-state material, indirect mechanisms have a substantial effect on the magnetic dipolar coupling. Conduction band electrons play a critical role in the coupling exhibited in metallic materials, whilst in transition metal oxides, an example of an insulating compound, the interaction occurs through intervening ligands *via* covalent bonding pathways.[92, 93] Discrete molecular magnets are a more complex class of magnetic materials that contain a backbone of insulating ligands through which intense coupling can occur between ionic electron spins, whilst the direct coupling between the magnetic ions themselves is comparatively, incredibly weak.

Exchange coupling is due to a combination of factors when considering electrons as localised spins, as in the Heitler-London (Valence Bond) model of chemical bonding.[94] The first exchange is dependent upon the direct overlap of relevant orbitals driving a quantum mechanical exchange between two sites. This overlap can cause a ferromagnetic or antiferromagnetic interaction defined by the exchange constant (J_{ab}).

Eq^{n} 13: $J_{ab} = \frac{1}{2}(E_+ - E_-) = \frac{J_{ex} - CS^2}{1 - S^4}$

Positive J_{ab} values indicate the interaction favours electrons with parallel spins and hence are indicative of ferromagnetic behaviour. Conversely, negative J_{ab} values instead indicate favour for interactions with electrons of antiparallel spin, suggesting antiferromagnetic behaviour.

The quantitative measure of the strength of exchange between neighbouring paramagnetic centres is given by (J). An example of the line shapes of graph produced from magnetic data are shown in **Figure 13** with J = 0 showing ideal Curie behaviour, J > 0 showing ferromagnetic exchange and J < 0 displaying antiferromagnetic exchange. These types of graphs are a common form for displaying magnetic data.

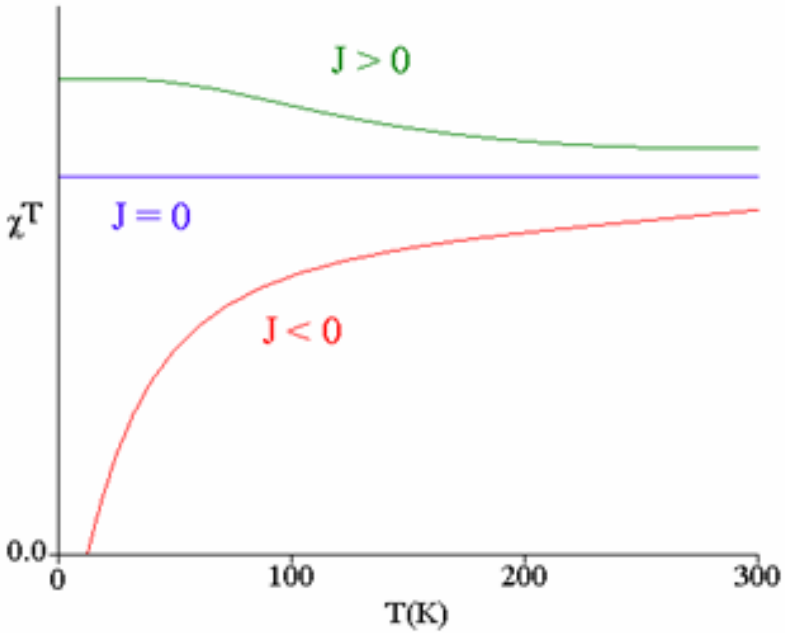

Figure 13- Overlaid representations of the general χ^T vs T line shapes for various exchange couplings.

Although the consequences of the exchange interaction are magnetic in nature, this simple mechanism, defined by Heisenberg in 1928,[95] is insufficient to explain the substantial coupling existing within many substances, especially those with insulating components. Additionally, the indirect pathways of interaction should be considered, a

covalency mediated mechanism between metal ions simultaneously binding to intervening ligands – superexchange.[96, 97]

Normally exchange interactions are very short ranged – as with intra-atomic exchange occurring when electrons are confined within orbitals of a single atom or in direct exchange between nearest neighbour atoms – superexchange breaks this trend by coupling across an intermediary atom. In the majority of non-metallic transition metal compounds, with simultaneous covalent bonding between metal ions of the same valency and their bridging ligands, superexchange proves to be the dominant source of coupling and most commonly leads to long range antiferromagnetic ordering. An example orbital overlap for superexchange in a linear Metal – Ligand – Metal (M – L – M) system is given in **Figure 14**, which results in an antiferromagnetic coupling of the bridged cations.

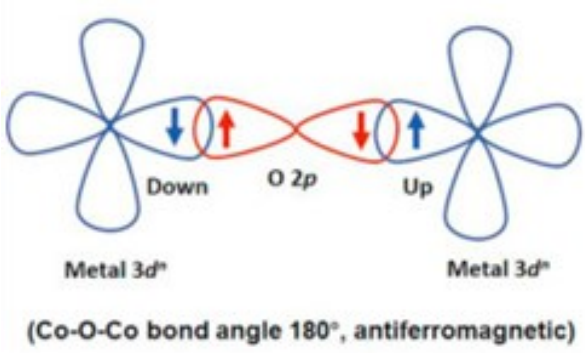

Figure 14- Schematic for an antiferromagnetic superexchange interaction according to the Goodenough-Kanemori rules.[98-100]

An example orbital overlap for superexchange in a 90° bent M – L – M system is given in **Figure 15**, which results in a ferromagnetic coupling of the bridged cations.

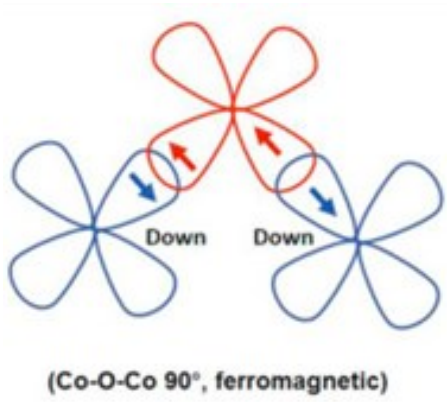

Figure 15- Schematic for a ferromagnetic superexchange interaction according to the Goodenough-Kanemori rules.[98-100]

The strength of the exchange coupling derived from M – L – M superexchange is highly dependent on the MLM bond angle. The superexchange is diminished as orbital overlap is reduced, either by distance or by angle, but the reduction in antiferromagnetic interaction as the bond angle moves away from linear may be met with an increase in ferromagnetic character as the overlapping orbitals approach perpendicular.

Another model of exchange interaction is the double exchange mechanism.[101, 102] Although the mechanism is superficially similar to superexchange, it requires a difference in charge between the two interacting metal ions to proceed. The process involves the transition of two electrons of the same spin *via* a ligand orbital. An example orbital overlap for double exchange in a linear Mn(III) – O – Mn(IV) system is given in **Figure 16**, which results in a ferromagnetic coupling of the bridged cations.

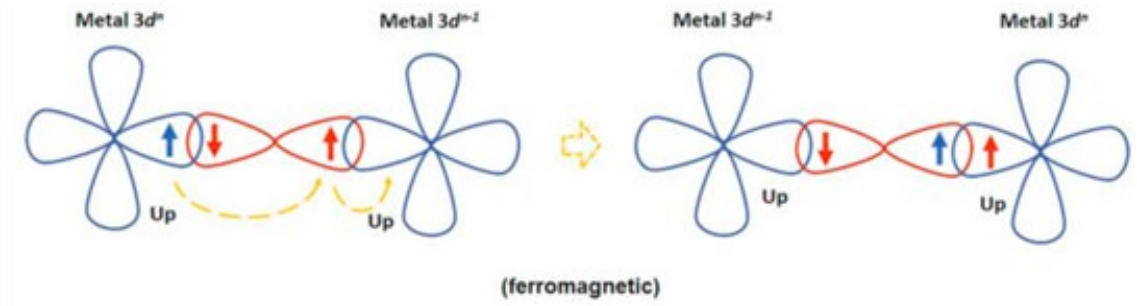

Figure 16- Schematic for a ferromagnetic double exchange interaction.[98-100]

If the transition between orbitals requires no change in spin direction to conserve Hund's Rule on the accepting species, and the electron is therefore delocalised over the

two neighbouring metal ions, then the overall energy saving can result in a ferromagnetic cooperative alignment.

As a result of the relationship seen between the molecular magnets structure and magneto- or physico-chemistry it is theoretically possible to use a high-throughput design method towards the creation of a QSAR (quantitative structure-activity relationship) like database. This could result in the construction of isolated molecules or assemblies with one, or multiple magnetic centres all contributing to the molecules sum-total properties. Long spin coherence times,[103] for example, could open the door for molecular magnets to act as candidates towards quantum computing *via* encoding a qubit[104] with its molecular spin, but beyond this, molecular magnets have even wider multidisciplinary uses in fields as diverse as catalysis[105] and biomimetic modelling.[106-109]

1.3.1 Single-Molecule Magnets (SMMs)

Single-molecule magnets (SMMs) are a class of nano-sized molecular magnets which exemplify this optimisation of physicochemical properties by structure variation. SMMs could represent the next step in information storage due to their ability to undergo slow relaxation of magnetisation.[110] An SMM is comprised of one (or many) magnetic ion(s) bound within a matrix of organic or organometallic ligands that isolate the magnetic centres and form the remainder of the complex or cluster.

The prototype SMM could be considered to be $[Mn_{12}O_{12}(O_2CR)_{16}(H_2O)_4]$ (R = Me or Ph), or Mn12-ac, as shown in **Figure 17**, published by Sessoli and Gatteschi *et al.*, in 1993.[111]

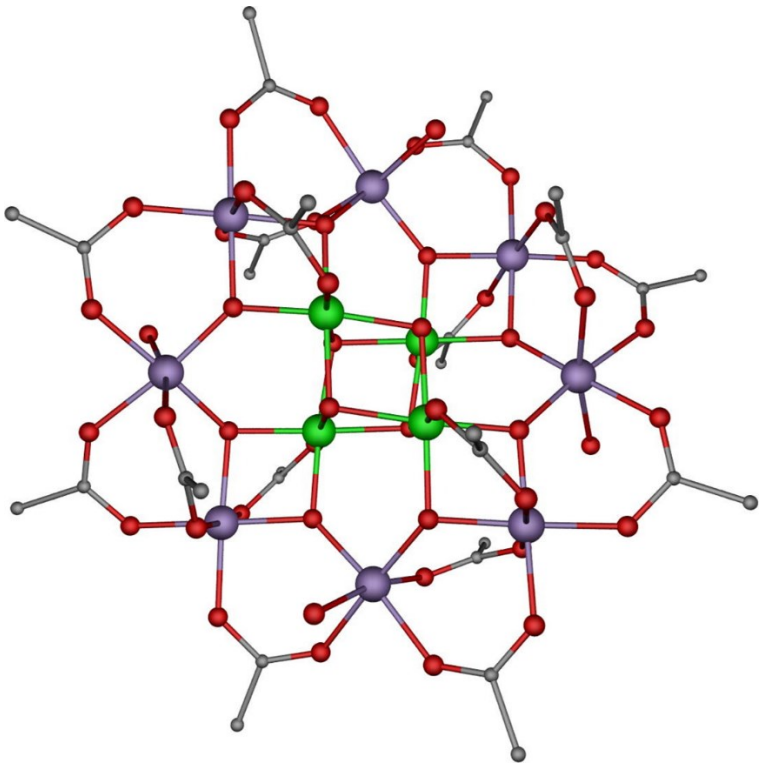

Figure 17- Molecular structure of Mn12-ac: C atoms, grey; O atoms, red; Mn^{III} ions, purple; Mn^{IV} atoms, green. H atoms have been omitted for clarity.[112]

Mn12-ac exhibits the required ability to store magnetic information at a molecular level and kickstarted the investigation of high spin transition metal complexes. The ability of an SMM to store information is hinged upon the molecules ability to differentiate between two distinct bi-switchable spin ground states separated by a high thermal barrier,[113, 114] U_{eff}, as demonstrated in **Figure 18**.

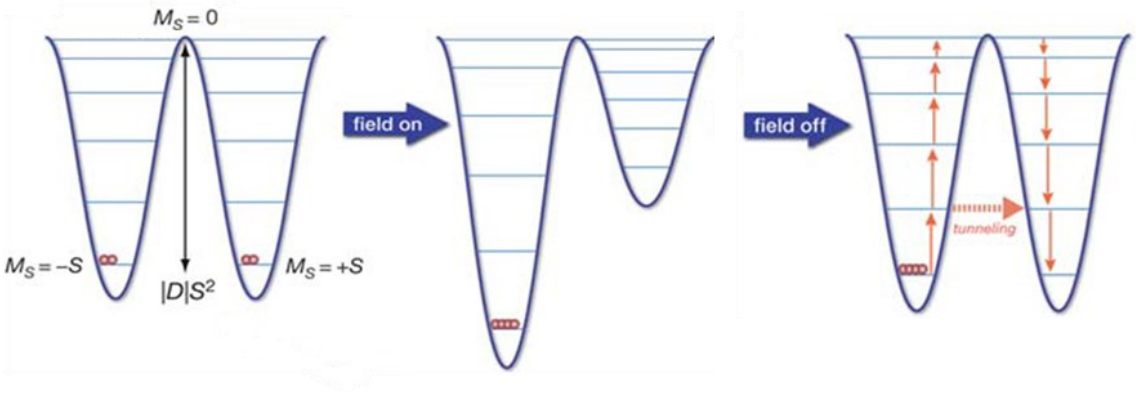

Figure 18- Double well diagram of a bi-switchable spin ground state and the effect observed with the application and removal of an external field. Relaxation pathways then revert the population skew over time.

In a system exhibiting a bi-switchable ground state, the application of an external field can trigger the population to skew towards the state in which the electron spins are aligned parallel to the field. As such the electrons are blocked in this spin orientation. As the field is removed, this orientation blocking is reduced. The skewed configuration is not indefinite upon the removal of the external field and will instead return to a state of thermal equilibrium. The time it takes for the artificial orientation skew in the molecule to fade is called the relaxation time (τ) and is predicated on the amount of thermal energy available to the system and the height of the energy barrier (U_{eff}). This process can also be described by a relaxation rate (1/τ).

Eqⁿ 14a: $\tau = \tau_0 \, . e^{U_{eff}/k_B T}$

Eqⁿ 14b: $1/\tau = 1/\tau_o \, . e^{-U_{eff}/k_B T}$

Eqⁿ 14c: $\ln(\tau) = \ln(\tau_0) + U_{eff}/k_B T$

The relaxation time can be measured at a specific temperature by extracting the frequency maximum (ν_{max}) from an alternating current (AC) experiment.

Eqⁿ 15: $\tau = \frac{1}{2\pi\nu_{max}}$

The manner by which the electrons return back to thermal equilibrium is dictated by which relaxation pathway is dominant. The three main relaxation pathways,[113, 115] Orbach, Raman and quantum tunnelling of magnetisation (QTM) are shown in **Figure 19**.

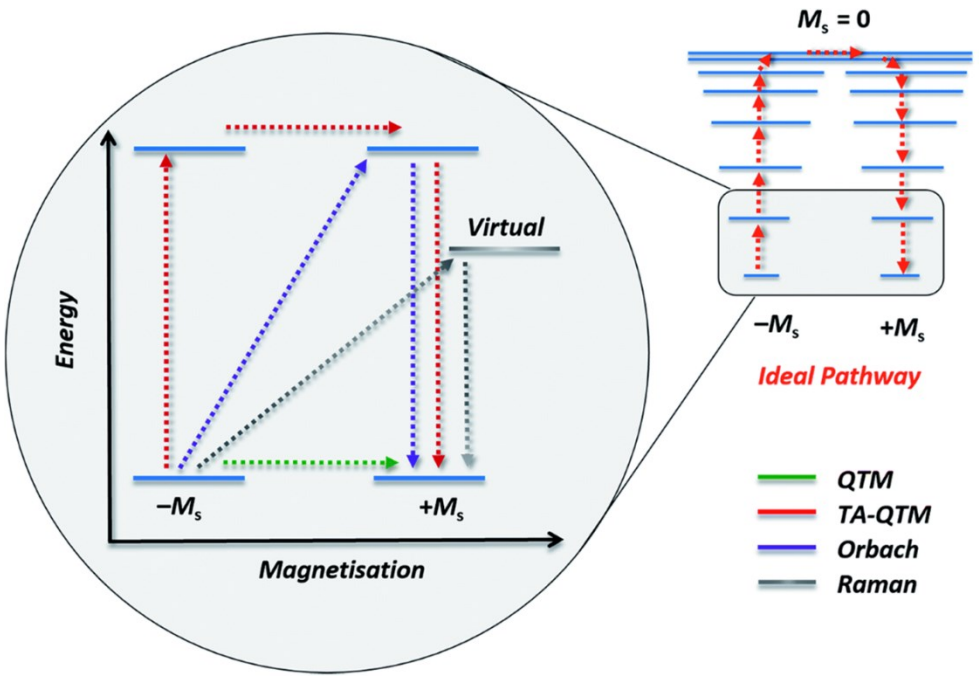

Figure 19- Simplified representation of the major magnetisation relaxation pathways commonly exhibited by molecular magnetic materials.[114]

Molecules are not isolated from their environment, instead the molecule and environment can influence each other. A direct interaction can occur in which an electron is elevated to a higher state by absorbing a packet of energy in the form of a phonon – a quantised vibrational mode of the lattice – which are essentially the microscopic origin of temperature. Multiple sequential direct interactions are collectively referred to as the Orbach process,[116, 117] and as the elevated electron falls back towards the ground state after passing the energy barrier phonons are released back to the environment. As a result, this process of spin-phonon transition is considered a two phonon process. The second pathway, Raman,[118] is again a two phonon process, but instead traverses the barrier *via* a "virtual" state. The third and final process, quantum tunnelling of magnetisation (QTM),[119] bypasses the energy barrier entirely by tunnelling between spin states without elevating in energy: there is no energy cost and no phonons are involved. Combinations of the pathways are viable, such as QTM between spin states from an excited energy level reached by a direct interaction, otherwise known as thermally activated quantum tunnelling of magnetisation (TA-QTM).[120, 121] In reality, multiple relaxation mechanisms are concurrently active for all molecules, with a certain mechanism dominant over any others often dependant on the temperature of the system, as shown in **Figure 20**.

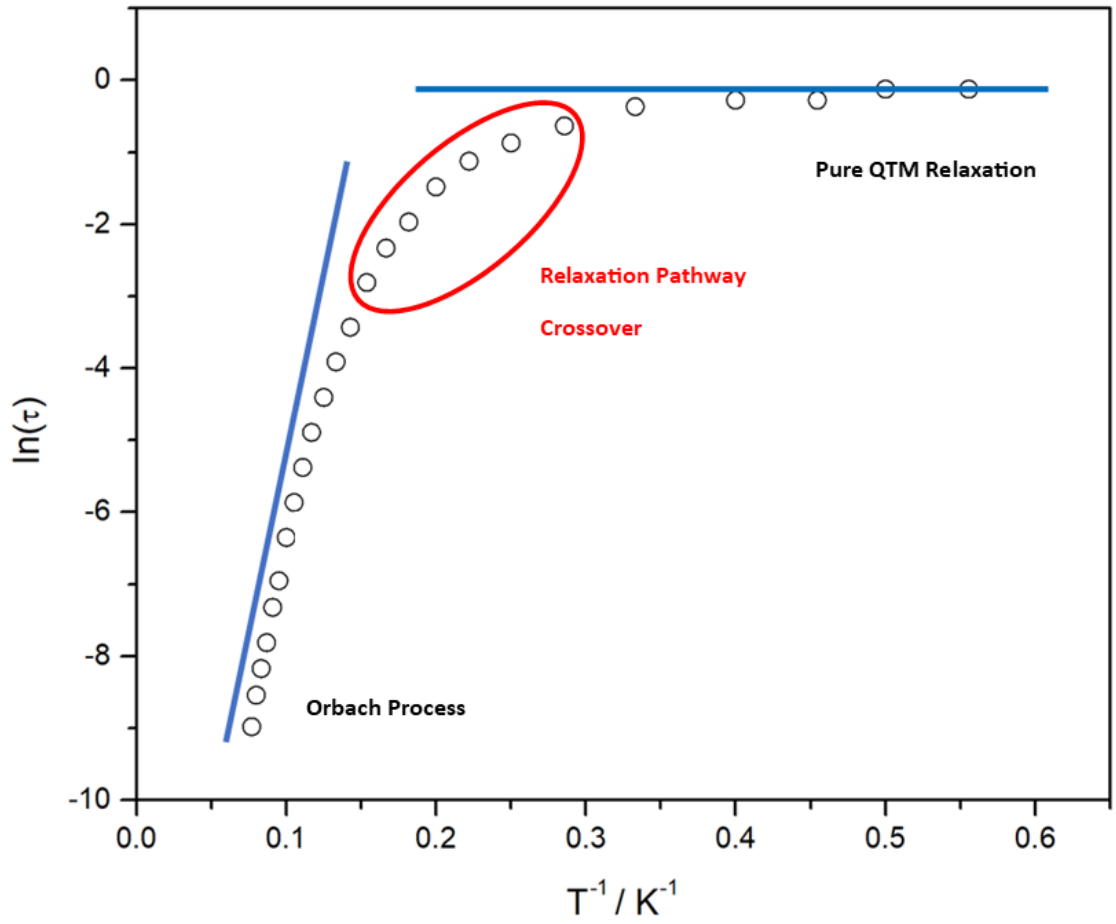

Figure 20- Arrhenius plot of ln(τ) vs T^{-1} showing the transition between dominant relaxation pathways with changing temperature.

On a molecular level, this balance of magnetisation and relaxation can be plotted as a hysteresis loop, an example of which is given in **Figure 21**. The terminal values on the Y axis of the hysteresis plot represent the sample at magnetisation saturation, in either direction, or a point at which the population is skewed entirely in favour of aligning to the strong applied field. The field is then swept back to zero before being applied in the opposite direction.

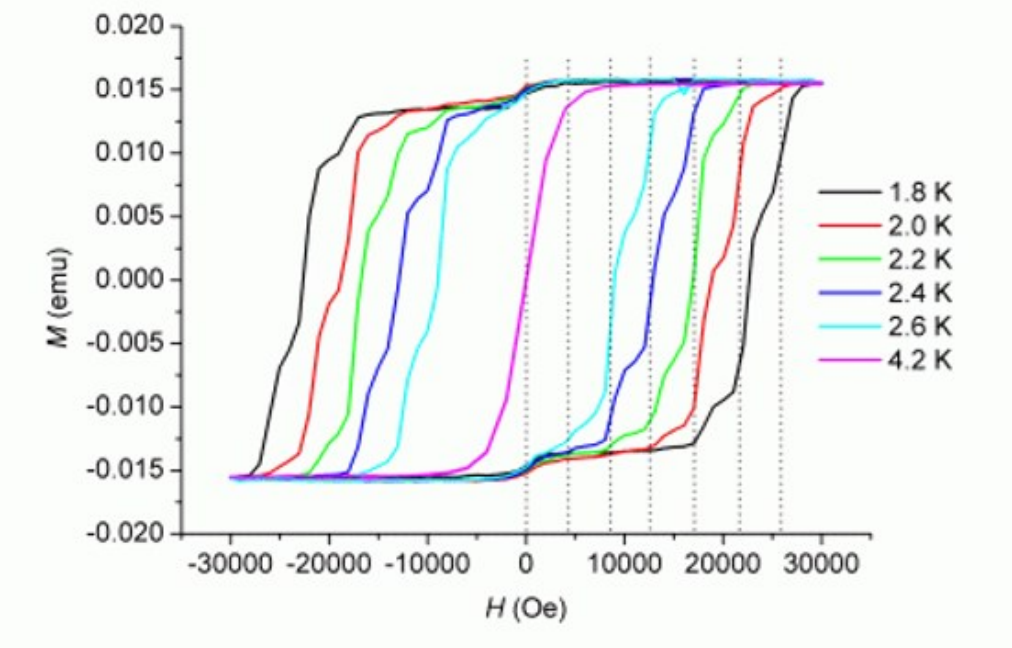

Figure 21- An example of a hysteresis plot of magnetisation vs applied field. Plot recreated from the data of Mn12-ac, originally published in 1993.[111, 122]

In a species where the splitting between energy levels is small, or the coupling within a molecule weak, the reduction in magnetisation will be severe with the reduction in field strength, to a point where at zero field the magnetisation is zero. At this point the hysteresis loop is said to be closed, as shown in the 4.2 K sweep of **Figure 21**. As such the two degenerate ground states are indistinguishable and the material will be unable to store information. However, at lower temperatures the Orbach relaxation pathway is less favourable due to less phonons being available to drive the loss of magnetisation.[123] In this case the remanence of the material leads to a retention of the magnetisation at zero field, and even beyond, until the QTM pathway and/or intensifying opposed magnetic field cause the magnetisation to collapse.[124] For any given hysteresis loop, the magnetic field at which the remanence is overcome, and the magnetisation is reduced to zero is called the coercive field.[125] The coercivity is therefore a measure of how hard it is to demagnetise a material. It is favourable to have a large coercive field at higher temperature for the purpose of storage, although an increase in temperature invariably leads to a drop in the coercive field. The hysteresis plot is then built up with progressive loops at higher and higher temperatures until the loop closes. The standard definition for whether a material would be viable for storage of information is the temperature at which the molecule remains magnetised for 100

seconds in the absence of a field.[126-128] This is referred to as the blocking temperature (T_B).

Quantum tunnelling can be driven by the presence of a field. Degenerate pairs of spin states diverge in energy as a result of the application of an external field. Where there is a crossover of different spin states at certain field strengths due to the Zeeman effect, a spontaneous loss of magnetisation can be observed.[129] When two states are in resonance an element of mixing occurs which can drive the loss of magnetisation. This results in the stepwise reductions in magnetisation often witnessed in hysteresis loops.

Synthetically producing molecules which exhibit higher spin-relaxation barriers, and thereby diminish the effects of the Orbach relaxation pathway, is primarily dictated by manipulation of three physical parameters; S, D and J; the spin ground state, the axial zero field splitting parameter and the exchange coupling constant, respectively. Current research is attempting to attack the production of SMMs from three major directions. These directions consist of 1) increasing the energy barrier to reversal of magnetisation (U_{eff}), 2) increasing the blocking temperature (T_B) at which the SMM can operate *via* exhibiting slow relaxation of magnetisation and 3) decreasing the molecules ability to undergo QTM, a process which bypasses the increased U_{eff} value of a molecule.[130] Recent publications have attempted to explain the phenomenon by which an increase in U_{eff} does not ensure a concomitant increase in T_B, as would initially be expected, with this disconnect expected to be a function of QTM. QTM allows for the spin to spontaneously access an efficient quantum relaxation pathway that supersedes the traditional phonon and thermal based relaxation pathways. As a result, developing a molecule or motif, which efficiently reduces or eliminates a molecules preference for QTM stands as a crux point to accelerating the production of SMMs to a practically usable frontier.

It should be noted that even an exceptionally large barrier of magnetisation reversal, a product of the parameters S and D, related by **Eq^n 16**, will not necessarily bring about a high blocking temperature if the exchange coupling is not strong.[131]

Eq^{n} 16: $U_{eff} = |D|S^2$

Where D is proportional to 1 / S^2

Improving magnetic bi-stability of the ground state has been studied extensively,[111, 120, 132-134] with the most efficient method of achieving a maximised barrier to reversal being through stabilisation of the high-spin ground state (S). However, this tactic is complicated by the inverse proportionality between S and D.[135] Raising the total spin of a molecular magnet (S) has the side effect of reducing the molecules anisotropy (related to D), factoring into a limitation on the pathway. Controlling the S and D parameters simultaneously, in such a way as to maximise the effective barrier to magnetisation reversal has therefore proven incredibly difficult.[136]

The third parameter, J, is critical as it plays a role in the separation between the molecules ground state and any elevated energy levels thereafter. Should this energy gap be insufficiently large, the slow magnetisation pathways will shut down in favour of quantum relaxation, a faster and spontaneous process that is far more difficult to influence and control, or fast spin relaxation involving the higher energy states. These alternate routes become especially prevalent at higher temperatures. Quantum processes can therefore eliminate the magnetisation remanence, which is stored in the sample as a result of magnetic hysteresis, leading to a loss of digital data.

1.3.2 Single-Chain Magnets (SCMs)

Compared to SMMs, single-chain magnets (SCMs) represent an interesting alternative to truly discrete molecular magnets in the construction of large, one-dimensional chains of repeating monomeric units. In this class materials exhibit high relaxation barriers to the reversal of magnetisation along the direction of the chain, thereby exhibiting magnetic hysteresis. A combination of three components best defines the interest now seen in SCM development:[137] strong intra-chain coupling and magnetic interactions, weak or negligible inter-chain magnetic interactions and a large uniaxial magnetic anisotropy, contributing to the material's overall behaviour. The lack of inter-chain interactions prevents the material from growing into a 3d arrangement or lattice. Three main strategies for construction have been seen in SCM design, as shown in **Figure 22**:

a ferromagnetic chain strategy, a ferrimagnetic chain strategy and a spin-canted chain strategy. Spin tunnelling of domain walls and inter-spin exchange interactions provide a pivotal role in the magnetisation relaxation pathways exhibited by SCMs.

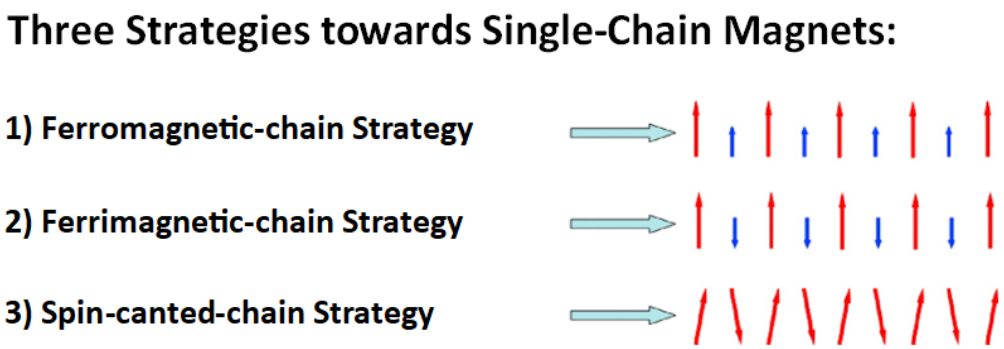

Figure 22- Strategies towards the construction of Single-Chain Magnets (SCMs).[138]

1.3.3 Frontiers of Molecular Magnetism

Molecular Magnetism, as a field, has exploded since the pioneering work of Sessoli and Gatteschi.[111] Their work introduced the ideas of quantum tunnelling of magnetisation and the broad requirements for stabilising a degenerate ground state towards information storage to the wider scientific community. The field was, at the time, based primarily in the study of transition metal clusters of increasing complexity with exceedingly large total spin values and peak blocking temperatures in the region of 2-3 K. This was until the seminal work of Ishikawa *et al*. on lanthanide double decker phthalocyanine complexes in 2003,[139] building upon the synthetic route described by Ohashi *et al.* in 1996.[140] The paper introduced the use of lanthanides into the design of SMMs and proved to be a turning point in the field in general, showing that comparable magnetic properties could be derived from a single ion centre rather than only from large arrays. Osa and Matsumoto *et al*.[141] took this one step further in 2004 with the first SMM consisting of d- and f-block elements, whilst also proving that the SMM behaviour observed was not intrinsic to the lanthanide centres alone.[141] In 2011 the first major leap forward was to be made. By this time the field leading SMMs exhibited blocking temperatures in the order of 5 K,[142, 143] but the work of Rinehart and Long *et al*. changed this. Initially the group attained a record-breaking blocking temperature of 8.3

K in May 2011,[144] then later reached a 100 second blocking temperature of 13.9 K whilst further exhibiting magnetic hysteresis at 14 K by August the same year,[127] through a series of N_2^{3-} radical-bridged dilanthanide complexes, $\{[(Me_3Si)_2N]_2(THF)Ln\}_2(\mu\text{-}\eta^2\text{:}\eta^2\text{-}N_2)^-$ (May, Ln = Gd, Dy; August, Ln = Tb, Ho, Er). A general structure for these complexes in shown in **Figure 23**. The blocking temperatures were achieved by merit of an N_2^{3-} radical bridge, which led to strong magnetic exchange coupling that hindered fast relaxation processes at zero field. And so, the record stood, occasionally imitated, but not convincingly beaten.[145-149]

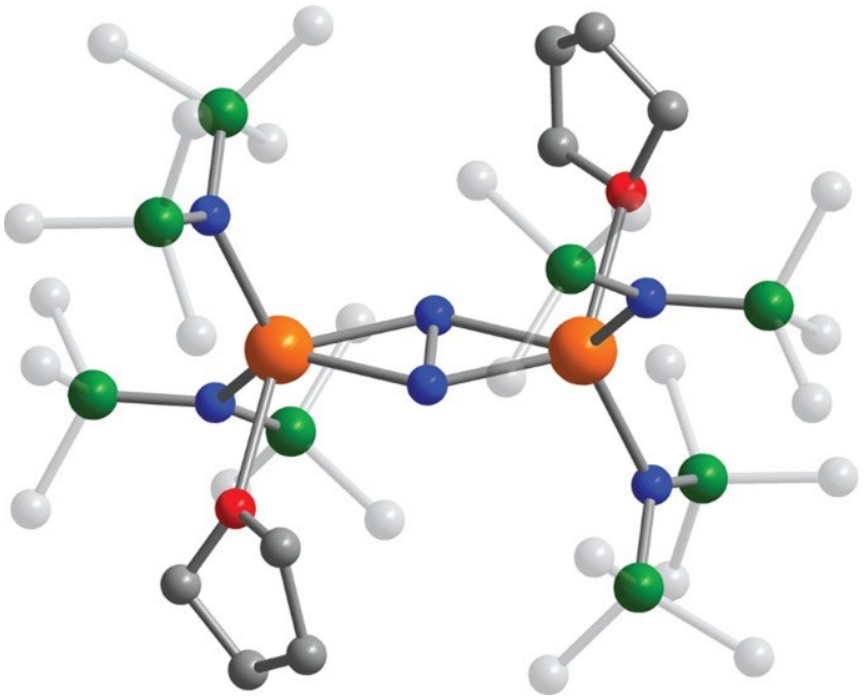

Figure 23- Molecular structure of the $\{[(Me_3Si)_2N]_2(THF)Ln]_2(\mu\text{-}\eta^2\text{:}\eta^2\text{-}N_2)^-$ anion published by Rinehart and Long *et al.*: C atoms, grey; O atoms, red; N atoms, blue; Si atoms, green; Ln ion, orange. H atoms have been omitted and methyl groups faded for clarity. Note, Ln = Gd for this specific figure.[144]

The frontier of molecular magnetism is currently dominated by the search for low coordination, high symmetry, near-linear homometallic complexes of 4f metals.[150] Metallocenes of dysprosium, or dysprosoceniums, are a new class of near-linear sandwich complexes combining the high anisotropy of a dysprosium (III) ion with two sterically bulky ligands bound within the axial direction of the ion[8] with, crucially, an incredibly bulky and weakly coordinating counter ion which balances the complexes charge without causing extensive delinearisation of the Ligand – Metal – Ligand (L – M

– L) bond angle. The structure best known, very polarising as it may be, is $[Dy(Cp^{ttt})_2][B(C_6F_5)_4]$ (Cp^{ttt}, 1,2,4-tri-tertbutylcyclopentadienyl), as shown in **Figure 24**. This work was seemingly simultaneously pioneered by the Mills[151] and Layfield[152] groups of the University of Manchester in 2017. Overnight the field was revolutionised – a pinnacle blocking temperature of 60 K utterly usurped the previous record holder of just 14 K. Later Layfield[153] published a follow up piece, using different η^5 capping ligands to push this astounding discovery even further whilst Mills[154, 155] broadened the field by creating analogues of the original complex utilising different lanthanide ions. Layfield's route focussed on proving that the original example was just a step on a design-based developmental ladder, whilst further proving that the motif still had greater opportunities for growth and development. Conversely Mills route attempted to explain the properties of the molecule his group had discovered and drill down to the underlying causes and properties of such an unprecedented discovery. The current field leading molecule is the dysprosocenium derivative, $[(Cp^{iPr5})Dy(Cp^*)][B(C_6F_5)_4]$ (Cp^{iPr5}, penta-iso-propylcyclopentadienyl; Cp*****, pentamethylcyclopentadienyl), also shown in **Figure 24** published by Layfield *et al*.[153] which exhibits an astounding blocking temperature of 80 K, above the tantalising liquid nitrogen operating threshold.

Figure 24- Structures of the Mills, left, and Layfield, right, dysprosoceniums. The weakly associated counter ion, $[B(C_6F_5)_4]^-$, is omitted from both structures.

Dysprosoceniums are in many ways, an exercise in simplicity. The use of three or four components, chosen with their physical and magnetic properties in mind, synergising to create the pinnacle of design-based molecular magnets.

1.4 Fundamentals of Lanthanide Magnetism

Lanthanides, or 4f elements, are a class of metallic elements that exhibit interesting and relatively uniform chemistry when compared to the transition metals of the d-block.[19] Lanthanide ions typically exist in the 3+ oxidation state, losing their two 6s electrons and either one 5d or one 4f electron as part of their ionisation, although exceptions to this preference do exist, primarily praseodymium (IV), samarium (II), europium (II) and terbium (IV).[156-159] Lanthanum itself is a lanthanoid rather than a lanthanide and is followed by the fourteen elements of the lanthanide group from cerium to lutetium. As the seven f-orbitals are equivalent energetically, progressive electrons fill the orbitals according to Hund's rules, whilst maintaining the Pauli exclusion principle, leading to isolated ions with potentially exceedingly high inherent spin. In this section we shall consider each lanthanide as its 3+ cation unless otherwise stated, defining them by their f^N configuration, where N is the number of f-electrons remaining after ionisation, *e.g.* $Ce^{III} = f^1$, $Gd^{III} = f^7$ and $Dy^{III} = f^9$.

The energy levels, ground and excited states can be denoted using term symbols of the form $^{2S+1}L_J$, and are calculated by consideration of the quantum properties of the ionic electrons. Derivation of term symbols requires the total spin quantum number S, such that $S = \Sigma m_s$, the total orbital quantum number L, such that $L = \Sigma m_l$, and the total angular momentum quantum number J, where $J = |L+S|$ or $|L-S|$ dependant on whether the f-orbital is above or below half occupancy, respectively. **Figure 25** visualises the process for Dy^{III}, Gd^{III} and Eu^{III}, whilst all the ground state Ln term symbols are given in **Table 2**.

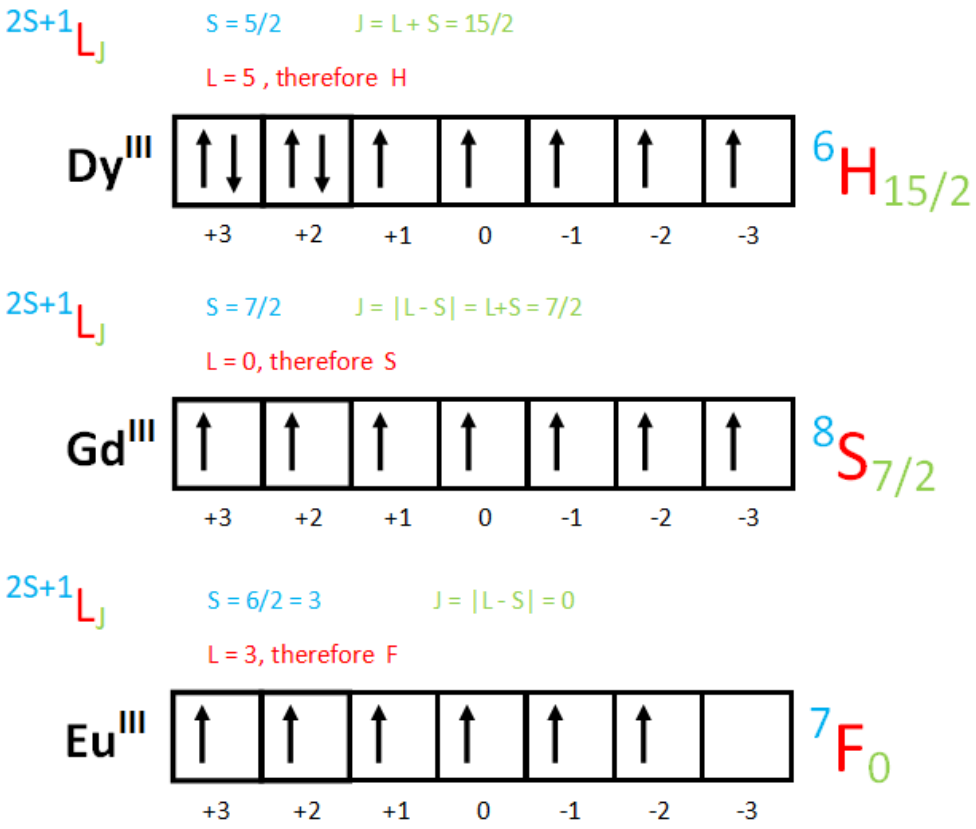

Figure 25- Discerning term symbols, $^{2S+1}L_J$, of lanthanide ions Dy^{III}, Gd^{III} and Eu^{III}.

The value for L, is denoted using spectroscopic notation within a term symbol such that: 0 → S, 1 → P, 2 → D, 3 → F, 4 → G, 5 → H, 6 → I *etc*.

Table 2- Ground state term symbols for all Ln^{III} ions.

Ce^{3+}	Pr^{3+}	Nd^{3+}	Pm^{3+}	Sm^{3+}	Eu^{3+}	Gd^{3+}
$^2F_{5/2}$	$^3H_4$	$^4I_{9/2}$	$^5I_4$	$^6H_{5/2}$	$^7F_0$	$^8S_{7/2}$
Tb^{3+}	**Dy^{3+}**	**Ho^{3+}**	**Er^{3+}**	**Tm^{3+}**	**Yb^{3+}**	**Lu^{3+}**
$^7F_6$	$^6H_{15/2}$	$^5I_8$	$^4I_{15/2}$	$^3H_6$	$^2F_{7/2}$	$^1S_0$

Table 3 details the values for the ground state S, L, J, g_J and theoretical n_{eff} value, based off the Hund-Landé equation for all the trivalent lanthanide ions from cerium through lutetium. It also offers details as to the classification of Kramers' ions,[160, 161] a requirement for SMM behaviour which links the degeneracy to spin. Kramers' degeneracy theorem contains the implication that all species of a half-integer spin will

exhibit an even degeneracy of every energy level – which increases the probability for a bi-stable ground state separated by an appreciable energy barrier.

Table 3- Ground state quantum terms for the trivalent lanthanide ions Ce-Lu and theoretical n_{eff} values as dictated by the Hund Landé Equation.

Ion	f^N Configuration	Ground State L	S	J	Landé g-Factor G_J	Kramers' Ion Y / N	Theoretical n_{eff}
Ce (III)	1	3	1/2	5/2	6/7	Y	2.54
Pr (III)	2	5	1	4	4/5	N	3.58
Nd (III)	3	6	3/2	9/2	8/11	Y	3.62
Pm (III)	4	6	2	4	3/5	N	2.68
Sm (III)	5	5	5/2	5/2	2/7	Y	0.85*
Eu (III)	6	3	3	0	-	N	0*
Gd (III)	7	0	7/2	7/2	2	Y	7.94
Tb (III)	8	3	3	6	3/2	N	9.72
Dy (III)	9	5	5/2	15/2	4/3	Y	10.63
Ho (III)	10	6	2	8	5/4	N	10.60
Er (III)	11	6	3/2	15/2	6/5	Y	9.57
Tm (III)	12	5	1	6	7/6	N	7.63
Yb (III)	13	3	1/2	7/2	8/7	Y	4.50
Lu (III)	14	0	0	0	-	N	0

*Species exhibit significant variation between the Hund Landé model and observed values

It should be noted that the Hund-Landé equation, **Eq^n 2**, fails to accurately represent the experimental magnetic moments of Sm(III) and Eu(III).[162] The Hund Landé equation is predicated upon the assumption that the electrons exist in their ground state term at ambient temperatures. Both europium and samarium exhibit much smaller splittings between their ground and first excited states than other trivalent lanthanides, thereby causing the electrons to be elevated to higher energy levels by the Boltzmann energy, k_BT, of the environment at ambient temperature. This invalidates the equation and accounts for the discrepancy between theoretical and observed values of n_{eff}. **Figure 26** provides an evaluation of the observed and theoretical values of n_{eff} for the trivalent lanthanide ions, and first row transition metals for comparative purposes.

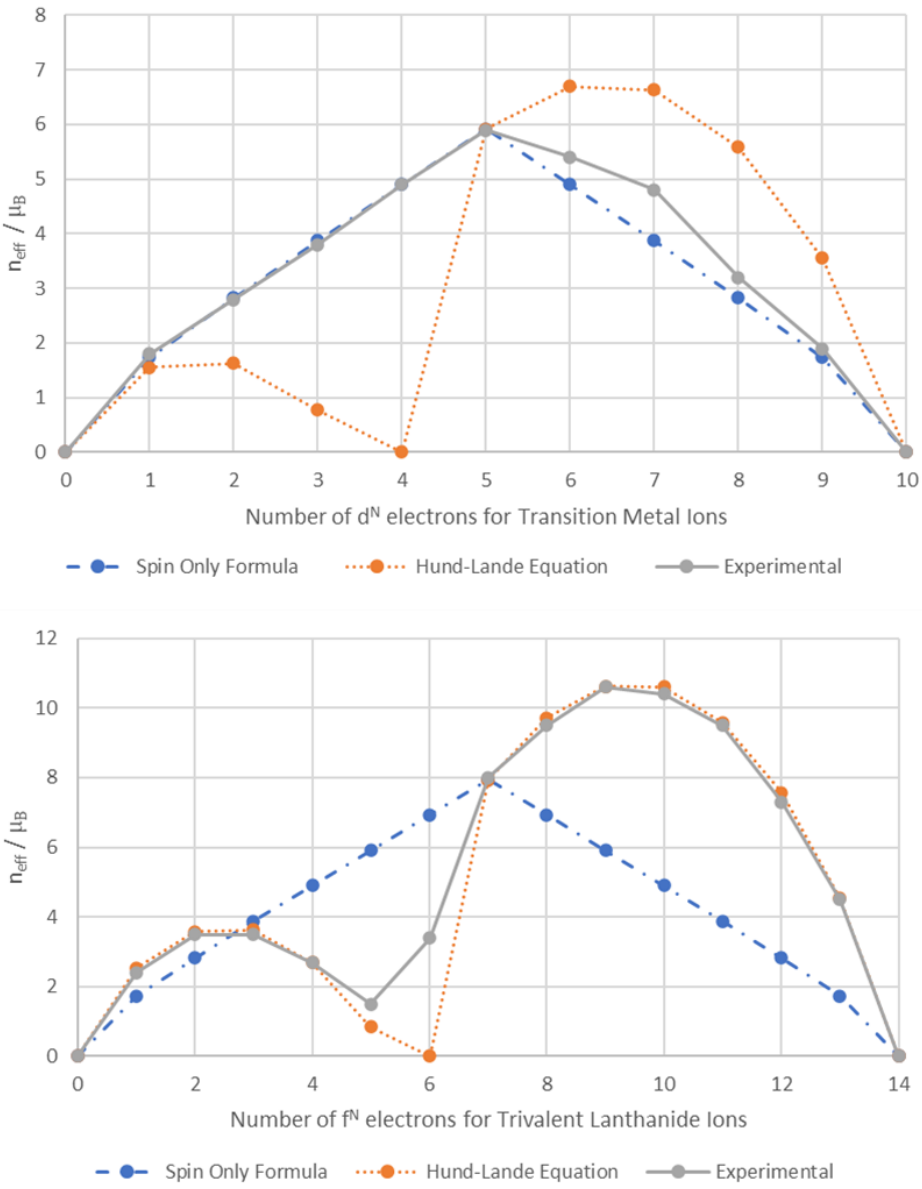

Figure 26- Graphical representation of typical experimental lanthanide n_{eff} values and those calculated by the Spin-Only formula and Hund-Lande equation, bottom; and for first row transition metals, top.

Paramagnetism within lanthanide elements can be primarily attributed to the incomplete 4f orbital, but the magnetic moment varies very little as a function of the ligand environment.[163] Typically, when measuring values around 300 K, lanthanide molecular moments do not vary any more than 15% for compounds of a particular lanthanide metal, and frequently less. Comparatively, molecular moments for compounds of a particular first transition series metal can exhibit variations of upwards of 200%. These observations are indicative of the 4f electrons having minimal

involvement in the covalent interactions with the ligand environment. For this to occur the outer electrons of the 4f orbitals must have very contracted radial functions,[164] acting more akin to core electrons than valence electrons. This can be seen in **Figure 27** which portrays the radial distribution functions of the higher order orbitals in a lanthanide or actinide species.

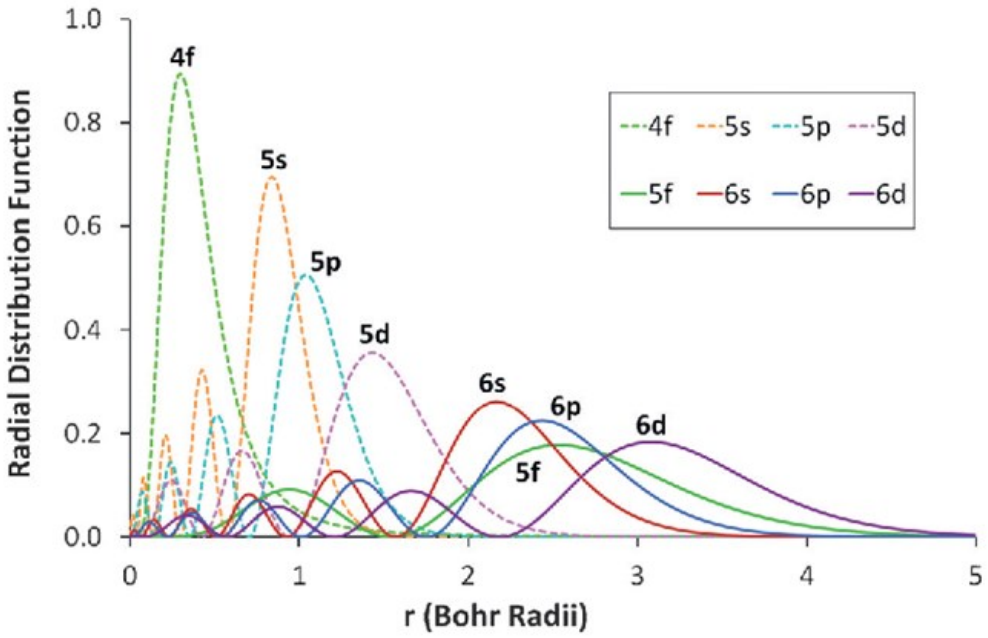

Figure 27- Radial Distribution Functions for the higher order orbitals of lanthanides and actinides. Note the comparatively core-like nature of the 4f orbitals.[165]

The contracted core-like nature of lanthanide 4f orbitals leaves very little protruding electron density to interact covalently with the ligand environment, and so this function is instead undertaken by the more radially dispersed 5d and 6s orbitals. This variation in only the electrons of core-like orbitals across the lanthanide series contributes largely to the uniformity exhibited in lanthanide chemistry whilst also explaining why the f-orbitals remain degenerate regardless of the ligand field it experiences, unlike with comparable effects for transition metals.

Due to the switch from transition metal based SMMs to lanthanide based SMMs it should be noted that there is a marked difference in the analysis of the magnetism of lanthanide ions compared to transition metal ions. Primarily TM SMMs can usually be described by the S quantum number with second order spin-orbit effects – whereas for lanthanide SMMs the spin, orbit and spin orbit coupling must explicitly be described.

The spin-orbit coupling constant (ζ_{nl}) shows significant periodicity for 4f elements.[166]

Eq^n 17: $\zeta_{nl} = \hbar^2 Z A \langle r \rangle^{-3}$

Where $A = \frac{\mu_0 e^2 g_e}{16\pi m_e^2}$

Due to their size and number of electrons, lanthanide radial wavefunctions are significantly distorted. Additionally, the electron orbitals are further deformed by the effects of special relativity whilst another contribution can be associated to the interaction between the spin magnetic moment of an electron with the magnetic fields generated by the orbital momentum of other surrounding electrons. These considerations are normally negligible for lighter elements, but in heavier atoms like lanthanides, their contribution becomes significant. Although **Eq^n 17** is insufficiently reliable to model larger species such as lanthanides, it still functions as an approximation in the first case.

Spin-orbit coupling is significant to the chemistry of lanthanide species. Most lanthanide ions, other than gadolinium (III) and lutetium (III), display large unquenched orbital angular momentums[167] which contribute to the strong spin-orbit couplings, as shown in **Figure 28**. Orbital contributions are predicated in the ability of the open shell electrons to circulate between equivalent orbitals with no associated energy cost.

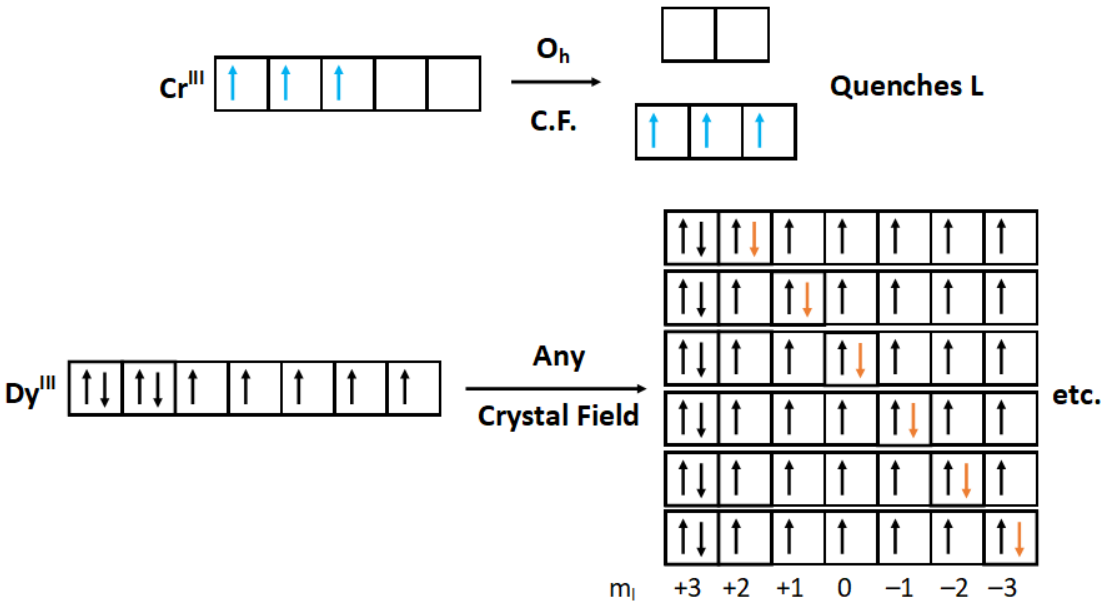

Figure 28- An example of Orbital Contributions and Spin-Orbit Coupling. In transition metals the ligand field quenches (or limits) the value of L, such that there is a negligible, or no, orbital magnetic moment. In f-block metals there is no crystal field splitting as the core-like f-orbitals do not experience the ligand field. As a result, the electrons can hop between orbitals with (nearly) no energy cost, resulting in a large orbital magnetic moment.

An unquenched orbital angular momentum must be considered when calculating magnetic moments, hence why the spin-only formula breaks down for f block elements. As each successive trivalent lanthanide ion is investigated the spin-orbit coupling constant, ζ_{4f}, is shown to increase, with a near five-fold increase in strength from 640 – 2940 cm^{-1} across the series in total. These large values are indicative of the high nuclear charge and contracted 4f orbitals known to exist within lanthanide elements. The Russell-Saunders model continues to hold even with these large spin-orbit coupling values, although the strain can be seen where mixing of multiplet states with the same J values becomes apparent: a step towards the model breaking down.

As a result of the strong spin-orbit contributions, the multiplet width and separation between the ground state and first excited state become exceedingly large for lanthanide ions, in the region of 5000-10000 cm^{-1} and 2000 cm^{-1}, respectively, once more excluding the outlier examples of samarium and europium.

Anisotropy is a quality that is imperative in the development of lanthanide-based molecular magnets.[168-170] Simple models portray the electron density of atoms and ions as spherical, but this is often not the case, especially in elements with a higher atomic number (Z). Lanthanide ions tend to exhibit some form of axiality, as explained by Rinehart and Long in 2011.[171] The electron density of an isolated lanthanide, in the majority of cases, exhibits compression or elongation of one axis when compared to the remaining two; akin to the bond distances exhibited in the Jahn-Teller distortion of octahedral transition metal complexes. The electron density of most lanthanide ions is therefore inherently oblate (axially squashed) or prolate (axially elongated), and this skew of electron density plays an important role in the potential design principles of SMMs. **Figure 29** shows the predicted shape of electron densities for the trivalent lanthanide ions. Note that gadolinium and lutetium remain spherical as a result of their half-filled and filled f-orbitals, respectively, quenching the angular orbital momentum of the electrons, thereby preventing the expected distortion.

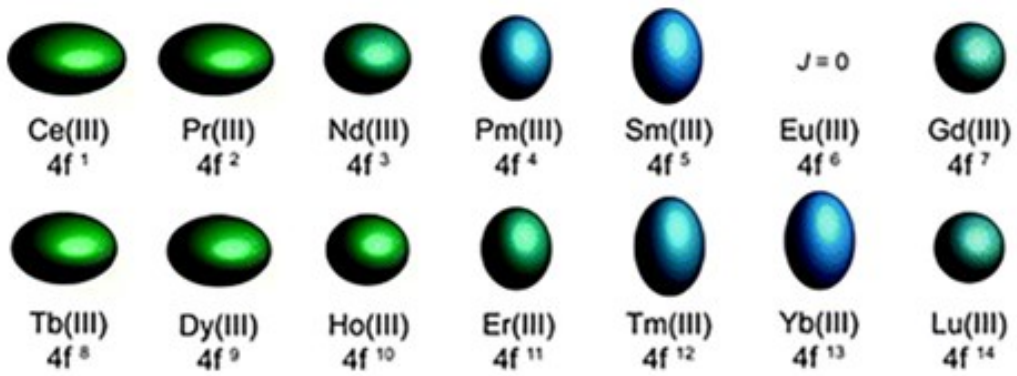

Figure 29- Predicted electron density distributions for the trivalent lanthanide ions.[171]

Knowing the effective shape of the electron density spheroid for specific rare earth metal ions defines a parameter by which the molecules anisotropy can be tweaked through structural variation, as shown in **Figure 30**. Reducing the electronic repulsion between the lanthanide ion electron density and the ligand donors with the largest electron densities will act to stabilise the ground state. As such, a Dy^{III} ion, with a predicted oblate electron density will see its ground state, with higher M_J values, stabilise as a result of highly electron donating ligand being placed on its anisotropy axis, z, which is perpendicular to the oblate density itself. Doing so minimises the overlap of the lanthanide orbitals with the ligand orbitals where the lanthanide-ligand (Ln-L) bond

lengths are shortest. In such a case, the absence of equatorial ligands, will see the oblate electron density expand along the plane enhancing the axial anisotropy further. Conversely, if the donor atoms do coordinate within the equatorial plane the electron distribution will become more isotropic, or sphere like, reducing the ions potential to behave as an SMM. However, this methodology is limited by the large ionic radii of lanthanide ions, which result in the favouring of high coordination numbers, often eight or higher, when considering ligands not themselves designed to be sterically hindering. Such high coordination complexes commonly have ligands exhibit a blend of axial and equatorial character, thereby complicating the design element.

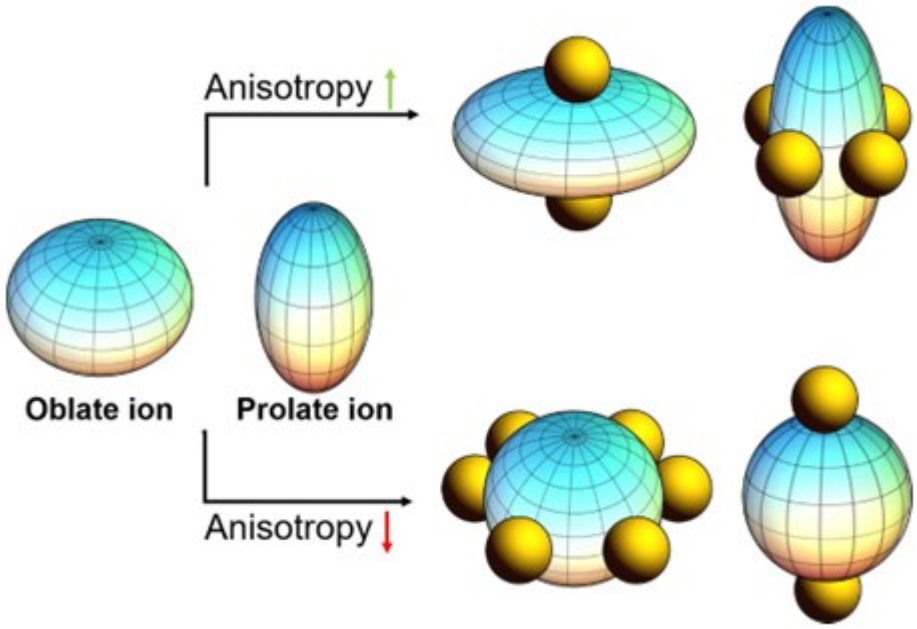

Figure 30- Design parameters for ligand coordination as an effect on the anisotropy of oblate and prolate electron densities of lanthanide ions.[112]

These principles of active design were nevertheless exemplified by the work of Murugesu *et al.* in 2013.[172] By producing a total of six very similar dinuclear $\{Dy^{III}_2\}$ complexes which were differentiated primarily by the electron donating character of an ancillary bidentate ligand, Rinehart and Long's hypothesis could be tested. As the core structure remained functionally the same any changes in the magnetic properties were assigned to the effect of the exchanged ligand. **Figure 31** shows three of these structures, with a nitrate ligand being replaced with an acetylacetonate (Acac) ligand or hexafluoroacetylacetonate (Hfac) ligand which are more and less electron donating respectively. The resultant structures validated the Rinehart and Long paper as

increasing the electron density on the equatorially coordinating oxygen donor atoms proved to negatively influence the values of U_{eff} of the resultant complex.

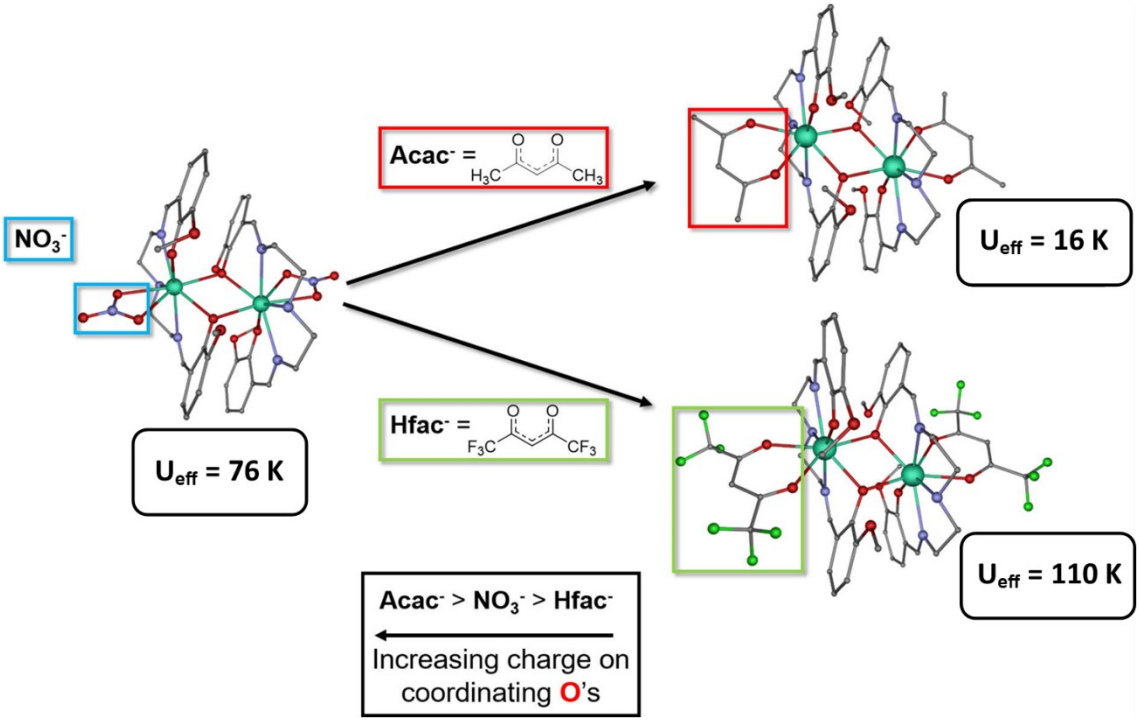

Figure 31- Three dinuclear $\{Dy^{III}_2\}$ complexes synthesised by the Murugesu group with inset U_{eff} values influenced by the donating character of the indicated ligands.[172]

As previously discussed, the magnitude of the barrier to magnetisation reversal, can be bypassed entirely by fast quantum tunnelling relaxation pathways, preventing the formation of hysteresis loops with significant coercive components. Lanthanides exhibit very weak intramolecular magnetic exchange and near-zero coupling between neighbouring lanthanide ions. Previous reports have indicated a relationship between exchange effects and zero-field quantum tunnelling of magnetisation, that sees a reduction in the loss of magnetisation.[173] In a relative sense the exchange coupling within a {3d-4f} complex could prove significantly more intense than in an equivalent {4f-4f} complex exhibiting the same structural motif. Inducing a strong magnetic exchange coupling[174] between 3d and 4f ions is therefore a potential route to the reduction of quantum tunnelling in complexes exhibiting a bi-stable ground state.

1.5 Magnetochemistry and Lepidoptery

Foundations for this project have been laid since the earliest days of the molecular magnetism renaissance, with the seminal work of Gatteschi *et al.*[175], in 1985, forming the basis for studies of magnetism in {3d-4f} coordination complexes. In combination with the work of Osa and Matsumoto *et al*.[141], in 2004, producing the first {3d-4f} SMM complex, which highlighted the transition metal-lanthanide ferromagnetic interaction and magnetic anisotropy within a discrete system, the principle of heterometallic {3d-4f} complexes with the required properties to exhibit a slow relaxation of magnetisation was cemented.

Many different synthetic strategies have been applied to this problem since the early 2000's with molecular motifs being discovered with diverse nuclearities and topologies, ranging from cages and balls to wheels and disks.[176-179] Even though {3d-4f} complexes have been thoroughly studied over decades by groups across the world correlations between magnetic and structural data still only provide the broadest of relationships. In diversifying the data available we move closer, as a collective, to uncovering further guiding principles of molecular magnetism – and subsequently being able to exploit these correlations in the tailored construction of further {3d-4f} complexes with more preferential magnetic properties: a worldwide collaborative, iterative collaboration, with communication at its heart.

This project focusses primarily on the coordination chemistry of amine polyalcohol ligands – of which a {3d-4f} butterfly motif is a common resulting structural topology. This motif, also commonly referred to as a defect dicubane, is composed of a $\{(3d)_2(4f)_2(\mu_3\text{-OR})_2(\mu_2\text{-OR'})_4\}$ core decorated with varying terminal and capping ligands to form a discrete molecular magnet with multiple, tuneable exchange pathways – and variations there upon. These coordination clusters have two common arrangements,[180] as shown in **Figure 32**: the Type I, or reverse butterfly, in which the more massive metal ion, typically a lanthanide, is held in the peripheral "wing" sites and the Type II, or butterfly topology, where the more massive metal ion is bound in the more core-like "body" sites.

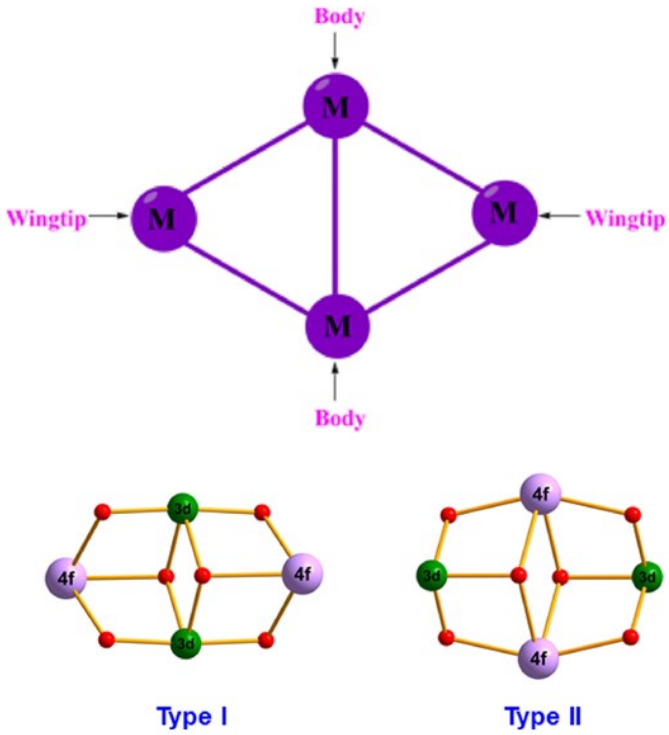

Figure 32- Defining type I and type II butterflies as a function of the ions found in the body and wing coordination sites of the complex. In the examples, bottom, 4f ions are coloured pink and 3d ions are coloured green.[180]

The $\{M_2Ln^{III}_2\}$ core of the butterfly family provides versatile opportunities for coupling interactions which can strongly influence the magnetism of said complex overall. The reverse butterfly topology (Type I) tends to see its magnetism directed by the M-Ln coupling present, although the central M-M coupling and Ln single ion magnetics can also prove to be significant perturbing effects. In such cases where the M ion is either non-diamagnetic or exhibits strong M-Ln and M-M coupling parameters the overall magnetic properties must be assessed as a cooperative entity.[180, 181] Switching to the butterfly topology (Type II) M-M coupling interactions are effectively removed, leaving only the Ln single ion effects and M-Ln couplings to drive the magnetic properties. In such instances the lanthanide single ion effects can be considered to be dominating.

In 2013, the Murray group reported the first $\{Cr^{III}_2Dy^{III}_2\}$ (Type II) butterfly complex, $[Cr^{III}_2Dy^{III}_2(OMe)_2(Benz)_4(MDEA)_2(NO_3)_2]$.[131] This complex shall act as the front-runner compound for our studies and is shown in **Figure 33**. The complex comprised of a $\{Cr^{III}_2Dy^{III}_2\}$ core bound together by two μ_3-OMe ligands and further supported at the

periphery by two doubly deprotonated N-methyldiethanolamine ligands ($MDEA^{2-}$) binding in a μ_3-η^2:η^1:η^2 (or Harris Notation 5.2.2.1, see later sections) coordination mode. The metallic core is additionally stabilised by four benzoate ligands, one bridging each adjacent Cr-Dy pair. The dysprosium atoms are then capped by chelating nitrate ions. The compound is described in the paper as showing ferrimagnetic coupling between the paramagnetic centres, whilst ab-initio calculations revealed stronger than usual antiferromagnetic interactions between the Cr and Dy ions ($J_{Cr\text{-}Dy}$ = 20.30 cm^{-1} and 16.7 cm^{-1}). Classic SMM behaviour was observed with maxima in the out-of-phase ac susceptibilities versus temperature and frequency plots from which U_{eff} = 77 K (53.5 cm^{-1}) and $\tau_0 = 5.1x10^{-8}$ s were extracted using the Arrhenius law. Hysteresis measurements exhibited an open loop up to 3.5 K, with a wide coercive field of approximately 2.7 T at 1.8 K, whilst the Cole-Cole plot suggests a single Orbach relaxation pathway. All examples of the magnetic data from the Langley and Murray *et al*. paper can be found in **Figure 34**. Overall, this dataset, alongside a further seven structural variants were produced which mimicked the core structure whilst varying the organic ligand field which collectively indicated that increasing exchange coupling between 3d and 4f ions can help to slow down the usually very fast relaxation of 4f ions.

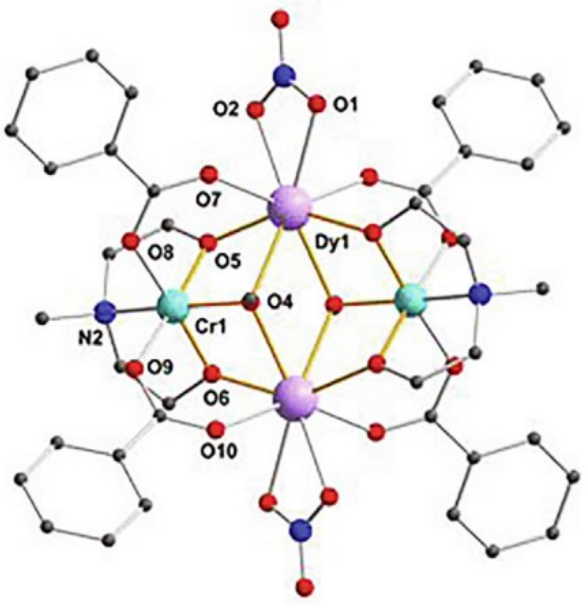

Figure 33- Molecular structure of $[Cr^{III}_2Dy^{III}_2(OMe)_2(Benz)_4(MDEA)_2(NO_3)_2]$: C atoms, grey; O atoms, red; N atoms, dark blue; Dy atoms, pink; Cr atoms, light blue. H atoms have been omitted for clarity.[131]

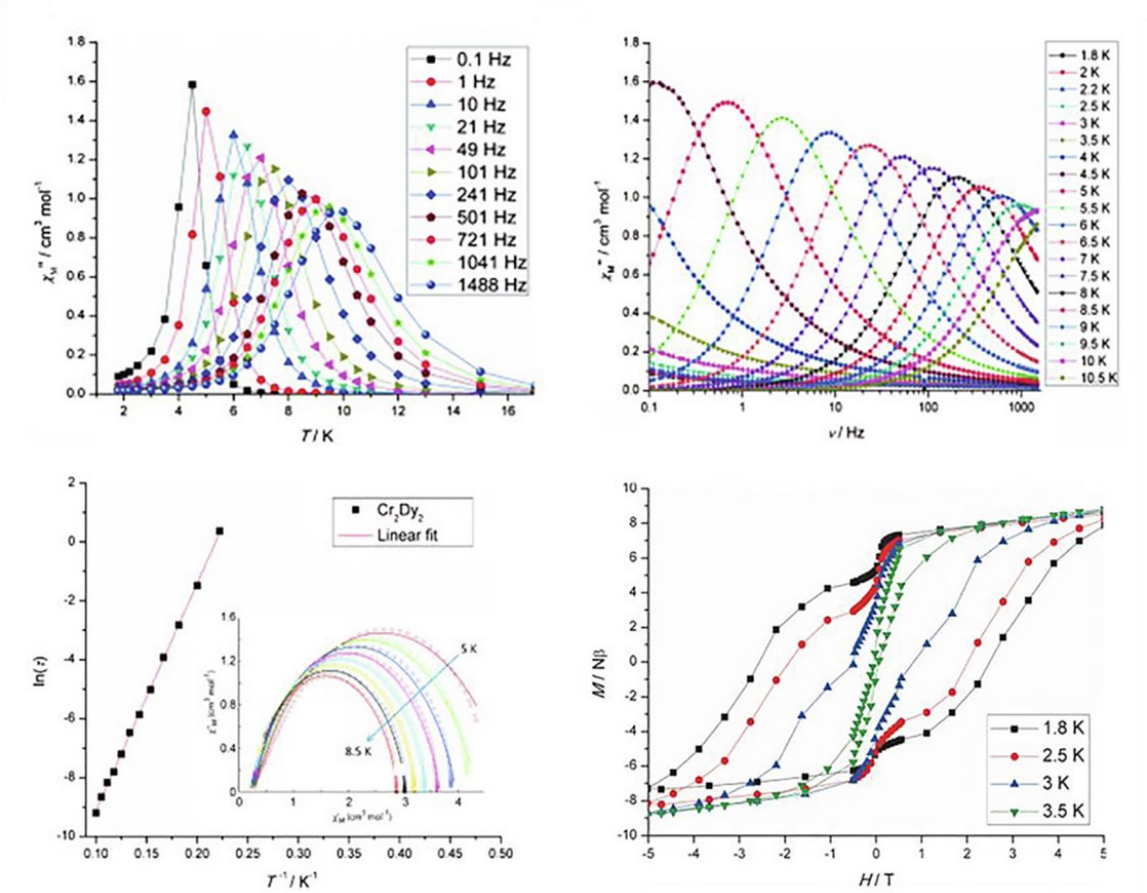

Figure 34- Magnetic data for[$Cr^{III}_2Dy^{III}_2(OMe)_2(Benz)_4(MDEA)_2(NO_3)_2$]: top left, χ" vs temperature; top right χ" vs frequency; bottom left, Argand diagram with inset Cole-Cole plot; bottom right, hysteresis plot in the temperature range 1.8-3.5 K.[131]

In the intervening near twenty years since the first {3d-4f} structures were codified towards magnetic study the field has bloomed. Studies of the butterfly topology have been undertaken on paramagnetic 3d ions,[182-187] diamagnetic 3d ions,[188, 189] and more esoteric systems such as with 4d ions[190] or even where M = Mg^{II} or Al^{III}.[191, 192] These studies are summarised by seven general conclusions suggested by Peng and Powell in 2021:[181]

a) *The coordination environments around the metal ions, the alignments of uniaxial-anisotropy axes, such as the Ising axes of Ln^{III} ions and J-T axes of Mn^{III} ions, and the exchange coupling between metal centres are the key tuning handles for the magnetic properties.*

b) *For most {3d-4f} SMMs, the primary contribution to the slow relaxation of the magnetization is from highly anisotropic Ln^{III} ions. The direction of the easy axis of*

magnetization may not necessarily coincide with the obvious molecular symmetry axis. The {3d-4f} interaction can also play a key role in suppressing QTM.

c) *Up to now, it has proved more challenging to exert the high degree of control over local ion coordination geometry which has been achieved for the 3d-SMMs and 4f-SMMs within the {3d-4f} systems.*

d) *It was found that in the Type I {3d-4f} butterfly systems (Ln in wingtips) simple substitutions around the Dy^{III} ions have little influence on the barrier height. This is in contrast to the Type II {$Co^{III}_2Dy_2$} complexes (Ln in body), in which the nature of the slow magnetic relaxation is a consequence of the single ion Dy^{III} anisotropy being influenced by subtle changes to the ligand field.*

e) *Introducing electron withdrawing groups in the butterfly system can help in enhancing the magnetic properties, such as increasing the barrier height to magnetisation reversal.*

f) *The 3d paramagnetic metal ions play an important role in determining the resulting static and dynamic magnetic properties. From ab initio calculations deleting the 3d contribution using diamagnetic metal ions can reduce QTM in favourable cases.*

g) *Clearly, the role of magnetic exchange and dipolar interactions between metal centres in {3d-4f} SMMs should be further studied both experimentally and theoretically.*

These seven statements codified the basis for further study into the motif and summarises the research of multiple groups over multiple decades into bitesize, actionable components, akin to a magneto-structural activity relationship.

So why lepidoptery? Our intention is to synthesise or “capture” new and previously unknown species of butterfly complex and further motifs before studying them comparatively with known isostructural analogues. In so doing the project can contribute to the growing knowledge base of this burgeoning field.

1.5.1 Polyalcohol Ligands

Typically, beyond the $\{(3d)_2(4f)_2(\mu_3\text{-}OR)_2(\mu_2\text{-}OR')_4\}$ core exhibited by the molecular butterfly motif, an additional multi-dentate ligand is required to support the self-assembly of the topology. These ligands often take the form of tridentate (or tetradentate) amine polyalcohol ligands such as derivatives of diethanolamine, collectively RDEA, with examples from prior publications given in **Figure 35**.

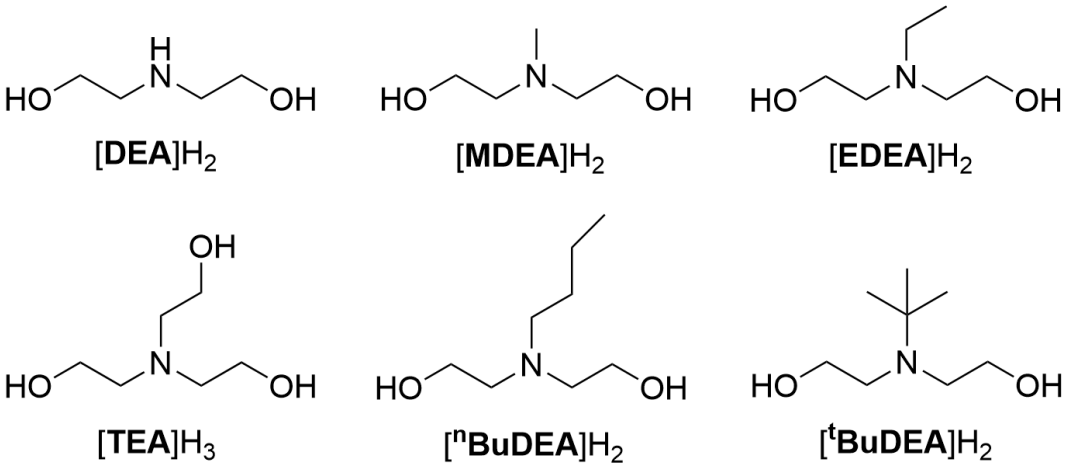

Figure 35- Previously used amine polyalcohol ligands for the serendipitous assembly of butterfly complexes.

Such amine polyalcohol ligands are typically cheap, freely available and have flexible uses in the chemistry of hard-acid metal ions, a classification amongst which lanthanide ions are considered. Amine polyalcohols exhibit (at least) two tuneable binding environments based around the softer N-atom and the harder O-atom. This is an ideal situation for the synthesis of heterometallic complexes where this trait can be exploited to guide specific ions to particular positions. Such ligands can also exhibit an exceedingly wide range of binding modes, especially in combination with a deprotonating agent, which is discussed at length in the review by Sharples and Collison,[193] in 2014. A selection of the observed binding modes realised by diethanolamine derivatives, including triethanolamine, across current literature can be found in **Figure 36**, overleaf.

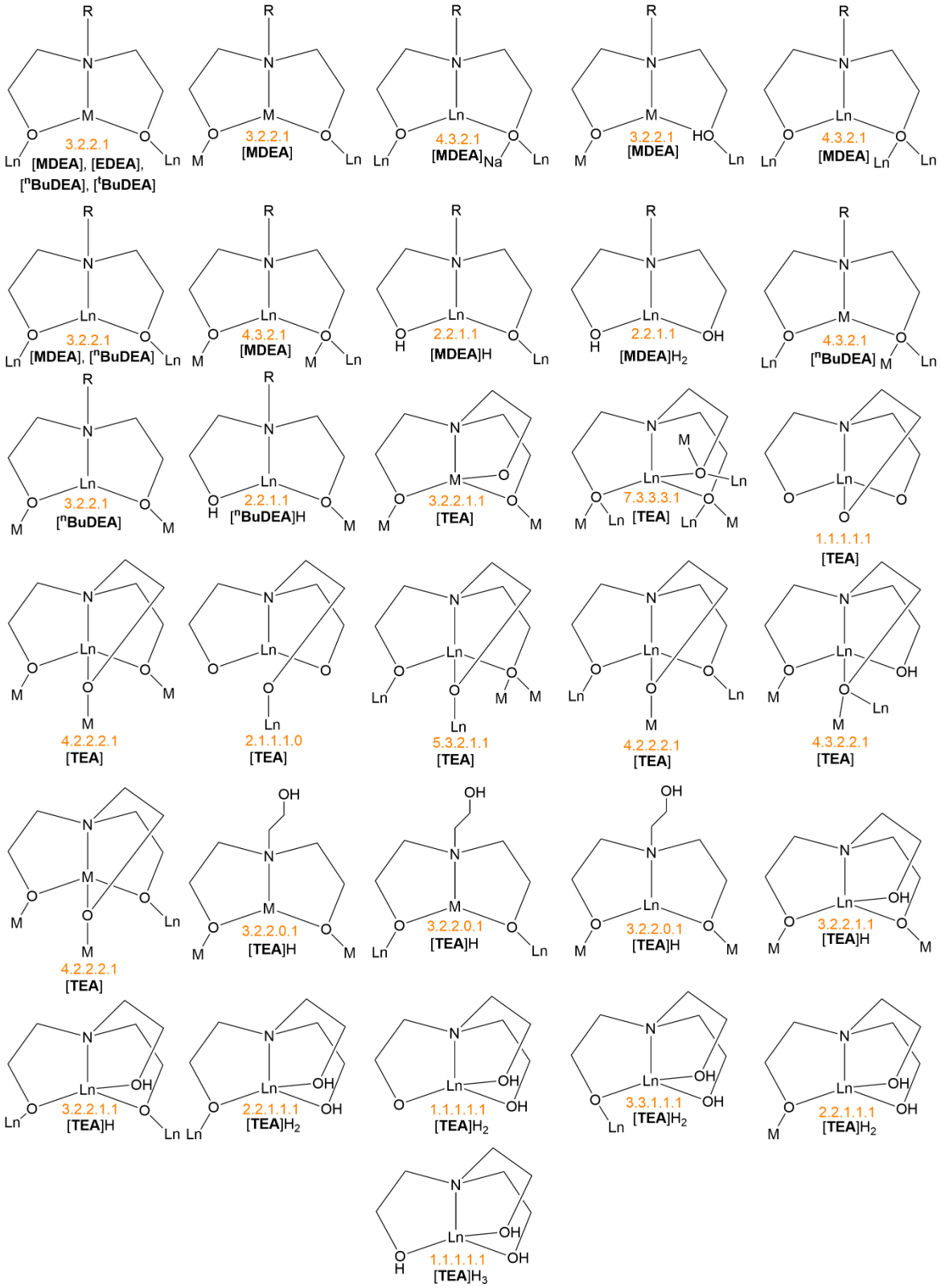

Figure 36- Binding modes of $[RDEA]H_x^{(2-x)-}$ and $[TEA]H_x^{(3-x)-}$ derivatives from previously published {3d-4f} and 4f structures, where M is a transition metal ion and Ln is a lanthanide ion. Binding modes are denoted by their Harris notations in orange. Adapted from the review of Sharples and Collison, 2014.[193]

The observed binding modes can be considered in two distinct way, either as a consideration of the denticity ($X\kappa^n$), bridging (μ_n) and hapticity (η^n) or by Harris notation,[194] as seen in the above figure. Denticity is the description of the number of available donor groups within a ligand that bind non-contiguously to a metal centre – this is not the same as the number of potential donor atoms. Bridging describes how a ligand connects metal centres as a function of the number of connected metal centres. Hapticity describes the coordination of a ligand to a metal by and uninterrupted series of contiguous atoms, such as with a terminal side on dinitrogen (η^2) occupying to metal coordination sites, or cyclopentadienyl ligands (η^5) binding facially *via* a contribution from the π systems of all five carbon atoms within the ligand collectively. The combination of these three notations can collectively impart the same information as Harris notation alone. Harris notation describes a ligand binding mode collectively, in the form $[X.Y_1Y_2Y_3\ldots Y_n]$ where X is the total number of distinct metal ions bound to the ligand, whilst the values of Y refer to the number of metal ions coordinated to each donor atom, typically ordered using the Cahn-Ingold-Prelog rules from Y_1 to Y_n. This alternative methodology has proven very applicable to coordination chemistry in general and shall be utilised in discussion, whilst the classical Greek notation shall be used in definitions or chemical naming notation.

It should be noted that although the Sharples and Collison review speaks to amine polyalcohol ligands as “a double-edged sword”, their primary concern appears to be a lack of application towards targeted synthesis, which shall be further discussed later alongside the merits of serendipitous assembly.

Previous research in butterfly synthesis has been dominated by higher symmetry amine polyalcohols, but the synthesis of simple asymmetric polyalcohols for coordination purposes remains a viable target of investigation. The structures of the targeted symmetric and asymmetric polyalcohol ligands are shown in **Figure 37**.

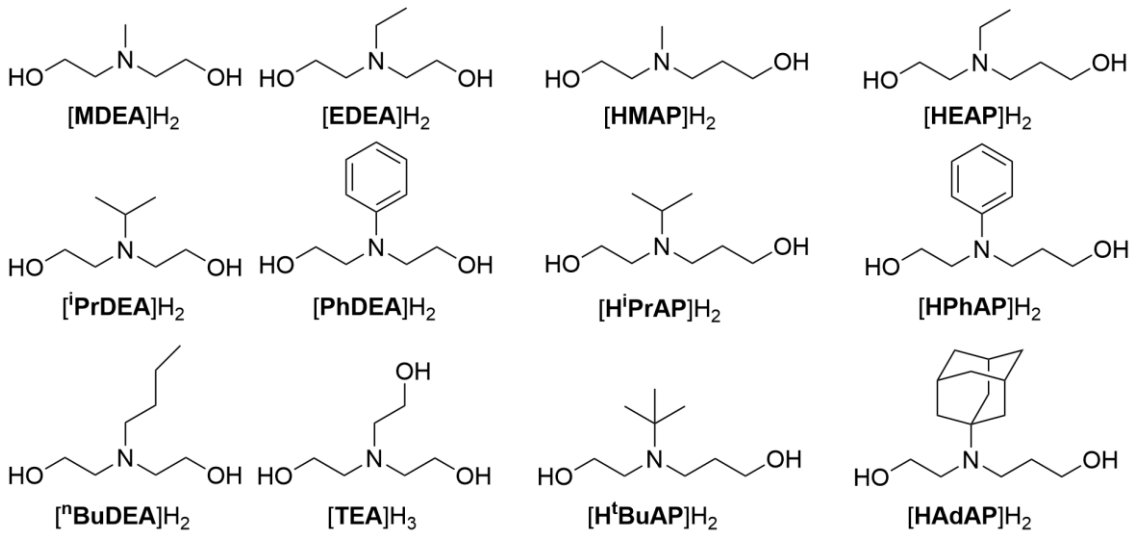

Figure 37- Target structures of symmetric, left, and asymmetric, right, polyalcohol ligands. Full IUPAC names can be found in **Section 1.9**.

Reviews of the previous literature on the synthesis of asymmetric amine polyalcohols exhibited three main pathways towards the production of the target molecules: epoxide alkylation,[195-198] base-promoted haloalkane nucleophilic substitution[199-202] and non-base-promoted haloalkane nucleophilic substitution.[203]

Epoxide alkylation has been well studied as a method of amine alkylation. It proceeds by a mechanism of ring opening, which can exhibit either greater S_N1 or S_N2 character depending on the epoxide used and the reaction conditions. The three-membered epoxide ring is incredibly sterically strained and so the opening of said ring can thermodynamically drive the reaction to completion, should the nucleophile prove strong enough in the respective slow reaction steps.

The reaction can proceed because of the nucleophilic amine triggering the ring opening mechanism of the three-membered ring epoxide. This mechanism of ring opening shows strong S_N2 character and could be considered a basic ring opening, as shown in **Scheme 1**. In the case of a basic ring opening the nucleophile will attack at the least sterically hindered site, forming a pseudo trigonal bipyramidal carbo-anion transition state, with the nucleophile approaching from the plane opposite the epoxide.

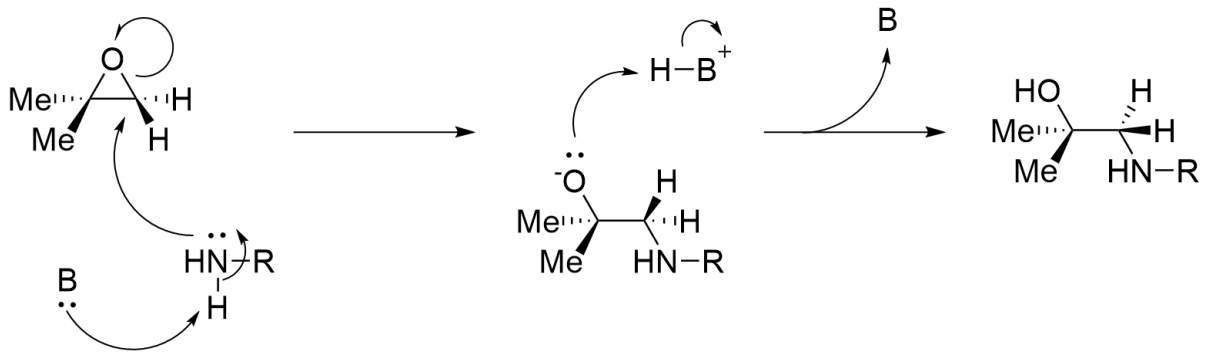

Scheme 1- Concerted mechanism of base-catalysed epoxide ring opening reactions.

In the case of an acidic ring opening, the mechanism would proceed differently, exhibiting a far greater S_N1 character, as shown in **Scheme 2**. The protonation of the epoxide will cause a shift in the electron density of the ring and a partial positive charge will begin to build on the most substituted epoxide ring carbon. This partial charge is stabilised by the inductive effect of the alkyl branches, whilst also making that carbon a more viable target for nucleophilic attack, once more approaching from the opposite plane to the epoxide. The opening will then proceed as normal but produces a unique structure different to that of the basic ring opening.

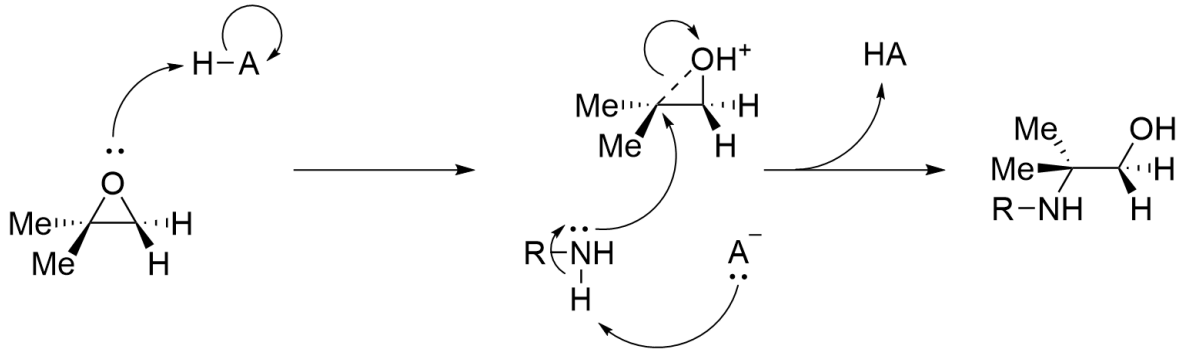

Scheme 2- Concerted mechanism of acid-catalysed epoxide ring opening reactions.

Scheme 1 and **Scheme 2** show the ring opening mechanisms for asymmetric epoxides - a regioselective and stereoselective process - as the final products are non-superimposable constitutional isomers of each other. This method of amine alkylation produces branched chain alkyl amines with superior yields and far wider applications than an equivalent amine halo-alkylation. The length of the resultant chain though is greatly restricted, as the three membered epoxide will always open to a 2-aminoethanol

derivative. However, most amine species are comparatively weak nucleophiles which may not be strong enough to drive these reactions. The amine nucleophile may also not be stable enough to the strongly acidic or basic conditions required for these reactions to proceed effectively. Undergoing these reactions without some form of catalyst to enhance the epoxide's electrophilicity, microwave irradiation or ultra-sonification in aqueous medium being employed will often result in long reaction times, lower yields or poor regioselectivity in the final product.

Base-promoted haloalkane nucleophilic substitution utilises an amine and haloalkane or haloalcohol dispersed in a polar solvent before using a strong base to deprotonate the amine and thereby increase its nucleophilicity to drive the reaction, as seen in **Scheme 3**. The free halide ion is then associated to the protonated base which can be removed as a salt by solvent separation methods. This is a commonly attempted method of synthesis; however stoichiometric control is problematic. Addition of successive alkyl chains to an amine nitrogen leads to an increased electron density about the nitrogen, therefore making it a stronger nucleophile. As such, for similar alkyl R-groups, $NH_3<NH_2R<NHR_2<NR_3$ in terms of nitrogen nucleophilicity. This often leads to a cascading effect where the reaction will push towards the tertiary or quaternary amine, unaffected by any attempted stoichiometric control and have a huge deductive effect on the final yield. As a result, this method is not suitable to produce the precursor molecules, which are typically secondary amines, and any purification method, whether by column chromatography or distillation, would be involved, intensive and time consuming.

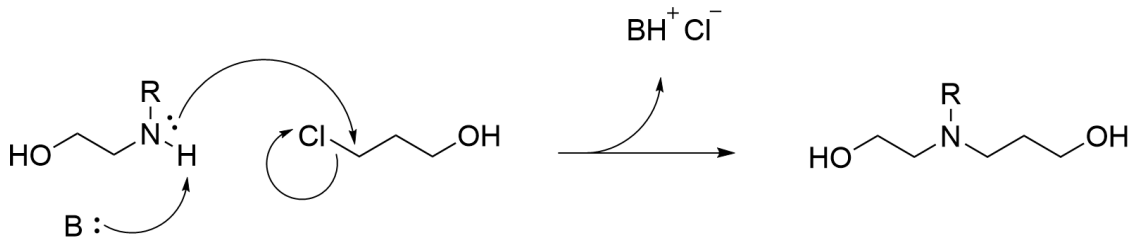

Scheme 3- Concerted mechanism for base-promoted haloalkane nucleophilic substitution.

As a result of these factors synthetic methods focus upon non-base-promoted haloalkane nucleophilic substitution in the first case, as shown in **Scheme 4**. Unlike with

the base-promoted variant of the method, the reactions are undertaken in a high boiling point, non-polar solvent and produce the hydro-halide salt of the amine product. As the ionic salts are far less able to dissociate in a non-polar solvent, the reactions are seen to proceed stepwise, allowing for the addition of one alkyl or alcohol chain at a time to produce a quaternary halide salt, which can then be collected, purified and freebased prior to further reaction steps and differentiation. This method, although labour intensive, is also the most likely to allow for the recovery of unused reagent from the reaction mix for use in further reactions and can be pushed with far more forcing conditions. Steric accessibility of the amine nitrogen is an exceedingly important factor in this reaction method, and so as the coordination sites of nitrogen become occupied with larger groups the reactions must be run in higher concentrations for more time to compensate.

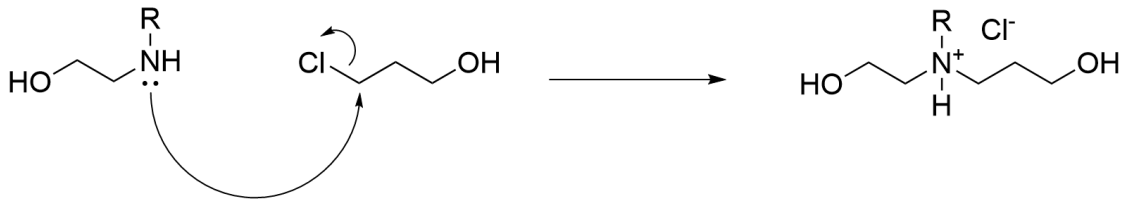

Scheme 4- Concerted mechanism for non-base-promoted haloalkane nucleophilic substitution.

1.6 Serendipitous Assembly

One-pot complexation reactions are planned as a combination of designed ligands and selected metal ions in a compatible solvent system, but then proceed by self-assembly principles. This manner of production, termed serendipitous assembly has led to a split amongst the molecular magnetism community. Which is favourable – synthesis using methods of designed-assembly or methods of self-assembly? This discordancy is discussed in Winpenny's seminal Dalton Perspectives piece (2002).[204] Coordination complexes can be multifaceted and intricate – arguably beyond the scope of a predicted design, but the results of directed synthesis are more likely to show the physico-properties which would be preferential for a specific use. Indeed, the serendipitous route may never produce the properties required for any single application, but each novel material represents new knowledge, more patterns and a wider spread of information on a material which may provide the perfect properties for another unthought of purpose.

As concluded by Winpenny "*The dichotomy between designed and serendipitous assembly can be exaggerated.*" One route does not invalidate the other. In fact, to apply our research to its maximal potential, a combination of both aspects is preferential. Synthetic work originated for serendipitous assemblies can be refined and exploited by further active design, but without a breadth of understanding of step 1, how can we predict the best product of step 2? In the area of molecular magnetism, SMMs were discovered by accident, but a field has flourished from those humble beginnings. However, if the hurdle of an ambient temperature SMM is ever to be overcome an element of design will be required, with considered criteria to create the next generation of materials. By elucidating the nature of {3d-4f} interactions, comparing isostructural materials and illuminating the magneto-structural relationships that reduce the effect of limiting factors, such as quantum tunnelling of the magnetisation, we step ever closer to reliability creating materials with specific properties. However, as stated by Peng and Powell in their 2021 review[181] – "*it is still a long journey towards this goal*".

1.7 Aims of the Project

This thesis aims to assess the effect of symmetry in amine polyalcohols acting as ligands within larger molecular arrangements, towards applications as single-molecule magnets. Attaining this goal will be based upon the analysis of synthesised compounds in comparison to known structures.

At its genesis this project was envisioned as a combination of four subsections:

1. Utilising a freely available ligand, 3-[N,N-bis(2-hydroxyethyl)amino]-2-hydroxypropane sulfonic acid ([**DIPSO**]H_4), to evaluate the impact asymmetry may have in the structural arrangement of heterometallic complexes.
2. Investigating amine synthesis in low polarity solvent environments to reduce the risk of reaction cascade as often found in alkylation reactions.
3. Synthesising and characterising precursor molecules and potential amine polyalcohol ligands with varying asymmetry and denticity. Targets include known compounds used as ligands in similar reactions, known compounds used in other chemical investigations and novel ligand molecules. The planned asymmetric ligands targeted for coordination into the butterfly motif are: 3-[(2-hydroxyethyl) (methyl) amino] propan-1-ol ([**HMAP**]H_2), 3-[(2-hydroxyethyl) (ethyl) amino] propan-1-ol ([**HEAP**]H_2), 3-[(2-hydroxyethyl) (iso-propyl) amino] propan-1-ol ([**H^{i}PrAP**]H_2), 3-[(2-hydroxyethyl) (phenyl) amino] propan-1-ol ([**HPhAP**]H_2), 3-[(2-hydroxyethyl) (tert-butyl) amino] propan-1-ol ([**H^{t}BuAP**]H_2), 3-[(2-hydroxyethyl) (adamantyl) amino] propan-1-ol ([**HAdAP**]H_2), 2,2'-[(3-hydroxypropyl) imino] bis-ethanol ([**^{n}Pr'DEA**]H_3).
4. Completing a coordination study to produce novel examples of heterometallic complexes. Analysis of such molecules will proceed by suitable structural and magnetic techniques.

In so doing this project hopes to discover new themes and patterns which will add to the codex of magneto-structural knowledge.

1.8 Summary of Chapters

In the course of this thesis the following topics shall be examined:

Chapter 2- Synthesis of Heterometallic DIPSO Containing Complexes.
This chapter forms the introduction to the synthetic methodology of the project by use of a readily available, freely purchasable ligand, which exhibits increased asymmetry compared to the commonly used triethanolamine.

Chapter 3- Synthesis Towards the Production of Amine Polyalcohol Ligands.
This chapter builds upon previous work by utilising known synthetic methods to create symmetric polyalcohol ligands and their asymmetric derivatives for use in later complexation reactions, alongside any precursor molecules that may be required.

Chapter 4- Synthesis of {3d-4f} Complexes with Amine Polyalcohol Ligands.
This chapter utilises the tridentate ligands synthesised in chapter 3 in reactions to form heterometallic {3d-4f} complexes with interesting magnetic properties. In addition, an example of a heterometallic toroidal compound is given in this chapter which could act as a template molecule for further research.

Chapter 5- Synthesis of {4d-4f} Complexes with Amine Polyalcohol Ligands.
This chapter utilises the tridentate ligands synthesised in chapter 3 in reactions to form heterometallic {4d-4f} complexes with interesting magnetic properties. In addition, an example of a {5p-4f} complex is given in this chapter for comparative purposes.

1.9 List of Target Precursors and Pro-Ligands

Precursors and Pro-Ligands	IUPAC Name
[**MAE**]H	2-(methylamino)ethan-1-ol
[**EAE**]H	2-(ethylamino)ethan-1-ol
[^{i}**PrAE**]H	2-(isopropylamino)ethan-1-ol
[^{t}**BuAE**]H	2-(tertbutylamino)ethan-1-ol
[**PhAE**]H	2-(phenylamino)ethan-1-ol
[**AdAE**]H	2-(adamantylamino)ethan-1-ol
[^{t}**BuAPr**]H	3-(tertbutlylamino)propan-1-ol
[**AdAPr**]H	3-(adamantylamino)propan-1-ol
[**MDEA**]H_2	N-methyldiethanolamine
[**EDEA**]H_2	N-ethyldiethanolamine
[^{i}**PrDEA**]H_2	N-isopropyldiethanolamine
[^{n}**BuDEA**]H_2	N-n-butyldiethanolamine
[**PhDEA**]H_2	N-phenyldiethanolamine
[**TEA**]H_3	Triethanolamine
[^{t}**BuDEA**]H_2	N-tertbutyldiethanolamine
[**AdDEA**]H_2	N-adamantyldiethanolamine
[**HMAP**]H_2	3-[(2-hydroxyethyl)(methyl)amino] propan-1-ol
[**HEAP**]H_2	3-[(2-hydroxyethyl)(ethyl)amino] propan-1-ol
[H^{i}**PrAP**]H_2	3-[(2-hydroxyethyl)(iso-propyl)amino] propan-1-ol
[**HPhAP**]H_2	3-[(2-hydroxyethyl)(phenyl)amino] propan-1-ol
[H^{t}**BuAP**]H_2	3-[(2-hydroxyethyl)(tert-butyl)amino] propan-1-ol
[**HAdAP**]H_2	3-[(2-hydroxyethyl)(adamantyl)amino] propan-1-ol
[^{n}**Pr'DEA**]H_3	2,2'-[(3-hydroxypropyl)imino] bis-ethanol

1.10 List of Coordination Complexes

Complex Number	Chemical Formula
C1	$[Cr^{III}_2Dy^{III}_2(OMe)_2(Benz)_4(DIPSOH)_2(MeOH)_2]\cdot 2MeOH\cdot H_2O$
C2	$[Co^{III}_2Dy^{III}_2(OMe)_2(o\text{-}Tol)_4(DIPSOH)_2(H_2O)_2]\cdot MeCN\cdot 3H_2O$
C3	$[Mn^{III}_2Dy^{III}_2(OH)_2(o\text{-}Tol)_4(DIPSOH)_2(H_2O)_2]\cdot 4MeCN\cdot 2H_2O$
C4	$[Mn^{II}_4Mn^{III}_2(O)_2(o\text{-}Tol)_{10}(MeCN)_3(H_2O)]\cdot MeCN$
C5	$[Mn^{III}_2Gd^{III}_2(OH)_2(Benz)_4(DIPSOH)_2(MeOH)_2]\cdot 2MeCN$
C6	$[Fe^{III}_2Dy^{III}_2(OH)_2(Benz)_2(DIPSOH)_2(NO_3)_2(H_2O)_2]\cdot MeCN\cdot 2H_2O$
C7	$[Fe^{III}_{12}Dy^{III}_4O_6(OH)_4(Benz)_{12}(DIPSO)_4(DIPSOH_2)_2]\cdot 5MeCN\cdot 8H_2O$
C8	$[Fe^{III}_2Dy^{III}_2(OH)_2(2I\text{-}Benz)_2(DIPSOH)_2(NO_3)_2]\cdot 3MeCN$
C9	$[Cr^{III}Dy^{III}_2(OH)(2,6Cl\text{-}Benz)_4(DIPSOH)(NO_3)_3]^{2-}\cdot(NEt_3H)^+_2$
C10	$[Fe^{III}_4Dy^{III}_6O_2(OH)_6(o\text{-}Tol)_{14}(DIPSOH)_2(MeOH)_2(H_2O)_4]\cdot 8MeOH$
C11	$[Co^{II}_2Co^{III}Dy^{III}(OMe)(DIPSOH_2)_2(DIPSO)(2Cl\text{-}Benz)]\cdot MeOH\cdot H_2O$
C12	$[Co^{II}_3Co^{III}_2Dy^{III}_2(OH)_2(OMe)_2(DIPSO)_2(2Cl\text{-}Benz)_6(MeOH)_2]\cdot 4MeOH$
C13	$[Co^{II}_3Co^{III}_2Dy^{III}_2(OH)_2(OMe)_2(DIPSO)_2(2Br\text{-}Benz)_6(MeOH)_2]\cdot 4MeOH$
C14	$[Co^{II}_3Co^{III}_2Dy^{III}_2(OH)_2(OMe)_2(DIPSO)_2(2I\text{-}Benz)_6(MeOH)_2]\cdot 2MeOH\cdot 2H_2O$
C15	$[Cr^{III}_2Dy^{III}_2(OMe)_2(Benz)_4(HMAP)_2(NO_3)_2]$
C16	$[Cr^{III}_2Dy^{III}_2(OMe)_2(Benz)_4(HEAP)_2(NO_3)_2]$
C17	$[Mn^{III}_2Dy^{III}_2(O)(Benz)_6(HMAP)_2]_n$
C18	$[Mn_2Gd^{III}_2(O)(Piv)_3(HEAP)_2(NO_3)_4]\cdot 0.5MeOH\cdot H_2O$
C19	$[Cr^{III}_4Dy^{III}_4(OH)_6(Benz)_{10}(HMAP)_4]\cdot 3H_2O$
C20	$[Cr^{III}Dy^{III}_6(OH)_8(o\text{-}Tol)_{13}(DMF)_3(MeOH)_2]$
C21	$[Ru^{III}_2Dy^{III}_2(OMe)_2(Benz)_4(MDEA)_2(NO_3)_2]$
C22	$[Ru^{III}_2Dy^{III}_2(OMe)_2(p\text{-}Tol)_4(MDEA)_2(MeOH)_4]Cl_2$
C23	$[Ru^{III}_2Dy^{III}_2(OMe)_2(Acac)_4(EDEA)_2(NO_3)_2]$
C24	$[Ru^{III}_2Dy^{III}_2(OMe)_2(2\text{-}F_3C\text{-}Benz)_4(MDEA)_2(NO_3)_2]$
C25	$[Ru^{III}_2Dy^{III}_2(OMe)_2(2,3,4,5\text{-}tet\text{-}F\text{-}Benz)_4(MDEA)_2(NO_3)_2]$
C26	$[Ru^{III}_2Dy^{III}_2(OMe)_2(2\text{-}Cl\text{-}4,5\text{-}F\text{-}Benz)_4(MDEA)_2(NO_3)_2]$
C27	$[Ru^{III}_2Gd^{III}_2(OMe)_2(Benz)_4(MDEA)_2(NO_3)_2]$
C28	$[Ru^{III}_2Gd^{III}_2(OMe)_2(Acac)_4(EDEA)_2(NO_3)_2]$
C29	$[Ru^{III}_2Dy^{III}_4(OH)_2(OMe)_2(Benz)_{10}(HMAP)_2(MeOH)_2]$
C30	$[In^{III}_{16}Dy^{III}_6(O)_6(OH)_{12}(OMe)_3(Benz)_{22}(HMAP)_6(NO_3)_5]$

2 Synthesis of Heterometallic DIPSO Containing Complexes

2.1 Introduction

As a part of the literature review that preceded this project, a gap in knowledge presented itself. Butterfly topologies are predicated around two bridging ligands, commonly amine polyalcohols such as [**MDEA**]H_2 and [**TEA**]H_3, supporting a core of two pairs of metallic ions, whether homo- or heterometallic. One pair of ions typically binds to the nitrogen atom of the amine polyalcohol whilst the hydroxide arms can then bridge ions between opposing pairs. The core is then further supported by two μ_3-hydroxide or methoxide ions. Invariably, these amine polyalcohols have been symmetric about the nitrogen, with hydroxide chains of equivalent length. And so, the question arose, by breaking this symmetry and elongating the length of one or more arms, could the coordination sites be meaningfully changed and how would this affect the magnetic properties of this new family of butterflies?

3-[N,N-bis(2-hydroxyethyl)amino]-2-hydroxypropane sulfonic acid, [**DIPSO**]H_4, was chosen as the prototype compound to test this hypothesis. [**DIPSO**]H_4 is an air and moisture stable, non-hazardous, relatively cheap molecule which could encapsulate our hypothesis without the need for lengthy organic studies.

In this chapter, the work exhibited proves the versatility of the aforementioned ligand, [**DIPSO**]H_4, towards the serendipitous assembly of novel heterometallic complexes with proclivity towards molecular magnetism. The ligand is capable of forming a wide array of different morphologies from simple butterflies to larger arrays.

2.2 Results and Discussion

This chapter describes the synthesis and characterisation of fourteen {3d-4f} coordination complexes utilising the ligand 3-[N,N-bis(2-hydroxyethyl)amino]-2-hydroxypropane sulfonic acid ([**DIPSO**]H_4), as shown in **Figure 38**, a freely purchasable prototype compound, as the main structural ligand. Additional bidentate ligands used to stabilise the complexes formed are also given in **Figure 39**. This work exhibits the

variation in structure which can occur in the products of chemically similar serendipitous arrangement reactions.

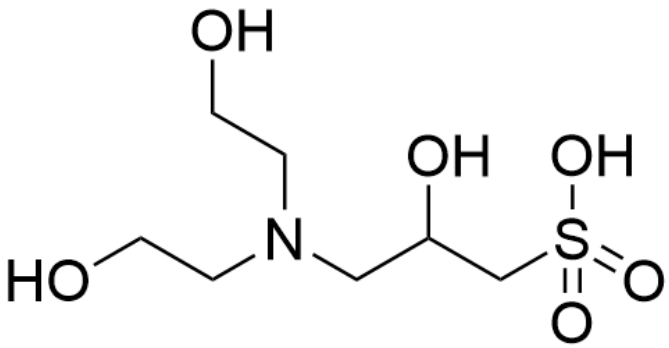

Figure 38- Structure of 3-[N,N-bis(2-hydroxyethyl)amino]-2-hydroxypropane sulphonic acid ([**DIPSO**]H_4).

The chapter also expounds upon how the binding modes of the polyalcohol can vary significantly between, or within, molecules. All the complexes produced, **C1**-**C14**, were initially produced in reactions using the same stoichiometric ratio (Ln : TM : Acid : Polyalcohol : Triethylamine, 2 : 2 : 4 : 2 : 8 respectively), prior to the synthesis being refined in an attempt to target specific, now known structures.

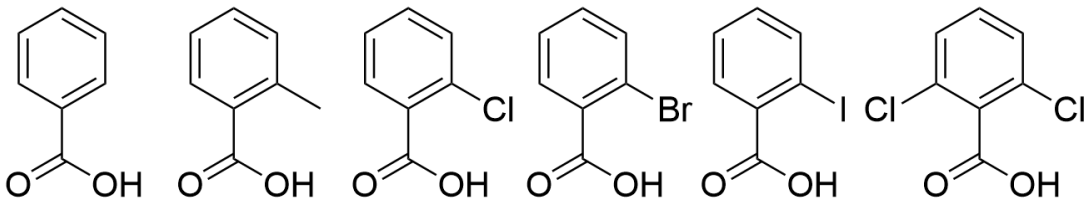

Figure 39- Bidentate ligands used in the synthesis described in chapter 2, from left to right: benzoic acid ([Benz]H), o-toluic acid ([o-Tol]H), 2-chlorobenzoic acid ([2Cl-Benz]H), 2-bromobenzoic acid ([2Br-Benz]H), 2-iodobenzoic acid ([2I-Benz]H), 2,6-dichlorobenzoic acid ([2,6Cl-Benz]H).

2.2.1 Notes on Metals for Coordination and Magnetism

Serendipitous assembly is an ideal methodology for broadening the knowledge of a known system, whilst also providing the opportunity to discover new and unexpected topologies, however elements of design are still required to guide or prove any specific hypothesis. On top of the ligands chosen for the synthetic methods described throughout this thesis, consideration was given to the metal ions utilised also.

Initially, lanthanides were chosen due to their highly anisotropic ground states and core-like 4f orbitals which limit the effect of the ligand field upon the ions magnetic properties. Our first choice was dysprosium, a common pick amongst magnetic research. Its high inherent magnetic moment, high spin, anisotropic nature and definition as a Kramers' ion whilst in its ubiquitous 3+ oxidation state makes it an ideal choice for analysis. In addition to this, two other lanthanides (or pseudo lanthanides) were selected that would provide the greatest comparative analysis: gadolinium and yttrium respectively. Gadolinium is a Kramers' ion in its 3+ oxidation state, and again has a relatively high inherent magnetic moment, however as its 4f orbital exhibits perfect half-occupancy (S = 7/2) in its 3+ oxidation state, the ion is paramagnetic but isotropic which is generally detrimental to SMM design. Similarly, yttrium in its diamagnetic 3+ oxidation state, although not a lanthanide has a sufficiently similar size and reactivity to mimic one in our structures. Ideally, by creating a series of isostructural complexes we can reveal how different traits considered important to the overall magnetism of a complex shapes the substances absolute properties.

As the project is targeting heterometallic complexes which can limit the effects of quantum tunnelling on the relaxation pathways, our design then turned to transition metals whose diffuse orbitals could interact with the core-like 4f orbitals of the lanthanides. We proposed a series of metals which were paramagnetic or diamagnetic, with variable preferred oxidation states, Kramers' ions or non-Kramers ions, that favoured low spin or high spin configurations within the octahedral ligand field and a selection of p-block post-transition metals. In sum total, eleven species were selected: aluminium, chromium, cobalt, copper, gallium, indium, iron, manganese, nickel, ruthenium, and zinc. The sources of the metals used throughout the synthesis for this project can be found in **Appendix A**.

2.2.2 Notes on the Binding Modes of Deprotonated [DIPSO]H_4

As a ligand [**DIPSO**]H_4 is significantly more versatile than the tridentate and tetradentate polyalcohol ligands that it mimics, and precedes, in this thesis. It contains five potential donor groups and so can bind in multiple modes within a complex. The hard, sterically unrestricted O-donors are likely to bridge multiple centres compared to the more sterically hindered sulphonic acid group or the tertiary N-donor. A summary of the binding modes found within the novel complexes synthesised for this project is shown in **Figure 40**. Where multiple binding modes of [**DIPSO**]H_4 or its deprotonated derivatives are present within a single complex, the crystal structure denotation Cn, where n = 1-14, is listed under multiple Harris notations.

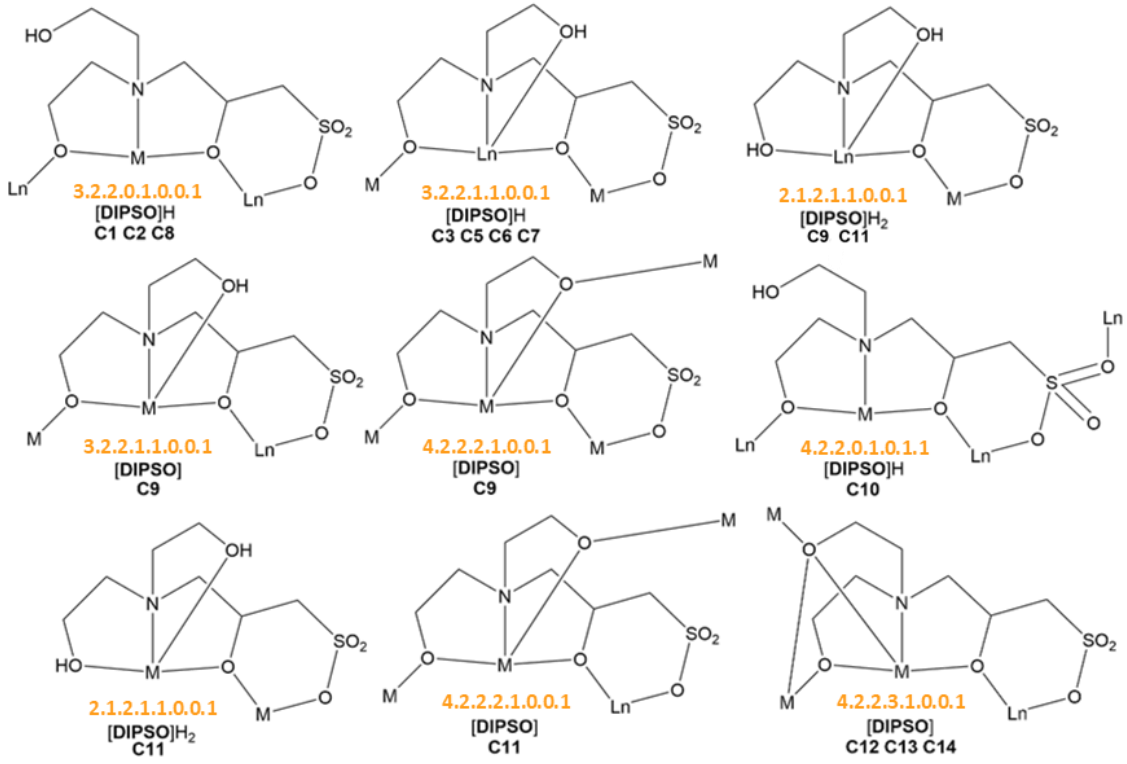

Figure 40- Binding modes of [**DIPSO**]$H_x^{(4-x)-}$ derivatives found in complexes **C1-C14**, where M is a transition metal ion and Ln is a lanthanide ion. Binding modes are denoted by their Harris notations in orange.

2.2.3 Notes on Crystallisation Methodologies

Crystallisation is a method of purification in which a structure grows as a result of changing physical or chemical properties imposed upon its system. The simplest form of crystallisation is precipitation from a solution, which can be driven by the influence of temperature on solubility. To be able to grow a crystal of sufficient quality for single crystal X-ray diffraction (SC-XRD) analysis, the rate of deposition must be kept low to ensure the structure orders itself in the most consistent pattern possible. High temperature crystallisation methods are therefore not applicable to crystal growth for SC-XRD. Instead by manipulating the solubility of our materials within their solvent systems, we can slowly induced nucleation and allow the crystal to grow over a prolonged period of time. The four main crystallisation methods used throughout this project are shown in **Figure 41**: slow deposition, slow evaporation, layer diffusion and vapour diffusion.

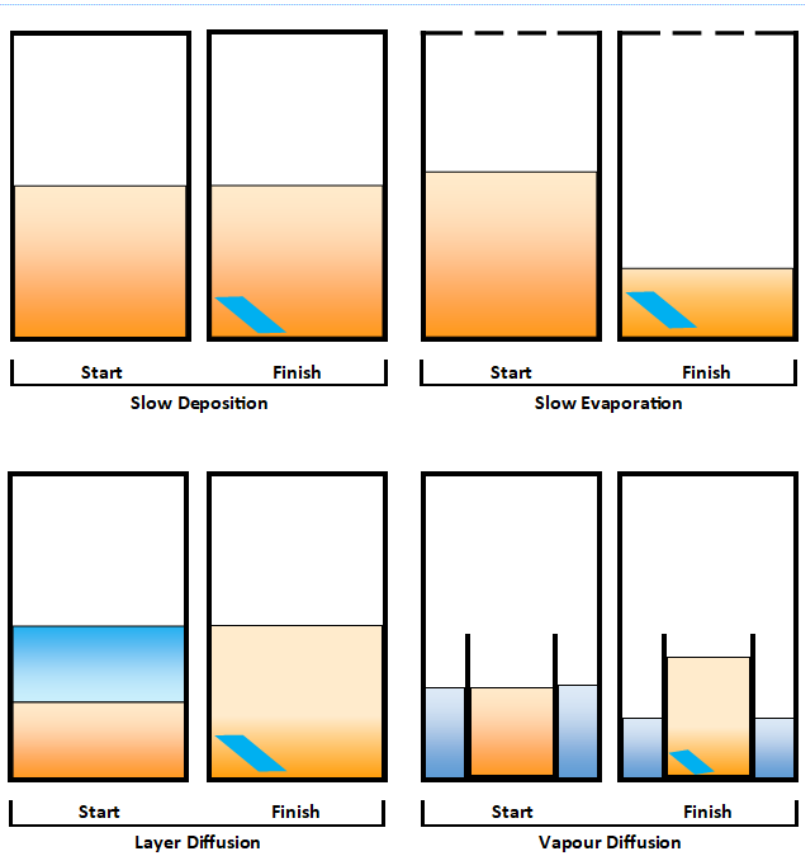

Figure 41- Crystallisation methodologies: slow deposition, top left; slow evaporation, top right; layer diffusion, bottom left; vapour diffusion, bottom right.

Slow deposition was the initial crystallisation method attempted for our samples, and assumes the material has a limited solubility in its synthetic solvent mixture. By sealing the system after filtering off any powder deposition, nucleation can occur, but often the material will prove sufficiently soluble in its chemical environment as to not progress through crystal growth. The second method, slow evaporation, then involves breaking the seal on the system, to allow the solvent (or solvent mixture) to slowly evaporate away. This has the effect of the resulting solution becoming more concentrated over time, thereby forcing the target material out of solution. This method can prove effective if the rate of evaporation is kept relatively consistent, but also consistently low thereby preventing the solid from quickly depositing as a powder rather than slowly growing into a larger crystalline structure. The third method, layer diffusion, involves the layering of a partially miscible solvent with a significant polarity difference to the original solvent (or solvent mix) that the target material is highly soluble in. By doing so, over time, the two solvent systems will slowly homogenise, and thereby make the overall new solvent system less favourable to the solute remaining in solution. This can prove exceedingly effective should sufficient thought be given to the identities of the component solvents. Finally, vapour diffusion is the technique with the slowest gradient of solubility change over time. Set up involves two containers, one smaller than the other: the smaller container holds the solute dissolved in a highly soluble solvent (or solvent mix), whilst the outer container holds a high volatility, low boiling point solvent antithetical to the solute, such as diethyl ether for polar solutes. Over time the outer solvent will evaporate and condense into the inner container, slowly lowering the overall solubility of the material in the new solvent mix. Nucleation can then occur within the inner container.

Crystallisation can be induced through the lowering of the samples temperature without effecting the quality of the crystals produced, but this methodology was not required for the crystalline samples discussed in this thesis.

It should be noted that the formation of a super-saturated solution does not guarantee the successful production of SC-XRD quality crystals, and often nucleation must be induced by providing an etched glass surface on which nucleation sites are more likely to form.

2.2.4 Structural Studies

Utilising [**DIPSO**]H_4 as our primary compound, the work in this chapter focussed upon the investigation of the coordination chemistry exhibited by the pentadentate ligand in heterometallic complexes. Complexes **C1**-**C14** were all realised by simple aerobic reactions to form novel complexes in solution by serendipitous assembly. In the following section each sample is discussed in terms of parameters extracted from single crystal X-ray diffraction (SC-XRD) analysis alongside pertinent synthetic details.

It should be noted, in both this chapter and all successive chapters, no powder X-ray diffraction (P-XRD) analysis, microanalysis or Fourier transform infrared (FT-IR) spectroscopy are presented for any coordination complex. As a result of the instrumentation for specialised techniques required for this project, namely single crystal X-ray diffraction (SC-XRD) analysis and superconducting quantum interference device (SQUID) magnetometry, residing at external institutions samples were prepared and shipped for analysis by technique specialists across the world. Unfortunately, many of these samples were destroyed in transit or were consumed in their entirety as part of these analyses. The decision was made by the team involved in this project that the time and funds required to repeat these experiments, to replicate the crystals described, was beyond that available for this project. The author is aware that this lack of analysis weakens any assertions made thereafter and aims to replicate this work prior to any attempts of publication.

The reaction of [**DIPSO**]H_4 with chromium (III) chloride hexahydrate, dysprosium (III) nitrate pentahydrate, benzoic acid and a suitable deprotonating agent (triethylamine) in a solvent mix of acetonitrile and methanol (4:1) produced a turquoise-grey mother liquor from which pink-purple crystals of $[Cr^{III}_2Dy^{III}_2(OMe)_2(Benz)_4(DIPSOH)_2(MeOH)_2]\cdot 2MeOH\cdot H_2O$, **C1**, were grown by layer diffusion using a methanol:diethyl ether (1:4) solvent system. Complex **C1** crystallises in the triclinic space group *P*-1, with the asymmetric unit containing half of the molecule. The unit cell of **C1** has a volume of 1495 $Å^3$ containing one molecule per unit cell and exhibiting the unit cell parameters: a = 11.6957(5) Å, b = 12.5208(5) Å, c = 12.5292(6) Å, α = 63.443(4)°, β = 69.211(4)°, γ = 69.673(4)° (See **Appendix B**, **Table S1**).

Complex **C1** is a heterometallic {3d-4f} tetranuclear complex with the metallic core displaying a planar butterfly-type topology, as shown in **Figure 42**.

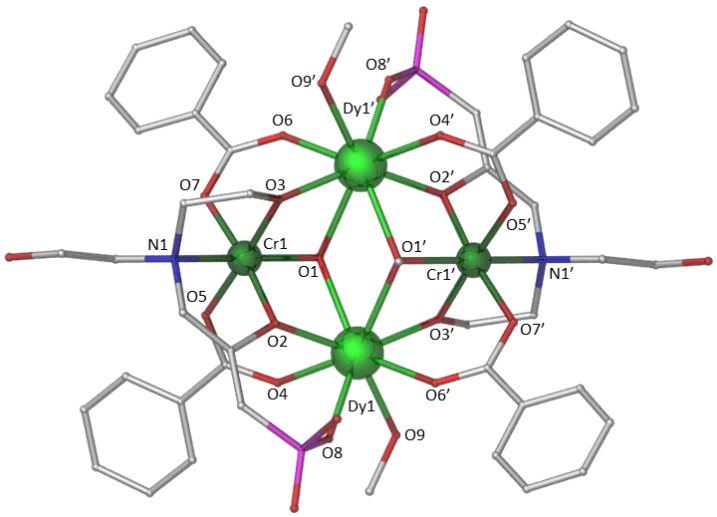

Figure 42- Molecular structure of **C1**: C atoms, grey; O atoms, red; N atoms, blue; S atoms, pink; Dy atoms, green; Cr atoms, dark green. H atoms have been omitted for clarity.

The asymmetric unit consists of half of the complex – thereby one chromium and one dysprosium ion each in the 3+ oxidation state – with the remainder generated by inversion symmetry. The two dysprosium (III) ions were found to be eight-coordinate with a distorted square antiprismatic geometry and occupy the 'body' sites of the butterfly. The two chromium (III) ions were found to be six-coordinate with a distorted octahedral geometry and occupy the 'wing' sites of the butterfly. Two μ_3 methoxide ligands bridge the two dysprosium (III) ions to each chromium (III) ion. Each chromium

(III) ion is further ligated by a triply deprotonated (**DIPSO**H)$^{3-}$ ligand, of Harris Notation 3.2.2.0.1.0.0.1, and two benzoate ligands completing the six-coordinate octahedral environment. The N-atom of the (**DIPSO**H)$^{3-}$ ligand chelates to the chromium (III) ion with the two deprotonated alkoxide arms bridging from the chromium (III) ions to the body dysprosium (III), moreover the sulphonate group further chelates to a dysprosium (III) ion from each ligand. The protonated alcohol arm of the (**DIPSO**H)$^{3-}$ ligands do not coordinate to the complex directly. The four carboxylate ligands each bridge from a chromium (III) ion to a dysprosium (III) ion in a μ_2 manner. The coordinate sphere of each dysprosium (III) ion is completed by a terminal methanol ligand.

Crystal packing diagrams for **C1** can be found in **Figure 43**. Intermolecular interactions are dominated by aromatic π, and C-H interactions derived from the benzoate ligands. Hydrogen bonds are present in the packing diagram such that the dysprosium bound methanol donates to the (**DIPSO**H)$^{3-}$ protonated free arm on an adjacent complex (1.977 Å, DHA angle 143.74°), and the (**DIPSO**H)$^{3-}$ protonated free arm donates to the dysprosium bound sulphate group on another adjacent complex (2.065 Å, DHA angle 135.66°).

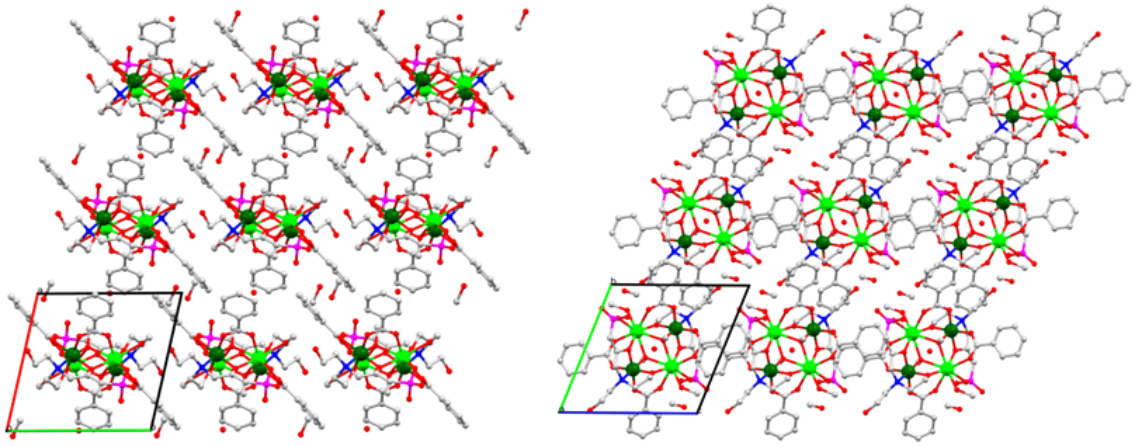

Figure 43- Crystal packing diagram of **C1** viewing the ab plane, left, and bc plane, right. Unit cell included for reference. C atoms, grey; O atoms, red; N atoms, blue; S atoms, pink; Dy atoms, green; Cr atoms, dark green. H atoms have been omitted for clarity.

The average Cr-$L_{N,O}$ bond length is found to be 1.99 Å with bond lengths ranging from 1.939-2.114 Å. The average Dy-O bond length is found to be 2.37 Å with bond lengths ranging from 2.278-2.512 Å. Selected bond lengths and bond angles are given below in **Table 4**.

Table 4- Selected bond lengths and bond angles for complex **C1**.

Atoms	Bond Length (Å)	Atoms	Bond Angle (°)
Dy1-O1	2.474	Dy1-O1-Cr1	96.19
Dy1-O1’	2.512	Dy1-O1’-Cr1’	96.06
Dy1-O3’	2.278	Dy1-O2-Cr1	102.10
Dy1-O6’	2.335	Dy1-O3’-Cr1’	104.90
Dy1-O9	2.412	Dy1-O1-Dy1’	116.02
Dy1-O8	2.340		
Dy1-O4	2.372		
Dy1-O2	2.307		
Cr1-O1	1.967		
Cr1-O2	1.956		
Cr1-O5	1.969		
Cr1-N1	2.114		
Cr1-O7	1.988		
Cr1-O3	1.939		
Dy1-Dy1’	4.229		
Dy1-Cr1	3.323		
Dy1-Cr1’	3.350		
Cr1-Cr1’	5.162		

The reaction of [**DIPSO**]H_4 with cobalt (II) nitrate hexahydrate, dysprosium (III) nitrate pentahydrate, o-toluic acid and triethylamine in a solvent mix of acetonitrile and methanol (4:1) produced a dark red mother liquor from which small green block crystals of $[Co^{III}_2Dy^{III}_2(OMe)_2(o\text{-}Tol)_4(DIPSOH)_2(H_2O)_2]\cdot MeCN\cdot 3H_2O$, **C2**, were grown by vapour diffusion using methanol:acetonitrile:diethyl ether (1:4:20) solvent system. Complex **C2** crystallises in the monoclinic space group *C 2/c*, with the asymmetric unit containing half of the molecule. The unit cell of **C2** has a volume of 7193 $Å^3$ containing four molecules per unit cell and exhibiting the unit cell parameters: a = 27.7298(7) Å, b = 12.9852(2) Å, c = 21.5187(4) Å, α = 90°, β = 111.828(2)°, γ = 90° (See **Appendix B**, **Table S1**).

Complex **C2** is a heterometallic {3d-4f} tetranuclear complex with the metallic core displaying a planar butterfly-type topology, as shown in **Figure 44**. The cobalt oxidation state was assigned through bond valence sum (BVS) calculations and balancing of charges.

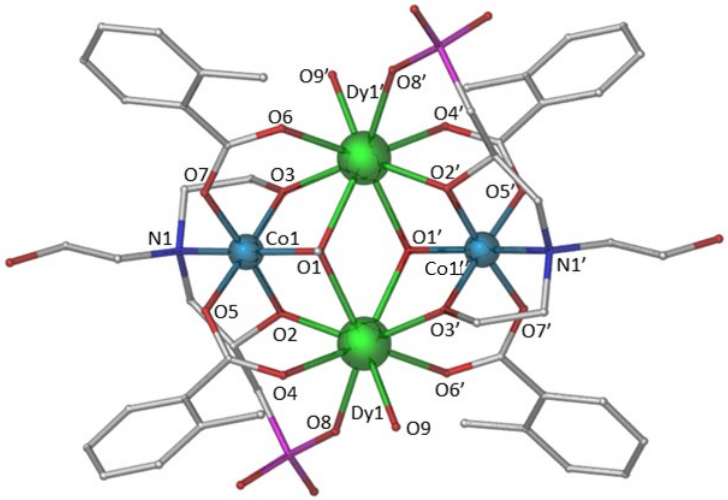

Figure 44- Molecular structure of **C2**: C atoms, grey; O atoms, red; N atoms, small blue; S atoms, pink; Dy atoms, green; Co atoms, large blue. H atoms have been omitted for clarity.

The asymmetric unit consists of half of the complex – thereby one cobalt and one dysprosium ion each in the 3+ oxidation state – with the remainder generated by inversion symmetry. The two dysprosium (III) ions were found to be eight-coordinate with a distorted square antiprismatic geometry and occupy the 'body' sites of the butterfly. The two cobalt (III) ions (BVS score = 2.92; **Table S7**) were found to be six-coordinate with a distorted octahedral geometry and occupy the 'wing' sites of the

butterfly. Two μ_3 methoxide ligands bridge the two dysprosium (III) ions to a cobalt (III) ion. Each cobalt (III) ion is further ligated by a triply deprotonated (**DIPSO**H)$^{3-}$ ligand, of Harris Notation 3.2.2.0.1.0.0.1, and two benzoate ligands completing the six-coordinate octahedral environment. The N-atom of the (**DIPSO**H)$^{3-}$ ligand chelates to the cobalt (III) ion with the two deprotonated alkoxide arms bridging from the cobalt (III) ions to the body dysprosium (III), moreover the sulphonate group further chelates to a dysprosium (III) ion from each ligand. The protonated alcohol arm of the (**DIPSO**H)$^{3-}$ ligand does not coordinate directly. The four carboxylate ligands each bridge from a cobalt (III) ion to a dysprosium (III) ion in a μ_2 manner. The coordination sphere of each dysprosium (III) ion is completed by a terminal water ligand.

Crystal packing diagrams for **C2** can be found in **Figure 45**. Intermolecular interactions are dominated by aromatic π, and C-H interactions derived from the o-toluate ligands. Hydrogen bonds are present in the crystal packing such that a water bound to dysprosium donates to the (**DIPSO**H)$^{3-}$ free arm on an adjacent complex (1.852 Å, DHA angle 151.52°) whilst the (**DIPSO**H)$^{3-}$ free arm concurrently donates to a dysprosium bound sulphate group on another adjacent complex (1.855 Å, DHA angle 170.32°)

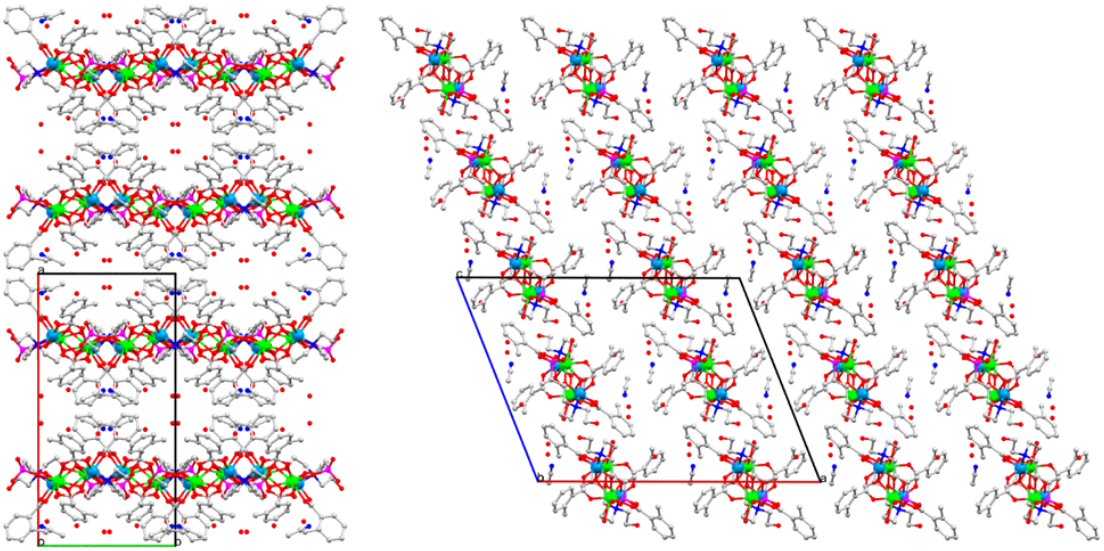

Figure 45- Crystal packing diagram of **C2** viewing the ab plane, left, and the ac plane, right. Unit cell included for reference. C atoms, grey; O atoms, red; N atoms, small blue; S atoms, pink; Dy atoms, green; Co atoms, large blue. H atoms have been omitted for clarity.

The average Co-$L_{N,O}$ bond length is found to be 1.92 Å with bond length ranging from 1.879-1.986 Å. The average Dy-O bond length if found to be 2.36 Å with bond lengths ranging from 2.270-2.449 Å. Selected bond lengths and bond angles are given below in **Table 5**.

Table 5- Selected bond lengths and bond angles for complex **C2**.

Atoms	Bond Length (Å)	Atoms	Bond Angle (°)
Dy1-O1	2.436	Dy1-O1-Co1	97.09
Dy1-O1’	2.449	Dy1-O1’-Co1’	97.85
Dy1-O3’	2.270	Dy1-O2-Co1	103.55
Dy1-O6’	2.336	Dy1-O3’-Co1’	106.13
Dy1-O9	2.400	Dy1-O1-Dy1’	113.60
Dy1-O8	2.376		
Dy1-O4	2.348		
Dy1-O2	2.294		
Co1-O1	1.939		
Co1-O2	1.888		
Co1-O5	1.921		
Co1-N1	1.986		
Co1-O7	1.924		
Co1-O3	1.879		
Dy1-Dy1’	4.088		
Dy1-Co1	3.295		
Dy1-Co1’	3.325		
Co1-Co1’	5.207		

The reaction of [**DIPSO**]H_4 with manganese (II) nitrate tetrahydrate, dysprosium (III) nitrate pentahydrate, o-toluic acid and triethylamine in a solvent mix of acetonitrile and methanol (4:1) produced a red-brown mother liquor from which small brown plate crystals of $[Mn^{III}_2Dy^{III}_2(OH)_2(o\text{-}Tol)_4(DIPSOH)_2(H_2O)_2]\cdot 4MeCN\cdot 2H_2O$, **C3**, were grown by vapour diffusion using methanol:acetonitrile:diethyl ether (1:4:20) solvent system. Complex **C3** crystallises in the triclinic space group *P*-1, with the asymmetric unit containing two halves of the molecule. The unit cell of **C3** has a volume of 1597 $Å^3$ containing one molecule per unit cell and exhibiting the unit cell parameters: a = 11.204(2) Å, b = 12.009(2) Å, c = 13.401(3) Å, α = 96.28(3)°, β = 110.18(3)°, γ = 104.78(3)° (See **Appendix B**, **Table S1**).

Complex **C3** is a heterometallic {3d-4f} tetranuclear complex with the metallic core displaying a planar reverse butterfly-type topology, as shown in **Figure 46**. The manganese oxidation state was assigned through bond valence sum (BVS) calculations and balancing of charges.

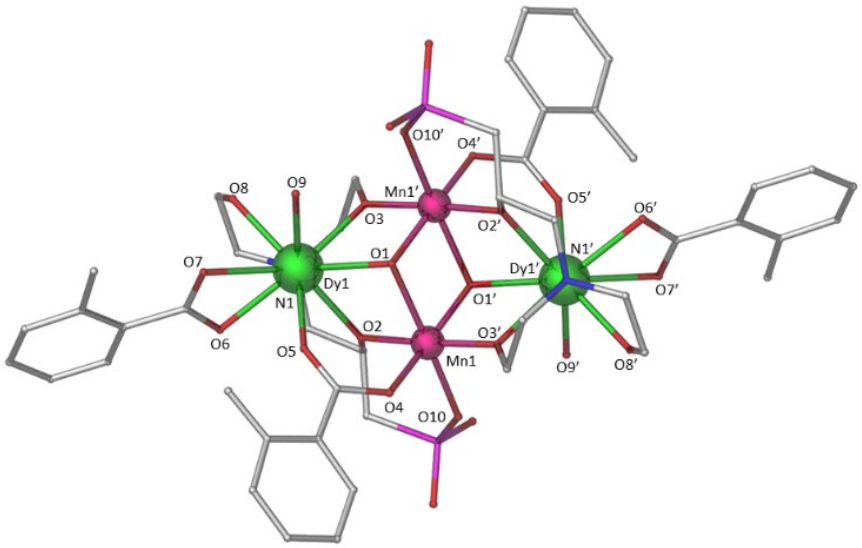

Figure 46- Molecular structure of **C3**: C atoms, grey; O atoms, red; N atoms, blue; S atoms, small pink; Dy atoms, green; Mn atoms, large pink. H atoms have been omitted for clarity.

The asymmetric unit consists of two halves of the complex – thereby one manganese and one dysprosium ion each in the 3+ oxidation state, per half – with the remainder generated by inversion symmetry. The two manganese (III) ions (BVS score = 3.22; **Table S8**) were found to be six-coordinate with a Jahn-Teller distorted octahedral geometry

and occupy the 'body' sites of the butterfly. The two dysprosium (III) ions were found to be nine-coordinate with a distorted capped square antiprismatic geometry and occupy the 'wing' sites of the butterfly. Two μ_3 methoxide ligands bridge the two manganese (III) ions to each dysprosium (III) ion. Each dysprosium (III) ion is further ligated by a triply deprotonated (**DIPSO**H)$^{3-}$ ligand, of Harris Notation 3.2.2.1.1.0.0.1, two o-toluate ligands, one bridging and one terminal, and a capping water ligand completing the nine-coordinate environment. The N-atom of the (**DIPSO**H)$^{3-}$ ligand chelates to the dysprosium (III) ion with the two deprotonated alkoxide arms bridging from the dysprosium (III) ions to the body manganese (III), moreover the sulphonate group further chelates to a manganese (III) ion from each ligand. The protonated alcohol arm of the (**DIPSO**H)$^{3-}$ ligand wraps around to coordinate with the same wing site dysprosium (III) as the N-atom. Two carboxylate ligands each bridge a dysprosium (III) ion to a manganese (III) ion in a μ_2 manner, whilst the remaining terminal carboxylates chelate as capping ligands.

Crystal packing diagrams for **C3** can be found in **Figure 47**. Intermolecular interactions are dominated by aromatic π, and C-H interactions derived from the o-toluate ligands. Hydrogen bonds are present in the crystal packing such that the short, protonated arm of (**DIPSO**H)$^{3-}$ bound to dysprosium only donates to a sulphate group on an adjacent complex (1.845 Å, DHA angle 167.01°), and an μ_3 hydroxide donates to an acetonitrile solvent molecule (2.135 Å, DHA angle 157.04). Within each complex a hydrogen bond is present such that a Dysprosium bound water donates to a sulphate group bound to a manganese ion (2.216 Å, DHA angle 148.7°).

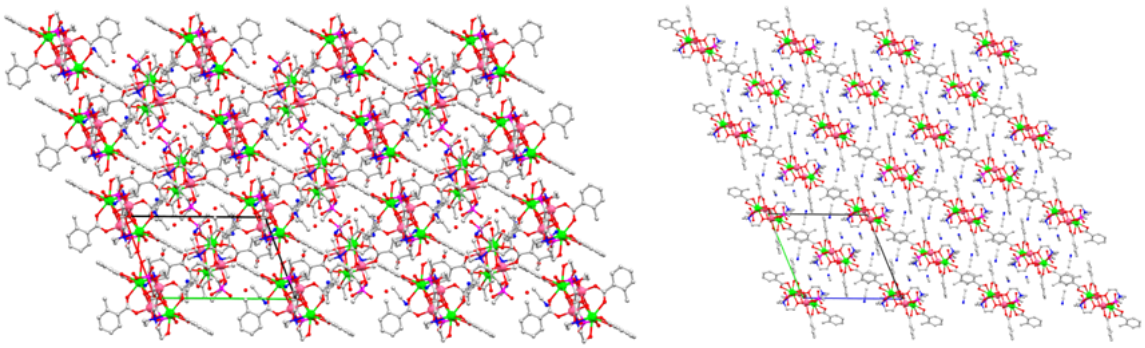

Figure 47- Crystal packing diagram of **C3** viewing the ab plane, left, and the bc plane, right. Unit cell included for reference. C atoms, grey; O atoms, red; N atoms, blue; S atoms, small pink; Dy atoms, green; Mn atoms, large pink. H atoms have been omitted for clarity.

The average Dy-$L_{N,O}$ bond length is found to be 2.43 Å with bond length ranging from 2.345-2.597 Å. The two manganese (III) ions display Jahn-Teller distorted octahedral geometries with the axially elongated axes lying parallel to each other, with average Mn-L_{ax} and Mn-L_{eq} bond lengths of 2.23 and 1.91 Å, respectively. Selected bond lengths and bond angles are given below in **Table 6**.

Table 6- Selected bond lengths and bond angles for complex **C3**.

Atoms	Bond Length (Å)	Atoms	Bond Angle (°)
Dy1-O1	2.424	Mn1-O1-Dy1	96.34
Dy1-O2	2.378	Mn1-O1'-Dy1'	105.44
Dy1-O5	2.414	Mn1-O2-Dy1	107.92
Dy1-O6	2.381	Mn1-O3'-Dy1'	110.38
Dy1-O7	2.468	Mn1-O1-Mn1'	99.24
Dy1-O8	2.451		
Dy1-O9	2.391		
Dy1-O3	2.347		
Dy1-N1	2.610		
Mn1-O1	2.235		
Mn1-O1'	1.944		
Mn1-O3'	1.888		
Mn1-O10	2.210		
Mn1-O4	1.918		
Mn1-O2	1.904		
Mn1-Mn1'	3.189		
Mn1-Dy1	3.474		
Mn1-Dy1'	3.487		
Dy1-Dy1'	6.188		

A second morphology, small brown hexagonal plate crystals of $[Mn^{II}_4Mn^{III}_2(O)_2(o\text{-}Tol)_{10}(MeCN)_3(H_2O)]\cdot MeCN$, **C4**, was concurrently produced from the reaction which produced crystals **C3**. Complex **C4** crystallises in the monoclinic space group *P 2₁/c*, with the asymmetric unit containing the entire molecule. The unit cell of **C4** has a volume of 1895 Å^3 containing four molecules per unit cell and exhibiting the unit cell parameters: a = 14.9870(2)Å, b = 32.0072(4) Å, c = 20.1982(3) Å, α = 90°, β = 107.958(2)°, γ = 90° (See **Appendix B**, **Table S1**).

Complex **C4** is a homometallic 3d hexanuclear complex with the metallic core displaying an edge-sharing dual distorted tetrahedra or face-sharing dual distorted cubane topology, as shown in **Figure 48**. The variable manganese oxidation states were assigned through bond valence sum (BVS) calculations and balancing of charges.

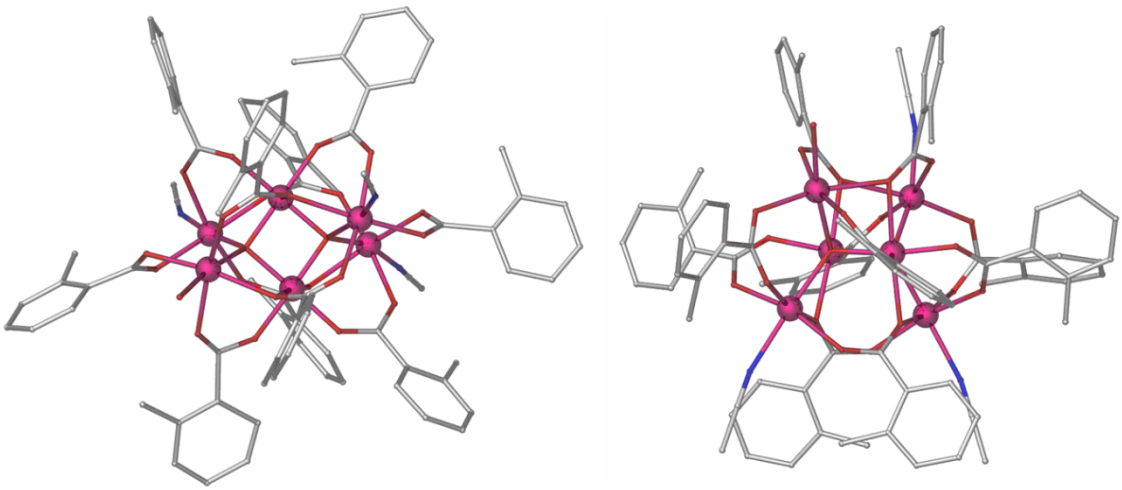

Figure 48- Molecular structure plan view (left) and front view (right)of **C4**: C atoms, grey; O atoms, red; N atoms, blue; Mn atoms, pink. H atoms have been omitted for clarity.

The asymmetric unit contains the entire complex – two manganese (III) ions and four manganese (II) ions. The two manganese (III) ions (BVS scores = 3.19, 3.11; **Table S9**) were found to be six-coordinate with a Jahn-Teller distorted octahedral geometry and occupy the most core-like sites of the complex. The Jahn-Teller axes of these two centres are non-parallel due to a twisting distortion. The four manganese (II) ions (BVS score = 2.16, 2.12, 1.99, 2.09; **Table S9**) were found to also be six-coordinate with a distorted octahedral geometry, exhibiting no Jahn-Teller distortion, whilst occupying the remaining vertices of the twisted tetrahedra. Two μ_4 oxide ligands bridge the two

manganese (III) ions to two manganese (II) ions each, forming the core of each distorted tetrahedron. Each core manganese (III) ion is further ligated by two μ_3 o-toluate ligands and two μ_2 o-toluate ligands which bind to the closest vertex manganese in each distorted tetrahedron, completing the six-coordinate environment. The outer manganese (II) ions are bound by four o-toluate ligands, three exhibiting a μ_2 binding mode whilst one exhibits a μ_3 binding mode and the μ_4 oxide ligand, leaving one open coordination site to be capped by a solvent molecule. This capping function is fulfilled by three acetonitrile molecules and one water molecule across the complex and breaking the complexes symmetry. A simplified skeletal form is given in **Figure 49**.

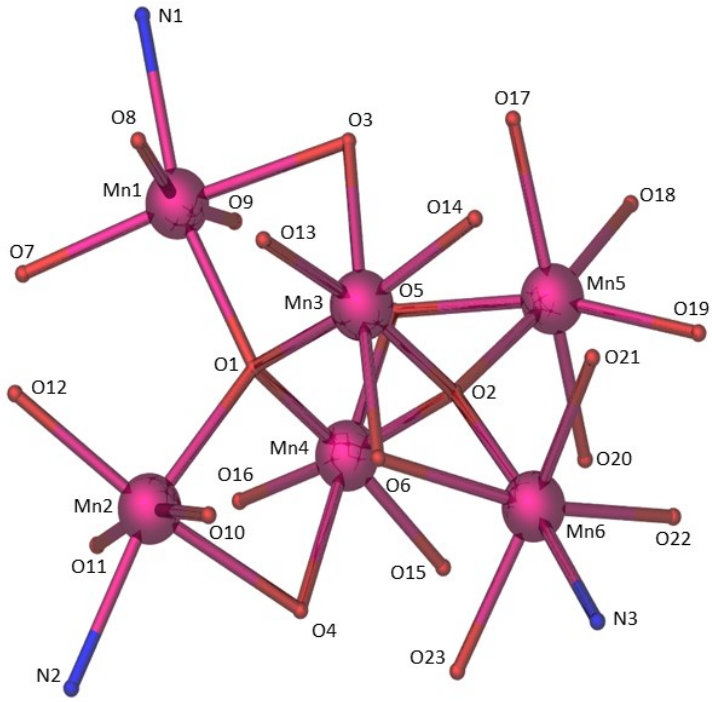

Figure 49- Skeletal form of **C4**: O atoms, red; N atoms, blue; Mn atoms, pink. H and C atoms have been omitted for clarity.

Crystal packing diagrams for **C4** can be found in **Figure 50**. Intermolecular interactions are dominated by aromatic π, and C-H interactions derived from the o-toluate ligands.

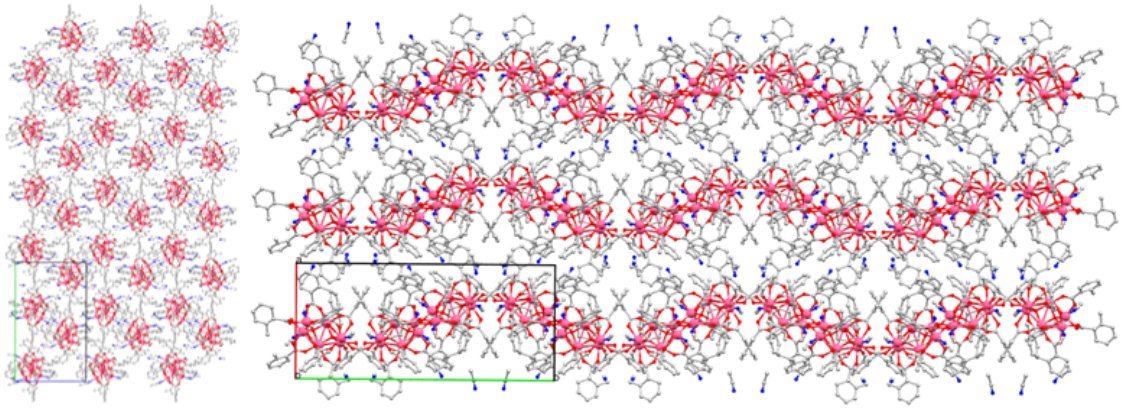

Figure 50- Crystal packing diagram of **C4** viewing the bc axis, left, and the ab axis, right. Unit cell included for reference. C atoms, grey; O atoms, red; N atoms, blue; Mn atoms, pink. H atoms have been omitted for clarity.

The average Mn^{II}-$L_{N,O}$ bond length is found to be 2.19 Å with bond length ranging from 2.090-2.326 Å. The two manganese (III) ions display Jahn-Teller distorted octahedral geometries with average Mn-L_{ax} and Mn-L_{eq} bond lengths of 2.21 and 1.93 Å, respectively. Selected bond lengths and bond angles are given below in **Table 7** and **Table 8**, respectively.

Table 7- Selected bond lengths for complex **C4**.

Atoms	Bond Length (Å)	Atoms	Bond Length (Å)
Mn1-O1	2.164	Mn4-O1	1.899
Mn1-O7	2.101	Mn4-O5	2.232
Mn1-O8	2.140	Mn4-O2	1.896
Mn1-N1	2.253	Mn4-O15	1.961
Mn1-O3	2.326	Mn4-O4	2.204
Mn1-O9	2.126	Mn4-O16	1.971
Mn2-O1	2.189	Mn5-O2	2.180
Mn2-O10	2.126	Mn5-O5	2.282
Mn2-O4	2.297	Mn5-O17	2.128
Mn2-N2	2.272	Mn5-O18	2.256
Mn2-O11	2.129	Mn5-O19	2.210
Mn2-O12	2.126	Mn5-O20	2.155
Mn3-O1	1.885	Mn6-O2	2.206
Mn3-O13	1.958	Mn6-O21	2.175
Mn3-O3	2.206	Mn6-O22	2.090
Mn3-O14	1.966	Mn6-N3	2.288
Mn3-O2	1.880	Mn6-O23	2.146
Mn3-O6	2.215	Mn6-O6	2.256

Table 8- Selected bond angles for complex **C4**.

Atoms	Bond Angle (°)	Atoms	Bond Angle (°)
Mn1-O1-Mn2	116.72	Mn3-O2-Mn4	95.95
Mn1-O1-Mn3	100.93	Mn3-O2-Mn5	119.93
Mn1-O1-Mn4	122.21	Mn3-O2-Mn6	99.87
Mn1-O3-Mn3	82.27	Mn3-O6-Mn6	89.01
Mn2-O1-Mn3	118.88	Mn4-O2-Mn5	100.39
Mn2-O1-Mn4	101.62	Mn4-O2-Mn6	120.84
Mn2-O4-Mn4	89.67	Mn4-O5-Mn5	88.02
Mn3-O1-Mn4	95.66	Mn5-O2-Mn6	118.78

The reaction of [**DIPSO**]H_4 with manganese (II) nitrate tetrahydrate, gadolinium (III) nitrate hexahydrate, benzoic acid and triethylamine in a solvent mix of acetonitrile and methanol (4:1) produced a red-brown mother liquor from which small green crystals of $[Mn^{III}_2Gd^{III}_2(OH)_2(Benz)_4(DIPSOH)_2(MeOH)_2]\cdot 2MeCN$, **C5**, were grown by vapour diffusion using methanol:acetonitrile:diethyl ether (1:4:20) solvent system. Complex **C5** crystallises in the triclinic space group *P*-1, with the asymmetric unit containing half of the molecule. The unit cell of **C5** has a volume of 1429 Å^3 containing one molecule per unit cell and exhibiting the unit cell parameters: a = 10.4655(4) Å, b = 10.6178(4) Å, c = 14.4781(5) Å, α = 83.2760(10)°, β = 73.4410(10)°, γ = 67.8960(10)° (See **Appendix B**, **Table S1**).

Complex **C5** is a heterometallic {3d-4f} tetranuclear complex with the metallic core displaying a planar reverse butterfly-type topology, as shown in **Figure 51**. The manganese oxidation state was assigned through bond valence sum (BVS) calculations and balancing of charges.

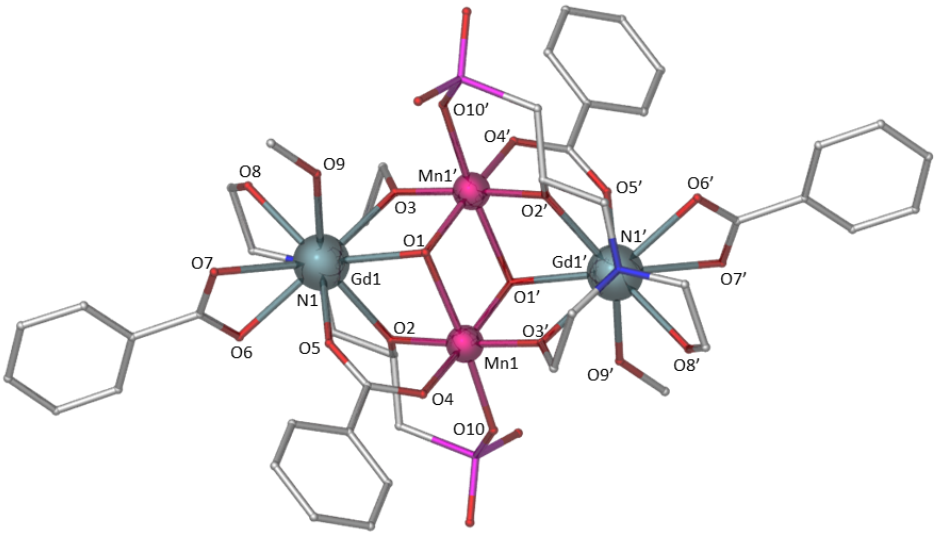

Figure 51- Molecular structure of **C5**: C atoms, grey; O atoms, red; N atoms, blue; S atoms, small pink; Gd atoms, silver; Mn atoms, large pink. H atoms have been omitted for clarity.

The asymmetric unit consists of half of the complex – thereby one manganese and one gadolinium ion each in the 3+ oxidation state – with the remainder generated by inversion symmetry. The two manganese (III) ions (BVS score = 3.22; **Table S10**) were found to be six-coordinate with a Jahn-Teller distorted octahedral geometry and occupy

the 'body' sites of the butterfly. The two gadolinium (III) ions were found to be nine-coordinate with a distorted capped square antiprismatic geometry and occupy the 'wing' sites of the butterfly. Two μ_3 hydroxide ligands bridge the two manganese (III) ions to each gadolinium (III) ion. Each gadolinium (III) ion is further ligated by a triply deprotonated (**DIPSO**H)$^{3-}$ ligand, of Harris Notation 3.2.2.1.1.0.0.1, two benzoate ligands – one bridging and one terminal – and a capping methanol ligand, completing the nine-coordinate environment. The N-atom of the (**DIPSO**H)$^{3-}$ ligand chelates to the gadolinium (III) ion with the two deprotonated alkoxide arms bridging from the gadolinium (III) ions to the body manganese (III), moreover the sulphonate group further chelates to a manganese (III) ion from each ligand. The protonated alcohol arm of the (**DIPSO**H)$^{3-}$ ligand wraps around to coordinate with the same wing site gadolinium (III) as the N-atom. Two carboxylate ligands bridge a gadolinium (III) ion to a manganese (III) ion in a μ_2 manner, whilst the remaining terminal carboxylates chelate as capping ligands.

Crystal packing diagrams for complex **C5** can be found in **Figure 52**. Intermolecular interactions are dominated by aromatic π, and C-H interactions derived from the benzoate ligands. Hydrogen bonds are present in the crystal packing such that the protonated short arm of (**DIPSO**H)$^{3-}$ bound only to gadolinium donates to a manganese bound sulphate group on an adjacent complex (1.753 Å, DHA angle 167.98°) and a μ_3-hydroxide binds to a solvent acetonitrile (2.139 Å, DHA angle 158.56°).

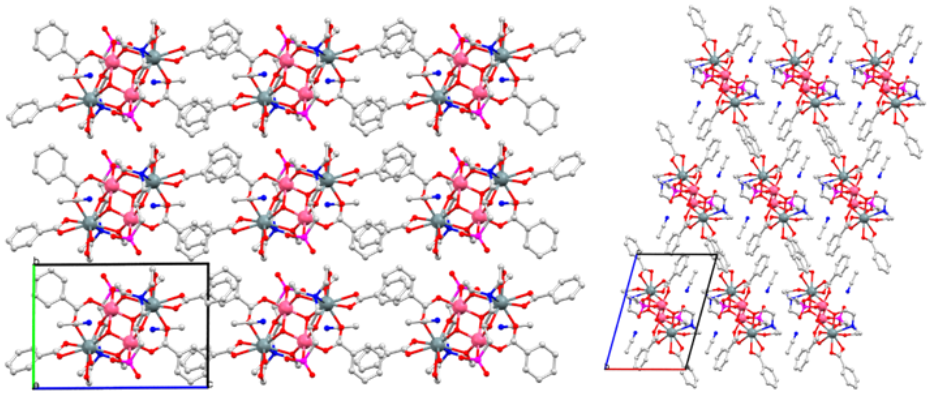

Figure 52- Crystal packing diagram of **C5** viewing the bc plane, left, and the ac plane, right. Unit cell included for reference. C atoms, grey; O atoms, red; N atoms, blue; S atoms, small pink; Gd atoms, silver; Mn atoms, large pink. H atoms have been omitted for clarity.

The average Gd-$L_{N,O}$ bond length is found to be 2.45 Å with bond length ranging from 2.380-2.618 Å. The two manganese (III) ions display Jahn-Teller distorted octahedral geometries with the axially elongated axes lying parallel to each other, with average Mn-L_{ax} and Mn-L_{eq} bond lengths of 2.22 and 1.91 Å, respectively. Selected bond lengths and bond angles are given below in **Table 9**.

Table 9- Selected bond lengths and bond angles for complex **C5**.

Atoms	Bond Length (Å)	Atoms	Bond Angle (°)
Gd1-O1	2.432	Mn1-O1-Gd1	95.56
Gd1-O2	2.382	Mn1-O1'-Gd1'	105.75
Gd1-O5	2.405	Mn1-O2-Gd1	108.41
Gd1-O6	2.410	Mn1-O3'-Gd1'	110.16
Gd1-O7	2.500	Mn1-O1-Mn1'	99.55
Gd1-O8	2.477		
Gd1-O9	2.424		
Gd1-O3	2.380		
Gd1-N1	2.618		
Mn1-O1	2.271		
Mn1-O1'	1.945		
Mn1-O3'	1.877		
Mn1-O10	2.169		
Mn1-O4	1.938		
Mn1-O2	1.899		
Mn1-Mn1'	3.228		
Mn1-Dy1	3.484		
Mn1-Dy1'	3.502		
Gd1-Gd1'	6.196		

The reaction of [**DIPSO**]H_4 with iron (III) nitrate nonahydrate, dysprosium (III) nitrate pentahydrate, benzoic acid and triethylamine in a solvent mix of acetonitrile and methanol (4:1) produced an orange mother liquor from which small golden-yellow octahedral prism crystals of $[Fe^{III}_2Dy^{III}_2(OH)_2(Benz)_2(DIPSOH)_2(NO_3)_2(H_2O)_2]\cdot MeCN\cdot 2H_2O$, **C6**, were grown by vapour diffusion using methanol:acetonitrile:diethyl ether (1:4:10) solvent system. Complex **C6** crystallises in the tetragonal space group *I* $4_1/a$, with the asymmetric unit containing half of the molecule. The unit cell of **C6** has a volume of 12163 $Å^3$ containing eight molecules per unit cell and exhibiting the unit cell parameters: a = 19.15160(10) Å, b = 19.15160(10)Å, c = 33.1601(2) Å, α = 90°, β = 90°, γ = 90° (See **Appendix B**, **Table S2**).

Complex **C6** is a heterometallic {3d-4f} tetranuclear complex with the metallic core displaying a planar reverse butterfly-type topology, as shown in **Figure 53**. The iron oxidation state was assigned through bond valence sum (BVS) calculations and balancing of charges.

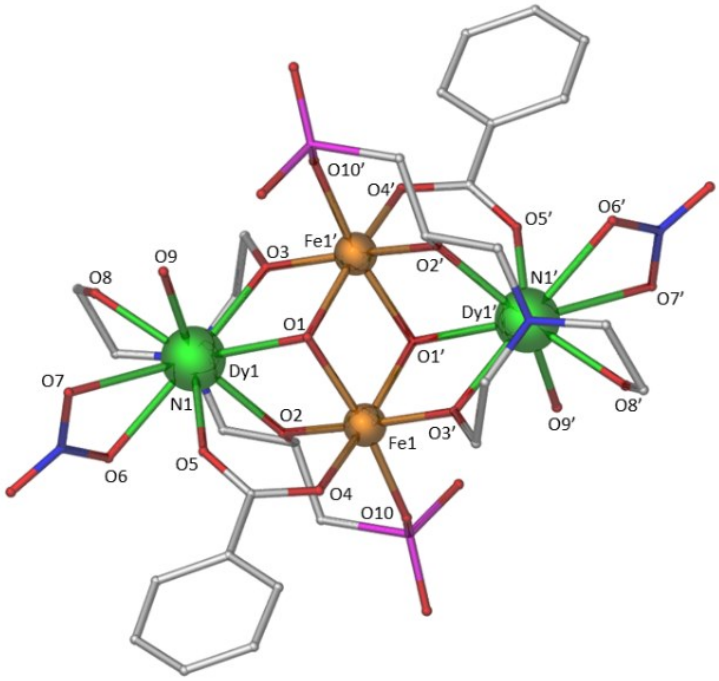

Figure 53- Molecular structure of **C6**: C atoms, grey; O atoms, red; N atoms, blue; S atoms, pink; Dy atoms, green; Fe atoms, orange. H atoms have been omitted for clarity.

The asymmetric unit consists of half of the complex – thereby one iron and one dysprosium ion each in the 3+ oxidation state – with the remainder generated by

inversion symmetry. The two iron (III) ions (BVS score = 2.99; **Table S11**) were found to be six-coordinate with a distorted octahedral geometry and occupy the 'body' sites of the butterfly. The two dysprosium (III) ions were found to be nine-coordinate with a distorted capped square antiprismatic geometry and occupy the 'wing' sites of the butterfly. Two μ_3 hydroxide ligands bridge the two iron (III) ions to each dysprosium (III) ion. Each dysprosium (III) ion is further ligated by a triply deprotonated (**DIPSO**H)$^{3-}$ ligand, of Harris Notation 3.2.2.1.1.0.0.1, a bridging benzoate ligand, a terminal nitrate ligand and a capping water ligand, completing the nine-coordinate environment. The N-atom of the (**DIPSO**H)$^{3-}$ ligand chelates to the dysprosium (III) ion with the two deprotonated alkoxide arms bridging from the dysprosium (III) ions to the body iron (III), moreover the sulphonate group further chelates to an iron (III) ion from each ligand. The protonated alcohol arm of the (**DIPSO**H)$^{3-}$ ligand wraps around to coordinate with the same wing site dysprosium (III) as the N-atom. Two carboxylate ligands bridge a dysprosium (III) ion to an iron (III) ion in a μ_2 manner, whilst the remaining terminal nitrates chelate as capping ligands.

Crystal packing diagrams for **C6** can be found in **Figure 54.** Intermolecular interactions are dominated by aromatic π, and C-H interactions derived from the benzoate ligands. Hydrogen bonds are present in the crystal packing such that a dysprosium bound water molecule donates to an iron bound sulphate group on an adjacent complex (1.981 Å, DHA angle 143.69°) and within the same complex (1.981 Å, DHA angle 116.44°). Additional hydrogen bonding includes the short, dysprosium bound only, arm of the (**DIPSO**H)$^{3-}$ ligand donating to an iron bound sulphate group on another adjacent complex (1.787 Å, DHA angle 170.92°) and a μ_3 hydroxide donating to a solvent water molecule (1.914 Å, DHA angle 172.37°)

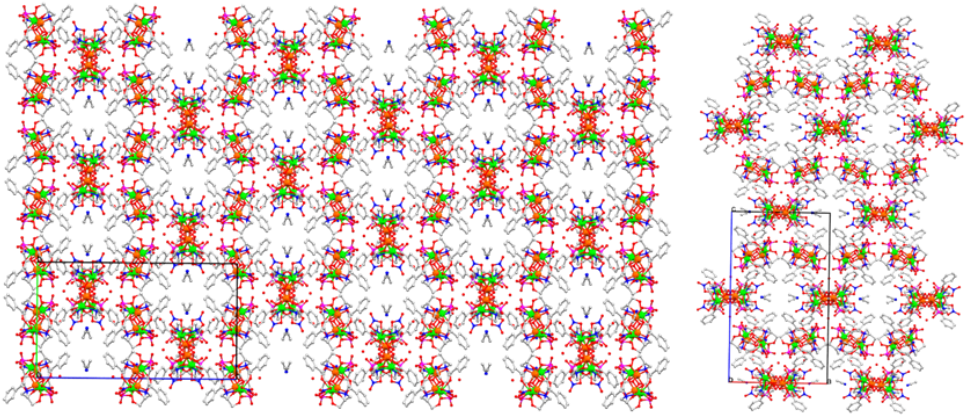

Figure 54- Crystal packing diagram of **C6** viewing the bc plane, left, and the ac plane, right. Unit cell included for reference. C atoms, grey; O atoms, red; N atoms, blue; S atoms, pink; Dy atoms, green; Fe atoms, orange. H atoms have been omitted for clarity.

The average Dy-$L_{N,O}$ bond length is found to be 2.43 Å with bond length ranging from 2.296-2.603 Å. The average Fe-O bond length if found to be 2.02 Å with bond lengths ranging from 1.935-2.072 Å. Selected bond lengths and bond angles are given below in **Table 10**.

Table 10- Selected bond lengths and bond angles for complex **C6**.

Atoms	Bond Length (Å)	Atoms	Bond Angle (°)
Dy1-O1	2.441	Fe1-O1-Dy1	98.19
Dy1-O2	2.296	Fe1-O1'-Dy1'	103.57
Dy1-O5	2.383	Fe1-O2-Dy1	104.74
Dy1-O6	2.464	Fe1-O3'-Dy1'	113.00
Dy1-O7	2.601	Fe1-O1-Fe1'	100.26
Dy1-O8	2.394		
Dy1-O9	2.336		
Dy1-O3	2.311		
Dy1-N1	2.603		
Fe1-O1	2.054		
Fe1-O1'	2.063		
Fe1-O3'	1.935		
Fe1-O10	2.072		
Fe1-O4	1.992		
Fe1-O2	2.000		
Fe1-Fe1'	3.160		
Fe1-Dy1	3.407		
Fe1-Dy1'	3.547		
Dy1-Dy1'	6.196		

A second morphology, small brown block crystals of $[Fe^{III}_{12}Dy^{III}_{4}O_6(OH)_4(Benz)_{12}(DIPSO)_4(DIPSOH_2)_2]\cdot 5MeCN\cdot 8H_2O$, **C7**, was concurrently produced from the reaction which produced crystals **C6**. Complex **C7** crystallises in the monoclinic space group *P* $2_1/c$, with the asymmetric unit containing half of the molecule. The unit cell of **C7** has a volume of 9228 $Å^3$ containing four molecules per unit cell and exhibiting the unit cell parameters: a = 16.0618(2) Å, b = 18.4844(2) Å, c = 31.3103(4) Å, α = 90°, β = 96.9390(10)°, γ = 90° (See **Appendix B**, **Table S2**).

Complex **C7** is a heterometallic {3d-4f} hexadecanuclear dimeric complex containing twelve iron (III) ions and four dysprosium (III) ions, as shown in **Figure 55**. The iron oxidation state was assigned through bond valence sum (BVS) calculations and balancing of charges.

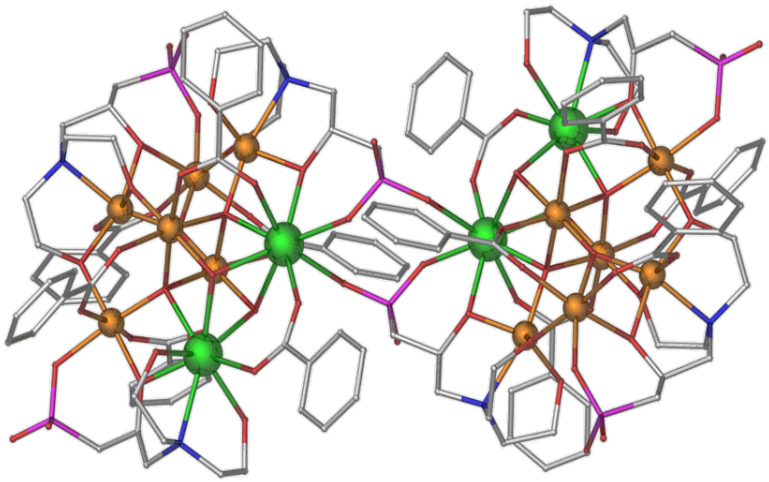

Figure 55- Molecular structure of **C7**: C atoms, grey; O atoms, red; N atoms, blue; S atoms, pink; Dy atoms, large green; Fe atoms, orange. H atoms have been omitted for clarity.

The asymmetric unit contains the monomeric unit, two dysprosium (III) and six iron (III) ions (BVS scores = 3.01, 3.12, 3.09, 2.88, 3.05, 2.81; **Table S12**), with the remaining ions generated by inversion symmetry. The complex is dimeric consisting of two $\{Fe_6Dy_2\}$ monomer units linked by two sulphonate bridges. Each monomer unit comprises of a distorted $\{Fe_2Dy_2\}$ cubane with two additional iron (III) ions binding to an iron-iron-dysprosium face by a core μ_4 oxide ligand. The remaining two iron ions in each monomeric unit form a puckered oxo-centred triangle with one of the $\{Fe_2Dy_2\}$ cubane iron vertices *via* a μ_3 oxide ligand. Both dysprosium (III) ions are eight-coordinate

displaying distorted square antiprismatic geometries and five of the six iron (III) ions have a distorted octahedral geometry whilst the final five-coordinate iron centre instead displays a distorted trigonal bipyramidal geometry. The five-coordinate iron is found in a position facially bound to the $\{Fe_2Dy_2\}$ cubane nearest to the sulphonate linking bridges. Each monomeric unit is bound together by three (**DIPSO**)H_4 ligand derivatives, one of which is doubly deprotonated and two of which are fully deprotonated, and each exhibits its own binding mode. The doubly deprotonated (**DIPSO**H_2)$^{2-}$ ligand binds in a 2.1.2.1.1.0.0.1 mode between the non-bridging dysprosium ion, *via* the N-atom and chelating with three of the alkoxide arms, and one of the face bound non-cubane iron ions, *via* the deprotonated alkoxide arm and sulphonate group. A fully deprotonated (**DIPSO**)$^{4-}$ ligand binds to the bridging dysprosium cubane vertex in a 3.2.2.1.1.0.0.1 manner to two iron ions, whilst the final deprotonated (**DIPSO**)$^{4-}$ ligand binds 4.2.2.2.1.0.0.1 between four of the iron ions, isolated from the dysprosium pair. The dysprosium pair itself is further bound together one benzoate ligand and two μ_3 methoxide ligands which stabilise the cubane structure. Each monomeric unit is further ligated by five additional benzoate ligands, all of which bind μ_2, completing the coordination environments of all the metal ions present. A simplified skeletal form is given in **Figure 56**.

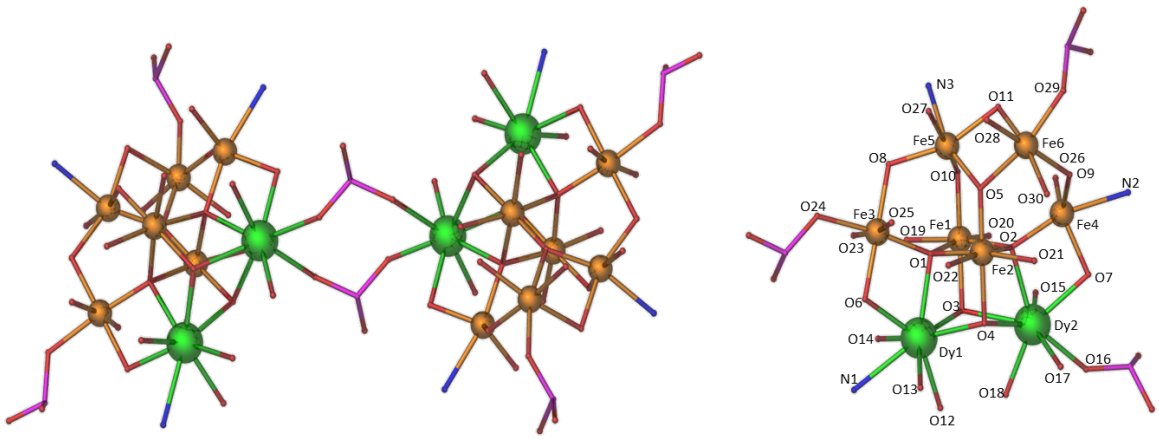

Figure 56- Skeletal form of the dimer (left) and monomeric unit (right) for **C7**: O atoms, red; N atoms, blue; S atoms, pink; Dy atoms, green; Fe atoms, orange. H and C atoms have been omitted for clarity.

Crystal packing diagrams of **C7** can be found in **Figure 57**. Intermolecular interactions are dominated by aromatic π, and C-H interactions derived from the benzoate ligands.

Hydrogen bonds are present in the crystal packing such that one short arm of (**DIPSO**H_2)$^{2-}$ singularly bound to dysprosium donates to a solvent water molecule (1.745 Å, DHA angle 160.56°) and the other short arm bound also to only dysprosium donates to a solvent acetonitrile molecule (1.932 Å, DHA angle 150.72°). It should be noted, additional hydrogen bonds are hypothesised to be present within this structure but due to the positional uncertainty of protons on unbound solvent water molecules it is not possible to accurately record hydrogen bond distances or angles associated to these interactions.

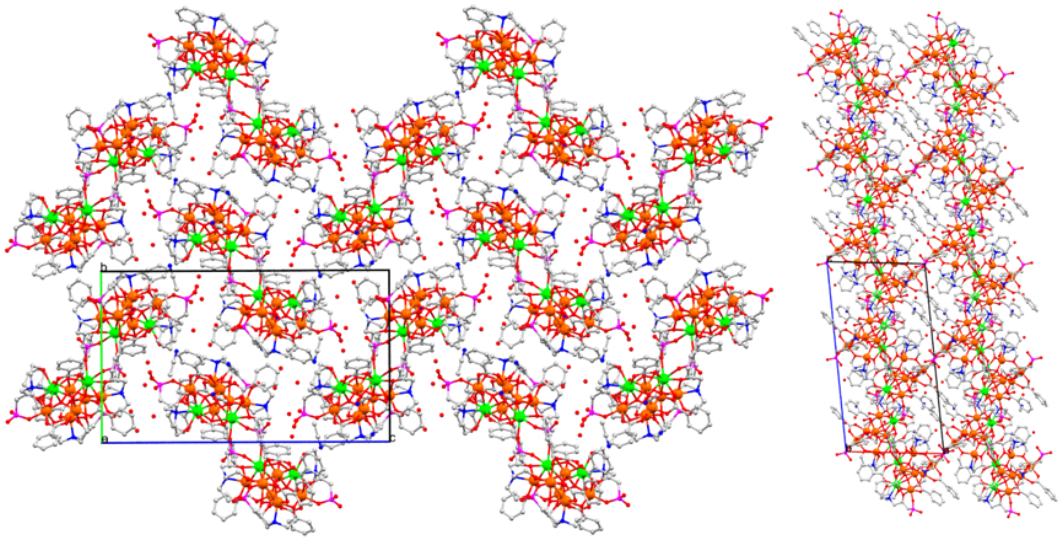

Figure 57- Crystal packing diagram of **C7** viewing the bc plane, left, and the ac plane, right. Cell unit included for reference. C atoms, grey; O atoms, red; N atoms, blue; S atoms, pink; Dy atoms, large green; Fe atoms, orange. H atoms have been omitted for clarity.

The average Dy-$L_{N,O}$ bond length is found to be 2.37 Å with bond length ranging from 2.266-2.593 Å. The average Fe- $L_{N,O}$ bond length if found to be 2.02 Å with bond lengths ranging from 1.860-2.252 Å. Selected bond lengths and bond angles are given below in **Table 11** and **Table 12**, respectively.

Table 11- Selected bond lengths for complex **C7**.

Atoms	Bond Length (Å)	Atoms	Bond Length (Å)
Fe1-O1	1.985	Fe5-O22	2.104
Fe1-O19	2.041	Fe5-N3	2.180
Fe1-O10	1.977	Fe5-O11	2.001
Fe1-O20	2.013	Fe6-O5	2.030
Fe1-O2	2.020	Fe6-O28	2.017
Fe1-O3	2.056	Fe6-O11	2.084
Fe2-O1	2.029	Fe6-O29	2.001
Fe2-O5	1.860	Fe6-O26	2.097
Fe2-O2	2.006	Fe6-O30	2.021
Fe2-O21	2.025	Dy1-O1	2.458
Fe2-O4	2.085	Dy1-O3	2.330
Fe2-O22	2.042	Dy1-O4	2.339
Fe3-O1	1.925	Dy1-O12	2.400
Fe3-O6	1.985	Dy1-O13	2.364
Fe3-O23	2.041	Dy1-N1	2.593
Fe3-O24	2.068	Dy1-O14	2.342
Fe3-O8	2.000	Dy1-O6	2.274
Fe3-O25	2.029	Dy2-O2	2.378
Fe4-O2	1.927	Dy2-O15	2.330
Fe4-O26	1.861	Dy2-O7	2.323
Fe4-O9	1.950	Dy2-O16	2.379
Fe4-N2	2.252	Dy2-O17	2.266
Fe4-O7	1.961	Dy2-O18	2.379
Fe5-O5	1.885	Dy2-O4	2.415
Fe5-O10	2.026	Dy2-O3	2.426
Fe5-O8	1.970		

Table 12- Selected bond angles for complex **C7**.

Atoms	Bond Angle (°)	Atoms	Bond Angle (°)
Fe1-O1-Dy1	103.66	Fe2-O4-Dy2	100.90
Fe1-O1-Fe2	95.51	Fe2-O5-Fe5	125.90
Fe1-O1-Fe3	126.63	Fe2-O5-Fe6	128.65
Fe1-O2-Dy2	103.45	Fe3-O1-Dy1	101.25
Fe1-O2-Fe2	95.17	Fe3-O6-Dy1	105.95
Fe1-O2-Fe4	125.23	Fe3-O8-Fe5	115.79
Fe1-O3-Dy1	105.92	Fe4-O2-Dy2	101.90
Fe1-O3-Dy2	100.71	Fe4-O7-Dy2	102.77
Fe1-O10-Fe 5	120.92	Fe4-O9-Fe6	130.57
Fe2-O1-Dy1	100.25	Fe5-O5-Fe6	100.23
Fe2-O1-Fe3	125.20	Fe5-O11-Fe6	94.70
Fe2-O2-Dy2	104.62	Dy1-O3-Dy2	106.96
Fe2-O2-Fe4	123.70	Dy1-O4-Dy2	107.05
Fe2-O4-Dy1	102.53		

The reaction of [**DIPSO**]H_4 with iron (III) nitrate nonahydrate, dysprosium (III) nitrate pentahydrate, 2-iodobenzoic acid and triethylamine in a solvent mix of acetonitrile and methanol (4:1) produced an orange mother liquor from which small yellow crystals of $[Fe^{III}_2Dy^{III}_2(OH)_2(2I\text{-}Benz)_2(DIPSOH)_2(NO_3)_2(MeOH)_2]\cdot 3MeCN$, **C8**, were grown by vapour diffusion using methanol:acetonitrile:diethyl ether (2:3:20) solvent system. Complex **C8** crystallises in the monoclinic space group *P 2₁/c*, with the asymmetric unit containing half of the molecule. The unit cell of **C8** has a volume of 2755 Å^3 containing two molecules per unit cell and exhibiting the unit cell parameters: a = 10.9709(5) Å, b = 18.3660(9) Å, c = 13.7053(7) Å, α = 90°, β = 94.0190(10)°, γ = 90° (See **Appendix B**, **Table S2**).

Complex **C8** is a heterometallic {3d-4f} tetranuclear complex with the metallic core displaying a planar reverse butterfly-type topology, as shown in **Figure 58**. The iron oxidation state was assigned through bond valence sum (BVS) calculations and balancing of charges.

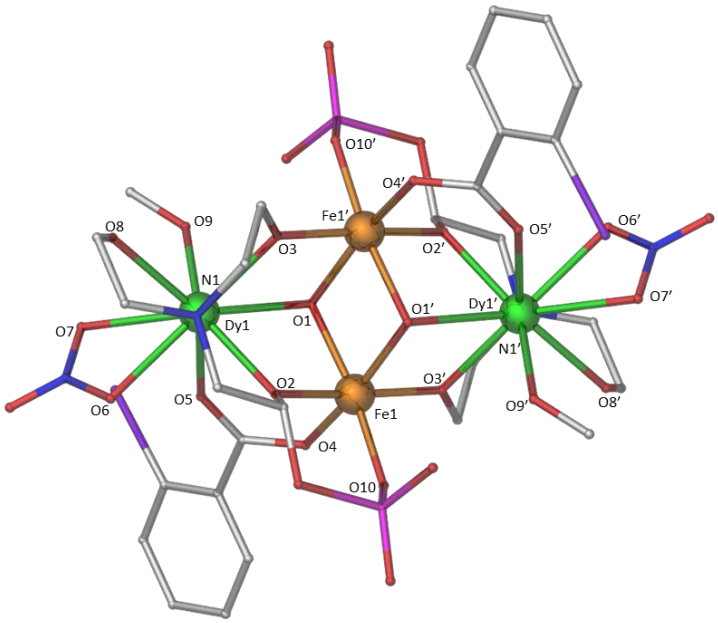

Figure 58- Molecular structure of **C8**: C atoms, grey; O atoms, red; N atoms, blue; S atoms, pink; I atoms, purple; Dy atoms, green; Fe atoms, orange. H atoms have been omitted for clarity.

The asymmetric unit consists of half of the complex – thereby one iron and one dysprosium ion each in the 3+ oxidation state – with the remainder generated by inversion symmetry. The two iron (III) ions (BVS score = 3.08; **Table S13**) were found to

be six-coordinate with a distorted octahedral geometry and occupy the 'body' sites of the butterfly. The two dysprosium (III) ions were found to be nine-coordinate with a distorted capped square antiprismatic geometry and occupy the 'wing' sites of the butterfly. The observed coordination environment of **C8** is the same as that described for **C6**, however, 2-I-benzoate is substituted in the place of the benzoate ligands and MeOH is the capping ligand rather than H_2O.

Crystal packing diagrams of **C8** can be found in **Figure 59**. Intermolecular interactions are dominated by aromatic π, and C-H interactions derived from the halo-benzoate ligands. Hydrogen bonds are present in the crystal packing such that a dysprosium bound methanol donates to a sulphate group within the same complex (1.886 Å, DHA 163.61°), no intermolecular hydrogen bonds were found.

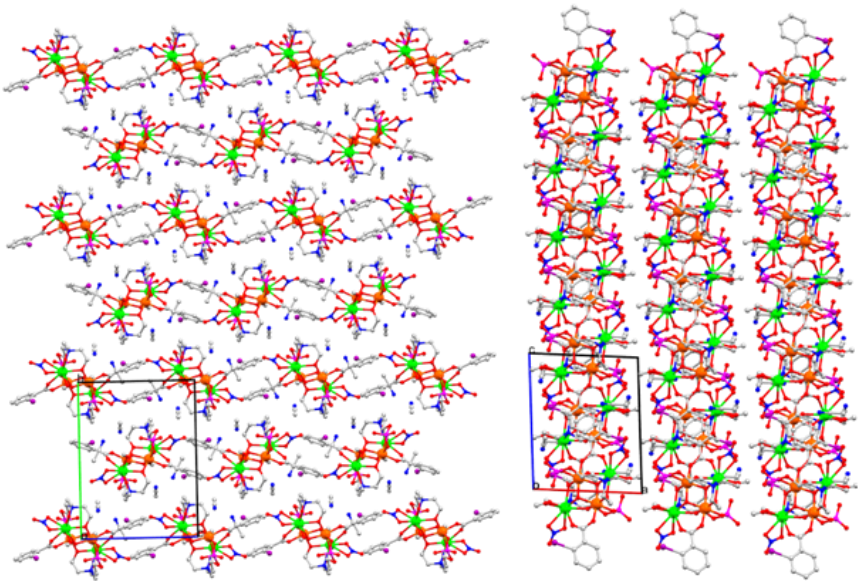

Figure 59- Crystal packing diagram of **C8** viewing the bc plane, left, and the ac plane, right. Unit cell included for reference. C atoms, grey; O atoms, red; N atoms, blue; S atoms, pink; I atoms, purple; Dy atoms, green; Fe atoms, orange. H atoms have been omitted for clarity.

The average Dy-$L_{N,O}$ bond length is found to be 2.42 Å with bond length ranging from 2.307-2.586 Å. The average Fe-O bond length if found to be 2.01 Å with bond lengths ranging from 1.929-2.069 Å. Selected bond lengths and bond angles are given below in **Table 13**.

Table 13- Selected bond lengths and bond angles for complex **C8**.

Atoms	Bond Length (Å)	Atoms	Bond Angle (°)
Dy1-O1	2.455	Fe1-O1-Dy1	98.11
Dy1-O2	2.307	Fe1-O1'-Dy1'	103.33
Dy1-O5	2.387	Fe1-O2-Dy1	105.85
Dy1-O6	2.453	Fe1-O3'-Dy1'	113.62
Dy1-O7	2.504	Fe1-O1-Fe1'	100.69
Dy1-O8	2.444		
Dy1-O9	2.368		
Dy1-O3	2.312		
Dy1-N1	2.586		
Fe1-O1	2.069		
Fe1-O1'	2.067		
Fe1-O3'	1.929		
Fe1-O10	2.043		
Fe1-O4	1.966		
Fe1-O2	1.981		
Fe1-Fe1'	3.185		
Fe1-Dy1	3.427		
Fe1-Dy1'	3.555		
Dy1-Dy1'	6.215		

The reaction of [**DIPSO**]H_4 with chromium (III) nitrate hexahydrate, dysprosium (III) nitrate pentahydrate, 2,6-dichlorobenzoic acid and triethylamine in a solvent mix of acetonitrile and methanol (4:1) produced a blue-grey mother liquor from which very small purple crystals of $[Cr^{III}Dy^{III}_2(OH)(2,6\text{-}Cl\text{-}Benz)_4(DIPSOH)(NO_3)_3]^{2-}\cdot(NEt_3H)^+_2$, **C9**, were grown by layer diffusion from a methanol:diethyl ether (1:4) solvent system. Complex **C9** crystallises in the triclinic space group *P-1*, with the asymmetric unit containing the entire molecule. The unit cell of **C9** has a volume of 3658 Å^3 containing two molecules per unit cell and exhibiting the unit cell parameters: a = 15.1726(2) Å, b = 15.7352(2) Å, c = 16.0390(3) Å, α = 104.481(2)°, β = 96.4280(10)°, γ = 95.0300(10)° (See **Appendix B**, **Table S2**).

Complex **C9** is a heterometallic {3d-4f} trinuclear complex with the metallic core displaying a planar triangular topology. This could also be considered an incomplete butterfly complex with a chromium (III) ion absent, as shown in **Figure 60**.

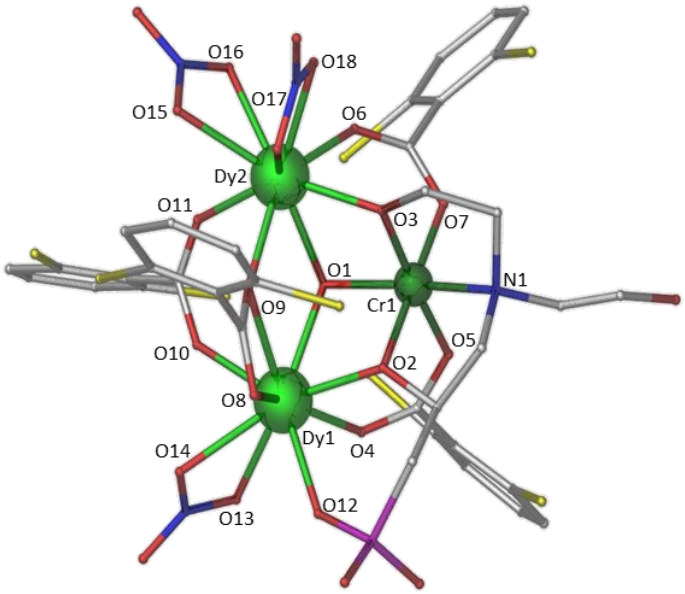

Figure 60- Molecular structure of **C9**: C atoms, grey; O atoms, red; N atoms, blue; S atoms, pink; Cl atoms, yellow; Dy atoms, large green; Cr atoms, small green. H atoms and counter-ions have been omitted for clarity.

The asymmetric unit consists of the entire complex – thereby one chromium and two dysprosium ions each in the 3+ oxidation state. The two dysprosium (III) ions were found to be nine-coordinate with a distorted capped square antiprismatic geometry and occupy the pseudo- 'body' sites of the partial butterfly. The chromium (III) ion was found

to be six-coordinate with a distorted octahedral geometry and occupy the pseudo-'wing' site of the partial butterfly. One μ_3 hydroxide ligand bridges the two dysprosium (III) ions to the chromium (III) ion. The chromium (III) ion is further ligated by a triply deprotonated (**DIPSO**H)$^{3-}$ ligand, of Harris Notation 3.2.2.0.1.0.0.1, and two halo-benzoate ligands completing the six-coordinate octahedral environment. The N-atom of the (**DIPSO**H)$^{3-}$ ligand chelates to the chromium (III) ion with the two deprotonated alkoxide arms bridging from the chromium (III) ions to the pseudo-body dysprosium (III). Moreover, the sulphonate group further chelates to one of the dysprosium (III) ions, which shall be further denoted as Dy(1). The protonated alcohol arm of the (**DIPSO**H)$^{3-}$ ligand does not coordinate to the complex directly. Two carboxylate ligands each bridge from the chromium (III) ion to a dysprosium (III) ion in a μ_2 manner. The remaining two carboxylates bridge the two dysprosium (III) ions in two different modes – one in the usual μ_2 motif, with one oxygen atom of the carboxylate group coordinating to each metal ion, whilst the second binds as a capping agent to Dy(1) whilst also bridging μ_2 to Dy(2), an uncommon structural motif. The coordinate sphere of Dy(1) is completed by a terminal nitrate ligand, whilst Dy(2) requires two terminal nitrates to similarly complete its coordination sphere. Charges are balanced by two triethylammonium cations associated to the complex.

Crystal packing diagrams of **C9** can be found in **Figure 61**. Intermolecular interactions are dominated by aromatic π, and C-H interactions derived from the halo-benzoate ligands. Hydrogen bonds are hypothesised to contribute to the association of the triethylammonium cation by interaction with a sulphate oxygen. However, protons are not present on the counterion making it impossible to confirm without further computation.

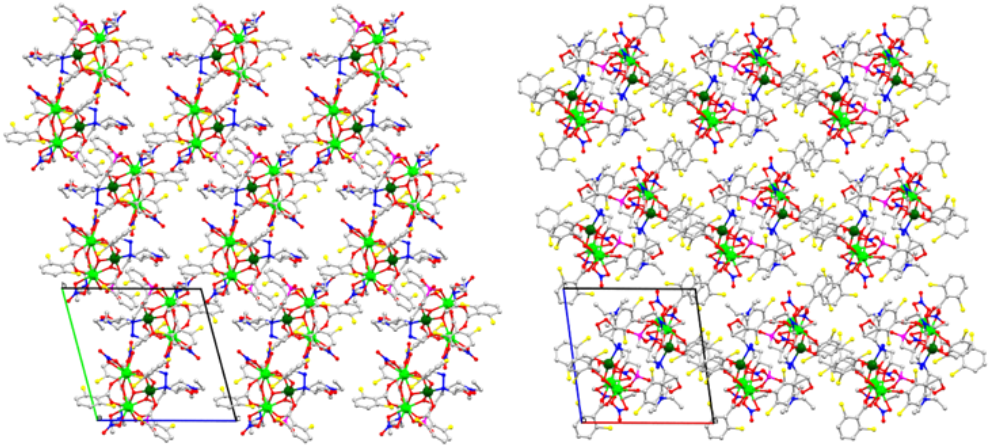

Figure 61- Crystal packing diagram of **C9** viewing the bc plane, left, and the ac plane, right. Unit cell included for reference. C atoms, grey; O atoms, red; N atoms, blue; S atoms, pink; Cl atoms, yellow; Dy atoms, large green; Cr atoms, small green. H atoms and counter-ions have been omitted for clarity.

The average Cr-$L_{N,O}$ bond length is found to be 1.98 Å with bond length ranging from 1.927-2.091 Å. The average Dy(1)-O bond length if found to be 2.42 Å with bond lengths ranging from 2.283-2.544 Å. The average Dy(2)-O bond length if found to be 2.40 Å with bond lengths ranging from 2.272-2.491 Å. Selected bond lengths and bond angles are given below in **Table 14**.

Table 14- Selected bond lengths and bond angles for complex **C9**.

Atoms	Bond Length (Å)	Atoms	Bond Length (Å)
Cr1-O1	1.947	Dy2-O15	2.460
Cr1-O3	1.927	Dy2-O16	2.491
Cr1-O7	1.986	Dy2-O17	2.476
Cr1-N1	2.091	Dy2-O18	2.452
Cr1-O5	1.990	Dy2-O6	2.366
Cr1-O2	1.927	Dy2-O3	2.272
Dy1-O1	2.407		
Dy1-O2	2.283		
Dy1-O4	2.425		
Dy1-O12	2.352		
Dy1-O13	2.429		
Dy1-O14	2.486	Atoms	Bond Angle (°)
Dy1-O8	2.480	Cr1-O1-Dy1	100.31
Dy1-O10	2.350	Cr1-O1-Dy2	98.85
Dy1-O9	2.544	Cr1-O2-Dy1	105.42
Dy2-O1	2.449	Cr1-O3-Dy2	105.74
Dy2-O9	2.336	Dy1-O1-Dy2	111.86
Dy2-O11	2.339	Dy1-O9-Dy2	110.98

The reaction of [**DIPSO**]H_4 with iron (III) nitrate nonahydrate, dysprosium (III) nitrate pentahydrate, o-toluic acid and triethylamine in acetonitrile produced an orange mother liquor from which orange-brown crystals of $[Fe^{III}_4Dy^{III}_6O_2(OH)_6(o\text{-}Tol)_{14}(DIPSOH)_2(MeOH)_2(H_2O)_4]\cdot 8MeOH$, **C10**, were grown by layer diffusion using a methanol:diethyl ether (2:3) solvent system. Complex **C10** crystallises in the monoclinic space group *P 2₁/n*, with the asymmetric unit containing half of the molecule. The unit cell of **C10** has a volume of 7816 Å^3 containing two molecules per unit cell and exhibiting the unit cell parameters: a = 15.650(3) Å, b = 29.970(6) Å, c = 16.862(3) Å, α = 90°, β = 98.77(3)°, γ = 90° (See **Appendix B**, **Table S2**).

Complex **C10** is a heterometallic {3d-4f} decanuclear complex containing four iron (III) ions and six dysprosium (III) ions, as shown in **Figure 62**. The iron oxidation state was assigned through bond valence sum (BVS) calculations and balancing of charges.

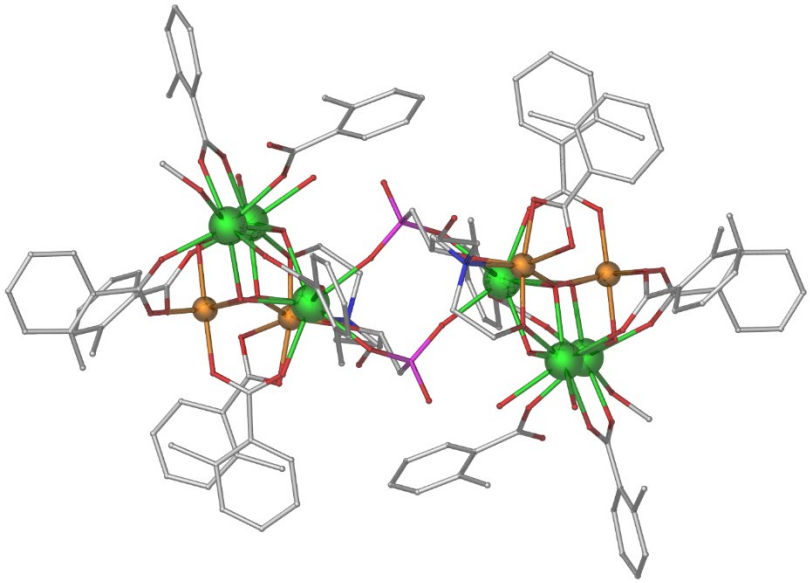

Figure 62- Molecular structure of **C10**: C atoms, grey; O atoms, red; N atoms, blue; S atoms, pink; Dy atoms, green; Fe atoms, orange. H atoms have been omitted for clarity.

The asymmetric unit contains half of the dimeric complex – three dysprosium (III) and two iron (III) ions – with the remaining ions generated by inversion symmetry. The metal ion core can be described in two ways. The first description is that of two distorted $\{Dy^{III}_3Fe^{III}O(OH)_3\}$ cubanes, each capped by an iron (III) ion that lies on the oxide vertex. The second view is that of two dysprosium (III) triangles with an iron (III) ion (BVS score

= 3.04; **Table S14**) lying below the centre of the triangle forming a tetrahedron, with the second iron (III) ion (BVS score = 2.95; **Table S14**) capping a triangular face. There are six hydroxide and two oxide ions, all form part of the cubane vertices – the hydroxide ligands are μ_3 bridging while the oxide is μ_4. Fourteen o-toluate ligands are present – ten are μ_2 bridging across five of the six faces of the two cubanes. Two chelate each to the capping iron (III) ion, while two lie terminal coordinating to a dysprosium (III) ion *via* a single O-atom. Two triply deprotonated (**DIPSO**H)$^{3-}$ ligands are found, of Harris Notation 4.2.2.0.1.0.1.1. The N-atom of the (**DIPSO**H)$^{3-}$ ligand chelates to the capping iron (III) atom with the two deprotonated alkoxide arms bridging from the iron (III) ions each to a cubane dysprosium (III) ion. The protonated alcohol arm of the (**DIPSO**H)$^{3-}$ ligand does not coordinate to the complex directly. The sulphonate group then forms a bridge between the two monomeric cubanes *via* two of its O-atoms. Four terminal water and two methanol ligands complete the coordination sphere of four of the dysprosium (III) ions. A simplified skeletal form is given in **Figure 63**.

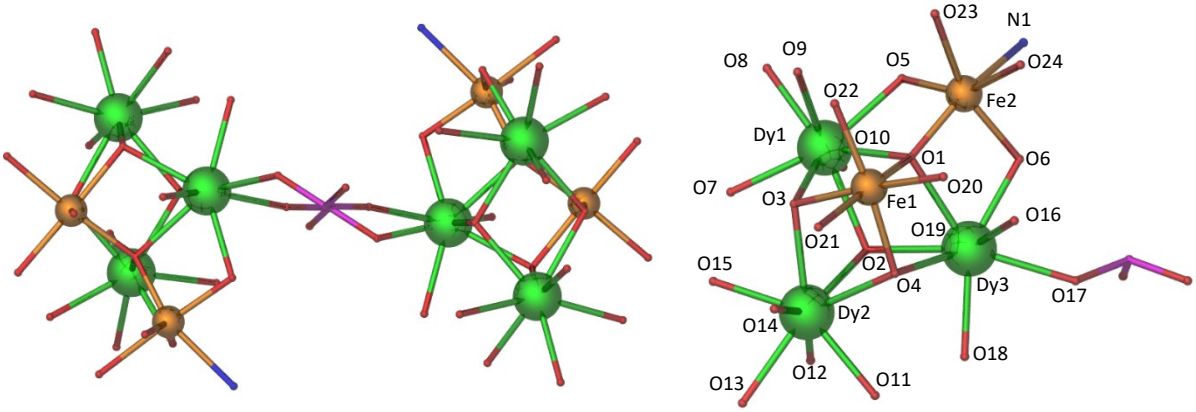

Figure 63- Skeletal form of the dimer (left) and monomeric unit (right) for **C10**: O atoms, red; N atoms, blue; S atoms, pink; Dy atoms, large green; Fe atoms, orange. H and C atoms have been omitted for clarity.

Crystal packing diagrams of **C10** can be found in **Figure 64**. Intermolecular interactions are dominated by aromatic π, and C-H interactions derived from the o-toluate ligands. Hydrogen bonds are present in the crystal packing such that a μ_3-hydroxide donates to an unbound solvent methanol (1.867 Å, DHA angle 170.60°), a second unbound solvent methanol donates to an o-toluate ligand bound to iron in the complex (1.903 Å, DHA angle 175.45°). Two water molecules terminally bound to a dysprosium ion donate to

the same, third, unbound solvent methanol (2.002 Å, DHA angle 143.10° and 1.900 Å, DHA angle 170.37° respectively). One of these water molecules additionally donates to a separate, fourth, unbound solvent methanol (1.906 Å, DHA angle 162.22°). The other water molecule additionally donates internally to the bridging sulphate group (1.839 Å, DHA angle 167.88°). Finally, another internal hydrogen bond is located between an accepting monodentate o-toluate ligand and donating capping methanol bound to the same dysprosium (1.727 Å, DHA angle 178.24°)

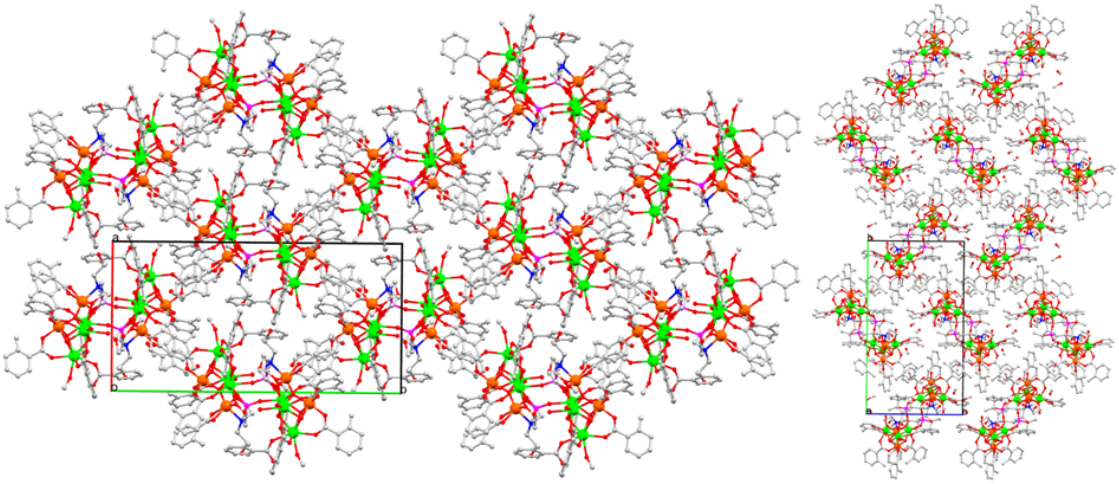

Figure 64- Crystal packing diagram of **C10** viewing the ab plane, left, and the bc plane, right. Cell unit included for reference. C atoms, grey; O atoms, red; N atoms, blue; S atoms, pink; Dy atoms, green; Fe atoms, orange. H atoms have been omitted for clarity.

All six dysprosium (III) ions are eight-coordinate with distorted square antiprismatic geometries, with an average Dy-O bond length of 2.36 Å. The four iron (III) ions display distorted octahedral geometries, with an average Fe-$L_{N,O}$ bond length of 2.03 Å. Selected bond lengths and bond angles are given below in **Table 15** and **Table 16**, respectively.

Table 15- Selected bond lengths for complex **C10**.

Atoms	Bond Length (Å)	Atoms	Bond Length (Å)
Dy1-O1	2.392	Dy3-O16	2.359
Dy1-O10	2.426	Dy3-O17	2.398
Dy1-O2	2.373	Dy3-O18	2.320
Dy1-O3	2.342	Dy3-O4	2.338
Dy1-O7	2.330	Dy3-O2	2.409
Dy1-O8	2.423	Dy3-O19	2.346
Dy1-O9	2.374	Fe1-O1	1.951
Dy1-O5	2.289	Fe1-O20	1.991
Dy2-O2	2.364	Fe1-O4	2.021
Dy2-O4	2.369	Fe1-O21	2.058
Dy2-O11	2.327	Fe1-O3	2.055
Dy2-O12	2.382	Fe1-O22	2.001
Dy2-O13	2.410	Fe2-O1	1.892
Dy2-O14	2.342	Fe2-O5	1.959
Dy2-O15	2.326	Fe2-O23	2.161
Dy2-O3	2.399	Fe2-N1	2.248
Dy3-O1	2.412	Fe2-O24	2.084
Dy3-O6	2.297	Fe2-O6	1.943

Table 16- Selected bond angles for complex **C10**.

Atoms	Bond Angle (°)	Atoms	Bond Angle (°)
Dy1-O1-Dy3	108.28	Dy2-O3-Fe1	102.27
Dy1-O1-Fe1	101.34	Dy2-O4-Dy3	106.78
Dy1-O1-Fe2	101.54	Dy2-O4-Fe1	104.36
Dy1-O2-Dy2	107.30	Dy3-O1-Fe1	100.18
Dy1-O2-Dy3	109.02	Dy3-O1-Fe2	101.08
Dy1-O3-Dy2	107.18	Dy3-O4-Fe1	100.59
Dy1-O3-Fe1	99.89	Dy3-O6-Fe2	103.64
Dy1-O5-Fe2	103.10	Fe1-O1-Fe2	141.85
Dy2-O2-Dy3	104.65		

The reaction of [**DIPSO**]H_4 with cobalt (II) nitrate hexahydrate, dysprosium (III) nitrate pentahydrate, 2-chlorobenzoic acid and triethylamine in acetonitrile produced a dark grey mother liquor from which blue-green crystals of $[Co^{II}_2Co^{III}Dy^{III}(OMe)(DIPSOH_2)_2(DIPSO)(2Cl\text{-}Benz)]\cdot MeOH\cdot H_2O$, **C11**, were grown by layer diffusion using a methanol:diethyl ether (2:3) solvent system. Complex **C11** crystallises in the monoclinic space group *P* 2(1)/c, with the asymmetric unit containing the entire molecule. The unit cell of **C11** has a volume of 4592 $Å^3$ containing four molecules per unit cell and exhibiting the unit cell parameters: a = 17.5291(4) Å, b = 12.6158(3) Å, c = 21.6165(5) Å, α = 90°, β = 106.116(2)°, γ = 90° (See **Appendix B**, **Table S3**).

Complex **C11** is a tetranuclear heterometallic {3d-4f} complex consisting of two cobalt (II), one cobalt (III) and one dysprosium (III) ion with the metallic core resembling a reverse butterfly arrangement, as shown in **Figure 65**. The variable cobalt oxidation states were assigned through bond valence sum (BVS) calculations and balancing of charges.

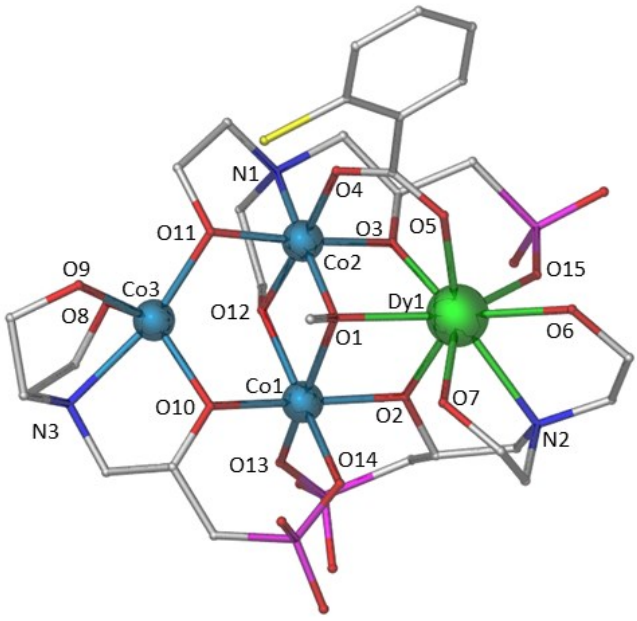

Figure 65- Molecular structure of **C11**: C atoms, grey; O atoms, red; N atoms, blue; S atoms, pink; Dy atoms, green; Fe atoms, orange. H atoms have been omitted for clarity.

Within the butterfly, the central 'body' sites are occupied by a cobalt (II) ion (BVS score = 2.04; **Table S15**) and cobalt (III) ion (BVS score = 3.09; **Table S15**), whilst the outer 'wing' sites comprise of a cobalt (II) ion (BVS score = 1.68; **Table S15**) and a dysprosium

(III) ion. The metallic core is stabilised by a methoxide ligand, a fully deprotonated (**DIPSO**)$^{4-}$ ligand, of Harris Notation 4.2.2.2.1.0.0.1, two doubly deprotonated (**DIPSO**H_2)$^{2-}$ ligands, of Harris Notation 2.1.2.1.1.0.0.1, and a carboxylate ligand. The methoxide forms a μ_3 bridge, bonding to the two central body ions, cobalt (II) and cobalt (III), to the outer wing dysprosium (III) ion. The fully deprotonated (**DIPSO**)$^{4-}$ ligand bridges to all four metal ions. The N-atom chelates to the body cobalt (III) ion, with the O-atoms of the three alkoxide arms each forming μ_2 bridges from the cobalt (III) ion to the two cobalt (II) and dysprosium (III) ion. The sulphonate group forms a chelate to the dysprosium (III) ion. The two (**DIPSO**H_2)$^{2-}$ ligands each chelate to an outer wing ion, cobalt (II) and dysprosium (III), *via* the N-atom and the two protonated alcohol arms. In both cases the alkoxide arm bridges from the outer wing ion to the central cobalt (II) ion, with the sulphonate group then also chelating to the central cobalt (II) ion. The complex is further stabilised by the carboxylic acid, 2-chlorobenzoic acid which forms a μ_2 bridge between the body cobalt (III) ion and the outer wing dysprosium (III) ion.

Crystal packing diagrams for **C11** can be found in **Figure 66**. Intermolecular interactions are dominated by aromatic π, and C-H interactions derived from the benzoate ligands. Hydrogen bonds are present in the crystal packing such that the short, dysprosium only bound, arm of (**DIPSO**H_2)$^{2-}$ donates to an unbound solvent methanol (1.867 Å, DHA angle 156.70°), that same unbound solvent methanol binds to a separate complex via a cobalt bound sulphate group (1.981 Å DHA angle 171.30°). Additionally, a cobalt only bound short arm of (**DIPSO**H_2)$^{2-}$ is donates to a dysprosium bound sulphate on an adjacent complex (1.869 Å, DHA angle 172.44°). Lastly, an internal hydrogen bond is present between a dysprosium bound short arm of (**DIPSO**H_2)$^{2-}$ donating a cobalt bound sulphate group (1.828, DHA angle 170.51°).

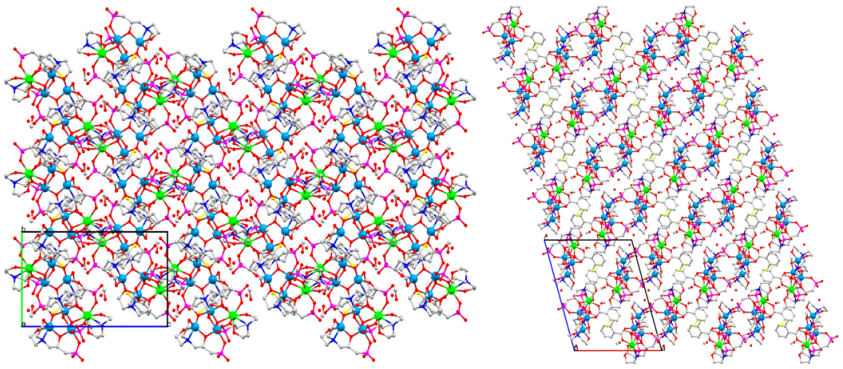

Figure 66- Crystal packing diagram of **C11** Viewing the bc plane, left, and the ac plane, right. Unit cell included as a reference.

The wing cobalt (II) ion is five-coordinate and adopts a distorted trigonal bipyramidal geometry with an average Co-$L_{N,O}$ bond length of 2.09 Å, with bond length ranging from 1.986-2.258 Å. The body cobalt (II) ion and the cobalt (III) ion are both six-coordinate displaying octahedral geometries, with average Co-$L_{N,O}$ bond lengths of 2.09 and 1.90 Å, respectively. The dysprosium (III) ion is eight-coordinate and with distorted square antiprismatic geometry, with an average Dy- $L_{N,O}$ bond length of 2.37 Å with bond length ranging from 2.214-2.588 Å. Selected bond lengths and bond angles are given below in **Table 17**.

Table 17- Selected bond lengths and bond angles for complex **C11**.

Atoms	Bond Length (Å)	Atoms	Bond Length (Å)
Dy1-O1	2.401	Co3-O9	2.092
Dy1-O3	2.271	Co3-O11	2.041
Dy1-O5	2.339	Co3-O10	1.986
Dy1-O15	2.338	Dy1-Co1	3.432
Dy1-O6	2.437	Dy1-Co2	3.281
Dy1-N2	2.588	Dy1-Co3	5.743
Dy1-O7	2.409	Co1-Co2	3.059
Dy1-O2	2.214	Co1-Co3	3.254
Co1-O1	2.186	Co2-Co3	3.200
Co1-O2	2.000		
Co1-O14	2.207		
Co1-O13	2.111		
Co1-O10	1.988		
Co1-O12	2.070	Atoms	Bond Angle (°)
Co2-O1	1.916	Dy1-O1-Co1	96.78
Co2-O12	1.870	Dy1-O1-Co2	98.29
Co2-O11	1.894	Dy1-O2-Co1	108.98
Co2-N1	1.912	Dy1-O3-Co2	103.35
Co2-O4	1.935	Co1-O1-Co2	96.21
Co2-O3	1.900	Co1-O12-Co2	101.74
Co3-N3	2.258	Co1-O10-Co3	109.94
Co3-O8	2.095	Co2-O11-Co3	108.80

The reaction of [**DIPSO**]H_4 with cobalt (II) nitrate hexahydrate, dysprosium (III) nitrate pentahydrate, 2-chlorobenzoic acid and triethylamine in a solvent mix of acetonitrile and methanol (4:1) produced a red-purple mother liquor from which small green plate crystals of $[Co^{II}_3Co^{III}_2Dy^{III}_2(OH)_2(OMe)_2(DIPSO)_2(2\text{-Cl-Benz})_6(MeOH)_2]\cdot 4MeOH$, **C12**, were grown by vapour diffusion using methanol:diethyl ether (1:3) solvent system. Complex **C12** crystallises in the triclinic space group *P-1*, with the asymmetric unit containing half of the molecule. The unit cell of **C12** has a volume of 2036 Å^3 containing one molecule per unit cell and exhibiting the unit cell parameters: a = 11.4314(6) Å, b = 12.7567(7) Å, c = 14.6825(8) Å, α = 102.3170(10)°, β = 96.101(2)°, γ = 100.1170(10)° (See **Appendix B**, **Table S3**).

Complex **C12** is a heterometallic {3d-4f} heptanuclear complex with the metallic core displaying an extended planar reverse-butterfly, or molecular disk, topology, as shown in **Figure 67**. The variable cobalt oxidation states were assigned through bond valence sum (BVS) calculations and balancing of charges.

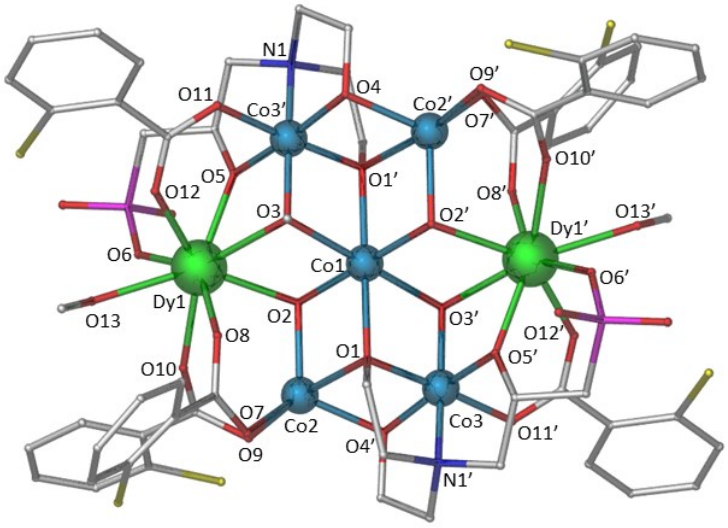

Figure 67- Molecular structure of **C12**: C atoms, grey; O atoms, red; N atoms, small blue; S atoms, pink; Cl atoms, yellow; Dy atoms, green; Co atoms, large blue. H atoms have been omitted for clarity.

The asymmetric unit consists of half of the complex – thereby one dysprosium ion and two cobalt ions each in the 3+ oxidation state in addition to a third half-occupancy cobalt ion of the same oxidation state which lies upon an inversion centre. Of the five cobalt atoms making up the pseudo- 'body' sites, two of the cobalt (II) ions (BVS score = 1.79;

Table S16) were found to be five-coordinate with a distorted trigonal bipyramidal geometry, the two cobalt (III) ions (BVS score = 3.00; **Table S16**) were found to be six-coordinate with a distorted octahedral geometry, whilst the final central cobalt (II) ion (BVS score = 1.96; **Table S16**) also exhibits a distorted octahedral geometry as a six-coordinate centre. The two dysprosium (III) ions were found to be eight-coordinate with a distorted square antiprismatic geometry and occupy the pseudo- 'wing' sites of the molecular disk. Two μ_3 hydroxide and two μ_3 methoxide ligands bridge two cobalt ions to each dysprosium (III) ion, respectively, with both the hydroxide and alkoxide ligands all coordinating to the central cobalt (II) ion. Each dysprosium (III) ion is further ligated by a fully deprotonated $(\mathbf{DIPSO})^{4-}$ ligand, three bridging halo-benzoate ligands and a capping methanol ligand, completing the eight-coordinate environment. Each $(\mathbf{DIPSO})^{4-}$ ligand coordinates as Harris Notation 4.2.2.3.1.0.0.1, binding to one dysprosium (III) and three cobalt ions each. The N-atom of the $(\mathbf{DIPSO})^{4-}$ ligand chelates to an octahedral cobalt (III) ion with the one deprotonated alkoxide arm bridging μ_3 between three cobalt centres, whilst another bridges μ_2 between two cobalt centres and the final alkoxide arm bridges μ_2 between a dysprosium (III) and an octahedral cobalt (III). The sulphonate group further chelates to a dysprosium (III) ion for each ligand. The six carboxylate ligands bridge from a dysprosium (III) ion to a cobalt ion in a μ_2 manner completing the coordination spheres of all the metal ions present. Crystal packing diagrams of **C12** can be found in **Figure 68**. Intermolecular interactions are dominated by aromatic π, and C-H interactions derived from the o-toluate ligands.

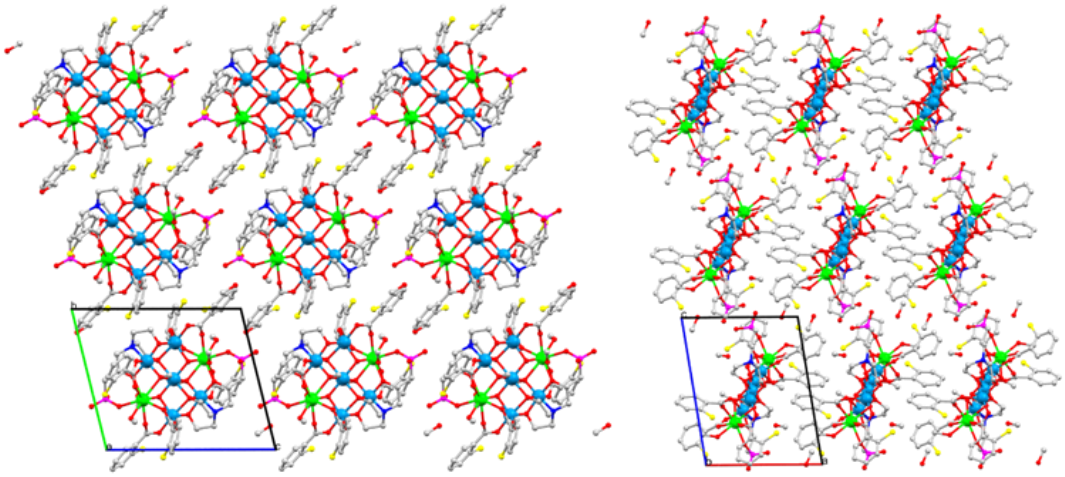

Figure 68- Crystal packing diagram of **C12** viewing the bc plane, left, and the ac plane, right. Unit cell included for reference. C atoms, grey; O atoms, red; N atoms, small blue; S atoms, pink; Cl atoms, yellow; Dy atoms, green; Co atoms, large blue. H atoms have been omitted for clarity.

The average Dy-O bond length is found to be 2.36 Å with bond lengths ranging from 2.300-2.508 Å. The average Co- $L_{N,O}$ bond length if found to be 2.01 Å with bond lengths ranging from 1.884-2.265 Å. Selected bond lengths and bond angles are given below in **Table 18** and **Table 19**, respectively.

Table 18- Selected bond lengths for complex **C12**.

Atoms	Bond Length (Å)	Atoms	Bond Length (Å)
Co1-O1	2.182	Dy1-O2	2.363
Co1-O2	2.029	Dy1-O8	2.268
Co1-O3	2.099	Dy1-O10	2.349
Co1-O1’	2.182	Dy1-O13	2.441
Co1-O2’	2.029	Dy1-O6	2.316
Co1-O3’	2.099	Dy1-O12	2.325
Co2-O1	2.265	Dy1-O5	2.300
Co2-O4’	1.996	Dy1-O3	2.508
Co2-O7	2.079	Co1-Co2	3.204
Co2-O9	2.032	Co1-Co3	3.093
Co2-O2	2.008	Co1-Dy1	3.532
Co3-O1	1.884	Co2-Co3	3.074
Co3-O3’	1.915	Co2-Dy1	3.462
Co3-O5’	1.906	Co3-Dy1’	3.355
Co3-O11’	1.931	Co2-Co2’	6.409
Co3-N1’	1.926	Co3-Co3’	6.185
Co3-O4’	1.924	Dy1-Dy1’	7.065

Table 19- Selected bond angles for complex **C12**.

Atoms	Bond Angle (°)	Atoms	Bond Angle (°)
Co1-O1-Co2	92.18	Co2-O1-Co3	95.21
Co1-O1-Co3	98.77	Co2-O2-Dy1	104.45
Co1-O2-Co2	105.06	Co2-O4’-Co3	103.26
Co1-O2-Dy1	106.81	Co3-O3’-Dy1’	97.76
Co1-O3-Dy1	99.76	Co3-O5’-Dy1’	105.43
Co1-O3-Co3’	100.68		

The reaction of [**DIPSO**]H_4 with cobalt (II) nitrate hexahydrate, dysprosium (III) nitrate pentahydrate, 2-bromobenzoic acid and triethylamine in a solvent mix of acetonitrile and methanol (4:1) produced a red-purple mother liquor from which small green plate crystals of $[Co^{II}_3Co^{III}_2Dy^{III}_2(OH)_2(OMe)_2(DIPSO)_2(2\text{-Br-Benz})_6(MeOH)_2]\cdot 4MeOH$, **C13**, were grown by vapour diffusion using methanol:diethyl ether (1:3) solvent system. Complex **C13** crystallises in the triclinic space group *P-1*, with the asymmetric unit containing half of the molecule. The unit cell of **C13** has a volume of 2075 $Å^3$ containing one molecule per unit cell and exhibiting the unit cell parameters: a = 11.5721(2) Å, b = 12.8228(2) Å, c = 14.7498(2) Å, α = 102.3290(10)°, β = 96.7710(10)°, γ = 100.4070(10)° (See **Appendix B**, **Table S3**).

Complex **C13** is a heterometallic {3d-4f} heptanuclear complex with the metallic core displaying a planar molecular disk topology, as shown in **Figure 69**. The variable cobalt oxidation states were assigned through bond valence sum (BVS) calculations and balancing of charges.

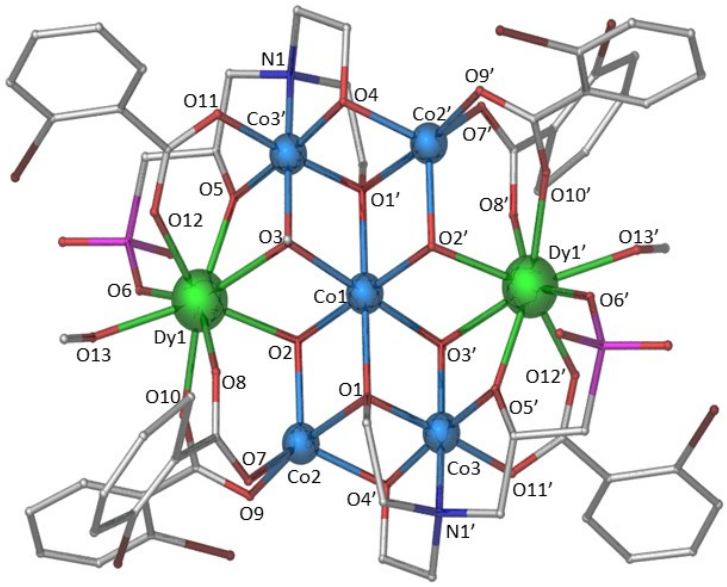

Figure 69- Molecular structure of **C13**: C atoms, grey; O atoms, red; N atoms, small blue; S atoms, pink; Br atoms, brown; Dy atoms, green; Co atoms, large blue. H atoms have been omitted for clarity.

The asymmetric unit consists of half of the complex – thereby one dysprosium ion and two cobalt ions each in the 3+ oxidation state in addition to a third half-occupancy cobalt ion of the same oxidation state which lies upon an inversion centre. Of the five cobalt

atoms making up the pseudo- 'body' sites, two of the cobalt (II) ions (BVS score = 1.78; **Table S17**) were found to be five-coordinate with a distorted trigonal bipyramidal geometry, the two cobalt (III) ions (BVS score = 3.02; **Table S17**) were found to be six-coordinate with a distorted octahedral geometry, whilst the final central cobalt (II) ion (BVS score = 2.01; **Table S17**) also exhibits a distorted octahedral geometry as a six-coordinate centre. The two dysprosium (III) ions were found to be eight-coordinate with a distorted square antiprismatic geometry and occupy the pseudo- 'wing' sites of the molecular disk. The observed coordination environment of **C13** is the same as that described for **C12**, however, 2-Br-benzoate is substituted in the place of the 2-Cl-benzoate ligands. Crystal packing diagrams of **C13** can be found in **Figure 70**. Intermolecular interactions are dominated by aromatic π, and C-H interactions derived from the o-toluate ligands.

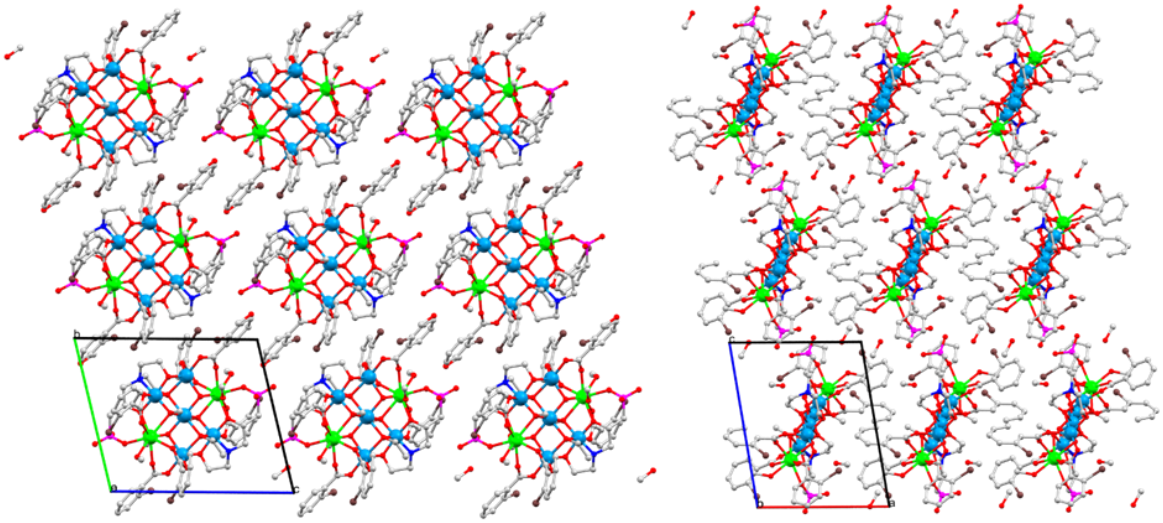

Figure 70- Crystal packing diagram of **C13** viewing the bc plane, left, and the ac plane, right. Unit cell included for reference. C atoms, grey; O atoms, red; N atoms, small blue; S atoms, pink; Br atoms, brown; Dy atoms, green; Co atoms, large blue. H atoms have been omitted for clarity.

The average Dy-O bond length is found to be 2.37 Å with bond lengths ranging from 2.278-2.521 Å. The average Co- $L_{N,O}$ bond length is found to be 2.01 Å with bond lengths ranging from 1.893-2.253 Å. Selected bond lengths and bond angles are given below in **Table 20** and **Table 21**, respectively.

Table 20- Selected bond lengths for complex **C13**.

Atoms	Bond Length (Å)	Atoms	Bond Length (Å)
Co1-O1	2.157	Dy1-O2	2.352
Co1-O2	2.039	Dy1-O8	2.278
Co1-O3	2.085	Dy1-O10	2.356
Co1-O1’	2.157	Dy1-O13	2.448
Co1-O2’	2.039	Dy1-O6	2.307
Co1-O3’	2.085	Dy1-O12	2.309
Co2-O1	2.253	Dy1-O5	2.299
Co2-O4’	2.022	Dy1-O3	2.521
Co2-O7	2.056	Co1-Co2	3.198
Co2-O9	2.038	Co1-Co3	3.091
Co2-O2	2.014	Co1-Dy1	3.531
Co3-O1	1.893	Co2-Co3	3.074
Co3-O3’	1.934	Co2-Dy1	3.456
Co3-O5’	1.904	Co3-Dy1’	3.353
Co3-O11’	1.928	Co2-Co2’	6.396
Co3-N1’	1.912	Co3-Co3’	6.182
Co3-O4’	1.903	Dy1-Dy1’	7.062

Table 21- Selected bond angles for complex **C13**.

Atoms	Bond Angle (°)	Atoms	Bond Angle (°)
Co1-O1-Co2	92.93	Co2-O1-Co3	95.30
Co1-O1-Co3	99.29	Co2-O2-Dy1	104.38
Co1-O2-Co2	104.17	Co2-O4’-Co3	103.06
Co1-O2-Dy1	106.81	Co3-O3’-Dy1’	96.76
Co1-O3-Dy1	99.66	Co3-O5’-Dy1’	105.40
Co1-O3-Co3’	100.48		

The reaction of [**DIPSO**]H_4 with cobalt (II) nitrate hexahydrate, dysprosium (III) nitrate pentahydrate, 2-iodobenzoic acid and triethylamine in a solvent mix of acetonitrile and methanol (4:1) produced a red-purple mother liquor from which small green plate crystals of $[Co^{II}_3Co^{III}_2Dy^{III}_2(OH)_2(OMe)_2(DIPSO)_2(2I\text{-}Benz)_6(MeOH)_2]\cdot 2MeOH\cdot 2H_2O$, **C14**, were grown by vapour diffusion using methanol:diethyl ether (1:3) solvent system. Complex **C14** crystallises in the triclinic space group *P-1*, with the asymmetric unit containing half of the molecule. The unit cell of **C14** has a volume of 2058 $Å^3$ containing one molecule per unit cell and exhibiting the unit cell parameters: a = 10.7878(2) Å, b = 14.5016(2) Å, c = 15.6902(2) Å, α = 113.376(2)°, β = 97.2310(10)°, γ = 107.789(2)° (See **Appendix B**, **Table S3**).

Complex **C14** is a heterometallic {3d-4f} heptanuclear complex with the metallic core displaying a planar molecular disk topology, as shown in **Figure 71**. The variable cobalt oxidation states were assigned through bond valence sum (BVS) calculations and balancing of charges.

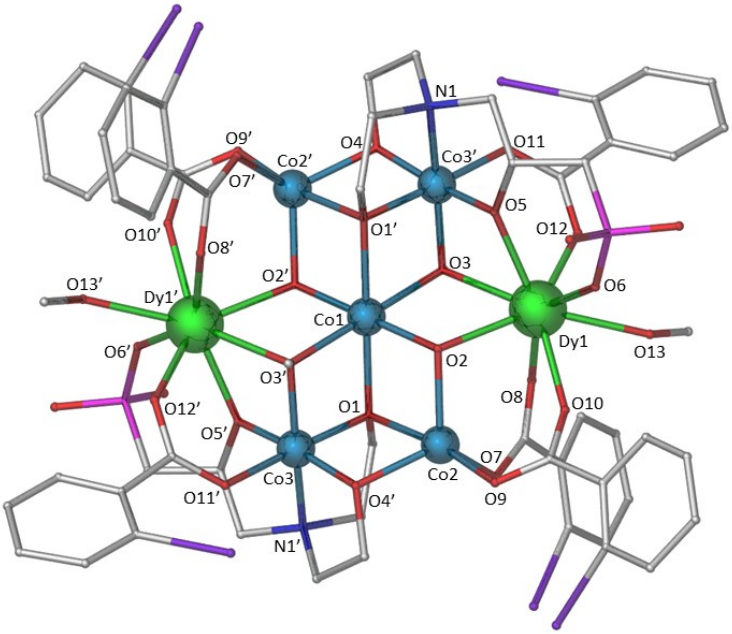

Figure 71- Molecular structure of **C14**: C atoms, grey; O atoms, red; N atoms, small blue; S atoms, pink; I atoms, purple; Dy atoms, green; Co atoms, large blue. H atoms have been omitted for clarity.

The asymmetric unit consists of half of the complex – thereby one dysprosium ion and two cobalt ions each in the 3+ oxidation state in addition to a third half-occupancy cobalt

ion of the same oxidation state which lies upon an inversion centre. Of the five cobalt atoms making up the pseudo- 'body' sites, two of the cobalt (II) ions (BVS score = 1.90; **Table S18**) were found to be five-coordinate with a distorted trigonal bipyramidal geometry, the two cobalt (III) ions (BVS score = 3.07; **Table S18**) were found to be six-coordinate with a distorted octahedral geometry, whilst the final central cobalt (II) ion (BVS score = 1.99; **Table S18**) also exhibits a distorted octahedral geometry as a six-coordinate centre. The two dysprosium (III) ions were found to be eight-coordinate with a distorted square antiprismatic geometry and occupy the pseudo- 'wing' sites of the molecular disk. The observed coordination environment of **C14** is the same as that described for **C12**, however, 2-I-benzoate is substituted in the place of the 2-Cl-benzoate ligands. Crystal packing diagrams of **C14** can be found in **Figure 72**. Intermolecular interactions are dominated by aromatic π, and C-H interactions derived from the o-toluate ligands.

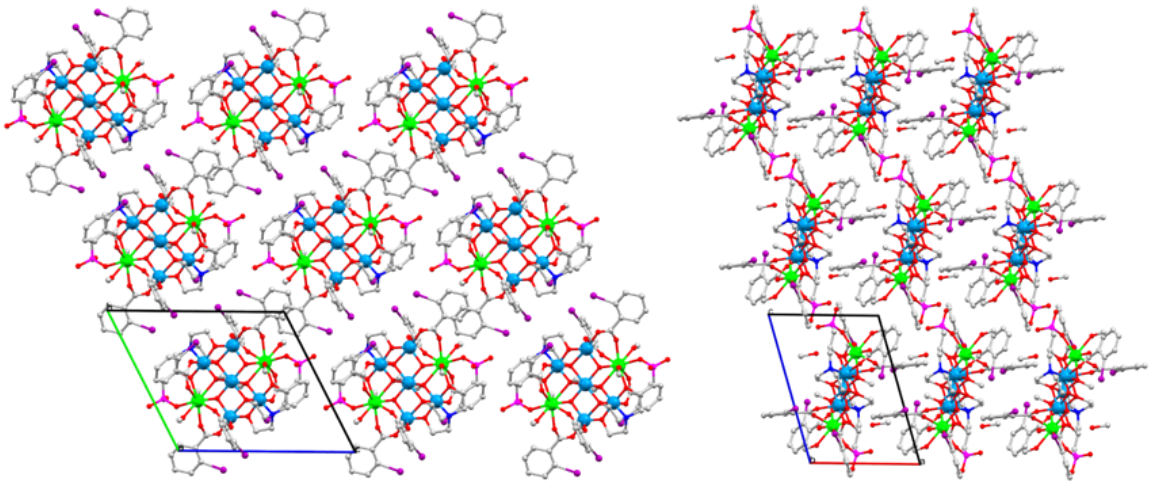

Figure 72- Crystal packing diagram of **C14** viewing the bc plane, left, and the ac plane, right. Unit cell included as a reference. C atoms, grey; O atoms, red; N atoms, small blue; S atoms, pink; I atoms, purple; Dy atoms, green; Co atoms, large blue. H atoms have been omitted for clarity.

The average Dy-O bond length is found to be 2.36 Å with bond lengths ranging from 2.256-2.560 Å. The average Co- $L_{N,O}$ bond length if found to be 2.00 Å with bond lengths ranging from 1.890-2.226 Å. Selected bond lengths and bond angles are given below in **Table 22** and **Table 23**, respectively.

Table 22- Selected bond lengths and bond angles for complex **C14**.

Atoms	Bond Length (Å)	Atoms	Bond Length (Å)
Co1-O1	2.162	Dy1-O2	2.342
Co1-O2	2.045	Dy1-O8	2.261
Co1-O3	2.084	Dy1-O10	2.386
Co1-O1’	2.162	Dy1-O13	2.408
Co1-O2’	2.045	Dy1-O6	2.301
Co1-O3’	2.084	Dy1-O12	2.316
Co2-O1	2.240	Dy1-O5	2.293
Co2-O4’	1.992	Dy1-O3	2.548
Co2-O7	2.020	Co1-Co2	3.156
Co2-O9	2.004	Co1-Co3	3.087
Co2-O2	2.011	Co1-Dy1	3.566
Co3-O1	1.887	Co2-Co3	3.058
Co3-O3’	1.915	Co2-Dy1	3.456
Co3-O5’	1.889	Co3-Dy1’	3.358
Co3-O11’	1.926	Co2-Co2’	6.313
Co3-N1’	1.919	Co3-Co3’	6.174
Co3-O4’	1.901	Dy1-Dy1’	7.133

Table 23- Selected bond angles and bond angles for complex **C14**.

Atoms	Bond Angle (°)	Atoms	Bond Angle (°)
Co1-O1-Co2	91.59	Co2-O1-Co3	95.21
Co1-O1-Co3	99.14	Co2-O2-Dy1	104.84
Co1-O2-Co2	102.19	Co2-O4’-Co3	103.48
Co1-O2-Dy1	108.57	Co3-O3’-Dy1’	96.59
Co1-O3-Dy1	100.21	Co3-O5’-Dy1’	106.09
Co1-O3-Co3’	100.98		

The bonding structures exhibited in the above work display similar characteristics to those observed in previous literature. Some broad similarities in motif are discussed below in relation to: diisopropanolamine, (dipa)H_3, N-(2-hydroxyethyl) iminodiacetic acid, (Heidi)H_3, and molecular disks.

(Dipa)H_3, as an adaptation upon diethanolamine, (**DEA**)H_2, represents a first step towards increasing asymmetry when compared to the three-fold symmetric triethanolamine, (**TEA**)H_3, ligand used in early amine polyalcohol assemblies. Work by Jones and Murray *et al.* exhibited the variability of structures and oxidation states which could be produced by the $[(dipa)H_x]^{(3-x)-}$ ligand in solution.[205] The work in this thesis looked to increase the asymmetry of the amine polyalcohol ligand whilst retaining steric and oxidation state flexibility, as is found in $[(\mathbf{DIPSO})H_x]^{(4-x)-}$.

(Heidi)H_3, alongside its methyl and ethyl branched chain offshoots, similarly inspired the research of more asymmetric (**TEA**)H_3 derivatives. The work of Powell and Pieralli *et al.* and the later work of Goodwin and Heath *et al.* exhibited the potential for similarly complex ligands to form larger arrays akin to nanoclusters.[206, 207] These larger arrays are expanded upon by structures **C7** and **C10**, which additionally exhibit the interactions of heterometallics within the large clusters.

Heptanuclear molecular disks similar to **C12**, **C13** and **C14** are a well-known motif within molecular magnetism. Early research, as is typical, focussed upon {3d} transition metal chemistry producing homometallic heptanuclear disks of manganese, iron, cobalt, nickel, and copper.[208-213] Later research has developed {3d-4f} examples of heptanuclear disks of a 3:4 TM:Ln ratio.[214] This is dissimilar to the examples given in this thesis which exhibit a 5:2 TM:Ln.

2.2.5 Magnetic Susceptibility Studies

This section discusses the magnetic data collected for four crystal samples: **C8**, **C12**, **C13** and **C14**:

C8- $[Fe^{III}_2Dy^{III}_2(OH)_2(2I\text{-}Benz)_2(DIPSOH)_2(NO_3)_2]\cdot 3MeCN$

C12- $[Co^{II}_3Co^{III}_2Dy^{III}_2(OH)_2(OMe)_2(DIPSO)_2(2Cl\text{-}Benz)_6(MeOH)_2]\cdot 4MeOH$

C13- $[Co^{II}_3Co^{III}_2Dy^{III}_2(OH)_2(OMe)_2(DIPSO)_2(2Br\text{-}Benz)_6(MeOH)_2]\cdot 4MeOH$

C14- $[Co^{II}_3Co^{III}_2Dy^{III}_2(OH)_2(OMe)_2(DIPSO)_2(2I\text{-}Benz)_6(MeOH)_2]\cdot 2MeOH\cdot 2H_2O$

Direct current (dc) magnetic susceptibility analysis was undertaken on polycrystalline samples of complexes **C8** and **C12-14**. Initial analysis was completed over the temperature range 2-300 K in dc field of 0.1 T. The resultant $\chi_M T$ vs. T plots can be found in **Figure 73**.

It should be noted, complexes **C12**-**C14** contain Co^{II} ions within their structures. The presence of Co^{II} complicates the modelling of collective ions within a heterometallic species, as its room temperature $\chi_M T$ value is often higher than that expected for a non-interacting, spin-only centre where S = 3/2 and g = 2. This phenomenon is discussed in detail in the work of Murrie, 2010.[215] The departure from the expected $\chi_M T$ value is conventionally assigned to the orbital contribution of high spin Co^{II} in octahedral geometries working in unison with the spin moment. In six coordinate systems the separation between ground state and first excited state can be very large as a result of a high axial anisotropy parameter, D, of the order 100 cm^{-1}. It is often found more effective to model Co^{II} as an effective S' = 1/2, with a very anisotropic principle effective g' >> 2, especially at low temperature where only the lowest lying Kramers' doublet would remain populated.

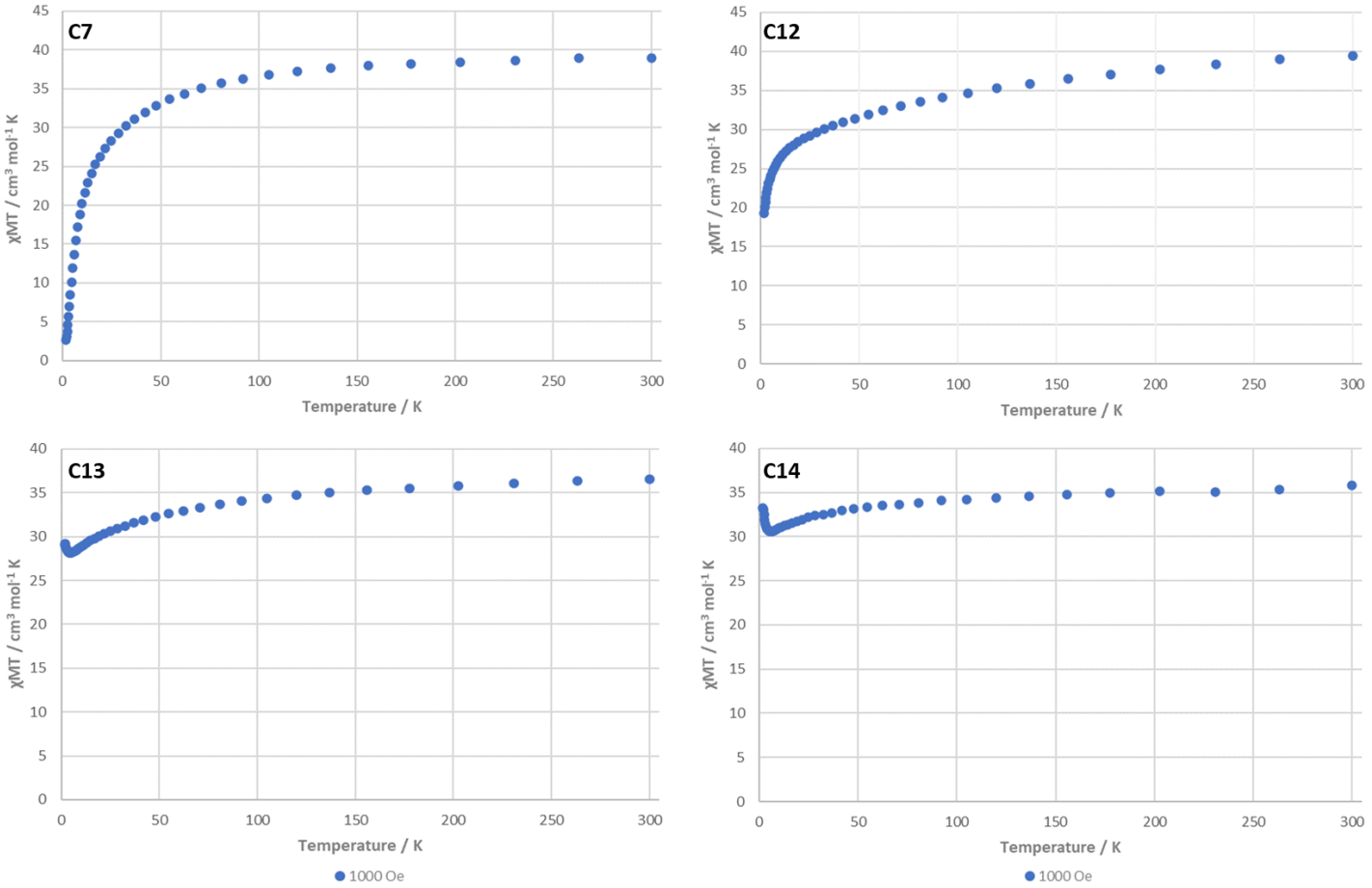

Figure 73- Plots of $\chi_M T$ vs T for samples **C8**, **C12**, **C13**, **C14** measured under a 1000 Oe (0.1 T) applied magnetic field.

Extracted from the data collected are values of the molar magnetic susceptibility times temperature, $\chi_M T$, of 39.43, 36.52 and 35.79 cm^3 K mol^{-1} for the $\{Co^{II}_3Co^{III}_2Dy^{III}_2\}$ complexes **C12**, **C13** and **C14** respectively at 300 K. These values broadly correlate with the calculated values for two Dy^{III} (S = 5/2, L = 5, J = 15/2, $^6H_{15/2}$, g_J = 4/3, C = 14.17 cm^3 K mol^{-1}) and three Co^{II} (S' = 1/2, g = 5.5, C = 2.84 cm^3 K mol^{-1}) and two Co^{III} (S = 0, g = 2.0, C = 0.00 cm^3 K mol^{-1}, Diamagnetic) non-interacting centres ((2 × 14.17) + (3 × 2.84) + (2 × 0) = 36.86 cm^3 K mol^{-1}). Values of C are calculated using equations 2, 5 and 9 found in **Chapter 1**. Similarly, the experimental value of $\chi_M T$ for the $\{Fe^{III}_2Dy^{III}_2\}$ complex **C8**, 39.01 at 300 K, correlates strongly with the calculated values for two Dy^{III} (As previous) and two Fe^{III} (S = 5/2, g_J = 2.0, C = 4.38 cm^3 K mol^{-1}) non-interacting centres ((2 × 14.17) + (2 × 4.38) = 37.1 cm^3 K mol^{-1}).

The profiles of the $\chi_M T$ vs. T plots for the four complexes are indicative of variations in the magnetic exchange interactions. As shown in the experiments at 0.1 T, the three near-isostructural $\{Co^{II}_3Co^{III}_2Dy^{III}_2\}$ complexes, **C12**, **C13** and **C14**, exhibit two distinct line shapes. Observed for **C12** is a steady decrease down to approximately 50 K, below which the gradient of the plot becomes steeper and the $\chi_M T$ fall off more distinct. The decrease is likely due to the gradual depopulation of the excited m_J magnetic states of Dy(III) ions as the temperature is decreased. At the lowest temperatures the magnetic exchange becomes the dominant factor. As observed for **C12,** a continual decrease would suggest a small magnetic ground state and dominant antiferromagnetic exchange behaviour. However, for **C13** and **C14** we instead observe an upturn indicating a larger "spin" ground state and possible dominant ferromagnetic interactions. This indicates non-negligible exchange interactions between the Co(II) and Dy(III) ions. Due to the similarities exhibited in the structures of samples **C12-14** we must reach the conclusion that small changes in the structure can influence the magnetic exchange pathways exhibited by the complexes. Furthermore, due to the competing magnetic interactions, small perturbations in exchange strength will greatly influence the energies of the coupled magnetic states. Additionally, for **C13** and **C14**, as the temperature decreases the $\chi_M T$ product also decreases until the before mentioned upturn, at about 5 K, is observed with the $\chi_M T$ product then continuing to increase until the lowest temperature recorded. This upturn could indicate ferromagnetic interactions or competing

antiferromagnetic interactions, akin to a metamagnetic switch at a critical temperature within a constant field.

The $\{Fe^{III}_2Dy^{III}_2\}$ complex, **C8**, demonstrates a similar profile to **C12**, exhibiting a curve of decreasing gradient as the temperature increases, becoming near linear above 75 K, without reaching saturation. It should be noted that the fall off of the $\chi_M T$ product is much more distinct for the iron complex, than for the cobalt complex. The decrease at higher temperatures due to depopulation of excited m_J states of the Dy(III) ion with an accelerating decrease down to 2.651 cm^3 K mol^{-1} at 2K indicating a small ground "spin" state and dominant antiferromagnetic interactions.

The isothermal magnetisation, M, plotted as a function of the magnetic field, H, was collected over three incremental steps within the temperature range of 2-6 K for each of the novel samples. These plots are shown in **Figure 74**. All three $\{Co^{II}_3Co^{III}_2Dy^{III}_2\}$ samples display a rapid increase in magnetisation up to 2 T, before reaching a steady, near-linear increase without attaining saturation. In combination with the field dependency demonstrated by the magnetic susceptibility plots, this would suggest the samples exhibit a significant magnetic anisotropy. Successive increases in the temperature at which the experiments were run prove to increase the overall linearity of the line shape. The $\{Fe^{III}_2Dy^{III}_2\}$ sample, **C8**, displays a moderate increase in magnetisation up to 3 T, before reaching a steady, near-linear increase without attaining saturation. In combination with the field dependency demonstrated by the magnetic susceptibility plots, this would suggest the samples exhibit a significant magnetic anisotropy. Successive increases in the temperature show far less distinct changes in plot profiles and these are much less pronounced than for samples **C12-14**.

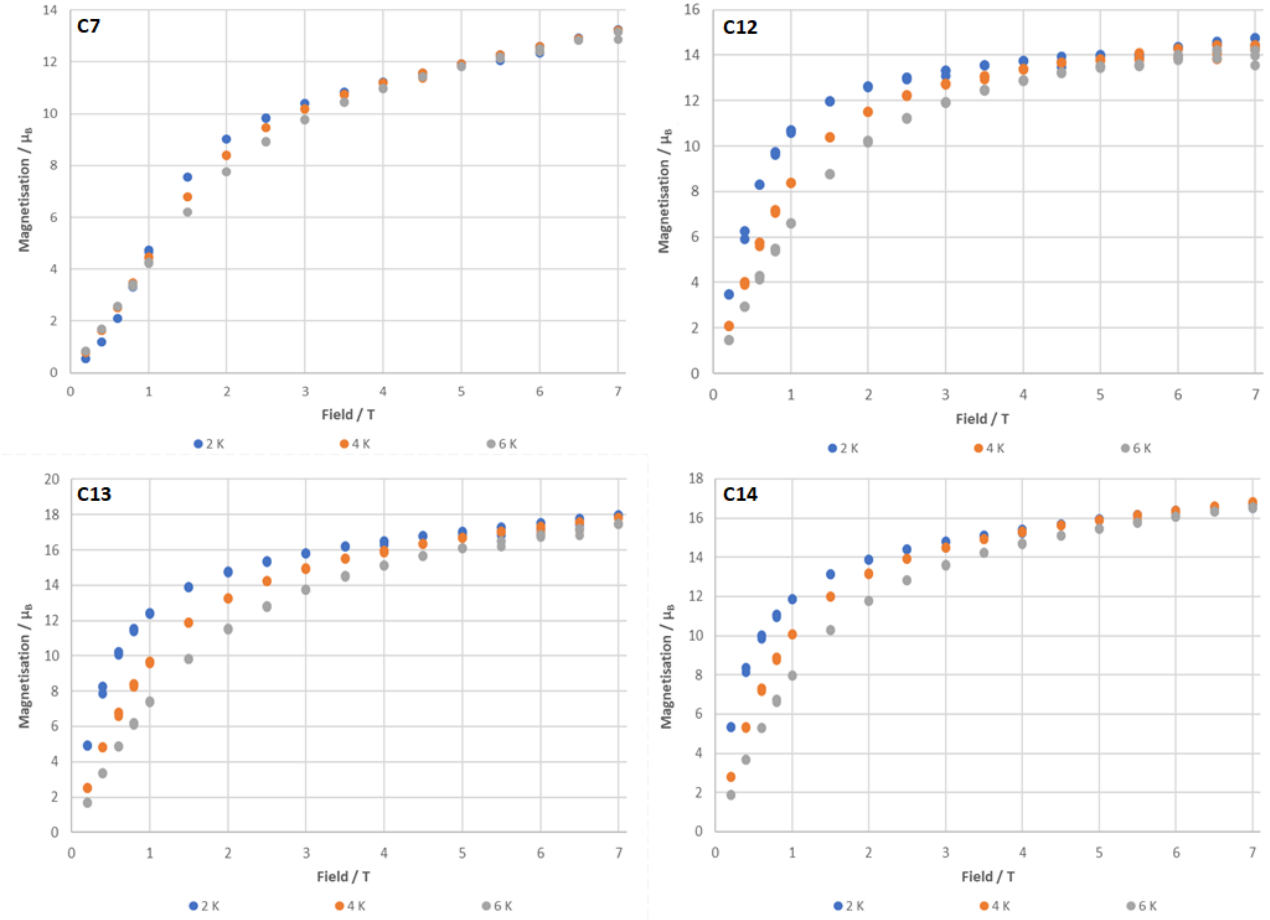

Figure 74- Plots of M vs H for samples **C8**, **C12**, **C13**, **C14**, taken in 2 K increments between 2-6 K.

Due to the suspected presence of magnetic anisotropy, ac magnetic susceptibility measurements were performed to probe for any SMM behaviour. However, no out-of-phase χ" signals were observed down to 2 K and 1500 Hz for all complexes. This indicates magnetic relaxation is too fast on the timescale of the experiment undertaken. Instead in an attempt to gather further data additional analysis would be required to probe the samples below 2 K in search of a further tail.

2.3 Chapter Summary

In this chapter the syntheses and analyses of fourteen complexes have been described, including thirteen [**DIPSO**] containing complexes, **C1**-**C3** and **C5**-**C14**, alongside one co-crystallised transition metal complex that does not contain the [**DIPSO**] ligand, **C4**. Structural data was collected for all the samples **C1**-**C14**, of which thirteen are thought to be novel at the time of research.

These structures show a substantial variation in the binding modes exhibited by the [**DIPSO**] ligand, both between and occasionally within complexes.

Magnetic analysis was undertaken on four samples, **C8** and **C12**-**14**, although none of the dc data collected proved viable enough to warrant further ac analysis at this point. Subtle differences in the dc magnetic susceptibility data were observed at low temperatures – possibly due to the nature of the bulky group at the 2 position of the benzoate ligand causing structural distortions that influence the exchange coupling This chapter has exhibited the viability of [**DIPSO**] as an asymmetric forebear ligand in the construction of butterfly-like complexes, but also larger arrangements with some more unusual configurations, such as $\{Fe^{III}_{12}Dy^{III}_{4}\}$, $\{Fe^{III}_{4}Dy^{III}_{6}\}$ or $\{Co_{5}Dy^{III}_{2}\}$, becoming apparent.

2.4 Experimental Methods

All information relating to the sourcing of chemicals, technical specifications of instrumentation, data processing procedures and software can be found in the appendices. Pertinent to this chapter are **Appendix A**, **B** and **F** for synthetic procedures, single-crystal X-ray diffraction analysis and magnetism respectively.

2.4.0 General Synthetic Method

The subsequent synthetic method and stoichiometries were used in all the following reactions, unless otherwise noted in the specific entry for each target molecule. In terms of this general method the transition metal nitrate hydrates, $TM(NO_3)_x{\cdot}yH_2O$, used throughout the project were chromium, manganese, iron and cobalt whilst the lanthanide metal nitrate hydrates, $Ln(NO_3)_3{\cdot}xH_2O$, used were dysprosium and gadolinium. The carboxylic acids used in the reaction series were benzoic acid, 2-chlorobenzoic acid, 2-bromobenzoic acid, 2-iodobenzoic acid, 2,6-dichlorobenzoic acid and o-toluic acid. No more than one transition metal, one lanthanide species and one carboxylic acid were involved in any one reaction.

In a small reaction vessel containing a stirrer bar, acetonitrile (20 mL) and methanol (5 mL) were dissolved $TM(NO_3)_x{\cdot}yH_2O$ (0.5 mmol), $Ln(NO_3)_3{\cdot}xH_2O$ (0.5 mmol), carboxylic acid (1 mmol) and [**DIPSO**]H_4 (0.5 mmol) respectively, ensuring each component was fully dissolved prior to addition of the next reagent. The solution was stirred continuously as the reaction was activated with triethylamine (2 mmol), dropwise over thirty seconds, and was then allowed to stir for a further two hours. Upon completion of the reaction, the solution was allowed to cool fully overnight, without stirring, and gravity filtered to remove any deposited solid material. The solvent was then removed by rotary evaporation to yield an oil which can be set up for crystallisation by any of the methods noted in **Section 2.2.1**.

2.4.1 $[Cr^{III}_2Dy^{III}_2(OMe)_2(benz)_4(DIPSOH)_2(MeOH)_2]\cdot 2MeOH\cdot H_2O$, C1

$CrCl_3\cdot 6H_2O$ (133 mg, 0.5 mmol), $Dy(NO_3)_3\cdot 5H_2O$ (219 mg, 0.5 mmol), benzoic acid (122 mg, 1 mmol) and [**DIPSO**]H_4 (131 mg, 0.5 mmol) were added consecutively to a solvent mixture of methanol (5mL) and acetonitrile (20 mL). The solution was then heated to 50 °C and stirred continuously as the reaction was activated with triethylamine (0.28 mL, 2 mmol), dropwise over thirty seconds. The reaction was then allowed to stir for a further two hours. The resultant turquoise-grey solution was left overnight, and gravity filtered to remove any deposited solids. Single crystals of **C1** were grown over 4-7 days by layer diffusion using a MeOH:Et_2O (1:4) solvent system, yielding small pink-purple crystals (27%). The title structure was confirmed by SC-XRD with a molecular formula: $C_{48}H_{72}Cr_2Dy_2N_2O_{27}S_2$.

2.4.2 $[Co^{III}_2Dy^{III}_2(OMe)_2(o\text{-}Tol)_4(DIPSOH)_2(H_2O)_2]\cdot MeCN\cdot 3H_2O$, C2

$Co(NO_3)_2\cdot 6H_2O$ (146 mg, 0.5 mmol), $Dy(NO_3)_3\cdot 5H_2O$ (219 mg, 0.5 mmol), o-toluic acid (136 mg, 1 mmol) and [**DIPSO**]H_4 (131 mg, 0.5 mmol) were added consecutively to a solvent mixture of methanol (5mL) and acetonitrile (20 mL). The solution was stirred continuously as the reaction was activated with triethylamine (0.28 mL, 2 mmol), dropwise over thirty seconds. The reaction was then allowed to stir for a further two hours. The resultant dark red solution was left overnight, and gravity filtered to remove any deposited solids. Single crystals of **C2** were grown over 10-14 days by vapour diffusion using a MeOH:MeCN:Et_2O (1:4:20) solvent system, yielding small green block crystals (35%). The title structure was confirmed by SC-XRD with a molecular formula: $C_{50}H_{75}Co_2Dy_2N_3O_{27}S_2$.

2.4.3 $[Mn^{III}_2Dy^{III}_2(OH)_2(o\text{-}Tol)_4(DIPSOH)_2(H_2O)_2]\cdot 4MeCN\cdot 2H_2O$, C3

Sample **C3** co-crystallised with sample **C4**, forming two distinct morphologies from solution.

$Mn(NO_3)_2\cdot 4H_2O$ (126 mg, 0.5 mmol), $Dy(NO_3)_3\cdot 5H_2O$ (219 mg, 0.5 mmol), o-toluic acid (136 mg, 1 mmol) and [**DIPSO**]H_4 (131 mg, 0.5 mmol) were added consecutively to a

solvent mixture of methanol (5mL) and acetonitrile (20 mL). The solution was stirred continuously as the reaction was activated with triethylamine (0.28 mL, 2 mmol), dropwise over thirty seconds. The reaction was then allowed to stir for a further two hours. The resultant red-brown solution was left overnight, and gravity filtered to remove any deposited solids. Single crystals of **C3** were grown over 14-20 days by layer diffusion using a MeOH:MeCN:Et_2O (1:4:20) solvent system, yielding small brown plate crystals. No crystal yield is given due to co-crystallisation of the sample. The title structure was confirmed by SC-XRD with a molecular formula: $C_{54}H_{78}Dy_2Mn_2N_6O_{26}S_2$.

2.4.4 $[Mn^{II}_4Mn^{III}_2(O)_2(o\text{-}Tol)_{10}(MeCN)_3(H_2O)]\cdot MeCN$, C4

Sample **C4** co-crystallised with sample **C3**, forming two distinct morphologies from solution.

$Mn(NO_3)_2\cdot 4H_2O$ (126 mg, 0.5 mmol), $Dy(NO_3)_3\cdot 5H_2O$ (219 mg, 0.5 mmol), o-toluic acid (136 mg, 1 mmol) and [**DIPSO**]H_4 (131 mg, 0.5 mmol) were added consecutively to a solvent mixture of methanol (5mL) and acetonitrile (20 mL). The solution was stirred continuously as the reaction was activated with triethylamine (0.28 mL, 2 mmol), dropwise over thirty seconds. The reaction was then allowed to stir for a further two hours. The resultant red-brown solution was left overnight, and gravity filtered to remove any deposited solids. Single crystals of **C4** were grown over 14-20 days by layer diffusion using a MeOH:MeCN:Et_2O (1:4:20) solvent system, yielding small brown hexagonal crystals. No crystal yield is given due to co-crystallisation of the sample. The title structure was confirmed by SC-XRD with a molecular formula: $C_{88}H_{84}Mn_6N_4O_{23}$.

2.4.5 $[Mn^{III}_2Gd^{III}_2(OH)_2(Benz)_4(DIPSOH)_2(MeOH)_2]\cdot 2MeCN$, C5

$Mn(NO_3)_2\cdot 4H_2O$ (126 mg, 0.5 mmol), $Gd(NO_3)_3\cdot 6H_2O$ (226 mg, 0.5 mmol), benzoic acid (122 mg, 1 mmol) and [**DIPSO**]H_4 (131 mg, 0.5 mmol) were added consecutively to a solvent mixture of methanol (5mL) and acetonitrile (20 mL). The solution was stirred continuously as the reaction was activated with triethylamine (0.28 mL, 2 mmol), dropwise over thirty seconds. The reaction was then allowed to stir for a further two hours. The resultant red-brown solution was left overnight, and gravity filtered to

remove any deposited solids. Single crystals of **C5** were grown over 4-7 days by vapour diffusion using a MeOH:MeCN:Et_2O (1:4:20) solvent system, yielding small green block crystals (22%). The title structure was confirmed by SC-XRD with a molecular formula: $C_{48}H_{64}Gd_2Mn_2N_4O_{24}S_2$.

2.4.6 $[Fe^{III}_2Dy^{III}_2(OH)_2(Benz)_2(DIPSOH)_2(NO_3)_2(H_2O)_2]\cdot MeCN\cdot 2H_2O$, C6

Sample **C6** co-crystallised with sample **C7**, forming two distinct morphologies from solution.

$Fe(NO_3)_3\cdot 9H_2O$ (202 mg, 0.5 mmol), $Dy(NO_3)_3\cdot 5H_2O$ (219 mg, 0.5 mmol), benzoic acid (122 mg, 1 mmol) and [**DIPSO**]H_4 (131 mg, 0.5 mmol) were added consecutively to a solvent mixture of methanol (5mL) and acetonitrile (20 mL). The solution was stirred continuously as the reaction was activated with triethylamine (0.28 mL, 2 mmol), dropwise over thirty seconds. The reaction was then allowed to stir for a further two hours. The resultant orange solution was left overnight, and gravity filtered to remove any deposited solids. Single crystals of **C6** were grown over 10-14 days by vapour diffusion using a MeOH:MeCN:Et_2O (1:4:20) solvent system, yielding small brown octahedral prism crystals. No crystal yield is given due to co-crystallisation of the sample. The title structure was confirmed by SC-XRD with a molecular formula: $C_{28}H_{48}Dy_2Fe_2N_4O_{28}S_2$.

2.4.7 $[Fe^{III}_{12}Dy^{III}_4O_6(OH)_4(Benz)_{12}(DIPSO)_4(DIPSOH_2)_2]\cdot 5MeCN\cdot 8H_2O$, C7

Sample **C7** co-crystallised with sample **C6**, forming two distinct morphologies from solution.

$Fe(NO_3)_3\cdot 9H_2O$ (202 mg, 0.5 mmol), $Dy(NO_3)_3\cdot 5H_2O$ (219 mg, 0.5 mmol), benzoic acid (122 mg, 1 mmol) and [**DIPSO**]H_4 (131 mg, 0.5 mmol) were added consecutively to a solvent mixture of methanol (5mL) and acetonitrile (20 mL). The solution was stirred continuously as the reaction was activated with triethylamine (0.28 mL, 2 mmol), dropwise over thirty seconds. The reaction was then allowed to stir for a further two hours. The resultant orange solution was left overnight, and gravity filtered to remove

any deposited solids. Single crystals of **C7** were grown over 10-14 days by vapour diffusion using a MeOH:MeCN:Et_2O (1:4:20) solvent system, yielding small brown block crystals. No crystal yield is given due to co-crystallisation of the sample. The title structure was confirmed by SC-XRD with a molecular formula: $C_{136}H_{177}Dy_4Fe_{12}N_{11}O_{78}S_6$.

2.4.8 $[Fe^{III}_2Dy^{III}_2(OH)_2(2I\text{-}Benz)_2(DIPSOH)_2(NO_3)_2]\cdot 3MeCN$, C8

$Fe(NO_3)_3\cdot 9H_2O$ (202 mg, 0.5 mmol), $Dy(NO_3)_3\cdot 5H_2O$ (219 mg, 0.5 mmol), 2-iodobenzoic acid (248 mg, 1 mmol) and [**DIPSO**]H_4 (131 mg, 0.5 mmol) were added consecutively to a solvent mixture of methanol (5mL) and acetonitrile (20 mL). The solution was stirred continuously as the reaction was activated with triethylamine (0.28 mL, 2 mmol), dropwise over thirty seconds. The reaction was then allowed to stir for a further two hours. The resultant orange solution was left overnight, and gravity filtered to remove any deposited solids. Single crystals of **C8** were grown over 10-14 days by vapour diffusion using a MeOH:MeCN:Et_2O (2:3:20) solvent system, yielding small yellow plate crystals (30%). The title structure was confirmed by SC-XRD with a molecular formula: $C_{36}H_{55}Dy_2Fe_2I_2N_7O_{26}S_2$.

2.4.9 $[Cr^{III}Dy^{III}_2(OH)(2,6Cl\text{-}Benz)_4(DIPSOH)(NO_3)_3]^{2-}\cdot(NEt_3H)^+_2$, C9

$Cr(NO_3)_3\cdot 9H_2O$ (200 mg, 0.5 mmol), $Dy(NO_3)_3\cdot 5H_2O$ (219 mg, 0.5 mmol), 2,6-dichlorobenzoic acid (191 mg, 1 mmol) and [**DIPSO**]H_4 (131 mg, 0.5 mmol) were added consecutively to a solvent mixture of methanol (5mL) and acetonitrile (20 mL). The solution was then heated to 40 °C and stirred continuously as the reaction was activated with triethylamine (0.28 mL, 2 mmol), dropwise over thirty seconds. The reaction was then allowed to stir for a further two hours. The resultant turquoise-grey solution was left overnight, and gravity filtered to remove any deposited solids. Single crystals of **C9** were grown over 4-7 days by layer diffusion using a MeOH:Et_2O (1:4) solvent system, yielding small purple plate crystals (15%). The title structure was confirmed by SC-XRD with a molecular formula: $C_{47}H_{59}Cl_8CrDy_2N_6O_{24}S_2$.

2.4.10 $[Fe^{III}_4Dy^{III}_6O_2(OH)_6(o\text{-}Tol)_{14}(DIPSOH)_2(MeOH)_2(H_2O)_4]\cdot 8MeOH$, C10

$Fe(NO_3)_3\cdot 9H_2O$ (202 mg, 0.5 mmol), $Dy(NO_3)_3\cdot 5H_2O$ (219 mg, 0.5 mmol), o-toluic acid (204 mg, 1.5 mmol) and [**DIPSO**]H_4 (61 mg, 0.25 mmol) were added consecutively to a solvent mixture of methanol (5mL) and acetonitrile (20 mL). The solution was stirred continuously as the reaction was activated with triethylamine (0.30 mL, 3 mmol), dropwise over thirty seconds. The reaction was then allowed to stir for a further two hours. The resultant orange solution was left overnight, and gravity filtered to remove any deposited solids. Single crystals of **C10** were grown over 15-21 days by layer diffusion using a MeOH:Et_2O (2:3) solvent system, yielding small orange-brown block crystals (18%). The title structure was confirmed by SC-XRD with a molecular formula: $C_{136}H_{180}Dy_6Fe_4N_2O_{62}S_2$.

2.4.11 $[Co^{II}_2Co^{III}Dy^{III}(OMe)(DIPSOH_2)_2(DIPSO)(2Cl\text{-}Benz)]\cdot MeOH\cdot H_2O$, C11

$Co(NO_3)_2\cdot 6H_2O$ (97 mg, 0.333 mmol), $Dy(NO_3)_3\cdot 5H_2O$ (90 mg, 0.2 mmol), 2-chlorobenzoic acid (117 mg, 0.75 mmol) and [**DIPSO**]H_4 (97 mg, 0.4 mmol) were added consecutively to acetonitrile (20 mL). The solution was stirred continuously as the reaction was activated with triethylamine (0.4 mL, 3 mmol), dropwise over thirty seconds. The reaction was then allowed to stir for a further two hours. The resultant dark grey solution was left overnight, and gravity filtered to remove any deposited solids. Single crystals of **C11** were grown over 10-14 days by layer diffusion using a MeOH:Et_2O (2:3) solvent system, yielding blue-green crystals (14%). The title structure was confirmed by SC-XRD with a molecular formula: $C_{30}H_{56}Co_3DyN_3O_{23}S_3$.

2.4.12 $[Co^{II}_3Co^{III}_2Dy^{III}_2(OH)_2(OMe)_2(DIPSO)_2(2Cl\text{-}Benz)_6(MeOH)_2]\cdot 4MeOH$, C12

$Co(NO_3)_2\cdot 6H_2O$ (146 mg, 0.5 mmol), $Dy(NO_3)_3\cdot 5H_2O$ (219 mg, 0.5 mmol), 2-chlorobenzoic acid (157 mg, 1 mmol) and [**DIPSO**]H_4 (131 mg, 0.5 mmol) were added consecutively to a solvent mixture of methanol (5mL) and acetonitrile (20 mL). The solution was stirred continuously as the reaction was activated with triethylamine (0.28 mL, 2 mmol), dropwise over thirty seconds. The reaction was then allowed to stir for a further two hours. The resultant red-purple solution was left overnight, and gravity filtered to

remove any deposited solids. Single crystals of **C12** were grown over 4-7 days by vapour diffusion using a MeOH:Et_2O (1:3) solvent system, yielding small green plate crystals (38%). The title structure was confirmed by SC-XRD with a molecular formula: $C_{64}H_{82}Cl_6Co_5Dy_2N_2O_{34}S_2$.

2.4.13 $[Co^{II}_3Co^{III}_2Dy^{III}_2(OH)_2(OMe)_2(DIPSO)_2(2Br\text{-}Benz)_6(MeOH)_2]\cdot 4MeOH$, C13

$Co(NO_3)_2\cdot 6H_2O$ (146 mg, 0.5 mmol), $Dy(NO_3)_3\cdot 5H_2O$ (219 mg, 0.5 mmol), 2-bromobenzoic acid (201 mg, 1 mmol) and [**DIPSO**]H_4 (131 mg, 0.5 mmol) were added consecutively to a solvent mixture of methanol (5mL) and acetonitrile (20 mL). The solution was stirred continuously as the reaction was activated with triethylamine (0.28 mL, 2 mmol), dropwise over thirty seconds. The reaction was then allowed to stir for a further two hours. The resultant red-purple solution was left overnight, and gravity filtered to remove any deposited solids. Single crystals of **C13** were grown over 4-7 days by vapour diffusion using a MeOH:Et_2O (1:3) solvent system, yielding small green plate crystals (35%). The title structure was confirmed by SC-XRD with a molecular formula: $C_{64}H_{82}Br_6Co_5Dy_2N_2O_{34}S_2$.

2.4.14 $[Co^{II}_3Co^{III}_2Dy^{III}_2(OH)_2(OMe)_2(DIPSO)_2(2I\text{-}Benz)_6(MeOH)_2]\cdot 2MeOH\cdot 2H_2O$, C14

$Co(NO_3)_2\cdot 6H_2O$ (146 mg, 0.5 mmol), $Dy(NO_3)_3\cdot 5H_2O$ (219 mg, 0.5 mmol), 2-iodobenzoic acid (248 mg, 1 mmol) and [**DIPSO**]H_4 (131 mg, 0.5 mmol) were added consecutively to a solvent mixture of methanol (5mL) and acetonitrile (20 mL). The solution was stirred continuously as the reaction was activated with triethylamine (0.28 mL, 2 mmol), dropwise over thirty seconds. The reaction was then allowed to stir for a further two hours. The resultant red-purple solution was left overnight, and gravity filtered to remove any deposited solids. Single crystals of **C14** were grown over 4-7 days by vapour diffusion using a MeOH:Et_2O (1:3) solvent system, yielding small green plate crystals (29%). The title structure was confirmed by SC-XRD with a molecular formula: $C_{62}H_{74}Co_5Dy_2I_6N_2O_{34}S_2$.

3 Synthesis Towards the Production of Amine Polyalcohol Ligands

3.1 Introduction

The targeted ligand from **Chapter 2**, [**DIPSO**]H_4, demonstrates a significant number of binding modes, leading to a variable but unpredictable final product. As a result the viability of comparative studies is somewhat sacrificed. By reducing the complexity of the primary ligand, from five donor groups to three donor groups, an additional element of design can be implemented. The form and function of a primary ligand that can result in the formation of a butterfly-like topology is wide and diverse, from more sterically restricted structures such as (2-hydroxymethyl)pyridine through o-vanillin and acetylacetone ([Acac]H) derivatives to the conformationally derestricted amine polyalcohols.[173, 216, 217] Of the ligands currently and commonly utilised in the production of butterfly complexes, tertiary amine polyalcohols had the perfect balance of structural symmetry and conformational freedom. Furthermore, a comparison could be made to the complexes produced by reactions with [**DIPSO**]H_4 whilst maintaining an element of steric and electronic tuning from the backbone R group as shown in **Figure 75**. The chemistry of amine polyalcohols is well known, but somewhat antiquated with plentiful studies from the late 1800s to the 1950s[218, 219] but with declining use thereafter. The chemistry is robust and well known, further innovation is far from a priority. Despite this, the molecules are ubiquitous with diverse synthetic uses as wide as dyes and polymers to pre-drugs and biomimetics.[199, 203, 220]

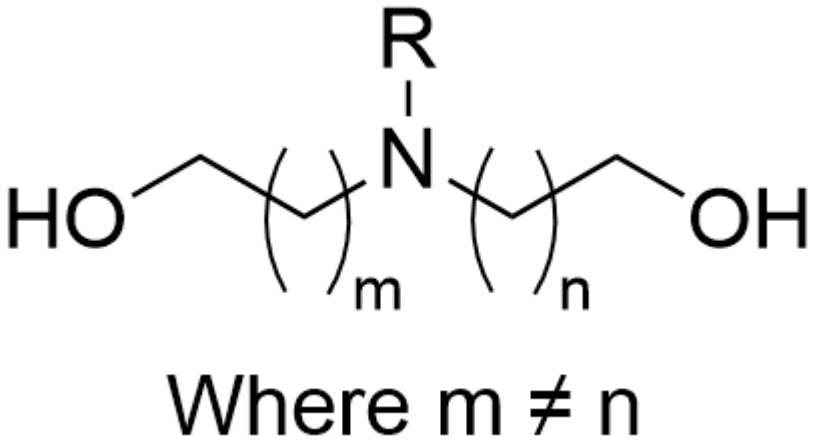

Figure 75- Generic structure of an asymmetric amine polyalcohol ligand.

In this chapter, the work exhibited broadens the applications of the syntheses reported by: Glowacki, Jeong, Shi and Hullio by adapting their methods, targets, and precursors as required. In so doing, novel pathways towards the synthesis of a collection of amine polyalcohols were discovered, although not without challenge, primarily in purification. Further to this, the work exhibits the utility of stepwise synthesis in ligand preparation when working with cascading reaction schemes, such as the alkylation of amines. Although the two potential novel samples, [**H^{t}BuAP**]H_2 and [**HAdAP**]H_2, were not fully characterised as a result of product impurities, the mass spectrometry undertaken indentures confidence that with time the synthesis could be driven to further success.

3.2 Results and Discussion

This chapter describes the synthesis and characterisation of eight polyalcohol precursor molecules, six symmetric polyalcohol ligands, and four asymmetric polyalcohol ligands of the form [**L**]H_1, [**L**]H_2 or [**L**]H_3, as appropriate. This work exhibits the versatility of the main synthetic route utilised, but also offers alternatives for examples where the preferred route proved invalid. All the symmetric and asymmetric ligands produced of the form [**L**]H_2 or [**L**]H_3 are viable as multidentate core binding ligands within butterfly complexes, as described in **Chapter 4** and **Chapter 5**.

Sequential numbering of carbons for analysis is allocated to the reaction product of the schemes situated throughout this chapter, denoted as C_n. This is for simplicity of discussion, and where appropriate, this allocation may refer to the carbons directly, or the protons directly associated to said carbon. Terminology such as nitrogen proximal protons, or oxygen proximal protons refers to the protons directly attached to the carbon adjacent to the heteroatom in question.

3.2.1 Notes on Vacuum Distillation

Vacuum distillation is a purification method performed at reduced pressure, allowing for substances with higher boiling points to be removed at nearer ambient temperatures. As a separation method, vacuum distillation functions by gently evaporating substances according to their volatility. By reducing the pressure of the

system, the temperature required to boil the mixture is greatly reduced, therefore lowering the likelihood of temperature dependant degradation of the product material. Invariably, increasing the amine order (*i.e.,* from similar primary amine to secondary amine) will result in a significant increase in the required temperature to reach boiling. In order to approximate the temperature required for a system to best separate the components of the mixture, considerations had to be made towards the boiling points of the reagents and products likely present in the crude mixture. This was achieved through a nomograph using the Clausius-Clapeyron equation (**Eq^{n} 18**), its derivatives and data from existing peer reviewed journals.

Eq^{n} 18a: $\frac{dP}{dT} = \frac{L}{T\Delta v}\frac{\Delta s}{\Delta v}$

Where L is the specific latent heat (of vaporisation or sublimination), T is the temperature, Δv is the specific volume change, and Δs is the specific entropy change of the phase transition. In this case *d*P/*d*T can be considered to be the tangent, or slope, of any point along a P-T curve which represents a phase transition, otherwise referred to as a coexistence curve. The expression can therefore be rewritten into a linear form, shown below, and regression performed to make approximations towards the temperature-pressure relation.

Eq^{n} 18b: $\frac{d\ln(P)}{dT} = \frac{\Delta H_{Molar}^{Vap}}{RT^2}$

Eq^{n} 18c: $\ln\left(\frac{P}{P^*}\right) = \frac{-\Delta H_{Vap}}{R}\left(\frac{1}{T} - \frac{1}{T^*}\right)$

The Clausius-Clapeyron equation assumes that the molar enthalpy of vaporisation does not vary over a given temperature range; this assumption proved reasonable for its function in this work. The equation was first used to estimate an expected boiling point at standard atmospheric pressure and this value was then used to further calculate the normalised boiling point at a fixed pressure of 20 mbar, as shown in **Table 24**. This pressure was chosen as it could be easily reached and maintained on the vacuum distillation set up used for this experimental series. Standard practice was to set the

temperature of the sand bath to 10 °C above the boiling point of the component to be removed, unless otherwise mentioned in the text of the experimental.

Table 24- Relationship between pressure and boiling point for a selection of pertinent reactants and products, for use in the calculation of vacuum distillation conditions.

	Boiling Point at Specific Pressures / °C			
	1013.2 mbar	100 mbar	50 mbar	20 mbar
[**MAE**]H	159	85.2	68.5	48.7
[**EAE**]H	170	95.0	78.0	57.8
[^{i}**PrAE**]H	172	96.8	79.7	59.4
[**PhAE**]H	282	195.1	174.5	150.1
[**MDEA**]H_2	248	164.7	145.2	122.1
[**EDEA**]H_2	252	168.3	148.7	125.3
[^{i}**PrDEA**]H_2	270	184.4	164.2	140.2
[**PhDEA**]H_2	N/A	N/A	N/A	N/A
2-ClEtOH	129	58.3	42.7	24.0
3-ClPrOH	162	87.8	71.1	51.2

All reaction products were freebased prior to vacuum distillation. Unreacted reagents collected by vacuum distillation were collected for NMR analysis prior to further use to ensure cross contamination did not occur.

3.2.2 Notes on Defining Synthetic Success

In the first case, synthetic success for this chapter's reactions was defined by ^{1}H NMR spectroscopy and correlated spectroscopy, or COSY. Most reactions proceeded *via* nucleophilic substitution of haloalcohols, with an amine moiety directly replacing the halogen group. In the ^{1}H NMR spectroscopy undertaken for this chapter, distinct regions were noted that could correlate to nitrogen proximal protons or oxygen proximal protons. It was also noted that the chlorine proximal protons on the chloro-alcohol reagents shared a similar grouping to the oxygen proximal protons, whilst both were

typically distinct enough from the nitrogen proximal proton region to indicate reaction progress. Within this dataset, terminal halogen groups attached to non-branched aliphatic alkyl or alcohol chains produce a triplet in the region of 3.529-3.869 ppm resulting from the two protons sharing a carbon centre with the halogen atom, whereas a similarly situated amine will produce a triplet in the region of 2.507-3.590 ppm. It should be mentioned, although the two ranges stated above overlap, in practice the regions remain distinct when considering each species individually, rather than as a collective. The distance between the two regions is on average 0.868 ppm, a large enough shift to indicate a group substitution. As the exchangeable protons on the amine group appear unreliably in ^{1}H NMR spectroscopy, this triplet shift between reagent spectrum and product spectrum is a far more reliable indicator of synthetic success. Subsequent COSY spectra were then used to ensure the newly shifted peak was associated to the remainder of the new chain. This second stage of confirmation becomes more important in reactions between precursor molecules and additional haloalkanes, as multiple triplets will then appear in the nitrogen-proximal region.

Additionally, specific to the production of tertiary amine products, IR spectroscopy can be used as an initial indication of reaction success. A tertiary amine product exhibits no N-H stretch, unlike for the secondary amine starting material, indicative of a complete reaction. It is important that this is attempted after a) freebasing any product hydrochloride salts and b) purifying the sample to remove any secondary amine reagents, as these contaminants would result in false N-H bond signals not associated to the target product.

3.2.3 Precursor Molecule Preparation

Preparations for eight precursor molecules proceeded as dictated in the Experimental Methods **Sections 3.4.1** - **3.4.8** and were subsequently characterised using nuclear magnetic resonance (NMR), infrared spectroscopy (IR) and mass spectrometry (MS). See the Experimental Methods **Section 3.4** for further details.

2-(methylamino) ethanol, [**MAE**]H, 2-(ethylamino) ethanol, [**EAE**]H, and 2-(isopropylamino) ethanol, [^{i}**PrAE**]H, as shown in **Figure 76**, were synthesised according

to, or adapted from literature methods.[221] These reaction proceeded by reaction of 2-amino ethanol with two stoichiometric equivalents of an aldehyde or ketone - paraformaldehyde, acetaldehyde and acetone respectively - in the presence of zinc chloride prior to in-situ reduction of the carbon-nitrogen double bond with sodium borohydride. The reaction was then quenched with sodium hydroxide to freebase the ammonium salt back to its target secondary amine form. These reactions were carried out primarily in accordance with the synthetic method described by Hullio *et al*.[221] The reactions were monitored throughout by TLC and, including their purification steps, require about 24 hours to reach completion. A longer reaction time may cause an increase in total yield, but the methods provided in this chapter proved sufficient for the project requirements.

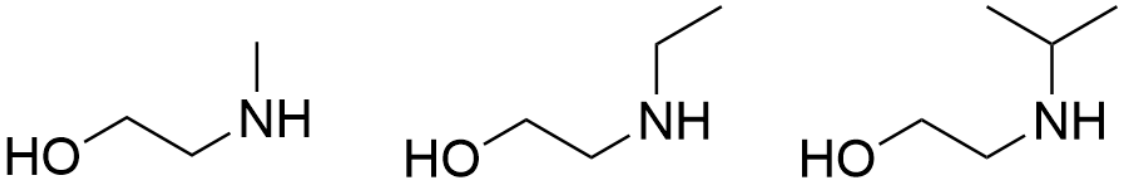

Figure 76- Structures for target molecules [**MAE**]H, left; [**EAE**]H, centre; and [^{i}**PrAE**]H, right.

In the case of [**MAE**]H, the desired product was produced as a near colourless liquid in high yield (74%), suitable for use in further reactions without additional purification required. The reaction proved very scalable and was successfully applied at a larger scale producing commensurate yields. The compound appears to be stable to both air and moisture for long term storage in its liquid state at room temperature and is soluble in the organic solvents commonly used throughout this project: chloroform, dichloromethane, methanol, acetonitrile and toluene.

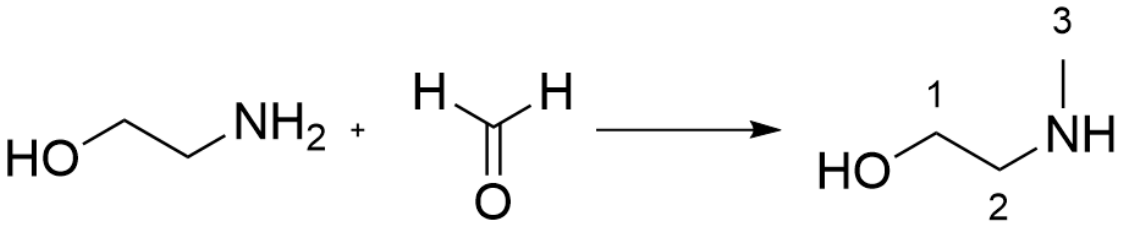

Scheme 5- Simplified synthesis of 2-(methylamino) ethan-1-ol. Stepwise: i) $ZnCl_2$ (2 eq), DCM (Dry), 1h, RT with stirring; ii) $NaBH_4$, 18h, RT with stirring; iii) NaOH (aq), 0.25h, DCM (3x10 mL), $MgSO_4$, flash column purification.

The ^{1}H NMR spectrum of [**MAE**]H, as shown in **Figure S1**, exhibited three peaks representative of the product: a singlet signal at 2.338 ppm associated to the protons on C_3 and two multiplet (pseudo-triplet) peaks at 2.656 and 3.601 ppm representative of the nitrogen proximal and oxygen proximal protons within the alcohol chain, C_2 and C_1, respectively. No broad proton signals for the exchangeable hydroxide or amine proton were observed. The ^{13}C NMR spectrum of [**MAE**]H, as shown in **Figure S3**, also exhibited three corresponding peaks: a 35.926 ppm methyl peak, C_3, alongside 53.412 and 60.320 ppm peaks representing the nitrogen proximal and oxygen proximal carbons, C_2 and C_1, respectively. These allocations were confirmed by COSY and HMQC analysis, given in **Figures S2** and **S4** respectively. The mass spectrum obtained of [**MAE**]H, as shown in **Figure S90**, gave rise to the three most abundant peaks at 76.0759, 98.0581 and 173.1284 representative of $\{M+H\}^+$, $\{M+Na\}^+$ and $\{2M+Na\}^+$ respectively. The FT-IR spectrum of [**MAE**]H, as shown in **Figure S72**, exhibited characteristic bands at 3288 and 3142 cm^{-1} consistent with the presence of an N-H and O-H bond, respectively.

In the case of [**EAE**]H, the desired product was produced as a near colourless liquid in a reasonable yield (59%). The product proved to be sufficiently pure, stable at room temperature to air and moisture and was soluble in all required organic solvents for use in further reactions.

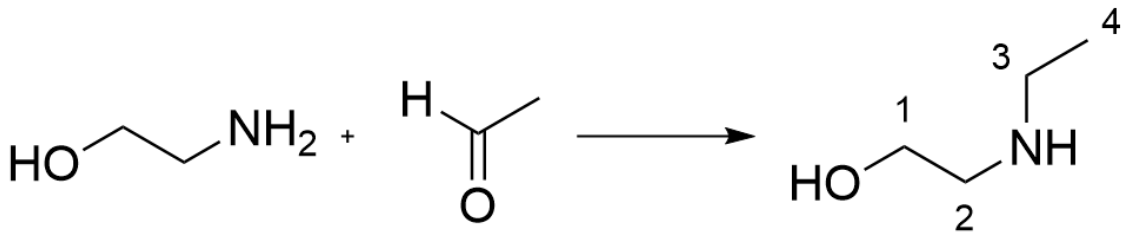

Scheme 6- Simplified synthesis of 2-(ethylamino) ethan-1-ol. Stepwise: i) $ZnCl_2$ (2 eq), DCM (Dry), 1h, RT with stirring; ii) $NaBH_4$, 18h, RT with stirring; iii) NaOH (aq), 0.25h, DCM (3x10 mL), $MgSO_4$, flash column purification.

The ^{1}H NMR spectrum of [**EAE**]H, as shown in **Figure S5**, exhibited four peaks representative of the product: a triplet signal at 1.050 ppm associated to the protons on C_4, a quartet within the range 2.575-2.618 ppm, related to the protons on C_3, and two triplets at 2.669 and 3.584 ppm representative of the protons within the alcohol chain, C_2 and C_1, respectively. No broad proton signals for the exchangeable hydroxide or amine proton were observed. The ^{13}C NMR Spectrum of [**EAE**]H, as shown in **Figure S7**, also exhibited four corresponding peaks: the side chain ethyl peaks, C_4 and C_3, at 14.948 and 43.680 ppm, alongside peaks for the alcohol chain at 51.130 and 60.430 ppm peaks representing C_2 and C_1, respectively. These allocations were confirmed by COSY and HMQC analysis, given in **Figures S6** and **S8** respectively. The mass spectrum of [**EAE**]H, as shown in **Figure S91**, gave rise to the three most abundant peaks at 90.0918, 112.0739 and 201.1595 representative of $\{M+H\}^+$, $\{M+Na\}^+$ and $\{2M+Na\}^+$ respectively. The FT-IR spectrum of [**EAE**]H, as shown in **Figure S73**, exhibited characteristic bands at 3263 and 3149 cm^{-1} consistent with the presence of an N-H and O-H bond, respectively.

In the case of [^{i}**PrAE**]H, the desired product was produced as a near colourless liquid in a moderate yield (35%). The product proved to be sufficiently pure, stable at room temperature to air and moisture and was soluble in all required organic solvents for use in further reactions.

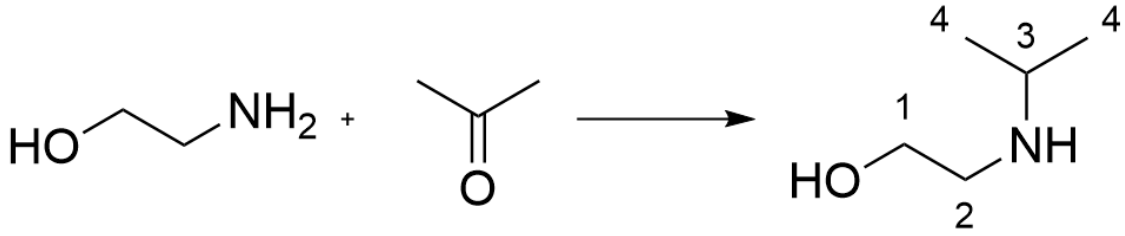

Scheme 7- Simplified synthesis of 2-(isopropylamino) ethan-1-ol. Stepwise: i) $ZnCl_2$ (2 eq), DCM (Dry), 1h, RT with stirring; ii) $NaBH_4$, 18h, RT with stirring; iii) NaOH (aq), 0.25h, DCM (3x10 mL), $MgSO_4$, flash column purification.

The ^{1}H NMR spectrum of [^{i}**PrAE**]H, as shown in **Figure S9**, exhibited four peaks representative of the product: a doublet signal in the region 1.010-1.022 ppm associated to the protons on C_4, a heptet centred at 2.749 ppm, related to the proton on C_3, and two triplets at 2.673 and 3.592 ppm representative of the protons within the alcohol chain, C_2 and C_1, respectively. No broad proton signals for the exchangeable hydroxide or amine proton were observed. The ^{13}C NMR Spectrum of [^{i}**PrAE**]H, as shown in **Figure S11**, also exhibited four corresponding peaks: the side chain isopropyl peaks, C_4 and C_3, at 22.808 and 48.754 ppm, alongside peaks for the alcohol chain at 48.559 and 60.892 ppm peaks representing C_2 and C_1, respectively. These allocations were confirmed by COSY and HMQC analysis, given in **Figures S10** and **S12** respectively. The mass spectrum of [^{i}**PrAE**]H, as shown in **Figure S92**, gave rise to the three most abundant peaks at 104.1074, 126.0896 and 229.1914 representative of $\{M+H\}^+$, $\{M+Na\}^+$ and $\{2M+Na\}^+$ respectively. The FT-IR spectrum of [^{i}**PrAE**]H, as shown in **Figure S74**, exhibited a characteristic band at 3142 cm^{-1} consistent with the presence of an O-H bond, although the expected weaker N-H stretch from the secondary amine does not appear in a region similar to other precursor molecules.

2-(tertbutylamino) ethanol, [^{t}**BuAE**]H, 2-(phenylamino) ethanol, [**PhAE**]H, 2-(adamantylamino) ethanol, [**AdAE**]H, 3-(tertbutylamino) propanol, [^{t}**BuAPr**]H and 3-(adamantylamino) propanol, [**AdAPr**]H, as shown in **Figure 77**, were synthesised according to, or adapted from, literature methods.[203] The syntheses proceeded by reaction of a primary amine – tertbutylamine, aniline or adamantylamine, as required – with an excess of chloroalcohol – 2-chloroethanol or 3-chloropropanol, as required – in a low polarity solvent, toluene. The products were isolated as quaternary hydrochloride salts of the target product and were freebased as part of the purification methods. These reactions were carried out by primarily adapting the synthetic methods described by Shi *et al.*[203], 2015 and Glowacki *et al.*[200], 2011. The reactions were undertaken at multiple scales and reaction lengths with the optimal conditions described within the Experimental Methods section below.

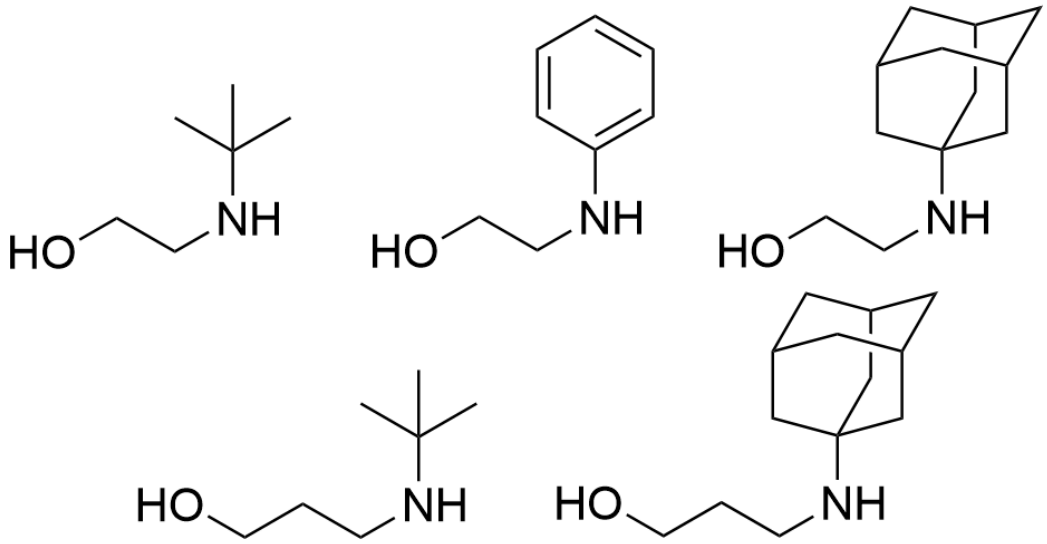

Figure 77- Structures for target molecules [^{t}**BuAE**]H, top left; [**PhAE**]H, top centre; [**AdAE**]H, top right; [^{t}**BuAPr**]H, bottom left, and [**AdAPr**]H, bottom right.

In the case of [^{t}**BuAE**]H, the desired product was produced as a low melting point colourless crystalline solid in a reasonable yield (54%). Handling this product proved challenging due to its near room temperature melting point. The product proved to be sufficiently pure, stable at room temperature to air and moisture and was soluble in all required organic solvents for use in further reactions.

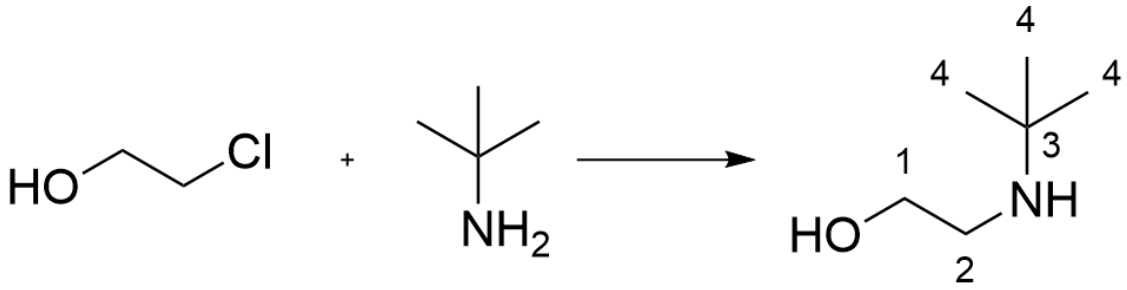

Scheme 8- Simplified synthesis of 2-(tertbutylamino) ethan-1-ol. Stepwise: i) Toluene (Dry), 24h, reflux with stirring; ii) Water, NaOH (aq), 0.25h, DCM (3x10 mL), $MgSO_4$, triturated with pentane at low temperature.

The ^{1}H NMR spectrum of [^{t}**BuAE**]H, as shown in **Figure S13**, exhibited three peaks representative of the product: a singlet signal at 1.090 ppm associated to the protons on C_4, and two triplets at 2.690 and 3.630 ppm representative of the protons within the alcohol chain, C_2 and C_1, respectively. C_3 has no associated protons and so exhibits no signal. No broad proton signals for the exchangeable hydroxide or amine proton were observed. The ^{13}C NMR spectrum of [^{t}**BuAE**]H, as shown in **Figure S15**, instead exhibited four corresponding peaks: the side chain tertbutyl peaks, C_4 and C_3, at 28.995 and 50.202 ppm, alongside peaks for the alcohol chain at 43.873 and 61.562 ppm peaks representing C_2 and C_1, respectively. These allocations were confirmed by COSY and HMQC analysis, given in **Figures S14** and **S16** respectively. The mass spectrum of [^{t}**BuAE**]H, as shown in **Figure S93**, gave rise to the three most abundant peaks at 118.1230, 140.1051 and 257.2227 representative of $\{M+H\}^+$, $\{M+Na\}^+$ and $\{2M+Na\}^+$ respectively. The FT-IR spectrum of [^{t}**BuAE**]H, as shown in **Figure S75**, exhibited characteristic bands at 3266 and 3114 cm^{-1} consistent with the presence of an N-H and O-H bond, respectively.

In the case of [**PhAE**]H, the desired product was produced as a near black viscous oil in a reasonable yield (58%). The product proved to be sufficiently pure, stable at room temperature to air and moisture in the short term and was sufficiently soluble in all required organic solvents for use in further reactions. With prolonged exposure in aerobic environments [**PhAE**]H will discolour to a dark blue, this did not result in a noticeable change to its action in further syntheses.

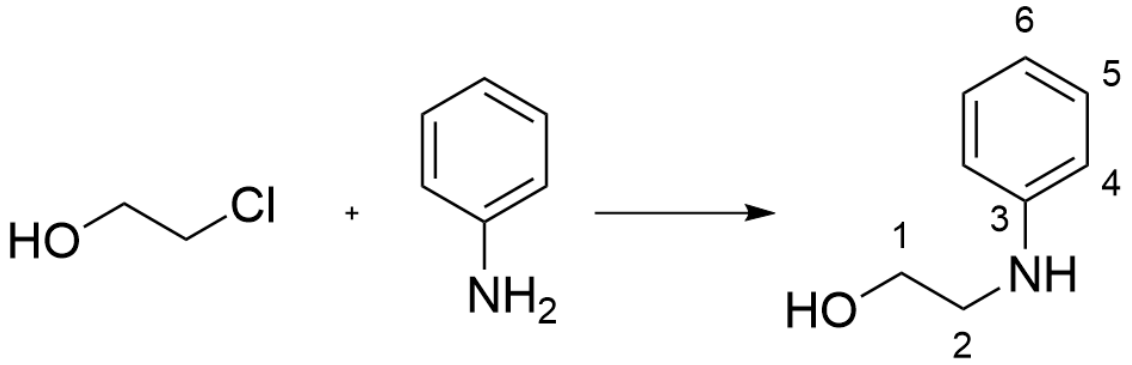

Scheme 9- Simplified synthesis of 2-(phenylamino) ethan-1-ol. Stepwise: i) Toluene (Dry), 24h, reflux with stirring; ii) Water, NaOH (aq), 0.25h, DCM (3x10 mL), $MgSO_4$, purified by vacuum distillation.

The ^{1}H NMR spectrum of [**PhAE**]H, as shown in **Figure S17**, exhibited four peaks representative of the product: two triplets at 3.265 and 3.782 ppm representative of the protons within the alcohol chain, C_2 and C_1, respectively, and two multiplet signals within the regions 6.647-6.784 ppm (three protons, ortho and para positions) and 7.195-7.234 ppm (two protons, meta positions) which collectively characterise the phenyl side group as a summation of the protons on C_4, C_5 and C_6. C_3 has no associated protons and so exhibits no signal. No broad proton signals for the exchangeable hydroxide or amine proton were observed. The ^{13}C NMR spectrum of [**PhAE**]H, as shown in **Figure S19**, instead exhibited five corresponding peaks: the side group phenyl peaks, C_6, C_5, C_4 and C_3, at 117.819, 129.208, 113.176 and 148.010 ppm, respectively, alongside peaks for the alcohol chain at 45.981 and 61.007 ppm peaks representing C_2 and C_1. These allocations were confirmed by COSY and HMQC analysis, given in **Figures S18** and **S20** respectively. The mass spectrum of [**PhAE**]H, as shown in **Figure S94**, gave rise to the three most abundant peaks at 120.0811, 138.0917 and 297.1591 representative of $\{M+H-[H_2O]\}^+$, $\{M+H\}^+$ and $\{2M+Na\}^+$ respectively. The FT-IR spectrum of [**PhAE**]H, as shown in **Figure S76**, exhibited characteristic bands at 3388 and 3346 cm^{-1} consistent with the presence

of an N-H and O-H bond, respectively. The phenyl group is also represented by signals at 1601 cm^{-1} and 1459 cm^{-1}.

In the case of [**AdAE**]H, the desired product was produced as an off-white solid in a high yield (89%). The product proved to be sufficiently pure, stable at room temperature to air and moisture and was soluble in all required organic solvents when heated for use in further reactions.

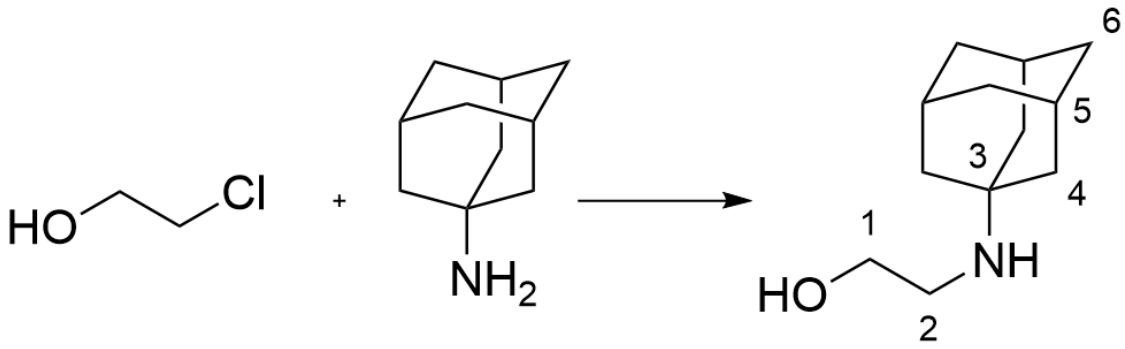

Scheme 10- Simplified synthesis of 2-(adamantylamino) ethan-1-ol. Stepwise: i) Toluene (Dry), 24h, reflux with stirring; ii) Water, NaOH (aq), 0.25h, DCM (4x50 mL), $MgSO_4$, concentrated under vacuo.

The ^{1}H NMR spectrum of [**AdAE**]H, as shown in **Figure S21**, exhibited four distinct peaks representative of the product: a multiplet signal within the range 1.579-1.672 ppm associated to the protons on the secondary carbons C_4 and C_6, alongside a broad singlet at 2.055, representative of the protons on the tertiary carbons, C_5, and two triplets at 2.716 and 3.580 ppm representative of the protons within the alcohol chain, C_2 and C_1, respectively. C_3 has no associated protons and so exhibits no signal. No broad proton signals for the exchangeable hydroxide or amine proton were observed. The ^{13}C NMR spectrum of [**AdAE**]H, as shown in **Figure S23**, instead exhibited six corresponding peaks: the side group adamantyl peaks, C_6, C_5, C_4 and C_3, at 36.658, 29.513, 42.862 and 50.173 ppm, respectively, alongside peaks for the alcohol chain at 41.706 and 61.739 ppm peaks representing C_2 and C_1. These allocations were confirmed by COSY and HMQC analysis, given in **Figures S22** and **S24** respectively. The mass spectrum of [**AdAE**]H, as shown in **Figure S95**, gave rise to the three most abundant peaks at 196.1699, 413.3239 and 429.2825 representative of $\{M+H\}^+$, $\{2M+Na\}^+$ and $\{2M+K\}^+$ respectively. The FT-IR spectrum of [**AdAE**]H, as shown in **Figure S77**, exhibited a characteristic band in the region 3378 cm^{-1} consistent with the presence of an N-H bond. The broad O-H bond seems to be heavily distorted by a strong amine stretch and is therefore difficult to assign.

In the case of [^{t}**BuAPr**]H, the desired product was produced as a low melting point colourless crystalline solid in a reasonable yield (54%). Handling this product proved challenging due to its near room temperature melting point. The product proved to be sufficiently pure, stable at room temperature to air and moisture and was soluble in all required organic solvents for use in further reactions.

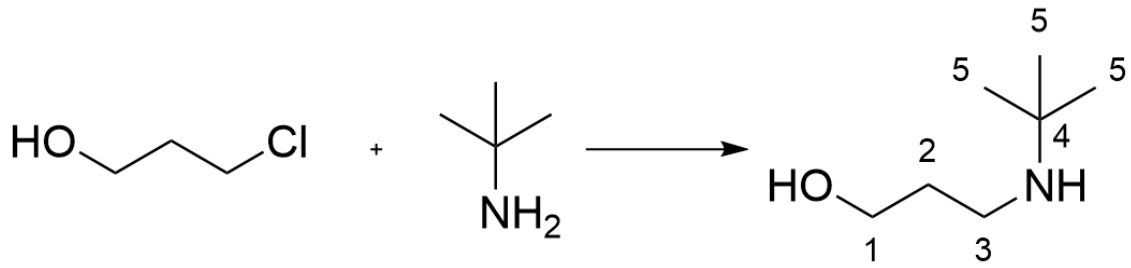

Scheme 11- Simplified synthesis of 3-(tertbutylamino) propan-1-ol. Stepwise: i) Toluene (Dry), 24h, reflux with stirring; ii) Water, NaOH (aq), 0.25h, DCM (3x25 mL), $MgSO_4$, triturated with pentane at low temperature.

The ^{1}H NMR spectrum of [^{t}**BuAPr**]H, as shown in **Figure S25**, exhibited four peaks representative of the product: a singlet signal at 1.440 ppm associated to the protons on C_5, and two triplets at 3.061 and 3.776 ppm and a pentet at 2.114 ppm representative of the protons within the alcohol chain, C_3, C_1 and C_2, respectively. C_4 has no associated protons and so exhibits no signal. No broad proton signals for the exchangeable hydroxide or amine proton were observed. The ^{13}C NMR spectrum of [^{t}**BuAPr**]H, as shown in **Figure S27**, instead exhibited five corresponding peaks: the side chain tertbutyl peaks, C_5 and C_4, at 25.789 and 57.012 ppm, alongside peaks for the alcohol chain at 39.824, 28.908 and 59.502 ppm peaks representing C_3, C_2 and C_1, respectively. These allocations were confirmed by COSY and HMQC analysis, given in **Figures S26** and **S28** respectively. The mass spectrum of [^{t}**BuAPr**]H, as shown in **Figure S96**, gave rise to peaks the three most abundant at 132.1390, 154.1209 and 263.2700 representative of $\{M+H\}^+$, $\{M+Na\}^+$ and $\{2M+H\}^+$ respectively. The FT-IR spectrum of [^{t}**BuAPr**]H, as shown in **Figure S78**, exhibited a characteristic band in the region 3378 cm^{-1} consistent with the presence of an N-H bond. The broad O-H bond seems to be heavily distorted by a strong amine stretch and is therefore difficult to assign.

In the case of [**AdAPr**]H, the desired product was produced as a white solid in a high yield (89%). The product proved to be sufficiently pure, stable at room temperature to air and moisture and was soluble in all required organic solvents when heated for use in further reactions.

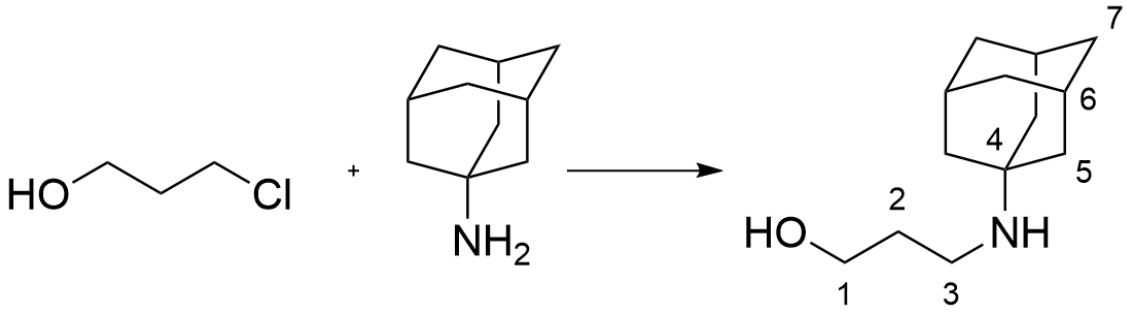

Scheme 12- Simplified synthesis of 3-(adamantylamino) propan-1-ol. Stepwise: i) Acetonitrile, 96h, reflux with stirring; ii) Hot filtration, cool filtrate, diethyl ether (4x5 mL) washes and dry in air.

The ^{1}H NMR spectrum of [**AdAPr**]H, as shown in **Figure S29**, exhibited four distinct peaks representative of the product: a multiplet signal within the range 1.580-1.679 ppm associated to the protons on the secondary carbons C_5 and C_7, alongside a broad singlet at 2.062, representative of the protons on the tertiary carbons, C_6, and two triplets at 2.869 and 3.804 ppm and a pentet overlapping with the adamantyl secondary carbons in the range 1.580-1.679 ppm (for a total integral of fourteen protons) representative of the protons within the alcohol chain, C_3, C_1 and C_2, respectively. C_4 has no associated protons and so exhibits no signal. No broad proton signals for the exchangeable hydroxide or amine proton were observed. The ^{13}C NMR spectrum of [**AdAPr**]H, as shown in **Figure S31**, instead exhibited seven corresponding peaks: the side group adamantyl peaks, C_7, C_6, C_5 and C_4, at 36.639, 29.446, 42.590 and 50.655 ppm, respectively, alongside peaks for the alcohol chain at 40.907, 31.545 and 64.997 ppm peaks representing C_3, C_2 and C_1. These allocations were confirmed by COSY and HMQC analysis, given in **Figures S30** and **S32** respectively. The mass spectrum of [**AdAPr**]H, as shown in **Figure S97**, gave rise to the three most abundant peaks at 210.1871, 232.1679 and 419.3634 representative of $\{M+H\}^+$, $\{M+Na\}^+$ and $\{2M+H\}^+$ respectively. The FT-IR spectrum of [**AdAPr**]H, as shown in **Figure S79**, exhibited characteristic bands at 3256 cm^{-1} and 3098 cm^{-1} consistent with the presence of an N-H and O-H bond, respectively.

Precursors [**MAE**]H, [**EAE**]H and [^{i}**PrAE**]H were produced by an alternate route due to the difficulty in procuring and handling the reagents which would be required for the chloroalcohol nucleophilic substitution route. Methylamine, ethylamine and isopropylamine all exhibit boiling points below 50 °C – well below the intended temperature for an acetonitrile or toluene reflux – potentially leading to handling issues or reaction vessel pressurisation. This led to the institution of the alternate methodology discussed.

3.2.4 Symmetric Polyalcohol Ligand Preparation

Preparations for six symmetric polyalcohol ligands proceeded as dictated in the Experimental Methods **Sections 3.4.9 - 3.4.14** and were subsequently characterised using nuclear magnetic resonance (NMR), infrared spectroscopy (IR) and mass spectrometry (MS). See the Experimental Methods **Section 3.4** for further details.

N-methyldiethanolamine, [**MDEA**]H_2, N-ethyldiethanolamine, [**EDEA**]H_2, N-isopropyldiethanolamine, [^{i}**PrDEA**]H_2 and N-phenyldiethanolamine, [**PhDEA**]H_2, as shown in **Figure 78**, were synthesised according to, or adapted from, literature methods.[203] N-tertbutyldiethanolamine, [^{t}**BuDEA**]H_2 and N-adamantyldiethanolamine, [**AdDEA**]H_2 syntheses were also attempted and shall be further discussed towards the end of this section. The syntheses proceeded by reaction of a secondary amine – [**MAE**]H, [**EAE**]H, [^{i}**PrAE**]H, [^{t}**BuAE**]H, [**PhAE**]H or [**AdAE**]H as required – with 2-chloroethanol, primarily in a low polarity solvent, toluene. The products were isolated as quaternary hydrochloride salts of the target product and were freebased as part of the purification methods. These reactions were carried out by adapting the synthetic methods described by Shi *et al*, 2015.[203] The reactions were undertaken at multiple scales, equivalencies and reaction lengths with the optimal conditions described within the Experimental Methods section below.

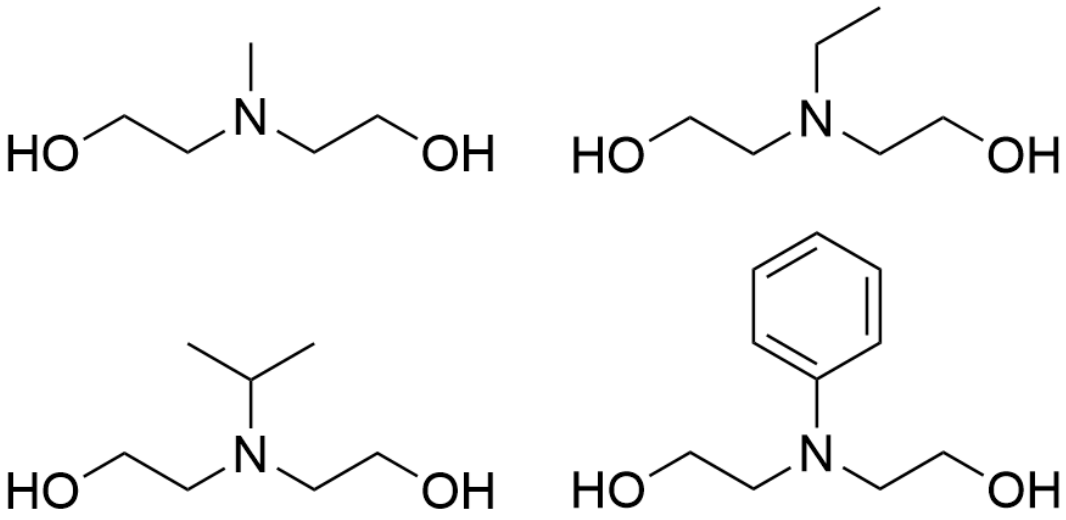

Figure 78- Structures for target molecules [**MDEA**]H_2, top left; [**EDEA**]H_2, top right; [^{i}**PrDEA**]H_2, bottom left; and [**PhDEA**]H_2, bottom right.

In the case of [**MDEA**]H_2, the desired product was produced as a near colourless oil in a reasonable yield (61%). The product proved to be sufficiently pure, stable at room temperature to air and moisture and was soluble in acetonitrile and methanol for use in complexation reactions.

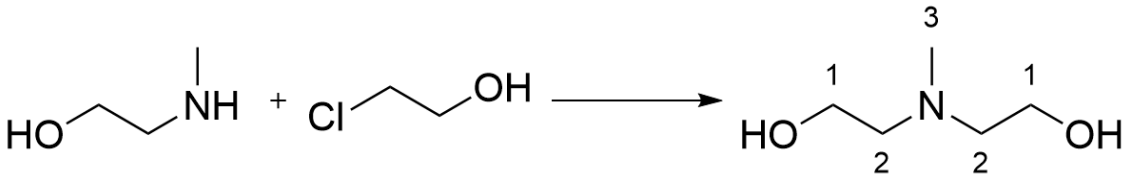

Scheme 13- Simplified synthesis of N-methyldiethanolamine. Stepwise: i) Toluene (Dry), 3h, reflux with stirring; ii) Water, NaOH (aq), 0.25h, DCM (3x20 mL), $MgSO_4$, purified by vacuum distillation.

The ^{1}H NMR spectrum of [**MDEA**]H_2, as shown in **Figure S33**, exhibited three peaks representative of the product: a singlet signal at 2.235 ppm associated to the protons on C_3 and two triplets at 2.507 and 3.578 ppm representative of the nitrogen proximal and oxygen proximal protons within the alcohol chain, C_2 and C_1, respectively. No broad proton signals for the exchangeable hydroxide or amine proton were observed. The ^{13}C NMR spectrum of [**MDEA**]H_2, as shown in **Figure S35**, also exhibited three corresponding peaks: a 41.994 ppm methyl peak, C_3, alongside 59.423 and 58.951 ppm peaks representing the nitrogen proximal and oxygen proximal carbons, C_2 and C_1, respectively. These allocations were confirmed by COSY and HMQC analysis, given in **Figures S34** and **S36** respectively. The mass spectrum of [**MDEA**]H_2, as shown in **Figure S98**, gave rise to the three most abundant peaks at 102.0918, 120.1031 and 142.0842 representative of $\{M+H-[H_2O]\}^+$, $\{M+H\}^+$ and $\{M+Na\}^+$ respectively. The FT-IR spectrum of [**MDEA**]H_2, as shown in **Figure S80**, exhibited a characteristic band at 3315 cm^{-1} consistent with the presence of an O-H bond.

In the case of [**EDEA**]H_2, the desired product was produced as a near colourless oil in a moderate yield (40%). The product proved to be sufficiently pure, stable at room temperature to air and moisture and was soluble in acetonitrile and methanol for use in complexation reactions.

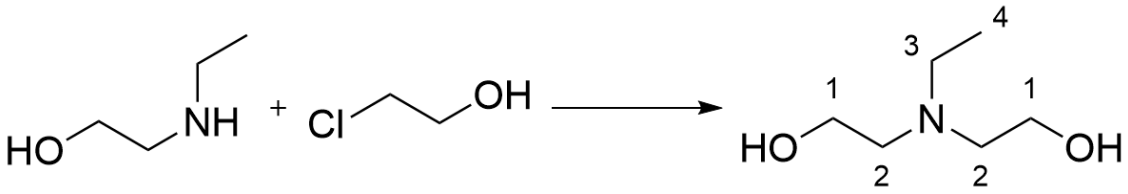

Scheme 14- Simplified synthesis of N-ethyldiethanolamine. Stepwise: i) Toluene (Dry), 3h, reflux with stirring; ii) Water, NaOH (aq), 0.25h, DCM (3x20 mL), $MgSO_4$, purified by vacuum distillation.

The ^{1}H NMR spectrum of [**EDEA**]H_2, as shown in **Figure S37**, exhibited four peaks representative of the product: a triplet signal at 1.001 ppm associated to the protons on C_4, a quartet within the range 2.586-2.612 ppm, related to the protons on C_3, and two triplets, one overlapping the quartet at 2.586-2.612 ppm and another at 3.570 ppm representative of the protons within the alcohol chain, C_2 and C_1, respectively. No broad proton signals for the exchangeable hydroxide or amine proton were observed. The ^{13}C NMR spectrum of [**EDEA**]H_2, as shown in **Figure S39**, also exhibited four corresponding peaks: the side chain ethyl peaks, C_4 and C_3, at 11.333 and 55.362 ppm, alongside peaks for the alcohol chain at 48.070 and 59.135 ppm peaks representing C_2 and C_1, respectively. These allocations were confirmed by COSY and HMQC analysis, given in **Figures S38** and **S40** respectively. The mass spectrum of [**EDEA**]H_2, as shown in **Figure S99**, gave rise to the three most abundant peaks at 116.1074, 134.1189 and 156.0998 representative of $\{M+H-[H_2O]\}^+$, $\{M+H\}^+$ and $\{M+Na\}^+$ respectively. The FT-IR spectrum of [**EDEA**]H_2, as shown in **Figure S81**, exhibited a characteristic band at 3324 cm^{-1} consistent with the presence of an O-H bond.

In the case of [^{i}**PrDEA**]H_2, the desired product was produced as a near colourless oil in a moderate yield (44%). The product proved to be sufficiently pure, stable at room temperature to air and moisture and was soluble in acetonitrile and methanol for use in complexation reactions.

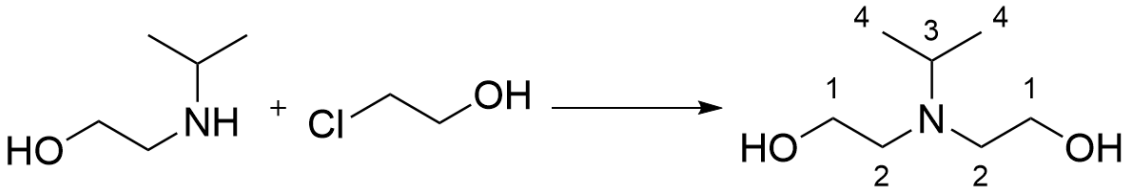

Scheme 15- Simplified synthesis of N-isopropyldiethanolamine. Stepwise: i) Toluene (Dry), 3h, reflux with stirring; ii) Water, NaOH (aq), 0.25h, DCM (3x20 mL), $MgSO_4$, purified by vacuum distillation.

The ^{1}H NMR spectrum of [^{i}**PrDEA**]H_2, as shown in **Figure S41**, exhibited four peaks representative of the product: a doublet signal in the region 0.976-0.990 ppm associated to the protons on C_4, a heptet centred at 2.931 ppm, related to the proton on C_3, and two triplets at 2.571 and 3.529 ppm representative of the protons within the alcohol chain, C_2 and C_1, respectively. No broad proton signals for the exchangeable hydroxide or amine proton were observed. The ^{13}C NMR spectrum of [^{i}**PrDEA**]H_2, as shown in **Figure S43**, also exhibited four corresponding peaks: the side chain isopropyl peaks, C_4 and C_3, at 18.029 and 50.927 ppm, alongside peaks for the alcohol chain at 51.552 and 59.993 ppm peaks representing C_2 and C_1, respectively. These allocations were confirmed by COSY and HMQC analysis, given in **Figures S42** and **S44** respectively. The mass spectrum of [^{i}**PrDEA**]H_2, as shown in **Figure S100**, gave rise to the three most abundant peaks at 130.1233, 148.1341 and 170.1156 representative of $\{M+H-[H_2O]\}^+$, $\{M+H\}^+$ and $\{M+Na\}^+$ respectively. The FT-IR spectrum of [^{i}**PrDEA**]H_2, as shown in **Figure S82**, exhibited a characteristic band at 3303 cm^{-1} consistent with the presence of an O-H bond.

In the case of [**PhDEA**]H_2, the desired product was produced as a white solid in a low yield (26%). The product proved to be sufficiently pure, stable at room temperature to air and moisture in the short term for use in complexation reactions. However [**PhDEA**]H_2 is only slightly soluble in acetonitrile and methanol limiting its use in complexation reactions.

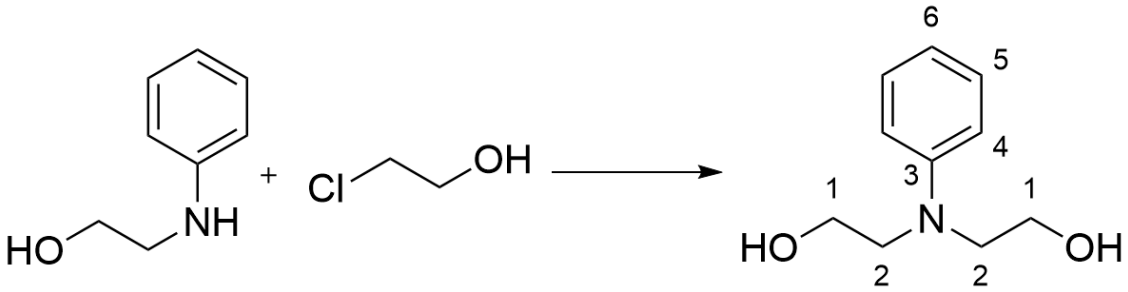

Scheme 16- Simplified synthesis of N-phenyldiethanolamine. Stepwise: i) Toluene (Dry), 6h, reflux with stirring; ii) Water, NaOH (aq), 0.25h, DCM (3x20 mL), $MgSO_4$, triturated with pentane.

The ^{1}H NMR spectrum of [**PhDEA**]H_2, as shown in **Figure S49**, exhibited four peaks representative of the product: two triplets at 3.590 and 3.869 ppm representative of the protons within the alcohol chain, C_2 and C_1, respectively, and two multiplet signals within the regions 6.712-6.758 ppm (three protons, ortho and para positions) and 7.218-7.251 ppm (two protons, meta positions) which collectively characterise the phenyl side group as a summation of the protons on C_4, C_5 and C_6. C_3 has no associated protons and so exhibits no signal. No broad proton signals for the exchangeable hydroxide or amine proton were observed. The ^{13}C NMR spectrum of [**PhDEA**]H_2, as shown in **Figure S51**, instead exhibited five corresponding peaks: the side group phenyl peaks, C_6, C_5, C_4 and C_3, at 117.085, 129.325, 112.764 and 147.891 ppm, respectively, alongside peaks for the alcohol chain at 55.253 and 60.887 ppm peaks representing C_2 and C_1. These allocations were confirmed by COSY and HMQC analysis, given in **Figures S50** and **S52** respectively. The mass spectrum of [**PhDEA**]H_2, as shown in **Figure S102**, gave rise to the three most abundant peaks at 164.1072, 182.1178 and 204.0998 representative of $\{M+H-[H_2O]\}^+$, $\{M+H\}^+$ and $\{M+Na\}^+$ respectively. The FT-IR spectrum of [**PhDEA**]H_2, as shown in **Figure S84**, exhibited a characteristic band at 3323 cm^{-1} consistent with the presence of an O-H bond. The phenyl group is also represented by signals at 1596 cm^{-1} and 1458 cm^{-1}.

N-n-butyldiethanolamine, [^{n}**BuDEA**]H_2, and triethanolamine, [**TEA**]H_3, as shown in **Figure 79**, were synthesised by adaption of literature methods.[200] As a result of the minimal solubility of diethanolamine in toluene, an alternate method of synthesis using a different solvent was required for [^{n}**BuDEA**]H_2 and [**TEA**]H_3. The syntheses proceeded by reaction of diethanolamine with an excess of 2-chloroethanol or 4-chlorobutane respectively in a high polarity solvent, water. The products were isolated as quaternary hydrochloride salts of the target product and were freebased as part of the purification methods. These reactions were carried out by primarily adapting the synthetic methods described by Glowacki *et al.*[200], 2011. The reactions were undertaken at multiple scales, equivalencies and reaction lengths with the optimal conditions described within the Experimental Methods section below.

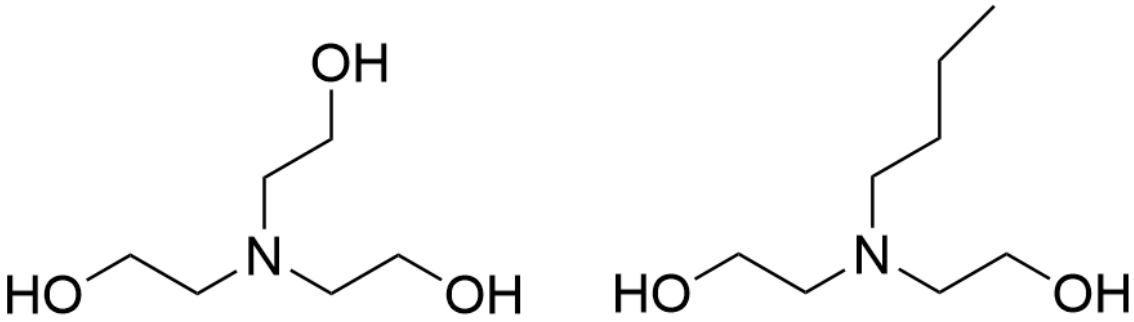

Figure 79- Structures for target molecules [**TEA**]H_3, left; and [^{n}**BuDEA**]H_2, right.

In the case of [^{n}**BuDEA**]H_2, the desired product was produced as a near colourless oil in a high yield (74%). The product proved to be sufficiently pure, stable at room temperature to air and moisture and was soluble in acetonitrile and methanol for use in complexation reactions.

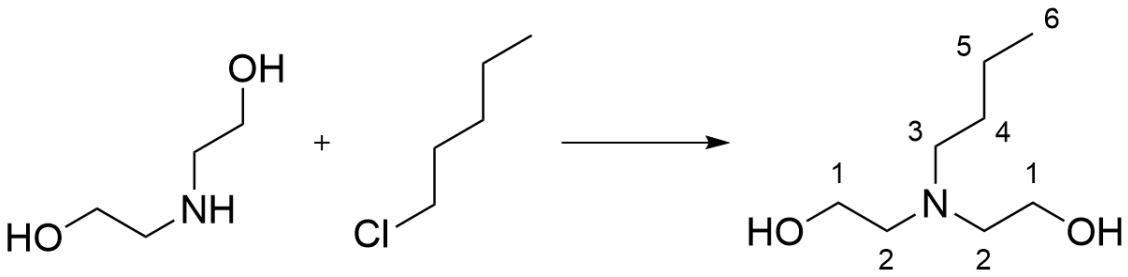

Scheme 17- Simplified synthesis of N-n-butyldiethanolamine. Stepwise: i) Water, 24h, reflux with stirring; ii) Water, NaOH (aq), 0.25h, DCM (3x20 mL), $MgSO_4$, purified by vacuum distillation.

The ^{1}H NMR spectrum of [^{n}**BuDEA**]H_2, as shown in **Figure S45**, exhibited six peaks representative of the product. Making up the butyl side chain were two triplet signals at 0.877 and 2.482 ppm associated to the protons on C_6 and C_3, a sextet and a pentet within the range 1.230-1.304 ppm and at 1.413 ppm, related to the protons on C_5 and C_4. Additionally, the alcohol chains were denoted by two triplets, at 2.601 ppm and 3.564 ppm representative of the protons on C_2 and C_1, respectively. No broad proton signals for the exchangeable hydroxide or amine proton were observed. The ^{13}C NMR spectrum of [^{n}**BuDEA**]H_2, as shown in **Figure S47**, also exhibited six corresponding peaks: the side chain ethyl peaks, C_6, C_5, C_4 and C_3, at 13.916, 20.426, 28.896 and 54.447 ppm respectively, alongside peaks for the alcohol chain at 56.023 and 59.514 ppm peaks representing C_2 and C_1. These allocations were confirmed by COSY and HMQC analysis, given in **Figures S46** and **S48** respectively. The mass spectrum of [^{n}**BuDEA**]H_2, as shown in **Figure S101**, gave rise to the three most abundant peaks at 144.1385, 162.1507 and 184.1309 representative of $\{M+H-[H_2O]\}^+$, $\{M+H\}^+$ and $\{M+Na\}^+$ respectively. The FT-IR spectrum of [^{n}**BuDEA**]H_2, as shown in **Figure S83**, exhibited a characteristic band at 3345 cm^{-1} consistent with the presence of an O-H bond.

In the case of [**TEA**]H_3, the desired product was produced as a colourless liquid in a high yield (96%). The product proved to be sufficiently pure, stable at room temperature to air and moisture and was soluble in acetonitrile and methanol for use in complexation reactions.

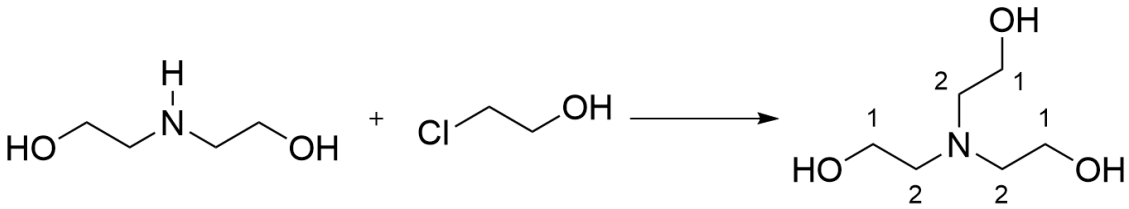

Scheme 18- Simplified synthesis of triethanolamine. Stepwise: i) Water, 24h, reflux with stirring; ii) Water, NaOH (aq), 0.25h, DCM (3x20 mL), $MgSO_4$, purified by vacuum distillation.

The ^{1}H NMR spectrum of [**TEA**]H_3, as shown in **Figure S53**, exhibited three peaks representative of the product: two triplets at 2.514 and 3.550 ppm representative of the nitrogen proximal and oxygen proximal protons within the alcohol chain, C_2 and C_1, respectively and a broad proton signal at 5.082 ppm for the exchangeable hydroxides. The ^{13}C NMR spectrum of [**TEA**]H_3, as shown in **Figure S55**, instead exhibited two corresponding peaks: 56.893 and 59.226 ppm peaks representing the nitrogen proximal and oxygen proximal carbons, C_2 and C_1, respectively. These allocations were confirmed by COSY and HMQC analysis, given in **Figures S54** and **S56** respectively. The mass spectrum of [**TEA**]H_3, as shown in **Figure S103**, gave rise to the three most abundant peaks at 132.1024, 150.1141 and 172.0946 representative of $\{M+H-[H_2O]\}^+$, $\{M+H\}^+$ and $\{M+Na\}^+$ respectively. The FT-IR spectrum of [**TEA**]H_3, as shown in **Figure S85**, exhibited a characteristic band at 3288 cm^{-1} consistent with the presence of an O-H bond.

As part of the synthetic methods untaken in the research for this chapter, further attempts were made to synthesise the ligands N-tertbutyldiethanolamine, [^{t}**BuDEA**]H_2 and N-adamantyldiethanolamine, [**AdDEA**]H_2, as shown in **Figure 80**.

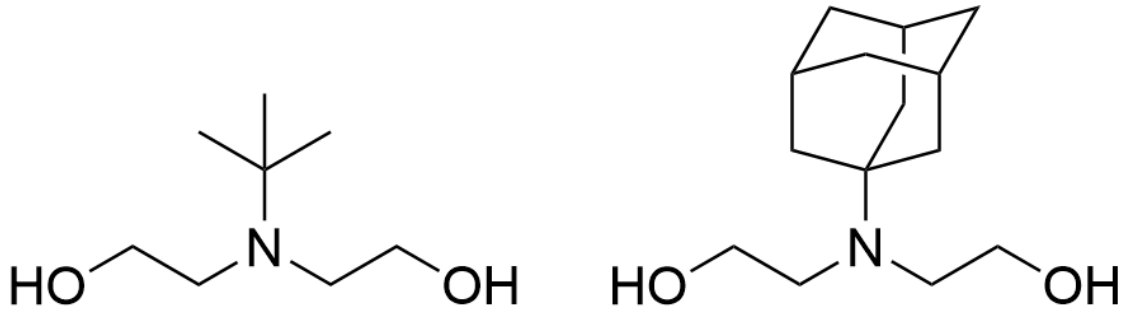

Figure 80- Structures for target molecules [^{t}**BuDEA**]H_2, left; and [**AdDEA**]H_2, right.

These syntheses proceeded broadly similarly to those previously mentioned by the reaction of 2-chloroethanol with the prerequisite precursor, [^{t}**BuAE**]H or [**AdAE**]H respectively. Even though these reactions were carried out with a stoichiometric excess of 2-chloroethanol, the increased steric bulk of the precursors proved to inhibit the reaction from moving to completion, with the final product remaining a mixture of the two reagents and target product. Purification methods viable for previous reactions, however, proved insufficient to separate these mixtures. Hot filtration of the adamantyl product resulted in the co crystallisation of product and precursor molecule, although this did expedite removal of the excess chloroethanol. Trituration of the tertbutyl product failed to initiate product crystallisation, even at sub room temperature levels. Thin layer chromatography (TLC) on silica plates, basified silica plates and alumina plates exhibited some separation of the precursor and product, whilst attempts at scaling this process up to column chromatography resulted in said components getting stuck on the silica column, with no amine species appearing in the first fifty eluate layers. Finally, vacuum distillation, although effective at removing the excess chloroethanol from the adamantyl reaction, was unable to remove the assumedly high boiling point [**AdAE**]H precursor, whilst the tert-butyl species seemingly degraded during the process. As a result, no pure [^{t}**BuDEA**]H_2 or [**AdDEA**]H_2 samples were obtained for structural analysis such as NMR or IR as the precursor too closely resembles the product to cleanly differentiate the two within a spectrum. However, the impure samples were still submitted for analysis by mass spectrometry as an indication of synthetic success.

The mass spectrum of [^{t}**BuDEA**]H_2, with the molecular formula $C_8H_{19}NO_2$, as shown in **Figure S104**, gave rise to peaks at 162.1493, 184.1308 and 305.2805 representative of $\{M+H\}^+$, $\{M+Na\}^+$ and $\{2M+H-[H_2O]\}^+$ respectively. Calculated $[M+H]^+ = 162.1494$.

The mass spectrum of [**AdDEA**]H_2, with the molecular formula $C_{14}H_{25}NO_2$, as shown in **Figure S105**, gave rise to peaks at 222.1825, 240.1966 and 262.1780 representative of $\{M+H-[H_2O]\}^+$, $\{M+H\}^+$ and $\{M+Na\}^+$ respectively. Calculated $[M+H]^+ = 240.1964$.

3.2.5 Asymmetric Polyalcohol Ligand Preparation

Preparations for four asymmetric polyalcohol ligands proceeded as dictated in the Experimental Methods **Sections 3.4.15 - 3.4.18** and were subsequently characterised using nuclear magnetic resonance (NMR), infrared spectroscopy (IR) and mass spectrometry (MS). See the Experimental Methods **Section 3.4** for further details.

3-[(2-hydroxyethyl)(methyl)amino] propan-1-ol, [**HMAP**]H_2, 3-[(2-hydroxyethyl)(ethyl)amino] propan-1-ol, [**HEAP**]H_2, 3-[(2-hydroxyethyl)(iso-propyl)amino] propan-1-ol, [**H^{i}PrAP**]H_2, 3-[(2-hydroxyethyl)(phenyl)amino] propan-1-ol, [**HPhAP**]H_2, as shown in **Figure 81**, were synthesised according to, or adapted from, literature methods.[203] 3-[(2-hydroxyethyl)(tert-butyl)amino] propan-1-ol, [**H^{t}BuAP**]H_2, 3-[(2-hydroxyethyl)(adamantyl)amino] propan-1-ol, [**HAdAP**]H_2, and 2,2'-[(3-hydroxypropyl)imino] bis-ethanol [**^{n}Pr'DEA**]H_3 syntheses were also attempted and shall be further discussed towards the end of this section. The syntheses proceeded by reaction of a secondary amine – [**MAE**]H, [**EAE**]H, [**^{i}PrAE**]H, [**^{t}BuAE**]H, [**PhAE**]H or [**AdAE**]H, as required – with 3-chloropropanol in a low polarity solvent, toluene. The products were isolated as quaternary hydrochloride salts of the target product and were freebased as part of the purification methods. These reactions were carried out by adapting the synthetic methods described by Shi *et al.*[203], 2015, and Glowacki *et al.*[200], 2011. The reactions were undertaken at multiple scales, equivalencies and reaction lengths with the optimal conditions described within the Experimental Methods section below.

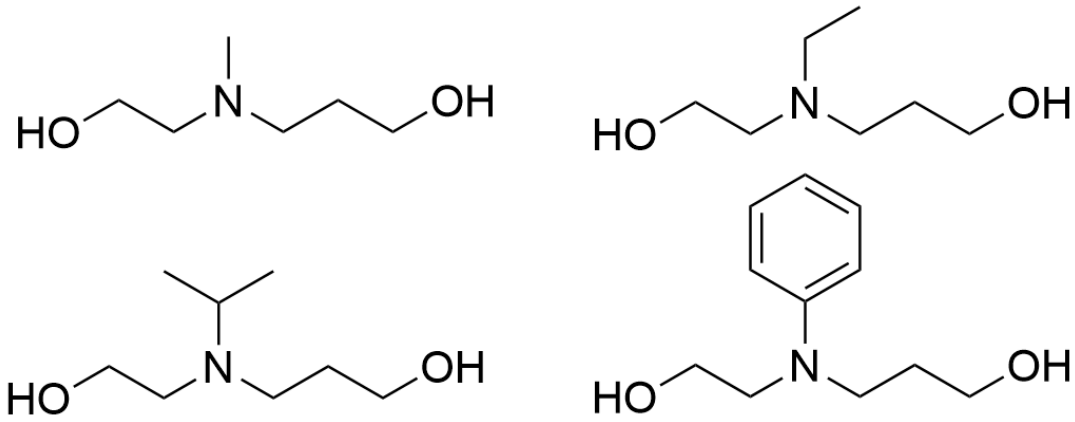

Figure 81- Structures for target molecules [**HMAP**]H_2, top left; [**HEAP**]H_2, top right; [**H^{i}PrAP**]H_2, bottom left; and [**HPhAP**]H_2, bottom right.

In the case of [**HMAP**]H_2, the desired product was produced as a near colourless oil in a reasonable yield (61%). The product proved to be sufficiently pure, stable at room temperature to air and moisture and was soluble in acetonitrile and methanol for use in complexation reactions.

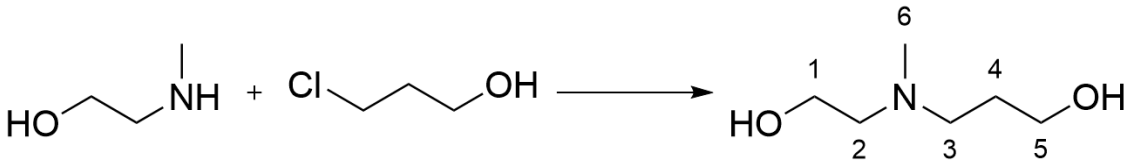

Scheme 19- Simplified synthesis of 3-[(2-hydroxyethyl)(methyl)amino]propan-1-ol. Stepwise: i) Toluene (Dry), 24h, reflux with stirring; ii) Water, NaOH (aq), 0.25h, DCM (3x20 mL), $MgSO_4$, concentrated under vacuo.

The ^{1}H NMR spectrum of [**HMAP**]H_2, as shown in **Figure S57**, exhibited six peaks representative of the product. The ethanol chain was represented by two triplet signals at 2.584 and 3.674 ppm associated to the protons on C_2 and C_1. The propanol chain was represented by two triplets and one pentet signal at 2.648, 3.759 and 1.724 ppm correlating to the protons on C_3, C_5 and C_4 respectively. Finally, the methyl side chain exhibits one singlet at 2.316 ppm, representing the protons on C_6. No broad proton signals for the exchangeable hydroxide or amine proton were observed. The ^{13}C NMR spectrum of [**HMAP**]H_2, as shown in **Figure S59**, also exhibited six corresponding peaks: a 42.166 ppm methyl peak, C_6, alongside 59.519 and 59.039 ppm peaks representing the protons on C_2 and C_1, together with the three signals from the propanol chain C_3, C_4 and C_5 at 56.860, 28.307, 63.038 ppm respectively. These allocations were confirmed by COSY and HMQC analysis, given in **Figures S58** and **S60** respectively. The mass spectrum of [**HMAP**]H_2, as shown in **Figure S106**, gave rise to the three most abundant peaks at 116.1074, 134.1183 and 156.0997 representative of $\{M+H-[H_2O]\}^+$, $\{M+H\}^+$ and $\{M+Na\}^+$ respectively. The FT-IR spectrum of [**HMAP**]H_2, as shown in **Figure S86**, exhibited characteristic bands at 3303 cm^{-1} consistent with the presence of an O-H bond.

In the case of [**HEAP**]H_2, the desired product was produced as a near colourless oil in a moderate yield (40%). The product proved to be sufficiently pure, stable at room temperature to air and moisture and was soluble in acetonitrile and methanol for use in complexation reactions.

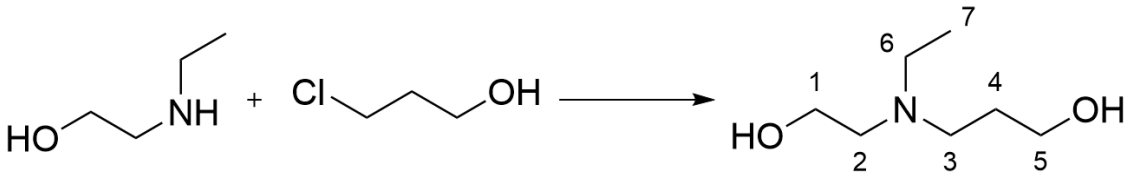

Scheme 20- Simplified synthesis of 3-[(2-hydroxyethyl)(ethyl)amino]propan-1-ol. Stepwise: i) Toluene (Dry), 24h, reflux with stirring; ii) Water, NaOH (aq), 0.25h, DCM (3x20 mL), $MgSO_4$, purified by vacuum distillation.

The ^{1}H NMR spectrum of [**HEAP**]H_2, as shown in **Figure S61**, exhibited seven peaks representative of the product. The ethanol chain was represented by two triplet signals at 2.557-2.613 and 3.654 ppm associated to the protons on C_2 and C_1. The propanol chain was represented by two triplets and one pentet signal at 2.667, 3.784 and 1.706 ppm correlating to the protons on C_3, C_5 and C_4 respectively. Finally, the ethyl side chain exhibits one triplet at 1.060 ppm, and one quartet overlapping the signal for C_2 at 2.557-2.613 ppm, representing the protons on C_7 and C_6 individually. No broad proton signals for the exchangeable hydroxide or amine proton were observed. The ^{13}C NMR spectrum of [**HEAP**]H_2, as shown in **Figure S63**, also exhibited seven corresponding peaks: two signals at 48.163 and 11.653 ppm comprising the ethyl group, C_6 and C_7, alongside 55.904 and 59.757 ppm peaks representing the protons on C_2 and C_1, together with the three signals from the propanol chain C_3, C_4 and C_5 at 53.245, 28.448, 63.544 ppm respectively. These allocations were confirmed by COSY and HMQC analysis, given in **Figures S62** and **S64** respectively. The mass spectrum of [**HEAP**]H_2, as shown in **Figure S107**, gave rise to the three most abundant peaks at 130.1231, 148.1343 and 170.1156 representative of $\{M+H-[H_2O]\}^+$, $\{M+H\}^+$ and $\{M+Na\}^+$ respectively. The FT-IR spectrum of [**HEAP**]H_2, as shown in **Figure S87**, exhibited characteristic bands at 3289 cm^{-1} consistent with the presence of an O-H bond.

In the case of [**H^{i}PrAP**]H_2, the desired product was produced as a near colourless oil in a moderate yield (44%). The product proved to be sufficiently pure, stable at room temperature to air and moisture and was soluble in acetonitrile and methanol for use in complexation reactions.

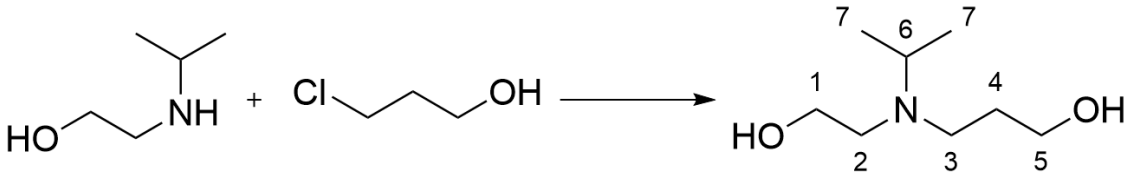

Scheme 21- Simplified synthesis of 3-[(2-hydroxyethyl)(isopropyl)amino]propan-1-ol. Stepwise: i) Toluene (Dry), 24h, reflux with stirring; ii) Water, NaOH (aq), 0.25h, DCM (3x20 mL), $MgSO_4$, purified by vacuum distillation

The ^{1}H NMR spectrum of [**H^{i}PrAP**]H_2, as shown in **Figure S65**, exhibited seven peaks representative of the product. The ethanol chain was represented by two triplet signals at 2.573 and 3.615 ppm associated to the protons on C_2 and C_1. The propanol chain was represented by two triplets and one pentet signal at 2.672, 3.745 and 1.679 ppm correlating to the protons on C_3, C_5 and C_4 respectively. Finally, the isopropyl side chain exhibits one doublet at 0.997-1.011 ppm, and one at 3.051 ppm, representing the protons on C_7 and C_6 individually. No broad proton signals for the exchangeable hydroxide or amine proton were observed. The ^{13}C NMR spectrum of [**H^{i}PrAP**]H_2, as shown in **Figure S67**, also exhibited seven corresponding peaks: two signals at 50.457 and 17.347 ppm comprising the isopropyl group, C_6 and C_7, alongside 51.561 and 59.826 ppm peaks representing the protons on C_2 and C_1, together with the three signals from the propanol chain C_3, C_4 and C_5 at 49.477, 28.765, 63.115 ppm respectively. These allocations were confirmed by COSY and HMQC analysis, given in **Figures S66** and **S68** respectively. The mass spectrum of [**H^{i}PrAP**]H_2, as shown in **Figure S108**, gave rise to the three most abundant peaks at 144.1388, 162.1502 and 184.1310 representative of $\{M+H-[H_2O]\}^+$, $\{M+H\}^+$ and $\{M+Na\}^+$ respectively. The FT-IR spectrum of [**H^{i}PrAP**]H_2, as shown in **Figure S88**, exhibited characteristic bands at 3288 cm^{-1} consistent with the presence of an O-H bond.

In the case of [**HPhAP**]H_2, the desired product was produced as a black oil in a low yield (25%). The product proved to be sufficiently pure, stable at room temperature to air and moisture in the short term for use in complexation reactions. However [**HPhAP**]H_2 is only slightly soluble in acetonitrile and methanol limiting its use in complexation reactions.

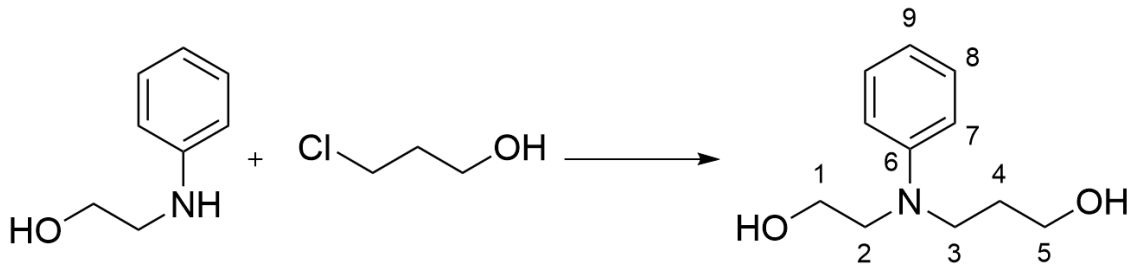

Scheme 22- Simplified synthesis of 3-[(2-hydroxyethyl)(phenyl)amino]propan-1-ol. Stepwise: i) Toluene (Dry), 48h, reflux with stirring; ii) Water, NaOH (aq), 0.25h, DCM (3x20 mL), $MgSO_4$, flash column purification.

The ^{1}H NMR spectrum of [**HPhAP**]H_2, as shown in **Figure S69**, exhibited six peaks representative of the product. Two triplets, overlap each other, becoming indistinguishable at 3.480-3.518 ppm, representing the nitrogen proximal protons in the alcohol chains, C_2 and C_3. Additionally, the ethanol side chain is represented by a triplet at 3.817 ppm, C_1, whilst the propanol chain is further represented by a triplet at 3.745 ppm and a pentet at 1.863 ppm, C_4 and C_5. Two multiplet signals within the regions 6.748-6.839 ppm (three protons, ortho and para positions) and 7.224-7.256 ppm (two protons, meta positions) collectively characterise the phenyl side group as a summation of the protons on C_7, C_8 and C_9. C_6 has no associated protons and so exhibits no signal. No broad proton signals for the exchangeable hydroxide or amine proton were observed. The ^{13}C NMR spectrum of [**PhDEA**]H_2 instead exhibited only eight corresponding peaks, extracted from the HMQC, as a result of the background noise interference and the low concentration of the sample tested. The side group phenyl peaks, C_9, C_8 and C_7 at 115.497, 129.648, 113.123, respectively. No signal for C6 was observable, individually or by association. Additionally peaks for the alcohol chains appear at 55.035 and 60.606 ppm representing C_2 and C_1, the ethanol chain, and at 49.370, 29.796 and 60.854 ppm representing C_3, C_4 and C_5, the propanol chain. These allocations were confirmed by COSY and HMQC analysis, given in **Figures S70** and **S71** respectively. The mass spectrum of [**HPhAP**]H_2, as shown in **Figure S109**, gave rise to

the three most abundant peaks at 178.1227, 196.1344 and 218.1150 representative of $\{M+H-[H_2O]\}^+$, $\{M+H\}^+$ and $\{M+Na\}^+$ respectively. The FT-IR spectrum of [**HPhAP**]H_2, as shown in **Figure S89**, exhibited characteristic bands at 3304 cm^{-1} consistent with the presence of an O-H bond. The phenyl group is also represented by signals at 1598 cm^{-1} and 1459 cm^{-1}.

As part of the synthetic methods untaken in the research for this chapter, further attempts were made to synthesise the ligands 3-[(2-hydroxyethyl)(tertbutyl)amino] propan-1-ol, [**H^{t}BuAP**]H_2, 3-[(2-hydroxyethyl)(adamantyl)amino] propan-1-ol, [**HAdAP**]H_2 and 2,2'-[(3-hydroxypropyl)imino] bis-ethanol [**^{n}Pr'DEA**]H_3; the structures for which can be found in **Figure 82**.

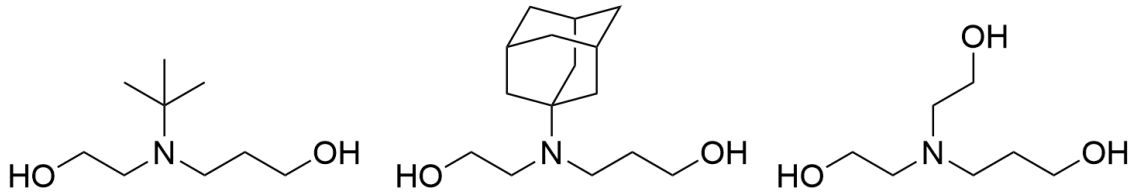

Figure 82- Structures for target molecules [**H^{t}BuAP**]H_2, left; [**HAdAP**]H_2, centre; and [**^{n}Pr'DEA**]H_3, right.

These syntheses proceeded broadly similarly to those previously mentioned, by the reaction of 3-chloropropanol with the prerequisite precursor, [**^{t}BuAE**]H, [**AdAE**]H or [**DEA**]H_2 respectively. It should also be noted synthetic attempts were made using the precursors [**^{t}BuAPr**]H and [**AdAPr**]H and 2-chloroethanol, also, but met with similar results. For the purpose of this section discussion will focus upon the aminoethanol precursor synthetic route. Even though these reactions were carried out with a stoichiometric excess of chloroalcohol, the final product remained a mixture of the two reagents and target product. Purification methods viable for previous reactions, however, proved insufficient to separate these mixtures. These included, but were not limited to hot filtration, trituration, TLC on silica plates, basified silica plates and alumina plates towards column chromatography, vacuum distillation and cold crystallisation from solution. As a result, no pure [**H^{t}BuAP**]H_2, [**HAdAP**]H_2 or [**^{n}Pr'DEA**]H_3 samples were obtained for structural analysis such as NMR or IR as the precursor too closely resembles the product to cleanly differentiate the two within a spectrum. However, the impure

samples were still submitted for analysis by mass spectrometry as an indication of synthetic success.

The mass spectrum of [**H^{t}BuAP**]H_2, with the molecular formula $C_9H_{21}NO_2$, as shown in **Figure S110**,gave rise to peaks at 176.1647, 198.1467 and 351.3208 representative of $\{M+H\}^+$, $\{M+Na\}^+$ and $\{2M+H]\}^+$ respectively. Calculated $[M+H]^+ = 176.1651$.

The mass spectrum of [**HAdAP**]H_2, with the molecular formula $C_{15}H_{27}NO_2$, as shown in **Figure S111**,gave rise to peaks at 254.2128, 276.1936 and 489.4055 representative of $\{M+H\}^+$, $\{M+Na\}^+$ and $\{2M+H-[H_2O]\}^+$ respectively. Calculated $[M+H]^+ = 254.2120$.

The mass spectrum of [^{n}**Pr'DEA**]H_3, with the molecular formula $C_7H_{17}NO_3$, as shown in **Figure S112**,gave rise to peaks at 146.1175, 164.1290 and 186.1103 representative of $\{M+H-[H_2O]\}^+$, $\{M+H\}^+$ and $\{M+Na\}^+$ respectively. Calculated $[M+H]^+ = 162.1287$.

These syntheses, although incomplete, are mentioned here as a result of the novelty they represent. Further effort towards the completion of these syntheses would be the next step in the advancement of the work presented in this chapter.

3.3 Chapter Summary

In this chapter the synthesis and analysis of a family of eighteen organic molecules has been described, including ten potential tri- or tetra-dentate polyalcohol ligands. In addition to this, five further syntheses were discussed, two of which are of novel structures at the time of research, [**H^{t}BuAP**]H_2 and [**HAdAP**]H_2. These symmetric and asymmetric polyalcohol ligands were purified for use in coordination reactions towards novel single-molecule magnets, targeting the butterfly motif stoichiometrically. This chapter has shown the scope of Shi-style nucleophilic substitution routes towards higher order amines. The use of stepwise additions to reduce the extent of unwanted by-products appears viable, although further study is required. Such stepwise reactions are labour intensive; however, they allow for access to simple polyalcohol products using cheaper, more readily available starting materials than current routes, that often utilise expensive catalysts or reducing agents to access higher yields.

The Hullio paper, codifies the production of [**MAE**]H by the reaction of paraformaldehyde with 2-amino ethanol for an overall yield of 74%, in comparison to the literature value of 72%. The method involved a condensation mechanism, to form an imine prior to complete reduction to the amine form. Although the paper in question did not specify whether this reaction had scope for further products from different carbonyl containing small molecule reagents, further syntheses towards the production of [**EAE**]H and [^{i}**PrAE**]H were attempted. These reactions proved successful even at significantly reduced yields, 59% and 35% respectively, compared to the [**MAE**]H example.

The Shi paper describes the reaction of imines with chloroalcohols, although functionally the “imine” examples given appear to be secondary amines. The starting materials for these reaction steps, viii in the paper, are dimethylamine, diethylamine, morpholine. Functionally therefore, these reactions appear to actually describe the stepwise synthesis of a secondary amine to a tertiary amine by addition of a chloroalcohol. No yields are given in the Shi paper for these steps, as they are functionally partial reaction steps towards the Shi paper targets, 19a-c, where the hydroxy group has been further substituted for a chloride group by reflux with $SOCl_2$. These reaction steps were modified and utilised to be applied to secondary amine and tertiary amine products with one or more alkoxide chains in the low polarity solvent, toluene. The Shi paper methodology

proved effective in this regard for a wide range of starting materials and products, with yields ranging from 26% to 83% for [**HPhAP**]H and [**HMAP**]H_2, respectively. It should be noted that to attain these yields, the reaction times are increased significantly to those described by the Shi paper. Once more our study proves the method described by the paper in question to have a far wider scope than is originally reported. Glowacki *et al*., conversely describes the direct synthesis of [**HMAP**]H_2 in a more polar solvent compared to that used in the Shi methodology, acetonitrile, with a reflux time of 5 days producing a yield of 85%. Our comparative Shi style reaction attains an 83% yield with a 24hr reflux period. In comparison to our synthetic targets, where the identity of the R group is varied, Glowacki *et al*., instead vary the alkoxide chains by adding branching moieties. Glowacki style reactions, when the R group increases in size, were found to have a diminishing return of percentage yield as the size increased. Shi style reactions are therefore primarily utilised unless the starting materials proved insufficiently soluble in the toluene reaction solvent, as is the case for [**DEA**]H_2. In these cases, the Glowacki method of synthesis proved consistently superior.

3.4 Experimental Methods

All information relating to the sourcing of chemicals, technical specifications of instrumentation, data processing procedures and software can be found in the appendices. Pertinent to this chapter are **Appendix A**, **C**, **D** and **E**, for synthetic procedures, NMR, IR and MS respectively, where the full spectra can also be found.

Sealed reaction vessels used in reactions for this chapter were based upon a three necked round bottom flask, sealed with rubber septums, an outlet pipe directed through a solvent trap and Dreschel bottle bubbler filled with silicon oil, and an inert gas inlet, *via* needle directly into the liquid layer, either directly from the fumehood, or through a Schlenk system. Additions were completed *via* the third neck, as and when required by pausing the inert gas flow to prevent blow back or damage to the addition funnel.

3.4.1 2-(methylamino)ethan-1-ol, [MAE]H

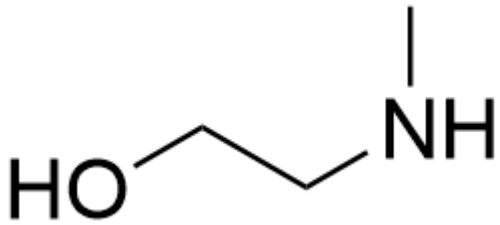

Figure 83- Skeletal structure of 2-(methylamino) ethanol, [**MAE**]H.

A mixture of 2-amino ethanol (3.054 g, 50 mmol), zinc chloride (13.630 g, 100 mmol) and dry dichloromethane (20 mL) in a sealed reaction vessel was degassed using an argon bubbler for five minutes. The reaction vessel was then charged with paraformaldehyde (3.003 g, 100 mmol) and allowed to stir for 1 h at room temperature under the dry atmosphere. Subsequently sodium borohydride (3.783 g, 100 mmol) was added, and the resulting mixture allowed to stir for another 18 h. The reaction was monitored using TLC. Upon completion, the reaction was basified with aqueous sodium hydroxide (25 mL, 2N) until universal indicator paper showed the solution was strongly basic (pH=14). The mixture was then stirred for a further 15 minutes and the organic layer separated. The aqueous layer was then extracted with dichloromethane (3x10 mL). The combined organic layers were then dried over anhydrous magnesium sulphate and concentrated under vacuo. The crude product was run through a flash column of neutral alumina using an eluent mixture of hexane:diethyl ether (3:1). The product, [**MAE**]H (2.786 g, 74%), was yielded as a near colourless liquid.

^{1}H NMR (**Fig. S1**, 500 MHz, $CDCl_3$): δ 2.338 (s, 3H, C**H**$_3$), 2.656 (m, 2H, C**H**$_2$N), 3.601 (m, 2H, C**H**$_2$O). ^{13}C NMR (**Fig. S3**, 125 MHz, $CDCl_3$): δ 35.926 (**C**H$_3$N), 53.412(**C**H$_3$O), 60.320 (**C**H$_2$O). HRMS (**Fig. S90**, ESI): M = C_3H_9NO Calc. $[M+H]^+$ = 76.0757, Found: $[M+H]^+$ = 76.0759. FT-IR ν(cm^{-1}) (**Fig. S72**): 3288, 3142 (br), 2935, 2840, 2795, 1475, 1450, 1350, 1236, 1143, 1114, 1054 (s), 1008, 897, 865, 820.

3.4.2 2-(ethylamino)ethan-1-ol, [EAE]H

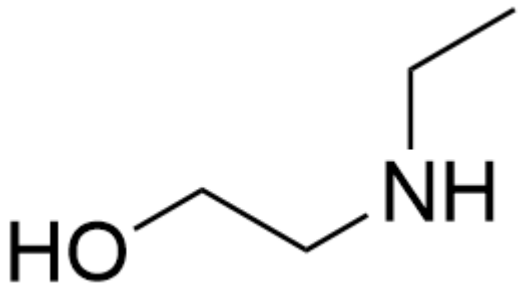

Figure 84- Skeletal structure of 2-(ethylamino) ethanol, [**EAE**]H.

A mixture of amino ethanol (3.054 g, 50 mmol), zinc chloride (13.630 g, 100 mmol) and dry dichloromethane (20 mL) in a sealed reaction vessel was degassed using an argon bubbler for five minutes. The reaction vessel was then charged with acetaldehyde (5.6 mL, 100 mmol) and allowed to stir for 1 h at room temperature under the dry atmosphere. Subsequently sodium borohydride (3.783 g, 100 mmol) was added, and the resulting mixture allowed to stir for another 18 h. The reaction was monitored using TLC. Upon completion, the reaction was basifying with aqueous sodium hydroxide (25 mL, 2N) until universal indicator paper showed the solution was strongly basic (pH=14). The mixture was then stirred for a further 15 minutes and the organic layer separated. The aqueous layer was further extracted with dichloromethane (3x10 mL). The combined organic layers and extracts were then dried over anhydrous magnesium sulphate and concentrated under vacuo. The crude product was run through a flash column of neutral alumina using an eluent mixture of hexane:diethyl ether (3:1). The product, [**EAE**]H (2.630 g, 59%), was yielded as a near colourless liquid.

^{1}H NMR (**Fig. S5**, 500 MHz, $CDCl_3$): δ 1.050 (t, 3H, C**H**$_3$), 2.575-2.618 (q, 2H, NC**H**$_2$CH$_3$), 2.669 (t, 2H, C**H**$_2$N), 3.584 (t, 2H, C**H**$_2$O). ^{13}C NMR (**Fig. S7**, 125 MHz, $CDCl_3$): δ 14.948 (**C**H$_3$CH$_2$), 43.680 (CH$_3$**C**H$_2$N), 51.130 (CH$_2$**C**H$_2$N), 60.430 (CH$_2$**C**H$_2$O). HRMS (**Fig. S91**, ESI): M = $C_4H_{11}NO$ Calc. $[M+H]^+$ = 90.0913, Found $[M+H]^+$ = 90.0918. FT-IR ν(cm^{-1}) (**Fig. S73**): 3263, 3149 (br), 2965, 2930, 2872, 2828, 1453, 1376, 1331, 1298, 1255, 1224, 1118, 1060 (s), 1040, 938, 916, 857, 829, 779, 663.

3.4.3 2-(isopropylamino)ethan-1-ol, [^{i}PrAE]H

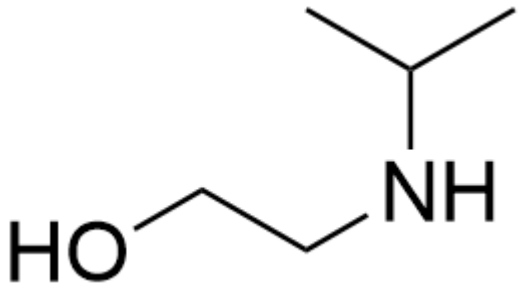

Figure 85- Skeletal structure of 2-(isopropylamino) ethanol, [^{i}**PrAE**]H.

A mixture of amino ethanol (3.054 g, 50 mmol), zinc chloride (13.630 g, 100 mmol) and dry dichloromethane (20 mL) in a sealed reaction vessel was degassed using an argon bubbler for five minutes. The reaction vessel was then charged with acetone (7.3 mL, 100 mmol) and allowed to stir for 1 h at room temperature under the dry atmosphere. Subsequently sodium borohydride (3.783 g, 100 mmol) was added, and the resulting mixture allowed to stir for another 18 h. The reaction was monitored using TLC. Upon completion, the reaction was basifying with aqueous sodium hydroxide (25 mL, 2N) until universal indicator paper showed the solution was strongly basic (pH=14). The mixture was then stirred for a further 15 minutes and the organic layer separated. The aqueous layer was further extracted with dichloromethane (3x10 mL). The combined organic layers and extracts were then dried over anhydrous magnesium sulphate and concentrated under vacuo. The crude product was run through a flash column of neutral alumina using an eluent mixture of hexane:diethyl ether (3:1). The product, [^{i}**PrAE**]H (1.805 g, 35%), was yielded as a near colourless liquid.

^{1}H NMR (**Fig. S9**, 500 MHz, $CDCl_3$): δ 1.010-1.022 (d, 6H, CH(C**H**$_3$)$_2$), 2.673 (t, 2H, NC**H**$_2$), 2.749 (h, 1H, NC**H**(CH$_3$)$_2$), 3.592 (t, 2H, C**H**$_2$O). ^{13}C NMR (**Fig. S11**, 125 MHz, $CDCl_3$): δ 22.808 (CH(**C**H$_3$)$_2$), 48.559 (**C**H$_2$N), 48.759 (N**C**H(CH$_3$)$_2$), 60.892 (**C**H$_2$O). HRMS (**Fig. S92**, ESI): M = $C_5H_{13}NO$ Calc. $[M+H]^+$ = 104.1070, Found $[M+H]^+$ = 104.1074. FT-IR ν(cm^{-1}) (**Fig. S74**): 3142 (br), 2964, 2870, 2835, 1469, 1382, 1369, 1339, 1322, 1261, 1220, 1176, 1136, 1094, 1058 (s), 990, 921, 876, 848, 803, 754.

3.4.4 2-(tertbutylamino)ethan-1-ol, [^{t}BuAE]H

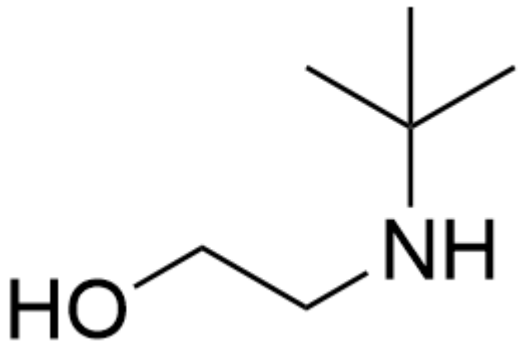

Figure 86- Skeletal structure of 2-(tertbutylamino) ethanol, [^{t}**BuAE**]H.

Tert-butylamine (15.75 mL, 150 mmol) was added to degassed toluene (25 mL) in a sealed system and stirred at room temperature whilst 2-chloroethanol (13.4 mL, 200 mmol) was added dropwise over five minutes. The mixture was then refluxed at 120°C for 24 h. After cooling, the mixture was filtered and the filtrate concentrated under vacuo to produce a yellow oil of the crude product hydrochloride salt (25.006 g, 108%). This oil was freebased by dissolving in a minimum amount of water (approx. 20 mL) and basifying with aqueous sodium hydroxide (12 mL, 2N) until universal indicator paper showed the solution was strongly basic (pH=14). The aqueous solution was then extracted with dichloromethane (3x25 mL). The combined organic layers were dried over anhydrous magnesium sulphate and concentrated under vacuo. The resultant orange oil was triturated with pentane (20 mL) and cooled in an acetone ice bath until a large amount of low melting point colourless crystals grew within the vessel. The orange pentane solution was decanted, the crystals collected on a Buchner funnel and washed with ice cold pentane until the filtrate ran colourless. The resultant colourless crystals were then collected and refrigerated prior to further use. The product, [**tBuAE**]H (9.471 g, 50%), was yielded as a colourless crystalline solid. Overall reaction yield of 54%.

^{1}H NMR (**Fig. S13**, 500 MHz, $CDCl_3$): δ 1.090 (s, 9H, NC($C\mathbf{H}_3$)$_3$), 2.690 (t, 2H, $C\mathbf{H}_2$N), 3.603 (t, 2H, $C\mathbf{H}_2$O). ^{13}C NMR (**Fig. S15**, 125 MHz, $CDCl_3$): δ 28.955 (NC($\mathbf{C}H_3$)$_3$), 43.873 ($\mathbf{C}H_2$N), 50.202 (N$\mathbf{C}$(CH_3)$_3$), 61.562 ($\mathbf{C}H_2$O). HRMS (**Fig. S93**, ESI): M = $C_6H_{15}NO$ Calc. $[M+H]^+$ = 118.1226, Found $[M+H]^+$ = 118.1230. FT-IR ν(cm^{-1}) (**Fig. S75**): 3266, 3114 (br), 2970, 2933, 2894, 2840, 2724, 2685, 2549, 1484, 1476, 1446, 1434, 1393, 1378, 1367, 1362, 1352, 1287, 1259, 1220, 1116, 1094, 1078 (s), 1024, 971, 939, 921, 878, 846, 764, 744.

3.4.5 2-(phenylamino)ethan-1-ol, [PhAE]H

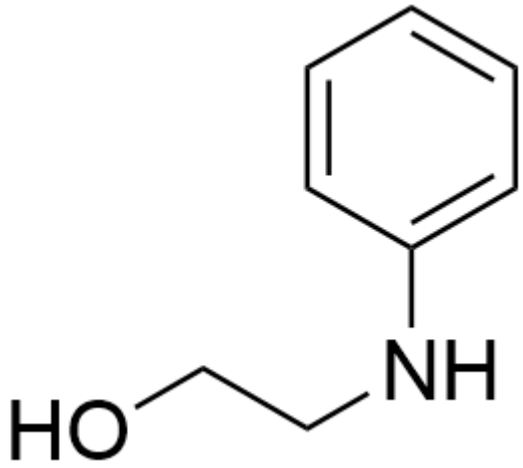

Figure 87- Skeletal structure of 2-(phenylamino) ethanol, [**PhAE**]H.

Aniline (4.66 mL, 50 mmol) dissolved in toluene was stirred at room temperature whilst 2-chloroethanol (8.36 mL, 100 mmol) was added dropwise over five minutes. The mixture was then refluxed at 120°C for 24 h. After cooling the mixture was filtered and the remaining solution was concentrated under vacuo to produce a brown oil of the product hydrochloride salt (5.223 g, 60%). This oil was freebased by dissolving in a minimum amount of water (approx. 10 mL) and basifying with aqueous sodium hydroxide (8 mL, 2N) until universal indicator paper showed the solution was strongly basic (pH=14). The aqueous solution was then extracted with dichloromethane (3x20 mL). The combined organic layers were then dried over anhydrous magnesium sulphate and concentrated under vacuo. The resultant oil was run through a vacuum distillation apparatus (110°C, 20 mbar) to leave the product in the Claisen flask after 2h. The product, [**PhAE**]H (4.004 g, 97%), was yielded as a near black, viscous oil. Overall reaction yield of 58%.

^{1}H NMR (**Fig. S17**, 500 MHz, $CDCl_3$): δ 3.265 (t, 2H, NC**H**$_2$), 3.782 (t, 2H, C**H**$_2$O), 6.647-6.784 (m, 3H, Ph), 7.193-7.234 (m, 2H, Ph). ^{13}C NMR (**Fig. S19**, 125 MHz, $CDCl_3$): δ 45.981 (**C**H_2N), 61.007 (**C**H_2O), 113.176 (Ph), 117.819 (Ph), 129.208 (Ph), 148.010 (Ph). HRMS (**Fig. S94**, ESI): M = $C_8H_{11}NO$ Calc. $[M+H]^+$ = 138.0917, Found $[M+H]^+$ = 138.0913. FT-IR ν(cm^{-1}) (**Fig. S76**): 3388, 3346 (br), 3050, 3021, 2941, 2875, 2840, 1601 (s), 1559, 1537, 1501, 1459, 1431, 1402, 1384, 1362, 1318, 1261, 1211, 1179, 1154, 1121, 1051 (s), 991, 896, 869, 820, 748 (s), 692, 664.

3.4.6 2-(adamantylamino)ethan-1-ol, [AdAE]H

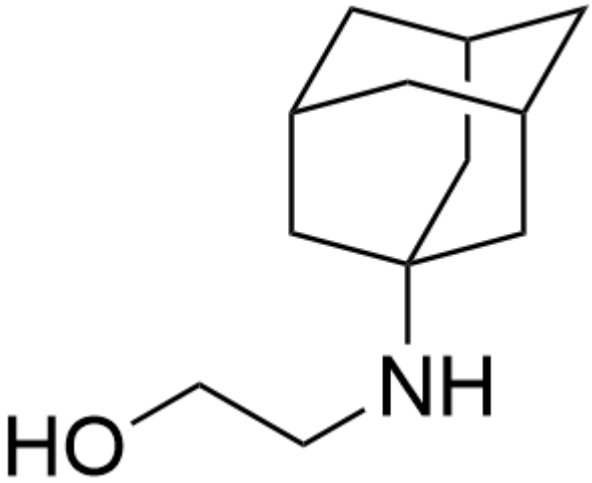

Figure 88- Skeletal structure of 2-(adamantylamino) ethanol, [**AdAE**]H.

1-aminoadamantane (7.663 g, 50 mmol) dissolved in toluene (40 mL) was stirred at room temperature whilst 2-chloroethanol (5.03 mL, 75 mmol) was added dropwise over five minutes. The mixture was then refluxed at 125°C for 24 h. The resulting solution was then allowed to cool to room temperature at which point white needles grew in the solution over 4 h. This white solid was filtered and washed with toluene until the filtrate ran colourless. The collected solid, the crude product hydrochloride salt (13.068 g, 113%), was freebased by dissolving in a minimum amount of water (approx. 15 mL) and basifying with aqueous sodium hydroxide (8 mL, 2N), producing a large amount of insoluble white solid which was collected by Buchner filtration. Portionwise, DCM (4x50 mL) was added to the solid until all the sparingly soluble product had fully dissolved. The combined organic layers were dried over anhydrous magnesium sulphate and concentrated under vacuo. The isolated off-white solid was found to be the target product, [**AdAE**]H (8.695 g, 79%), with no further purification required. Overall reaction yield of 89%.

^{1}H NMR (**Fig. S21**, 500 MHz, $CDCl_3$): δ 1.579-1.672 (m, 12H, Ad), 2.055 (s, 3H, Ad), 2.716 (t, 2H, C**H**$_2$N), 3.580 (t, 2H, C**H**$_2$O). ^{13}C NMR (**Fig. S23**, 125 MHz, $CDCl_3$): δ 29.513 (**C**H$(CH_2)_3$, Ad), 36.658 (**C**H$_2(CH)_2$, Ad), 41.706 (**C**H$_2$N), 42.862 (C**C**H$_2$CH, Ad), 50.173 (N**C**$(CH_2)_3$, Ad), 61.739 (**C**H$_2$O). HRMS (**Fig. S95**, ESI): M = $C_{12}H_{21}NO$ Calc. $[M+H]^+$ = 196.1696, Found $[M+H]^+$ = 196.1699. FT-IR ν(cm^{-1}) (**Fig. S77**): 3378 (s), 2979, 2931, 2881,

2788 (s), 2701, 2647, 2619, 2531, 2448, 2366, 1487, 1474, 1454, 1420, 1401, 1385, 1368, 1321, 1310, 1275, 1255, 1226, 1198, 1142, 1091, 1063 (s), 1008, 948, 907, 879, 870, 777.

3.4.7 3-(tertbutylamino)propan-1-ol, [^{t}BuAPr]H

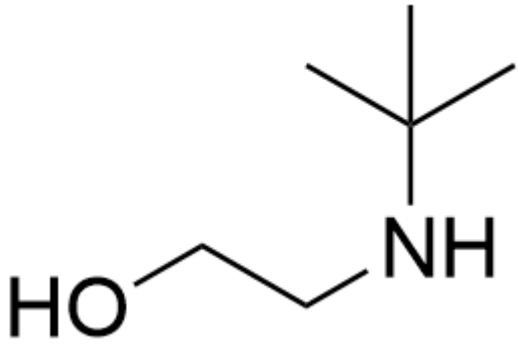

Figure 89- Skeletal structure of 3-(tertbutylamino) propanol, [^{t}**BuAPr**]H.

Tert-butylamine (15.75 mL, 150 mmol) was added to degassed toluene (25 mL) in a sealed system and stirred at room temperature whilst 3-chloropropanol (13.4 mL, 200 mmol) was added dropwise over five minutes. The mixture was then refluxed at 120°C for 24 h. After cooling, the mixture was filtered and the filtrate concentrated under vacuo to produce a yellow oil of the crude product hydrochloride salt (25.006 g, 108%). This oil was freebased by dissolving in a minimum amount of water (approx. 20 mL) and basifying with aqueous sodium hydroxide (12 mL, 2N) until universal indicator paper showed the solution was strongly basic (pH=14). The aqueous solution was then extracted with dichloromethane (3x25 mL). The combined organic layers were dried over anhydrous magnesium sulphate and concentrated under vacuo. The resultant orange oil was triturated with pentane and cooled in an acetone ice bath until a large amount of low melting point colourless crystals grew within the vessel. The orange pentane solution was decanted, the crystals collected on a Buchner funnel and washed with ice cold pentane until the filtrate ran colourless. The resultant colourless crystals were then collected and refrigerated prior to further use. The product, [^{t}**BuAPr**]H (9.4714 g, 50%), was yielded as a colourless crystalline solid. Overall reaction yield of 54%.

^{1}H NMR (**Fig. S25**, 500 MHz, $CDCl_3$): δ 1.440 (s, 9H, $C(CH_3)_3$), 2.114 (p, 2H, $CH_2CH_2CH_2$), 3.061 (t, 2H, NCH_2), 3.776 (t, 2H, OCH_2: inc. impurity overlap). ^{13}C NMR (**Fig. S27**, 125

MHz, $CDCl_3$): δ 25.789 (C(**C**H_3)$_3$), 28.908 (CH_2**C**H_2CH_2), 39.824 (N**C**H_2), 57.012 (**C**(CH_3)$_3$), 59.502 (O**C**H_2). HRMS (**Fig. S96**, ESI): M = $C_7H_{17}NO$ Calc. $[M+H]^+$ = 132.1383, Found $[M+H]^+$ = 132.1390. FT-IR ν(cm^{-1}) (**Fig. S78**): 3378 (s), 2979, 2880, 2788 (s), 2701, 2647, 2619, 2531, 2448, 1487, 1474, 1454, 1420, 1401, 1385, 1368, 1321, 1310, 1274, 1255, 1226, 1198, 1091, 1063 (s), 1008, 948, 907, 879, 870.

3.4.8 3-(adamantylamino)propan-1-ol, [AdAPr]H

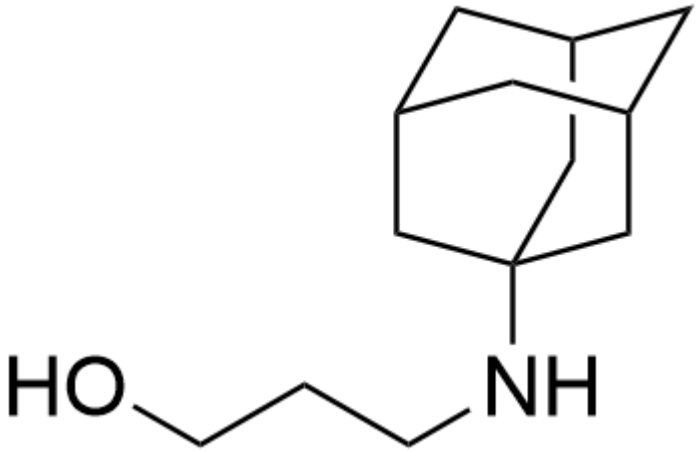

Figure 90- Skeletal structure of 3-(adamantylamino)-propanol, [**AdAPr**]H.

1-aminoadamantane (2.495 g, 16.5 mmol) dissolved in acetonitrile (25 mL) was stirred at room temperature whilst 3-chloropropanol (2.79 mL, 33 mmol) was added dropwise over five minutes. Potassium carbonate was added, and the mixture was then refluxed at 80°C for 96 h. The resulting solution was then hot filtrated and allowed to cool to room temperature at which point white needles grew in the solution over 4 h. This white solid was filtered and washed with diethyl ether (4x5 mL) before being allowed to dry thoroughly in air. The isolated solid was found to be the target product, [**AdAPr**]H (2.863 g, 89%), with no further purification required.

^{1}H NMR (**Fig. S29**, 500 MHz, $CDCl_3$): δ 1.580-1.679 (m+p, 12H+2H, Ad (C**H**$_2$) + CH_2C**H**$_2$$CH_2$), 2.062 (s, 3H, Ad (C**H**)), 2.869 (t, 2H, NC**H**$_2$), 3.804 (t, 2H, OC**H**$_2$). ^{13}C NMR (**Fig. S31**, 125 MHz, $CDCl_3$): δ 29.466 (**C**H(CH_2)$_3$), 31.545 (CH_2**C**H_2CH_2), 36.639 (**C**H_2(CH)$_2$), 40.917 (N**C**H_2), 42.590 (NC**C**H_2CH), 50.655 (N**C**(CH_2)$_3$), 64.977(O**C**H_2). HRMS (**Fig. S97**, ESI): M = $C_{13}H_{23}NO$ Calc. $[M+H]^+$ = 210.1852, Found $[M+H]^+$ = 210.1871. FT-IR ν(cm^{-1}) (**Fig. S79**): 3256, 3098 (br), 2906 (s), 2844, 2701, 1487, 1451, 1429, 1357, 1342, 1309, 1290, 1264,

1228, 1178, 1137, 1113, 1104, 1097, 1070, 1058 (s), 991, 975, 950, 931, 912, 894, 816, 800, 773, 720.

3.4.9 N-methyldiethanolamine, [MDEA]H_2

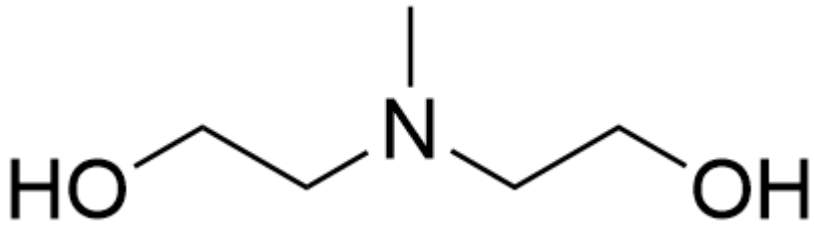

Figure 91- Skeletal structure of N-methyldiethanolamine, [**MDEA**]H_2.

Compound [**MAE**]H (4.02 mL, 50 mmol) dissolved in toluene (20 mL) was stirred at room temperature whilst 2-chloroethanol (3.35 mL, 50 mmol) was added dropwise over five minutes. The mixture was then refluxed at 120°C for 3 h. The resulting solution was then hot filtrated and allowed to cool to room temperature. After a second cold filtration the remaining solution was concentrated under vacuo to produce a near colourless oil of the product hydrochloride salt (6.412 g, 82%). This oil was freebased by dissolving in a minimum amount of water (approx. 2 mL) and basifying with aqueous sodium hydroxide (8 mL, 2N) until universal indicator paper showed the solution was strongly basic (pH=14). The aqueous solution was then extracted with dichloromethane (3x20 mL). The combined organic layers were then dried over anhydrous magnesium sulphate and concentrated under vacuo. The resultant oil was then run through a vacuum distillation apparatus (70°C, 20 mbar) to leave the product in the Claisen flask after 2h. The product, [**MDEA**]H_2 (3.660 g, 74%), was yielded as a near colourless liquid. Overall reaction yield of 61%.

^{1}H NMR (**Fig. S33**, 500 MHz, $CDCl_3$): δ 2.235 (s, 3H, NC**H**$_3$), 2.507 (t, 4H, C**H**$_2$N), 3.578 (t, 4H, C**H**$_2$O). ^{13}C NMR (**Fig. S35**, 125 MHz, $CDCl_3$): δ 41.994 (N**C**H$_3$), 58.951 (**C**H$_2$O), 59.423 (**C**H$_2$N). HRMS (**Fig. S98**, ESI): M = $C_5H_{13}NO_2$ Calc. $[M+H]^+$ = 120.1019, Found $[M+H]^+$ = 120.1031. FT-IR ν(cm^{-1}) (**Fig. S80**): 3315 (br), 2945, 2842, 2796, 1456, 1355, 1299, 1242, 1196, 1133, 1076, 1030 (s), 949, 877, 750.

3.4.10 N-ethyldiethanolamine, [EDEA]H_2

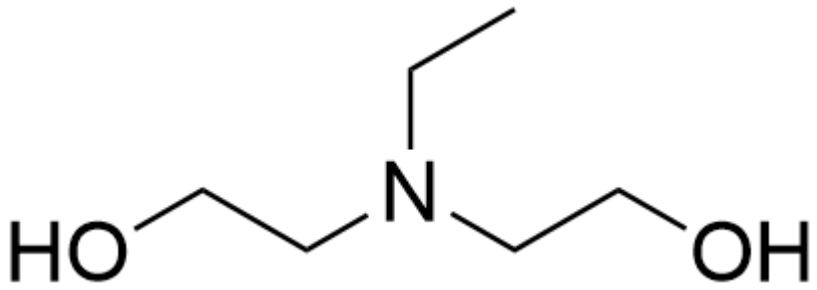

Figure 92- Skeletal structure of N-ethyldiethanolamine, [**EDEA**]H_2.

Compound [**EAE**]H (2.44 mL, 25 mmol) dissolved in toluene (20 mL) was stirred at room temperature whilst 2-chloroethanol (3.35 mL, 50 mmol) was added dropwise over five minutes. The mixture was then refluxed at 120°C for 3 h. The resulting solution was then hot filtrated and allowed to cool to room temperature. After a second cold filtration the remaining solution was concentrated under vacuo to produce a near colourless oil of the crude product hydrochloride salt (4.275 g, 101%). This oil was freebased by dissolving in a minimum amount of water (approx. 5 mL) and basifying with aqueous sodium hydroxide (8 mL, 2N) until universal indicator paper showed the solution was strongly basic (pH=14). The aqueous solution was then extracted with dichloromethane (3x20 mL). The combined organic layers were then dried over anhydrous magnesium sulphate and concentrated under vacuo. The resultant oil was then run through a vacuum distillation apparatus (70°C, 20 mbar) to leave the product in the Claisen flask after 2h. The product, [**EDEA**]H_2 (1.331 g, 40%), was yielded as a near colourless liquid. Overall reaction yield of 40%.

^{1}H NMR (**Fig. S37**, 500 MHz, $CDCl_3$): δ 1.001 (t, 3H, C**H**$_3$CH$_2$), 2.586-2.612 (t+q, 4H+2H, NC**H**$_2$ + NC**H**$_2$CH$_3$), 3.570 (t, 4H, OC**H**$_2$). ^{13}C NMR (**Fig. S39**, 125 MHz, $CDCl_3$): δ 11.333 (**C**H$_3$CH$_2$), 48.070 (CH$_3$**C**H$_2$N), 55.362 (N**C**H$_2$CH$_2$), 59.135 (O**C**H$_2$CH$_2$). HRMS (**Fig. S99**, ESI): M = $C_6H_{15}NO_2$ Calc. $[M+H]^+$ = 134.1176, Found $[M+H]^+$ = 134.1189. FT-IR ν(cm^{-1}) (**Fig. S81**): 3324 (br), 2938, 2874, 2819, 1458, 1374, 1297, 1236, 1181, 1153, 1035 (s), 907, 874, 729.

3.4.11 N-isopropyldiethanolamine, [^{i}PrDEA]H_2

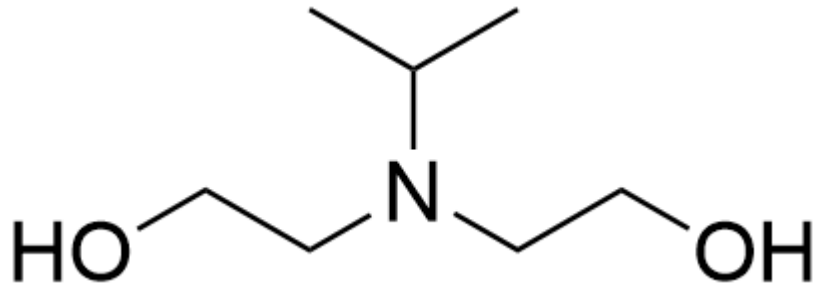

Figure 93- Skeletal structure of N-isopropyldiethanolamine, [^{i}**PrDEA**]H_2.

Compound [^{i}**PrAE**]H (2.88 mL, 25 mmol) dissolved in toluene (20 mL) was stirred at room temperature whilst 2-chloroethanol (3.35 mL, 50 mmol) was added dropwise over five minutes. The mixture was then refluxed at 120°C for 3 h. The resulting solution was then hot filtrated and allowed to cool to room temperature. After a second cold filtration the remaining solution was concentrated under vacuo to produce a near colourless oil of the product hydrochloride salt (4.419 g, 96%). This oil was freebased by dissolving in a minimum amount of water (approx. 5 mL) and basifying with aqueous sodium hydroxide (8 mL, 2N) until universal indicator paper showed the solution was strongly basic (pH=14). The aqueous solution was then extracted with dichloromethane (3x20 mL). The combined organic layers were then dried over anhydrous magnesium sulphate and concentrated under vacuo. The resultant oil was then run through a vacuum distillation apparatus (90°C, 20 mbar) to leave the product in the Claisen flask after 2h. The product, [^{i}**PrDEA**]H_2 (1.607 g, 45%), was yielded as a near colourless liquid. Overall reaction yield of 44%.

^{1}H NMR (**Fig. S41**, 500 MHz, $CDCl_3$): δ 0.976-0.990 (d, 6H, CH(C**H**$_3$)$_2$), 2.571 (t, 4H, NC**H**$_2$), 2.931 (h, 1H, NC**H**$(CH_3)_2$), 3.529 (t, 4H, OC**H**$_2$). ^{13}C NMR (**Fig. S43**, 125 MHz, $CDCl_3$): δ 18.029 (CH(**C**$H_3)_2$), 50.927 (N**C**$H(CH_3)_2$), 51.552 (N**C**H_2CH_2), 59.993 (O**C**H_2CH_2). HRMS (**Fig. S100**, ESI): M = $C_7H_{17}NO_2$ Calc. $[M+H]^+$ = 148.1332, Found $[M+H]^+$ = 148.1341. FT-IR ν(cm^{-1}) (**Fig. S82**): 3303 (br), 2962, 2872, 2835, 1463, 1383, 1362, 1278, 1225, 1173, 1121, 1041 (s), 951, 907, 875, 709.

3.4.12 N-n-butyldiethanolamine, [^{n}**BuDEA**]H_2

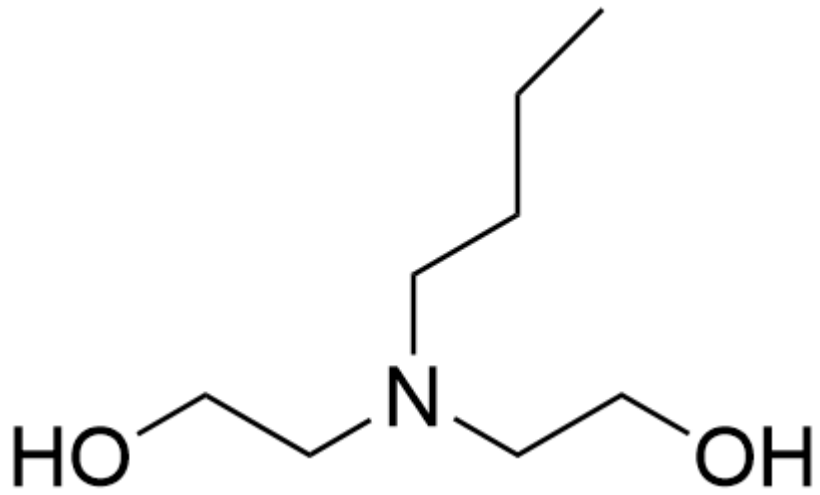

Figure 94- Skeletal structure of N-n-butyldiethanolamine, [^{n}**BuDEA**]H_2.

Diethanolamine (4.79 mL, 50 mmol) dissolved in water (20 mL) was stirred at room temperature whilst 1-chlorobutane (7.88 mL, 75 mmol) was added dropwise over five minutes. The mixture was then refluxed at 120°C for 24 h. The resulting solution was then hot filtrated and allowed to cool to room temperature. After a second cold filtration the remaining solution was concentrated under vacuo to produce a near colourless oil of the product hydrochloride salt (7.656 g, 77%). This oil was freebased by dissolving in a minimum amount of water (approx. 5 mL) and basifying with aqueous sodium hydroxide (5 mL, 2N) until universal indicator paper showed the solution was strongly basic (pH=14). The aqueous solution was then extracted with dichloromethane (3x20 mL). The combined organic layers were dried over anhydrous magnesium sulphate and concentrated under vacuo. The resultant oil was then run through a vacuum distillation apparatus (50°C, 20 mbar) to leave the product in the Claisen flask after 2h. The product, [^{n}**BuDEA**]H_2 (6.001 g, 96%), was yielded as a colourless liquid. Overall reaction yield of 74%.

^{1}H NMR (**Fig. S45**, 500 MHz, $CDCl_3$): δ 0.877 (t, 3H, $CH_2C\mathbf{H}_3$), 1.230-1.304 (sx, 2H, $CH_2C\mathbf{H}_2CH_3$), 1.413 (p, 2H, $CH_2C\mathbf{H}_2CH_2$), 2.482 (t, 2H, $CH_2CH_2C\mathbf{H}_2N$), 2.601 (t, 4H, $NC\mathbf{H}_2$), 3.564 (t, 4H, $OC\mathbf{H}_2$). ^{13}C NMR (**Fig. S47**, 125 MHz, $CDCl_3$): δ 13.916 ($CH_2\mathbf{C}H_3$), 20.426 ($CH_2\mathbf{C}H_2CH_3$), 28.986 ($CH_2\mathbf{C}H_2CH_2$), 54.447 ($CH_2CH_2\mathbf{C}H_2N$), 56.023 ($N\mathbf{C}H_2$), 59.514 ($O\mathbf{C}H_2$). HRMS (**Fig. S101**, ESI): M = $C_8H_{19}NO_2$ Calc. $[M+H]^+$ = 162.1489, Found $[M+H]^+$ = 162.1507.

FT-IR ν(cm^{-1}) (**Fig. S83**): 3345 (br), 2954, 2932, 2871, 2814, 1458, 1403, 1364, 1278, 1241, 1160, 1037 (s), 902, 875, 731.

3.4.13 N-phenyldiethanolamine, [PhDEA]H_2

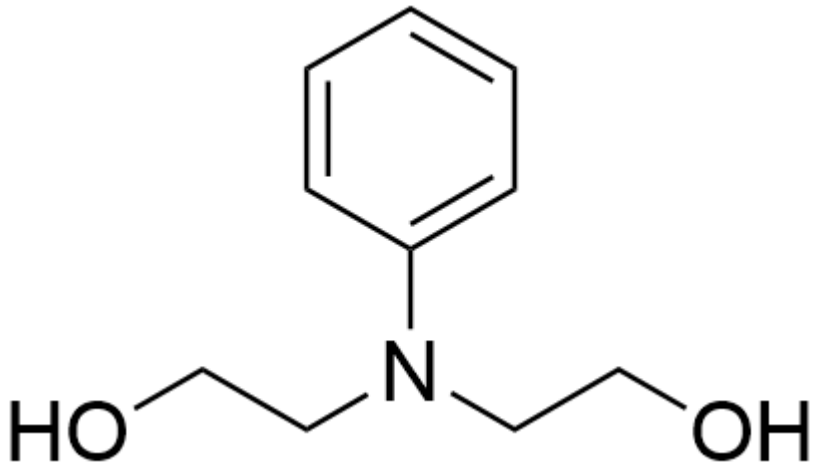

Figure 95- Skeletal structure of N-phenyldiethanolamine, [**PhDEA**]H_2.

Compound [**PhAE**]H (6.27 mL, 50 mmol) dissolved in toluene (20 mL) was stirred at room temperature whilst 2-chloroethanol (5.03 mL, 75 mmol) was added dropwise over five minutes. The mixture was then refluxed at 120°C for 6 h. The resulting solution was then hot filtrated and allowed to cool to room temperature. After a second cold filtration the remaining solution was concentrated under vacuo to produce a dark brown oil of the crude product hydrochloride salt (8.224 g, 76%). This oil was freebased by dissolving in a minimum amount of water (approx. 2 mL) and basifying with aqueous sodium hydroxide (8 mL, 2N) until universal indicator paper showed the solution was strongly basic (pH=14). The aqueous solution was then extracted with dichloromethane (3x20 mL). The combined organic layers were then dried over anhydrous magnesium sulphate and concentrated under vacuo to leave a viscous oil. After trituration with pentane (2x5 mL) the product, [**PhDEA**]H_2 (2.339 g, 34%), was yielded as a white solid, which slowly turns pink with exposure to air. Overall reaction yield of 26%.

^{1}H NMR (**Fig. S49**, 500 MHz, $CDCl_3$): δ 3.590 (t, 4H, NC**H**$_2$), 3.869 (t, 4H, OC**H**$_2$), 6.712-6.758 (m, 3H, Ph), 7.218-7.251 (m, 2H, Ph). ^{13}C NMR (**Fig. S51**, 125 MHz, $CDCl_3$): δ 55.253 (N**C**H_2), 60.887 (O**C**H_2), 112.764 (Ph), 117.085 (Ph), 129.325 (Ph), 147.891 (Ph). HRMS (**Fig. S102**, ESI): M = $C_{10}H_{15}NO_2$ Calc. $[M+H]^+$ = 182.1176, Found $[M+H]^+$ = 182.1178. FT-

IR v(cm^{-1}) (**Fig. S84**): 3323 (br), 3062, 2927, 2877, 1596, 1572, 1503, 1484, 1458, 1439, 1416, 1388, 1357, 1311, 1288, 1273, 1255, 1236, 1216, 1185, 1157, 1125, 1088, 1060, 1046, 1027 (s), 991, 980, 910, 860, 792, 752 (s), 694.

3.4.14 Triethanolamine, [TEA]H_3

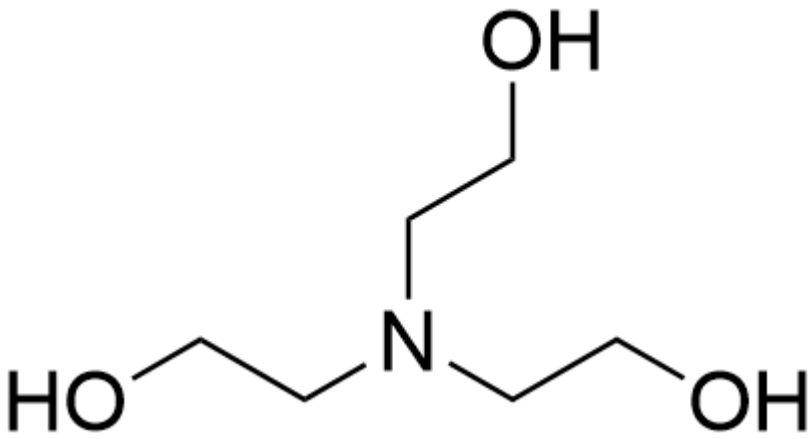

Figure 96- Skeletal structure of triethanolamine, [**TEA**]H_3.

Diethanolamine (4.79 mL, 50 mmol) dissolved in water (20 mL) was stirred at room temperature whilst 2-chloroethanol (5.03 mL, 75 mmol) was added dropwise over five minutes. The mixture was then refluxed at 120°C for 24 h. The resulting solution was then hot filtrated and allowed to cool to room temperature. After a second cold filtration the remaining solution was concentrated under vacuo to produce a near colourless oil of the product hydrochloride salt (9.006 g, 97%). This oil was freebased by dissolving in a minimum amount of water (approx. 2 mL) and basifying with aqueous sodium hydroxide (4 mL, 2N) until universal indicator paper showed the solution was strongly basic (pH=14). The aqueous solution was then extracted with dichloromethane (3x20 mL). The combined organic layers were dried over anhydrous magnesium sulphate and concentrated under vacuo. The resultant oil was then run through a vacuum distillation apparatus (110°C, 20 mbar) to leave the product in the Claisen flask after 2h. The product, [**TEA**]H_3 (7.193 g, 99%), was yielded as a colourless liquid. Overall reaction yield of 96%.

^{1}H NMR (**Fig. S53**, 500 MHz, $CDCl_3$): δ 2.514 (t, 6H, NC**H**$_2$), 3.550 (t, 6H, OC**H**$_2$), 5.082 (br s, 3H, O**H**). ^{13}C NMR **Fig. S55**, 125 MHz, $CDCl_3$): δ 56.893 (N**C**H_2), 59.226 (O**C**H_2). HRMS (**Fig. S103**, ESI): M = $C_6H_{15}NO_3$ Calc. $[M+H]^+$ = 150.1125, Found $[M+H]^+$ = 150.1141. FT-

IR ν(cm^{-1}) (**Fig. S85**): 3288 (br), 2947, 2876, 2616, 1450, 1403, 1358, 1279, 1248, 1152, 1067, 1029 (s), 907, 880.

3.4.15 3-[(2-hydroxyethyl)(methyl)amino]propan-1-ol, [HMAP]H_2

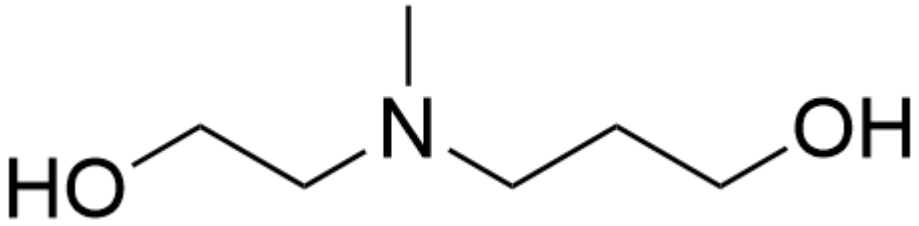

Figure 97- Skeletal structure of 3-[(2-hydroxyethyl)(methyl)amino] propan-1-ol, [**HMAP**]H_2.

Compound [**MAE**]H (4.02 mL, 50 mmol) dissolved in toluene (20 mL) was stirred at room temperature whilst 3-chloropropanol (4.18 mL, 50 mmol) was added dropwise over five minutes. The mixture was then refluxed at 120°C for 24 h. The resulting solution was then hot filtrated and allowed to cool to room temperature. After a second cold filtration the remaining solution was concentrated under vacuo to produce a yellow oil of the product hydrochloride salt (8.135 g, 96%). This oil was freebased by dissolving in a minimum amount of water (approx. 2 mL) and basifying with aqueous sodium hydroxide (8 mL, 2N) until universal indicator paper showed the solution was strongly basic (pH=14). The aqueous solution was then extracted with dichloromethane (3x20 mL). The combined organic layers were then dried over anhydrous magnesium sulphate and concentrated under vacuo. The resultant oil required no further purification. The product, [**HMAP**]H_2 (5.510 g, 88%), was yielded as a near colourless oil. Overall reaction yield of 83%.

^{1}H NMR (**Fig. S57**, 500 MHz, $CDCl_3$): δ 1.724 (p, 2H, $CH_2C\mathbf{H}_2CH_2$), 2.316 (s, 3H, $NC\mathbf{H}_3$), 2.584 (t, 2H, $CH_2C\mathbf{H}_2N$), 2.648 (t, 2H, $CH_2CH_2C\mathbf{H}_2N$), 3.674 (t, 2H, $CH_2C\mathbf{H}_2O$), 3.759 (t, 2H, $CH_2CH_2C\mathbf{H}_2O$). ^{13}C NMR (**Fig. S59**, 125 MHz, $CDCl_3$): δ 28.307 ($CH_2C\mathbf{H}_2CH_2$), 42.166 ($NC\mathbf{H}_3$), 56.860 ($CH_2CH_2C\mathbf{H}_2N$), 59.039 ($CH_2C\mathbf{H}_2O$), 59.519 ($CH_2C\mathbf{H}_2N$), 63.038 ($CH_2CH_2C\mathbf{H}_2O$). HRMS (**Fig. S106**, ESI): M = $C_6H_{15}NO_2$ Calc. $[M+H]^+$ = 134.1176, Found $[M+H]^+$ = 134.1183. FT-IR ν(cm^{-1}) (**Fig. S86**): 3303 (br), 2950, 2880, 2794, 2463, 2362, 1464, 1330, 1247, 1137, 1057 (s), 1032 (s), 915.

3.4.16 3-[(2-hydroxyethyl)(ethyl)amino]propan-1-ol, [**HEAP**]H_2

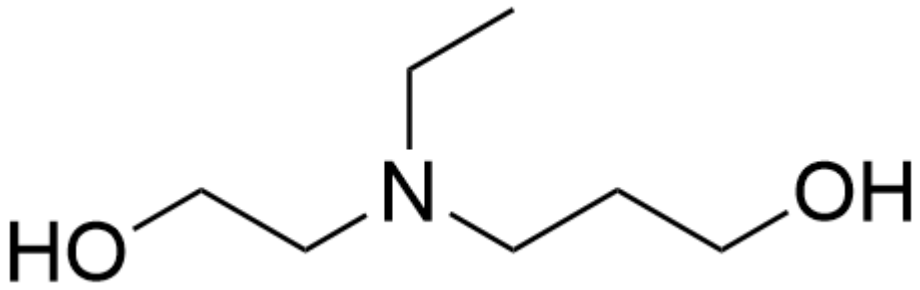

Figure 98- Skeletal structure of 3-[(2-hydroxyethyl)(ethyl)amino] propan-1-ol, [**HEAP**]H_2.

Compound [**EAE**]H (7.31 mL, 75 mmol) dissolved in toluene was stirred at room temperature whilst 3-chloropropanol (4.18 mL, 50 mmol) was added dropwise over five minutes. The mixture was then refluxed at 120°C for 24 h. The resulting solution was then hot filtrated and allowed to cool to room temperature. After a second cold filtration the remaining solution was concentrated under vacuo to produce a yellow oil of the product hydrochloride salt (8.857 g, 96%). This oil was freebased by dissolving in a minimum amount of water (approx. 2 mL) and basifying with aqueous sodium hydroxide (8 mL, 2N) until universal indicator paper showed the solution was strongly basic (pH=14). The aqueous solution was then extracted with dichloromethane (3x20 mL). The combined organic layers were then dried over anhydrous magnesium sulphate and concentrated under vacuo. The resultant oil was then run through a vacuum distillation apparatus (70°C, 20 mbar) to leave the product in the Claisen flask after 2h. The product, [**HEAP**]H_2 (5.453 g, 77%), was yielded as a near colourless oil. Overall reaction yield of 74%.

^{1}H NMR (**Fig. S61**, 500 MHz, $CDCl_3$): δ 1.060 (t, 3H, C**H**$_3$CH_2N), 1.706 (p, 2H, CH_2C**H**$_2$CH_2), 2.557-2.613 (t+q, 2H + 2H, NC**H**$_2$CH_3 + NC**H**$_2$CH_2O), 2.677 (t, 2H, CH_2CH_2C**H**$_2$N), 3.654 (t, 2H, NCH_2C**H**$_2$O), 3.784 (t, 2H, CH_2CH_2C**H**$_2$O). ^{13}C NMR (**Fig. S63**, 125 MHz, $CDCl_3$): δ 11.653 (NCH_2**C**H_3), 28.448 (CH_2**C**H_2CH_2), 48.163 (N**C**H_2CH_3), 53.245 (N**C**H_2CH_2), 55.904 (N**C**H_2CH_2O), 59.757 (NCH_2**C**H_2O), 63.544(CH_2**C**H_2O). HRMS (**Fig. S107**, ESI): M = $C_7H_{17}NO_2$ Calc. $[M+H]^+$ = 148.1332, Found $[M+H]^+$ = 148.1343. FT-IR ν(cm^{-1}) (**Fig. S87**): 3289 (br), 2944, 2875, 2359, 1466, 1375, 1216, 1052 (s), 922.

3.4.17 3-[(2-hydroxyethyl)(iso-propyl)amino]propan-1-ol, [H^{i}PrAP]H$_2$

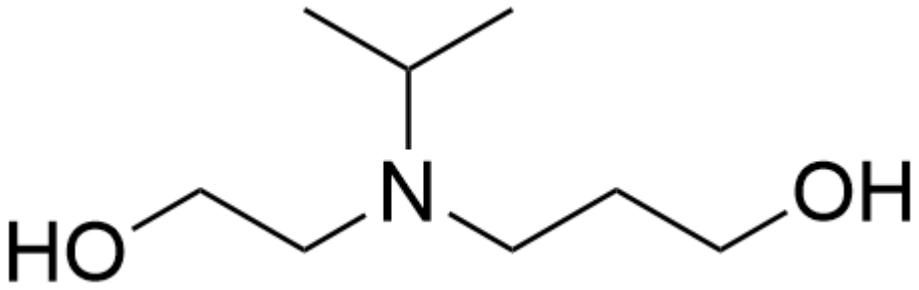

Figure 99- Skeletal structure of 3-[(2-hydroxyethyl)(isopropyl)amino] propan-1-ol, [H^{i}PrAP]H$_2$.

Compound [^{i}PrAE]H (5.73 mL, 50 mmol) dissolved in toluene was stirred at room temperature whilst 3-chloropropanol (8.36 mL, 100 mmol) was added dropwise over five minutes. The mixture was then refluxed at 120°C for 24 h. The resulting solution was then hot filtrated and allowed to cool to room temperature. After a second cold filtration the remaining solution was concentrated under vacuo to produce a yellow oil of the product hydrochloride salt (7.714 g, 78%). This oil was freebased by dissolving in a minimum amount of water (approx. 2 mL) and basifying with aqueous sodium hydroxide (8 mL, 2N) until universal indicator paper showed the solution was strongly basic (pH=14). The aqueous solution was then extracted with dichloromethane (3x20 mL). The combined organic layers were then dried over anhydrous magnesium sulphate and concentrated under vacuo. The resultant oil was then run through a vacuum distillation apparatus (70°C, 20 mbar) to leave the product in the Claisen flask after 2h. The product, [H^{i}PrAP]H$_2$ (5.335 g, 85%), was yielded as a near colourless oil. Overall reaction yield of 66%.

^{1}H NMR (**Fig. S65**, 500 MHz, $CDCl_3$): δ 0.997-1.011 (d, 6H, NCH(C**H**$_3$)$_2$), 1.679 (p, 2H, CH$_2$C**H**$_2$CH$_2$), 2.573 (t, 2H, OCH$_2$C**H**$_2$N), 2.672 (t, 2H, CH$_2$CH$_2$C**H**$_2$N), 3.051 (h, 1H, NC**H**(CH$_3$)$_2$), 3.615 (t, 2H, NCH$_2$C**H**$_2$O), 3.745 (t, 2H, CH$_2$CH$_2$C**H**$_2$O). ^{13}C NMR (**Fig. S67**, 125 MHz, $CDCl_3$): δ 17.347 (NCH(**C**H$_3$)$_2$), 28.765 (CH$_2$**C**H$_2$CH$_2$), 49.477 (N**C**H$_2$CH$_2$CH$_2$), 50.457 (N**C**H(CH$_3$)$_2$), 51.561 (N**C**H$_2$CH$_2$O), 59.826 (NCH$_2$**C**H$_2$O), 63.115 (CH$_2$**C**H$_2$OH). HRMS (**Fig. S108**, ESI): M = $C_8H_{19}NO_2$ Calc. $[M+H]^+$ = 162.1489, Found $[M+H]^+$ = 162.1502. FT-IR ν(cm^{-1}) (**Fig. S88**): 3288 (br), 2962, 2871, 2360, 1463, 1384, 1363, 1298, 1215, 1168, 1122, 1050 (s), 916, 874.

3.4.18 3-[(2-hydroxyethyl)(phenyl)amino]propan-1-ol, [HPhAP]H_2

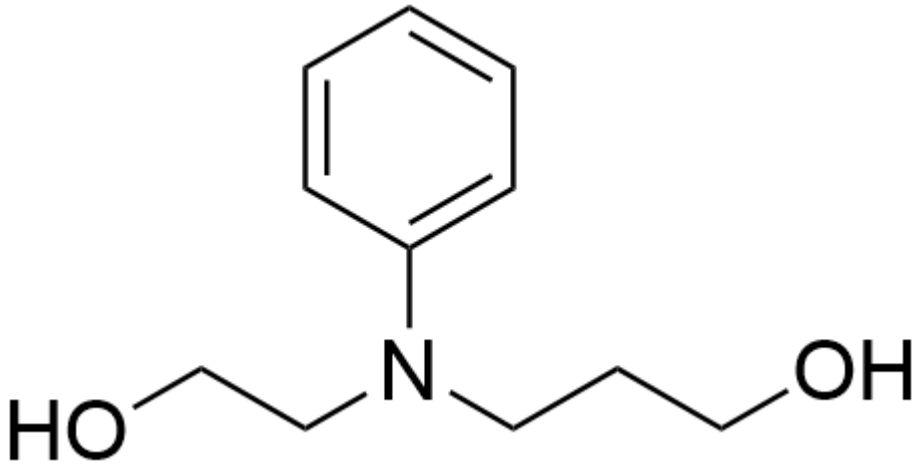

Figure 100- Skeletal structure of 3-[(2-hydroxyethyl)(phenyl)amino] propan-1-ol, [**HPhAP**]H_2.

Compound [**PhAE**]H (12.62 mL, 100 mmol) dissolved in toluene was stirred at room temperature whilst 3-chloropropanol (4.18 mL, 50 mmol) was added dropwise over five minutes. The mixture was then refluxed at 120°C for 48 h. The resulting solution was then hot filtrated and allowed to cool to room temperature. After a second cold filtration the remaining solution was concentrated under vacuo to produce a brown oil of the product hydrochloride salt (9.427 g, 81%). This oil was freebased by dissolving in a minimum amount of water (approx. 16 mL) and basifying with aqueous sodium hydroxide (8 mL, 2N) until universal indicator paper showed the solution was strongly basic (pH=14). The aqueous solution was then extracted with dichloromethane (3x20 mL). The combined organic layers were then dried over anhydrous magnesium sulphate and concentrated under vacuo. The crude product (7.522 g, 95%) was then run through a flash column of neutral silica using an eluent mixture of hexane:ethyl acetate (1:4). The product, [**HPhAP**]H_2 (2.407g, 32%), was yielded as a near black, viscous oil. Overall reaction yield of 26%.

^{1}H NMR (**Fig. S69**, 500 MHz, $CDCl_3$): δ 1.863 (p, 2H, $CH_2C\mathbf{H}_2CH_2$), 3.480-3.518 (t+t, 2H + 2H, $NC\mathbf{H}_2CH_2O$ + $NC\mathbf{H}_2CH_2CH_2$), 3.745 (t, 2H, $OC\mathbf{H}_2CH_2CH_2$), 3.817 (t, 2H, $OC\mathbf{H}_2CH_2N$), 6.748-6.839 (m, 3H, Ph), 7.224-7.256 (m, 2H, Ph). ^{13}C NMR (125 MHz, $CDCl_3$): δ 29.796 ($CH_2\mathbf{C}H_2CH_2$), 49.370 ($N\mathbf{C}H_2CH_2CH_2$), 55.035 ($OCH_2\mathbf{C}H_2N$), 60.606 ($O\mathbf{C}H_2CH_2N$), 60.854 ($O\mathbf{C}H_2CH_2CH_2$), 113.123(Ph), 115.497(Ph), 129.648 (Ph). Values extracted from HMQC

analysis. HRMS (**Fig. S109**, ESI): M = $C_{11}H_{17}NO_2$ Calc. $[M+H]^+$ = 196.1332, Found $[M+H]^+$ = 196.1341. FT-IR ν(cm^{-1}) (**Fig. S89**): 3304 (br), 3054, 2942, 2879, 2676, 2362, 1599, 1504, 1459, 1434, 1367, 1320, 1264, 1195, 1180, 1161, 1057 (s), 990, 917, 866, 749 (s), 693 (s).

4 Synthesis of {3d-4f} Complexes with Amine Polyalcohol Ligands

4.1 Introduction

Early research into potential molecular magnets focussed upon homometallic structures, whether composed entirely of {3d} or {4f} ions. However, both options have their drawbacks. Purely transition metal complexes were ideal for targeting S as a parameter to enhance U_{eff} and thereby overall magnetic properties. Conversely, pure lanthanide schemes exhibited a higher inherent magnetic moment, n_{eff}, and higher axial anisotropy, D, but due to weak coupling to ligands or other lanthanide centres the tunnelling pathway saw the coercive field collapse. By mixing the properties of both methodologies, a combination stronger than the sum of its parts could be forged. Previous investigations into {3d-4f} combinatorial systems demonstrated how the more diffuse {3d} orbitals could interact with the buried lanthanide {4f} orbitals, inducing stronger magnetic exchange, reducing QTM and thereby increasing the relaxation time significantly.

Magnetism, being an inherently unbalanced phenomenon, inspired this project to synthesise the asymmetric ligands described in **Chapter 3**, and here their utility shall be challenged. In this chapter, the work exhibited broadens the examples of known {3d-4f} molecular magnetic structures. It also attempts to explain the response of increasing ligand asymmetry within a known motif, before defining any effects this change may have had on the complexes magnetic behaviour. Additionally, the final sample described within this chapter, **C20**, demonstrates the versatility of serendipitous self-assembly with the production of the $\{Cr^{III}Dy^{III}_6\}$ toroid.

4.2 Results and Discussion

This chapter describes the synthesis and characterisation of five {3d-4f} coordination complexes utilising the asymmetric ligands, shown below in **Figure 101**, whose syntheses were described in **Chapter 3**. Additional bidentate ligands used to stabilise the complexes formed are also given in **Figure 102**. This work exhibits the variation in structure which can occur in the products of chemically similar serendipitous

arrangement reactions. It also expounds upon how the binding modes of the polyalcohol can vary significantly between, or within, molecules.

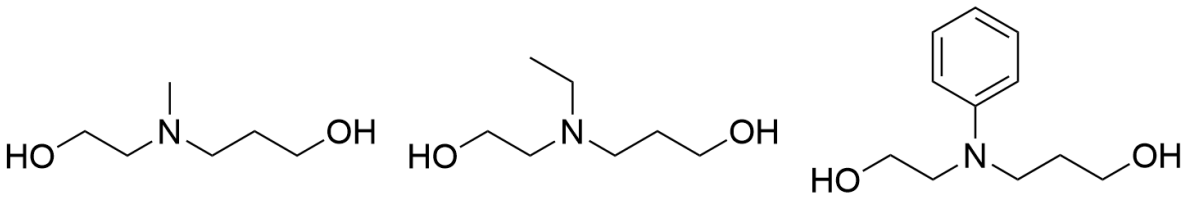

Figure 101- Structures of the three asymmetric polyalcohol ligands used in chapter 4, from left to right: [(2-hydroxyethyl)(methyl)amino]propan-1-ol ([**HMAP**]H_2), [(2-hydroxyethyl)(ethyl)amino]propan-1-ol ([**HEAP**]H_2), [(2-hydroxyethyl)(phenyl)amino]propan-1-ol ([**HPhAP**]H_2).

All the complexes produced, **C15**-**C19**, were initially produced in reactions using the same stoichiometric ratio (Ln : TM : Acid : Polyalcohol : Triethylamine, 2 : 2 : 4 : 2 : 8 respectively), prior to the synthesis being refined in an attempt to target specific, then known structures. Sample **C20** was produced by this same method, but failed to coordinate the polyalcohol ligand, leading to a distinct structural motif.

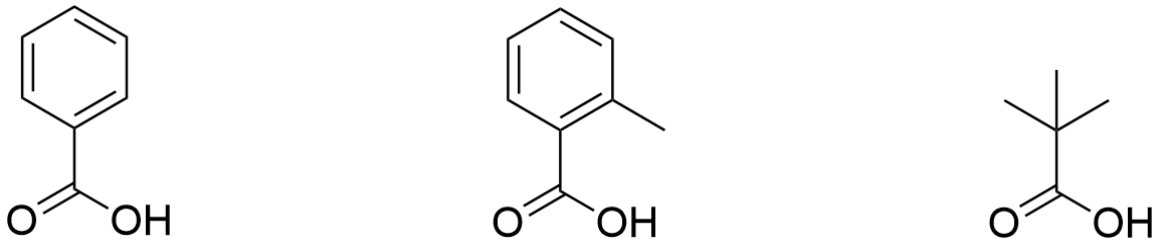

Figure 102- Bidentate ligands used in the synthesis described in chapter 4, from left to right: benzoic acid ([Benz]H), o-toluic acid ([o-Tol]H), pivalic acid ([Piv]H).

4.2.1 Structural Studies

Utilising the synthesised symmetric and asymmetric ligands described in **Chapter 3**, the work in this chapter focussed upon the investigation of the coordination chemistry exhibited by the tetradentate ligands in {3d-4f} heterometallic complexes. Complexes **C15**-**C20** were all realised by simple aerobic reactions to form novel complexes in solution by serendipitous assembly. In the following section each sample is discussed in terms of parameters extracted from single crystal X-ray diffraction (SC-XRD) analysis alongside pertinent synthetic details.

The reaction of [**HMAP**]H_2 with chromium (III) nitrate nonahydrate, dysprosium (III) nitrate pentahydrate, benzoic acid and a suitable deprotonating agent (triethylamine) in a solvent mix of acetonitrile and methanol (4:1) produced a blue-grey mother liquor from which small purple block crystals of $[Cr^{III}_2Dy^{III}_2(OMe)_2(Benz)_4(HMAP)_2(NO_3)_2]$, **C15**, were grown by layer diffusion using a methanol:diethyl ether (1:4) solvent system. Complex **C15** crystallises in the monoclinic space group *P* $2_1/n$, with the asymmetric unit containing half of the molecule. The unit cell of **C15** has a volume of 2422 $Å^3$ containing two molecules per unit cell and exhibiting the unit cell parameters: a = 7.9293(4) Å, b = 17.3924(8) Å, c = 17.5915(8) Å, α =9 0°, β = 93.3700(10)°, γ = 90° (See **Appendix B**, **Table S3**).

Complex **C15** is a heterometallic {3d-4f} tetranuclear complex with the metallic core displaying a planar butterfly-type topology, as shown in **Figure 103**.

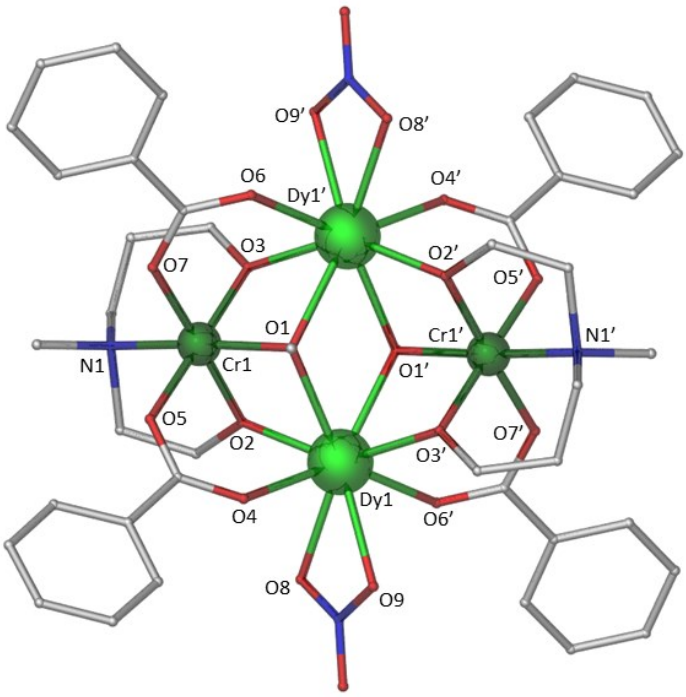

Figure 103- Molecular structure of **C15**: C atoms, grey; O atoms, red; N atoms, blue; Dy atoms, large green; Cr atoms, small green. H atoms have been omitted for clarity.

The asymmetric unit consists of half of the complex – thereby one chromium and one dysprosium ion each in the 3+ oxidation state – with the remainder generated by inversion symmetry. The two dysprosium (III) ions were found to be eight-coordinate with a distorted square antiprismatic geometry and occupy the 'body' sites of the

butterfly. The two chromium (III) ions were found to be six-coordinate with a distorted octahedral geometry and occupy the 'wing' sites of the butterfly. Two μ_3 methoxide ligands bridge the two dysprosium (III) ions to each chromium (III) ion. Each chromium (III) ion is further ligated by a fully deprotonated **HMAP**$^{2-}$ ligand, of Harris Notation 3.2.2.1, and two benzoate ligands completing the six-coordinate octahedral environment. The N-atom of the **HMAP**$^{2-}$ ligand chelates to the chromium (III) ion with the two deprotonated alkoxide arms bridging from the chromium (III) ion to the body dysprosium (III) ions. The four carboxylate ligands each bridge from a chromium (III) ion to a dysprosium (III) ion in a μ_2 manner. The coordinate sphere of each dysprosium (III) ion is completed by a capping nitrate ligand. Crystal packing diagrams of **C15** can be found in **Figure 104**. Intermolecular interactions are dominated by aromatic π, and C-H interactions derived from the benzoate ligands.

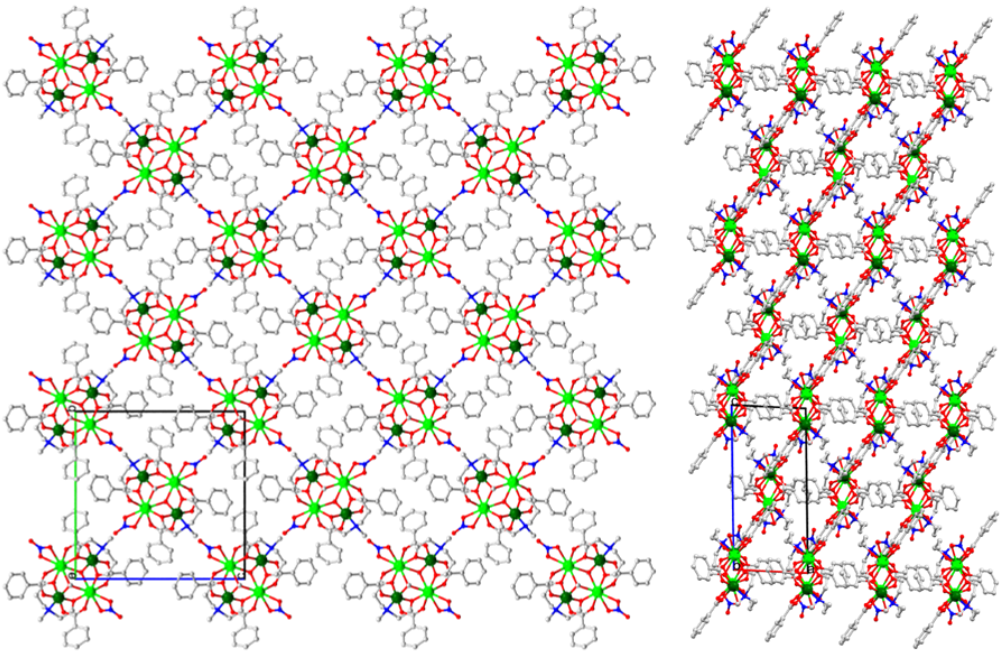

Figure 104- Crystal packing diagram of **C15** viewing the bc plane, left, and the ac plane, right. Unit cell included as a reference. C atoms, grey; O atoms, red; N atoms, blue; Dy atoms, large green; Cr atoms, small green. H atoms have been omitted for clarity.

The average Cr-$L_{N,O}$ bond length is found to be 1.99 Å with bond length ranging from 1.950-2.079 Å. The average Dy-O bond length is found to be 2.37 Å with bond lengths ranging from 2.243-2.447 Å. Selected bond lengths and bond angles are given below in **Table 25**.

Table 25- Selected bond lengths and bond angles for complex **C15**.

Atoms	Bond Length (Å)	Atoms	Bond Angle (°)
Dy1-O1	2.447	Dy1-O1-Cr1	96.35
Dy1-O1’	2.420	Dy1-O1’-Cr1’	96.92
Dy1-O3’	2.250	Dy1-O2-Cr1	104.27
Dy1-O6’	2.354	Dy1-O3’-Cr1’	103.59
Dy1-O9	2.444	Dy1-O1-Dy1’	113.70
Dy1-O8	2.432		
Dy1-O4	2.337		
Dy1-O2	2.243		
Cr1-O1	1.983		
Cr1-O2	1.950		
Cr1-O5	1.983		
Cr1-N1	2.079		
Cr1-O7	1.980		
Cr1-O3	1.954		
Dy1-Dy1’	4.075		
Dy1-Cr1	3.316		
Dy1-Cr1’	3.308		
Cr1-Cr1’	5.222		

The reaction of [**HEAP**]H_2 with chromium (III) nitrate nonahydrate, dysprosium (III) nitrate pentahydrate, benzoic acid and triethylamine in a solvent mix of acetonitrile and methanol (4:1) produced a pale blue mother liquor from which small purple plate crystals of $[Cr^{III}_2Dy^{III}_2(OMe)_2(Benz)_4(HEAP)_2(NO_3)_2]$, **C16**, were grown by layer diffusion using a methanol:diethyl ether (1:4) solvent system. Complex **C16** crystallises in the monoclinic space group *P 2₁/n*, with the asymmetric unit containing half of the molecule. The unit cell of **C16** has a volume of 2491 Å^3 containing two molecules per unit cell and exhibiting the unit cell parameters: a = 7.8874(4) Å, b = 17.7343(8) Å, c = 17.8886(8) Å, α = 90°, β = 94.4690(10)°, γ = 90° (See **Appendix B**, **Table S4**).

Complex **C16** is a heterometallic {3d-4f} tetranuclear complex with the metallic core displaying a planar butterfly-type topology, as shown in **Figure 105**.

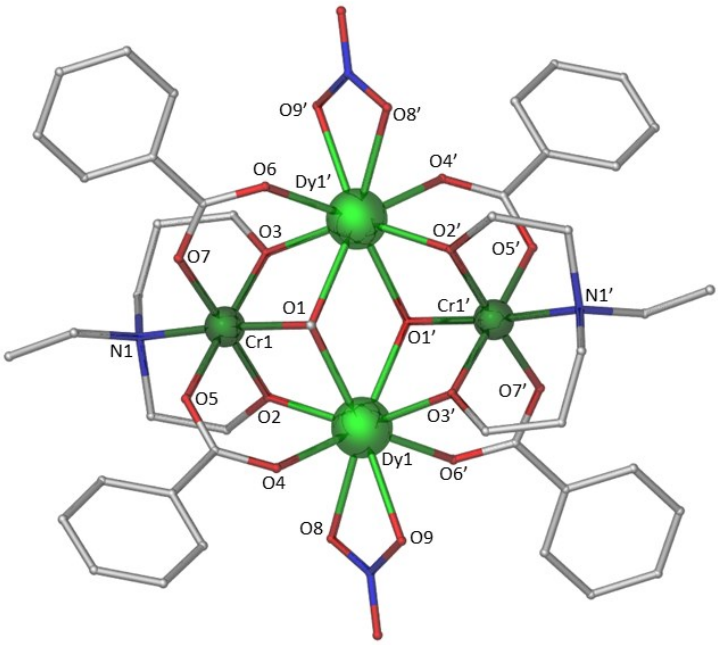

Figure 105- Molecular structure of **C16**: C atoms, grey; O atoms, red; N atoms, blue; Dy atoms, large green; Cr atoms, small green. H atoms have been omitted for clarity.

The asymmetric unit consists of half of the complex – thereby one chromium and one dysprosium ion each in the 3+ oxidation state – with the remainder generated by inversion symmetry. The two dysprosium (III) ions were found to be eight-coordinate with a distorted square antiprismatic geometry and occupy the 'body' sites of the butterfly. The two chromium (III) ions were found to be six-coordinate with a distorted octahedral geometry and occupy the 'wing' sites of the butterfly. Two μ_3 methoxide

ligands bridge the two dysprosium (III) ions to each chromium (III) ion. Each chromium (III) ion is further ligated by a fully deprotonated **HEAP**$^{2-}$ ligand, of Harris Notation 3.2.2.1, and two benzoate ligands completing the six-coordinate octahedral environment. The N-atom of the **HEAP**$^{2-}$ ligand chelates to the chromium (III) ion with the two deprotonated alkoxide arms bridging from the chromium (III) ion to the body dysprosium (III) ions. The four carboxylate ligands each bridge from a chromium (III) ion to a dysprosium (III) ion in a μ_2 manner. The coordinate sphere of each dysprosium (III) ion is completed by a capping nitrate ligand. Crystal packing diagrams of complex **C16** can be found in **Figure 106**. Intermolecular interactions are dominated by aromatic π, and C-H interactions derived from the benzoate ligands.

The average Cr-$L_{N,O}$ bond length is found to be 1.99 Å with bond length ranging from 1.946-2.101 Å. The average Dy-O bond length is found to be 2.37 Å with bond lengths ranging from 2.242-2.443 Å. Selected bond lengths and bond angles are given below in **Table 26**.

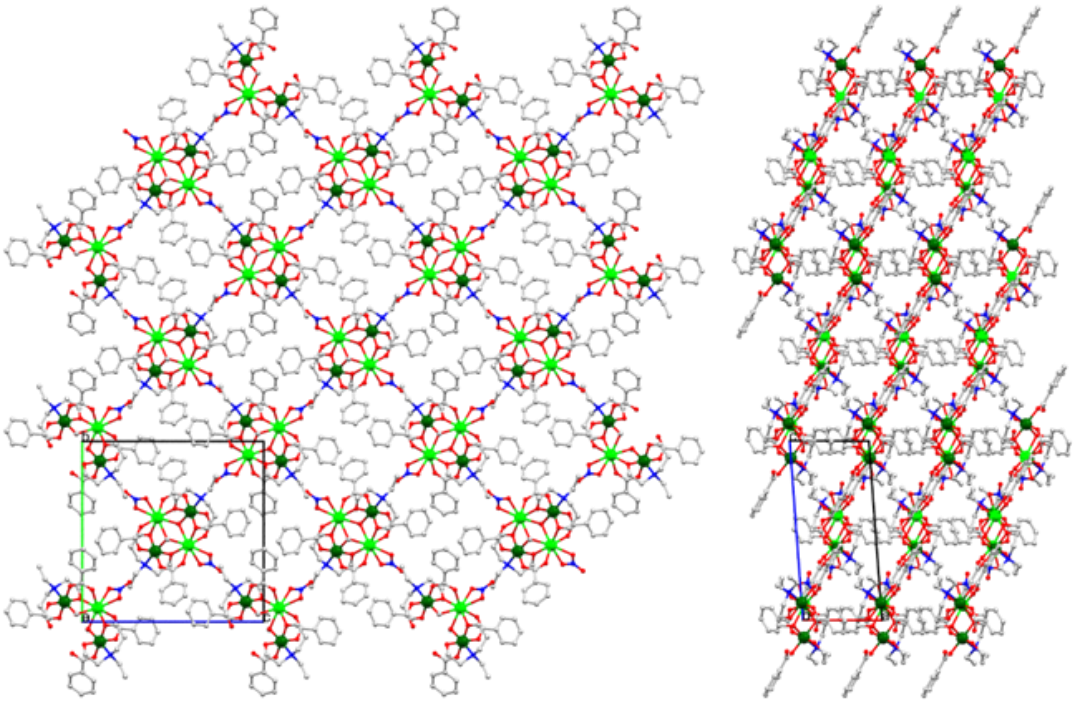

Figure 106- Crystal packing diagram of **C16** viewing the bc plane, left, and the ac plane, right. Unit cell included as a reference. C atoms, grey; O atoms, red; N atoms, blue; Dy atoms, large green; Cr atoms, small green. H atoms have been omitted for clarity.

Table 26- Selected bond lengths and bond angles for complex **C16**.

Atoms	Bond Length (Å)	Atoms	Bond Angle (°)
Dy1-O1	2.410	Dy1-O1-Cr1	97.59
Dy1-O1’	2.442	Dy1-O1’-Cr1’	96.22
Dy1-O3’	2.242	Dy1-O2-Cr1	103.88
Dy1-O6’	2.350	Dy1-O3’-Cr1’	104.22
Dy1-O9	2.443	Dy1-O1-Dy1’	113.73
Dy1-O8	2.431		
Dy1-O4	2.362		
Dy1-O2	2.253		
Cr1-O1	1.987		
Cr1-O2	1.957		
Cr1-O5	1.971		
Cr1-N1	2.101		
Cr1-O7	1.990		
Cr1-O3	1.946		
Dy1-Dy1’	4.062		
Dy1-Cr1	3.319		
Dy1-Cr1’	3.310		
Cr1-Cr1’	5.239		

The reaction of [**HMAP**]H_2 with manganese (II) nitrate tetrahydrate, dysprosium (III) nitrate pentahydrate, benzoic acid and triethylamine in a solvent mix of acetonitrile and methanol (4:1) produced a dark red mother liquor from which dark red needle crystals of $[Mn^{III}_2Dy^{III}_2(O)(Benz)_6(HMAP)_2]_n$, **C17**, were grown by slow deposition from the reaction solvent system. Complex **C17** crystallises in the orthorhombic space group *P m n* 2_1, with the asymmetric unit containing half of the monomeric unit. The unit cell of **C17** has a volume of 3065 $Å^3$ containing two molecules per unit cell and exhibiting the unit cell parameters: a = 15.5742(9) Å, b = 20.1115(13) Å, c = 9.7842(4) Å, α = 90°, β = 90°, γ = 90° (See **Appendix B**, **Table S4**).

Complex **C17** is a heterometallic {3d-4f} chain composed of a tetranuclear monomer component with the metallic core displaying a concave butterfly-type topology, as shown in **Figure 107**. The manganese oxidation state was assigned through bond valence sum (BVS) calculations and balancing of charges.

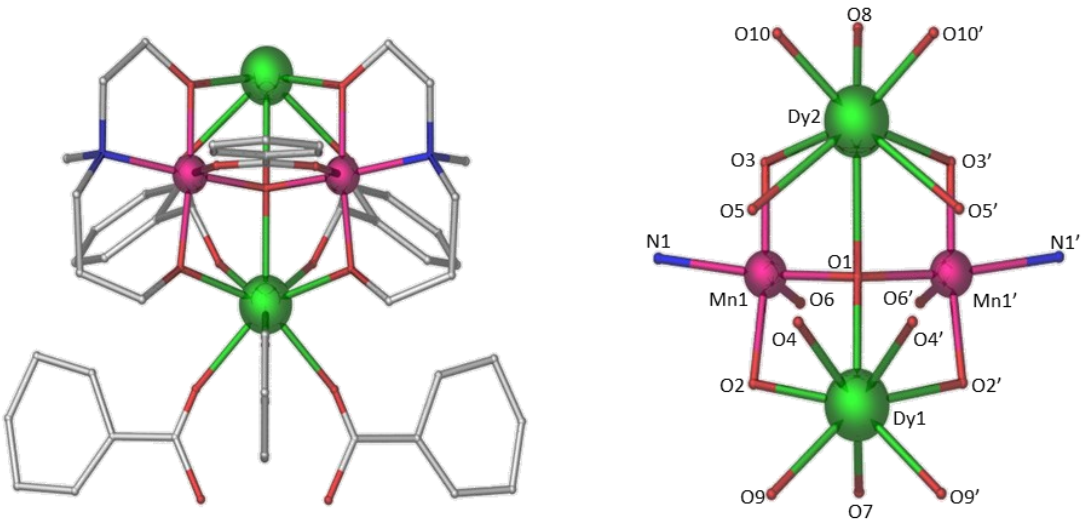

Figure 107- Molecular structure (left) and skeletal form (right) of the **C17** monomer: C atoms, grey; O atoms, red; N atoms, blue; Dy atoms, green; Mn atoms, pink. H atoms have been omitted from both structures and C atoms have been omitted from the skeletal form for clarity.

The asymmetric unit consists of half of the complex monomer – thereby one manganese and two half occupancy dysprosium ions each in the 3+ oxidation state – with the remainder generated by inversion symmetry. The two dysprosium (III) ions were found to be eight-coordinate with a distorted square antiprismatic geometry and occupy the

pseudo-'wing' sites of the butterfly. The two manganese (III) ions (BVS score = 3.17; **Table S19**) were found to be five-coordinate with a distorted square pyramidal geometry and occupy the pseudo-'body' sites of the butterfly. A μ_4 oxide ligand bridges the two dysprosium (III) ions to the two manganese (III) ions, resulting in the observed curvature to the normally planar butterfly topology. Each manganese (III) ion is further ligated by a fully deprotonated **HMAP**$^{2-}$ ligand, of Harris Notation 3.2.2.1, and one benzoate ligand between the two manganese ions completing the five-coordinate octahedral environment. The N-atom of the **HMAP**$^{2-}$ ligand chelates to the manganese (III) ion with the two deprotonated alkoxide arms bridging from the manganese (III) ion to the wing dysprosium (III) ions. The four remaining carboxylate ligands each bridge between two dysprosium (III) ion in a μ_2 manner. One of these ligands binds intra-monomerically and three inter-monomerically. Each monomer is bridged onwards to its adjacent monomer by this tri-benzoate linker system, as shown in **Figure 108**.

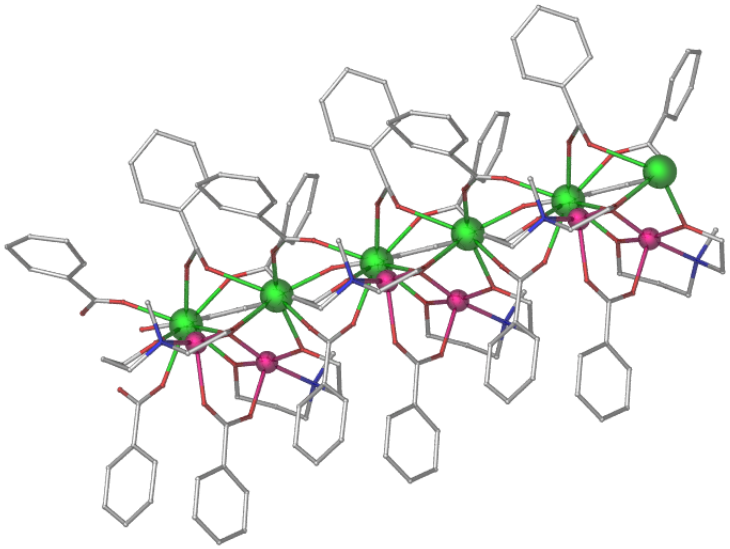

Figure 108- Molecular structure of the **C17** chain with three benzoate linkers bridging each pair of monomer components. C atoms, grey; O atoms, red; N atoms, blue; Dy atoms, green; Mn atoms, pink. H atoms have been omitted from both structures and C atoms have been omitted from the skeletal form for clarity.

Crystal packing diagrams of complex **C17** can be found in **Figure 109**. Intermolecular interactions are dominated by aromatic π, and C-H interactions derived from the benzoate ligands.

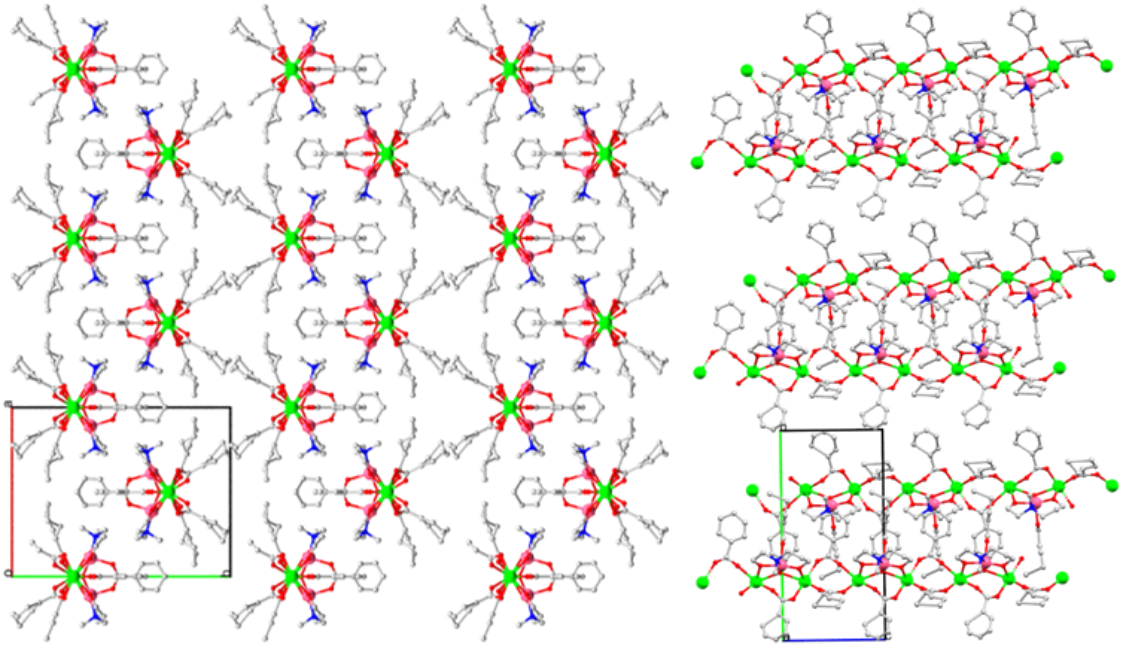

Figure 109- Crystal packing diagram of **C17** viewing the ab plane, left, and the bc plane, right. Unit cell included for reference. C atoms, grey; O atoms, red; N atoms, blue; Dy atoms, green; Mn atoms, pink. H atoms have been omitted from both structures and C atoms have been omitted from the skeletal form for clarity.

The average Mn-$L_{N,O}$ bond length is found to be 1.96 Å with bond length ranging from 1.834-2.169 Å. The average Dy-O bond length is found to be 2.37 Å with bond lengths ranging from 2.211-2.642 Å. Selected bond lengths and bond angles are given below in **Table 27**.

Table 27- Selected bond lengths and bond angles for complex **C17**.

Atoms	Bond Length (Å)	Atoms	Bond Angle (°)
Mn1-O1	1.862	Mn1-O1-Mn1’	133.95
Mn1-O6	2.169	Mn1-O1-Dy1	93.46
Mn1-O2	1.834	Mn1-O1-Dy2	101.63
Mn1-N1	2.060	Mn1-O2-Dy1	103.63
Mn1-O3	1.889	Mn1-O3-Dy2	102.25
Dy1-O1	2.609	Dy1-O1-Dy2	140.10
Dy1-O4’	2.642		
Dy1-O2’	2.340		
Dy1-O9’	2.211		
Dy1-O7	2.346		
Dy2-O1	2.356		
Dy2-O5	2.309		
Dy2-O3	2.316		
Dy2-O10	2.370		
Dy2-O8	2.303		
Mn1-Mn1’	3.427		
Mn1-Dy1	3.296		
Mn1-Dy2	3.284		
Dy1-Dy2	4.668		

The reaction of [**HEAP**]H_2 with manganese (II) nitrate tetrahydrate, gadolinium (III) nitrate pentahydrate, benzoic acid and triethylamine in a solvent mix of acetonitrile and methanol (4:1) produced a red mother liquor from which red-brown block crystals of $[Mn_2Gd^{III}_2(O)(Piv)_3(HEAP)_2(NO_3)_4]\cdot 0.5MeOH\cdot H_2O$, **C18**, were grown by layer diffusion from a methanol:diethyl ether (2:3) solvent system. Complex **C18** crystallises in the monoclinic space group *P 2₁/c*, with the asymmetric unit containing the entire molecule. The unit cell of **C18** has a volume of 5702 Å^3 containing four molecules per unit cell and exhibiting the unit cell parameters: a = 19.7059(8) Å, b = 15.4226(6) Å, c = 20.9323(8) Å, α = 90°, β = 116.3220(10)°, γ = 90° (See **Appendix B**, **Table S4**).

Complex **C18** is a heterometallic {3d-4f} tetranuclear monomer complex with the metallic core displaying a concave butterfly-type topology, as shown in **Figure 110**. The manganese oxidation state was assigned through bond valence sum (BVS) calculations and balancing of charges.

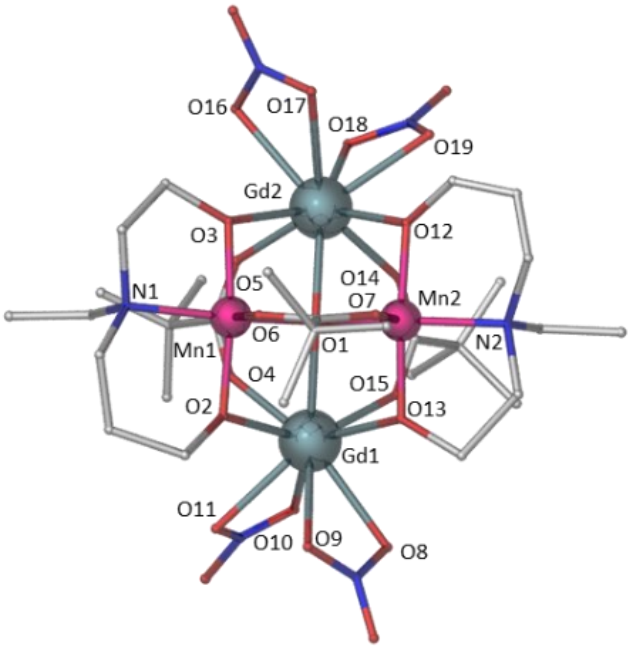

Figure 110- Molecular structure of **C18**: C atoms, grey; O atoms, red; N atoms, blue; Gd atoms, silver; Mn atoms, pink. H atoms have been omitted for clarity.

The two gadolinium (III) ions were found to be nine-coordinate with a distorted capped square antiprismatic geometry and occupy the pseudo-'wing' sites of the butterfly. The two manganese (III) ions (BVS scores = 3.25, 3.29; **Table S20**) were found to be five-coordinate with a distorted square pyramidal geometry and occupy the pseudo-'body'

sites of the butterfly. A μ_4 oxide ligand bridges the two gadolinium (III) ions to the two manganese (III) ions, resulting in the observed curvature to the normally planar butterfly topology. Each manganese (III) ion is further ligated by a fully deprotonated **HEAP**$^{2-}$ ligand, of Harris Notation 3.2.2.1, and one carboxylate ligand between the two manganese ions completing the five-coordinate octahedral environment. The N-atom of the **HEAP**$^{2-}$ ligand binds to the manganese (III) ion with the two deprotonated alkoxide arms bridging from the manganese (III) ion to the wing gadolinium (III) ions. The two remaining carboxylate ligands each bridge between two gadolinium (III) ion in a μ_2 manner. The coordination sphere for the gadolinium (III) ions is completed by a pair of capping nitrate ligands on each lanthanide ion.

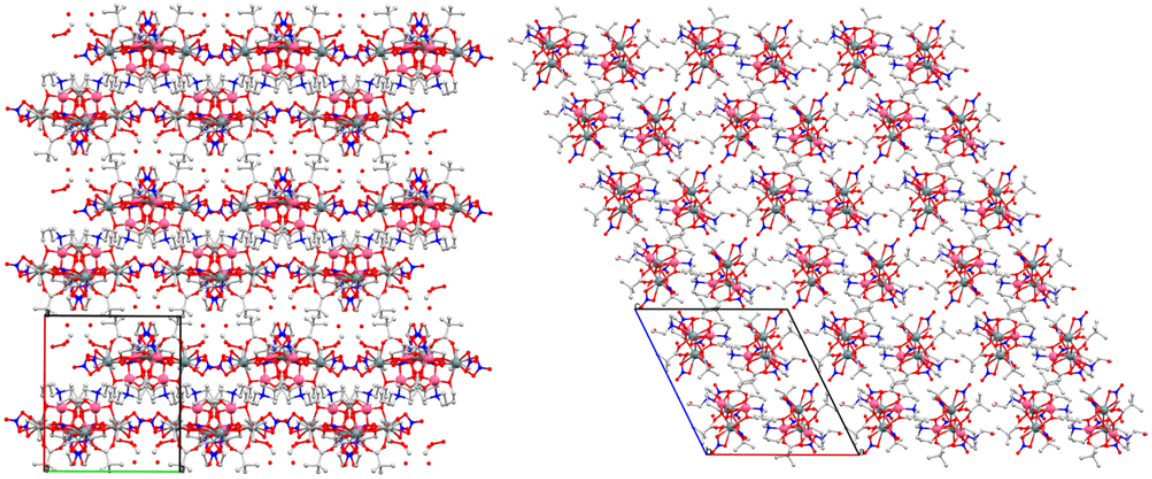

Figure 111- Crystal packing diagram of **C18** viewing the ab plane, left, and the ac plane, right. Unit cell included as a reference. C atoms, grey; O atoms, red; N atoms, blue; Gd atoms, silver; Mn atoms, pink. H atoms have been omitted for clarity.

Crystal packing diagrams of **C18** can be found in **Figure 111**. Intermolecular interactions are dominated by C-H interactions derived from the bulky pivalate ligands.

The average Mn-$L_{N,O}$ bond length is found to be 1.94 Å with bond length ranging from 1.860-2.081 Å. The average Gd-O bond length is found to be 2.44 Å with bond lengths ranging from 2.304-2.561 Å. Selected bond lengths and bond angles are given below in **Table 28** and **Table 29**, respectively.

Table 28- Selected bond lengths for complex **C18**.

Atoms	Bond Length (Å)	Atoms	Bond Length (Å)
Gd1-O1	2.406	Gd2-O16	2.492
Gd1-O15	2.306	Gd2-O17	2.541
Gd1-O13	2.415	Gd2-O18	2.538
Gd1-O8	2.514	Gd2-O19	2.526
Gd1-O9	2.512	Gd2-O12	2.362
Gd1-O10	2.542	Gd2-O14	2.362
Gd1-O11	2.561	Mn2-O1	1.862
Gd1-O2	2.358	Mn2-O7	2.078
Gd1-O4	2.376	Mn2-O12	1.877
Mn1-O1	1.866	Mn2-N2	2.018
Mn1-O6	2.081	Mn2-O13	1.860
Mn1-O2	1.874	Gd1-Gd2	4.419
Mn1-N1	2.035	Gd1-Mn1	3.307
Mn1-O3	1.866	Gd1-Mn2	3.360
Gd2-O1	2.411	Gd2-Mn1	3.359
Gd2-O5	2.304	Gd2-Mn2	3.292
Gd2-O3	2.432	Mn1-Mn2	3.213

Table 29- Selected bond angles for complex **C18**.

Atoms	Bond Angle (°)	Atoms	Bond Angle (°)
Gd1-O1-Mn1	100.72	Gd2-O1-Mn2	99.98
Gd1-O1-Gd2	133.08	Gd2-O1-Mn1	102.75
Gd1-O1-Mn2	103.14	Gd2-O12-Mn2	101.28
Gd1-O2-Mn1	102.20	Gd2-O3-Mn1	102.00
Gd1-O13-Mn2	102.86	Mn1-O1-Mn2	119.07

The reaction of [**HMAP**]H_2 with chromium (III) chloride hexahydrate, dysprosium (III) nitrate pentahydrate, benzoic acid and triethylamine in a solvent mix of acetonitrile and methanol (4:1) produced a blue-green mother liquor from which purple-green block crystals of $[Cr^{III}_4Dy^{III}_4(OH)_6(Benz)_{10}(HMAP)_4]\cdot 3H_2O$, **C19**, were grown by vapour diffusion from a methanol:acetonitrile:diethyl ether (1:4:15) solvent system. Complex **C19** crystallises in the monoclinic space group *P 2₁/c*, with the asymmetric unit containing the entire molecule. The unit cell of **C19** has a volume of 11505 Å^3 containing four molecules per unit cell and exhibiting the unit cell parameters: a = 14.8531(2) Å, b = 14.8534(2) Å, c = 52.4751(9) Å, α =90°, β = 96.4020(10)°, γ = 90° (See **Appendix B**, **Table S4**).

Complex **C19** is a heterometallic {3d-4f} octanuclear complex with the metallic core displaying a square-in-square topology, as shown in **Figure 112**.

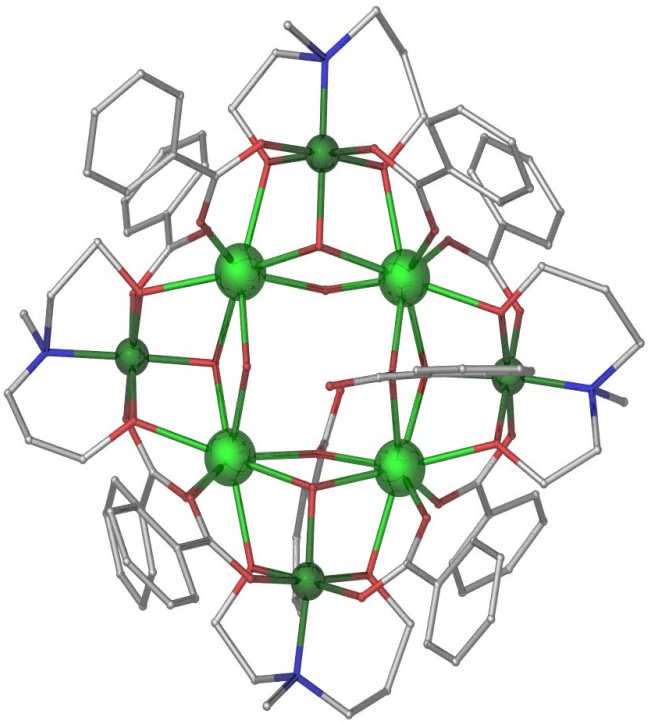

Figure 112- Molecular structure of **C19**: C atoms, grey; O atoms, red; N atoms, blue; Dy atoms, large green; Cr atoms, small green. H atoms have been omitted for clarity.

The asymmetric unit contains the entire complex – thereby four chromium and four dysprosium ions all in the 3+ oxidation state. The four dysprosium (III) ions were found to be eight-coordinate with a distorted square antiprismatic geometry and occupy the inner coordination sites of the complex. The four chromium (III) ions were found to be

six-coordinate with a distorted octahedral geometry and occupy the outer coordination sites. Four μ_3 hydroxide ligands bridge the two dysprosium (III) ions to their closest chromium (III) ion, forming a triangular arrangement. Two μ_2 hydroxide ligands and two μ_2 benzoate ligands, bridging through a single oxygen donor each, then bridge between the dysprosium (III) ions to form the square dysprosium tetramer core. Each chromium (III) ion is further ligated by a fully deprotonated **HMAP**$^{2-}$ ligand, of Harris Notation 3.2.2.1, and two benzoate ligands completing the six-coordinate octahedral environment. The N-atom of the **HMAP**$^{2-}$ ligand chelates to the chromium (III) ion with the two deprotonated alkoxide arms bridging from the chromium (III) ion to the proximal core dysprosium (III) ions. The chromium (III) ions do not reside within the plane of the core dysprosium tetramer, instead occupying alternating sites above and below the tetramer plane, moving around the complex. The eight remaining carboxylate ligands each bridge from a chromium (III) ion to a dysprosium (III) ion in a μ_2 manner. The coordinate sphere of each dysprosium (III) ion is completed without further capping ligands. A simplified skeletal form is given in **Figure 113**.

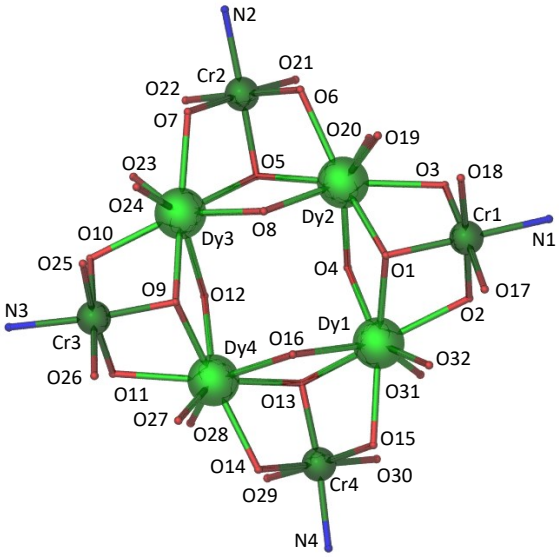

Figure 113- Skeletal forms of the complex **C19**: O atoms, red; N atoms, blue; Dy atoms, large green; Cr atoms, small green. H and C atoms have been omitted for clarity.

Crystal packing diagrams of **C19** can be found in **Figure 114**. Intermolecular interactions are dominated by aromatic π, and C-H interactions derived from the benzoate ligands.

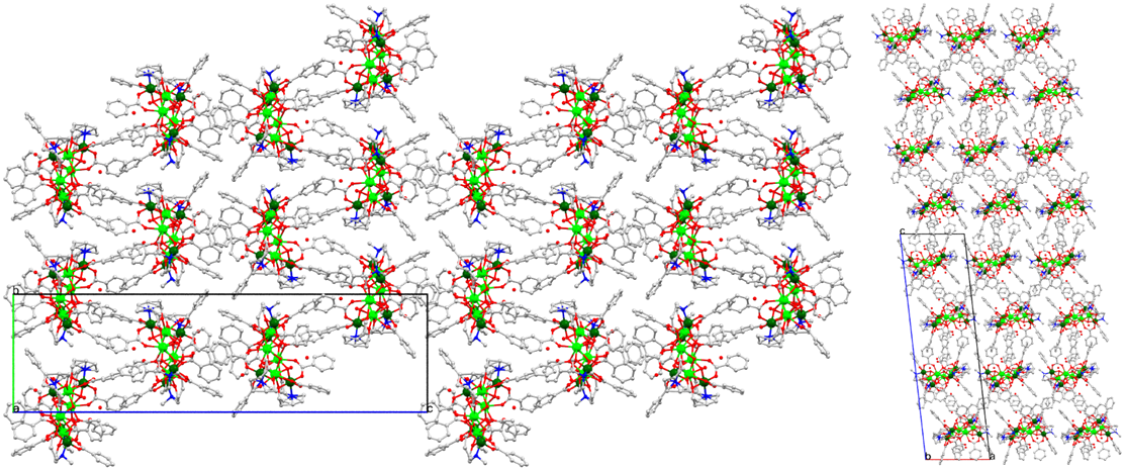

Figure 114- Crystal packing diagram of **C19** viewing the bc plane, left, and the ac plane, right. Unit cell included as a reference. C atoms, grey; O atoms, red; N atoms, blue; Dy atoms, large green; Cr atoms, small green. H atoms have been omitted for clarity.

The average Cr-$L_{N,O}$ bond length is found to be 1.92 Å with bond length ranging from 1.869-2.004 Å. The average Dy-O bond length is found to be 2.36 Å with bond lengths ranging from 2.250-2.442 Å. Selected bond lengths, inter-metal distances and bond angles are given below in **Table 30**, **Table 31** and **Table 32**, respectively.

Table 30- Selected bond lengths for complex **C19**.

Atoms	Bond Length (Å)	Atoms	Bond Length (Å)
Cr1-O1	1.915	Dy1-O15	2.358
Cr1-O3	1.894	Dy1-O13	2.375
Cr1-O18	1.928	Dy1-O16	2.417
Cr1-N1	1.979	Dy1-O4	2.268
Cr1-O17	1.917	Dy2-O1	2.409
Cr1-O2	1.894	Dy2-O4	2.250
Cr2-O5	1.928	Dy2-O8	2.285
Cr2-O7	1.892	Dy2-O5	2.402
Cr2-O22	1.895	Dy2-O6	2.361
Cr2-N2	2.004	Dy2-O20	2.400
Cr2-O21	1.924	Dy2-O19	2.405
Cr2-O6	1.892	Dy2-O2	2.359
Cr3-O9	1.927	Dy3-O5	2.374
Cr3-O11	1.904	Dy3-O8	2.263
Cr3-O26	1.913	Dy3-O12	2.428
Cr3-N3	1.991	Dy3-O9	2.406
Cr3-O25	1.935	Dy3-O10	2.331
Cr3-O10	1.869	Dy3-O24	2.384
Cr4-O13	1.919	Dy3-O23	2.381
Cr4-O15	1.896	Dy3-O7	2.358
Cr4-O30	1.904	Dy4-O9	2.334
Cr4-N4	1.966	Dy4-O12	2.442
Cr4-O29	1.920	Dy4-O16	2.416
Cr4-O14	1.879	Dy4-O13	2.353
Dy1-O1	2.383	Dy4-O14	2.310
Dy1-O2	2.349	Dy4-O28	2.376
Dy1-O32	2.354	Dy4-O27	2.375
Dy1-O31	2.391	Dy4-O11	2.336

-

Table 31- Selected inter-metal distances for complex **C19**.

Atoms	Distance (Å)	Atoms	Distance (Å)
Cr1-Dy1	3.345	Cr1-Cr4	6.667
Cr1-Dy2	3.362	Cr2-Cr3	6.684
Cr2-Dy2	3.350	Cr2-Cr4	8.754
Cr2-Dy3	3.351	Cr3-Cr4	6.625
Cr3-Dy3	3.367	Dy1-Dy2	3.810
Cr3-Dy4	3.326	Dy1-Dy3	5.479
Cr4-Dy4	3.327	Dy1-Dy4	3.916
Cr4-Dy1	3.366	Dy2-Dy3	3.827
Cr1-Cr2	6.648	Dy2-Dy4	5.470
Cr1-Cr3	8.811	Dy3-Dy4	3.935

Table 32- Selected bond angles for complex **C19**.

Atoms	Bond Angle (°)	Atoms	Bond Angle (°)
Cr1-O1-Dy1	101.65	Cr3-O9-Dy3	101.41
Cr1-O1-Dy2	101.47	Cr3-O9-Dy4	102.21
Cr1- O2-Dy1	103.55	Cr3-O10-Dy3	106.06
Cr1-O3-Dy2	103.93	Cr3-O11-Dy4	102.86
Dy1-O1-Dy2	105.35	Dy3-O9-Dy4	112.22
Dy1-O4-Dy2	114.99	Dy3-O12-Dy4	107.78
Cr2-O5-Dy2	100.77	Cr4-O13-Dy4	101.80
Cr2-O5-Dy3	101.82	Cr4-O13-Dy1	102.67
Cr2- O6-Dy2	103.35	Cr4-O14-Dy4	104.66
Cr2-O7-Dy3	103.57	Cr4-O15-Dy1	104.03
Dy2-O5-Dy3	106.49	Dy4-O13-Dy1	111.81
Dy2-O8-Dy3	114.59	Dy4-O16-Dy1	108.22

The reaction [**HPhAP**]H_2 with chromium (III) chloride hexahydrate, dysprosium (III) nitrate pentahydrate, o-toluic acid and triethylamine in acetonitrile produced a green mother liquor from which dark green crystals of $[Cr^{III}Dy^{III}_6(OH)_8(o\text{-}Tol)_{13}(DMF)_3(MeOH)_2]$, **C20**, were grown by layer diffusion from a methanol:dimethyl formamide (1:4) solvent system. Complex **C20** failed to coordinate the asymmetric amine polyalcohol used in this reaction, likely the result of the low solubility of [**HPhAP**]H_2 in the reaction solvent mix. Complex **C20** crystallises in the triclinic space group *P-1*, with the asymmetric unit containing half of the molecule. The unit cell of **C20** has a volume of 3380 $Å^3$ containing one molecule per unit cell and exhibiting the unit cell parameters: a = 15.49940(10) Å, b = 15.67110(10) Å, c = 17.09800(10) Å, α = 106.2720(10)°, β = 102.2070(10)°, γ = 114.0440(10)° (See **Appendix B**, **Table S4**).

Complex **C20** is a heterometallic {3d-4f} heptanuclear complex with the metallic core displaying an hourglass-like topology, as shown in **Figure 115**.

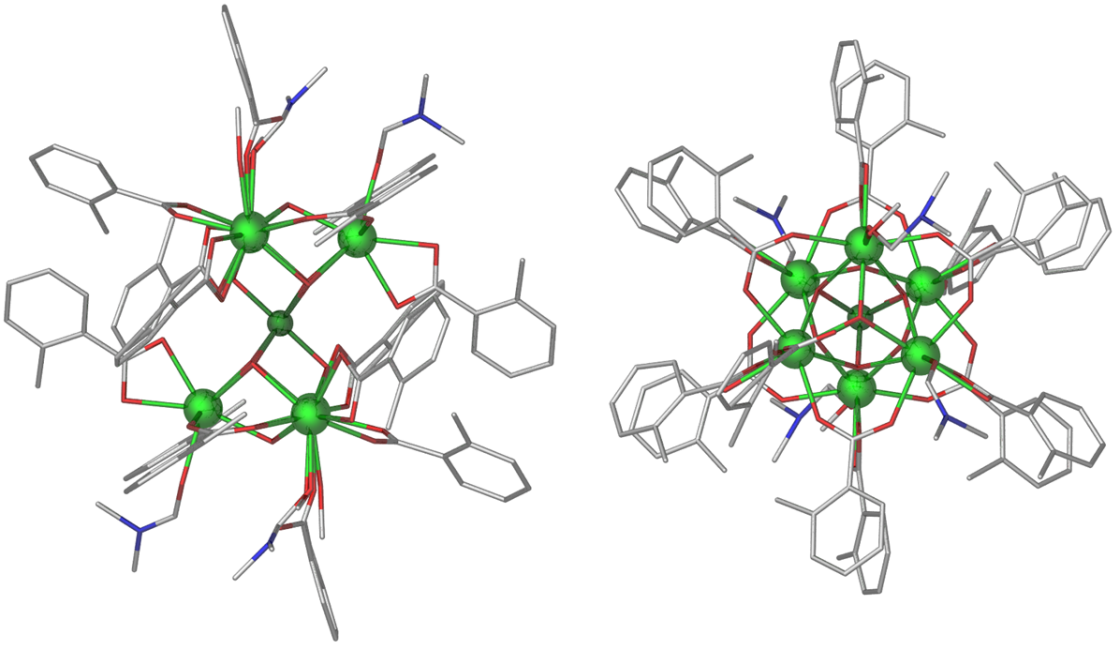

Figure 115- Molecular structure of **C20**, front view (left) and plan view (right): C atoms, grey; O atoms, red; N atoms, blue; Dy atoms, large green; Cr atoms, small green. H atoms have been omitted for clarity.

The asymmetric unit contains half the complex – thereby three dysprosium ions all in the 3+ oxidation state and a half occupancy chromium ion of the same oxidation state which lies upon an inversion centre. The six dysprosium (III) ions are divided into two

planar triangular disks, with an intercalating chromium (III) ion acting as the crux of the molecule. The dysprosium (III) ions were found to be eight-coordinate with distorted square antiprismatic geometries. The chromium (III) ion was found to be six-coordinate with a distorted octahedral geometry at the core of the complex. Six μ_3 hydroxide ligands complete the coordination environment of the chromium (III) ion with each bridging to a unique pair of adjacent dysprosium (III) ions within a disk. Two final μ_3 hydroxide ligands bridge the three dysprosium (III) ions within a disk together, one per disk. Adjacent dysprosium ions are also bridged by one μ_2 o-toluate ligand per triangular edge. Each dysprosium (III) ion is then further ligated by a terminal o-toluate ligand and one capping ligand per centre. The capping species present were concluded to be three DMF ligands, two water ligands and one non-chelating o-toluate ligand binding through a single oxygen donor atom, when partial occupancies were accounted for. A simplified skeletal form is given in **Figure 116**.

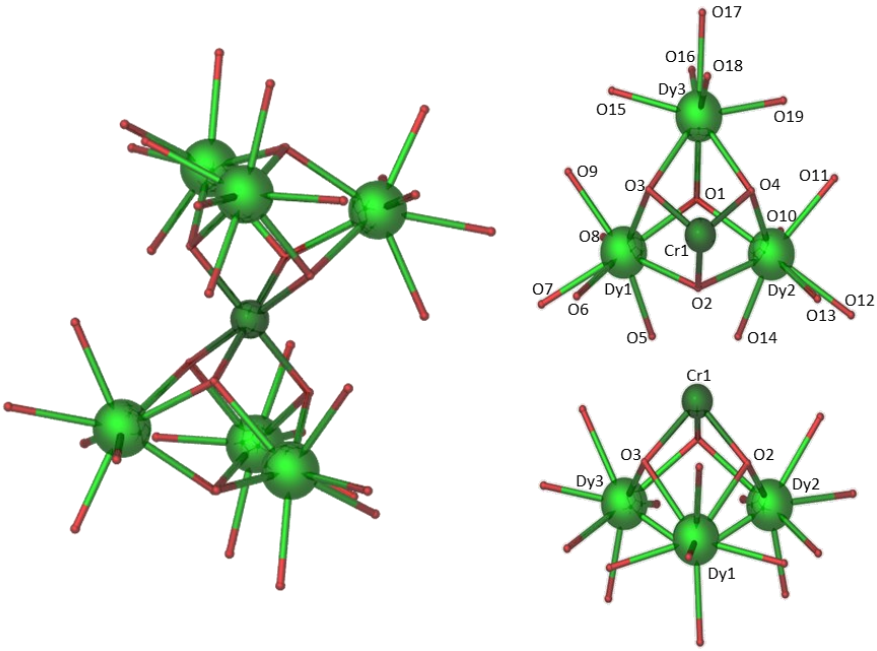

Figure 116- Skeletal forms of the complex (left) and asymmetric unit (right) of **C20**: O atoms, red; N atoms, blue; Dy atoms, large green; Cr atoms, small green. H and C atoms have been omitted for clarity.

Crystal packing diagrams of **C20** can be found in **Figure 117**. Intermolecular interactions are dominated by aromatic π, and C-H interactions derived from the o-toluate ligands.

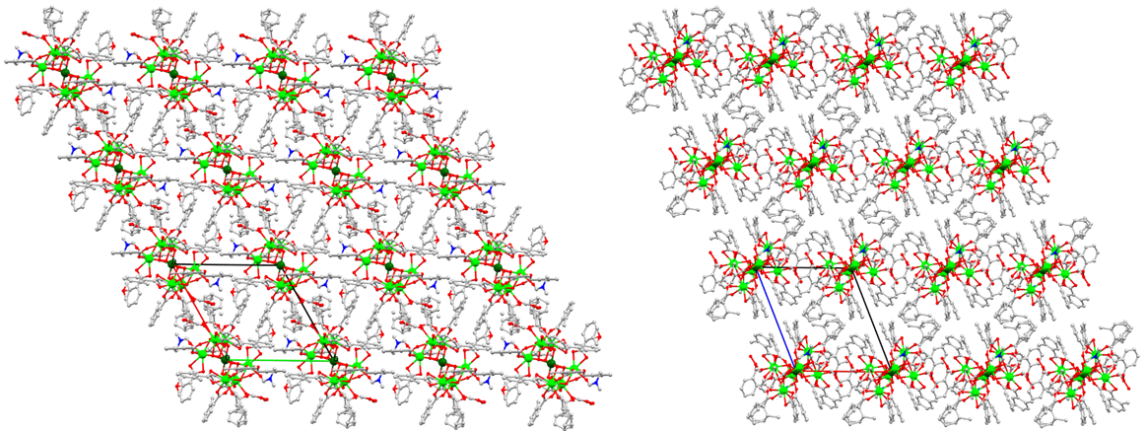

Figure 117- Crystal packing diagram of **C20** viewing the ab plane, left, and ac plane, right. Unit cell included for reference. C atoms, grey; O atoms, red; N atoms, blue; Dy atoms, large green; Cr atoms, small green. H atoms have been omitted for clarity.

The average Cr-O bond length is found to be 1.97 Å with bond length ranging from 1.958-1.976 Å. The average Dy-O bond length is found to be 2.37 Å with bond lengths ranging from 2.268-2.476 Å. Selected bond lengths and bond angles are given below in **Table 33** and **Table 34**, respectively.

Table 33- Selected bond lengths for the asymmetric unit of complex **C20**.

Atoms	Bond Length (Å)	Atoms	Bond Length (Å)
Cr1-O2	1.976	Dy2-O14	2.306
Cr1-O3	1.958	Dy2-O2	2.428
Cr1-O4	1.964	Dy3-O1	2.343
Dy1-O1	2.329	Dy3-O3	2.396
Dy1-O2	2.428	Dy3-O15	2.313
Dy1-O5	2.324	Dy3-O16	2.268
Dy1-O6	2.420	Dy3-O17	2.412
Dy1-O7	2.418	Dy3-O18	2.392
Dy1-O8	2.369	Dy3-O19	2.285
Dy1-O9	2.320	Dy3-O4	2.414
Dy1-O3	2.400	Cr1-Dy1	3.476
Dy2-O1	2.360	Cr1-Dy2	3.461
Dy2-O4	2.390	Cr1-Dy3	3.448
Dy2-O10	2.297	Dy1-Dy2	3.788
Dy2-O11	2.367	Dy1-Dy3	3.729
Dy2-O12	2.476	Dy2-Dy3	3.740
Dy2-O12	2.388		

Table 34- Selected bond angles for the asymmetric unit of complex **C20**.

Atoms	Bond Angle (°)	Atoms	Bond Angle (°)
Cr1-O2-Dy1	103.75	Dy1-O1-Dy2	107.77
Cr1-O2-Dy2	103.11	Dy1-O1-Dy3	105.92
Cr1-O3-Dy1	105.33	Dy1-O2-Dy2	102.52
Cr1-O3-Dy3	104.65	Dy1-O3-Dy3	102.37
Cr1-O4-Dy2	104.90	Dy2-O1-Dy3	105.40
Cr1-O4-Dy3	103.47	Dy2-O4-Dy3	102.27

The bonding structures exhibited in the above work display similar characteristics to those observed in previous literature. Some broad similarities in motif are discussed below in relation to: diethanolamine, (**DEA**)H_2, and triethanolamine, (**TEA**)H_3.

Prior literature demonstrates the extensive use of the aforementioned ligands. These uses generate structures of varying topologies from disk to saddles, and rings to icosanuclear clusters, however most importantly for this chapter they can produce the butterfly motif.[222-238] (**TEA**)H_3, (**DEA**)H_2, and their N-substituted variants *i.e.* (**MDEA**)H_2, (**EDEA**)H_2 *etc.* are near ubiquitous in molecular magnets of the butterfly motif. This work utilised asymmetric variants of these archetypical amine polyalcohols. In doing so only minor structural variations were found in early compounds, **C15** and **C16**. These small changes have the ability to greatly influence the super exchange of the metallic core. Later structures exhibited more extreme variation, such as the breaking of the TM_2-Ln_2 planarity to a more concave core built around a μ_4-oxide ion, as seen for **C17** and **C18**. It is hypothesised however, that a larger asymmetrical skew would be required to engender more distinct structural changes.

Complex **C19** exhibits the square-in-square topology with a typical TM_4-Ln_4 metallic core. Structures are known utilising the amine polyalcohols: (**TEA**)H_3, (**MDEA**)H_2 and (**^{t}BuDEA**)H_2.[115, 239, 240] Comparatively structure **C19** replaces the symmetric polyalcohols with an asymmetric polyalcohol seamlessly without causing significant distortion to the metallic core.

Compound **C20** in the absence of sufficient amine polyalcohol ligand in reaction solution instead formed as a toroid complex. Toroids typically consist of one or more homometallic disks whose spin vectors align in the direction of the disk rather than up or down, as such the spins align clockwise or anti-clockwise around the disk.[241-244] This system is known and of current research interest but divert significantly from the butterfly motif.

4.2.2 Magnetic Susceptibility Studies

This section discusses the magnetic data collected for three crystal samples: **C15**, **C16** and **C17**:

C15- $[Cr^{III}_2Dy^{III}_2(OMe)_2(Benz)_4(HMAP)_2(NO_3)_2]$

C16- $[Cr^{III}_2Dy^{III}_2(OMe)_2(Benz)_4(HEAP)_2(NO_3)_2]$

C17- $[Mn^{III}_2Dy^{III}_2(O)(Benz)_6(HMAP)_2]_n$

Direct current (dc) magnetic susceptibility analysis was undertaken on polycrystalline samples of complexes **C15-17**. Initial analysis was completed over the temperature range 2-300 K in a dc field of 0.1 T. The resultant $\chi_M T$ vs. T plots can be found in **Figure 118**.

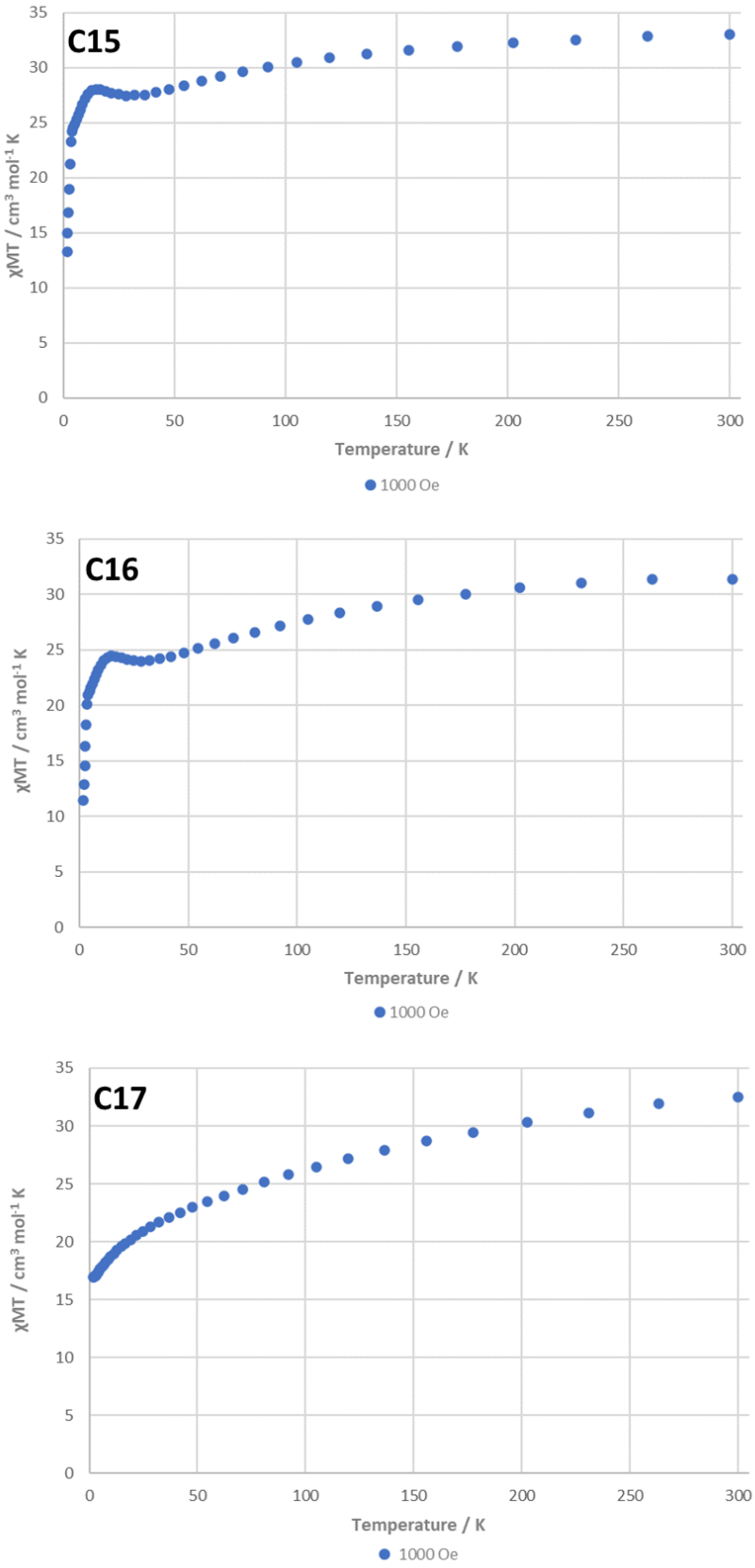

Figure 118- Plots of $\chi_M T$ vs T for samples **C15**, **C16**, **C17** measured under a 1000 Oe (0.1 T) applied magnetic field.

Extracted from the data collected are values of the molar magnetic susceptibility times temperature, $\chi_M T$, of 33.06 and 31.38 cm^3 K mol^{-1} for the $\{Cr^{III}_2Dy^{III}_2\}$ complexes **C15** and **C16** respectively at 300 K. These values broadly correlate with the calculated values for two Dy^{III} (S = 5/2, L = 5, J = 15/2, $^6H_{15/2}$, g_J = 4/3, C = 14.17 cm^3 K mol^{-1}) and two Cr^{III} (S = 3/2, g = 2, C = 1.88 cm^3 K mol^{-1}) non-interacting centres ((2 × 14.17) + (2 × 1.88) = 32.1 cm^3 K mol^{-1}). Values of C are calculated using equations 2, 5 and 9 found in **Chapter 1**. Similarly, the experimental value of $\chi_M T$ for the $\{Mn^{III}_2Dy^{III}_2\}$ complex **C17**, 32.53 at 300 K, correlates strongly with the calculated values for two Dy^{III} (As previous) and two Mn^{III} (S = 2, g = 1.9, C = 2.71 cm^3 K mol^{-1}) non-interacting centres ((2 × 14.17) + (2 × 2.71) = 33.76 cm^3 K mol^{-1}).

The profiles of the $\chi_M T$ vs. T plots for the three complexes are indicative of variations in the magnetic exchange interactions. As shown by the experiments at 0.1 T, the two near-isostructural $\{Cr^{III}_2Dy^{III}_2\}$ complexes, **C15** and **C16**, exhibit a line shape where, as the temperature decreases the $\chi_M T$ product also decreases until reaching about 30 K. At 30 K an upward turn is observed as ferromagnetic interactions begin to dominate. The upturn indicates significant magnetic exchange interactions with a peak observed at 15 K, beyond which the $\chi_M T$ product falls off swiftly down to the lowest temperature recorded as the magnetic susceptibility product collapses, reaching 8.077 and 11.421 cm^3 K mol^{-1}, respectively. This shouldering is indicative of a ferrimagnetic coupling interaction occurring between metal centres. Conversely, the $\{Mn^{III}_2Dy^{III}_2\}_n$ chain complex, **C17**, exhibits no such shoulder, exhibiting a curve of decreasing gradient as the temperature increases. The decrease is likely due to the gradual depopulation of the excited m_J magnetic states of Dy(III) ions as the temperature is decreased. At the lowest temperatures the magnetic exchange becomes the dominant factor. As observed for **C17,** a continual decrease would suggest a small magnetic ground state and dominant antiferromagnetic exchange behaviour.

The isothermal magnetisation, M, plotted as a function of the magnetic field, H, was collected over three incremental steps within the temperature range of 2-6 K for each of the novel samples. These plots are shown in **Figure 119**. The $\{Mn^{III}_2Dy^{III}_2\}_n$ sample, **C17**, displays a rapid increase in magnetisation up to 2 T, before reaching a steady, near-linear increase without attaining saturation. In combination with the field dependency demonstrated by the magnetic susceptibility plots, this would suggest the samples

exhibit a significant magnetic anisotropy. Successive increases in the temperature at which the experiments were run prove to increase the overall linearity of the line shape. Both of the $\{Cr^{III}_2Dy^{III}_2\}$ samples also display a rapid increase in magnetisation up to 2 T, before reaching a steady, near-linear increase without reaching saturation at 4 K and 6 K. However, the 2 K plot shows a significantly different shape, with steady increase between 0-2 T before a sharper increase in magnetisation between 2-4 T, which then once again reaches a near linear increase after 5 T, without attaining saturation. This distinctive s-shaped profile, present in both **C15** and **C16**, would suggest the samples encounter a blocking artefact below 2 K that is lost by 4 K, which is indicative of possible slow magnetic relaxation.

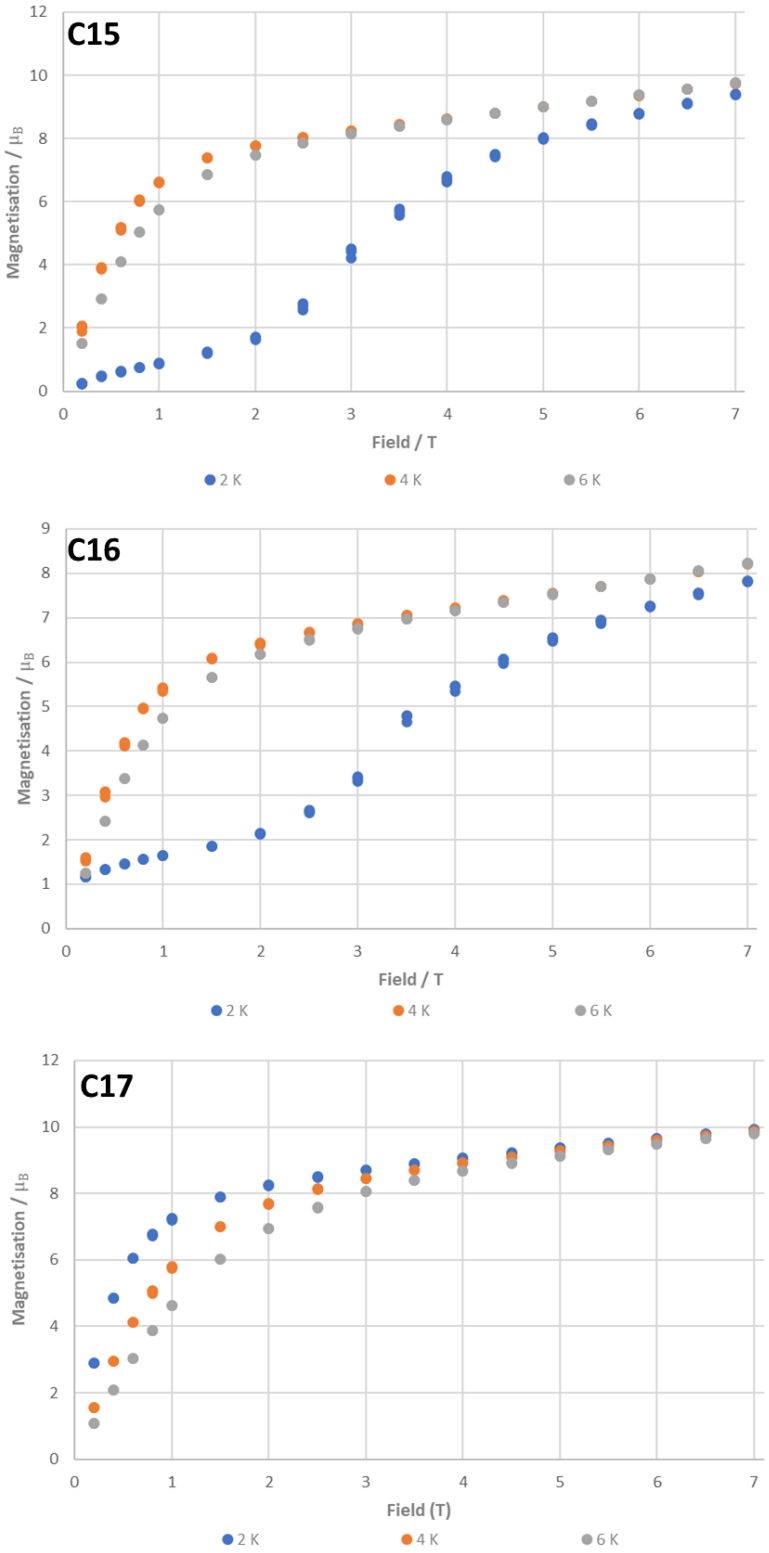

Figure 119- Plots of M vs H for samples **C15**, **C16**, **C17**, taken in 2 K increments between 2-6 K.

As a result of the distinct line shape observed, further variable field magnetisation measurements were performed to probe the relaxation time over a longer time scale,

which would reveal the presence of magnetic hysteresis. Using sweep rates of an average 0.001 T s^{-1} on a polycrystalline sample of **C15**, magnetic hysteresis was observed at increments of 0.5 K from 2 K up to 3.5 K whilst at 4 K the hysteresis loop was shown to collapse, as shown in **Figure 120**. The hysteretic behaviour observed between 2.0 and 3.5 K indicates a loss of magnetisation at zero field, as a result of some QTM, but the loop maintains a large coercive field regardless, of approximately 2.5 T at 2.0 K. As the temperature increases the coercive field depletes, as expected for an SMM.

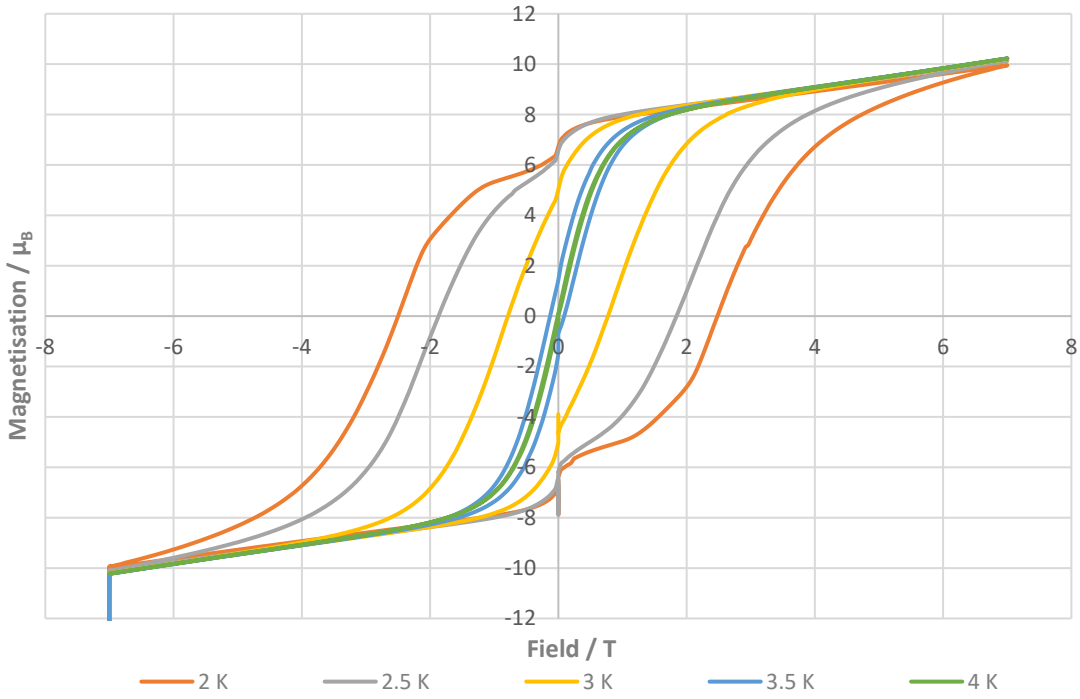

Figure 120- Hysteresis measurements of sample **C15**, taken in 0.5 K increments between 2-4 K.

Similarly, sample **C16** also exhibits this behaviour, as shown in **Figure 121**, but with a smaller step at zero field as a result of QTM and a coercive field of 2.78 T at 2.0 K, or 2.98 T at 1.8 K. This coercive field is slightly larger than that for the previously published complex $[Cr^{III}_2Dy^{III}_2(OMe)_2(Benz)_4(MDEA)_2(NO_3)_2]$, of approximately 2.8 T at 1.8 K.

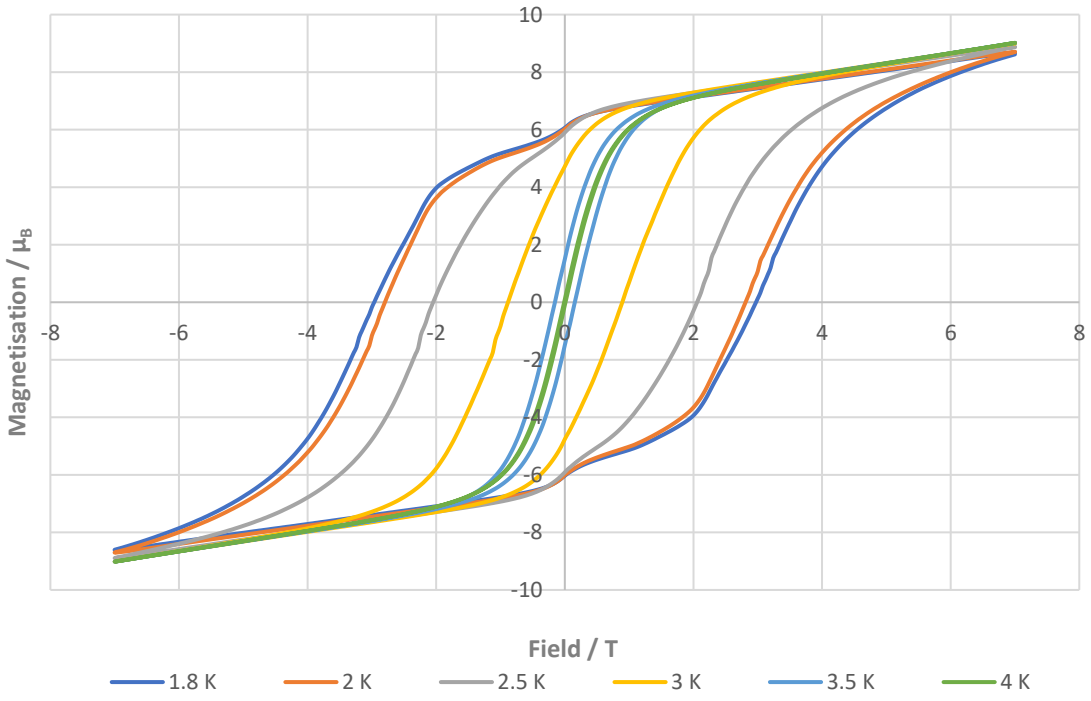

Figure 121- Hysteresis measurements of sample **C16**, taken between 1.8-4 K.

In order to further probe for slow magnetic relaxation within the $\{Cr^{III}_2Dy^{III}_2\}$ complexes additional experiments were performed to ascertain alternating current (ac) susceptibility measurements. These experiments were performed in an oscillating ac field of 3.5 Oe under a zero applied dc field. This resulted in two types of plot, the out-of-phase molar magnetic susceptibility, χ''_M, plotted against either variable temperature or variable frequency. These measurements revealed clear frequency and temperature dependant maxima (1.8-5 K) in the out-of-phase component for samples **C15** and **C16**. These maxima are indicative of SMM behaviour. Plots of χ''_M vs frequency and χ'_M vs frequency for samples **C15** and **C16** can be found in **Figure 122**.

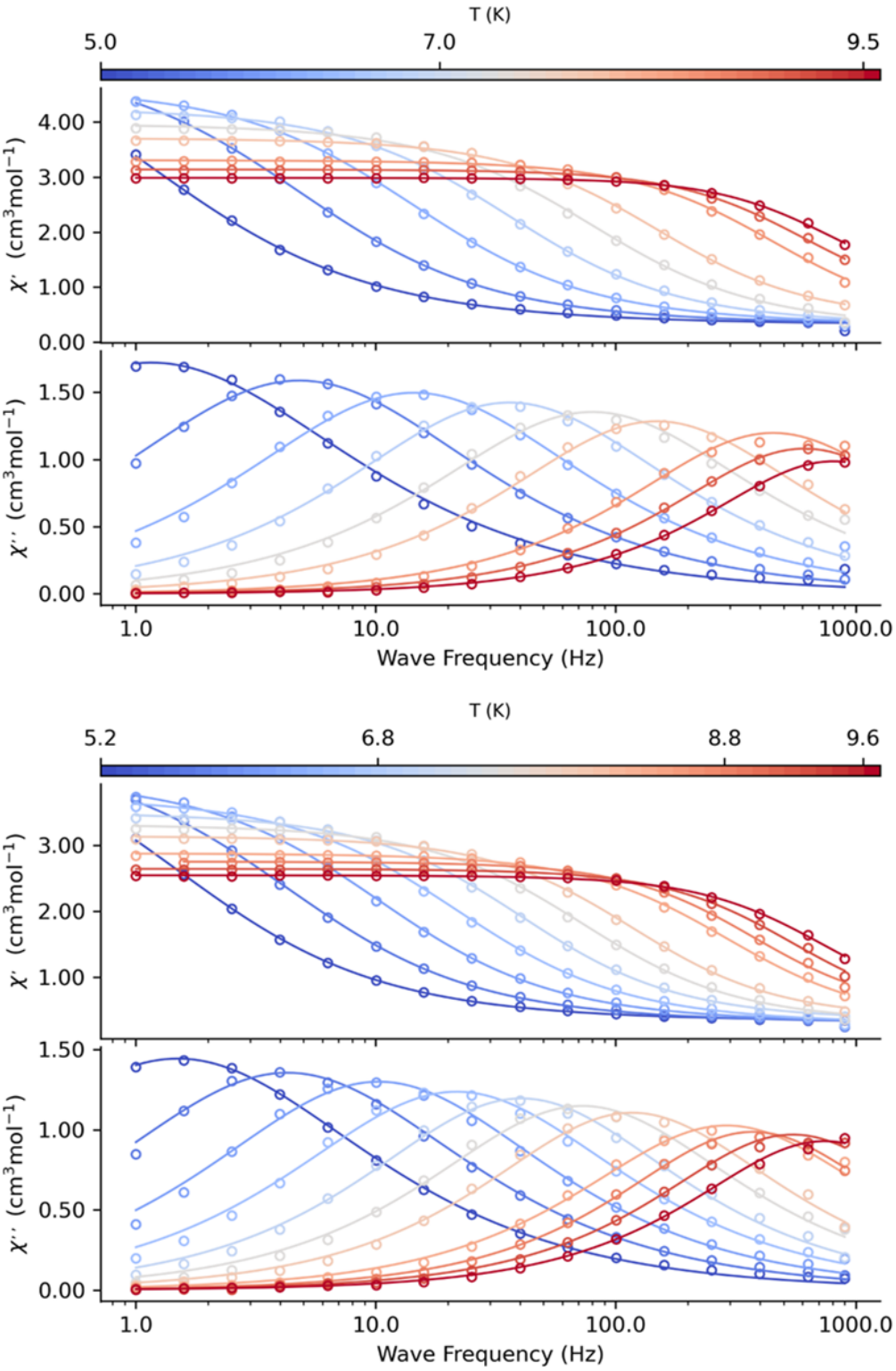

Figure 122- Plots of χ' vs Frequency and χ'' vs Frequency for samples **C15**, top; and **C16**, bottom.

Cole-Cole plots for said samples communicate semicircular profiles, as seen in **Figure 123**, these are suggestive of complexes undergoing a single relaxation process.

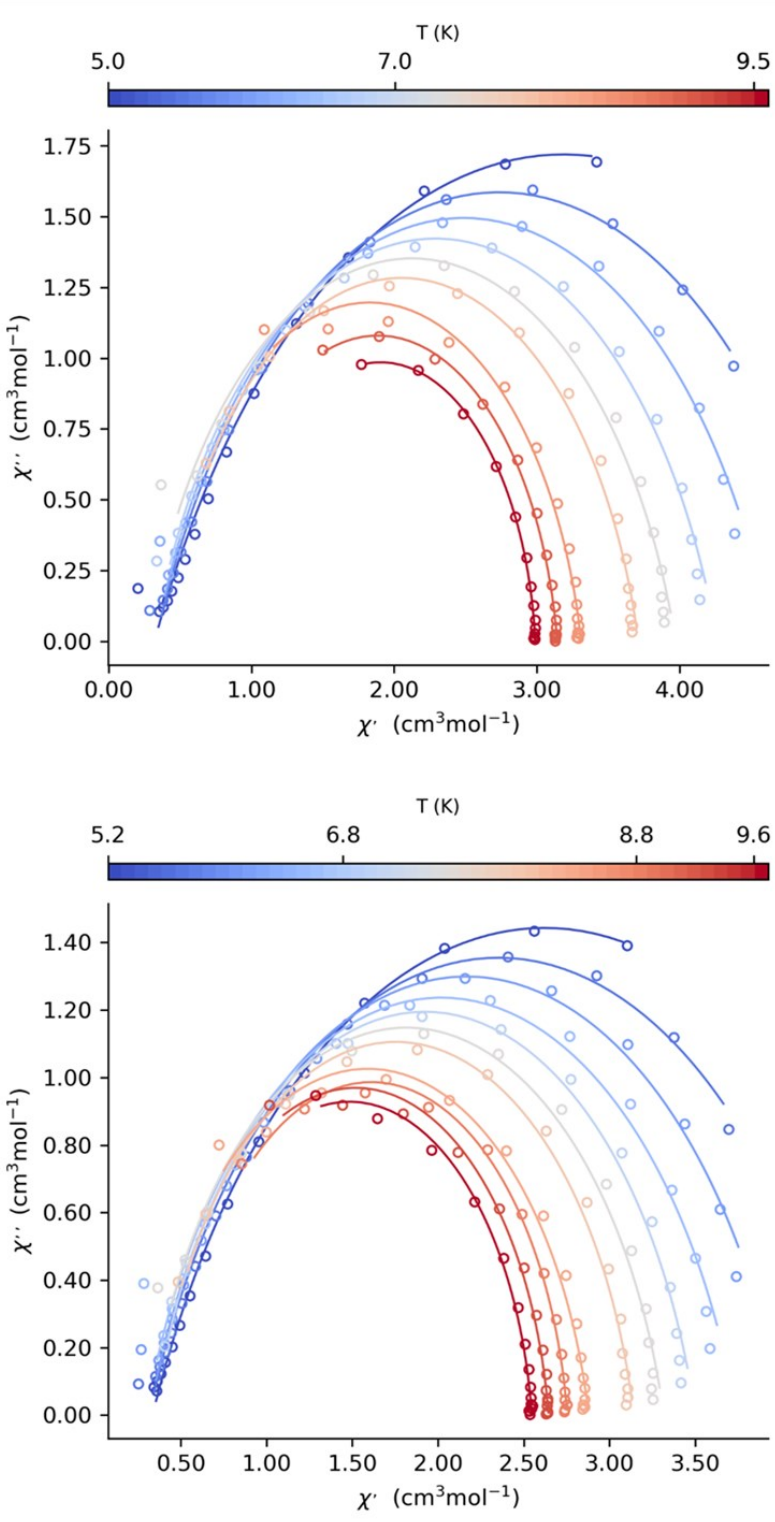

Figure 123- Cole-Cole plots of χ'' vs χ' for samples **C15**, top; and **C16**, bottom.

Initial analysis of argand plots, τ^{-1} vs T, for samples **C15** and **C16** produced fits, *via* CC-FIT[245] from which values of U_{eff} and τ_0, were extracted, as follows: **C15**, U_{eff} = 70 (10) K, $\tau_0 = 10^{-6.8(6)}$s; **C16**, U_{eff} = 70 (10) K, $\tau_0 = 10^{-6.8(6)}$s. These argand plots can be found in **Appendix F**. The results indicate that the slight structural variance between the samples

has minimal effect on the relaxation pathway or energy barrier, beyond the previously discussed variation in coercive field.

Complexes **C15** and **C16** are directly isostructural to the $\{Cr^{III}_2Dy^{III}_2\}$ complex proposed by Langley and Murray *et al*., in 2013,[131] other than the replacement of [**MDEA**]$^{2-}$ with [**HMAP**]$^{-2}$ and [**HEAP**]$^{-2}$ respectively. It would be remiss to not compare the magnetic properties of these three structures in the understanding that any variation in the magnetic properties of the complex is likely the result of the changes to the structural motif. The Murray group $\{Cr^{III}_2Dy^{III}_2\}$ complex exhibits a faster relaxation time and a higher barrier to magnetisation reversal than either **C15** or **C16**. The hysteresis loop of all three structures collapses between 3.5 K and 4 K. However, the coercive field of **C16** outstrips the Murray group complex and **C15** with coercive field values of 2.98 T, 2.7 T and 2.5 T (at a higher temperature at 2 K rather than 1.8 K) respectively. Furthermore, it is hypothesized that the reduction in coercive field exhibited by the Murray group complex is a result of the zero-field step observed in the magnetic hysteresis loop. Such steps are indicative of a loss of magnetisation as a result of QTM. Although, the percentage of magnetisation lost cannot be greater than 30% for the Murray complex, no step of such extent is observed in the hysteresis loop of **C16** which only loses approximately 15% total magnetisation as a result of what is assumed to be a stronger 3d-4f coupling. Values of magnetisation loss were extrapolated by geometric analysis of the hysteresis plots provided. As a result of this analysis, we can say that the structural variance observed has a significant effect on the magnetic properties of the isostructural $\{Cr^{III}_2Dy^{III}_2\}$ core. According to the data available here, we can say that the introduced asymmetry has a slight weakening effect on all four parameters discussed, however upon exchange of the methyl R group for an ethyl R group, the resulting increase in inductive effect seemingly counteracts and exceeds this penalty in terms of the resultant coercive field. To draw further conclusions from this dataset would require the synthesis and analysis of an [**EDEA**]$^{2-}$ isostructural analogue.

4.3 Chapter Summary

In this chapter the syntheses and analyses of six {3d-4f} complexes have been described, including four discrete asymmetric amine polyalcohol ligand containing complexes, **C15, C16**, **C18** and **C19**, and one chain asymmetric amine polyalcohol ligand containing complex, **C17**, alongside one toroidal {3d-4f} complex that does not contain any amine polyalcohol ligand, **C20**. Structural data was collected for all the samples **C15**-**C20**, of which five are thought to be novel at the time of research. Magnetic analysis was undertaken on three samples, **C15**, **C16** and **C17**, with dc data collected for all three samples, and ac data provided for the $[Cr^{III}_2Dy^{III}_2]$ samples **C15** and **C16**. This analysis concluded in the production of hysteresis loops for samples **C15** and **C16**, with strong coercive fields of 2.5 T at 2 K and 2.98 T at 1.8 K, respectively. These values are indicative of the expected strong exchange interactions between the transition metal and lanthanide centres which see a reduction in the QTM relaxation pathway at low temperatures.

4.4 Experimental Methods

All information relating to the sourcing of chemicals, technical specification of instrumentation, data processing procedures and software can be found in the appendices. Pertinent to this chapter are **Appendix A**, **B** and **F** for synthetic procedures, single-crystal X-ray diffraction analysis and magnetism respectively.

4.4.0 General Synthetic Method

The subsequent synthetic method and stoichiometries were used in the following reactions, unless otherwise noted in the specific entry for each target molecule. In terms of this general method the transition metal nitrate hydrates, $TM(NO_3)_x{\cdot}yH_2O$, used within this chapter were chromium and manganese whilst the lanthanide metal nitrate hydrates, $Ln(NO_3)_3{\cdot}xH_2O$, used were dysprosium and gadolinium. The carboxylic acids used in the reaction series were benzoic acid, pivalic acid and o-toluic acid. No more than one transition metal, one lanthanide species and one carboxylic acid were involved in any one reaction.

In a small reaction vessel containing a stirrer bar, acetonitrile (20 mL) and methanol (5 mL) were dissolved $TM(NO_3)_x{\cdot}yH_2O$ (0.5 mmol), $Ln(NO_3)_3{\cdot}xH_2O$ (0.5 mmol), carboxylic acid (1 mmol) and [**DIPSO**]H_4 (0.5 mmol) respectively, ensuring each component was fully dissolved prior to addition of the next reagent. The solution was stirred continuously as the reaction was activated with triethylamine (2 mmol), dropwise over thirty seconds, and was then allowed to stir for a further two hours. Upon completion of the reaction, the solution was allowed to cool fully overnight, without stirring, and gravity filtered to remove any deposited solid material. The solvent was then removed by rotary evaporation to yield an oil prior to successive, portionwise crystallisation attempts.

4.4.1 $[Cr^{III}_2Dy^{III}_2(OMe)_2(Benz)_4(HMAP)_2(NO_3)_2]$, C15

$Cr(NO_3)_3{\cdot}9H_2O$ (200 mg, 0.5 mmol), $Dy(NO_3)_3{\cdot}5H_2O$ (219 mg, 0.5 mmol), benzoic acid (122 mg, 1 mmol) and [**HMAP**]H_2 (67 mg, 0.5 mmol) were added consecutively to a solvent mixture of methanol (5mL) and acetonitrile (20 mL). The solution was then heated to 40 °C and stirred continuously as the reaction was activated with triethylamine (0.28 mL, 2 mmol), dropwise over thirty seconds. The reaction was then allowed to stir for a further two hours. The resultant blue-grey solution was left overnight, and gravity filtered to remove any deposited solids. Single crystals of **C15** were grown over 4-7 days by layer diffusion using a MeOH:Et_2O (1:4) solvent system, yielding small purple plate crystals (20%). The title structure was confirmed by SC-XRD with a molecular formula: $C_{42}H_{52}Cr_2Dy_2N_4O_{20}$.

4.4.2 $[Cr^{III}_2Dy^{III}_2(OMe)_2(Benz)_4(HEAP)_2(NO_3)_2]$, C16

$Cr(NO_3)_3{\cdot}9H_2O$ (200 mg, 0.5 mmol), $Dy(NO_3)_3{\cdot}5H_2O$ (219 mg, 0.5 mmol), benzoic acid (122 mg, 1 mmol) and [**HEAP**]H_2 (74 mg, 0.5 mmol) were added consecutively to a solvent mixture of methanol (5mL) and acetonitrile (20 mL). The solution was then heated to 40 °C and stirred continuously as the reaction was activated with triethylamine (0.28 mL, 2 mmol), dropwise over thirty seconds. The reaction was then allowed to stir for a further two hours. The resultant pale blue solution was left

overnight, and gravity filtered to remove any deposited solids. Single crystals of **C16** were grown over 4-7 days by layer diffusion using a MeOH:Et_2O (1:4) solvent system, yielding small purple plate crystals (16%). The title structure was confirmed by SC-XRD with a molecular formula: $C_{44}H_{56}Cr_2Dy_2N_4O_{20}$.

4.4.3 $[Mn^{III}_2Dy^{III}_2(O)(Benz)_6(HMAP)_2]_n$, C17

$Mn(NO_3)_2{\cdot}4H_2O$ (126 mg, 0.5 mmol), $Dy(NO_3)_3{\cdot}5H_2O$ (219 mg, 0.5 mmol), benzoic acid (122 mg, 1 mmol) and [**HMAP**]H_2 (67 mg, 0.5 mmol) were added consecutively to a solvent mixture of methanol (5mL) and acetonitrile (20 mL). The solution was stirred continuously as the reaction was activated with triethylamine (0.28 mL, 2 mmol), dropwise over thirty seconds. The reaction was then allowed to stir for a further two hours. The resultant dark red solution was left overnight, and gravity filtered to remove any deposited solids. Single crystals of **C17** were grown over 1-3 days by slow deposition from the reaction solvent system, yielding fine red needle-like crystals (46%). The title structure was confirmed by SC-XRD with a molecular formula: $C_{54}H_{56}Dy_2Mn_2N_2O_{17}$.

4.4.4 $[Mn_2Gd^{III}_2(O)(Piv)_3(HEAP)_2(NO_3)_4]{\cdot}0.5MeOH{\cdot}H_2O$, C18

$Mn(NO_3)_2{\cdot}4H_2O$ (126 mg, 0.5 mmol), $Gd(NO_3)_3{\cdot}6H_2O$ (226 mg, 0.5 mmol), pivalic acid (102 mg, 1 mmol) and [**HEAP**]H_2 (74 mg, 0.5 mmol) were added consecutively to a solvent mixture of methanol (5mL) and acetonitrile (20 mL). The solution was stirred continuously as the reaction was activated with triethylamine (0.28 mL, 2 mmol), dropwise over thirty seconds. The reaction was then allowed to stir for a further two hours. The resultant red solution was left overnight, and gravity filtered to remove any deposited solids. Single crystals of **C18** were grown over 4-7 days by layer diffusion using a MeOH:Et_2O (2:3) solvent system, yielding small red-brown plate crystals (23%). The title structure was confirmed by SC-XRD with a molecular formula: $C_{29.5}H_{61}Gd_2Mn_2N_6O_{24.5}$.

4.4.5 $[Cr^{III}_4Dy^{III}_4(OH)_6(Benz)_{10}(HMAP)_4]\cdot 3H_2O$, C19

$CrCl_3\cdot 6H_2O$ (133 mg, 0.5 mmol), $Dy(NO_3)_3\cdot 5H_2O$ (219 mg, 0.5 mmol), benzoic acid (122 mg, 1 mmol) and [**HMAP**]H_2 (67 mg, 0.5 mmol) were added consecutively to a solvent mixture of methanol (5mL) and acetonitrile (20 mL). The solution was then heated to 40 °C and stirred continuously as the reaction was activated with triethylamine (0.28 mL, 2 mmol), dropwise over thirty seconds. The reaction was then allowed to stir for a further two hours. The resultant blue-green solution was left overnight, and gravity filtered to remove any deposited solids. Single crystals of **C19** were grown over 15-21 days by vapour diffusion using a MeOH:MeCN:Et_2O (1:4:15) solvent system, yielding small purple-green plate crystals (19%). The title structure was confirmed by SC-XRD with a molecular formula: $C_{94}H_{114}Cr_4Dy_4N_4O_{37}$.

4.4.6 $[Cr^{III}Dy^{III}_6(OH)_8(o\text{-}Tol)_{13}(DMF)_3(MeOH)_2]$, C20

$CrCl_3\cdot 6H_2O$ (27 mg, 0.1 mmol), $Dy(NO_3)_3\cdot 5H_2O$ (274 mg, 0.6 mmol), o-toluic acid (136 mg, 1 mmol) and [**HPhAP**] (98mg, 0.5 mmol) were dissolved consecutively in acetonitrile (10mL). The solution was then heated to 40 °C and stirred continuously as the reaction was activated with triethylamine (0.28 mL, 2 mmol), dropwise over thirty seconds. The reaction was then allowed to stir for a further four hours. The resultant green-purple solution was left overnight, and gravity filtered to remove any deposited solids. Single crystals of **C19** were grown over 2-4 weeks by layer diffusion followed by slow evaporation using a MeOH:DMF (4:1) solvent system, yielding small dark green crystals (21%). The title structure was confirmed by SC-XRD with a molecular formula: $C_{115}H_{128}CrDy_6N_3O_{39}$.

5 Synthesis of {4d-4f} Complexes with Amine Polyalcohol Ligands

5.1 Introduction

Magnetic exchange interactions are crucial to the quenching of quantum tunnelling that could improve the function of discrete SMMs. Current research themes broadly focus upon enhancing this crucial parameter, and thereby a species' inherent SMM properties. The magnetic exchange coupling can be enhanced by careful design parameters: considering the shape of the ion electron distribution in comparison to its ligand environment, the use of radical bridges or by the combination of specific metal ions within an array. Previous investigations into heteronuclear SMMs have focussed primarily in {3d-4f} heterometallic arrays and work reported by Powell *et al.*[181] has revealed the importance of the {3d-4f} magnetic exchange interactions in directing the nature of the SMM properties observed. Due to the diffuse nature of {4d} orbitals in second row transition metal ions a higher exchange is expected with lanthanide ions such as dysprosium (III) in {4d-4f} SMMs. Some pure {4d} homometallic complexes can exhibit extremely strong exchange interactions of up to J = -800.6 cm^{-1}, as shown by the Ru^{III} homometallic hexameric cluster described by Upadhyay and Shanmugam *et al.*[246] The very first {4d-4f} butterfly, $\{Ru_2^{III}Dy_2^{III}\}$, was reported by Langley *et al.* in 2015,[247] $[Ru^{III}_2Dy^{III}_2(OMe)_2(Benz)_4(MDEA)_2(NO_3)_2]$, **C21** in this thesis. However, the results it provided proved contrary to the hypothesised higher exchange expected from a {4d-4f} system in relation to an isostructural {3d-4f} analogue.

In this chapter, the work exhibited broadens the examples of known {4d-4f} molecular magnetic structures and attempts to identify and explain any differences in SMM behaviour, focussing on the role of the ruthenium (III) ions within the complexes. In furtherance of this we also present the crystal structure of a novel {5p-4f} system, **C30**.

5.2 Results and Discussion

This chapter describes the synthesis and characterisation of ten coordination {4d-4f} complexes utilising the ligands, symmetric and asymmetric, shown below in **Figure 124,** whose syntheses were described in **Chapter 3**. Additional bidentate ligands used to stabilise the complexes formed are also given in **Figure 125**. These ligands were chosen to indicate the effect of varied electron withdrawing character upon the magnetic properties of the total complex as indicated by Murugesu *et al*.[172]

This work also exhibits the variation in structure which can occur in the products of chemically similar serendipitous arrangement reactions. It expounds upon how the binding modes of the polyalcohol can vary significantly between, or within, molecules.

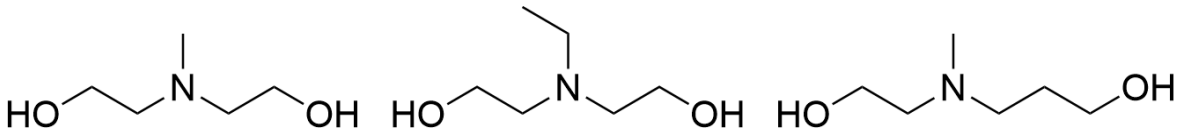

Figure 124- Symmetric and asymmetric ligands used in the synthesis described in chapter 5, N-methyldiethanolamine ([**MDEA**]H_2), N-ethyldiethanolamine ([**EDEA**]H_2), [(2-hydroxyethyl)(methyl)amino]propan-1-ol ([**HMAP**]H_2).

All the complexes produced, **C21**-**C30**, were initially produced in reactions using the same stoichiometric ratio (Ln : TM : Acid : Polyalcohol : Triethylamine, 2 : 2 : 4 : 2 : 8 respectively), prior to the synthesis being refined in an attempt to target specific, then known structures. Sample **C30**, substitutes a {5p} metal source in the place of the {4d} metal source utilised for the samples, **C21**-**C29**.

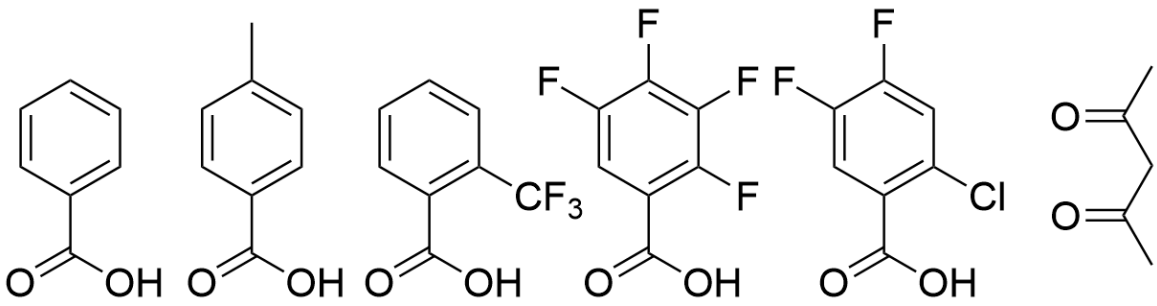

Figure 125- Bidentate ligands used in the synthesis described in chapter 5, from left to right: benzoic acid ([Benz]H), p-toluic acid ([p-Tol]H), 2-trifluoromethylbenzoic acid ([2-F_3C-Benz]H), 2,3,4,5-tetrafluorobenzoic acid ([2,3,4,5-tet-F-Benz]H), 2-chloro-4,5-difluorobenzoic acid ([2-Cl-4,5-F-Benz]H), acetylacetone ([Acac]H).

5.2.1 Structural Studies

Utilising the synthesised symmetric and asymmetric ligands described in **Chapter 3**, the work in this chapter focussed upon the investigation of the coordination chemistry exhibited by the tridentate ligands in {4d-4f} and {5p-4f} heterometallic complexes. Complexes **C21**-**C30** were all realised by simple aerobic reactions to form novel complexes in solution by serendipitous assembly. In the following section each sample is discussed in terms of parameters extracted from single crystal X-ray diffraction (SC-XRD) analysis alongside pertinent synthetic details.

The reaction of [**MDEA**]H_2 with ruthenium (III) chloride trihydrate, dysprosium (III) nitrate pentahydrate, benzoic acid and a suitable deprotonating agent (triethylamine) in acetonitrile produced a brown mother liquor from which yellow crystals of $[Ru^{III}_2Dy^{III}_2(OMe)_2(Benz)_4(MDEA)_2(NO_3)_2]$, **C21**, were grown by layer diffusion of a methanol:diethyl ether (1:3) solvent system. Complex **C21** crystallises in the monoclinic space group *P 2₁/n*, with the asymmetric unit containing half of the molecule. The unit cell of **C21** has a volume of 2380 $Å^3$ containing two molecules per unit cell and exhibiting the unit cell parameters: a = 8.0960(16) Å, b = 17.161(3) Å, c = 17.146(3) Å, α = 90°, β = 92.44(3)°, γ = 90° (See **Appendix B**, **Table S5**).

Complex **C21** is a heterometallic {4d-4f} tetranuclear complex with the metallic core displaying a planar butterfly-type topology, as shown in **Figure 126**.

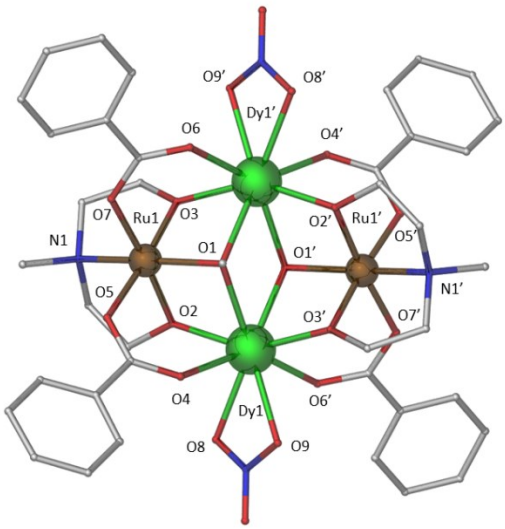

Figure 126- Molecular structure of **C21**: C atoms, grey; O atoms, red; N atoms, blue; Dy atoms, green; Ru atoms, brown. H atoms have been omitted for clarity.

The asymmetric unit consists of half of the complex – thereby one ruthenium and one dysprosium ion each in the 3+ oxidation state – with the remainder generated by inversion symmetry. The two dysprosium (III) ions were found to be eight-coordinate with a distorted square antiprismatic geometry and occupy the 'body' sites of the butterfly. The two ruthenium (III) ions were found to be six-coordinate with a distorted octahedral geometry and occupy the 'wing' sites of the butterfly. Two μ_3 methoxide ligands bridge the two dysprosium (III) ions to each ruthenium (III) ion. Each ruthenium (III) ion is further ligated by a fully deprotonated **MDEA**$^{2-}$ ligand, of Harris Notation

3.2.2.1, and two benzoate ligands completing the six-coordinate octahedral environment. The N-atom of the **MDEA**$^{2-}$ ligand chelates to the ruthenium (III) ion with the two deprotonated alkoxide arms bridging from the ruthenium (III) ion to the body dysprosium (III) ions. The four carboxylate ligands each bridge from a ruthenium (III) ion to a dysprosium (III) ion in a μ_2 manner. The coordinate sphere of each dysprosium (III) ion is completed by a capping nitrate ligand. Crystal packing diagrams of **C21** can be found in **Figure 127**. Intermolecular interactions are dominated by aromatic π, and C-H interactions derived from the benzoate ligands.

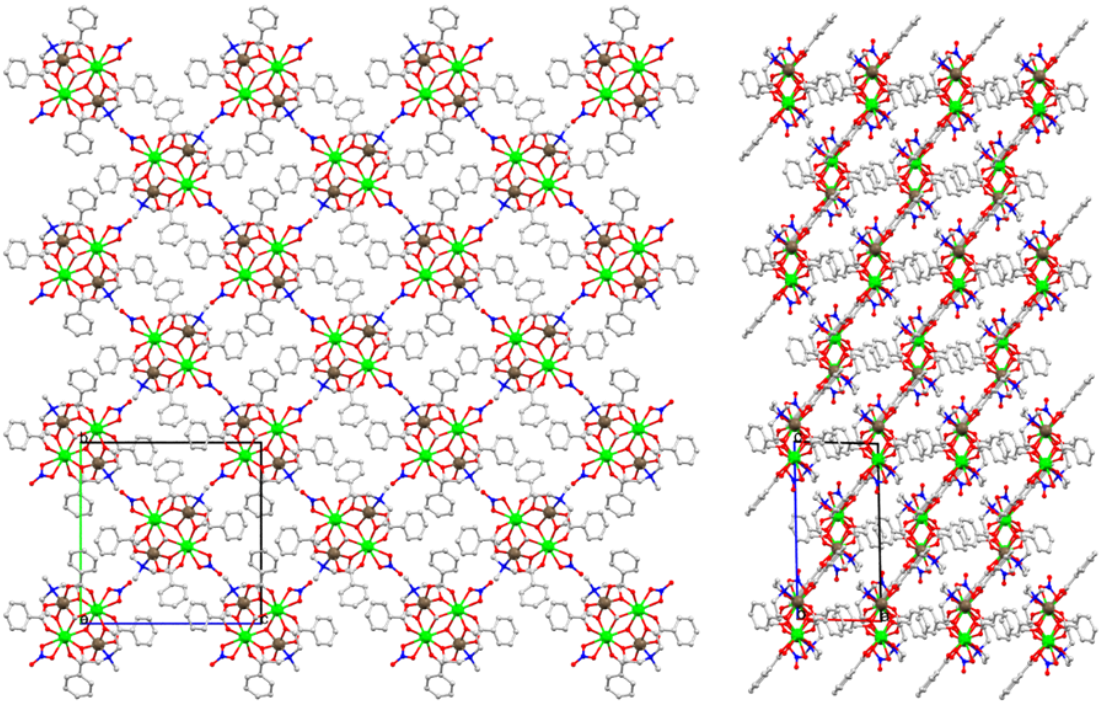

Figure 127- Crystal packing diagram of **C21** viewing the bc plane, left, and ac plane, right. Unit cell included for reference. C atoms, grey; O atoms, red; N atoms, blue; Dy atoms, green; Ru atoms, brown. H atoms have been omitted for clarity.

The average Ru-$L_{N,O}$ bond length is found to be 2.04 Å with bond length ranging from 1.977-2.120 Å. The average Dy-O bond length is found to be 2.36 Å with bond lengths ranging from 2.267-2.443 Å. Selected bond lengths and bond angles are given below in **Table 35**.

Table 35- Selected bond lengths and bond angles for complex **C21**.

Atoms	Bond Length (Å)	Atoms	Bond Angle (°)
Dy1-O1	2.389	Dy1-O1-Ru1	91.62
Dy1-O1’	2.392	Dy1-O1’-Ru1’	92.77
Dy1-O3’	2.269	Dy1-O2-Ru1	99.24
Dy1-O6’	2.350	Dy1-O3’-Ru1’	100.47
Dy1-O9	2.434	Dy1-O1-Dy1’	112.72
Dy1-O8	2.443		
Dy1-O4	2.353		
Dy1-O2	2.267		
Ru1-O1	2.102		
Ru1-O2	1.977		
Ru1-O5	2.052		
Ru1-N1	2.069		
Ru1-O7	2.050		
Ru1-O3	1.982		
Dy1-Dy1’	3.980		
Dy1-Ru1	3.239		
Dy1-Ru1’	3.273		
Ru1-Ru1’	5.153		

The reaction of [**MDEA**]H_2 with ruthenium (III) chloride trihydrate, dysprosium (III) nitrate pentahydrate, p-toluic acid and triethylamine in acetonitrile produced a brown mother liquor from which yellow crystals of $[Ru_2Dy_2(OMe)_2(p\text{-}Tol)_4(MDEA)_2(MeOH)_4]Cl_2$, **C22**, were grown by layer diffusion of a methanol:diethyl ether (1:3) solvent system. Complex **C22** crystallises in the hexagonal space group *P* -6 2c, with the asymmetric unit containing half of the molecule. The unit cell of **C22** has a volume of 10413 $Å^3$ containing six molecules per unit cell and exhibiting the unit cell parameters: a = 20.986(3) Å, b = 20.986(3) Å, c = 27.302(6) Å, α = 90°, β = 90°, γ = 120° (See **Appendix B**, **Table S5**).

Complex **C22** is a heterometallic {4d-4f} tetranuclear complex with the metallic core displaying a planar butterfly-type topology, as shown in **Figure 128**.

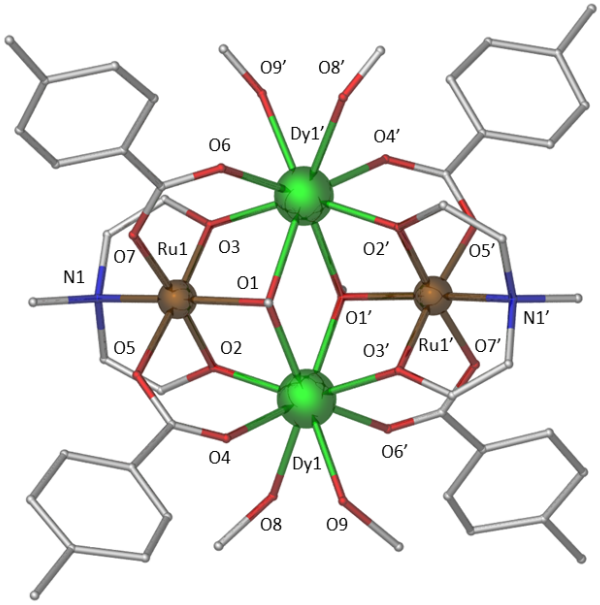

Figure 128- Molecular structure of **C22**: C atoms, grey; O atoms, red; N atoms, blue; Dy atoms, green; Ru atoms, brown. H atoms have been omitted for clarity.

The asymmetric unit consists of half of the complex, thereby one ruthenium and two half-occupancy dysprosium ions each in the 3+ oxidation state, with the remainder of the molecule generated by symmetry inversion. The two dysprosium (III) ions were found to be eight-coordinate with a distorted square antiprismatic geometry and occupy the 'body' sites of the butterfly. The two ruthenium (III) ions were found to be six-coordinate with a distorted octahedral geometry and occupy the 'wing' sites of the butterfly. Two μ_3 methoxide ligands bridge the two dysprosium (III) ions to each ruthenium (III) ion. Each ruthenium (III) ion is further ligated by a fully deprotonated

MDEA^{2-} ligand, of Harris Notation 3.2.2.1, and two p-toluate ligands completing the six-coordinate octahedral environment. The N-atom of the **MDEA**$^{2-}$ ligand chelates to the ruthenium (III) ion with the two deprotonated alkoxide arms bridging from the ruthenium (III) ion to the body dysprosium (III) ions. The four carboxylate ligands each bridge from a ruthenium (III) ion to a dysprosium (III) ion in a μ_2 manner. The coordinate sphere of each dysprosium (III) ion is completed by two terminal methanol ligands. Charges are balanced by two chloride anions associated to the complex.

Crystal packing diagrams of **C22** can be found in **Figure 129**. Intermolecular interactions are dominated by aromatic π, and C-H interactions derived from the p-toluate ligands.

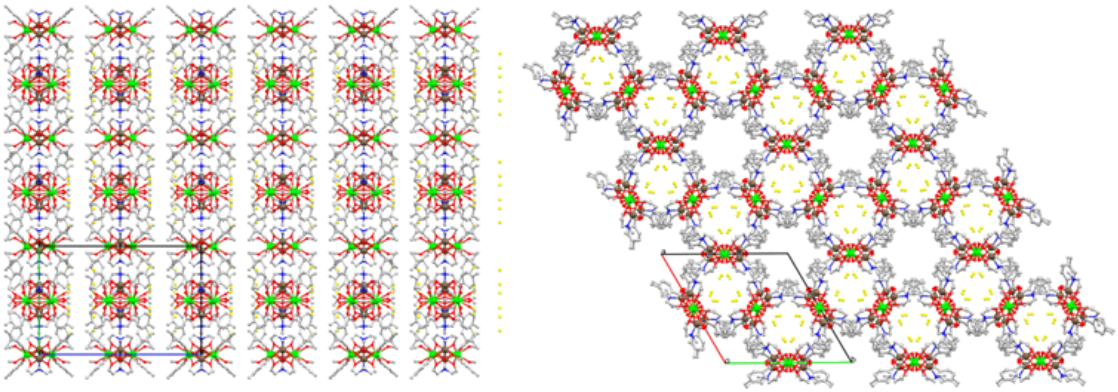

Figure 129- Crystal packing diagram of **C22** viewing the bc plane, left, and the ab plane, right. Unit cell included for reference. C atoms, grey; O atoms, red; N atoms, blue; Dy atoms, green; Ru atoms, brown. H atoms have been omitted for clarity.

The average Ru-$L_{N,O}$ bond length is found to be 2.04 Å with bond length ranging from 1.934-2.125 Å. The average Dy-O bond length is found to be 2.37 Å with bond lengths ranging from 2.278-2.467 Å. Selected bond lengths and bond angles are given below in **Table 36**.

Table 36- Selected bond lengths and bond angles for complex **C22**.

Atoms	Bond Length (Å)	Atoms	Bond Angle (°)
Dy1-O1	2.381	Dy1-O1-Ru1	93.42
Dy1-O1’	2.381	Dy1-O1-Ru1’	93.42
Dy1-O3’	2.282	Dy1-O2-Ru1	100.36
Dy1-O6’	2.312	Dy1-O3’-Ru1’	100.36
Dy1-O9	2.455	Dy1-O1-Dy1’	114.79
Dy1-O8	2.455		
Dy1-O4	2.312		
Dy1-O2	2.282		
Ru1-O1	2.124		
Ru1-O2	1.987		
Ru1-O5	2.125		
Ru1-N1	2.087		
Ru1-O7	2.011		
Ru1-O3	1.934		
Dy1-Dy1’	4.085		
Dy1-Ru1	3.284		
Dy1-Ru1’	3.284		
Ru1-Ru1’	5.147		

The reaction of [**EDEA**]H_2 with ruthenium (III) chloride trihydrate, dysprosium (III) nitrate pentahydrate, acetylacetone and triethylamine in acetonitrile produced a brown mother liquor from which yellow crystals of $[Ru^{III}_2Dy^{III}_2(OMe)_2(Acac)_4(EDEA)_2(NO_3)_2]$, **C23**, were grown by layer diffusion of a methanol:diethyl ether (1:3) solvent system. Complex **C23** crystallises in the triclinic space group *P-1*, with the asymmetric unit containing half of the molecule. The unit cell of **C23** has a volume of 1154 Å^3 containing one molecule per unit cell and exhibiting the unit cell parameters: a = 10.367(2) Å, b = 11.169(2) Å, c = 11.256(2) Å, α = 67.16(3)°, β = 73.88(3)°, γ = 83.77(3)° (See **Appendix B**, **Table S5**).

Complex **C23** is a heterometallic {4d-4f} tetranuclear complex with the metallic core displaying a planar butterfly-type topology, as shown in **Figure 130**.

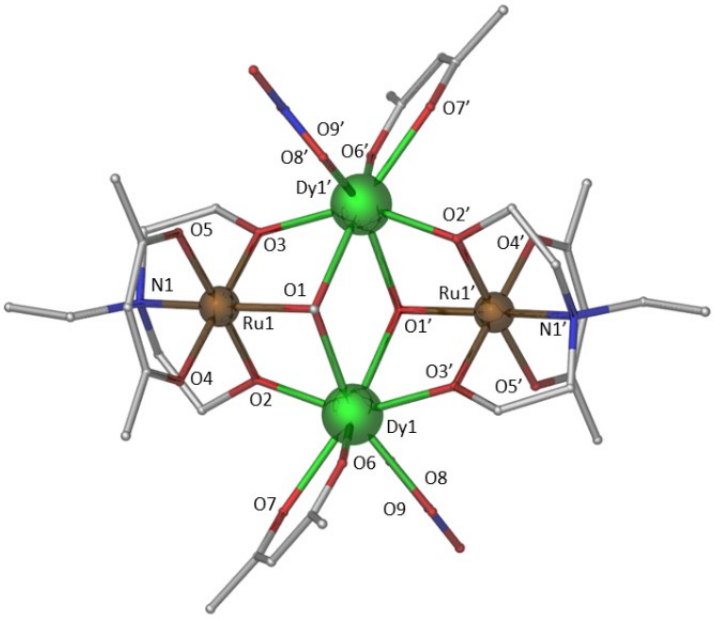

Figure 130- Molecular structure of **C23**: C atoms, grey; O atoms, red; N atoms, blue; Dy atoms, green; Ru atoms, brown. H atoms have been omitted for clarity.

The asymmetric unit consists of half of the complex – thereby one ruthenium and one dysprosium ion each in the 3+ oxidation state – with the remainder generated by inversion symmetry. The two dysprosium (III) ions were found to be eight-coordinate with a distorted square antiprismatic geometry and occupy the 'body' sites of the butterfly. The two ruthenium (III) ions were found to be six-coordinate with a distorted octahedral geometry and occupy the 'wing' sites of the butterfly. Two μ_3 methoxide ligands bridge the two dysprosium (III) ions to each ruthenium (III) ion. Each ruthenium

(III) ion is further ligated by a fully deprotonated **EDEA**$^{2-}$ ligand, of Harris Notation 3.2.2.1, and a capping acetylacetonate ligand completing the six-coordinate octahedral environment. The N-atom of the **EDEA**$^{2-}$ ligand chelates to the ruthenium (III) ion with the two deprotonated alkoxide arms bridging from the ruthenium (III) ion to the body dysprosium (III) ions. The remaining two acetylacetonate ligands similarly complete the coordinate sphere of each dysprosium (III) ion as capping ligands.

Crystal packing diagrams of **C23** can be found in **Figure 131**. Intermolecular interactions are dominated by C-H interactions derived from acetylacetonate and polyalcohol ligands.

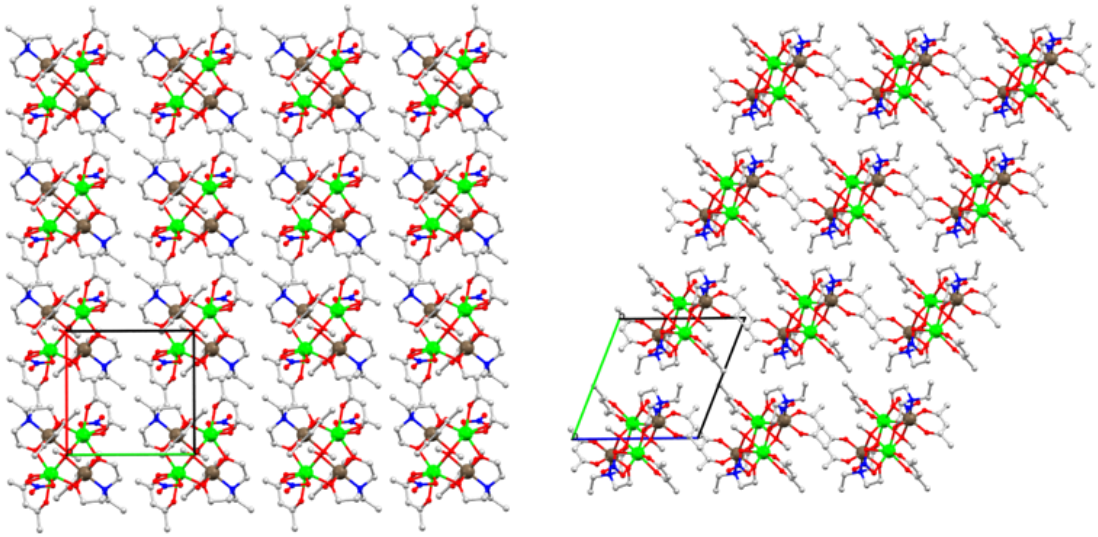

Figure 131- Crystal packing diagram of **C23** viewing the ab plane, left, and bc plane, right. Unit cell included for reference. C atoms, grey; O atoms, red; N atoms, blue; Dy atoms, green; Ru atoms, brown. H atoms have been omitted for clarity.

The average Ru-$L_{N,O}$ bond length is found to be 2.03 Å with bond length ranging from 1.960-2.116 Å. The average Dy-O bond length is found to be 2.38 Å with bond lengths ranging from 2.277-2.491 Å. Selected bond lengths and bond angles are given below in **Table 37**.

Table 37- Selected bond lengths and bond angles for complex **C23**.

Atoms	Bond Length (Å)	Atoms	Bond Angle (°)
Dy1-O1	2.428	Dy1-O1-Ru1	93.86
Dy1-O1’	2.491	Dy1-O1’-Ru1’	94.49
Dy1-O3’	2.291	Dy1-O2-Ru1	102.71
Dy1-O8	2.450	Dy1-O3’-Ru1’	105.63
Dy1-O9	2.484	Dy1-O1-Dy1’	112.14
Dy1-O6	2.276		
Dy1-O7	2.336		
Dy1-O2	2.277		
Ru1-O1	2.116		
Ru1-O2	1.976		
Ru1-O4	2.033		
Ru1-N1	2.086		
Ru1-O5	2.030		
Ru1-O3	1.960		
Dy1-Dy1’	4.082		
Dy1-Ru1	3.327		
Dy1-Ru1’	3.393		
Ru1-Ru1’	5.338		

The reaction of [**MDEA**]H_2 with ruthenium (III) chloride trihydrate, dysprosium (III) nitrate pentahydrate, 2-(trifluoromethyl)benzoic acid and triethylamine in acetonitrile produced a brown mother liquor from which dark purple crystals of $[Ru^{III}_2Dy^{III}_2(OMe)_2(2\text{-}F_3C\text{-}Benz)_4(MDEA)_2(NO_3)_2]$, **C24**, were grown by layer diffusion of a methanol:diethyl ether (1:3) solvent system. Complex **C24** crystallises in the triclinic space group *P-1*, with the asymmetric unit containing half of the molecule. The unit cell of **C24** has a volume of 1325 $Å^3$ containing one molecule per unit cell and exhibiting the unit cell parameters: a = 10.0637(3) Å, b = 11.1366(3) Å, c = 13.1405(4) Å, α = 68.9850(10)°, β = 75.3770(10)°, γ = 89.5200(10)° (See **Appendix B**, **Table S5**).

Complex **C24** is a heterometallic {4d-4f} tetranuclear complex with the metallic core displaying a planar butterfly-type topology, as shown in **Figure 132**.

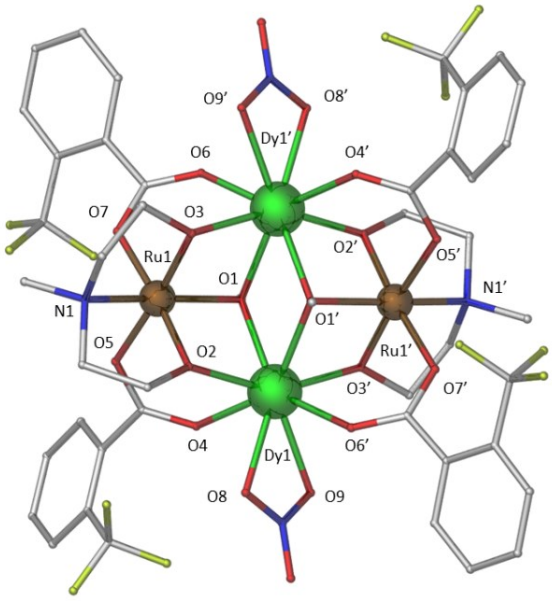

Figure 132- Molecular structure of **C24**: C atoms, grey; O atoms, red; N atoms, blue; F atoms, yellow; Dy atoms, green; Ru atoms, brown. H atoms have been omitted for clarity.

The asymmetric unit consists of half of the complex – thereby one ruthenium and one dysprosium ion each in the 3+ oxidation state – with the remainder generated by inversion symmetry. The two dysprosium (III) ions were found to be eight-coordinate with a distorted square antiprismatic geometry and occupy the 'body' sites of the butterfly. The two ruthenium (III) ions were found to be six-coordinate with a distorted octahedral geometry and occupy the 'wing' sites of the butterfly. Two μ_3 methoxide

ligands bridge the two dysprosium (III) ions to each ruthenium (III) ion. Each ruthenium (III) ion is further ligated by a fully deprotonated **MDEA**$^{2-}$ ligand, of Harris Notation 3.2.2.1, and two halo-toluate ligands completing the six-coordinate octahedral environment. The N-atom of the **MDEA**$^{2-}$ ligand chelates to the ruthenium (III) ion with the two deprotonated alkoxide arms bridging from the ruthenium (III) ion to the body dysprosium (III) ions. The four carboxylate ligands each bridge from a ruthenium (III) ion to a dysprosium (III) ion in a μ_2 manner. The coordinate sphere of each dysprosium (III) ion is completed by a capping nitrate ligand.

Crystal packing diagrams of **C24** can be found in **Figure 133**. Intermolecular interactions are dominated by aromatic π, and C-H interactions derived from the halo-toluate ligands.

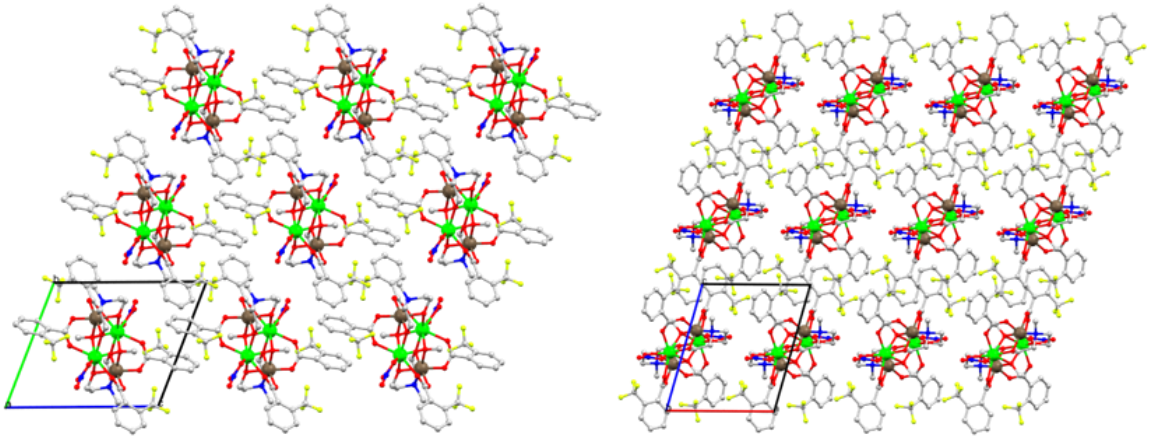

Figure 133- Crystal packing diagram of **C24** viewing the bc plane, left, and ab plane, right. Unit cell included for reference. C atoms, grey; O atoms, red; N atoms, blue; F atoms, yellow; Dy atoms, green; Ru atoms, brown. H atoms have been omitted for clarity.

The average Ru-$L_{N,O}$ bond length is found to be 2.05 Å with bond length ranging from 1.972-2.141 Å. The average Dy-O bond length is found to be 2.37 Å with bond lengths ranging from 2.265-2.462 Å. Selected bond lengths and bond angles are given below in **Table 38**.

Table 38- Selected bond lengths and bond angles for complex **C24**.

Atoms	Bond Length (Å)	Atoms	Bond Angle (°)
Dy1-O1	2.385	Dy1-O1-Ru1	91.64
Dy1-O1’	2.390	Dy1-O1’-Ru1’	91.45
Dy1-O3’	2.277	Dy1-O2-Ru1	99.97
Dy1-O6’	2.365	Dy1-O3’-Ru1’	99.00
Dy1-O9	2.462	Dy1-O1-Dy1’	112.11
Dy1-O8	2.429		
Dy1-O4	2.349		
Dy1-O2	2.265		
Ru1-O1	2.141		
Ru1-O2	1.972		
Ru1-O5	2.054		
Ru1-N1	2.074		
Ru1-O7	2.049		
Ru1-O3	1.989		
Dy1-Dy1’	3.961		
Dy1-Ru1	3.250		
Dy1-Ru1’	3.249		
Ru1-Ru1’	5.152		

The reaction of [**MDEA**]H_2 with ruthenium (III) chloride trihydrate, dysprosium (III) nitrate pentahydrate, 2,3,4,5-tetrafluorobenzoic acid and triethylamine in acetonitrile produced a brown mother liquor from which brown crystals of $[Ru^{III}_2Dy^{III}_2(OMe)_2(2,3,4,5\text{-tet-F-Benz})_4(MDEA)_2(NO_3)_2]$, **C25**, were grown by layer diffusion of a methanol:diethyl ether (1:3) solvent system. Complex **C25** crystallises in the monoclinic space group *P 2₁/c*, with the asymmetric unit containing half of the molecule. The unit cell of **C25** has a volume of 2568 Å^3 containing two molecules per unit cell and exhibiting the unit cell parameters: a = 10.4794(7) Å, b = 22.2231(13) Å, c = 11.1383(7) Å, α = 90°, β = 98.183(6)°, γ = 90° (See **Appendix B**, **Table S5**).

Complex **C25** is a heterometallic {4d-4f} tetranuclear complex with the metallic core displaying a planar butterfly-type topology, as shown in **Figure 134**.

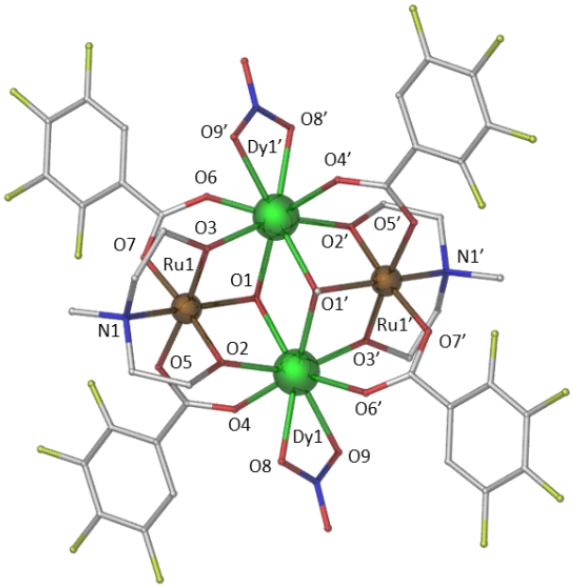

Figure 134- Molecular structure of **C25**: C atoms, grey; O atoms, red; N atoms, blue; F atoms, yellow; Dy atoms, green; Ru atoms, brown. H atoms have been omitted for clarity.

The asymmetric unit consists of half of the complex – thereby one ruthenium and one dysprosium ion each in the 3+ oxidation state – with the remainder generated by inversion symmetry. The two dysprosium (III) ions were found to be eight-coordinate with a distorted square antiprismatic geometry and occupy the 'body' sites of the butterfly. The two ruthenium (III) ions were found to be six-coordinate with a distorted octahedral geometry and occupy the 'wing' sites of the butterfly. Two μ_3 methoxide

ligands bridge the two dysprosium (III) ions to each ruthenium (III) ion. Each ruthenium (III) ion is further ligated by a fully deprotonated **MDEA**$^{2-}$ ligand, of Harris Notation 3.2.2.1, and two halo-benzoate ligands completing the six-coordinate octahedral environment. The N-atom of the **MDEA**$^{2-}$ ligand chelates to the ruthenium (III) ion with the two deprotonated alkoxide arms bridging from the ruthenium (III) ion to the body dysprosium (III) ions. The four carboxylate ligands each bridge from a ruthenium (III) ion to a dysprosium (III) ion in a μ_2 manner. The coordinate sphere of each dysprosium (III) ion is completed by a capping nitrate ligand.

Crystal packing of **C25** can be found in **Figure 135**. Intermolecular interactions are dominated by aromatic π, and C-H interactions derived from the halo-benzoate ligands.

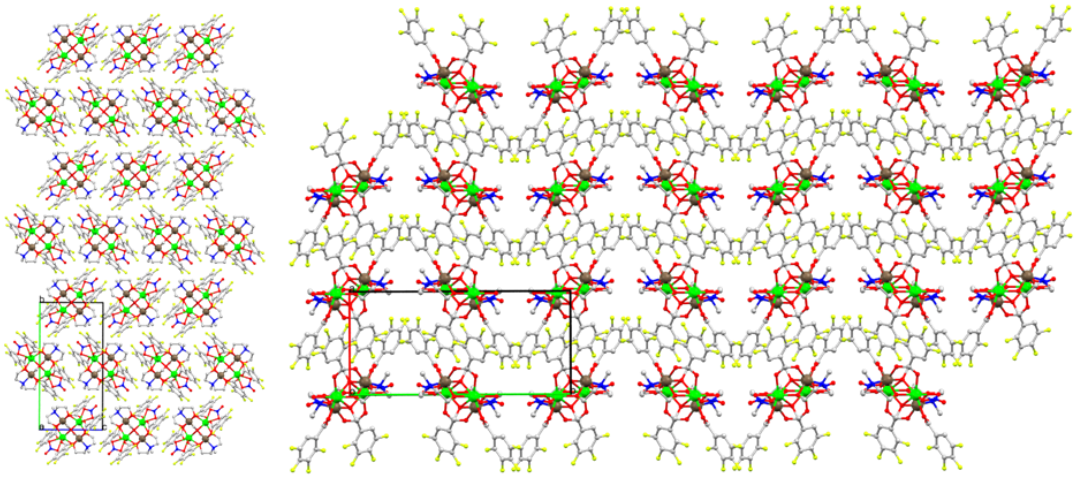

Figure 135- Crystal packing diagram of **C25** viewing the bc plane, left, and the ab plane, right. Unit cell included for reference C atoms, grey; O atoms, red; N atoms, blue; F atoms, yellow; Dy atoms, green; Ru atoms, brown. H atoms have been omitted for clarity.

The average Ru-$L_{N,O}$ bond length is found to be 2.05 Å with bond length ranging from 1.979-2.133 Å. The average Dy-O bond length is found to be 2.37 Å with bond lengths ranging from 2.269-2.438 Å. Selected bond lengths and bond angles are given below in **Table 39**.

Table 39- Selected bond lengths and bond angles for complex **C25**.

Atoms	Bond Length (Å)	Atoms	Bond Angle (°)
Dy1-O1	2.386	Dy1-O1-Ru1	91.53
Dy1-O1’	2.395	Dy1-O1’-Ru1’	92.06
Dy1-O3’	2.271	Dy1-O2-Ru1	99.25
Dy1-O6’	2.371	Dy1-O3’-Ru1’	100.10
Dy1-O9	2.436	Dy1-O1-Dy1’	113.05
Dy1-O8	2.438		
Dy1-O4	2.364		
Dy1-O2	2.268		
Ru1-O1	2.132		
Ru1-O2	1.980		
Ru1-O5	2.055		
Ru1-N1	2.081		
Ru1-O7	2.052		
Ru1-O3	1.979		
Dy1-Dy1’	3.988		
Dy1-Ru1	3.242		
Dy1-Ru1’	3.263		
Ru1-Ru1’	5.139		

The reaction of [**MDEA**]H_2 with ruthenium (III) chloride trihydrate, dysprosium (III) nitrate pentahydrate, 2-chloro-4,5-difluorobenzoic acid and triethylamine in acetonitrile produced a brown mother liquor from which yellow crystals of $[Ru^{III}_2Dy^{III}_2(OMe)_2(2\text{-Cl-}4,5\text{-F-Benz})_4(MDEA)_2(NO_3)_2]$, **C26**, were grown by layer diffusion of a methanol:diethyl ether (1:3) solvent system. Complex **C26** crystallises in the monoclinic space group *C 2/m*, with the asymmetric unit containing half of the molecule. The unit cell of **C26** has a volume of 2601 Å^3 containing two molecules per unit cell and exhibiting the unit cell parameters: a = 15.536(3) Å, b = 16.010(3) Å, c = 12.208(2) Å, α = 90°, β = 121.06(3)°, γ = 90° (See **Appendix B**, **Table S6**).

Complex **C26** is a heterometallic {4d-4f} tetranuclear complex with the metallic core displaying a planar butterfly-type topology, as shown in **Figure 136**.

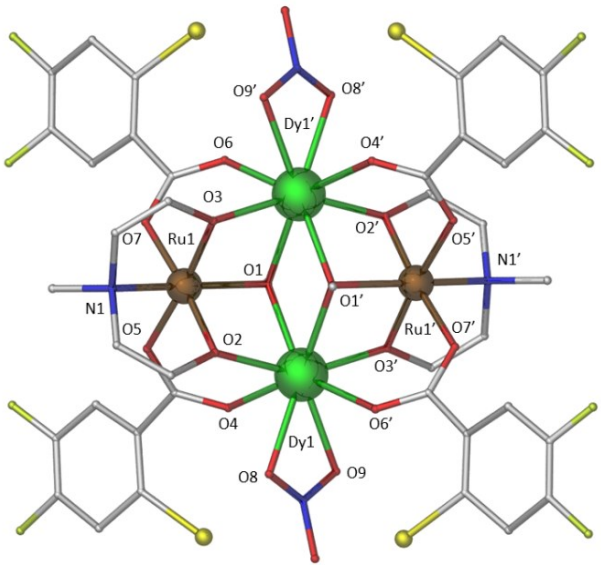

Figure 136- Molecular structure of **C26**: C atoms, grey; O atoms, red; N atoms, blue; F atoms, small yellow; Cl atoms, large yellow; Dy atoms, green; Ru atoms, brown. H atoms have been omitted for clarity.

The asymmetric unit consists of half of the complex – thereby one ruthenium and one dysprosium ion each in the 3+ oxidation state – with the remainder generated by inversion symmetry. The two dysprosium (III) ions were found to be eight-coordinate with a distorted square antiprismatic geometry and occupy the 'body' sites of the butterfly. The two ruthenium (III) ions were found to be six-coordinate with a distorted octahedral geometry and occupy the 'wing' sites of the butterfly. Two μ_3 methoxide ligands bridge the two dysprosium (III) ions to each ruthenium (III) ion. Each ruthenium

(III) ion is further ligated by a fully deprotonated **MDEA**$^{2-}$ ligand, of Harris Notation 3.2.2.1, and two halo-benzoate ligands completing the six-coordinate octahedral environment. The N-atom of the **MDEA**$^{2-}$ ligand chelates to the ruthenium (III) ion with the two deprotonated alkoxide arms bridging from the ruthenium (III) ion to the body dysprosium (III) ions. The four carboxylate ligands each bridge from a ruthenium (III) ion to a dysprosium (III) ion in a μ_2 manner. The coordinate sphere of each dysprosium (III) ion is completed by a capping nitrate ligand.

Crystal packing diagrams of **C26** can be found in **Figure 137**. Intermolecular interactions are dominated by aromatic π, and C-H interactions derived from the halo-benzoate ligands.

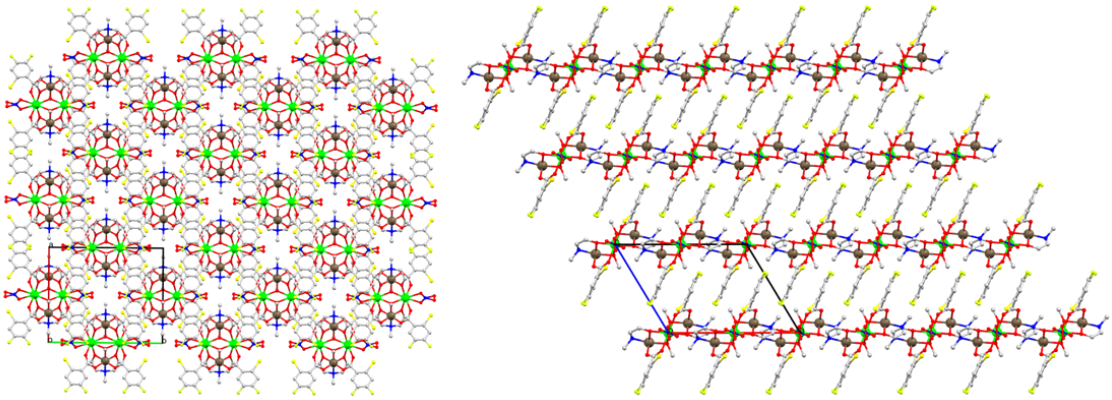

Figure 137- Crystal packing diagram of **C26** viewing the ac plane, left, and the ab plane, right. Unit cell included for reference. C atoms, grey; O atoms, red; N atoms, blue; F atoms, small yellow; Cl atoms, large yellow; Dy atoms, green; Ru atoms, brown. H atoms have been omitted for clarity.

The average Ru-$L_{N,O}$ bond length is found to be 2.04 Å with bond length ranging from 1.979-2.131 Å. The average Dy-O bond length is found to be 2.36 Å with bond lengths ranging from 2.274-2.419 Å. Selected bond lengths and bond angles are given below in **Table 40**.

Table 40- Selected bond lengths and bond angles for complex **C26**.

Atoms	Bond Length (Å)	Atoms	Bond Angle (°)
Dy1-O1	2.387	Dy1-O1-Ru1	91.95
Dy1-O1’	2.387	Dy1-O1’-Ru1’	91.95
Dy1-O3’	2.274	Dy1-O2-Ru1	99.58
Dy1-O6’	2.378	Dy1-O3’-Ru1’	99.58
Dy1-O9	2.419	Dy1-O1-Dy1’	113.79
Dy1-O8	2.419		
Dy1-O4	2.378		
Dy1-O2	2.274		
Ru1-O1	2.131		
Ru1-O2	1.979		
Ru1-O5	2.049		
Ru1-N1	2.050		
Ru1-O7	2.049		
Ru1-O3	1.979		
Dy1-Dy1’	3.998		
Dy1-Ru1	3.253		
Dy1-Ru1’	3.253		
Ru1-Ru1’	5.133		

The reaction of [**MDEA**]H_2 with ruthenium (III) chloride trihydrate, gadolinium (III) nitrate hexahydrate, benzoic acid and triethylamine in acetonitrile produced a brown mother liquor from which yellow crystals of $[Ru^{III}_2Gd^{III}_2(OMe)_2(Benz)_4(MDEA)_2(NO_3)_2]$, **C27**, were grown by layer diffusion of a methanol:diethyl ether (1:3) solvent system. Complex **C27** crystallises in the monoclinic space group *P* 2(1)/n, with the asymmetric unit containing half of the molecule. The unit cell of **C27** has a volume of 2392 $Å^3$ containing two molecules per unit cell and exhibiting the unit cell parameters: a = 8.0820(16) Å, b = 17.209(3) Å, c = 17.212(3) Å, α = 90°, β = 92.35(3)°, γ = 90° (See **Appendix B**, **Table S6**).

Complex **C27** is a heterometallic {4d-4f} tetranuclear complex with the metallic core displaying a planar butterfly-type topology, as shown in **Figure 138**.

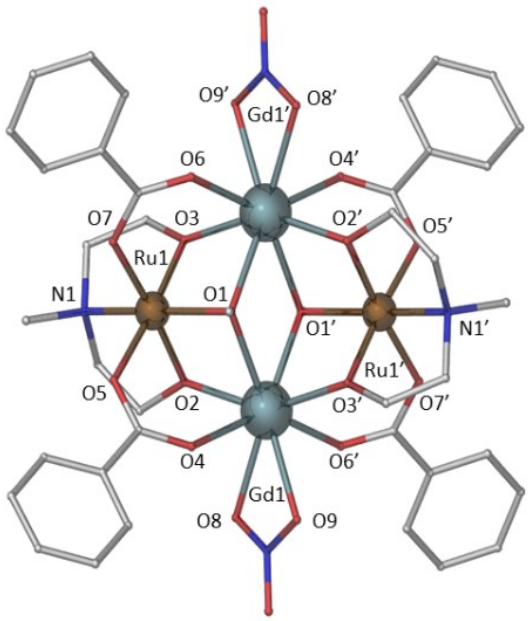

Figure 138- Molecular structure of **C27**: C atoms, grey; O atoms, red; N atoms, blue; Gd atoms, silver; Ru atoms, brown. H atoms have been omitted for clarity.

The asymmetric unit consists of half of the complex – thereby one ruthenium and one gadolinium ion each in the 3+ oxidation state – with the remainder generated by inversion symmetry. The two gadolinium (III) ions were found to be eight-coordinate with a distorted square antiprismatic geometry and occupy the 'body' sites of the butterfly. The two ruthenium (III) ions were found to be six-coordinate with a distorted octahedral geometry and occupy the 'wing' sites of the butterfly. Two μ_3 methoxide ligands bridge the two gadolinium (III) ions to each ruthenium (III) ion. Each ruthenium

(III) ion is further ligated by a fully deprotonated **MDEA**$^{2-}$ ligand, of Harris Notation 3.2.2.1, and two benzoate ligands completing the six-coordinate octahedral environment. The N-atom of the **MDEA**$^{2-}$ ligand chelates to the ruthenium (III) ion with the two deprotonated alkoxide arms bridging from the ruthenium (III) ion to the body gadolinium (III) ions. The four carboxylate ligands each bridge from a ruthenium (III) ion to a gadolinium (III) ion in a μ_2 manner. The coordinate sphere of each gadolinium (III) ion is completed by a capping nitrate ligand. As a result of this analysis **C21** and **C27** can be said to be isostructural. Crystal packing of **C27** can be found in **Figure 139**. Intermolecular interactions are dominated by aromatic π, and C-H interactions derived from the benzoate ligands.

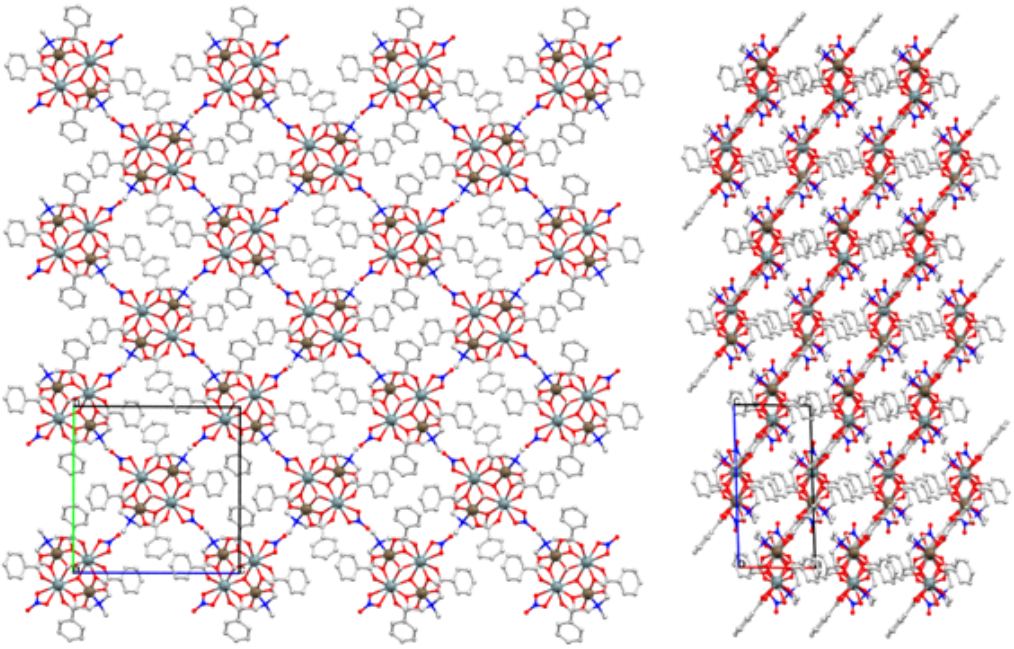

Figure 139- Crystal packing diagram of **C27** viewing the bc plane, left, and the ac plane, right. Unit cell included for reference. C atoms, grey; O atoms, red; N atoms, blue; Gd atoms, silver; Ru atoms, brown. H atoms have been omitted for clarity.

The average Ru-$L_{N,O}$ bond length is found to be 2.05 Å with bond length ranging from 1.986-2.128 Å. The average Gd-O bond length is found to be 2.39 Å with bond lengths ranging from 2.301-2.463 Å. Selected bond lengths and bond angles are given below in **Table 41**.

Table 41- Selected bond lengths and bond angles for complex **C27**.

Atoms	Bond Length (Å)	Atoms	Bond Angle (°)
Gd1-O1	2.407	Gd1-O1-Ru1	91.93
Gd1-O1’	2.407	Gd1-O1’-Ru1’	92.84
Gd1-O3’	2.303	Gd1-O2-Ru1	98.95
Gd1-O6’	2.367	Gd1-O3’-Ru1’	100.34
Gd1-O9	2.454	Gd1-O1-Gd1’	112.87
Gd1-O8	2.463		
Gd1-O4	2.371		
Gd1-O2	2.301		
Ru1-O1	2.128		
Ru1-O2	1.988		
Ru1-O5	2.052		
Ru1-N1	2.071		
Ru1-O7	2.052		
Ru1-O3	1.986		
Gd1-Gd1’	4.023		
Gd1-Ru1	3.266		
Gd1-Ru1’	3.301		
Ru1-Ru1’	5.190		

The reaction of [**EDEA**]H_2 with ruthenium (III) chloride trihydrate, gadolinium (III) nitrate hexahydrate, acetylacetone and triethylamine in acetonitrile produced a brown mother liquor from which yellow crystals of $[Ru^{III}_2Gd^{III}_2(OMe)_2(Acac)_4(EDEA)_2(NO_3)_2]$, **C28**, were grown by layer diffusion of a methanol:diethyl ether (1:3) solvent system. Complex **C28** crystallises in the triclinic space group *P-1*, with the asymmetric unit containing half of the molecule. The unit cell of **C28** has a volume of 1157 $Å^3$ containing one molecule per unit cell and exhibiting the unit cell parameters: a = 10.343(2) Å, b = 11.205(2) Å, c = 11.250(2) Å, α = 67.17(3)°, β = 74.35(3)°, γ = 84.09(3)° (See **Appendix B**, **Table S6**).

Complex **C28** is a heterometallic {4d-4f} tetranuclear complex with the metallic core displaying a planar butterfly-type topology, as shown in **Figure 140**.

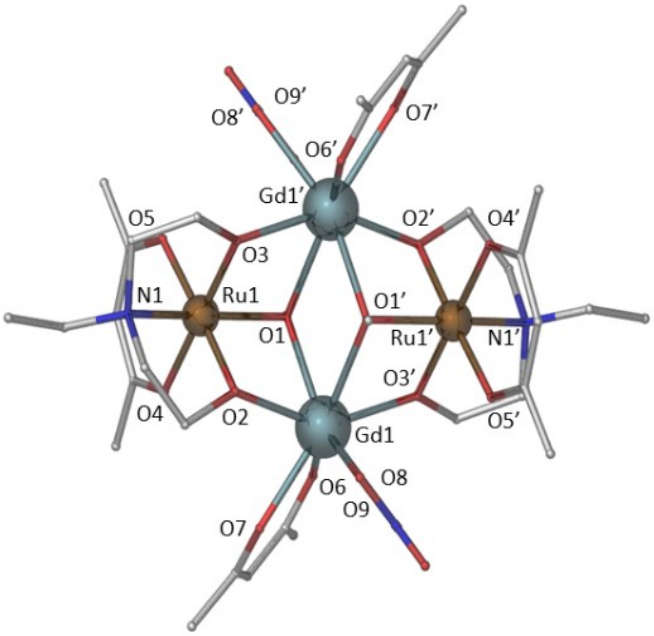

Figure 140- Molecular structure of **C28**: C atoms, grey; O atoms, red; N atoms, blue; Gd atoms, silver; Ru atoms, brown. H atoms have been omitted for clarity.

The asymmetric unit consists of half of the complex – thereby one ruthenium and one gadolinium ion each in the 3+ oxidation state – with the remainder generated by inversion symmetry. The two gadolinium (III) ions were found to be eight-coordinate with a distorted square antiprismatic geometry and occupy the 'body' sites of the butterfly. The two ruthenium (III) ions were found to be six-coordinate with a distorted octahedral geometry and occupy the 'wing' sites of the butterfly. Two μ_3 methoxide ligands bridge the two gadolinium (III) ions to each ruthenium (III) ion. Each ruthenium

(III) ion is further ligated by a fully deprotonated **EDEA**$^{2-}$ ligand, of Harris Notation 3.2.2.1, and a capping acetylacetonate ligand completing the six-coordinate octahedral environment. The N-atom of the **EDEA**$^{2-}$ ligand chelates to the ruthenium (III) ion with the two deprotonated alkoxide arms bridging from the ruthenium (III) ion to the body gadolinium (III) ions. The remaining two acetylacetonate ligands similarly complete the coordinate sphere of each gadolinium (III) ion as capping ligands. As a result of this analysis, **C23** and **C28** can be said to be isostructural.

Crystal packing diagrams of **C28** can be found in **Figure 141**. Intermolecular interactions are dominated by C-H interactions derived from acetylacetonate and polyalcohol ligands.

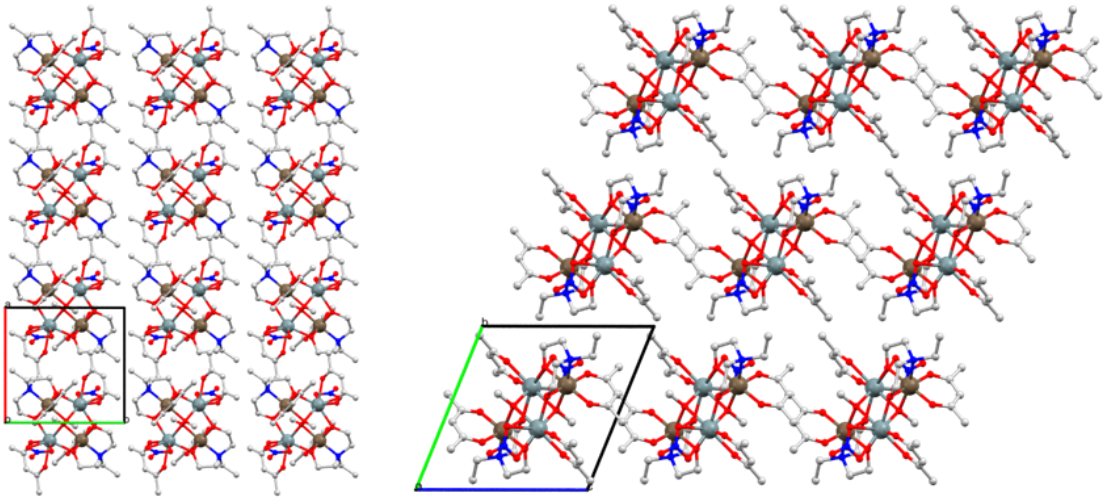

Figure 141- Crystal packing diagram of **C28** viewing the ac plane, left, and bc plane, right. Unit cell included for reference. C atoms, grey; O atoms, red; N atoms, blue; Gd atoms, silver; Ru atoms, brown. H atoms have been omitted for clarity.

The average Ru-$L_{N,O}$ bond length is found to be 2.04 Å with bond length ranging from 1.961-2.124 Å. The average Gd-O bond length is found to be 2.40 Å with bond lengths ranging from 2.303-2.505 Å. Selected bond lengths and bond angles are given below in **Table 42**.

Table 42- Selected bond lengths and bond angles for complex **C28**.

Atoms	Bond Length (Å)	Atoms	Bond Angle (°)
Gd1-O1	2.447	Gd1-O1-Ru1	94.01
Gd1-O1’	2.512	Gd1-O1’-Ru1’	94.64
Gd1-O3’	2.324	Gd1-O2-Ru1	102.55
Gd1-O8	2.505	Gd1-O3’-Ru1’	105.50
Gd1-O9	2.477	Gd1-O1-Gd1’	112.31
Gd1-O6	2.303		
Gd1-O7	2.355		
Gd1-O2	2.312		
Ru1-O1	2.124		
Ru1-O2	1.974		
Ru1-O4	2.035		
Ru1-N1	2.090		
Ru1-O5	2.030		
Ru1-O3	1.961		
Gd1-Gd1’	4.119		
Gd1-Ru1	3.350		
Gd1-Ru1’	3.418		
Ru1-Ru1’	5.371		

The reaction of [**HMAP**]H_2 with ruthenium (III) chloride trihydrate, dysprosium (III) nitrate pentahydrate, benzoic acid and triethylamine in a solvent mix of acetonitrile and methanol (4:1) produced a dark brown mother liquor from which red-brown crystals of $[Ru_2Dy_4(OH)_2(OMe)_2(Benz)_{10}(HMAP)_2(MeOH)_2]$, **C29**, were grown by slow deposition from the reaction mixture solvent system. Complex **C29** crystallises in the monoclinic space group *P 2₁/c*, with the asymmetric unit containing two halves of the molecule. The unit cell of **C29** has a volume of 9452 Å^3 containing four molecules per unit cell and exhibiting the unit cell parameters: a = 19.4315(2) Å, b = 19.4429(2) Å, c = 25.2337(4) Å, α = 90°, β = 97.4900(10)°, γ = 90° (See **Appendix B**, **Table S6**).

Complex **C29** is a heterometallic {4d-4f} hexanuclear complex containing two ruthenium (III) ions and four dysprosium (III) ions, with a metallic core resembling a planar butterfly-type topology, as shown in **Figure 142**.

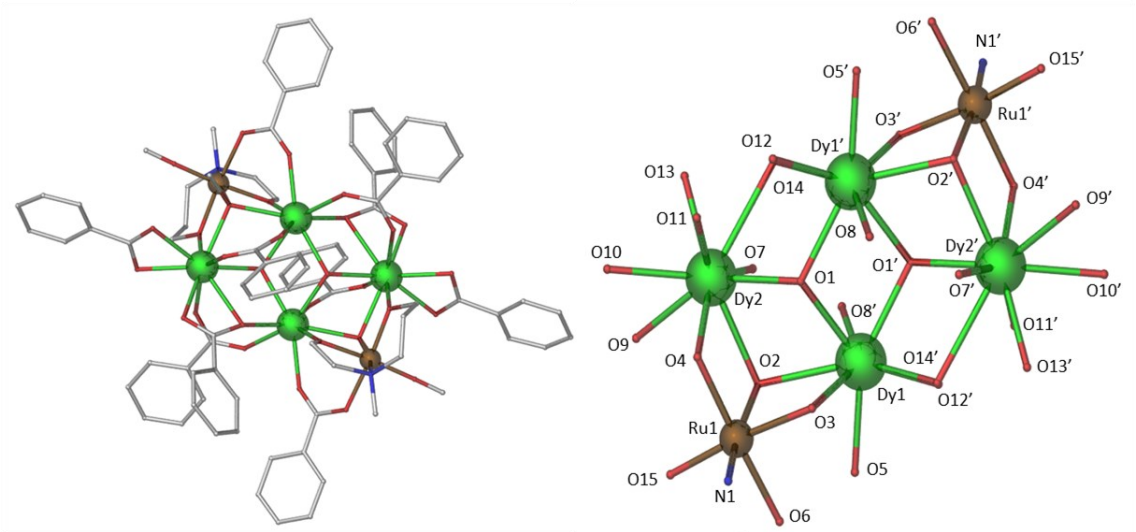

Figure 142- Molecular structure (left) and skeletal form (right) of **C29**: C atoms, grey; O atoms, red; N atoms, blue; F atoms, small yellow; Cl atoms, large yellow; Dy atoms, green; Ru atoms, brown. H atoms have been omitted from both structures and C atoms have been omitted from the skeletal form for clarity.

The asymmetric unit consists of two halves of the complex – thereby two ruthenium and four dysprosium ions each in the 3+ oxidation state in total – with the remainder generated by inversion symmetry. The two halves of the molecule in the asymmetric unit are not equivalent as a result of the molecular packing of the complexes. The four dysprosium (III) ions occupy all four sites of the butterfly core. Two of the dysprosium

(III) ions were found to be eight-coordinate with a distorted square antiprismatic geometry and occupy the 'body' sites of the butterfly. The remaining two dysprosium (III) ions were found to be nine-coordinate with a distorted tricapped trigonal prismatic geometry and occupy the 'wing' sites of the butterfly. The two ruthenium (III) ions were found to be six-coordinate with a distorted octahedral geometry and are bound between an eight-coordinate and nine-coordinate dysprosium ion to form a triangular arrangement, with the ruthenium (III) ion laying outside of the dysprosium plane. Two μ_3 hydroxide ligands bridge the two eight-coordinate dysprosium (III) ions to each nine-coordinate dysprosium (III) ion, whilst two μ_3 methoxide ligands bridge an eight-coordinate dysprosium (III) ion and a nine-coordinate dysprosium (III) ion to the peripheral ruthenium (III) ion, stabilising the triangular arrangement. Each ruthenium (III) ion is further ligated by a fully deprotonated **HMAP**$^{2-}$ ligand, of Harris Notation 3.2.2.1, one benzoate ligand and a terminal methanol ligand completing the six-coordinate octahedral environment. The N-atom of the **HMAP**$^{2-}$ ligand chelates to the ruthenium (III) ion with the one deprotonated alkoxide arms each bridging from the ruthenium (III) ion to a body dysprosium (III) ion and a wing dysprosium (III) ion, respectively. The remaining eight carboxylate ligands bind in three different modes: four bridge the body and wing site dysprosium (III) ions in a conventional μ_2 manner, two bridge the body and wing site dysprosium (III) ions in a μ_2 manner whilst acting as a capping agent to the wing site dysprosium (III) and the third mode completes each wing site dysprosium (III) ions coordinate sphere as a capping ligand.

Crystal packing diagrams of **C29** can be found in **Figure 143**. Intermolecular interactions are dominated by aromatic π, and C-H interactions derived from the benzoate ligands.

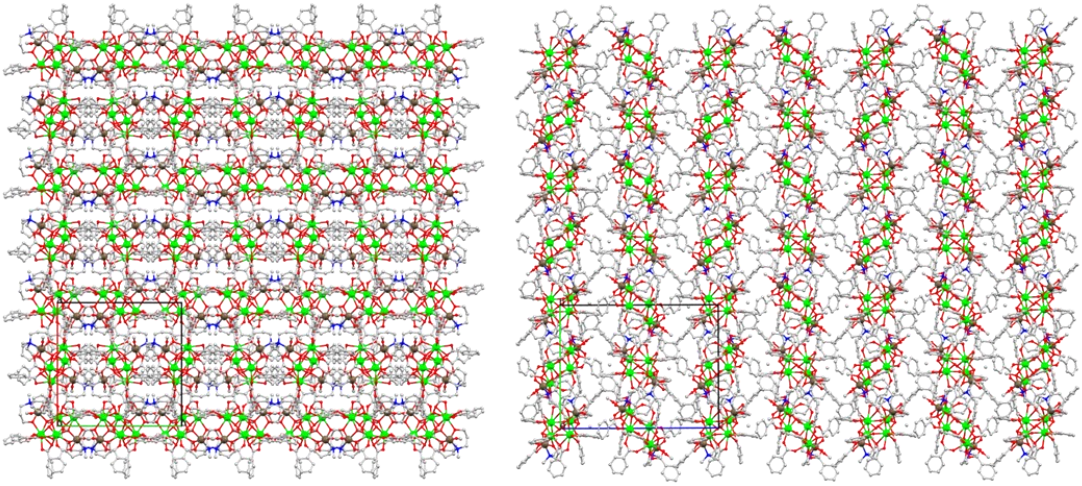

Figure 143- Crystal packing diagram of **C29** viewing the ab plane, left, and the bc plane, right. Unit cell included for reference. C atoms, grey; O atoms, red; N atoms, blue; F atoms, small yellow; Cl atoms, large yellow; Dy atoms, green; Ru atoms, brown. H atoms have been omitted for clarity.

The average Ru-$L_{N,O}$ bond length is found to be 2.01 Å with bond length ranging from 1.814-2.132 Å. The average Dy-O bond length is found to be 2.40 Å with bond lengths ranging from 2.294-2.733 Å. Selected bond lengths, inter-metal distances and bond angles are given below in **Table 43**.

Table 43- Selected bond lengths and bond angles for complex **C29**.

Atoms	Bond Length (Å)	Atoms	Inter-Atom Distance (Å)
Dy1-O1	2.373	Ru1-Ru1'	8.919
Dy1-O8	2.278	Dy1-Dy1'	3.907
Dy1-O1'	2.375	Dy1-Dy2	3.897
Dy1-O12'	2.352	Dy1-Dy2'	3.980
Dy1-O14'	2.362	Dy2-Dy2'	6.840
Dy1-O5	2.347	Dy1-Ru1	3.486
Dy1-O3	2.370	Dy2-Ru1	3.575
Dy1-O2	2.492		
Dy2-O1	2.303		
Dy2-O2	2.507		
Dy2-O4	2.370		
Dy2-O9	2.429		
Dy2-O10	2.440		
Dy2-O11	2.347	Atoms	Bond Angle (°)
Dy2-O13	2.374	Dy1-O1-Dy2	112.90
Dy2-O14	2.846	Dy1-O1'-Dy2'	116.58
Dy2-O7	2.356	Dy1-O2-Dy2	102.43
Ru1-O2	2.055	Dy1-O14'-Dy2'	99.27
Ru1-O3	1.997	Dy1-O1-Dy1'	110.78
Ru1-O6	2.089	Dy1-O2-Ru1	99.67
Ru1-N1	2.131	Dy1-O3-Ru1	105.64
Ru1-O15	1.838	Dy2-O2-Ru1	102.72
Ru1-O4	1.982	Dy2-O4-Ru1	110.11

The reaction of [**HMAP**]H_2 with indium (III) nitrate hexahydrate, dysprosium (III) nitrate pentahydrate, benzoic acid and triethylamine in a solvent mix of acetonitrile and methanol (4:1) produced a translucent mother liquor from which colourless crystals of $[In_{16}Dy_6(O)_6(OH)_{12}(OMe)_3(Benz)_{22}(HMAP)_6(NO_3)_5]$, **C30**, were grown by slow evaporation from a methanol:acetonitrile (1:4) solvent system. Complex **C30** crystallises in the triclinic space group *P-1*, with the asymmetric unit containing the entire molecule. The unit cell of **C30** has a volume of 13188 $Å^3$ containing two molecules per unit cell and exhibiting the unit cell parameters: a = 22.7373(3) Å, b = 23.8381(5) Å, c = 24.8983(5) Å, α = 93.571(2)°, β = 91.8860(10)°, γ = 101.4280(10)° (See **Appendix B**, **Table S6**).

Complex **C30** is a heterometallic {5p-4f} icosidyo-nuclear complex containing sixteen indium (III) ions and six dysprosium (III) ions in a propeller-like structure such that the metals are arranged in a $\{In(In_5Dy_2)_3\}$ system, as shown in **Figure 144**.

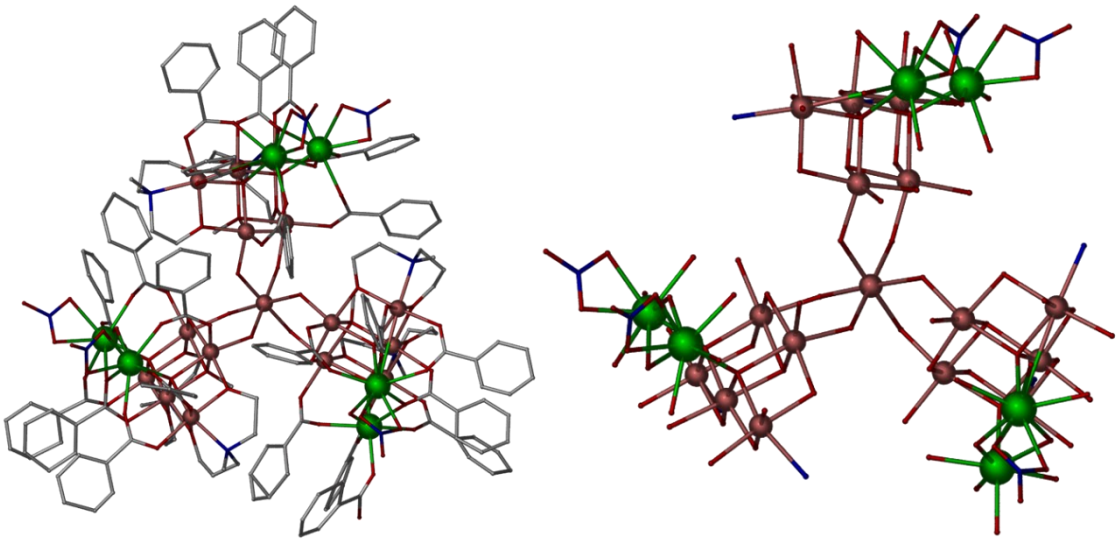

Figure 144- Molecular structure (left) and skeletal form (right) of **C30**: C atoms, grey; O atoms, red; N atoms, blue; Dy atoms, green; In atoms, pink. H atoms have been omitted from both structures and C atoms have been omitted from the skeletal form for clarity.

The central indium (III) ion was found to be six-coordinate and has a distorted octahedral geometry, with the remainder of the complex acting as three cis-binding organometallic ligands, or "blades" comprised of an additional five indium (III) ions and two dysprosium (III) ions each. The remaining indium (III) ions were also found to be six-coordinate with distorted octahedral geometries. Five of the dysprosium (III) ions were found to be eight-

coordinate with distorted square antiprismatic geometries, whilst one dysprosium (III) ion is instead seven coordinate exhibiting a distorted pentagonal bipyramidal geometry, breaking the molecules otherwise three-fold symmetry. All three blades are connected to the central indium(III) ion by two μ_2 hydroxide linkers, which also bind to one of the two most proximal of the outer indium (III) ions. Each blade is comprised of a pair of indium-dysprosium tetrahedra with a shared indium vertex where the five indium atoms are in a planar arrangement, akin to an incomplete molecular disk. The two dysprosium atoms then lie above the indium plane on the leading edge of the blade. Each $\{In_3Dy\}$ tetrahedron is stabilised by a core μ_4-oxide ligand, whilst the partial indium disk is bound by one μ_3 methoxide ligand and one μ_2 hydroxide ligand. A final μ_2 hydroxide ligand bridges the dysprosium pairs of each blade together. The two most distal/peripheral indium (III) ions of each blade are further ligated by two fully deprotonated $(\mathbf{HMAP})^{2-}$ ligands, of Harris Notation 3.2.2.1, with the N-atom and both deprotonated alkoxide arms chelating to said indium and bridging onwards to the two adjacent indium atoms *via* the alkoxide arms. Finally, seven benzoate ligands bind each blade together, securing the dysprosium pair to the partial indium disk. Six exhibit a μ_2 binding mode between an indium (III) and dysprosium (III) ion respectively, whilst the seventh, most central benzoate instead exhibits a binding mode of Harris Notation 3.2.1, binding both the ions in the dysprosium pair, through a single donor oxygen, to the central indium ion of each blade. A skeletal diagram for each propeller blade is given in **Figure 145** to assist in visualising the intricate arrangement of this complex.

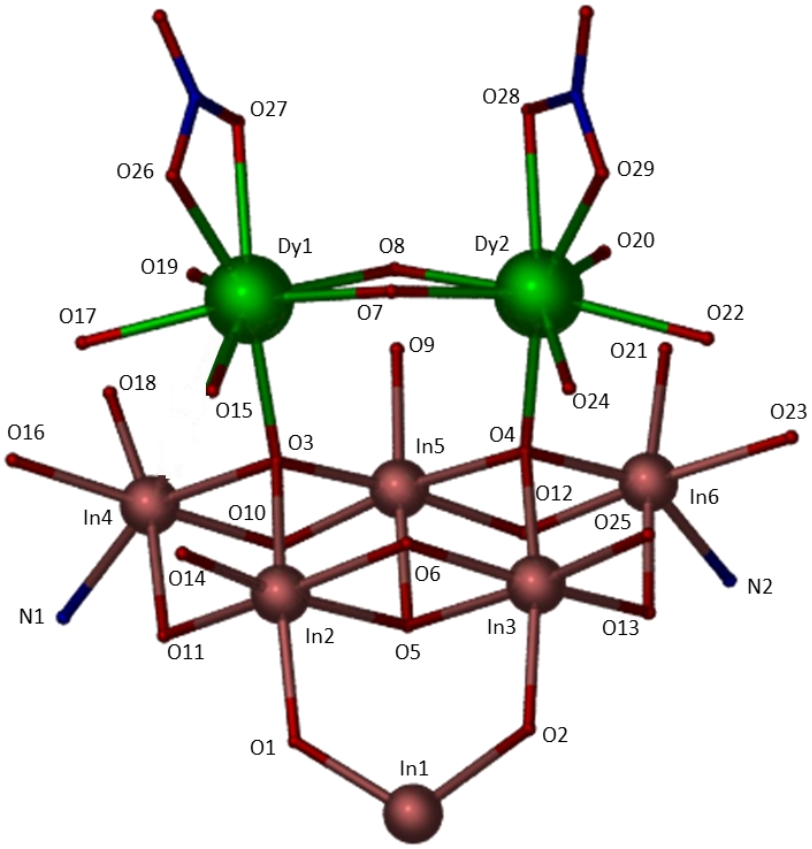

Figure 145- Skeletal form of a blade unit of complex **C30**. H and C atoms have been omitted for clarity. Note – the molecule does not exhibit perfect three-fold symmetry and so the capping ligands may differ between blades.

Finally, each dysprosium (III) ion is capped by a ligand to complete its coordination environment. In five of the six cases, this ligand is a bidentate nitrate, whilst in the sixth case this is instead a monodentate benzoate. This change in connectivity explains the one seven coordinate dysprosium mentioned earlier, whilst also breaking the otherwise three-fold symmetry of the complex overall.

Crystal packing of **C30** can be found in **Figure 146**. Intermolecular interactions are dominated by aromatic π, and C-H interactions derived from the benzoate ligands.

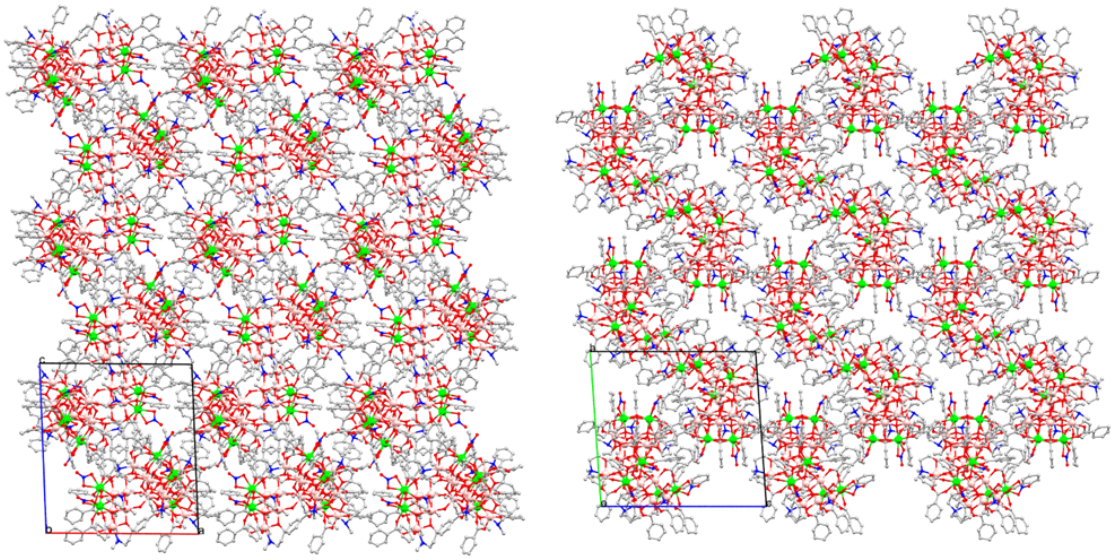

Figure 146- Crystal packing diagram of **C30** viewing the ac plane, left, and the bc plane, right. Unit cell included for reference. C atoms, grey; O atoms, red; N atoms, blue; Dy atoms, green; In atoms, pink. H atoms have been omitted for clarity.

The average Dy-O bond length is found to be 2.35 Å with bond lengths ranging from 2.216-2.478 Å. The average In-$L_{N,O}$ bond length within a blade is found to be 2.16 Å with bond lengths ranging from 2.061-2.327 Å, whilst the average In-O bond length for the central ion is instead 2.15 Å with bond lengths ranging from 2.131-2.193 Å. Selected bond lengths and bond angles are given below in **Table 44** and **Table 45**, respectively.

Table 44- Selected bond lengths for complex **C30**. Values are given for a single blade of the propeller-like structure.

Atoms	Bond Length (Å)	Atoms	Bond Length (Å)
In1-O1	2.154	In5-O4	2.164
In1-O2	2.145	In5-O12	2.105
In2-O1	2.090	In6-O13	2.130
In2-O11	2.090	In6-O12	2.163
In2-O14	2.149	In6-O4	2.163
In2-O3	2.192	In6-O21	2.132
In2-O6	2.145	In6-O23	2.163
In2-O5	2.281	In6-N2	2.327
In3-O2	2.101	Dy1-O3	2.313
In3-O5	2.249	Dy1-O15	2.379
In3-O6	2.115	Dy1-O17	2.258
In3-O4	2.207	Dy1-O19	2.353
In3-O25	2.173	Dy1-O26	2.430
In3-O13	2.104	Dy1-O27	2.441
In4-O11	2.125	Dy1-O8	2.431
In4-N1	2.275	Dy1-O7	2.216
In4-O16	2.182	Dy2-O4	2.288
In4-O18	2.143	Dy2-O7	2.219
In4-O3	2.192	Dy2-O8	2.422
In4-O10	2.174	Dy2-O28	2.447
In5-O5	2.201	Dy2-O29	2.478
In5-O10	2.107	Dy2-O20	2.351
In5-O3	2.169	Dy2-O22	2.266
In5-O9	2.126	Dy2-O24	2.319

Table 45- Selected bond angles for complex **C30**. Values are given for a single blade of the propeller-like structure.

Atoms	Bond Angles (°)	Atoms	Bond Angles (°)
In1-O1-In2	132.24	In3-O4-In6	98.99
In1-O2-In3	133.78	In3-O13-In6	103.42
In2-O11-In4	104.19	In4-O3-Dy1	111.62
In2-O3-In4	98.66	In4-O3-In5	99.27
In2-O3-Dy1	122.20	In4-O10-In5	101.84
In2-O3-In5	102.37	In5-O4-Dy2	121.56
In2-O5-In5	98.62	In5-O4-In6	100.19
In2-O5-In3	97.79	In5-O12-In6	102.10
In2-O6-In3	106.49	Dy1-O7-Dy2	121.22
In3-O4-In5	101.94	Dy1-O8-Dy2	105.54
In3-O4-Dy2	119.12		

The molecular magnetism of {3d} transition metals has been investigated significantly for decades as a result of their accessibility and low cost. As the research area matured eyes fell upon the later parts of the periodic table, in particular ruthenium. Initially this appears to have been in the form of {3d-4d} ruthenium heterometallic complexes, of which numerous examples are known.[248-253] In the mid to late 2000s a transition occurred to pure {4d} homometallic molecular magnets of ruthenium, and later other {4d} metals.[190, 254-257] Once again a transition was seen in the early 2010s towards lanthanide based complexes, with the first {4d-4f} ruthenium complex described by Norel and Rigaut *et. al.* producing a carbon-rich ruthenium decorated dysprosium SMM.[258] This work catalysed further investigations into {4d-4f} molecules within more typically recognisable motifs, such as the $\{Ru_2Dy_2\}$ butterfly, first synthesised by Langley et al.[247] and described as **C21** in this thesis. This was the starting point for the investigations discussed in this chapter, leading to the characterisation of seven novel complexes with the recognisable butterfly motif. The number of known {4d-4f} heterometallic complexes is low to this day, and the information therein represents a significant expansion to the body of knowledge. Additionally, an expanded butterfly, **C29**, is described, which appears to be a unique configuration in the literature.

The bonding structure exhibited in **C30** displays similar characteristics to those observed in previous literature for tris-bidentate octahedral transition metal complexes and may in fact exhibit similar optical properties through isomerism. If we consider each blade component to act as a bidentate ligand around the central indium atom, we can consider the structure as represented in **Figure 144** to be a delta, Δ, optical isomer. It is possible that the large residuals in **Table S6** may result from the crystal growing from a racemic mixture of the two enantiomers. Similar serendipitous assemblies of racemic Δ/Λ propeller complexes have been detailed in the work of Novitchi and Powell et al., as a supramolecular "double-propeller" dimer of hexanuclear $\{Cu_3Dy_3\}$ complexes.[259]

5.2.2 Magnetic Susceptibility Studies

This section discusses the magnetic data collected for six crystal samples: **C21**, **C22**, **C23**, **C26**, **C27** and **C28**:

C21- $[Ru^{III}_2Dy^{III}_2(OMe)_2(Benz)_4(MDEA)_2(NO_3)_2]$

C22- $[Ru^{III}_2Dy^{III}_2(OMe)_2(p\text{-}Tol)_4(MDEA)_2(MeOH)_4]Cl_2$

C23- $[Ru^{III}_2Dy^{III}_2(OMe)_2(Acac)_4(EDEA)_2(NO_3)_2]$

C26- $[Ru^{III}_2Dy^{III}_2(OMe)_2(2\text{-}Cl\text{-}4,5\text{-}F\text{-}Benz)_4(MDEA)_2(NO_3)_2]$

C27- $[Ru^{III}_2Gd^{III}_2(OMe)_2(Benz)_4(MDEA)_2(NO_3)_2]$

C28- $[Ru^{III}_2Gd^{III}_2(OMe)_2(Acac)_4(EDEA)_2(NO_3)_2]$

Direct current (dc) magnetic susceptibility analysis was undertaken on polycrystalline samples of complexes **C21-23** and **C26-28**. Initial analysis was completed over the temperature range 2-300 K in dc fields of 0.1 T and 1.0 T. The resultant $\chi_M T$ vs. T plots can be found in **Figure 147** and **Figure 148**. Data for the initial compound, **C21,** has been previously published[247] and can be found in **Appendix F**. Extracted from the data collected are values of the molar magnetic susceptibility times temperature, $\chi_M T$, of 28.83, 29.96 and 29.12 $cm^3\ K\ mol^{-1}$ for the $\{Ru^{III}_2Dy^{III}_2\}$ complexes **C22**, **C23** and **C26** respectively at 300 K. These values broadly correlate with the calculated values for two Dy^{III} ($S = 5/2$, $L = 5$, $J = 15/2$, $^6H_{15/2}$, $g_J = 4/3$, $C = 14.17\ cm^3\ K\ mol^{-1}$) and two Ru^{III} ($S = 1/2$, $g = 2.0$, $C = 0.37\ cm^3\ K\ mol^{-1}$) non-interacting centres ($(2 \times 14.17) + (2 \times 0.37) = 29.08\ cm^3\ K\ mol^{-1}$). Values of C are calculated using equations 2, 5 and 9 found in **Chapter 1**. Similarly, the experimental values of $\chi_M T$ for **C27** and **C28**, 16.61 and 16.69 respectively at 300 K, correlate strongly with the calculated values for two Ru^{III} (As previous) and two Gd^{III} ($S = 7/2$, $L = 0$, $J = 7/2$, $^8S_{7/2}$, $g_J = 2.0$, $C = 7.88\ cm^3\ K\ mol^{-1}$) non-interacting centres ($(2 \times 7.88) + (2 \times 0.37) = 16.52\ cm^3\ K\ mol^{-1}$).

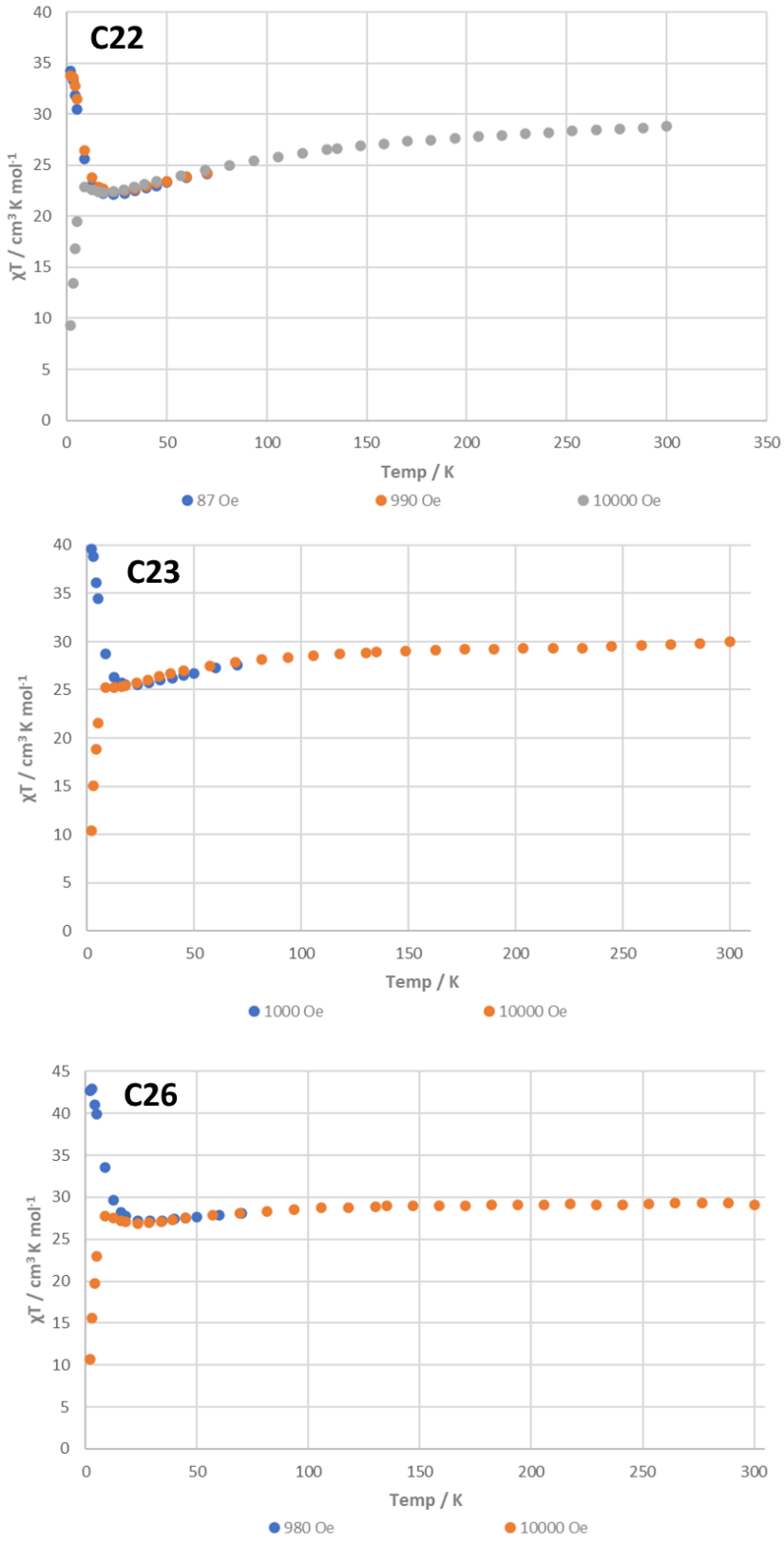

Figure 147- Plots of $\chi_M T$ vs T for the dysprosium containing samples **C22**, **C23**, **C26** measured under an applied magnetic field of different strength.

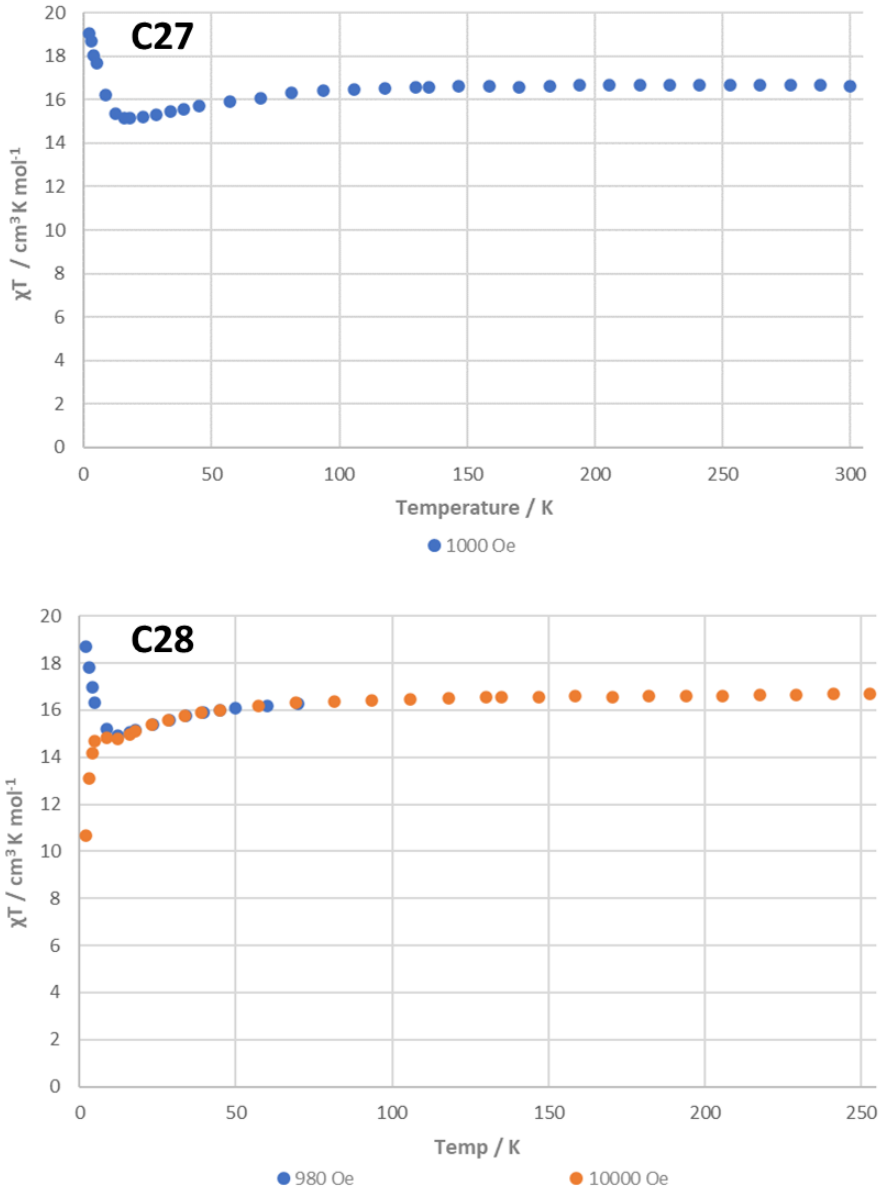

Figure 148- Plots of $\chi_M T$ vs T for gadolinium analogues, samples **C27**, **C28** measured under an applied magnetic field of different strengths.

The profiles of the $\chi_M T$ vs. T plots for the dysprosium analogues are indicative of variations in the magnetic exchange interactions. This is likely a result of subtle differences in the structure of the complexes and therefore different bridging pathways. As shown by the experiments at 1 T, for all three novel dysprosium containing samples, as the temperature decreases the $\chi_M T$ product also decreases until reaching about 25 K. At this point a differentiation in shape is observed, as samples **C22** and **C26** exhibit an upturn, whilst sample **C23** instead plateaus. Experiments at 0.1 T for all three samples instead exhibit a large upturn under 25 K. This low temperature behaviour can be

attributed to the Zeeman splitting of the ground state multiplet and is therefore field dependant. This further suggests non-negligible exchange interactions between the ion centres. As the temperature decreases from 300-25 K the $\chi_M T$ value slowly decreases which can be attributed to the depopulation of the excited m_J states of the Dy^{III} ions, although this effect is less apparent for **C26**. The dc magnetic susceptibility measurements on polycrystalline samples of the Gd^{III} analogues, complexes **C27** and **C28** have also been performed over the same temperature range and in the same dc field strengths.

The isothermal magnetisation, M, plotted as a function of the magnetic field, H, was collected over six incremental steps within the temperature range of 2-20 K for each of the novel samples. These plots are shown in **Figure 149** and **Figure 150**. All five samples display a rapid increase in magnetisation up to 2 T, before reaching a steady, near-linear increase without attaining saturation. In combination with the field dependency demonstrated by the magnetic susceptibility plots, this would suggest the samples exhibit a significant magnetic anisotropy. Successive increases in the temperature at which the experiments were run prove to increase the overall linearity of the line shape.

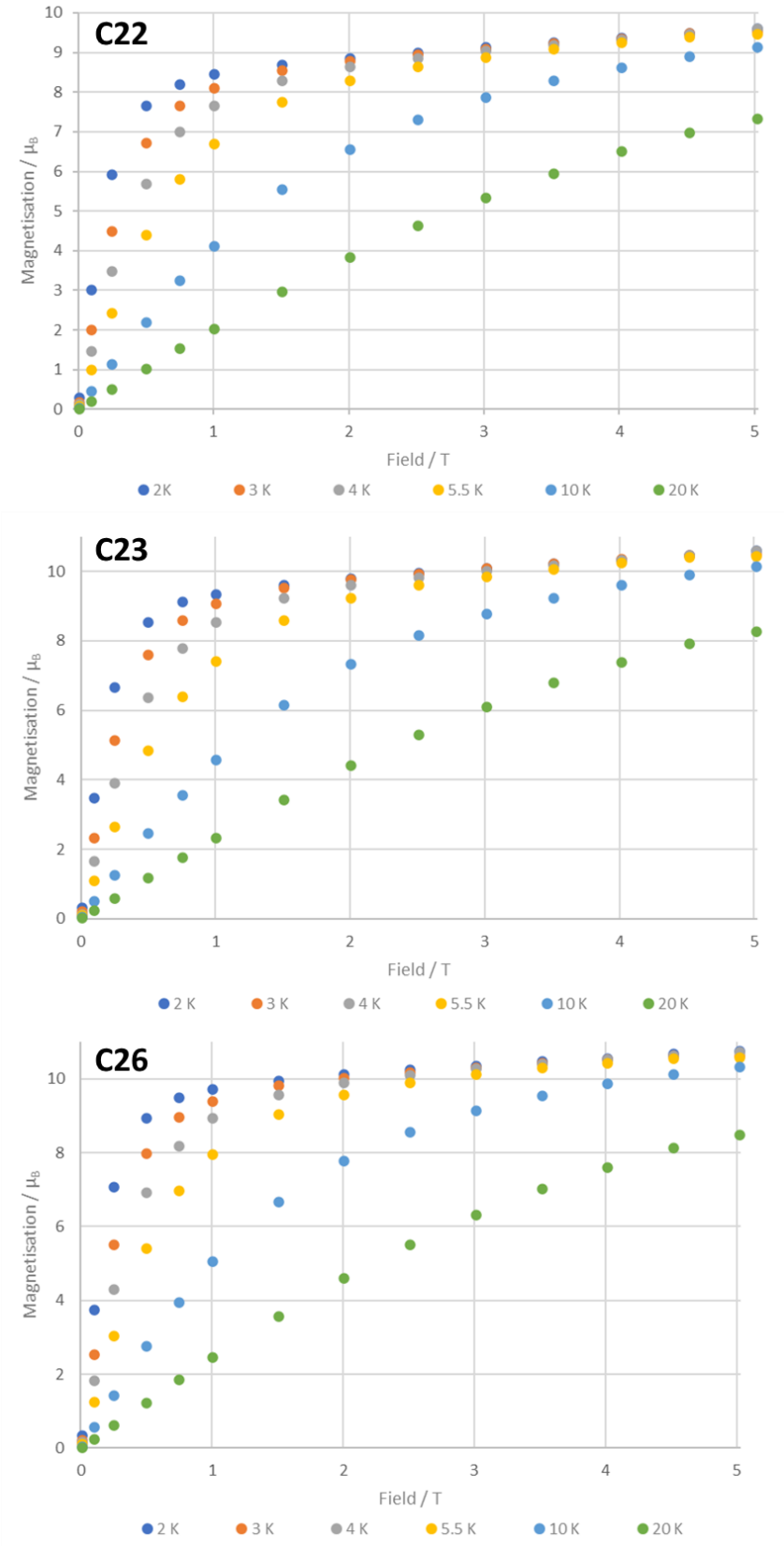

Figure 149- Plots of M vs H for the dysprosium containing samples **C22**, **C23**, **C26**, taken in increments between 2-20 K.

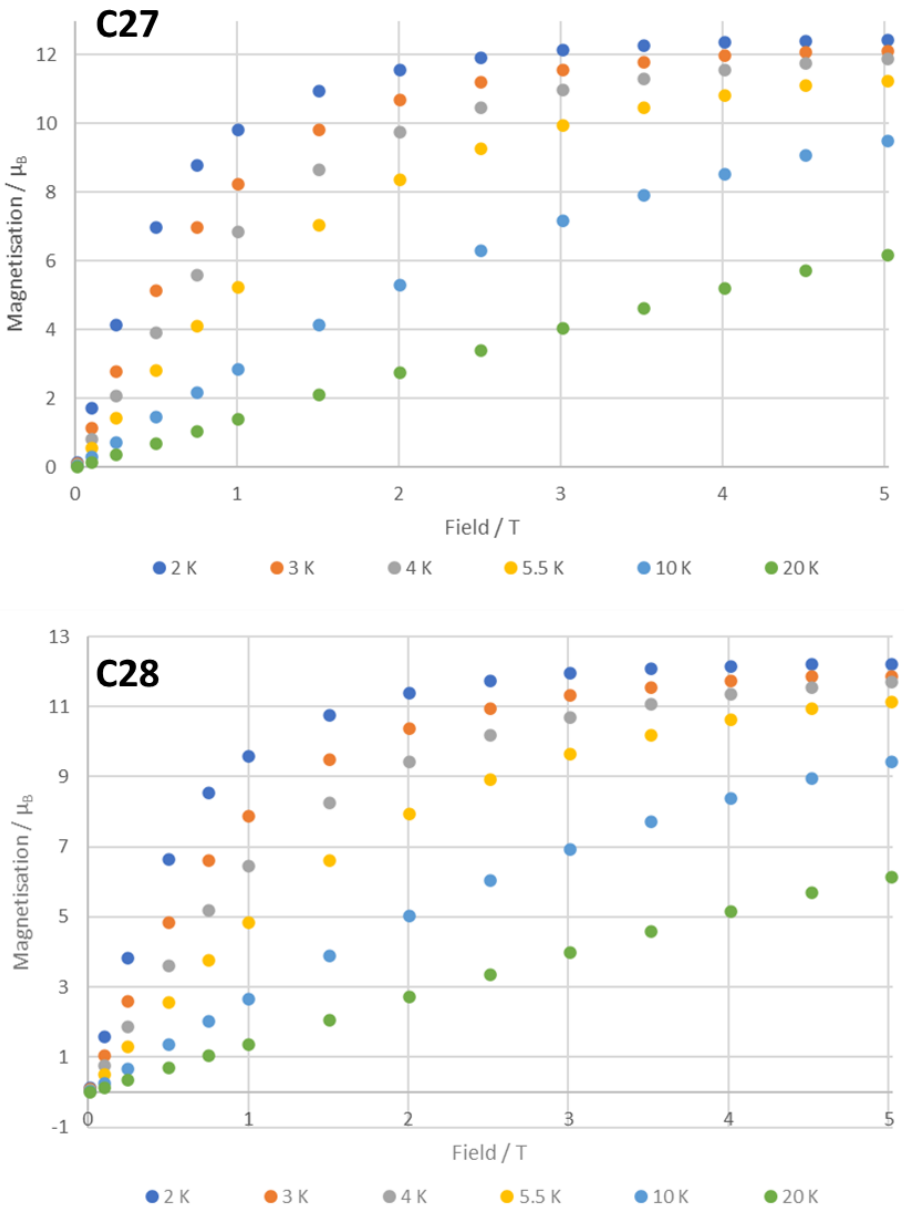

Figure 150- Plots of M vs H for gadolinium analogues, samples **C27**, **C28**, taken in increments between 2-20 K.

In order to further probe for slow magnetic relaxation within the $\{Ru^{III}_2Dy^{III}_2\}$ complexes additional experiments were performed to ascertain alternating current (ac) susceptibility measurements. These experiments were performed in an oscillating ac field of 3.5 Oe under a zero applied dc field. This resulted in two types of plot, the out-of-phase molar magnetic susceptibility, χ''_M, plotted against either variable temperature or variable frequency. These measurements revealed clear frequency and temperature dependant maxima (1.8-5 K) in the out-of-phase component for samples **C21** and **C26**. These maxima are indicative of SMM behaviour. Similar analysis for samples **C22** and

C23 revealed tails of peaks at the lowest temperatures measured; further analysis below 1.8 K would be necessary to fully characterise these complexes. As a result of slow relaxation being exhibited at higher temperatures, samples **C21** and **C26** can be considered better SMMs than samples **C22** and **C23**. Plots of χ''_M vs frequency for samples **C21** and **C26** can be found in **Figure 151**.

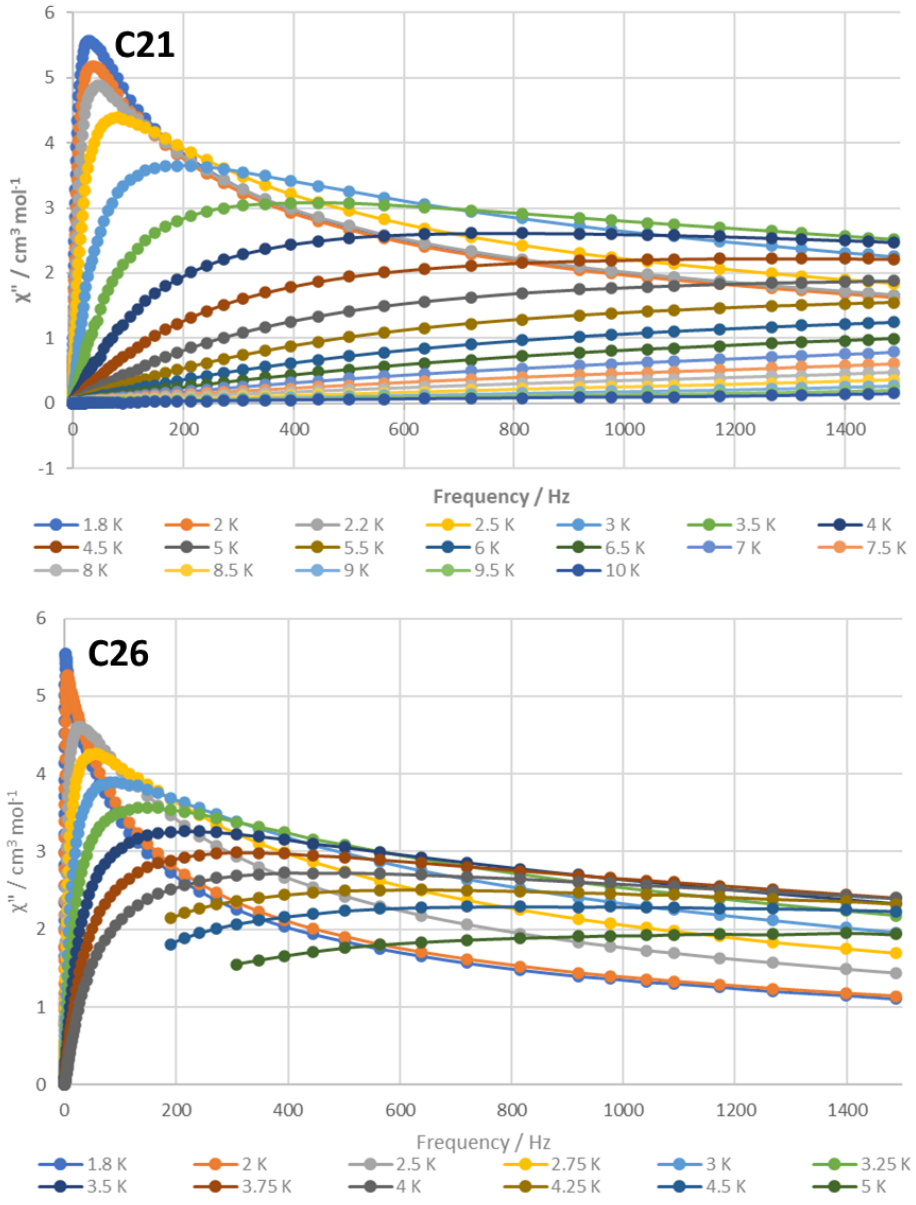

Figure 151- Plots of χ'' vs Frequency for samples **C21**, **C26**.

Cole-Cole plots for said samples communicate semicircular profiles, as seen in **Figure 152**, these are suggestive of complexes undergoing a single relaxation process.

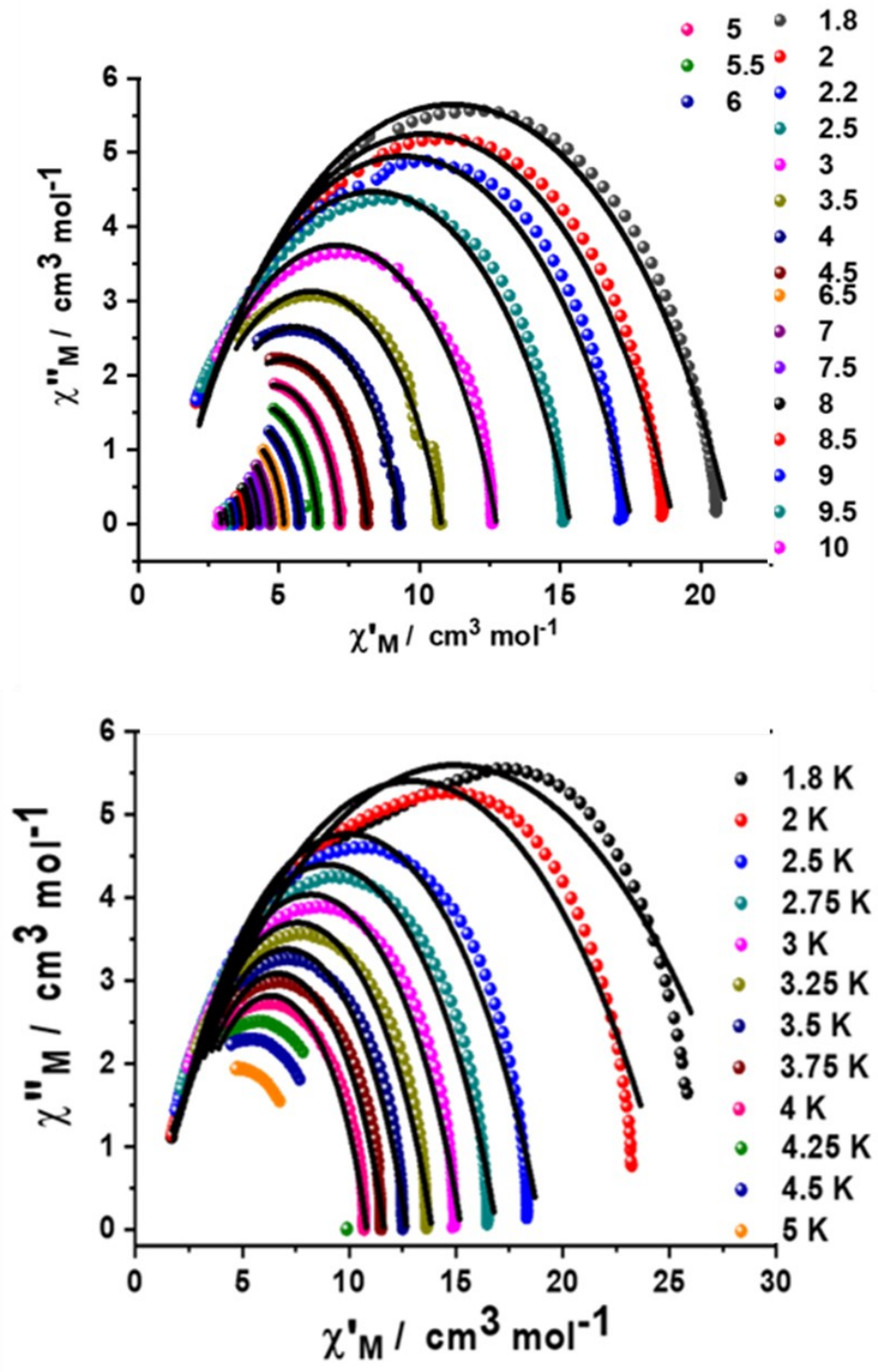

Figure 152- Cole-Cole plots of χ'' vs χ' for samples **C21**, top; and **C26**, bottom.

Samples **C22** and **C23** only show out-of-phase signals beginning to appear under a zero dc field down to temperatures of 1.8 K, however an out-of-phase signal is observed in the presence of a static dc field of 500 Oe and 2000 Oe, respectively, as shown in **Figure 153**. It is hypothesised that the appearance of these maxima can be assigned to the quenching of the QTM relaxation processes often found in Ln^{III} SMMs.

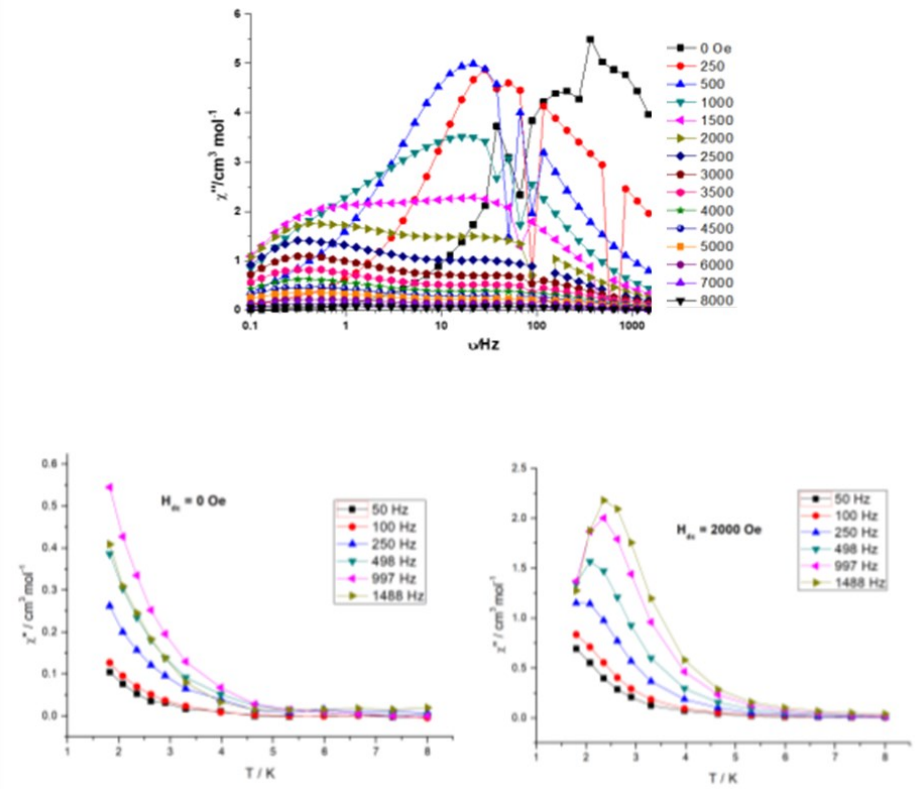

Figure 153- Plots of χ'' data for samples **C22**, top; and **C23**, bottom.

Similarly, the $\{Ru^{III}_2Gd^{III}_2\}$ complexes, **C27** and **C28**, exhibited no signal in a zero applied field, although **C28** produced out-of-phase tails at 2000 Oe, **Figure 154**. This tail is presumed to be due to the presence of anisotropic Ru^{III} ions within the complex.

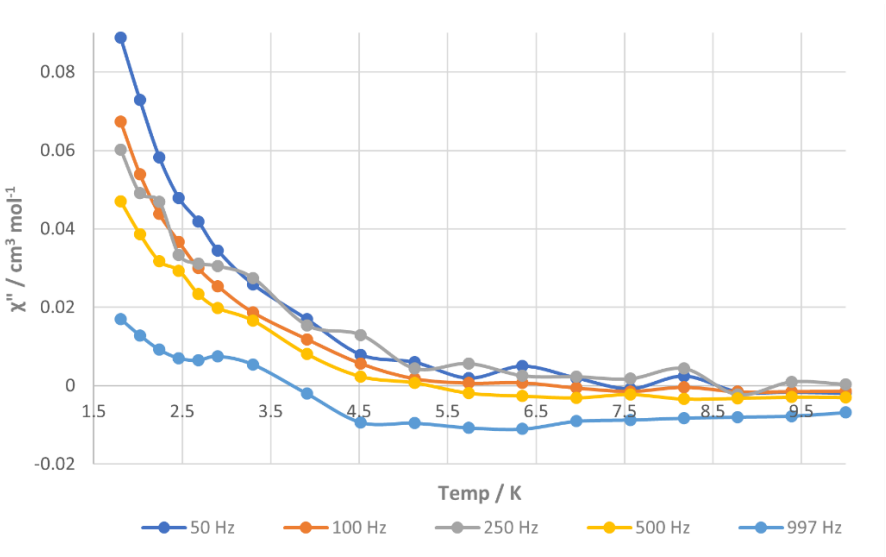

Figure 154- Plot of χ'' vs T at 2000 Oe for sample **C28**.

Previously published[247] analysis of sample **C21** produced a U_{eff} parameter of 10.4 cm^{-1}, but this calculation only considers the Orbach relaxation processes. The further analysis, for both **C21** and **C26**, presented for this thesis and published in 2021,[260] utilises the temperature dependant relaxation data and CC-FIT[245] to extract the relaxation times in consideration of all possible relaxation pathways. This is completed by fitting the data for both samples to **Eq^n 19**, given below.

Eq^n 19: $$\frac{1}{\tau} = \frac{1}{\tau_{QTM}} + CT^n + {\tau_0}^{-1} \cdot e^{U_{eff}/k_B T}$$

Where the red component corresponds to relaxation by a quantum tunnelling pathway, the blue component corresponds to relaxation by Raman processes and the green component accounts for relaxation by Orbach processes.

The values extracted from the best fit are as follows: **C21**, n = 6.3 ± 0.1, C = 1.0 ± 0.1 s^{-1} $K^{-6.3}$, U_{eff} = 41 ± 1 K (28 cm^{-1}) and τ_0 = 1.01 ± 0.02 × 10^{-11} s, τ_{QTM} = 0.0006 s; **C26**, n = 6.0 ± 0.2, C = 0.9 ± 0.1 s^{-1} K^{-6} , U_{eff} = 45 ± 2 K (31 cm^{-1}) and τ_0 = 1.01 ± 0.02 × 10^{-10} s, τ_{QTM} = 0.04 s. The variance between the values of U_{eff} for sample **C21** between purely Orbach processes and when considering all possible relaxation pathways is distinct and reveals the importance of undertaking a complete analysis of relaxation data for these {4d-4f} complexes.

5.3 Chapter Summary

In this chapter the syntheses and analyses of ten complexes have been described, including eight conventional butterfly complexes, **C21-28**, one asymmetric amine polyalcohol ligand containing complex, **C29**, alongside another larger {5p-4f} asymmetric amine polyalcohol ligand containing complex, **C30**. Structural data was collected for all the samples **C21**-**C30**, of which nine are thought to be novel at the time of research. Not only are these structures novel, but examples of $\{Ru^{III}_2\text{-}Ln^{III}_2\}$ complexes such as **C22**-**C28**, prove exceedingly rare within the literature at the time of research. Magnetic analysis was undertaken on six samples, **C21-23** and **C26-28**, with ac and dc data collected for all six samples. No hysteresis was observed from any of the samples tested, and fits were undertaken to model the relaxation of samples **C21** and **C26** as a combination of Orbach, Raman and QTM processes, in comparison to the previously published fits for **C21** as an Orbach only relaxation process. U_{eff} values were extrapolated for samples **C21** and **C26** of 41±1 K and 45±2 K respectively. Given the very similar core structures, of **C21** and **C26** we can begin to allocate the differences in magnetic properties as a result of the structural variations between the two. The immediately apparent structural difference between the two complexes is the replacement of benzoates in **C21** with the far more electron withdrawing moiety 2-chloro-4,5-difluoro benzoate. In addition to this the change in ligand may have influenced the bond angles within the $\{Ru^{III}_2\text{-}Dy^{III}_2\}$ cores. Small variations of these values can cause large variations in the complexes magnetic properties as described qualitatively by the Goodenough-Kanamori rules.

5.4 Experimental

All information relating to the sourcing of chemicals, technical specification of instrumentation, data processing procedures and software can be found in the appendices. Pertinent to this chapter are **Appendix A**, **B** and **F** for synthetic procedures, single-crystal X-ray diffraction analysis and magnetism respectively.

5.4.0 General Synthetic Method

The subsequent synthetic method and stoichiometries were used in the following reactions, unless otherwise noted in the specific entry for each target molecule. In terms of this general method the transition metal nitrate hydrates, $TM(NO_3)_x{\cdot}yH_2O$, used within this chapter were ruthenium and indium whilst the lanthanide metal nitrate hydrates, $Ln(NO_3)_3{\cdot}xH_2O$, used were dysprosium and gadolinium. The bidentate ligands used in the reaction series were benzoic acid, 2-trifluoromethylbenzoic acid, 2,3,4,5-tetrafluorobenzoic acid, 2-chloro-4,5-difluorobenzoic acid, p-toluic acid and acetyl acetone. No more than one transition metal, one lanthanide species and one bidentate ligand were involved in any one reaction.

In a small reaction vessel containing a stirrer bar, acetonitrile (20 mL) and methanol (5 mL) were dissolved $TM(NO_3)_x{\cdot}yH_2O$ (0.5 mmol), $Ln(NO_3)_3{\cdot}xH_2O$ (0.5 mmol), carboxylic acid (1 mmol) and [**L**]H_2 (0.5 mmol) respectively, ensuring each component was fully dissolved prior to addition of the next reagent. The solution was stirred continuously as the reaction was activated with triethylamine (2 mmol), dropwise over thirty seconds, and was then allowed to stir for a further two hours. Upon completion of the reaction, the solution was allowed to cool fully overnight, without stirring, and gravity filtered to remove any deposited solid material. The solvent was then removed by rotary evaporation to yield an oil, prior to successive, portionwise crystallisation attempts.

5.4.1 $[Ru^{III}_2Dy^{III}_2(OMe)_2(Benz)_4(MDEA)_2(NO_3)_2]$, C21

$RuCl_3{\cdot}3H_2O$ (131 mg, 0.5 mmol), $Dy(NO_3)_3{\cdot}5H_2O$ (219 mg, 0.5 mmol), benzoic acid (122 mg, 1 mmol) and [**MDEA**]H_2 (60 mg, 0.5 mmol) were added consecutively to acetonitrile (20 mL). The solution was stirred continuously as the reaction was activated with triethylamine (0.28 mL, 2 mmol), dropwise over thirty seconds. The reaction was then allowed to stir for a further two hours. The resultant brown solution was left overnight, and gravity filtered to remove any deposited solids, after which time the solvent was removed to give a brown oil. Single crystals of **C21** were grown over 5-7 days by layer diffusion using methanol to redissolve the oil which was then layered with diethyl ether, yielding small yellow block crystals (approx. 46%). The title structure was confirmed by SC-XRD with a molecular formula: $C_{40}H_{48}Dy_2N_4O_{20}Ru_2$.

5.4.2 $[Ru^{III}_2Dy^{III}_2(OMe)_2(p\text{-}Tol)_4(MDEA)_2(MeOH)_4]Cl_2$, C22

$RuCl_3{\cdot}3H_2O$ (131 mg, 0.5 mmol), $Dy(NO_3)_3{\cdot}5H_2O$ (219 mg, 0.5 mmol), p-toluic acid (136 mg, 1 mmol) and [**MDEA**]H_2 (60 mg, 0.5 mmol) were added consecutively to acetonitrile (20 mL). The solution was stirred continuously as the reaction was activated with triethylamine (0.28 mL, 2 mmol), dropwise over thirty seconds. The reaction was then allowed to stir for a further two hours. The resultant solution was left overnight, and gravity filtered to remove any deposited solids, after which time the solvent was removed to give a brown oil. Single crystals of **C22** were grown over 5-7 days by layer diffusion using methanol to redissolve the oil, which was then layered with diethyl ether, yielding small yellow plate crystals (approx. 33%). The title structure was confirmed by SC-XRD with a molecular formula: $C_{48}H_{72}Cl_2Dy_2N_2O_{18}Ru_2$.

5.4.3 $[Ru^{III}_2Dy^{III}_2(OMe)_2(Acac)_4(EDEA)_2(NO_3)_2]$, C23

$RuCl_3{\cdot}3H_2O$ (131 mg, 0.5 mmol), $Dy(NO_3)_3{\cdot}5H_2O$ (219 mg, 0.5 mmol), acetylacetone (100 mg, 1 mmol) and [**EDEA**]H_2 (67 mg, 0.5 mmol) were added consecutively to acetonitrile (20 mL). The solution was stirred continuously as the reaction was activated with triethylamine (0.28 mL, 2 mmol), dropwise over thirty seconds. The reaction was then allowed to stir for a further two hours. The resultant solution was left overnight, and

gravity filtered to remove any deposited solids, after which time the solvent was removed to give a brown oil. Single crystals of **C23** were grown over 5-7 days by layer diffusion using a MeOH:Et_2O (1:3) solvent system, yielding small yellow plate crystals (approx. 33%). The title structure was confirmed by SC-XRD with a molecular formula: $C_{34}H_{60}Dy_2N_4O_{20}Ru_2$.

5.4.4 $[Ru^{III}_2Dy^{III}_2(OMe)_2(2\text{-}F_3C\text{-}Benz)_4(MDEA)_2(NO_3)_2]$, C24

$RuCl_3{\cdot}3H_2O$ (131 mg, 0.5 mmol), $Dy(NO_3)_3{\cdot}5H_2O$ (219 mg, 0.5 mmol), 2-trifluoromethylbenzoic acid (190 mg, 1 mmol) and [**MDEA**]H_2 (60 mg, 0.5 mmol) were added consecutively to acetonitrile (20 mL). The solution was stirred continuously as the reaction was activated with triethylamine (0.28 mL, 2 mmol), dropwise over thirty seconds. The reaction was then allowed to stir for a further two hours. The resultant brown solution was left overnight, and gravity filtered to remove any deposited solids. Single crystals of **C24** were grown over 5-7 days by layer diffusion using a MeOH:Et_2O (1:3) solvent system, yielding small dark purple plate crystals (28%). The title structure was confirmed by SC-XRD with a molecular formula: $C_{44}H_{44}Dy_2F_{12}N_4O_{20}Ru_2$.

5.4.5 $[Ru^{III}_2Dy^{III}_2(OMe)_2(2,3,4,5\text{-}tet\text{-}F\text{-}Benz)_4(MDEA)_2(NO_3)_2]$, C25

$RuCl_3{\cdot}3H_2O$ (131 mg, 0.5 mmol), $Dy(NO_3)_3{\cdot}5H_2O$ (219 mg, 0.5 mmol), 2,3,4,5-tetrafluorobenzoic acid (194 mg, 1 mmol) and [**MDEA**]H_2 (60 mg, 0.5 mmol) were added consecutively to acetonitrile (20 mL). The solution was stirred continuously as the reaction was activated with triethylamine (0.28 mL, 2 mmol), dropwise over thirty seconds. The reaction was then allowed to stir for a further two hours. The resultant brown solution was left overnight, and gravity filtered to remove any deposited solids. Single crystals of **C25** were grown over 5-7 days by layer diffusion using a MeOH:Et_2O (1:3) solvent system, yielding small brown plate crystals (23%). The title structure was confirmed by SC-XRD with a molecular formula: $C_{40}H_{32}Dy_2F_{16}N_4O_{20}Ru_2$.

5.4.6 $[Ru^{III}_2Dy^{III}_2(OMe)_2(2\text{-Cl-}4,5\text{-F-Benz})_4(MDEA)_2(NO_3)_2]$, C26

$RuCl_3{\cdot}3H_2O$ (131 mg, 0.5 mmol), $Dy(NO_3)_3{\cdot}5H_2O$ (219 mg, 0.5 mmol), 2-chloro-4,5-difluorobenzoic acid (193 mg, 1 mmol) and [**MDEA**]H_2 (60 mg, 0.5 mmol) were added consecutively to acetonitrile (20 mL). The solution was stirred continuously as the reaction was activated with triethylamine (0.28 mL, 2 mmol), dropwise over thirty seconds. The reaction was then allowed to stir for a further two hours. The resultant solution was left overnight, and gravity filtered to remove any deposited solids, after which time the solvent was removed to give a brown oil. Single crystals of **C26** were grown over 5-7 days by layer diffusion using a MeOH:Et_2O (1:3) solvent system, yielding small brown plate crystals (approx. 33%). The title structure was confirmed by SC-XRD with a molecular formula: $C_{40}H_{36}Cl_4Dy_2F_8N_4O_{20}Ru_2$.

5.4.7 $[Ru^{III}_2Gd^{III}_2(OMe)_2(Benz)_4(MDEA)_2(NO_3)_2]$, C27

$RuCl_3{\cdot}3H_2O$ (131 mg, 0.5 mmol), $Gd(NO_3)_3{\cdot}6H_2O$ (226 mg, 0.5 mmol), benzoic acid (122 mg, 1 mmol) and [**MDEA**]H_2 (60 mg, 0.5 mmol) were added consecutively to acetonitrile (20 mL). The solution was stirred continuously as the reaction was activated with triethylamine (0.28 mL, 2 mmol), dropwise over thirty seconds. The reaction was then allowed to stir for a further two hours. The resultant solution was left overnight, and gravity filtered to remove any deposited solids, after which time the solvent was removed to give a brown oil. Single crystals of **C27** were grown over 5-7 days by layer diffusion using a MeOH:Et_2O (1:3) solvent system, yielding small brown plate crystals (approx. 33%). The title structure was confirmed by SC-XRD with a molecular formula: $C_{40}H_{48}Gd_2N_4O_{20}Ru_2$.

5.4.8 $[Ru^{III}_2Gd^{III}_2(OMe)_2(Acac)_4(EDEA)_2(NO_3)_2]$, C28

$RuCl_3{\cdot}3H_2O$ (131 mg, 0.5 mmol), $Gd(NO_3)_3{\cdot}6H_2O$ (226 mg, 0.5 mmol), acetylacetone (100 mg, 1 mmol) and [**EDEA**]H_2 (67 mg, 0.5 mmol) were added consecutively to acetonitrile (20 mL). The solution was stirred continuously as the reaction was activated with triethylamine (0.28 mL, 2 mmol), dropwise over thirty seconds. The reaction was then allowed to stir for a further two hours. The resultant solution was left overnight, and

gravity filtered to remove any deposited solids, after which time the solvent was removed to give a brown oil. Single crystals of **C28** were grown over 5-7 days by layer diffusion using a MeOH:Et_2O (1:3) solvent system, yielding small yellow plate crystals (approx. 33%). The title structure was confirmed by SC-XRD with a molecular formula: $C_{34}H_{60}Gd_2N_4O_{20}Ru_2$.

5.4.9 $[Ru^{III}_2Dy^{III}_4(OH)_2(OMe)_2(Benz)_{10}(HMAP)_2(MeOH)_2]$, C29

$RuCl_3{\cdot}3H_2O$ (131 mg, 0.5 mmol), $Dy(NO_3)_3{\cdot}5H_2O$ (219 mg, 0.5 mmol), benzoic acid (122 mg, 1 mmol) and [**HMAP**]H_2 (67 mg, 0.5 mmol) were added consecutively to a solvent mixture of methanol (5mL) and acetonitrile (20 mL). The solution was stirred continuously as the reaction was activated with triethylamine (0.28 mL, 2 mmol), dropwise over thirty seconds. The reaction was then allowed to stir for a further two hours. The resultant dark brown solution was left overnight, and gravity filtered to remove any deposited solids. Single crystals of **C29** were grown over 4-6 weeks by slow deposition from the mixed reaction solvents, yielding small red-brown plate crystals (approx. 25%). The title structure was confirmed by SC-XRD with a molecular formula: $C_{86}H_{92}Dy_4N_2O_{30}Ru_2$.

5.4.10 $[In^{III}_{16}Dy^{III}_6(O)_6(OH)_{12}(OMe)_3(Benz)_{22}(HMAP)_6(NO_3)_5]$, C30

$In(NO_3)_3{\cdot}6H_2O$ (204 mg, 0.5 mmol), $Dy(NO_3)_3{\cdot}5H_2O$ (219 mg, 0.5 mmol), benzoic acid (122 mg, 1 mmol) and [**HMAP**]H_2 (67 mg, 0.5 mmol) were added consecutively to a solvent mixture of methanol (5mL) and acetonitrile (20 mL). The solution was stirred continuously as the reaction was activated with triethylamine (0.28 mL, 2 mmol), dropwise over thirty seconds. The reaction was then allowed to stir for a further four hours. The resultant clear solution was left overnight, and gravity filtered to remove any deposited solids. Single crystals of **C30** were grown over 6-8 weeks by slow evaporation from the mixed reaction solvents, yielding small colourless block crystals (approx. 12%). The title structure was confirmed by SC-XRD with a molecular formula: $C_{193}H_{209}Dy_6In_{16}N_{11}O_{92}$.

6 Conclusions

In the course of this body of work, four major targets were identified in their relevant chapters, each chapter developing its own synthetic series. For the [**DIPSO**]H_4 synthetic series, fourteen complexes were successfully derived and structurally elucidated. These complexes demonstrate a wide variety of binding modes for [**DIPSO**]H_4 in its partially or fully deprotonated states which can therefore influence the magneto-structural properties of the overall complex. [**DIPSO**]H_4, as our binding ligand paradigm, along with a serendipitous method of self-assembly generated thirteen novel complexes **C1-3** and **C5-13.** In addition, the [**DIPSO**]H_4 structure proved not only to be an effective serendipitous chelator but also a potential bridging ligand between monomers within larger structural arrays.

The second synthetic series produced in chapter 3, of amine polyalcohol ligands and precursors, should also be considered successful, in a considerably different manner. Although none of the compounds reported as pure were themselves novel, the pathways to attain them were. These previously unreported synthetic pathways provide generally significant improvements over previous methods, whether in terms of yield produced or reaction time. Furthermore, the method developed as an adaptation of the Shi synthetic method, proved to be effective at preventing reaction cascades in the haloalkane substitutions by creating a stepwise methodology. These materials once sufficiently pure were also usable in the complexation for later chapters.

The third synthetic series were those produced by targeting {3d-4f} complexes bound by asymmetric polyalcohol ligands, synthesised as part of synthetic series two. These six complexes not only grow the motif of the butterfly complex by introducing new potential bridging ligands to the motif to modify the core structure, but they also provide credence to the fact that asymmetry would have a perceivable effect on the butterfly complex, as shown in the magnetic data of complex **C16**. This material demonstrates improved parameters such as the coercivity of its hysteresis loop. As a result of the effects on the exchange interactions observed, these novel complexes confirm the need

for additional research into this phenomenon towards the improvement of magnetic properties of molecules.

The final synthetic series, based upon both symmetric and asymmetric ligands produced as a part of synthetic series two resulted in eight new $\{Ru^{III}_2\text{-}Ln^{III}_n\}$ structures and a new indium based {5p-4f} topology. Not only are these complexes exceedingly rare in the field of molecular magnetism, but they also show how the modification of capping ligands to more electron withdrawing groups can influence or even improve the magnetic properties of the materials whilst also further enhancing the breadth of the motif with asymmetric ligands.

The work presented in this thesis has contributed to the following publications which can be found attached in Appendix G:

K. R. Vignesh, **R. B. C. Martin**, G. Miller, G. Rajaraman, K. S. Murray and S. K. Langley, Polyhedron, 2019, **170**, 508.

A. Swain, **R. Martin**, K. R. Vignesh, G. Rajaraman, K. S. Murray and S. K. Langley, Dalton Trans., 2021, **50**, 12265–12274.

6.1 Future Work

In the course of this thesis, eighteen organic molecules, thirty complexes and magnetic datasets for thirteen samples were collated. In the first case, the aim of any future work should be to equalise the number of complexes and datasets available. By doing so, we are able to extract more pertinent information that may reveal patterns not yet apparent in our current dataset. To do so, repeat syntheses should be attempted at both the original stoichiometries and in stoichiometries derived from our target product.

On top of extending our dataset with magnetic data extracted from samples not yet tested, attempts should also be made to improve the quantity and quality of information extrapolated from our currently available datasets. To do so, computational studies should be undertaken to extrapolate J exchange coupling values and further elucidate relaxation pathways undertaken by the complexes. These J values can then be used to develop magneto-structural correlations for complexes to see if any patterns can be found. Such correlations could then be used as predictive tools for future butterfly SMM synthesis. In the case of samples where molecular magnetic properties are seemingly present but no out-of-phase χ'' is seen at 2K, further low temperature studies should be targeted.

Following in the path of Langley and Murray further complexes should be targeted with highly electron withdrawing character allocated to its ligands. Similarly, to the process shown in chapter 5 for the ruthenium {4d-4f} complexes exchanging the benzoic acid component can have a substantial effect on the magnetic profile of the material. As shown by Langley *et al.,* in 2016, by replacing the benzoic acid ligands with a more electron withdrawing group, 2-chloro-4,5 difluorobenzoic acid, the coercive magnetic field can be increased to 4.4 T.[184] As previously discussed in **Chapter 4**, the coercive field was also increased from the original 2.8 T[131] in the Langley and Murray *et al.* paper, 2013, to 3 T for sample **C16** by replacement of the [**MDEA**]$^{2-}$ ligand with our [**HEAP**]$^{2-}$ ligand. With these facts in mind, a further study should be conducted to determine whether these processes are constructive for the overall magnetic properties, or do they lie as another mutually exclusive parameter that must be fine-tuned for the greatest properties to manifest?

Finally, our studies of {4d-4f} complexes have been very limited in their scope, focussing entirely on Ru(III). But Wang and Dunbar *et al.,* in 2011 collated the studies of {4d} and {5d} transition metals in molecular magnetic materials which could inspire new targets. In addition, in 2021, Darago and Long *et al.* described a series of MoS_4^{3-}-bridged dilanthanide complexes that further elucidated a potentially generalisable route to enhanced {nd-4f} magnetic exchange. These studies indicate a feasibility for magnetic interactions for molybdenum, rhenium, tungsten, and niobium. Molybdenum and niobium should exhibit similarly diffuse orbitals to ruthenium whilst tungsten and rhenium could theoretically exemplify this facet to an even greater extent. In their common oxidation states Nb(V), Mo(VI), W(VI) and Re(VII) would behave diamagnetically but if the metals could be held in their other stable oxidation states, Mo(IV), W(IV), Re(VI), Re (IV), Re(II), they would behave paramagnetically in an octahedral ligand field. Ideally, studying the chemistry of Mo(III), a less common oxidation state, or Re (IV) in an octahedral field, could see a quenching of orbital momentum similar to that observed in Cr(III) with a half-filled t_{2g} ground state.

7 References

1. P. W. Selwood, *Magnetochemistry*, Read Books Ltd, 2013.
2. R. Boča, *A Handbook of Magnetochemical Formulae*, 2012.
3. A. Etcheverry-Berrios, S. Parsons, K. V. Kamenev, M. R. Probert, S. A. Moggach, M. Murrie and E. K. Brechin, *Journal*, 2020, **6**.
4. A. Palii, B. Tsukerblat, J. M. Clemente-Juan and E. Coronado, *International Reviews in Physical Chemistry*, 2010, **29**, 135-230.
5. E. Coronado, *Nature Reviews Materials*, 2020, **5**, 87-104.
6. H. Günther, *NMR Spectroscopy: Basic Principles, Concepts and Applications in Chemistry*, John Wiley & Sons, 2013.
7. S. Shaw and S. Constantinides, 2012.
8. N. F. Chilton, C. A. P. Goodwin, D. P. Mills and R. E. P. Winpenny, *Chemical Communications*, 2015, **51**, 101-103.
9. M. A. Riley, A. D. Walmsley, J. D. Speight and I. R. Harris, *Materials Science and Technology*, 2002, **18**, 1-12.
10. G. Bulai and O. F. Caltun, in *Ferrite Nanostructured Magnetic Materials*, eds. J. Pal Singh, K. H. Chae, R. C. Srivastava and O. F. Caltun, Woodhead Publishing, 2023, DOI: https://doi.org/10.1016/B978-0-12-823717-5.00028-0, pp. 3-15.
11. S. S. Eaton and G. R. Eaton, *Journal of Magnetic Resonance*, 2012, **223**, 151-163.
12. E. D. Commins, *Annual Review of Nuclear and Particle Science*, 2012, **62**, 133-157.
13. R. R. Li, N. C. Rubin and A. E. DePrince, III, *Journal of Chemical Theory and Computation*, 2022, **18**, 5966-5977.
14. N. W. Ashcroft, Mermin, N. D., *Solid State Physics*, Saunders College Publishing, United States, 1976.
15. R. A. Guirado-López, J. Dorantes-Dávila and G. M. Pastor, *Physical Review Letters*, 2003, **90**, 226402.
16. S.-Q. Su, S.-Q. Wu, M. L. Baker, P. Bencok, N. Azuma, Y. Miyazaki, M. Nakano, S. Kang, Y. Shiota, K. Yoshizawa, S. Kanegawa and O. Sato, *Journal of the American Chemical Society*, 2020, **142**, 11434-11441.
17. K. Hentschel, *Journal*, 2009.

18. H. C. Aspinall, *Chemistry of the f-Block Elements*, Routledge, 2018.
19. S. A. Cotton, in *Encyclopedia of Inorganic and Bioinorganic Chemistry*, 2012, DOI: https://doi.org/10.1002/9781119951438.eibc2013.
20. P. Marcon and K. Ostanina, 2012.
21. F. Martín-Hernández and E. C. Ferré, *Journal of Geophysical Research: Solid Earth*, 2007, **112**.
22. N. Matsumoto and K. Kato, *Metrologia*, 2012, **49**, 530.
23. A. A. Kaufman, R. O. Hansen and R. L. K. Kleinberg, in *Methods in Geochemistry and Geophysics*, eds. A. A. Kaufman, R. O. Hansen and R. L. K. Kleinberg, Elsevier, 2008, vol. 42, pp. 207-254.
24. T. Panczyk and P. J. Camp, *Journal of Molecular Liquids*, 2021, **330**, 115701.
25. L. Bovo, L. D. C. Jaubert, P. C. W. Holdsworth and S. T. Bramwell, *Journal of Physics: Condensed Matter*, 2013, **25**, 386002.
26. A. I. Zhernovoi and S. V. Dyachenko, *Russian Physics Journal*, 2015, **58**, 133-137.
27. E. Maurat and P.-A. Hervieux, *New Journal of Physics*, 2009, **11**, 103031.
28. J. F. Schenck, *Medical Physics*, 1996, **23**, 815-850.
29. A. Ivanyi, *Physica B: Condensed Matter*, 2000, **275**, 107-113.
30. A. F. Orchard, *Magnetochemistry*, Oxford University Press, United Kingdom, 2007.
31. D. Gatteschi and R. Sessoli, *Angewandte Chemie International Edition*, 2003, **42**, 268-297.
32. A. Srivastava, M. Sidler, A. V. Allain, D. S. Lembke, A. Kis and A. Imamoğlu, *Nature Physics*, 2015, **11**, 141-147.
33. M. Georgiev and H. Chamati, *ACS Omega*, 2022, **7**, 42664-42673.
34. R. Boča, *Coordination Chemistry Reviews*, 2004, **248**, 757-815.
35. A. Cabot, A. P. Alivisatos, V. F. Puntes, L. Balcells, Ò. Iglesias and A. Labarta, *Physical Review B*, 2009, **79**, 094419.
36. A. T. Catherall, K. A. Benedict, P. J. King and L. Eaves, *Physical Review E*, 2003, **68**, 037302.
37. Magnetic Susceptibility of Chemical Elements, Encyclopedia Britannica, https://www.britannica.com/science/magnetism/Induced-and-permanent-atomic-magnetic-dipoles#/media/1/357334/1361, (accessed 24-09-23, 2023).

38. T. Phys and I. Kulik, *Turkish Journal of Physics*, 2003, **27**.
39. B. Stojanovic, *Magnetic, Ferroelectric, and Multiferroic Metal Oxides*, Elsevier, 2018.
40. S. Nagappan and C.-S. Ha, *Journal of Materials Chemistry A*, 2015, **3**, 3224-3251.
41. K. H. J. Buschow, de Boer, F.R., *Physics of Magnetism and Magnetic Materials*, Springer, Boston, MA, United States, 2003.
42. M. Suzuki, N. Kawamura, H. Miyagawa, J. S. Garitaonandia, Y. Yamamoto and H. Hori, *Physical Review Letters*, 2012, **108**, 047201.
43. J. J. Stephanos and A. W. Addison, *Electrons, Atoms, and Molecules in Inorganic Chemistry: A Worked Examples Approach*, Academic Press, 2017.
44. Y. Xin, W. Li, Q. Dong, T. Yang, B. Tian and Q. Li, *Superconductor Science and Technology*, 2020, **33**, 055004.
45. P. Sadhukhan and M. Sadhukhan, *Molecular Physics*, 2022, DOI: 10.1080/00268976.2022.2136114, e2136114.
46. S. Tarucha, D. G. Austing, T. Honda, R. J. van der Hage and L. P. Kouwenhoven, *Physical Review Letters*, 1996, **77**, 3613-3616.
47. S. Saini, Frankel, R. B., Stark, D. D. Ferruci Jr, J. T. , *American Journal of Roentgenology*, 1988, **150**, 735-743.
48. C. R. Quade, R. W. Mires, W. H. Brumage and C. F. Dorman, *The Journal of Chemical Physics*, 2003, **118**, 5506-5509.
49. S. Blundell, *Magnetism in Condensed Matter*, OUP Oxford, 2001.
50. Y.-R. Lee, T. T. Wang, T. M. Rvachov, J.-H. Choi, W. Ketterle and M.-S. Heo, *Physical Review A*, 2013, **87**, 043629.
51. X. Ji, H. Xie, C. Zhu, Y. Zou, A. U. Mu, M. Al-Hashimi, K. R. Dunbar and L. Fang, *Journal of the American Chemical Society*, 2020, **142**, 641-648.
52. F. Palacio, *Molecular Crystals and Liquid Crystals Science and Technology. Section A. Molecular Crystals and Liquid Crystals*, 1997, **305**, 385-399.
53. T. Jungwirth, X. Marti, P. Wadley and J. Wunderlich, *Nature Nanotechnology*, 2016, **11**, 231-241.
54. M. Tadic, D. Nikolic, M. Panjan and G. R. Blake, *Journal of Alloys and Compounds*, 2015, **647**, 1061-1068.
55. S. Mugiraneza and A. M. Hallas, *Communications Physics*, 2022, **5**, 95.

56. Y. Feng, R. Jaramillo, G. Srajer, J. C. Lang, Z. Islam, M. S. Somayazulu, O. G. Shpyrko, J. J. Pluth, H. k. Mao, E. D. Isaacs, G. Aeppli and T. F. Rosenbaum, *Physical Review Letters*, 2007, **99**, 137201.
57. J. F. Bondi, K. D. Oyler, X. Ke, P. Schiffer and R. E. Schaak, *Journal of the American Chemical Society*, 2009, **131**, 9144-9145.
58. K. Fabian, V. P. Shcherbakov and S. A. McEnroe, *Geochemistry, Geophysics, Geosystems*, 2013, **14**, 947-961.
59. P. P. Rout, S. K. Pradhan, S. K. Das, S. Samantaray and B. K. Roul, *Journal of Magnetism and Magnetic Materials*, 2013, **345**, 106-110.
60. X. W. Li, A. Gupta, T. R. McGuire, P. R. Duncombe and G. Xiao, *Journal of Applied Physics*, 1999, **85**, 5585-5587.
61. S. Velasco and F. L. Román, *The Physics Teacher*, 2007, **45**, 387-389.
62. M. H. Ferri Aliabadi, and Winston O. Soboyejo, *Comprehensive Structural Integrity*, 2 edn., 2023.
63. K. H. J. Buschow, R. W. Cahn, M. C. Flemings, B. Ilschner, E. J. Kramer, S. Mahajan and P. Veyssière, *Encyclopedia of Materials: Science and Technology*, 2001.
64. H. R. Kirchmayr, *Journal of Physics D: Applied Physics*, 1996, **29**, 2763.
65. D. C. Jiles and D. L. Atherton, *Journal of Physics D: Applied Physics*, 1984, **17**, 1265.
66. H. Zhang, B. Xia and D. Gao, *Journal of Magnetism and Magnetic Materials*, 2023, **569**, 170428.
67. A. Sundaresan and C. N. R. Rao, *Nano Today*, 2009, **4**, 96-106.
68. R. H. Victora, L. M. Falicov and S. Ishida, *Physical Review B*, 1984, **30**, 3896-3902.
69. J. Xie, X. Ren, Y. Song, Y. Zou and Q. Meng, *Journal of the Chemical Society, Dalton Transactions*, 2002, DOI: 10.1039/B201936C, 2868-2872.
70. X.-M. Zhang, P. Li, W. Gao, J.-P. Liu and E.-Q. Gao, *Dalton Transactions*, 2015, **44**, 13581-13585.
71. S. K. Malik and R. Vijayaraghavan, *Physical Review B*, 1975, **12**, 1098-1100.
72. J. Paulovič, F. Cimpoesu, M. Ferbinteanu and K. Hirao, *Journal of the American Chemical Society*, 2004, **126**, 3321-3331.

73. Y. Yafet and C. Kittel, *Physical Review*, 1952, **87**, 290-294.
74. L. Néel, *Proceedings of the Physical Society. Section A*, 1952, **65**, 869.
75. L. Néel, *Physical Chemical & Earth Sciences*, 1984, 18.
76. E. Stryjewski and N. Giordano, *Advances in Physics*, 1977, **26**, 487-650.
77. A. Thamizhavel, T. Takeuchi, T. D Matsuda, Y. Haga, K. Sugiyama, R. Settai and Y. Ōnuki, *Journal of the Physical Society of Japan*, 2005, **74**, 1858-1864.
78. J. Gómez-Segura, J. Veciana and D. Ruiz-Molina, *Chemical Communications*, 2007, DOI: 10.1039/B616352A, 3699-3707.
79. N. F. Chilton, *Annual Review of Materials Research*, 2022, **52**, 79-101.
80. A. S. Hoagland, *Computer*, 1979, **12**, 12-18.
81. M. Re, *Tech Talk on HDD Areal Density*, Seagate, Seagate, 2015.
82. C. A. Mack, *IEEE Transactions on Semiconductor Manufacturing*, 2011, **24**, 202-207.
83. A. J. Tasiopoulos, A. Vinslava, W. Wernsdorfer, K. A. Abboud and G. Christou, *Angewandte Chemie International Edition*, 2004, **43**, 2117-2121.
84. J. Ferrando-Soria, J. Vallejo, M. Castellano, J. Martínez-Lillo, E. Pardo, J. Cano, I. Castro, F. Lloret, R. Ruiz-García and M. Julve, *Coordination Chemistry Reviews*, 2017, **339**, 17-103.
85. E. L. Gavey, M. Al Hareri, J. Regier, L. D. Carlos, R. A. S. Ferreira, F. S. Razavi, J. M. Rawson and M. Pilkington, *Journal of Materials Chemistry C*, 2015, **3**, 7738-7747.
86. R. Lescouëzec, J. Vaissermann, C. Ruiz-Pérez, F. Lloret, R. Carrasco, M. Julve, M. Verdaguer, Y. Dromzee, D. Gatteschi and W. Wernsdorfer, *Angewandte Chemie International Edition*, 2003, **42**, 1483-1486.
87. T. Glaser, *Chemical Communications*, 2011, **47**, 116-130.
88. K. S. Pedersen, J. Dreiser, H. Weihe, R. Sibille, H. V. Johannesen, M. A. Sørensen, B. E. Nielsen, M. Sigrist, H. Mutka, S. Rols, J. Bendix and S. Piligkos, *Inorganic Chemistry*, 2015, **54**, 7600-7606.
89. I. A. Kühne, G. E. Kostakis, C. E. Anson and A. K. Powell, *Inorganic Chemistry*, 2016, **55**, 4072-4074.
90. A. I. Kuznetsov, A. E. Miroshnichenko, Y. H. Fu, J. Zhang and B. Luk'yanchuk, *Scientific Reports*, 2012, **2**, 492.

91. S. Ng and C. H. Sederholm, *The Journal of Chemical Physics*, 2004, **40**, 2090-2094.
92. V. Laget, C. Hornick, P. Rabu, M. Drillon and R. Ziessel, *Coordination Chemistry Reviews*, 1998, **178-180**, 1533-1553.
93. H. Wang, K. Qian, K. Wang, Y. Bian, J. Jiang and S. Gao, *Chemical Communications*, 2011, **47**, 9624-9626.
94. J. Gerratt, D. L. Cooper, P. B. Karadakov and M. Raimondi, *Chemical Society Reviews*, 1997, **26**, 87-100.
95. J. C. Slater, *Reviews of Modern Physics*, 1953, **25**, 199-210.
96. P. W. Anderson, *Physical Review*, 1950, **79**, 350-356.
97. H. Weihe and H. U. Güdel, *Inorganic Chemistry*, 1997, **36**, 3632-3639.
98. J. B. Goodenough, *Physical Review*, 1955, **100**, 564-573.
99. J. B. Goodenough, *Journal of Physics and Chemistry of Solids*, 1958, **6**, 287-297.
100. J. Kanamori, *Journal of Physics and Chemistry of Solids*, 1959, **10**, 87-98.
101. C. Zener, *Physical Review*, 1951, **82**, 403-405.
102. M. Azhar and M. Mostovoy, *Physical Review Letters*, 2017, **118**, 027203.
103. D. Aravena and E. Ruiz, *Dalton Transactions*, 2020, **49**, 9916-9928.
104. S. Bertaina, S. Gambarelli, T. Mitra, B. Tsukerblat, A. Müller and B. Barbara, *Nature*, 2008, **453**, 203-206.
105. J. L. S. Milani, Á. F. A. da Mata, I. S. Oliveira, A. K. S. M. Valdo, F. T. Martins, R. Rabelo, D. Cangussu, J. Cano, F. Lloret, M. Julve and R. P. das Chagas, *Dalton Transactions*, 2022, **51**, 12258-12270.
106. O. Roubeau and R. Clérac, *European Journal of Inorganic Chemistry*, 2008, DOI: https://doi.org/10.1002/ejic.200800603, 4325-4342.
107. M. A. Halcrow and G. Christou, *Chemical Reviews*, 1994, **94**, 2421-2481.
108. E. I. Solomon, U. M. Sundaram and T. E. Machonkin, *Chemical Reviews*, 1996, **96**, 2563-2606.
109. I. A. Koval, P. Gamez, C. Belle, K. Selmeczi and J. Reedijk, *Chemical Society Reviews*, 2006, **35**, 814-840.
110. U. Albold, H. Bamberger, P. P. Hallmen, J. van Slageren and B. Sarkar, *Angewandte Chemie International Edition*, 2019, **58**, 9802-9806.

111. R. Sessoli, D. Gatteschi, A. Caneschi and M. A. Novak, *Nature*, 1993, **365**, 141-143.

112. A. Zabala-Lekuona, J. M. Seco and E. Colacio, *Coordination Chemistry Reviews*, 2021, **441**, 213984.

113. A. Caneschi, D. Gatteschi and F. Totti, *Coordination Chemistry Reviews*, 2015, **289-290**, 357-378.

114. J. M. Frost, K. L. M. Harriman and M. Murugesu, *Chemical Science*, 2016, **7**, 2470-2491.

115. K. R. Vignesh, S. K. Langley, K. S. Murray and G. Rajaraman, *Chemistry – A European Journal*, 2017, **23**, 1654-1666.

116. A. Bhunia, M. T. Gamer, L. Ungur, L. F. Chibotaru, A. K. Powell, Y. Lan, P. W. Roesky, F. Menges, C. Riehn and G. Niedner-Schatteburg, *Inorganic Chemistry*, 2012, **51**, 9589-9597.

117. Y.-S. Ding, K.-X. Yu, D. Reta, F. Ortu, R. E. P. Winpenny, Y.-Z. Zheng and N. F. Chilton, *Nature Communications*, 2018, **9**, 3134.

118. M. Gregson, N. F. Chilton, A.-M. Ariciu, F. Tuna, I. F. Crowe, W. Lewis, A. J. Blake, D. Collison, E. J. L. McInnes, R. E. P. Winpenny and S. T. Liddle, *Chemical Science*, 2016, **7**, 155-165.

119. E. K. Brechin, C. Boskovic, W. Wernsdorfer, J. Yoo, A. Yamaguchi, E. C. Sañudo, T. R. Concolino, A. L. Rheingold, H. Ishimoto, D. N. Hendrickson and G. Christou, *Journal of the American Chemical Society*, 2002, **124**, 9710-9711.

120. R. J. Blagg, L. Ungur, F. Tuna, J. Speak, P. Comar, D. Collison, W. Wernsdorfer, E. J. L. McInnes, L. F. Chibotaru and R. E. P. Winpenny, *Nature Chemistry*, 2013, **5**, 673-678.

121. L. Ungur and L. F. Chibotaru, *Inorganic Chemistry*, 2016, **55**, 10043-10056.

122. J. V. Slageren, *Lecutre Notes, University of Stuttgart*, 2014, 21.

123. L. Gu, J. Li and R. Wu, *Journal of Magnetism and Magnetic Materials*, 2022, **564**, 170138.

124. F. Ortu, D. Reta, Y.-S. Ding, C. A. P. Goodwin, M. P. Gregson, E. J. L. McInnes, R. E. P. Winpenny, Y.-Z. Zheng, S. T. Liddle, D. P. Mills and N. F. Chilton, *Dalton Transactions*, 2019, **48**, 8541-8545.

125. X. Zhang, S. Liu, V. Vieru, N. Xu, C. Gao, B.-W. Wang, W. Shi, L. F. Chibotaru, S. Gao, P. Cheng and A. K. Powell, *Chemistry – A European Journal*, 2018, **24**, 6079-6086.

126. D. R. McCamey, J. Van Tol, G. W. Morley and C. Boehme, *Science*, 2010, **330**, 1652-1656.

127. J. D. Rinehart, M. Fang, W. J. Evans and J. R. Long, *Journal of the American Chemical Society*, 2011, **133**, 14236-14239.

128. D. Gatteschi, Sessoli, R., Villain, J., *Molecular Nanomagnets*, Oxford University Press, Oxford, 2006.

129. Y. Horii, K. Katoh, K. Sugimoto, R. Nakanishi, B. K. Breedlove and M. Yamashita, *Chemistry – A European Journal*, 2019, **25**, 3098-3104.

130. T. Gupta, M. F. Beg and G. Rajaraman, *Inorganic Chemistry*, 2016, **55**, 11201-11215.

131. S. K. Langley, D. P. Wielechowski, V. Vieru, N. F. Chilton, B. Moubaraki, B. F. Abrahams, L. F. Chibotaru and K. S. Murray, *Angewandte Chemie International Edition*, 2013, **52**, 12014-12019.

132. F. Donati, S. Rusponi, S. Stepanow, C. Wäckerlin, A. Singha, L. Persichetti, R. Baltic, K. Diller, F. Patthey, E. Fernandes, J. Dreiser, Ž. Šljivančanin, K. Kummer, C. Nistor, P. Gambardella and H. Brune, *Science*, 2016, **352**, 318-321.

133. D. Gatteschi, A. Caneschi, L. Pardi and R. Sessoli, *Science*, 1994, **265**, 1054-1058.

134. D. P. Mills, F. Moro, J. McMaster, J. van Slageren, W. Lewis, A. J. Blake and S. T. Liddle, *Nature Chemistry*, 2011, **3**, 454-460.

135. P. Shukla, S. Das, P. Bag and A. Dey, *Inorganic Chemistry Frontiers*, 2023, **10**, 4322-4357.

136. E. Ruiz, J. Cirera, J. Cano, S. Alvarez, C. Loose and J. Kortus, *Chemical Communications*, 2008, 52-54.

137. Y.-Z. Zheng, W. Xue, M.-L. Tong, X.-M. Chen and S.-L. Zheng, *Inorganic Chemistry*, 2008, **47**, 11202-11211.

138. H.-L. Sun, Z.-M. Wang and S. Gao, *Coordination Chemistry Reviews*, 2010, **254**, 1081-1100.

139. N. Ishikawa, M. Sugita, T. Ishikawa, S.-y. Koshihara and Y. Kaizu, *Journal of the American Chemical Society*, 2003, **125**, 8694-8695.

140. N. Koike, H. Uekusa, Y. Ohashi, C. Harnoode, F. Kitamura, T. Ohsaka and K. Tokuda, *Inorganic Chemistry*, 1996, **35**, 5798-5804.

141. S. Osa, T. Kido, N. Matsumoto, N. Re, A. Pochaba and J. Mrozinski, *Journal of the American Chemical Society*, 2004, **126**, 420-421.

142. P.-H. Lin, T. J. Burchell, L. Ungur, L. F. Chibotaru, W. Wernsdorfer and M. Murugesu, *Angewandte Chemie International Edition*, 2009, **48**, 9489-9492.

143. C. J. Milios, A. Vinslava, W. Wernsdorfer, S. Moggach, S. Parsons, S. P. Perlepes, G. Christou and E. K. Brechin, *Journal of the American Chemical Society*, 2007, **129**, 2754-2755.

144. J. D. Rinehart, M. Fang, W. J. Evans and J. R. Long, *Nature Chemistry*, 2011, **3**, 538-542.

145. M. G. F. Vaz, R. A. A. Cassaro, H. Akpinar, J. A. Schlueter, P. M. Lahti and M. A. Novak, *Chemistry – A European Journal*, 2014, **20**, 5460-5467.

146. R. A. A. Cassaro, S. G. Reis, T. S. Araujo, P. M. Lahti, M. A. Novak and M. G. F. Vaz, *Inorganic chemistry*, 2015, **54**, 9381-9383.

147. Y.-C. Chen, J.-L. Liu, L. Ungur, J. Liu, Q.-W. Li, L.-F. Wang, Z.-P. Ni, L. F. Chibotaru, X.-M. Chen and M.-L. Tong, *Journal of the American Chemical Society*, 2016, **138**, 2829-2837.

148. Y.-S. Ding, N. F. Chilton, R. E. P. Winpenny and Y.-Z. Zheng, *Angewandte Chemie International Edition*, 2016, **55**, 16071-16074.

149. S. Demir, M. I. Gonzalez, L. E. Darago, W. J. Evans and J. R. Long, *Nature Communications*, 2017, **8**, 2144.

150. V. S. Parmar, D. P. Mills and R. E. P. Winpenny, *Chemistry*, 2021, **27**, 7625-7645.

151. C. A. P. Goodwin, F. Ortu, D. Reta, N. F. Chilton and D. P. Mills, *Nature*, 2017, **548**, 439-442.

152. F.-S. Guo, B. M. Day, Y.-C. Chen, M.-L. Tong, A. Mansikkamäki and R. A. Layfield, *Angewandte Chemie International Edition*, 2017, **56**, 11445-11449.

153. F.-S. Guo, B. M. Day, Y.-C. Chen, M.-L. Tong, A. Mansikkamäki and R. A. Layfield, *Science*, 2018, **362**, 1400-1403.

154. J. Liu, D. Reta, J. A. Cleghorn, Y. X. Yeoh, F. Ortu, C. A. P. Goodwin, N. F. Chilton and D. P. Mills, *Chemistry – A European Journal*, 2019, **25**, 7749-7758.

155. C. A. P. Goodwin, D. Reta, F. Ortu, N. F. Chilton and D. P. Mills, *Journal of the American Chemical Society*, 2017, **139**, 18714-18724.

156. C. T. Palumbo, I. Zivkovic, R. Scopelliti and M. Mazzanti, *Journal of the American Chemical Society*, 2019, **141**, 9827-9831.

157. A. N. Selikhov, I. V. Lapshin, A. V. Cherkasov, G. K. Fukin and A. A. Trifonov, *Organometallics*, 2021, **40**, 3042-3049.

158. R. M. Diaz-Rodriguez, D. A. Gálico, D. Chartrand, E. A. Suturina and M. Murugesu, *Journal of the American Chemical Society*, 2022, **144**, 912-921.

159. A. R. Willauer, C. T. Palumbo, F. Fadaei-Tirani, I. Zivkovic, I. Douair, L. Maron and M. Mazzanti, *Journal of the American Chemical Society*, 2020, **142**, 5538-5542.

160. M. J. Klein, *American Journal of Physics*, 1952, **20**, 65-71.

161. D. N. Woodruff, R. E. Winpenny and R. A. Layfield, *Chem Rev*, 2013, **113**, 5110-5148.

162. S. Ullmann, P. Hahn, L. Blömer, A. Mehnert, C. Laube, B. Abel and B. Kersting, *Dalton Transactions*, 2019, **48**, 3893-3905.

163. D. Parker, E. A. Suturina, I. Kuprov and N. F. Chilton, *Accounts of Chemical Research*, 2020, **53**, 1520-1534.

164. R. B. Jordan, *Inorganic Chemistry*, 2023, **62**, 3715-3721.

165. S. T. Liddle, *Angewandte Chemie International Edition*, 2015, **54**, 8604-8641.

166. B. Wang, S. Jiang, X. Wang and S. Gao, *Science in China Series B: Chemistry*, 2009, **52**, 1739-1758.

167. D. Ray, M. S. Oakley, A. Sarkar, X. Bai and L. Gagliardi, *Inorganic Chemistry*, 2023, **62**, 1649-1658.

168. S. K. Singh, T. Gupta and G. Rajaraman, *Inorganic Chemistry*, 2014, **53**, 10835-10845.

169. N. F. Chilton, D. Collison, E. J. L. McInnes, R. E. P. Winpenny and A. Soncini, *Nature Communications*, 2013, **4**, 2551.

170. H. M. Nicholas, M. Vonci, C. A. P. Goodwin, S. W. Loo, S. R. Murphy, D. Cassim, R. E. P. Winpenny, E. J. L. McInnes, N. F. Chilton and D. P. Mills, *Chemical Science*, 2019, **10**, 10493-10502.

171. J. D. Rinehart and J. R. Long, *Chemical Science*, 2011, **2**, 2078-2085.

172. F. Habib, G. Brunet, V. Vieru, I. Korobkov, L. F. Chibotaru and M. Murugesu, *Journal of the American Chemical Society*, 2013, **135**, 13242-13245.

173. S. K. Langley, D. P. Wielechowski, V. Vieru, N. F. Chilton, B. Moubaraki, L. F. Chibotaru and K. S. Murray, *Chemical Science*, 2014, **5**, 3246-3256.

174. L. E. Darago, M. D. Boshart, B. D. Nguyen, E. Perlt, J. W. Ziller, W. W. Lukens, F. Furche, W. J. Evans and J. R. Long, *Journal of the American Chemical Society*, 2021, **143**, 8465-8475.

175. A. Bencini, C. Benelli, A. Caneschi, R. L. Carlin, A. Dei and D. Gatteschi, *Journal of the American Chemical Society*, 1985, **107**, 8128-8136.

176. X.-J. Kong, L.-S. Long, Z. Zheng, R.-B. Huang and L.-S. Zheng, *Accounts of Chemical Research*, 2010, **43**, 201-209.

177. Y.-Y. Li, F. Gao, J. E. Beves, Y.-Z. Li and J.-L. Zuo, *Chemical Communications*, 2013, **49**, 3658-3660.

178. E. Loukopoulos, B. Berkoff, A. Abdul-Sada, G. J. Tizzard, S. J. Coles, A. Escuer and G. E. Kostakis, *European Journal of Inorganic Chemistry*, 2015,

, 2646-2649.

179. A. Yamashita, A. Watanabe, S. Akine, T. Nabeshima, M. Nakano, T. Yamamura and T. Kajiwara, *Angewandte Chemie International Edition*, 2011, **50**, 4016-4019.

180. Y. Peng, H. Kaemmerer and A. K. Powell, *Chemistry – A European Journal*, 2021, **27**, 15044-15066.

181. Y. Peng and A. K. Powell, *Coordination Chemistry Reviews*, 2021, **426**, 213490.

182. Y. Peng, V. Mereacre, C. E. Anson and A. K. Powell, *Dalton Transactions*, 2017, **46**, 5337-5343.

183. I. A. Kühne, K. Griffiths, A.-J. Hutchings, O. P. E. Townrow, A. Eichhöfer, C. E. Anson, G. E. Kostakis and A. K. Powell, *Crystal Growth & Design*, 2017, **17**, 5178-5190.

184. S. K. Langley, D. P. Wielechowski, B. Moubaraki and K. S. Murray, *Chemical Communications*, 2016, **52**, 10976-10979.

185. H.-H. Zou, L.-B. Sheng, F.-P. Liang, Z.-L. Chen and Y.-Q. Zhang, *Dalton Transactions*, 2015, **44**, 18544-18552.

186. A. Baniodeh, V. Mereacre, N. Magnani, Y. Lan, J. A. Wolny, V. Schünemann, C. E. Anson and A. K. Powell, *Chemical Communications*, 2013, **49**, 9666-9668.

187. C. Papatriantafyllopoulou, K. A. Abboud and G. Christou, *Inorganic Chemistry*, 2011, **50**, 8959-8966.

188. H. Ke, W. Wei, Y. Yang, J. Zhang, Y.-Q. Zhang, G. Xie and S. Chen, *Dalton Transactions*, 2019, **48**, 7844-7852.

189. A. V. Funes, L. Carrella, Y. Rechkemmer, J. van Slageren, E. Rentschler and P. Alborés, *Dalton Transactions*, 2017, **46**, 3400-3409.

190. X.-Y. Wang, C. Avendaño and K. R. Dunbar, *Chemical Society Reviews*, 2011, **40**, 3213-3238.

191. Y. Peng, V. Mereacre, C. E. Anson and A. K. Powell, *Physical Chemistry Chemical Physics*, 2016, **18**, 21469-21480.

192. E. Moreno Pineda, N. F. Chilton, F. Tuna, R. E. P. Winpenny and E. J. L. McInnes, *Inorganic Chemistry*, 2015, **54**, 5930-5941.

193. J. W. Sharples and D. Collison, *Coordination Chemistry Reviews*, 2014, **260**, 1-20.

194. R. A. Coxall, S. G. Harris, D. K. Henderson, S. Parsons, P. A. Tasker and R. E. P. Winpenny, *Journal of the Chemical Society, Dalton Transactions*, 2000, DOI: 10.1039/B001404O, 2349-2356.

195. R. R. P. Kuppusamy, A. Zade and S. Neogi, *Chemical Papers*, 2023, **77**, 1887-1906.

196. X. Leng, B. Yang, Y. Liu, Y. Xie and J. Tong, 2011, **66**, 930-934.

197. J. S. Mistry, D. J. Abraham and I. Hanin, *Journal of Medicinal Chemistry*, 1986, **29**, 376-380.

198. W. E. Hanby and H. N. Rydon, *Journal of the Chemical Society (Resumed)*, 1947, DOI: 10.1039/JR9470000513, 513-519.

199. E. Jeong, H. S. Freeman and L. D. Claxton, *Dyes and Pigments*, 2010, **87**, 100-108.

200. B. Glowacki, R. Pallach, M. Lutter, F. Roesler, H. Alnasr, C. Thomas, D. Schollmeyer and K. Jurkschat, *Chemistry – A European Journal*, 2018, **24**, 19266-19279.

201. Q. Yang, J. Lin and F. Li, *Synthetic Communications*, 2001, **31**, 2817-2822.

202. N. Salvarese, F. Refosco, R. Seraglia, M. Roverso, A. Dolmella and C. Bolzati, *Dalton Transactions*, 2017, **46**, 9180-9191.

203. Z.-H. Shi, N.-G. Li, Q.-P. Shi, W. Zhang, Z.-X. Dong, Y.-P. Tang, P.-X. Zhang, T. Gu, W.-Y. Wu, F. Fang, X. Xin, H.-M. Li, J.-P. Yang and J.-A. Duan, *Bioorganic & Medicinal Chemistry*, 2015, **23**, 6875-6884.

204. R. E. P. Winpenny, *Journal of the Chemical Society, Dalton Transactions*, 2002, DOI: 10.1039/B107118C, 1-10.

205. L. F. Jones, P. Jensen, B. Moubaraki, J. D. Cashion, K. J. Berry and K. S. Murray, *Dalton Transactions*, 2005, DOI: 10.1039/B504270D, 3344-3352.

206. A. K. Powell, S. L. Heath, D. Gatteschi, L. Pardi, R. Sessoli, G. Spina, F. Del Giallo and F. Pieralli, *Journal of the American Chemical Society*, 1995, **117**, 2491-2502.

207. J. C. Goodwin, R. Sessoli, D. Gatteschi, W. Wernsdorfer, A. K. Powell and S. L. Heath, *Journal of the Chemical Society, Dalton Transactions*, 2000, DOI: 10.1039/B002135K, 1835-1840.

208. N. C. Harden, M. A. Bolcar, W. Wernsdorfer, K. A. Abboud, W. E. Streib and G. Christou, *Inorganic Chemistry*, 2003, **42**, 7067-7076.

209. L. F. Jones, P. Jensen, B. Moubaraki, K. J. Berry, J. F. Boas, J. R. Pilbrow and K. S. Murray, *Journal of Materials Chemistry*, 2006, **16**, 2690-2697.

210. M. Moragues-Canovás, C. E. Talbot-Eeckelaers, L. Catala, F. Lloret, W. Wernsdorfer, E. K. Brechin and T. Mallah, *Inorganic Chemistry*, 2006, **45**, 7038-7040.

211. J. J. Henkelis, L. F. Jones, M. P. de Miranda, C. A. Kilner and M. A. Halcrow, *Inorganic Chemistry*, 2010, **49**, 11127-11132.

212. S. T. Meally, G. Karotsis, E. K. Brechin, G. S. Papaefstathiou, P. W. Dunne, P. McArdle and L. F. Jones, *CrystEngComm*, 2010, **12**, 59-63.

213. Y. Jiao, Y. Li, Y. Zhou, P. Cen, Y. Ding, Y. Guo and X. Liu, *Chinese Chemical Letters*, 2024, **35**, 109082.

214. J. Liu, C. Ma, H. Chen, M. Hu, H. Wen, H. Cui and C. Chen, *Dalton Transactions*, 2013, **42**, 3787-3790.

215. M. Murrie, *Chemical Society Reviews*, 2010, **39**, 1986-1995.

216. J.-P. Costes, L. Vendier and W. Wernsdorfer, *Dalton Transactions*, 2011, **40**, 1700-1706.

217. L. Sun, H. Chen, C. Ma and C. Chen, *Inorganic Chemistry Communications*, 2016, **70**, 132-135.

218. F. F. Blicke and E.-P. Tsao, *Journal of the American Chemical Society*, 1953, **75**, 3999-4002.

219. Knorr, *Chemische Berichte*, 1889, **22**, 2084.

220. K. Hegetschweiler, *Chemical Society Reviews*, 1999, **28**, 239-249.

221. A. A. Hullio, Mastoi, G.M., and Khan, K.M., *Asian Journal of Chemistry*, 2011, **23**, 5411-5418.

222. J. Bertrand, E. Fujita and D. VanDerveer, *Inorganic Chemistry*, 1979, **18**, 230-233.

223. V. N. Kokozay and O. Y. Vassilyeva, *Transition Metal Chemistry*, 2002, **27**, 693-699.

224. V. Tudor, G. Marin, V. Kravtsov, Y. A. Simonov, J. Lipkowski, M. Brezeanu and M. Andruh, *Inorganica Chimica Acta*, 2003, **353**, 35-42.

225. D. S. Nesterov, V. G. Makhankova, O. Y. Vassilyeva, V. N. Kokozay, L. A. Kovbasyuk, B. W. Skelton and J. Jezierska, *Inorganic Chemistry*, 2004, **43**, 7868-7876.

226. M. Murugesu, W. Wernsdorfer, K. A. Abboud and G. Christou, *Angewandte Chemie International Edition*, 2005, **44**, 892-896.

227. D. S. Nesterov, V. N. Kokozay, V. V. Dyakonenko, O. V. Shishkin, J. Jezierska, A. Ozarowski, A. M. Kirillov, M. N. Kopylovich and A. J. L. Pombeiro, *Chemical Communications*, 2006, DOI: 10.1039/B608790F, 4605-4607.

228. R. Prakash, R. W. Saalfrank, H. Maid, A. Scheurer, F. W. Heinemann, A. X. Trautwein and L. H. Böttger, *Angewandte Chemie International Edition*, 2006, **45**, 5885-5889.

229. T. Liu, B.-W. Wang, Y.-H. Chen, Z.-M. Wang and S. Gao, *Zeitschrift für anorganische und allgemeine Chemie*, 2008, **634**, 778-783.

230. V. Tudor, G. Marin, F. Lloret, V. C. Kravtsov, Y. A. Simonov, M. Julve and M. Andruh, *Inorganica Chimica Acta*, 2008, **361**, 3446-3452.

231. A. M. Ako, V. Mereacre, Y. Lan, W. Wernsdorfer, R. Clérac, C. E. Anson and A. K. Powell, *Inorganic Chemistry*, 2010, **49**, 1-3.

232. S. K. Langley, B. Moubaraki, K. J. Berry and K. S. Murray, *Dalton Transactions*, 2010, **39**, 4848-4855.

233. S. K. Langley, B. Moubaraki and K. S. Murray, *Dalton Transactions*, 2010, **39**, 5066-5069.

234. V. Tudor, A. Madalan, V. Lupu, F. Lloret, M. Julve and M. Andruh, *Inorganica Chimica Acta*, 2010, **363**, 823-826.

235. A. M. Ako, V. Mereacre, Y. Lan, C. E. Anson and A. K. Powell, *Chemistry – A European Journal*, 2011, **17**, 4366-4370.

236. A. Baniodeh, I. J. Hewitt, V. Mereacre, Y. Lan, G. Novitchi, C. E. Anson and A. K. Powell, *Dalton Transactions*, 2011, **40**, 4080-4086.

237. S. K. Langley, N. F. Chilton, B. Moubaraki and K. S. Murray, *Dalton Transactions*, 2012, **41**, 1033-1046.

238. S. K. Langley, L. Ungur, N. F. Chilton, B. Moubaraki, L. F. Chibotaru and K. S. Murray, *Inorganic Chemistry*, 2014, **53**, 4303-4315.

239. V. Mereacre, M. N. Akhtar, Y. Lan, A. M. Ako, R. Clérac, C. E. Anson and A. K. Powell, *Dalton Transactions*, 2010, **39**, 4918-4927.

240. J. Rinck, G. Novitchi, W. Van den Heuvel, L. Ungur, Y. Lan, W. Wernsdorfer, C. E. Anson, L. F. Chibotaru and A. K. Powell, *Angewandte Chemie International Edition*, 2010, **49**, 7583-7587.

241. J. M. Ashtree, I. Borilović, K. R. Vignesh, A. Swain, S. H. Hamilton, Y. L. Whyatt, S. L. Benjamin, W. Phonsri, C. M. Forsyth, W. Wernsdorfer, A. Soncini, G. Rajaraman, S. K. Langley and K. S. Murray, *European Journal of Inorganic Chemistry*, 2021, **2021**, 435-444.

242. K. Hymas and A. Soncini, *Magnetochemistry*, 2022, **8**, 58.

243. K. Irländer and J. Schnack, *Physical Review Research*, 2023, **5**, 013192.

244. A. Swain, T. Sharma and G. Rajaraman, *Chemical Communications*, 2023, **59**, 3206-3228.

245. N. F. Chilton, CC-Fit, https://www.nfchilton.com/cc-fit, (accessed 25-09-2023).

246. A. Upadhyay, J. Rajpurohit, M. Kumar Singh, R. Dubey, A. Kumar Srivastava, A. Kumar, G. Rajaraman and M. Shanmugam, *Chemistry – A European Journal*, 2014, **20**, 6061-6070.

247. S. K. Langley, D. P. Wielechowski, V. Vieru, N. F. Chilton, B. Moubaraki, L. F. Chibotaru and K. S. Murray, *Chemical Communications*, 2015, **51**, 2044-2047.

248. J. Larionova, B. Mombelli, J. Sanchiz and O. Kahn, *Inorganic Chemistry*, 1998, **37**, 679-684.

249. E. Coronado, J. R. Galán-Mascarós, C. J. Gómez-García, J. M. Martínez-Agudo, E. Martínez-Ferrero, J. C. Waerenborgh and M. Almeida, *Journal of Solid State Chemistry*, 2001, **159**, 391-402.

250. H.-Y. Shen, D.-Z. Liao, Z.-H. Jiang and S.-P. Yan, *Synthesis and Reactivity in Inorganic and Metal-Organic Chemistry*, 2002, **32**, 69-80.

251. W.-F. Yeung, P.-H. Lau, T.-C. Lau, H.-Y. Wei, H.-L. Sun, S. Gao, Z.-D. Chen and W.-T. Wong, *Inorganic Chemistry*, 2005, **44**, 6579-6590.

252. L. M. Toma, L. D. Toma, F. S. Delgado, C. Ruiz-Pérez, J. Sletten, J. Cano, J. M. Clemente-Juan, F. Lloret and M. Julve, *Coordination Chemistry Reviews*, 2006, **250**, 2176-2193.

253. J.-F. Guo, X.-T. Wang, B.-W. Wang, G.-C. Xu, S. Gao, L. Szeto, W.-T. Wong, W.-Y. Wong and T.-C. Lau, *Chemistry – A European Journal*, 2010, **16**, 3524-3535.

254. H. Miyasaka, T. Izawa, N. Takahashi, M. Yamashita and K. R. Dunbar, *Journal of the American Chemical Society*, 2006, **128**, 11358-11359.

255. C.-K. Kuo, I. P.-C. Liu, C.-Y. Yeh, C.-H. Chou, T.-B. Tsao, G.-H. Lee and S.-M. Peng, *Chemistry – A European Journal*, 2007, **13**, 1442-1451.

256. W.-L. Man, H.-K. Kwong, W. W. Y. Lam, J. Xiang, T.-W. Wong, W.-H. Lam, W.-T. Wong, S.-M. Peng and T.-C. Lau, *Inorganic Chemistry*, 2008, **47**, 5936-5944.

257. C.-Y. Wong, F.-W. Lee, C.-M. Che, Y. F. Cheng, D. L. Phillips and N. Zhu, *Inorganic Chemistry*, 2008, **47**, 10308-10316.

258. L. Norel, K. Bernot, M. Feng, T. Roisnel, A. Caneschi, R. Sessoli and S. Rigaut, *Chemical Communications*, 2012, **48**, 3948-3950.

259. G. Novitchi, W. Wernsdorfer, L. F. Chibotaru, J.-P. Costes, C. E. Anson and A. K. Powell, *Angewandte Chemie International Edition*, 2009, **48**, 1614-1619.

260. A. Swain, R. Martin, K. R. Vignesh, G. Rajaraman, K. S. Murray and S. K. Langley, *Dalton Transactions*, 2021, **50**, 12265-12274.

261. N. E. Brese, and M. O'Keeffe, *Acta Crystallographica Section B*, 1991, **47**, 192-197.

262. I. D. Brown, and D. Altermatt, *Acta Crystallographica Section B*, 1985, **41**, 244-247.

263. K. Nakamoto, *nfrared and Raman Spectra of Inorganic and Coordination Compounds, Part A: Theory and Applications in Inorganic Chemistry*, Wiley-Interscience, 2009.

264. I. Fleming and D. Williams, *Spectroscopic Methods in Organic Chemistry*, Springer, 7 edn., 2020.

8 Appendices

Appendix A – Synthesis and Chemical Procurement

The synthesis of novel heterometallic arrays for this thesis proceeded employing a methodology analogous to high throughput screening used in biological testing, but on a smaller scale due to the limitations imposed by a lack of appropriate mechanisation. Chemicals listed below were utilised in this project but may have been excluded from the thesis at collation. All starting reagents and materials were sourced from the companies as listed below.

Sigma Aldrich: 1-chlorobutane, 2,3,4,5-tetrafluorobenzoic acid (2,3,4-tet-F-Benz), 2-chloro-4,5-difluorobenzoic acid (2-Cl-4,5-F-Benz), 2-iodobenzoic acid (2-I Benz), 2-isopropylaminoethanol ([^{i}**PrAE**]H), 2-trifluoromethylbenzoic acid (2-F3C-Benz), 3-chloropropanol, aniline, chromium (III) chloride hexahydrate, diethanolamine ([**DEA**]H_2), dimethylformamide (DMF), dysprosium (III) nitrate pentahydrate, N-ethyldiethanolamine ([**EDEA**]H_2), magnesium sulphate, manganese (II) nitrate hydrate, paraformaldehyde, potassium carbonate, p-toluic acid (p-Tol), triethylamine, zinc (II) chloride.

Alfa Aesar: 2-aminoethanol, 2-chloroethanol, 2-ethylamino ethanol ([**EAE**]H), 2-phenylamino ethanol ([**PhAE**]H), aluminium (III) nitrate hydrate, benzoic acid (Benz), cobalt (III) nitrate hexahydrate, chromium (III) nitrate nonahydrate, copper (II) nitrate hemipentahydrate, 3-[N,N-bis(2-hydroxyethyl)amino]-2-hydroxypropane sulfonic acid ([**DIPSO**]H_4), dysprosium (III) nitrate pentahydrate, iron (III) nitrate nonahydrate, gallium (III) nitrate hexahydrate, gadolinium (III) nitrate hexahydrate, indium(III) nitrate hexahydrate, nickel (II) nitrate hexahydrate, pentane, sodium borohydride, tert-butylamine, yttrium (III) nitrate hydrate, zinc (II) nitrate hexahydrate, zinc (II) chloride anhydrous.

Fisher Scientific: acetone, acetonitrile (MeCN), chloroform, dichloromethane, diethyl ether, hexane, methanol (MeOH), sodium hydroxide.

Acros Organics: 2,6-dichlorobenzoic acid (2,6-Cl-Benz), 2-chlorobenzoic acid (2-Cl-Benz), acetaldehyde, acetyl acetone (Acac), diethanolamine ([**DEA**]H_2), N-isopropyldiethanol

amine ([^{i}**PrDEA**]H_2), N-methyldiethanol amine ([**MDEA**]H_2), N-n-butyldiethanol amine ([^{n}**BuDEA**]H_2), N-phenyldiethanol amine ([**PhDEA**]H_2), triethanolamine ([**TEA**]H_3).

Tokyo Chemistry Industry (TCI): 2-isopropylamino ethanol ([**iPrAE**]H), 2-methylamino ethanol ([**MAE**]H), pivalic acid (Piv).

Manchester Organics: ruthenium (III) chloride hydrate.

Apollo Scientific: 1-amino adamantane.

Avocado Research Chemicals Ltd: o-toluic acid (o-Tol).

Unless otherwise stated, all reagents and solvents were used without further purification. Solvents were of general use or HPLC grade, unless specifically stated. Drying solvents over anhydrous potassium carbonate proved sufficient for use.

Deionised water was purified with a Merck Millipore Milli-Q Integral water purification system or a Merck Millipore gradient A10 water purification system.

The syntheses of the polyalcohol and precursor molecules were carried out in Fisher Quickfit™ round bottom flasks, with sand or silicon oil as heating medium, dependant on the reaction length and temperature, as appropriate. Inorganic serendipitous assemblies were performed in Fisherbrand™ 28 mL glass screw neck specimen vials with Fisherbrand™ micro (flea) Teflon magnetic stirrer bars as agitators. Reactions were completed in simultaneous batches of three to four per stirrer plate.

TLC monitoring made use of Merck Millipore aluminium backed silica gel F254 plates, whilst silica gel chromatography utilised Merck Millipore Geduran® silica gel 60 as a stationary phase. In such cases where silica proved disadvantageous for sample chromatography instead Merck TLC aluminium oxide 60 F_{254}, neutral plates and Acros aluminium oxide 97% was employed.

Vacuum distillation was undertaken using a conventional set up based around a Syntheware™ vacuum jacketed short path distillation head, whilst the vacuum strength was monitored from a separate vacuum tap on the same line using a Vacuubrand DVR 2Pro vacuum gauge.

Sonication, as a part of solvation or freebasing, employed a 475H Langford Sonomatic ultrasonic cleaner where necessary.

Appendix B – Single-Crystal X-Ray Diffraction Analysis

Single crystal X-ray diffraction measurements were undertaken at multiple institutions, on equipment as specified below:

SC-XRD measurements for samples **C1**-**C18** and **C20** were carried out at the University of Southampton, using a Bruker D8 QUEST diffractometer with MoKα radiation and a photon 50 CMOS detector. The data collection and integration were performed within the APEX 3 software program.

SC-XRD measurements for **C19**, **C29** and **C30** were carried out by Nottingham Trent University at 173 K using an Oxford Xcalibur diffractometer with Mo Kα radiation and a Sapphire3 detector. The data collection and integration were performed within the CrysAlisPro software program.

SC-XRD measurements for **C21**-**C28** were performed at 150(2) K at the Australian synchrotron MX1 beam-line. The data collection and integration were performed within Blu-Ice21 and XDS22 software programs.

Compounds **C1 – C30** were revealed by direct methods (SHELXS-97) and refined (SHELXL-97) by full least matrix least-squares on all F*2* data.

The structures of the novel complexes produced within this thesis were derived through a combination of SC-XRD and bond valence sum (BVS) calculations using the **Eq^{n}s 20a** and **20b**. These equations and values of R_{ij} are taken from the work of Brese and O'Keeffe, 1991.[261]

Eq^{n} 20a: $v_{ij} = e^{(R_{ij} - d_{ij})/b}$

Eq^{n} 20b: $V_i = \sum_j v_{ij}$

Where V_i is the valence of atom i, v_{ij} is the valence of the bond between atoms i and j, R_{ij} is the bond valence parameter, d_{ij} is the length of the bond i-j and b is a universal constant, 0.37, defined by Brown and Altermatt, 1985.[262]

Table S1- Crystallographic specifications for samples **C1-C5**.

	C1	**C2**	**C3**	**C4**	**C5**
Formula[a]	$Cr_2Dy_2C_{48}H_{72}N_2O_{27}S_2$	$Co_2Dy_2C_{50}H_{75}N_3O_{27}S_2$	$Mn_2Dy_2C_{52}H_{80}N_2O_{28}S_2$	$Mn_6C_{88}H_{84}N_4O_{23}$	$Mn_2Gd_2C_{48}H_{64}N_4O_{24}S_2$
M, $gmol^{-1}$	1602.18	1657.06	1680.18	1895.25	1569.53
Crystal system	Triclinic	Monoclinic	Triclinic	Monoclinic	Triclinic
Space group	*P-1*	*C 2/c*	*P-1*	*P 2₁/c*	*P-1*
a/[Å]	11.6957(5)	27.7298(7)	11.204(2)	14.9870(2)	10.4655(4)
b/[Å]	12.5208(5)	12.9852(2)	12.009(2)	32.0072(4)	10.6178(4)
c/[Å]	12.5292(6)	21.5187(4)	13.401(3)	20.1982(3)	14.4781(5)
α/[°]	63.443(4)	90	96.28(3)	90	83.2760(10)
β/[°]	69.211(4)	111.828(2)	110.18(3)	107.958(2)	73.4410(10)
γ/[°]	69.673(4)	90	104.78(3)	90	67.8960(10)
V/[$Å^3$]	1494.76(13)	7192.9(3)	1597.2(7)	9216.9(2)	1428.66(9)
T/K	173(2)	120(2)	173(2)	150(2)	150.00
Z	1	4	1	4	1
ρ_{calc} [g cm^{-3}]	1.778	1.525	1.747	1.364	1.824
λ/ [Å]	0.71073	0.71073	0.71073	0.71073	0.71073
Data Measured	27836	40069	19975	187292	38021
Ind. Reflns	6852	8017	6874	22855	8715
R_{int}	0.0391	0.0230	0.0204	0.0519	0.0349
Reflns with I > 2σ(I)	6062	7089	6525	17889	7819
Para-meters	403	428	419	1289	382
Restraints	20	43	3	1	7
R_1[b](obs), wR_2[b](all)	0.0424, 0.0979	0.0503, 0.1378	0.0352, 0.0863	0.0792, 0.2286	0.0311, 0.0550
goodness of fit	1.074	1.106	1.108	1.061	1.053
Largest residuals/ [e $Å^{-3}$]	2.484, -0.973	2.116, -1.324	1.727, -1,616	1.211, -0.578	1.240, -1.067

[a]Includes solvate molecules.

[b] $R_1=\Sigma||Fo| - |Fc||/\Sigma|Fo|$, $wR_2= \{\Sigma[w(Fo^2-Fc^2)^2]/\Sigma[w(Fo^2)^2]\}^{1/2}$.

Table S2- Crystallographic specifications for samples **C6-C10**.

	C6	**C7**	**C8**	**C9**	**C10**
Formula[a]	$Fe_2Dy_2C_{30}H_{51}N_5O_{28}S_2$	$Fe_{12}Dy_4C_{136}H_{177}N_{11}O_{78}S_6$	$Fe_2Dy_2C_{36}H_{55}I_2N_7O_{26}S_2$	$CrDy_2C_{47}H_{59}Cl_8N_6O_{24}S$	$Fe_4Dy_6C_{136}H_{180}N_2O_{62}S_2$
M, $gmol^{-1}$	1430.57	4726.31	1756.49	1784.66	4097.33
Crystal system	Tetragonal	Monoclinic	Monoclinic	Triclinic	Monoclinic
Space group	*I 4₁/a*	*P 2₁/c*	*P 2₁/c*	*P-1*	*P 2₁/n*
a/[Å]	19.15160(10)	16.0618(2)	10.9709(5)	15.1726(2)	15.650(3)
b/[Å]	19.15160(10)	18.4844(2)	18.3660(9)	15.7352(2)	29.970(6)
c/[Å]	33.1601(2)	31.3103(4)	13.7053(7)	16.0390(3)	16.862(3)
α/[°]	90	90	90	104.481(2)	90
β/[°]	90	96.9390(10)	94.0190(10)	96.4280(10)	98.77(3)
γ/[°]	90	90	90	95.0300(10)	90
V/[$Å^3$]	12162.59(15)	9227.71(19)	2754.7(2)	3657.53(10)	7816(3)
T/K	173(2)	173(2)	150(2)	173(2)	173(2)
Z	8	4	2	2	2
ρ_{calc} [g cm^{-3}]	1.563	1.695	2.118	1.620	1.741
λ/ [Å]	1.54178	1.54178	0.71073	1.54178	0.71073
Data Measured	29484	90947	51859	65505	132689
Ind. Reflns	6067	18460	9129	13374	18206
R_{int}	0.0294	0.0533	0.0237	0.0638	0.0331
Reflns with I > 2σ(I)	5652	15882	8840	11403	16145
Para-meters	344	1187	384	841	998
Restraints	6	31	24	101	18
R_1[b](obs), wR_2[b](all)	0.0451, 0.1493	0.0921, 0.2220	0.0304, 0.0648	0.0679, 0.1949	0.0506, 0.1215
goodness of fit	1.100	1.130	1.251	1.040	1.056
Largest residuals/ [e $Å^{-3}$]	1.720, -0.765	3.569, -1.351	1.758, -1.286	1.544, -1.383	1.551, -3.480

[a]Includes solvate molecules.

[b] $R_1=\Sigma||Fo| - |Fc||/\Sigma|Fo|$, $wR_2= \{\Sigma[w(Fo^2-Fc^2)^2]/\Sigma[w(Fo^2)^2]\}^{1/2}$.

Table S3- Crystallographic specifications for samples **C11-C15**.

	C11	**C12**	**C13**	**C14**	**C15**
Formula[a]	$Co_3DyC_{30}H_{56}N_3O_{23}S_3$	$Co_5Dy_2C_{64}H_{82}Cl_6N_2O_{34}S_2$	$Co_5Dy_2C_{64}H_{82}Br_6N_2O_{34}S_2$	$Co_5Dy_2C_{62}H_{78}I_6N_2O_{34}S_2$	$Cr_2Dy_2C_{42}H_{52}N_4O_{20}$
M, $gmol^{-1}$	1297.68	2319.78	2586.54	2840.40	1361.87
Crystal system	Monoclinic	Triclinic	Triclinic	Triclinic	Monoclinic
Space group	*P 2₁/c*	*P-1*	*P-1*	*P-1*	*P 2₁/n*
a/[Å]	17.5291(4)	11.4314(6)	11.5721(2)	10.7878(2)	7.9293(4)
b/[Å]	12.6158(3)	12.7567(7)	12.8228(2)	14.5016(2)	17.3924(8)
c/[Å]	21.6165(5)	14.6825(8)	14.7498(2)	15.6902(2)	17.5915(8)
α/[°]	90.00	102.3170(10)	102.3290(10)	113.376(2)	90
β/[°]	106.116(2)	96.101(2)	96.7710(10)	97.2310(10)	93.3700(10)
γ/[°]	90.00	100.1170(10)	100.4070(10)	107.789(2)	90
V/[$Å^3$]	4592.49(18)	2036.16(19)	2074.95(6)	2057.87(7)	2421.8(2)
T/K	123(2)	150(2)	100(2)	100(2)	150(2)
Z	4	1	1	1	2
$\rho_{, calc}$ [g cm^{-3}]	1.874	1.892	2.070	2.289	1.868
λ/ [Å]	0.71073	0.71073	1.54178	0.71075	0.71073
Data Measured	87384	36495	39213	56545	47193
Ind. Reflns	10453	8997	7810	12312	8118
R_{int}	0.0612	0.0579	0.0413	0.0485	0.0295
Reflns with I > 2σ(I)	8591	6615	7051	10099	7247
Para-meters	596	580	578	594	318
Restraints	2	150	42	42	31
R_1[b](obs), wR_2[b](all)	0.0593, 0.1037	0.1055, 0.2313	0.0779, 0.2254	0.0713, 0.1498	0.0373, 0.0713
goodness of fit	1.039	1.077	1.024	1.059	1.151
Largest residuals/ [e $Å^{-3}$]	2.088, -1.619	4.422, -2.626	4.400, -2.390	5.351, -2.994	1.959, -1.241

[a]Includes solvate molecules.

[b] $R_1=\Sigma||Fo| - |Fc||/\Sigma|Fo|$, $wR_2= \{\Sigma[w(Fo^2-Fc^2)^2]/\Sigma[w(Fo^2)^2]\}^{1/2}$.

Table S4- Crystallographic specifications for samples **C16-C20**.

	C16	**C17**	**C18**	**C19**	**C20**
Formula[a]	$Cr_2Dy_2C_{44}H_{56}N_4O_{20}$	$Mn_2Dy_2C_{54}H_{56}N_2O_{17}$	$Mn_2Gd_2C_{29.5}H_{61}N_6O_{24.5}$	$Cr_4Dy_4C_{94}H_{114}N_4O_{37}$	$CrDy_6C_{115}H_{128}N_3O_{39}$
M, gmol^{-1}	1389.92	1439.88	1316.20	2749.90	3203.24
Crystal system	Monoclinic	Orthorhombic	Monoclinic	Monoclinic	Triclinic
Space group	*P 2$_1$/n*	*P m n 2$_1$*	*P 2$_1$/c*	*P 2$_1$/c*	*P-1*
a/[Å]	7.8874(4)	15.5742(9)	19.7059(8)	14.8531(2)	15.49940(10)
b/[Å]	17.7343(8)	20.1115(13)	15.4226(6)	14.8534(2)	15.67110(10)
c/[Å]	17.8886(8)	9.7842(4)	20.9323(8)	52.4751(9)	17.09800(10)
α/[°]	90	90	90	90	106.2720(10)
β/[°]	94.4690(10)	90	116.3220(10)	96.4020(10)	102.2070(10)
γ/[°]	90	90	90	90	114.0440(10)
V/[Å^3]	2491.4(2)	3064.6(3)	5702.1(4)	11504.8(3)	3380.27(5)
T/K	150(2)	173(2)	150(2)	150(2)	173(2)
Z	2	2	4	4	1
ρ, calc [g cm^{-3}]	1.853	1.560	1.531	1.582	1.569
λ/ [Å]	0.71073	0.71073	0.71073	1.54184	0.71075
Data Measured	38698	20319	109375	112260	537124
Ind. Reflns	7525	7637	12603	22749	15503
R_{int}	0.0223	0.0416	0.1069	0.0533	0.0521
Reflns with I > 2σ(I)	6895	5854	9165	18722	13344
Para-meters	327	366	614	1393	764
Restraints	0	158	42	107	20
R_1[b](obs), wR_2[b](all)	0.0336, 0.0777	0.1044, 0.2324	0.0999, 0.1875	0.0883, 0.2190	0.0656, 0.1677
goodness of fit	1.040	1.060	1.111	1.059	1.070
Largest residuals/ [e Å^{-3}]	4.142, -1.058	4.040, -2.427	2.439, -1.426	2.190, -1.463	3.881, -1.164

[a]Includes solvate molecules.

[b] $R_1=\Sigma||Fo| - |Fc||/\Sigma|Fo|$, $wR_2= \{\Sigma[w(Fo^2-Fc^2)^2]/\Sigma[w(Fo^2)^2]\}^{1/2}$.

Table S5- Crystallographic specifications for samples **C21-C25**.

	C21	**C22**	**C23**	**C24**	**C25**
Formula[a]	$Ru_2Dy_2C_{40}H_{48}N_4O_{20}$	$Ru_2Dy_2C_{48}H_{72}Cl_2N_2O_{18}$	$Ru_2Dy_2C_{34}H_{60}N_4O_{20}$	$Ru_2Dy_2C_{44}H_{44}F_{12}N_4O_{20}$	$Ru_2Dy_2C_{40}H_{32}F_{16}N_4O_{20}$
M, $gmol^{-1}$	1431.96	1563.11	1372.00	1703.97	1719.80
Crystal system	Monoclinic	Hexagonal	Triclinic	Triclinic	Monoclinic
Space group	*P 2₁/n*	*P -6 2 c*	*P-1*	*P-1*	*P 2₁/c*
a/[Å]	8.0960(16)	20.986(3)	10.367(2)	10.0637(3)	10.4794(7)
b/[Å]	17.161(3)	20.986(3)	11.169(2)	11.1366(3)	22.2231(13)
c/[Å]	17.146(3)	27.302(6)	11.256(2)	13.1405(4)	11.1383(7)
α/[°]	90	90	67.16(3)	68.9850(10)	90
β/[°]	92.44(3)	90	73.88(3)	75.3770(10)	98.183(6)
γ/[°]	90	120	83.77(3)	89.5200(10)	90
V/[$Å^3$]	2380.0(8)	10413(4)	1153.9(5)	1324.73(7)	2567.5(3)
T/K	100(2)	150(2)	150(2)	150(2)	173(2)
Z	2	6	1	1	2
$\rho_{, calc}$ [g cm^{-3}]	1.998	1.495	1.974	2.136	2.219
λ/ [Å]	0.71073	0.71073	0.71073	0.71073	0.71073
Data Measured	44448	189257	19324	24168	17452
Ind. Reflns	6208	9808	4973	7978	6921
R_{int}	0.0742	0.0607	0.0175	0.0191	0.0367
Reflns with I > 2σ(I)	5858	8590	4805	7170	5606
Para-meters	309	362	286	381	391
Restraints	0	37	0	0	0
R_1[b](obs), wR_2[b](all)	0.0381, 0.0944	0.0561, 0.1719	0.0269, 0.0645	0.0307, 0.0638	0.0505, 0.0787
goodness of fit	1.055	1.049	1.066	1.061	1.038
Largest residuals/ [e Å $^{-3}$]	1.294, -1.295	1.677, -2.967	1.246, -1.385	2.440, -0.735	1.336, -0.835

[a]Includes solvate molecules.

[b] $R_1=\Sigma||Fo| - |Fc||/\Sigma|Fo|$, $wR_2= \{\Sigma[w(Fo^2-Fc^2)^2]/\Sigma[w(Fo^2)^2]\}^{1/2}$.

Table S6- Crystallographic specifications for samples **C26-C30**.

	C26	**C27**	**C28**	**C29**	**C30**
Formula[a]	$Ru_2Dy_2C_{40}H_{36}Cl_4F_8N_4O_{20}$	$Ru_2Gd_2C_{40}H_{48}N_4O_{20}$	$Ru_2Gd_2C_{34}H_{60}N_4O_{20}$	$Ru_2Dy_4C_{86}H_{92}N_2O_{30}$	$In_{16}Dy_6C_{193}H_{209}N_{11}O_{92}$
M, $gmol^{-1}$	1713.66	1421.46	1361.50	2485.78	6966.84
Crystal system	Monoclinic	Monoclinic	Triclinic	Monoclinic	Triclinic
Space group	*C 2/m*	*P 2₁/n*	*P-1*	*P 2₁/c*	*P-1*
a/[Å]	15.536(3)	8.0820(16)	10.343(2)	19.4315(2)	22.7373(3)
b/[Å]	16.010(3)	17.209(3)	11.205(2)	19.4429(2)	23.8381(5)
c/[Å]	12.208(2)	17.212(3)	11.250(2)	25.2337(4)	24.8983(5)
α/[°]	90	90.00	67.17(3)	90	93.571(2)
β/[°]	121.06(3)	92.35(3)	74.35(3)	97.4900(10)	91.8860(10)
γ/[°]	90	90.00	84.09(3)	90	101.4280(10)
V/[$Å^3$]	2601.1(11)	2391.9(8)	1157.1(5)	9452.1(2)	13187.9(4)
T/K	123(2)	123(2)	150(2)	150(2)	150(2)
Z	2	2	1	4	2
$\rho_{, calc}$ [g cm^{-3}]	2.229	1.974	1.954	1.745	1.751
λ/ [Å]	0.71073	0.71073	0.71073	1.54184	1.54184
Data Measured	9794	38797	17332	91240	154883
Ind. Reflns	2239	5612	3959	19322	52344
R_{int}	0.0306	0.0538	0.0377	0.0619	0.1091
Reflns with I > 2σ(I)	2234	5454	3899	15237	34976
Para-meters	195	309	286	1131	2863
Restraints	12	0	0	5	3
R_1[b](obs), wR_2[b](all)	0.1288, 0.3014	0.0338, 0.0807	0.0268, 0.0636	0.0960, 0.2083	0.1888, 0.4155
goodness of fit	1.207	1.087	1.086	1.060	1.524
Largest residuals/ [e $Å^{-3}$]	6.542, -4.786	1.733, -1.011	1.622, -0.821	1.984, -2.277	14.249, -4.256

[a]Includes solvate molecules.

[b] $R_1=\Sigma||Fo| - |Fc||/\Sigma|Fo|$, $wR_2= \{\Sigma[w(Fo^2-Fc^2)^2]/\Sigma[w(Fo^2)^2]\}^{1/2}$.

Table S7- Bond Valence Sum (BVS) calculations and scores for variable oxidation state transition metal centres in complex **C2**. Only ions in the asymmetric unit are considered for simplicity.

C2	Bond	Distance / Å	R_0	b	Valence	Total Score
(III)	Co1 - O1	1.939	1.637	0.37	0.44	**2.92**
	Co1 - O2	1.888	1.637	0.37	0.51	
	Co1 - O5	1.921	1.637	0.37	0.46	
	Co1 - N1	1.986	1.75	0.37	0.53	
	Co1 - O7	1.924	1.637	0.37	0.46	
	Co1 - O3	1.879	1.637	0.37	0.52	

Table S8- Bond Valence Sum (BVS) calculations and scores for variable oxidation state transition metal centres in complex **C3**. Only ions in the asymmetric unit are considered for simplicity.

C3	Bond	Distance / Å	R_0	b	Valence	Total Score
(III)	Mn1 - O1	2.235	1.76	0.37	0.28	**3.22**
	Mn1 - O1'	1.944	1.76	0.37	0.61	
	Mn1 - O3'	1.888	1.76	0.37	0.71	
	Mn1 - O10	2.21	1.76	0.37	0.30	
	Mn1 - O4	1.918	1.76	0.37	0.65	
	Mn1 - O2	1.904	1.76	0.37	0.68	

Table S9- Bond Valence Sum (BVS) calculations and scores for variable oxidation state transition metal centres in complex **C4**. Only ions in the asymmetric unit are considered for simplicity.

C4	Bond	Distance / Å	R_0	b	Valence	Total Score
(II)	Mn1-O1	2.164	1.79	0.37	0.36	**2.16**
	Mn1-O7	2.101	1.79	0.37	0.43	
	Mn1-O8	2.14	1.79	0.37	0.39	
	Mn1-N1	2.253	1.85	0.37	0.34	
	Mn1-O3	2.326	1.79	0.37	0.23	
	Mn1-O9	2.126	1.79	0.37	0.40	
(II)	Mn2-O1	2.189	1.79	0.37	0.34	**2.12**
	Mn2-O10	2.126	1.79	0.37	0.40	
	Mn2-O4	2.297	1.79	0.37	0.25	
	Mn2-N2	2.272	1.85	0.37	0.32	
	Mn2-O11	2.129	1.79	0.37	0.40	
	Mn2-O12	2.126	1.79	0.37	0.40	
(III)	Mn3-O1	1.885	1.76	0.37	0.71	**3.19**
	Mn3-O13	1.958	1.76	0.37	0.59	
	Mn3-O3	2.206	1.76	0.37	0.30	
	Mn3-O14	1.966	1.76	0.37	0.57	
	Mn3-O2	1.88	1.76	0.37	0.72	
	Mn3-O6	2.215	1.76	0.37	0.29	
(III)	Mn4-O1	1.899	1.76	0.37	0.69	**3.11**
	Mn4-O5	2.232	1.76	0.37	0.28	
	Mn4-O2	1.896	1.76	0.37	0.69	
	Mn4-O15	1.961	1.76	0.37	0.58	
	Mn4-O4	2.204	1.76	0.37	0.30	
	Mn4-O16	1.971	1.76	0.37	0.57	
(II)	Mn5-O2	2.18	1.79	0.37	0.35	**1.99**
	Mn5-O5	2.282	1.79	0.37	0.26	
	Mn5-O17	2.128	1.79	0.37	0.40	
	Mn5-O18	2.256	1.79	0.37	0.28	
	Mn5-O19	2.21	1.79	0.37	0.32	
	Mn5-O20	2.155	1.79	0.37	0.37	
(II)	Mn6-O2	2.206	1.79	0.37	0.32	**2.09**
	Mn6-O21	2.175	1.79	0.37	0.35	
	Mn6-O22	2.09	1.79	0.37	0.44	
	Mn6-N3	2.288	1.85	0.37	0.31	
	Mn6-O23	2.146	1.79	0.37	0.38	
	Mn6-O6	2.256	1.79	0.37	0.28	

Table S10- Bond Valence Sum (BVS) calculations and scores for variable oxidation state transition metal centres in complex **C5**. Only ions in the asymmetric unit are considered for simplicity.

C5	Bond	Distance / Å	R_0	b	Valence	Total Score
(III)	Mn1 - O1	2.271	1.76	0.37	0.25	**3.22**
	Mn1 - O1'	1.945	1.76	0.37	0.61	
	Mn1 - O3'	1.877	1.76	0.37	0.73	
	Mn1 - O10	2.169	1.76	0.37	0.33	
	Mn1 - O4	1.938	1.76	0.37	0.62	
	Mn1 - O2	1.899	1.76	0.37	0.69	

Table S11- Bond Valence Sum (BVS) calculations and scores for variable oxidation state transition metal centres in complex **C6**. Only ions in the asymmetric unit are considered for simplicity.

C6	Bond	Distance / Å	R_0	b	Valence	Total Score
(III)	Fe1-O1	2.054	1.759	0.37	0.45	**2.99**
	Fe1-O1’	2.063	1.759	0.37	0.44	
	Fe1-O3’	1.935	1.759	0.37	0.62	
	Fe1-O10	2.072	1.759	0.37	0.43	
	Fe1-O4	1.992	1.759	0.37	0.53	
	Fe1-O2	2.000	1.759	0.37	0.52	

Table S12- Bond Valence Sum (BVS) calculations and scores for variable oxidation state transition metal centres in complex **C7**. Only ions in the asymmetric unit are considered for simplicity.

C7	Bond	Distance / Å	R_0	b	Valence	Total Score
(III)	Fe1-O1	1.985	1.759	0.37	0.54	**3.01**
	Fe1-O19	2.041	1.759	0.37	0.47	
	Fe1-O10	1.977	1.759	0.37	0.55	
	Fe1-O20	2.013	1.759	0.37	0.50	
	Fe1-O2	2.02	1.759	0.37	0.49	
	Fe1-O3	2.056	1.759	0.37	0.45	
(III)	Fe2-O1	2.029	1.759	0.37	0.48	**3.12**
	Fe2-O5	1.86	1.759	0.37	0.76	
	Fe2-O2	2.006	1.759	0.37	0.51	
	Fe2-O21	2.025	1.759	0.37	0.49	
	Fe2-O4	2.085	1.759	0.37	0.41	
	Fe2-O22	2.042	1.759	0.37	0.47	
(III)	Fe3-O1	1.925	1.759	0.37	0.64	**3.09**
	Fe3-O6	1.985	1.759	0.37	0.54	
	Fe3-O23	2.041	1.759	0.37	0.47	
	Fe3-O24	2.068	1.759	0.37	0.43	
	Fe3-O8	2	1.759	0.37	0.52	
	Fe3-O25	2.029	1.759	0.37	0.48	
(III)	Fe4-O2	1.927	1.759	0.37	0.64	**2.88**
	Fe4-O26	1.861	1.759	0.37	0.76	
	Fe4-O9	1.95	1.759	0.37	0.60	
	Fe4-N2	2.252	1.815	0.37	0.31	
	Fe4-O7	1.961	1.759	0.37	0.58	
(III)	Fe5-O5	1.885	1.759	0.37	0.71	**3.05**
	Fe5-O10	2.026	1.759	0.37	0.49	
	Fe5-O8	1.97	1.759	0.37	0.57	
	Fe5-O22	2.104	1.759	0.37	0.39	
	Fe5-N3	2.18	1.815	0.37	0.37	
	Fe5-O11	2.001	1.759	0.37	0.52	
(III)	Fe6-O5	2.03	1.759	0.37	0.48	**2.81**
	Fe6-O28	2.017	1.759	0.37	0.50	
	Fe6-O11	2.084	1.759	0.37	0.42	
	Fe6-O29	2.001	1.759	0.37	0.52	
	Fe6-O26	2.097	1.759	0.37	0.40	
	Fe6-O30	2.021	1.759	0.37	0.49	

Table S13- Bond Valence Sum (BVS) calculations and scores for variable oxidation state transition metal centres in complex **C8**. Only ions in the asymmetric unit are considered for simplicity.

C8	Bond	Distance / Å	R_0	b	Valence	Total Score
(III)	Fe1-O1	2.069	1.759	0.37	0.43	**3.08**
	Fe1-O1’	2.067	1.759	0.37	0.43	
	Fe1-O3’	1.929	1.759	0.37	0.63	
	Fe1-O10	2.043	1.759	0.37	0.46	
	Fe1-O4	1.966	1.759	0.37	0.57	
	Fe1-O2	1.981	1.759	0.37	0.55	

Table S14- Bond Valence Sum (BVS) calculations and scores for variable oxidation state transition metal centres in complex **C10**. Only ions in the asymmetric unit are considered for simplicity.

C10	Bond	Distance / Å	R_0	b	Valence	Total Score
(III)	Fe1-O1	1.951	1.759	0.37	0.60	**3.04**
	Fe1-O20	1.991	1.759	0.37	0.53	
	Fe1-O4	2.021	1.759	0.37	0.49	
	Fe1-O21	2.058	1.759	0.37	0.45	
	Fe1-O3	2.055	1.759	0.37	0.45	
	Fe1-O22	2.001	1.759	0.37	0.52	
(III)	Fe2-O1	1.892	1.759	0.37	0.70	**2.95**
	Fe2-O5	1.959	1.759	0.37	0.58	
	Fe2-O23	2.161	1.759	0.37	0.34	
	Fe2-N1	2.248	1.815	0.37	0.31	
	Fe2-O24	2.084	1.759	0.37	0.42	
	Fe2-O6	1.943	1.759	0.37	0.61	

Table S15- Bond Valence Sum (BVS) calculations and scores for variable oxidation state transition metal centres in complex **C11**. Only ions in the asymmetric unit are considered for simplicity.

C11	Bond	Distance / Å	R_0	b	Valence	Total Score
(II)	Co1-O1	2.186	1.685	0.37	0.26	**2.04**
	Co1-O2	2	1.685	0.37	0.43	
	Co1-O14	2.207	1.685	0.37	0.24	
	Co1-O13	2.111	1.685	0.37	0.32	
	Co1-O10	1.988	1.685	0.37	0.44	
	Co1-O12	2.07	1.685	0.37	0.35	
(III)	Co2-O1	1.916	1.637	0.37	0.47	**3.09**
	Co2-O12	1.87	1.637	0.37	0.53	
	Co2-O11	1.894	1.637	0.37	0.50	
	Co2-N1	1.912	1.75	0.37	0.65	
	Co2-O4	1.935	1.637	0.37	0.45	
	Co2-O3	1.9	1.637	0.37	0.49	
(II)	Co3-N3	2.258	1.65	0.37	0.19	**1.68**
	Co3-O8	2.095	1.685	0.37	0.33	
	Co3-O9	2.092	1.685	0.37	0.33	
	Co3-O11	2.041	1.685	0.37	0.38	
	Co3-O10	1.986	1.685	0.37	0.44	

Table S16- Bond Valence Sum (BVS) calculations and scores for variable oxidation state transition metal centres in complex **C12**. Only ions in the asymmetric unit are considered for simplicity.

C12	Bond	Distance / Å	R_0	b	Valence	Total Score
(II)	Co1-O1	2.182	1.685	0.37	0.26	**1.96**
	Co1-O2	2.029	1.685	0.37	0.39	
	Co1-O3	2.099	1.685	0.37	0.33	
	Co1-O1’	2.182	1.685	0.37	0.26	
	Co1-O2’	2.029	1.685	0.37	0.39	
	Co1-O3’	2.099	1.685	0.37	0.33	
(II)	Co2-O1	2.265	1.685	0.37	0.21	**1.79**
	Co2-O4’	1.996	1.685	0.37	0.43	
	Co2-O7	2.079	1.685	0.37	0.34	
	Co2-O9	2.032	1.685	0.37	0.39	
	Co2-O2	2.008	1.685	0.37	0.42	
(III)	Co3-O1	1.884	1.637	0.37	0.51	**3.00**
	Co3-O3’	1.915	1.637	0.37	0.47	
	Co3-O5’	1.906	1.637	0.37	0.48	
	Co3-O11’	1.931	1.637	0.37	0.45	
	Co3-N1’	1.926	1.75	0.37	0.62	
	Co3-O4’	1.924	1.637	0.37	0.46	

Table S17- Bond Valence Sum (BVS) calculations and scores for variable oxidation state transition metal centres in complex **C13**. Only ions in the asymmetric unit are considered for simplicity.

C13	Bond	Distance / Å	R_0	b	Valence	Total Score
(II)	Co1-O1	2.157	1.685	0.37	0.28	**2.01**
	Co1-O2	2.039	1.685	0.37	0.38	
	Co1-O3	2.085	1.685	0.37	0.34	
	Co1-O1’	2.157	1.685	0.37	0.28	
	Co1-O2’	2.039	1.685	0.37	0.38	
	Co1-O3’	2.085	1.685	0.37	0.34	
(II)	Co2-O1	2.253	1.685	0.37	0.22	**1.78**
	Co2-O4’	2.022	1.685	0.37	0.40	
	Co2-O7	2.056	1.685	0.37	0.37	
	Co2-O9	2.038	1.685	0.37	0.39	
	Co2-O2	2.014	1.685	0.37	0.41	
(III)	Co3-O1	1.893	1.637	0.37	0.50	**3.02**
	Co3-O3’	1.934	1.637	0.37	0.45	
	Co3-O5’	1.904	1.637	0.37	0.49	
	Co3-O11’	1.928	1.637	0.37	0.46	
	Co3-N1’	1.912	1.75	0.37	0.65	
	Co3-O4’	1.903	1.637	0.37	0.49	

Table S18- Bond Valence Sum (BVS) calculations and scores for variable oxidation state transition metal centres in complex **C14**. Only ions in the asymmetric unit are considered for simplicity.

C14	Bond	Distance / Å	R_0	b	Valence	Total Score
(II)	Co1-O1	2.162	1.685	0.37	0.28	**1.99**
	Co1-O2	2.045	1.685	0.37	0.38	
	Co1-O3	2.084	1.685	0.37	0.34	
	Co1-O1'	2.162	1.685	0.37	0.28	
	Co1-O2'	2.045	1.685	0.37	0.38	
	Co1-O3'	2.084	1.685	0.37	0.34	
(II)	Co2-O1	2.24	1.685	0.37	0.22	**1.90**
	Co2-O4'	1.992	1.685	0.37	0.44	
	Co2-O7	2.02	1.685	0.37	0.40	
	Co2-O9	2.004	1.685	0.37	0.42	
	Co2-O2	2.011	1.685	0.37	0.41	
(III)	Co3-O1	1.887	1.637	0.37	0.51	**3.07**
	Co3-O3'	1.915	1.637	0.37	0.47	
	Co3-O5'	1.889	1.637	0.37	0.51	
	Co3-O11'	1.926	1.637	0.37	0.46	
	Co3-N1'	1.919	1.75	0.37	0.63	
	Co3-O4'	1.901	1.637	0.37	0.49	

Table S19- Bond Valence Sum (BVS) calculations and scores for variable oxidation state transition metal centres in complex **C17**. Only ions in the asymmetric unit are considered for simplicity.

C17	Bond	Distance / Å	R_0	b	Valence	Total Score
(III)	Mn1-O1	1.862	1.76	0.37	0.76	**3.17**
	Mn1-O6	2.169	1.76	0.37	0.33	
	Mn1-O2	1.834	1.76	0.37	0.82	
	Mn1-N1	2.06	1.84	0.37	0.55	
	Mn1-O3	1.889	1.76	0.37	0.71	

Table S20- Bond Valence Sum (BVS) calculations and scores for variable oxidation state transition metal centres in complex **C18**. Only ions in the asymmetric unit are considered for simplicity.

C18	Bond	Distance / Å	R_0	b	Valence	Total Score
(III)	Mn1-O1	1.866	1.76	0.37	0.75	**3.25**
	Mn1-O6	2.081	1.76	0.37	0.42	
	Mn1-O2	1.874	1.76	0.37	0.73	
	Mn1-N1	2.035	1.84	0.37	0.59	
	Mn1-O3	1.866	1.76	0.37	0.75	
(III)	Mn2-O1	1.862	1.76	0.37	0.76	**3.29**
	Mn2-O7	2.078	1.76	0.37	0.42	
	Mn2-O12	1.877	1.76	0.37	0.73	
	Mn2-N2	2.018	1.84	0.37	0.62	
	Mn2-O13	1.86	1.76	0.37	0.76	

Appendix C – Nuclear Magnetic Resonance Spectroscopy

Synthesised organic compounds were characterised by NMR spectroscopy with data collected on a JEOL ECS-500 FT NMR in the solvent described with chemical shifts (δ) quoted in ppm. Spectra were collected at a frequency of 500 MHz for ^{1}H spectra and 125 MHz for ^{13}C spectra.

NMR processing was carried out making use of Delta version 6.1.0.

Deuterated solvents were procured from Sigma Aldrich with ≥99.8% deuterium labelling.

Figure S1- 2-(methylamino)ethan-1-ol, [**MAE**]H, ^{1}H NMR

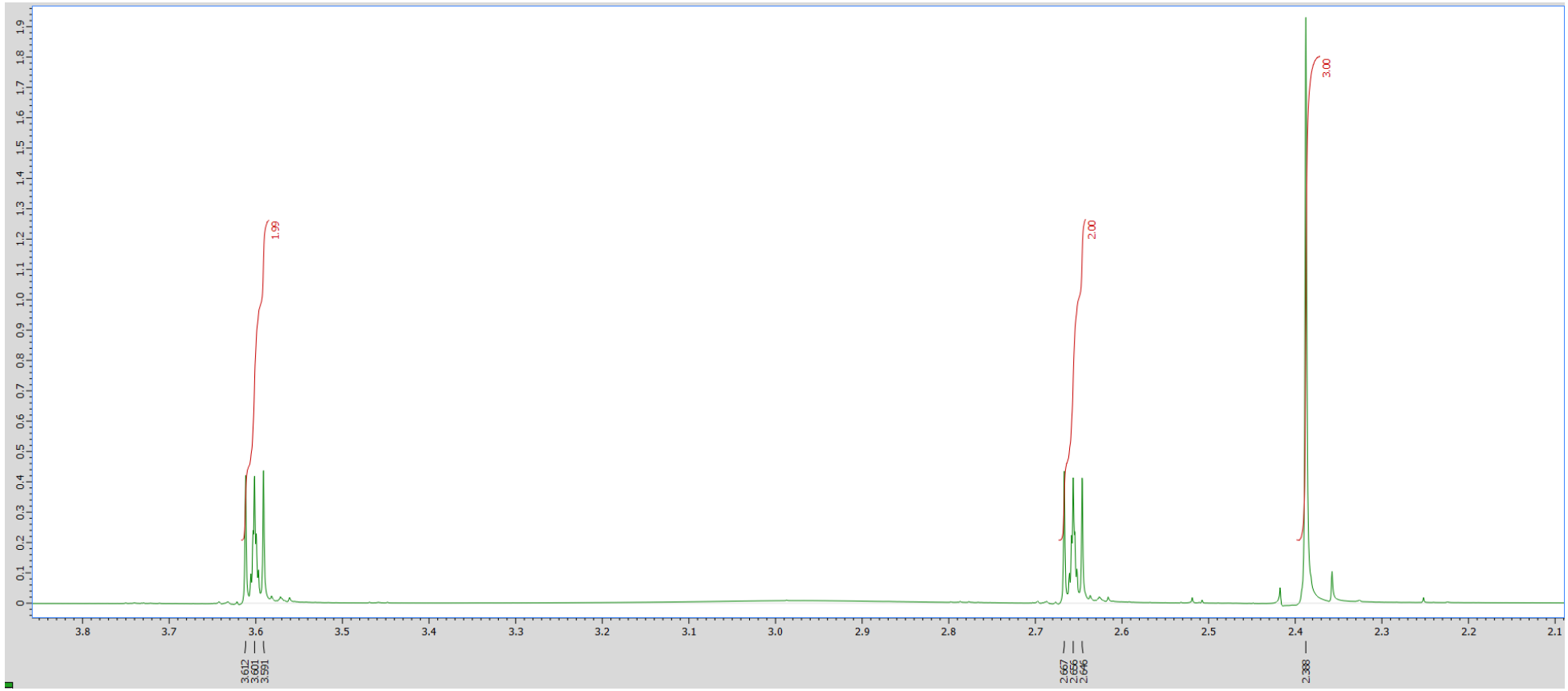

Figure S2- 2-(methylamino)ethan-1-ol, [**MAE**]H, COSY

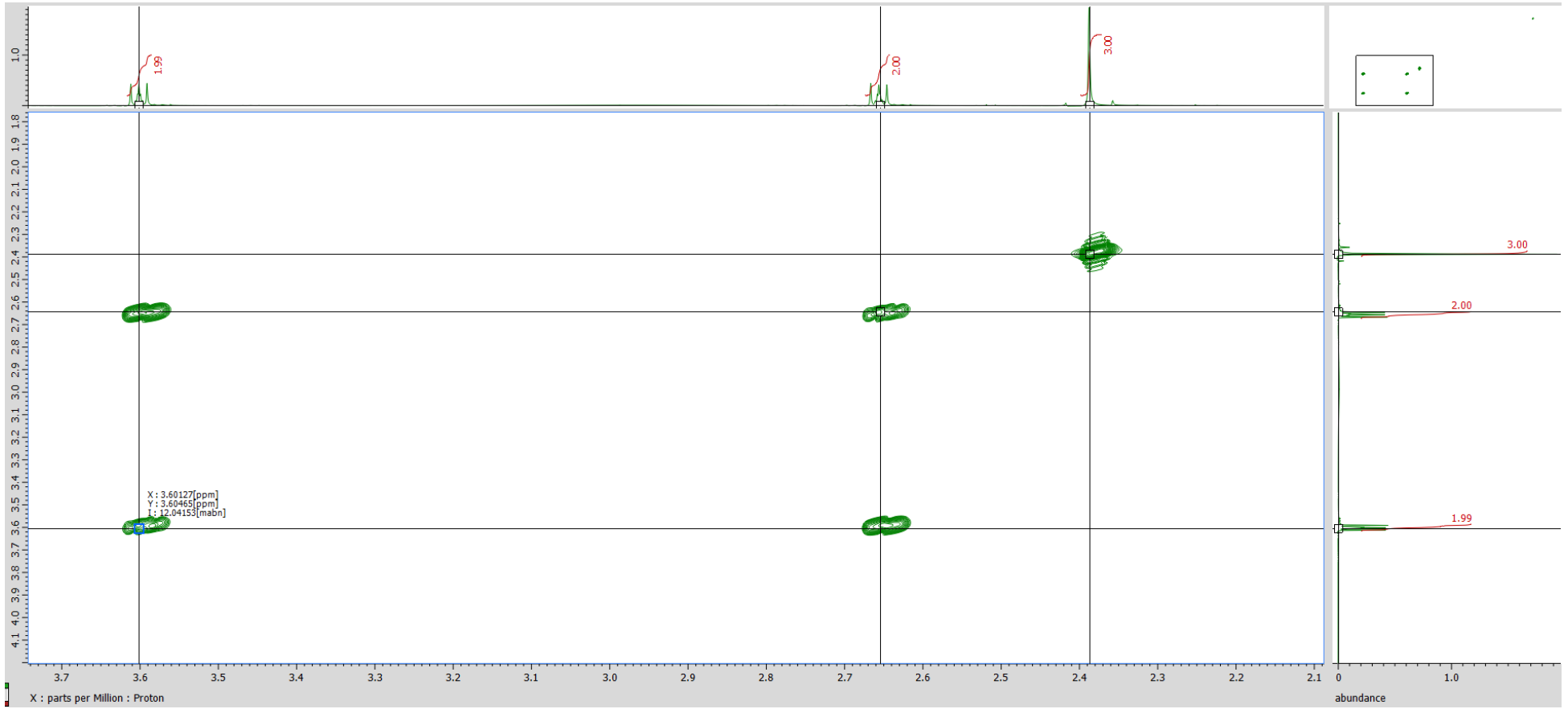

Figure S3- 2-(methylamino)ethan-1-ol, [**MAE**]H, ^{13}C NMR

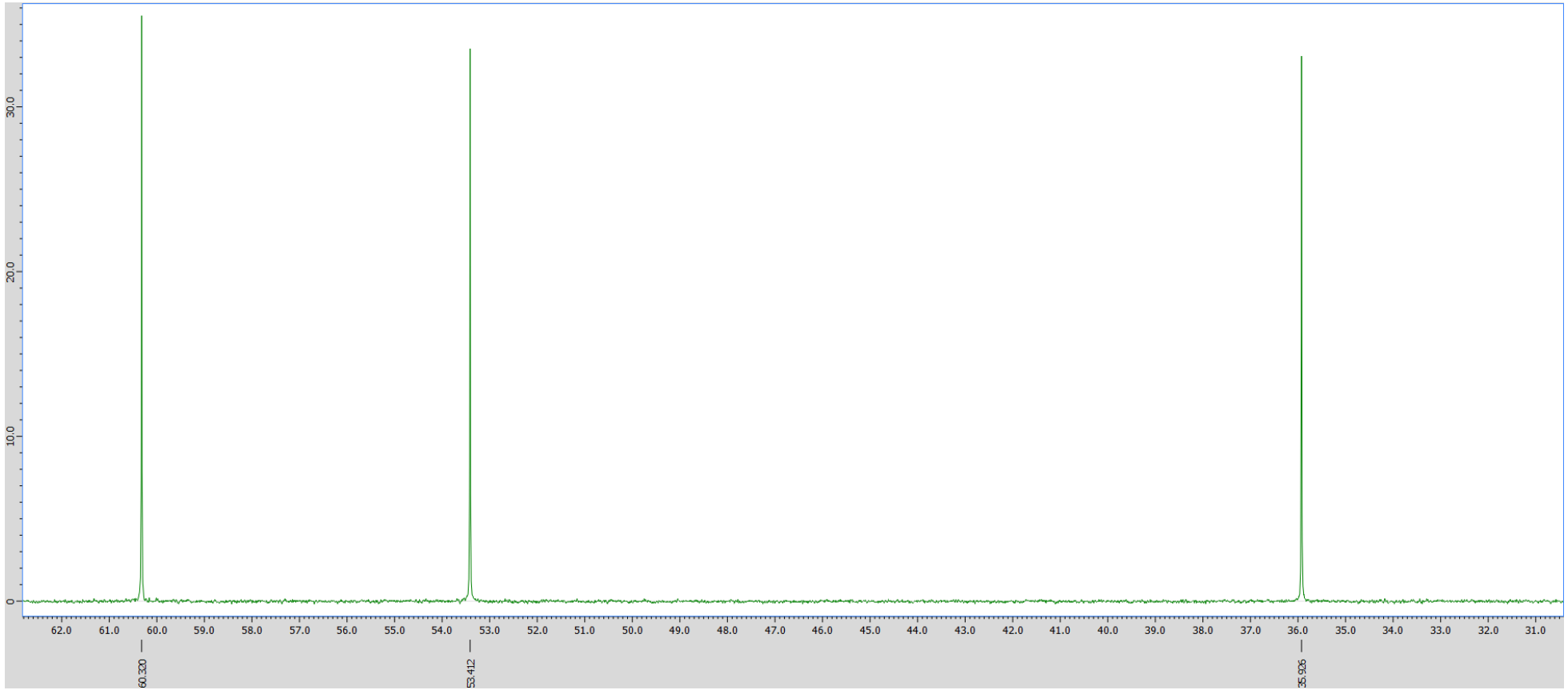

Figure S4- 2-(methylamino)ethan-1-ol, [**MAE**]H, HMQC

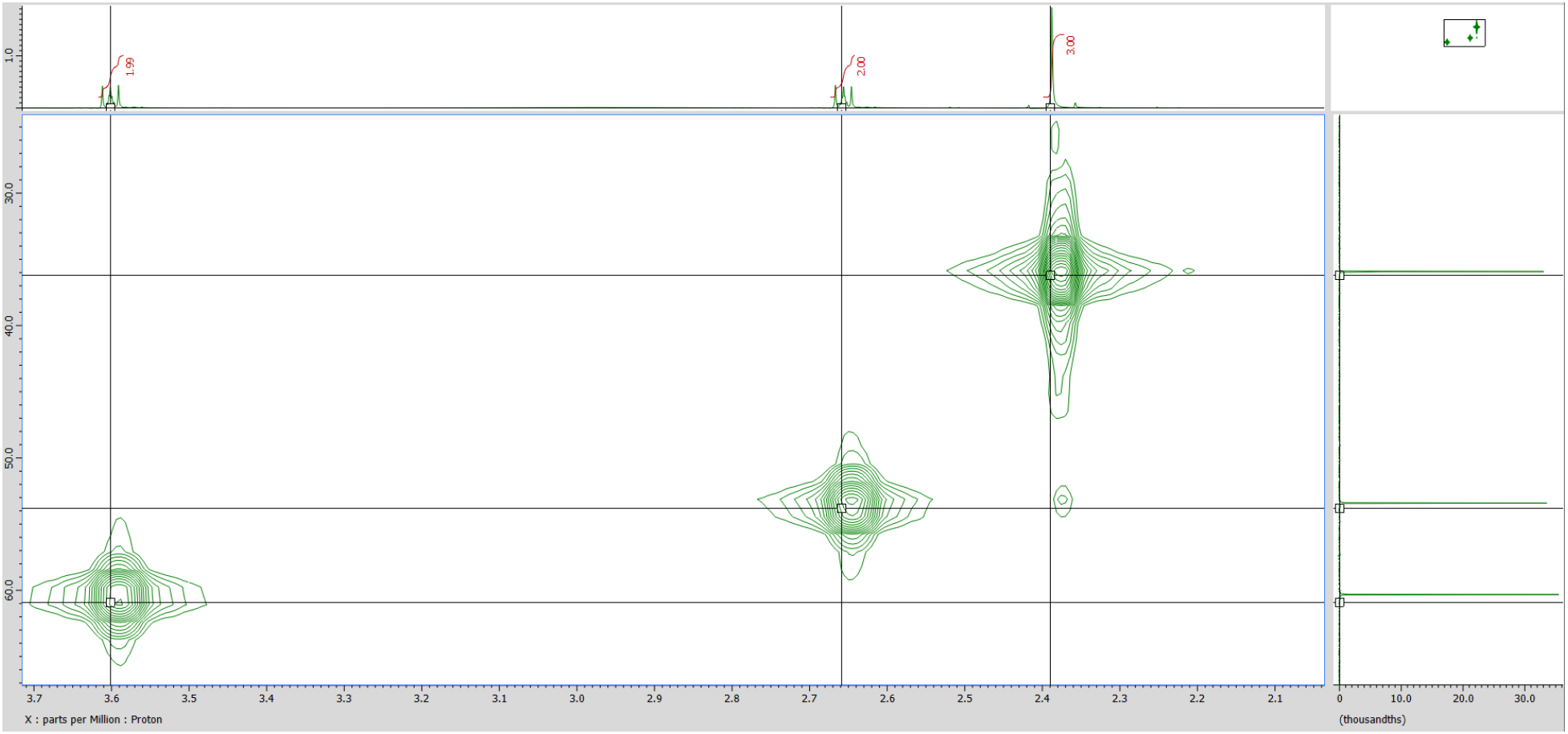

Figure S5- 2-(ethylamino)ethan-1-ol, [**EAE**]H, ^{1}H NMR

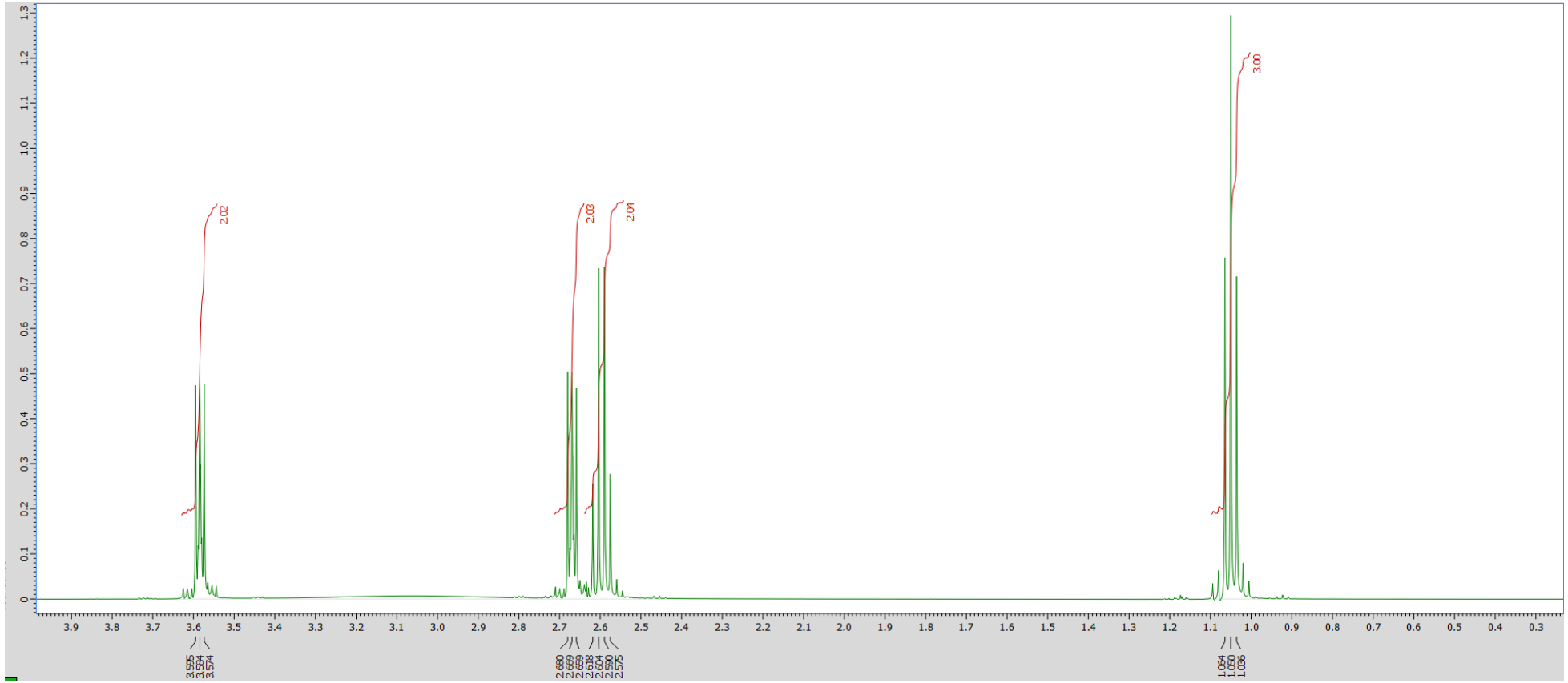

Figure S6- 2-(ethylamino)ethan-1-ol, [**EAE**]H, COSY

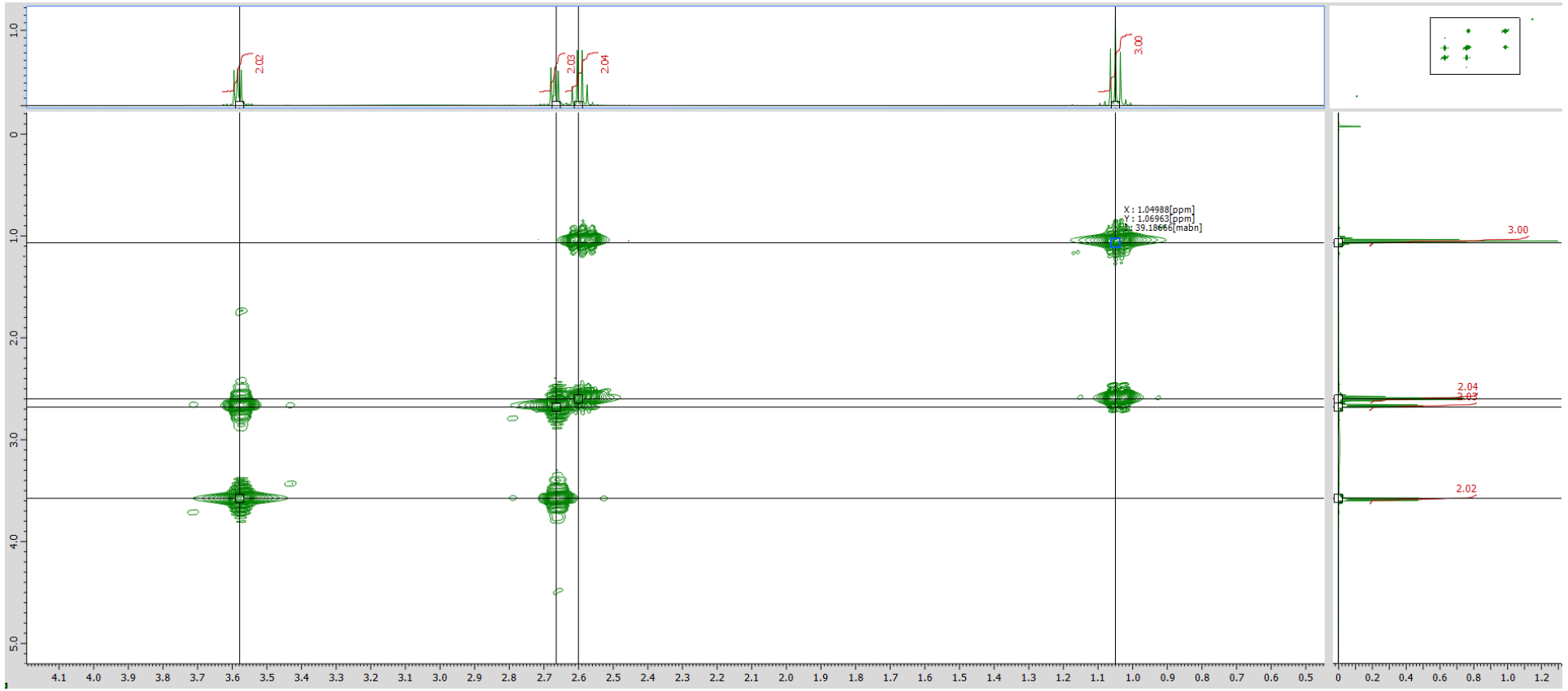

Figure S7- 2-(ethylamino)ethan-1-ol, [**EAE**]H, ^{13}C NMR

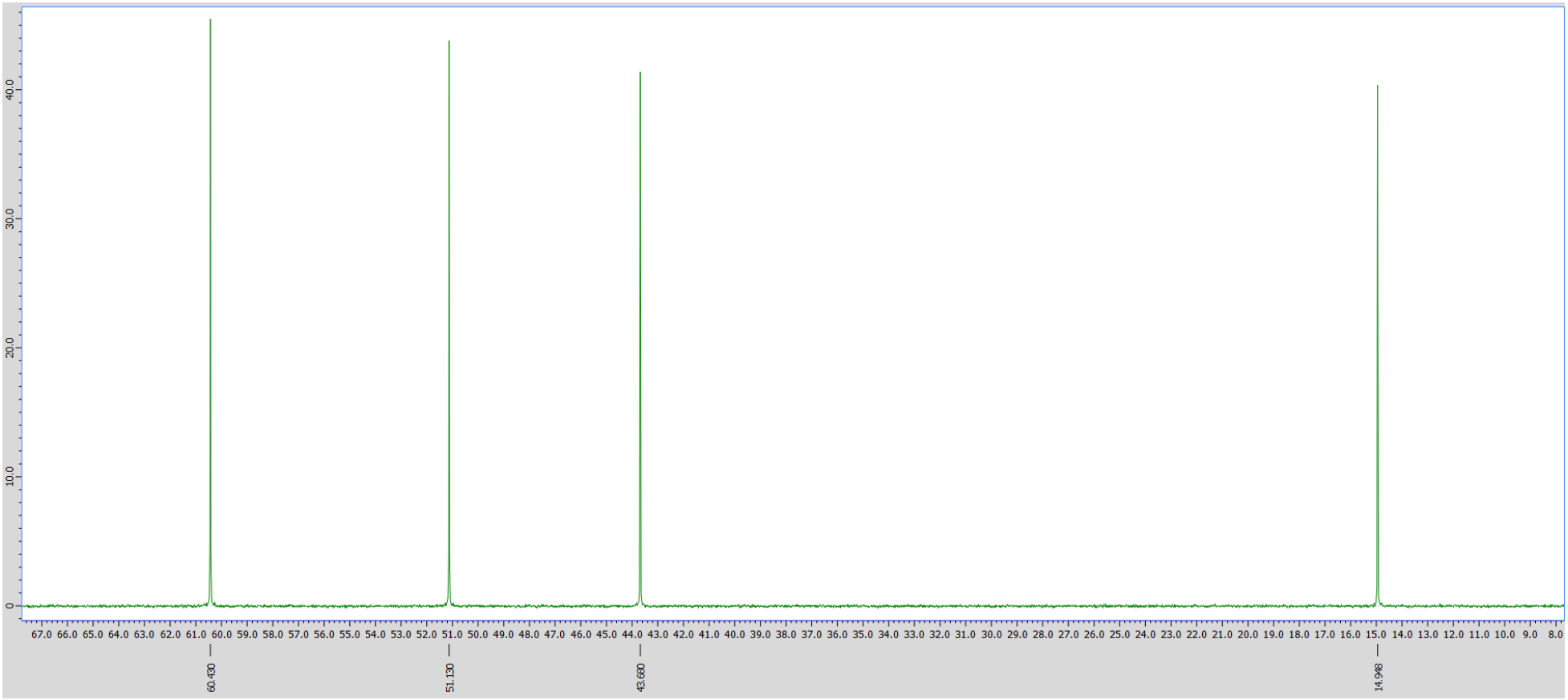

Figure S8- 2-(ethylamino)ethan-1-ol, [**EAE**]H, HMQC

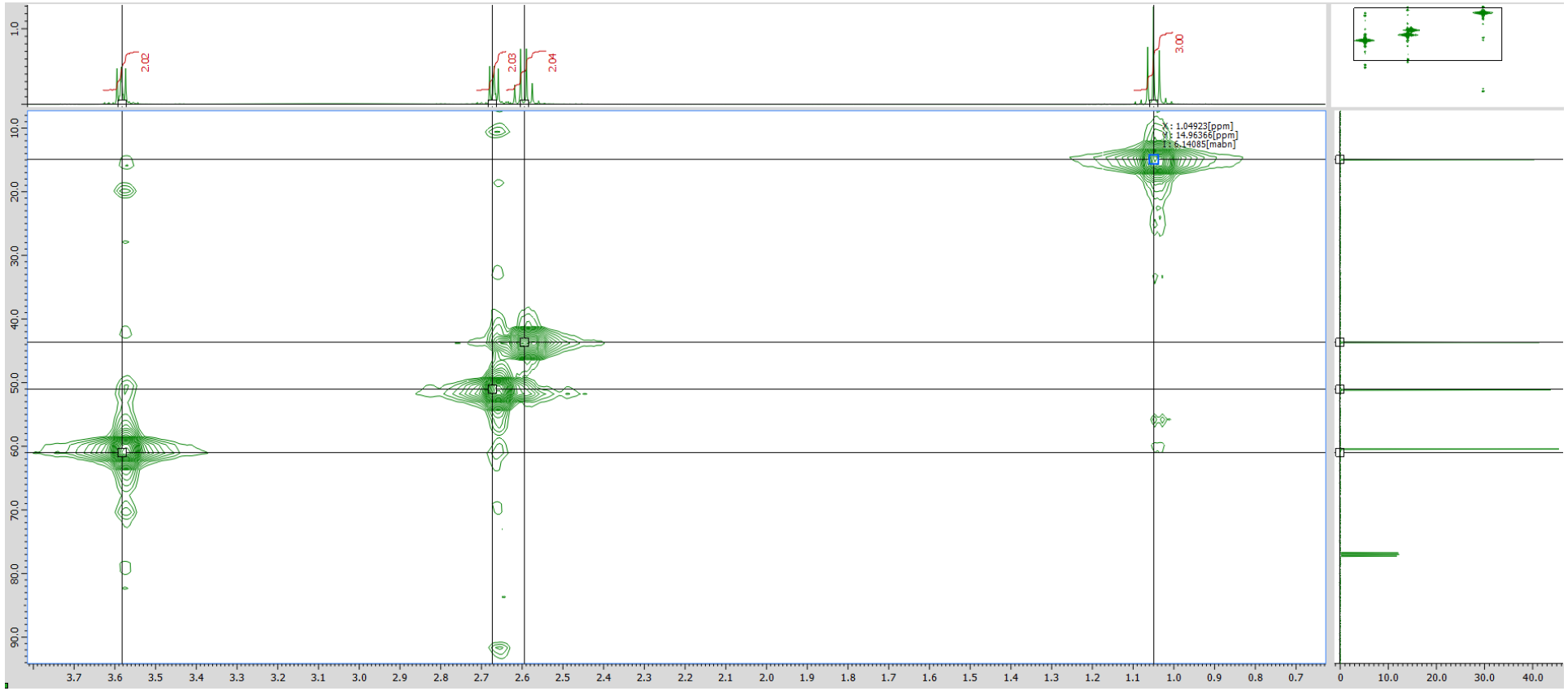

Figure S9- 2-(isopropylamino)ethan-1-ol, [^{i}**PrAE**]H, ^{1}H NMR

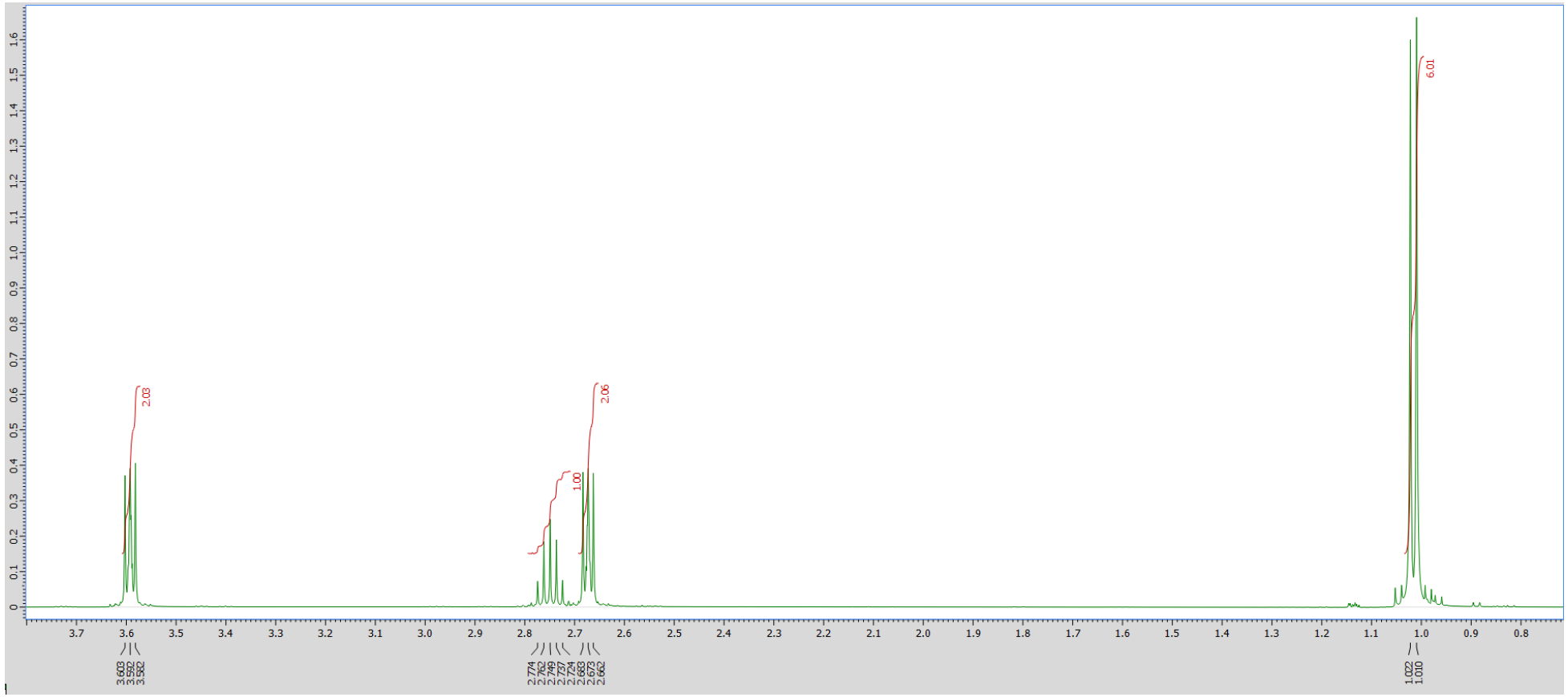

Figure S10- 2-(isopropylamino)ethan-1-ol, [^{i}**PrAE**]H, COSY

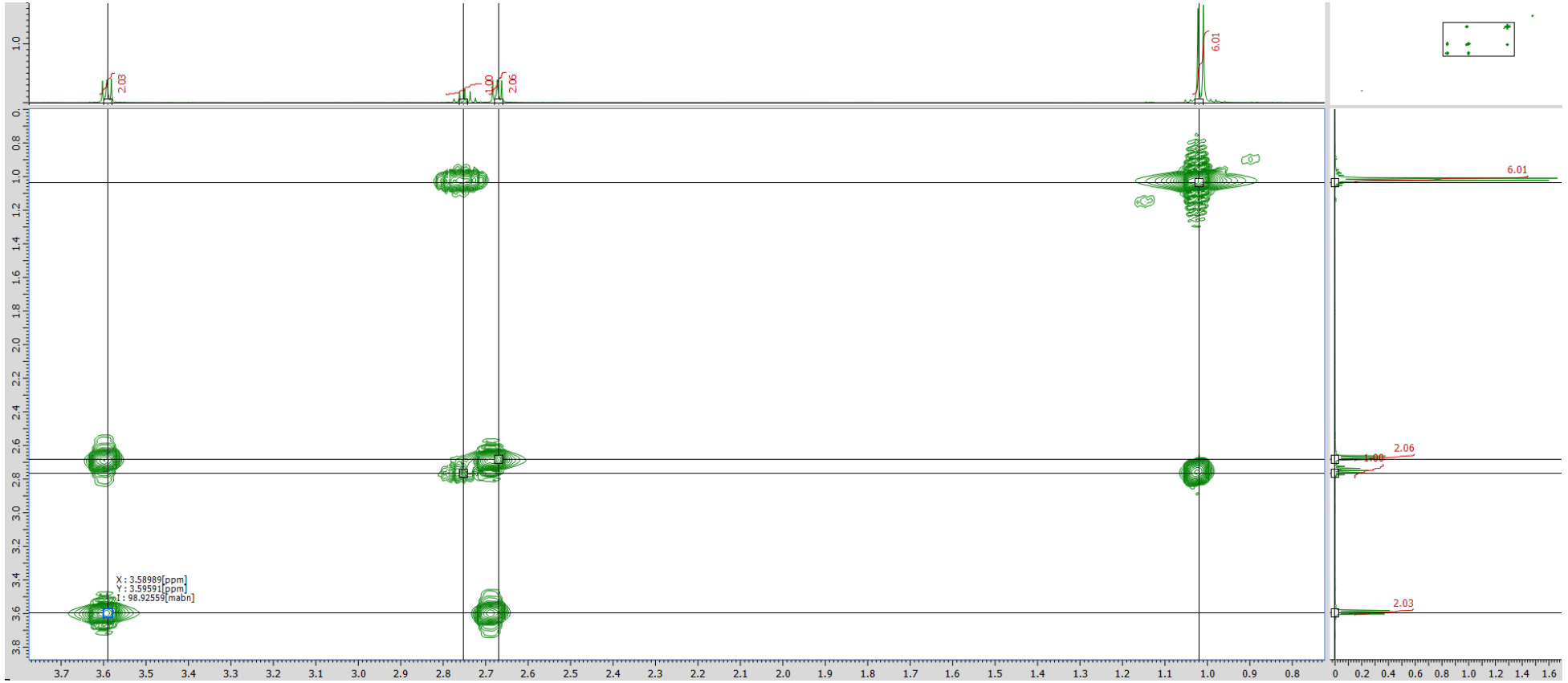

Figure S11- 2-(isopropylamino)ethan-1-ol, [^{i}**PrAE**]H, ^{13}C NMR

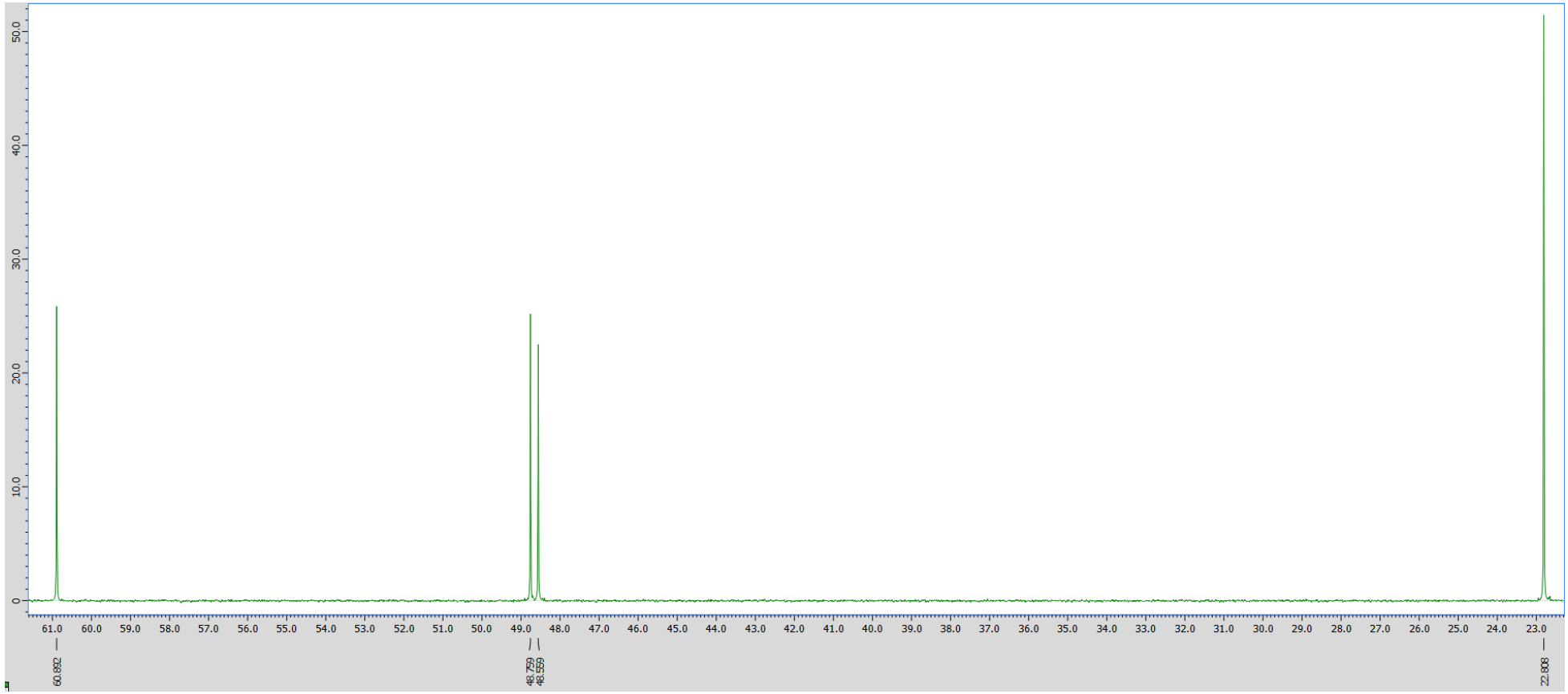

Figure S12- 2-(isopropylamino)ethan-1-ol, [^{i}**PrAE**]H, HMQC

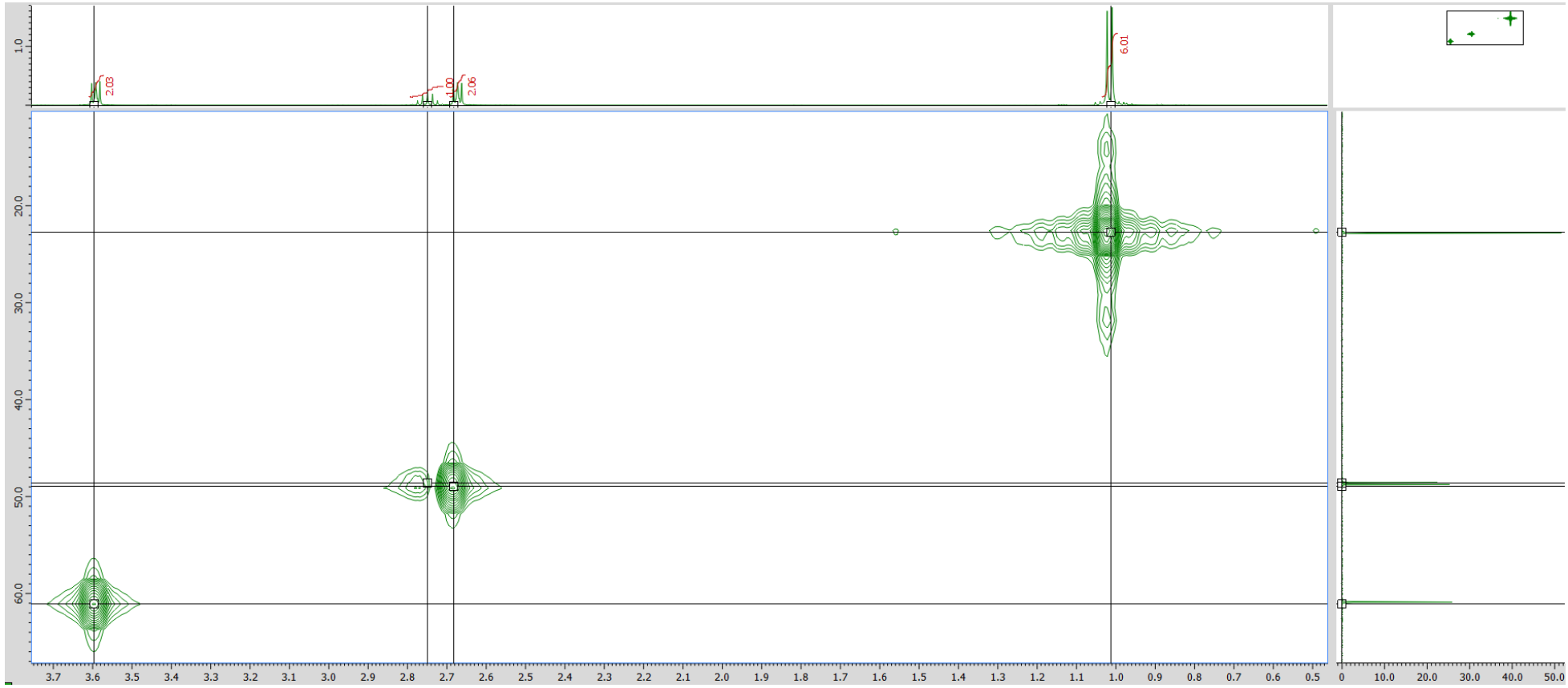

Figure S13- 2-(tertbutylamino)ethan-1-ol, [^{t}**BuAE**]H, ^{1}H NMR

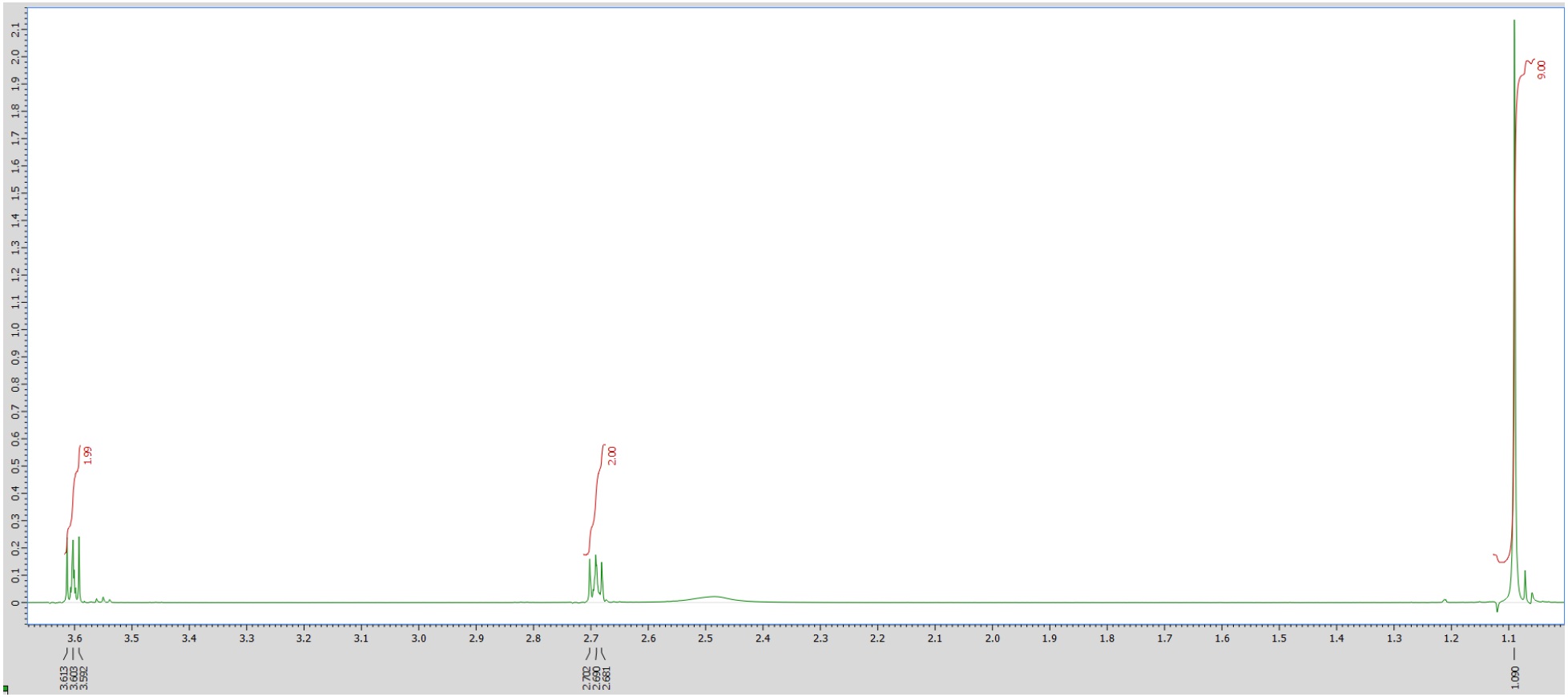

Figure S14- 2-(tertbutylamino)ethan-1-ol, [^{t}**BuAE**]H, COSY

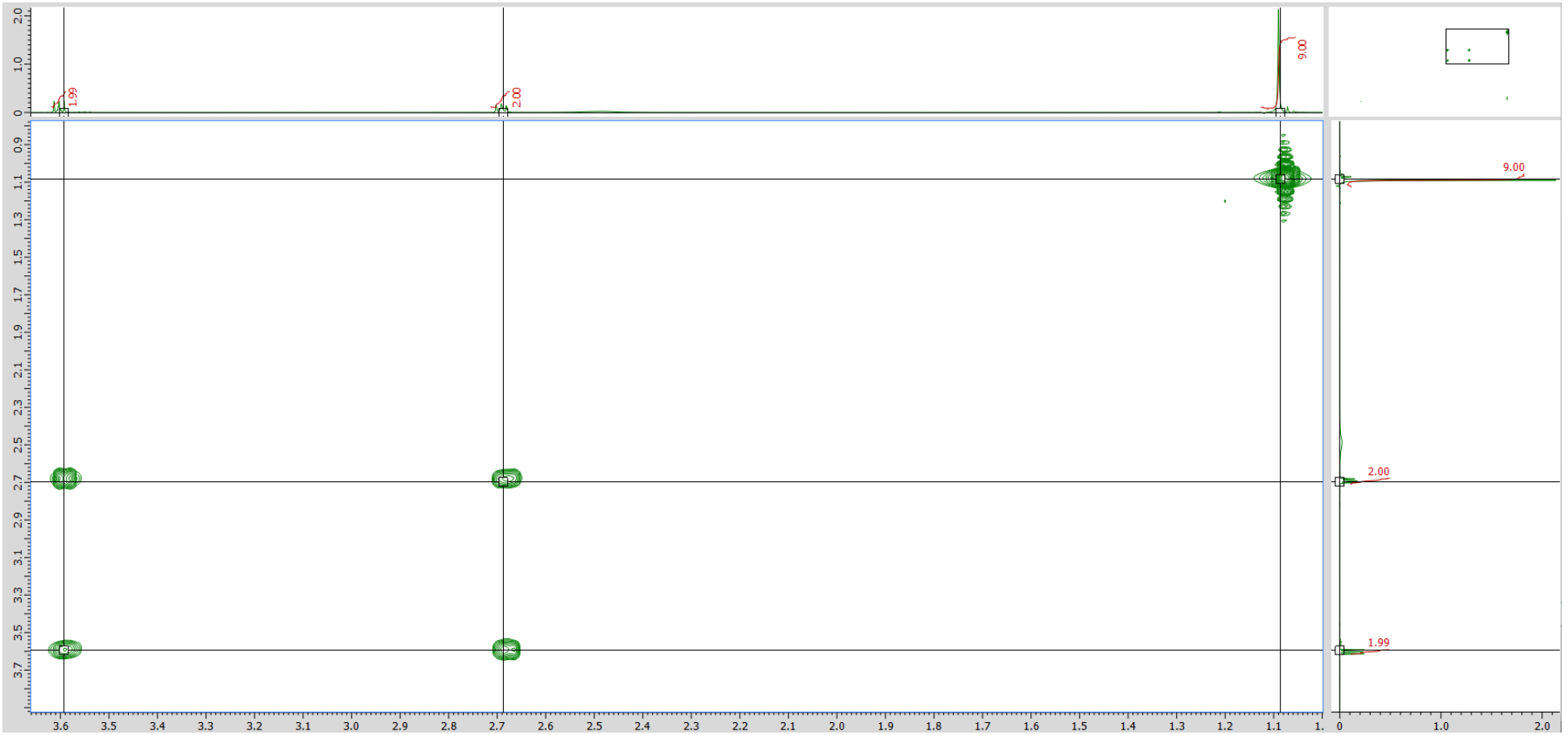

Figure S15- 2-(tertbutylamino)ethan-1-ol, [^{t}**BuAE**]H, ^{13}C NMR

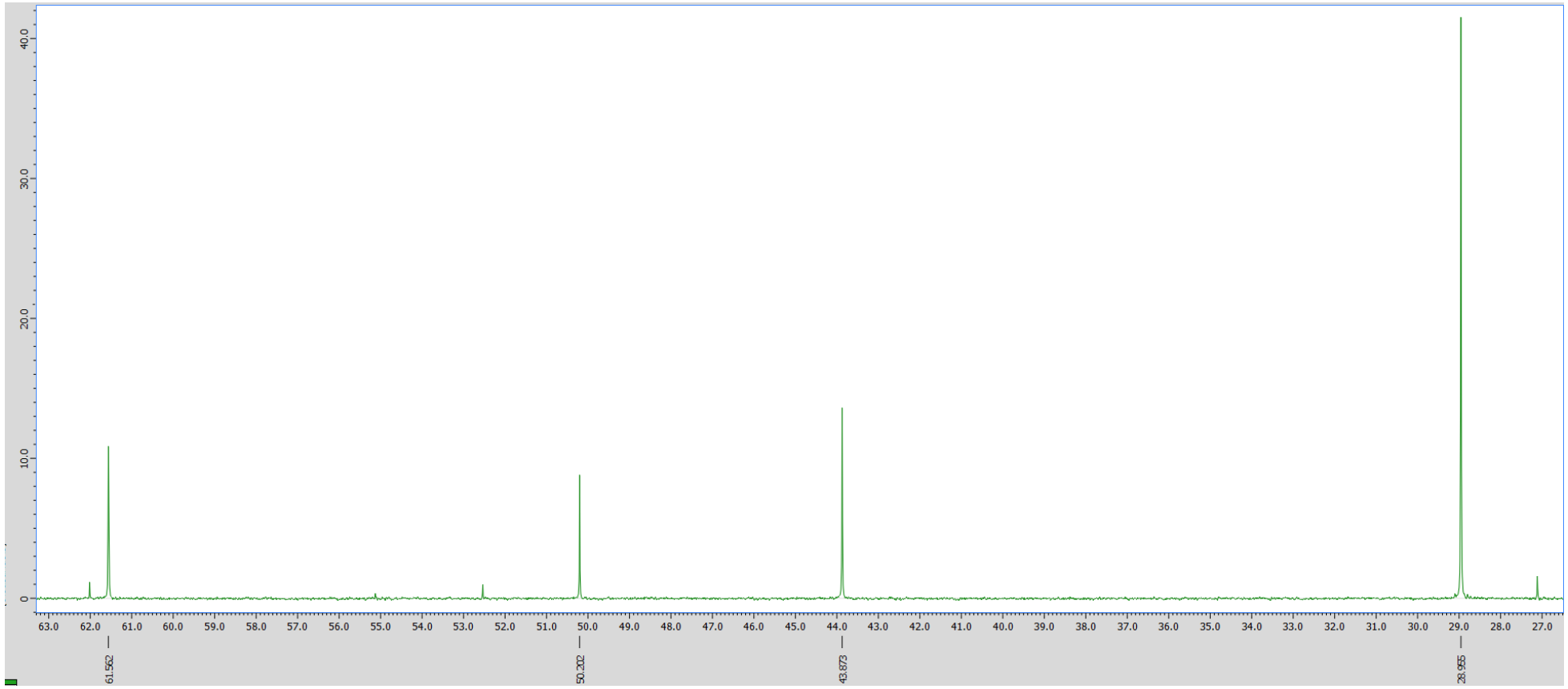

Figure S16- 2-(tertbutylamino)ethan-1-ol, [^{t}**BuAE**]H, HMQC

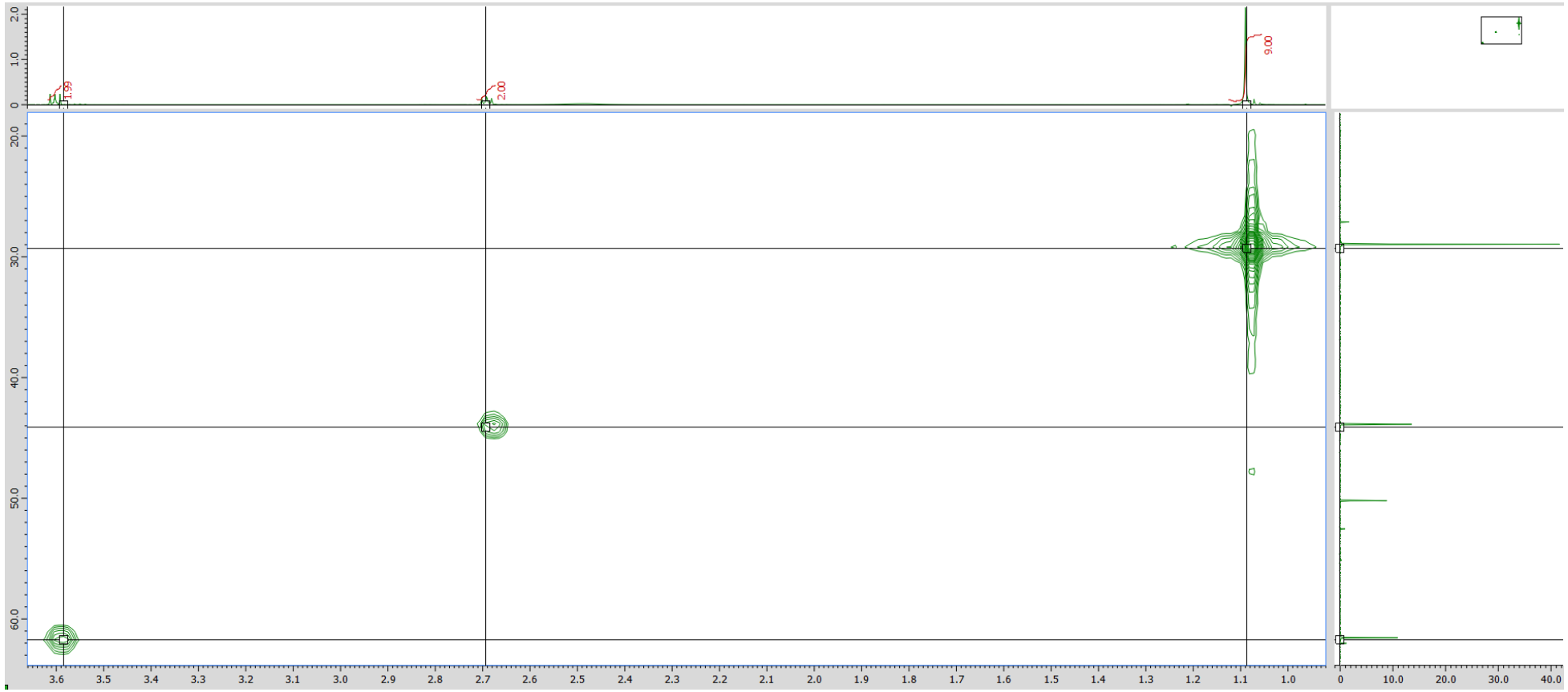

Figure S17- 2-(phenylamino)ethan-1-ol, [**PhAE**]H, ^{1}H NMR

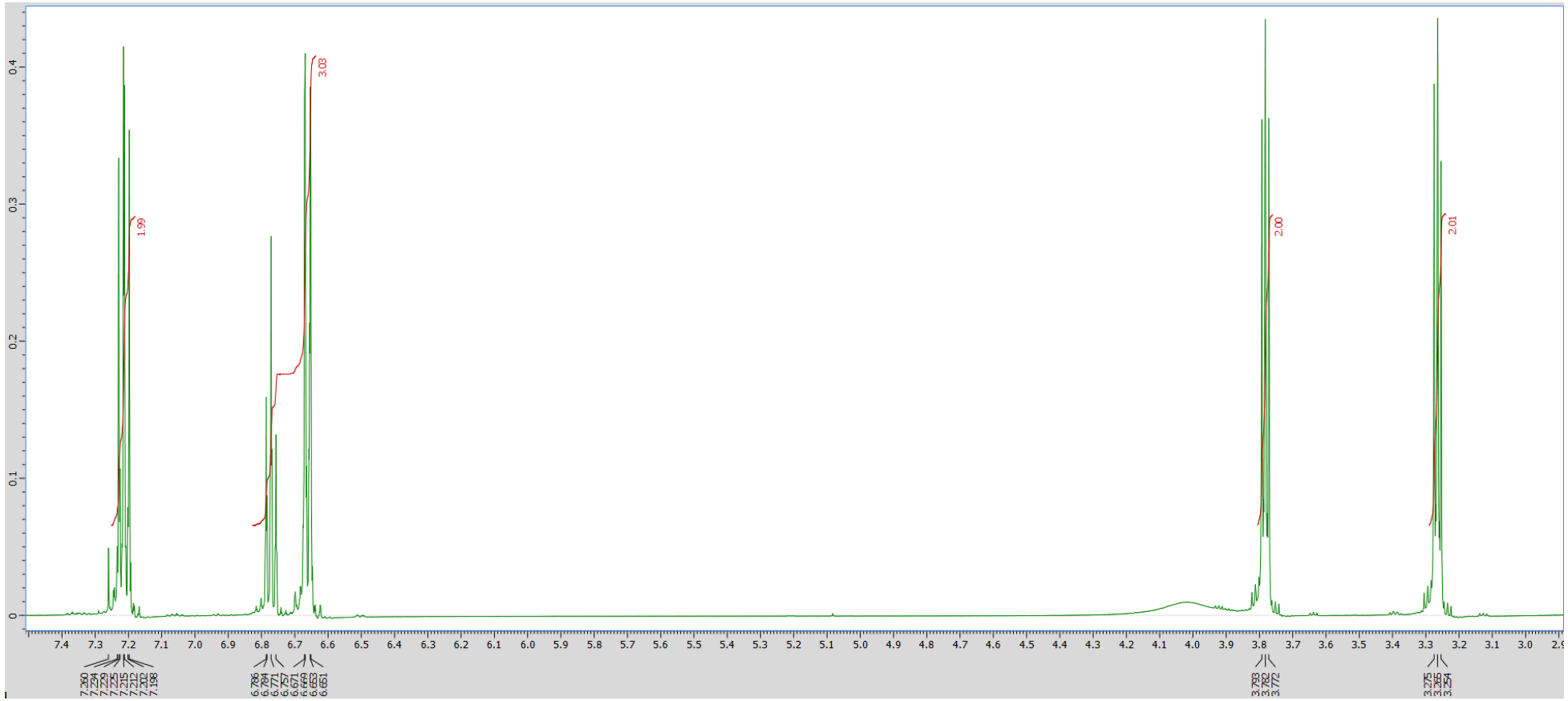

Figure S18- 2-(phenylamino)ethan-1-ol, [**PhAE**]H, COSY

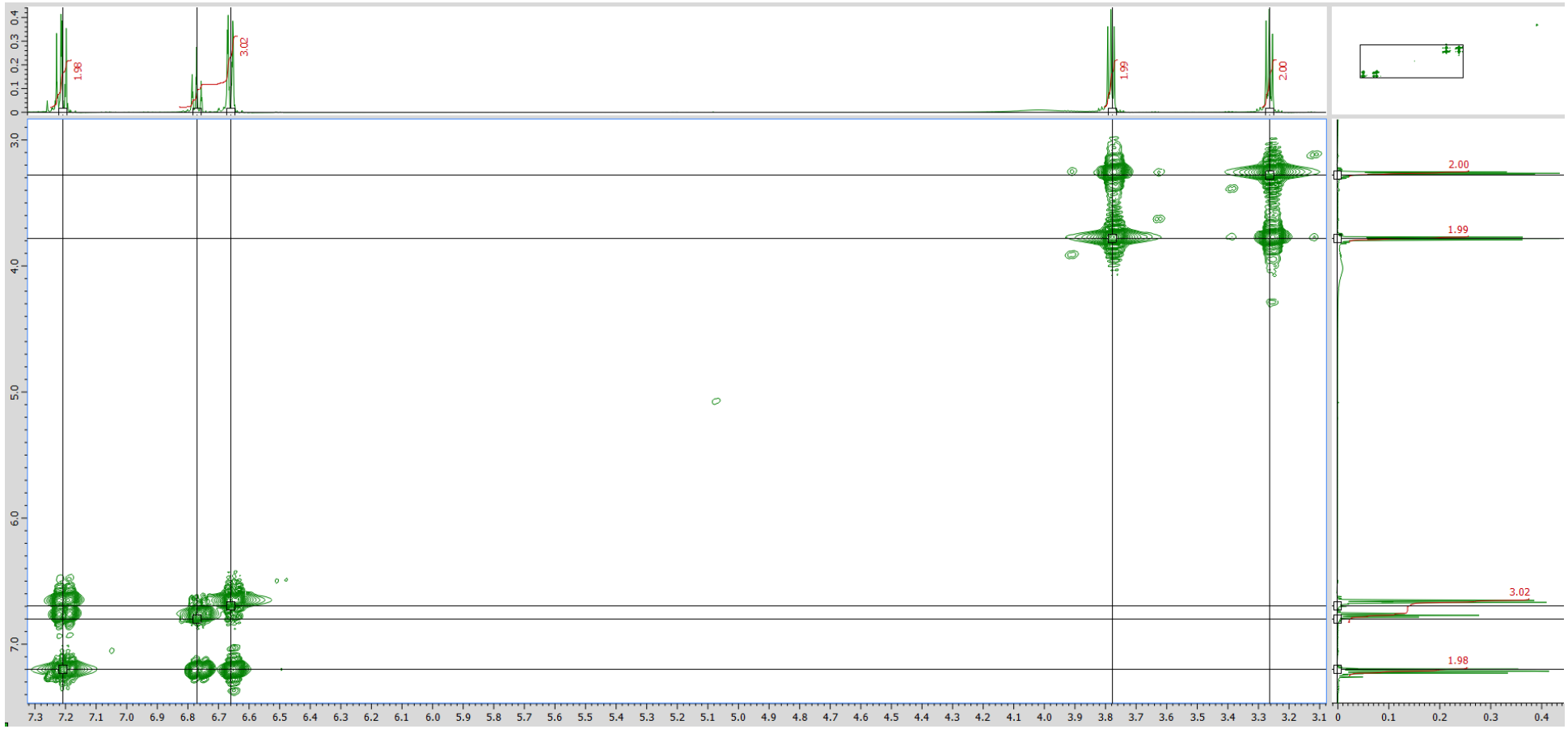

Figure S19- 2-(phenylamino)ethan-1-ol, [**PhAE**]H, ^{13}C NMR

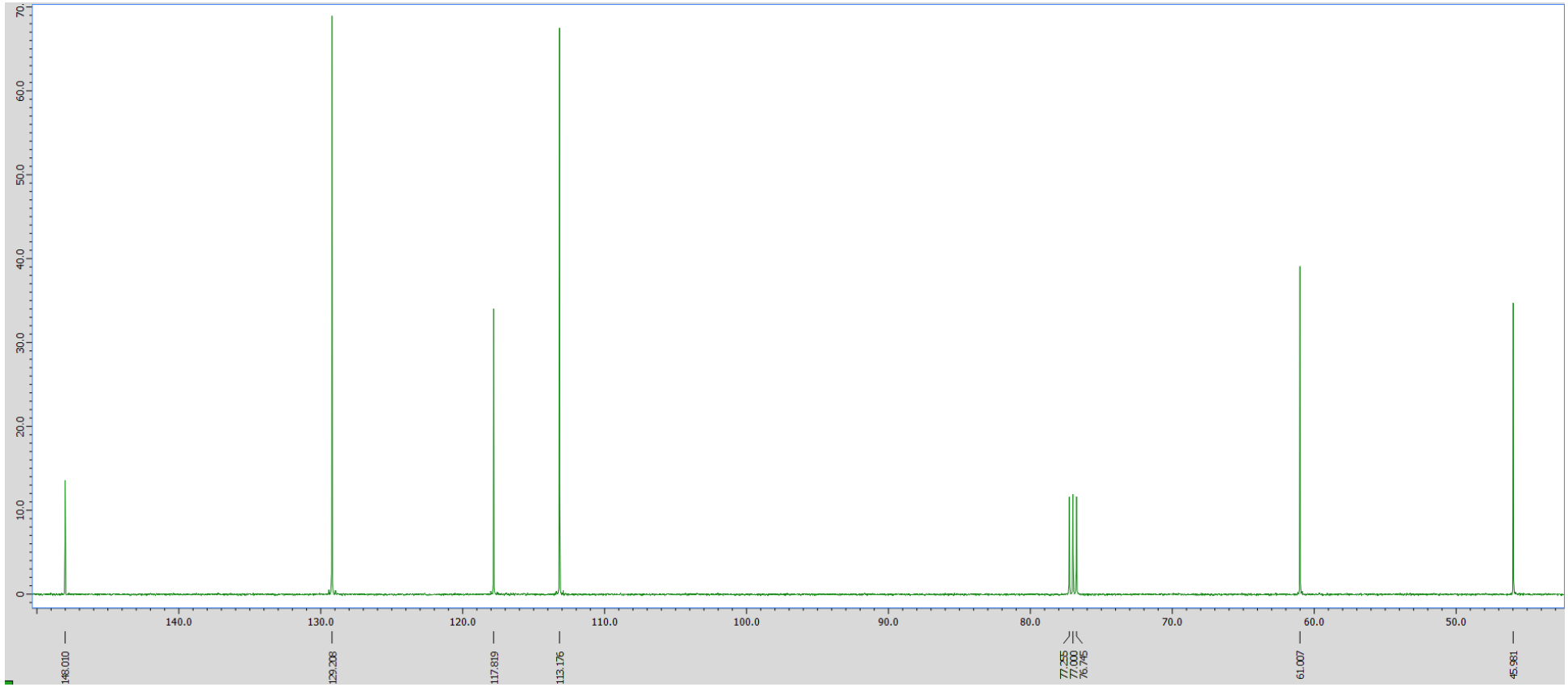

Figure S20- 2-(phenylamino)ethan-1-ol, [**PhAE**]H, HMQC

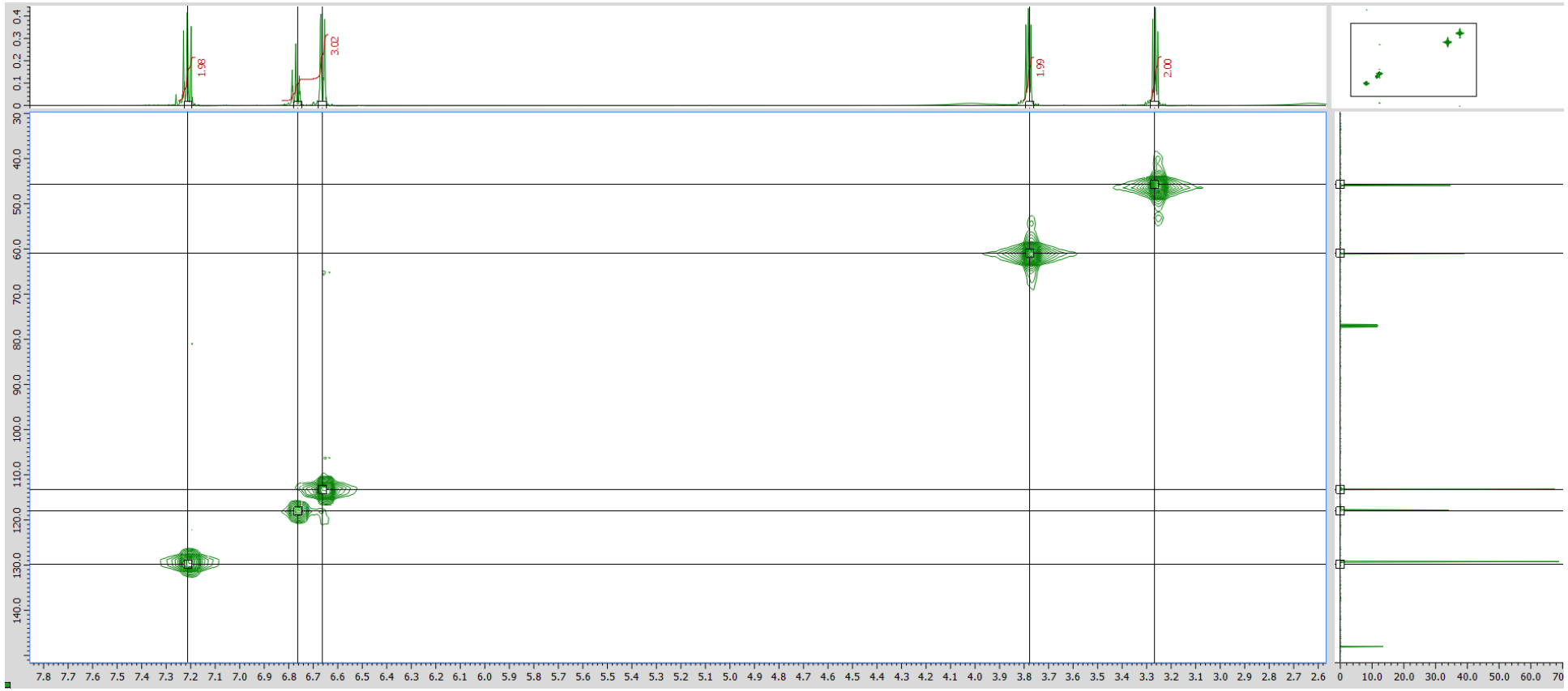

Figure S21- 2-(adamantylamino)ethan-1-ol, [**AdAE**]H, ^{1}H NMR

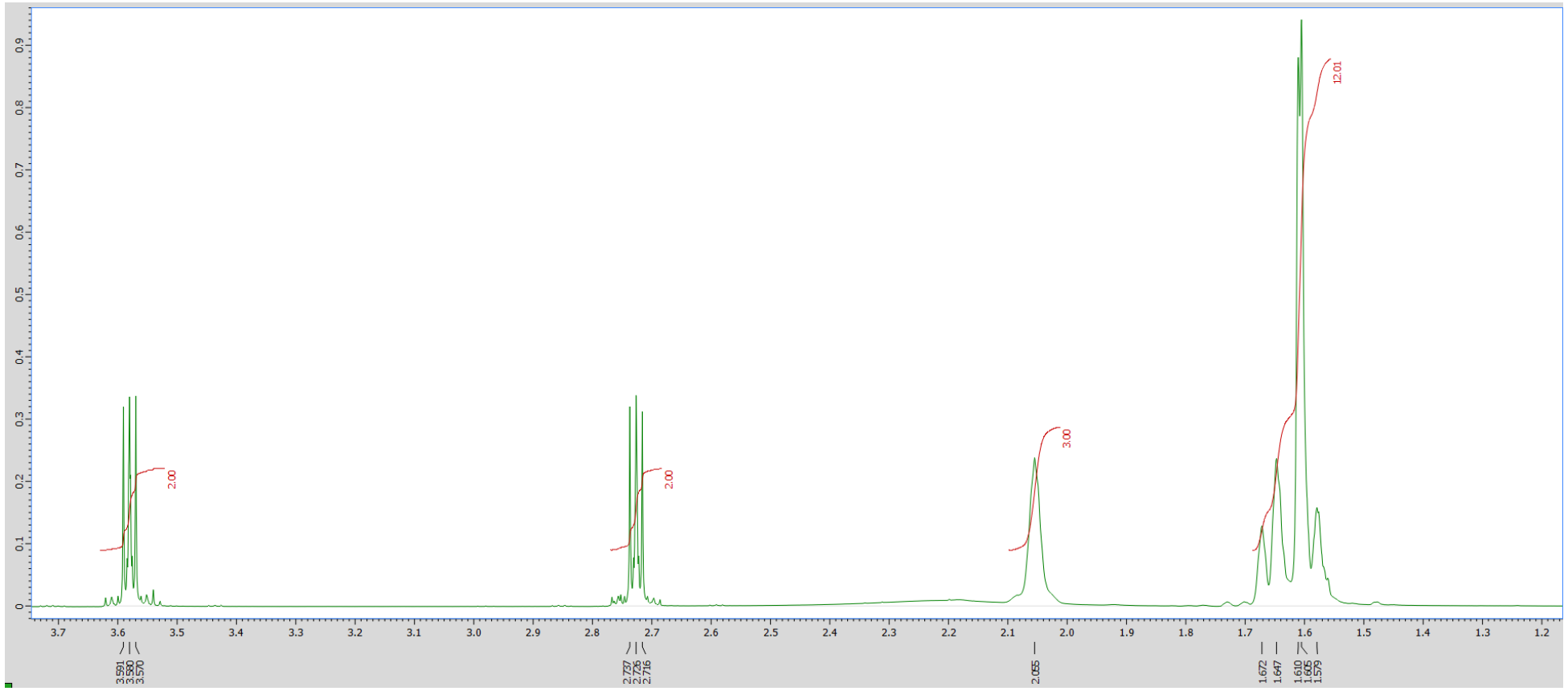

Figure S22- 2-(adamantylamino)ethan-1-ol, [**AdAE**]H, COSY

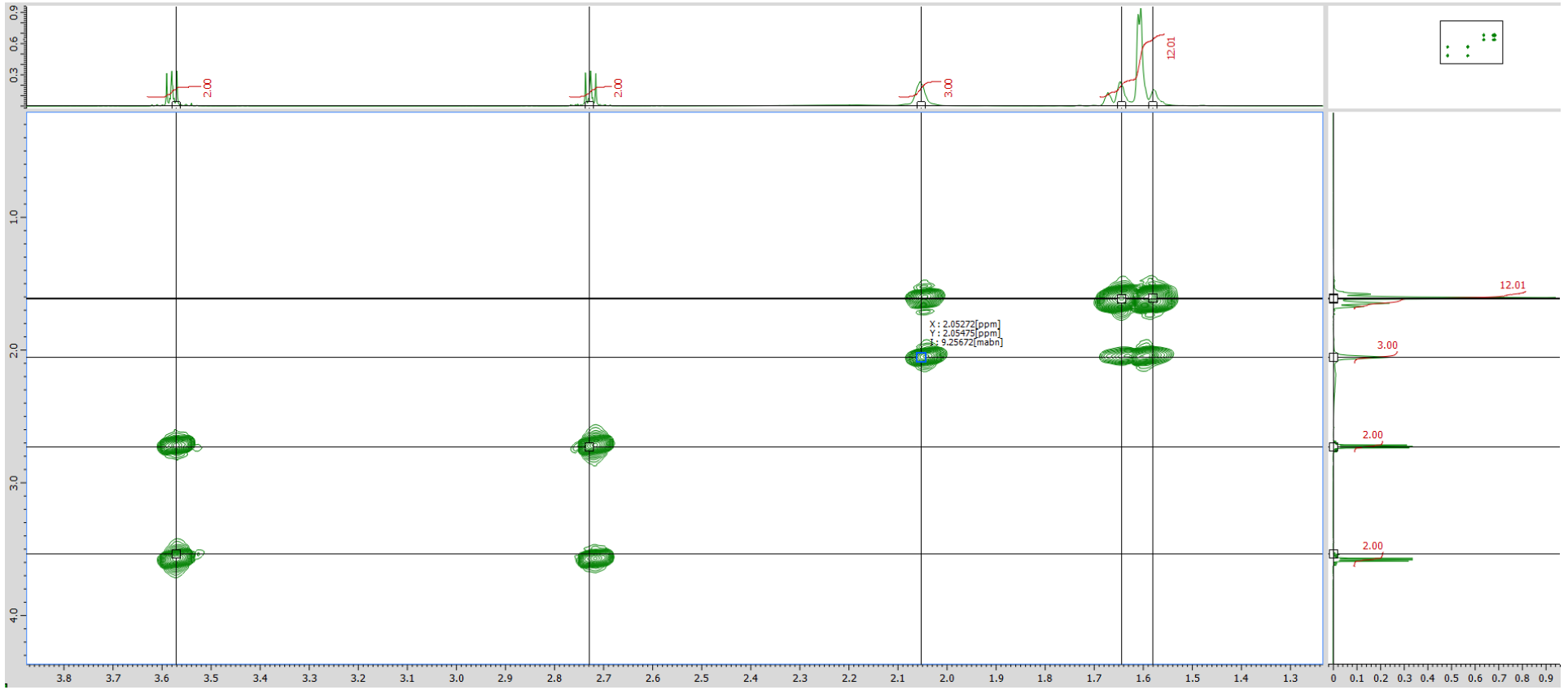

Figure S23- 2-(adamantylamino)ethan-1-ol, [**AdAE**]H, ^{13}C NMR

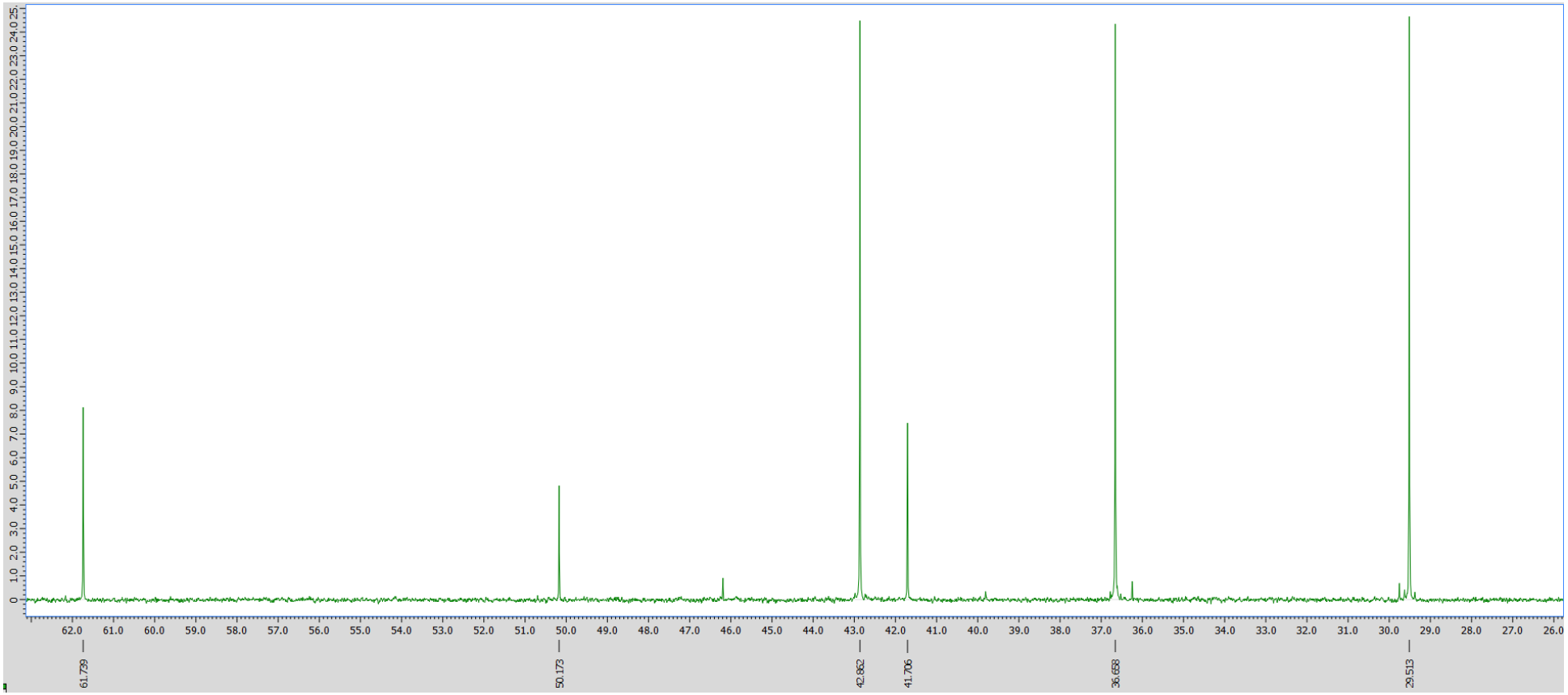

Figure S24- 2-(adamantylamino)ethan-1-ol, [**AdAE**]H, HMQC

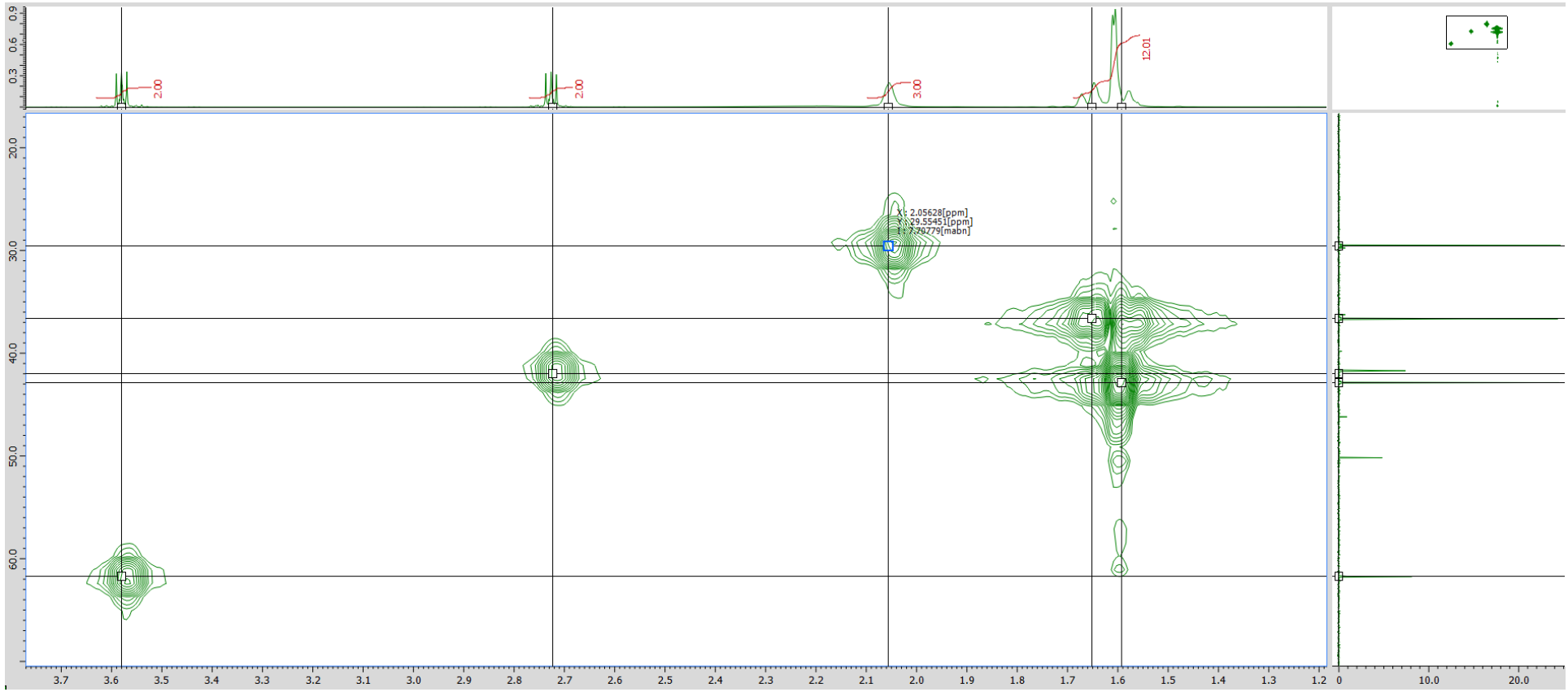

Figure S25- 3-(tertbutylamino)propan-1-ol, [^{t}**BuAPr**]H, ^{1}H NMR

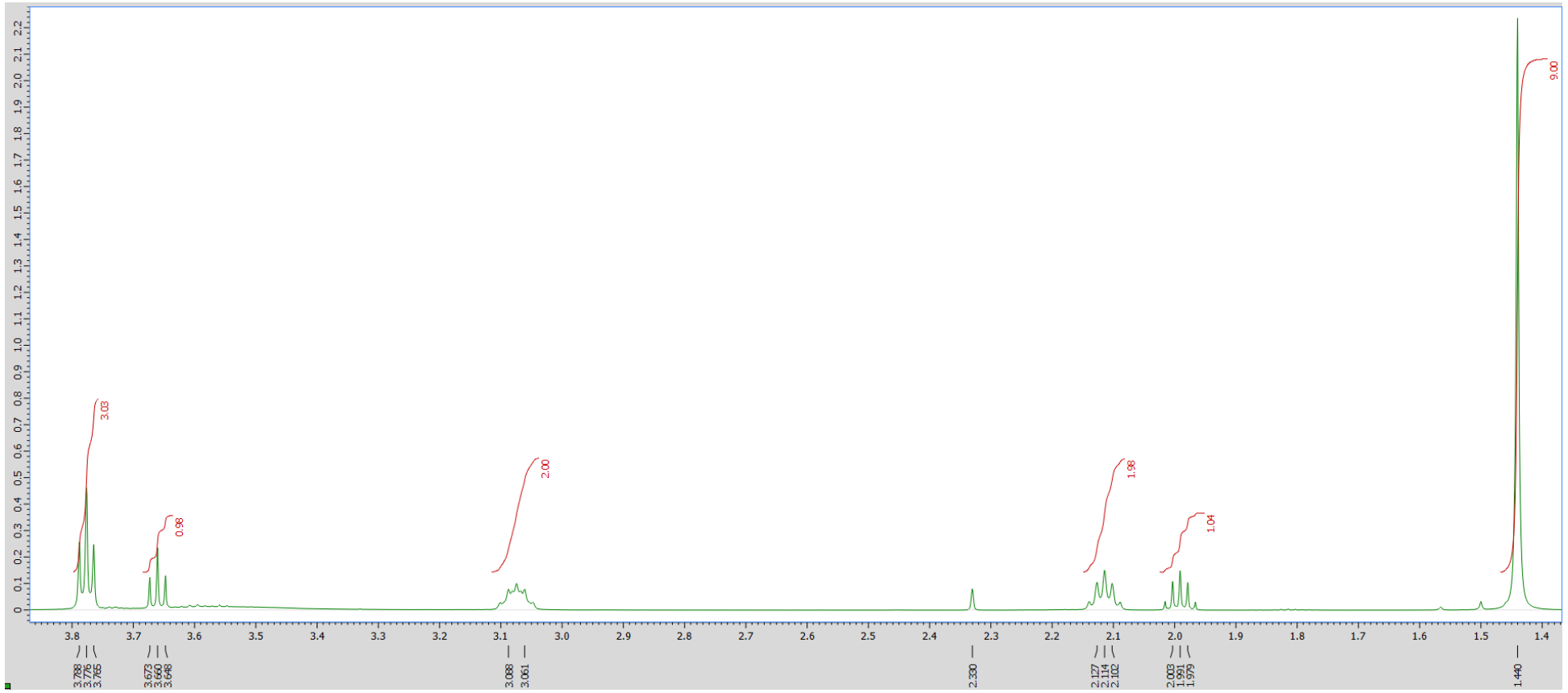

Figure S26- 3-(tertbutylamino)propan-1-ol, [^{t}**BuAPr**]H, COSY

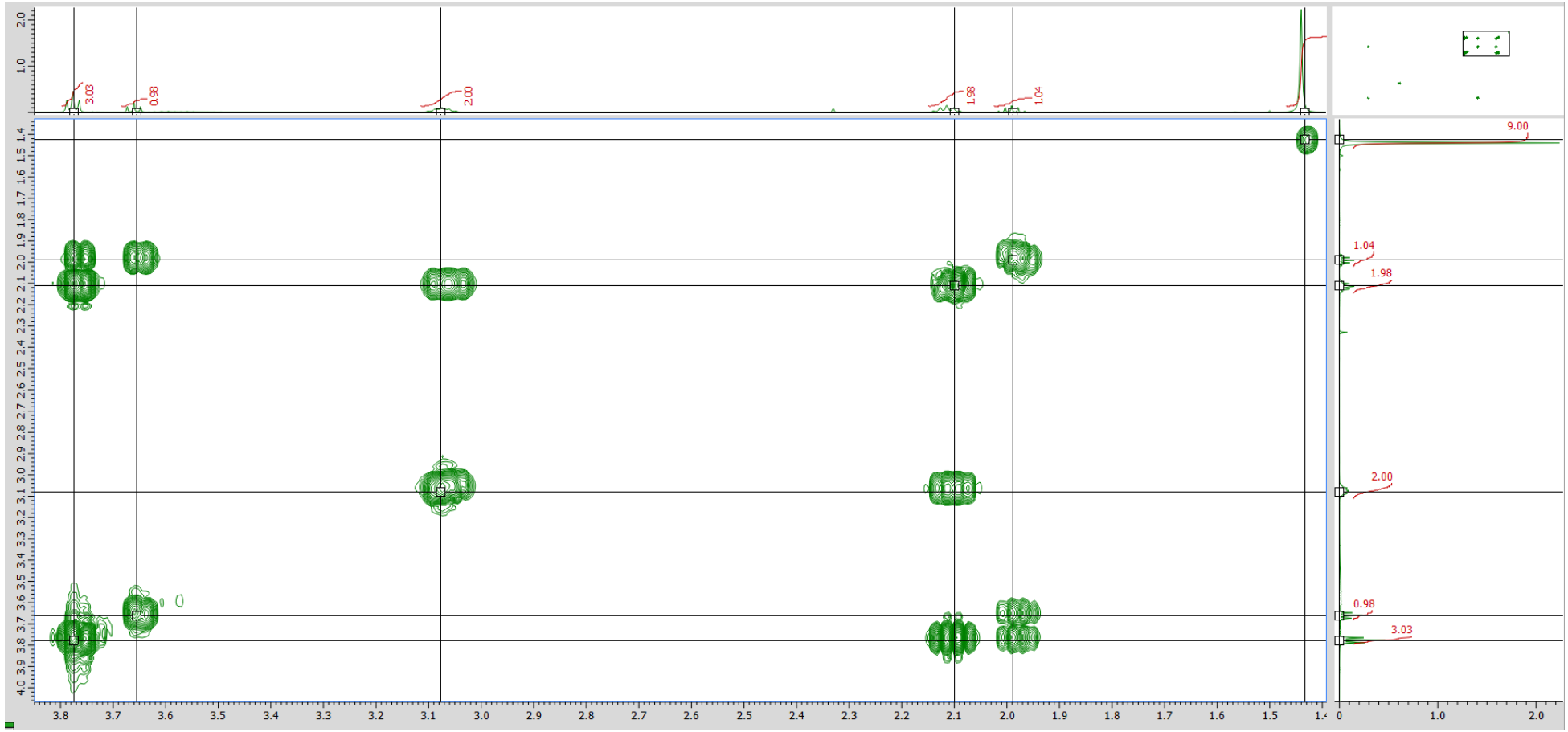

Figure S27- 3-(tertbutylamino)propan-1-ol, [^{t}**BuAPr**]H, ^{13}C NMR

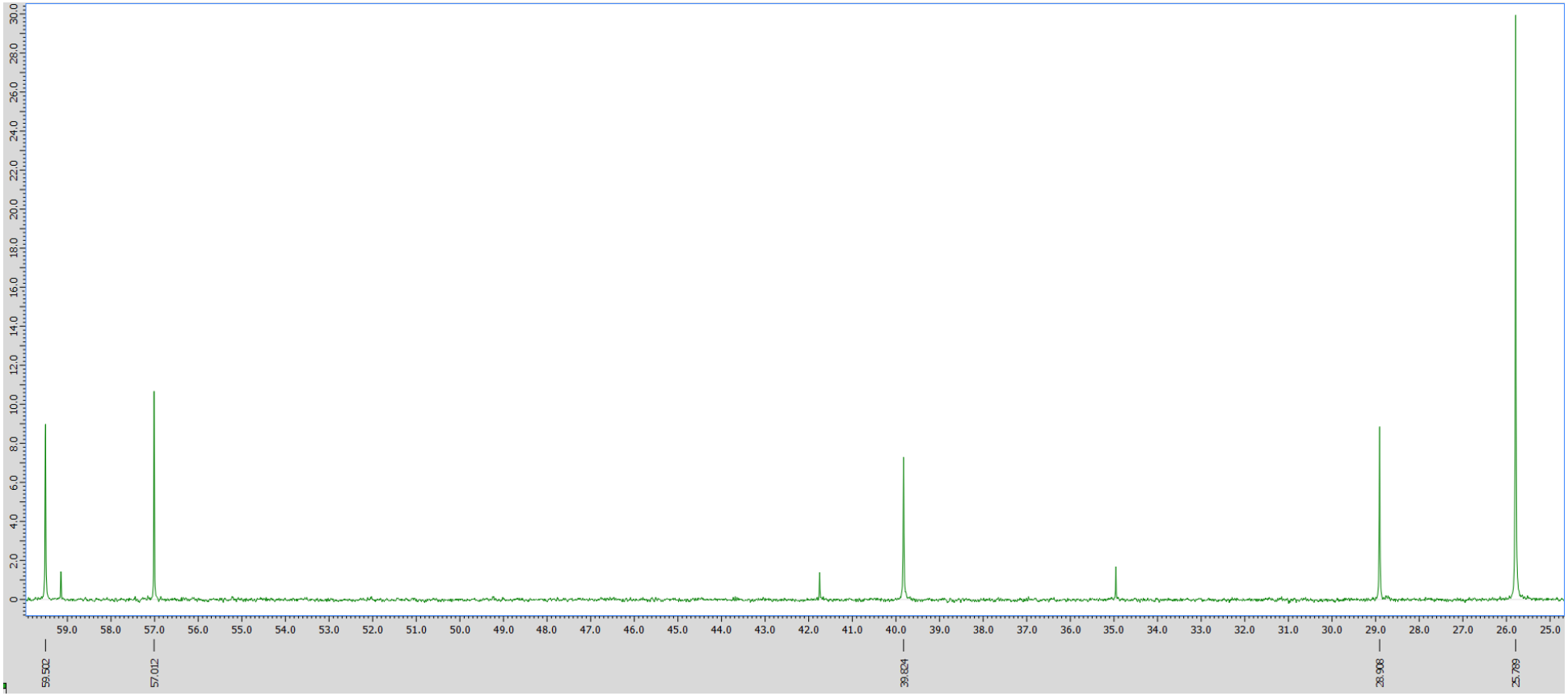

Figure S28- 3-(tertbutylamino)propan-1-ol, [^{t}**BuAPr**]H, HMQC

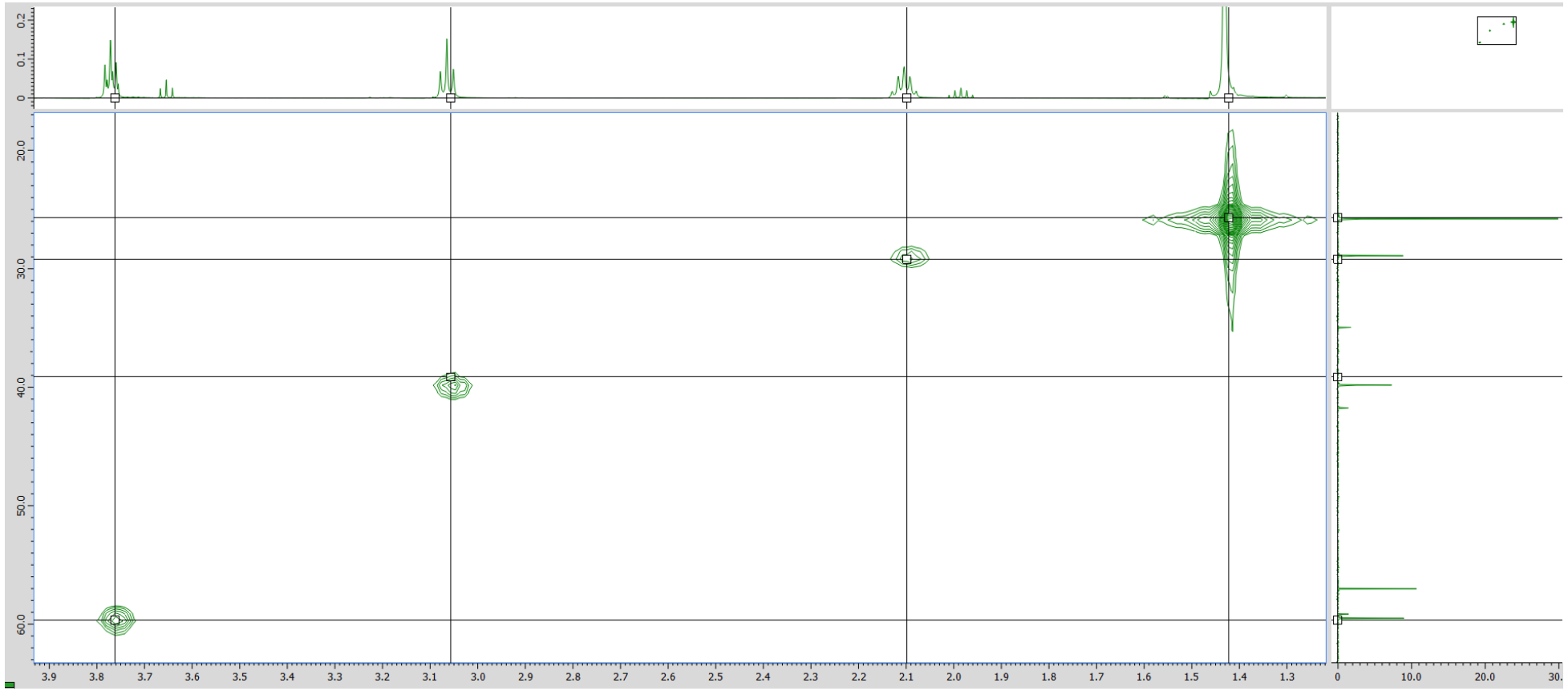

Figure S29- 3-(adamantylamino)propan-1-ol, [**AdAPr**]H, ^{1}H NMR

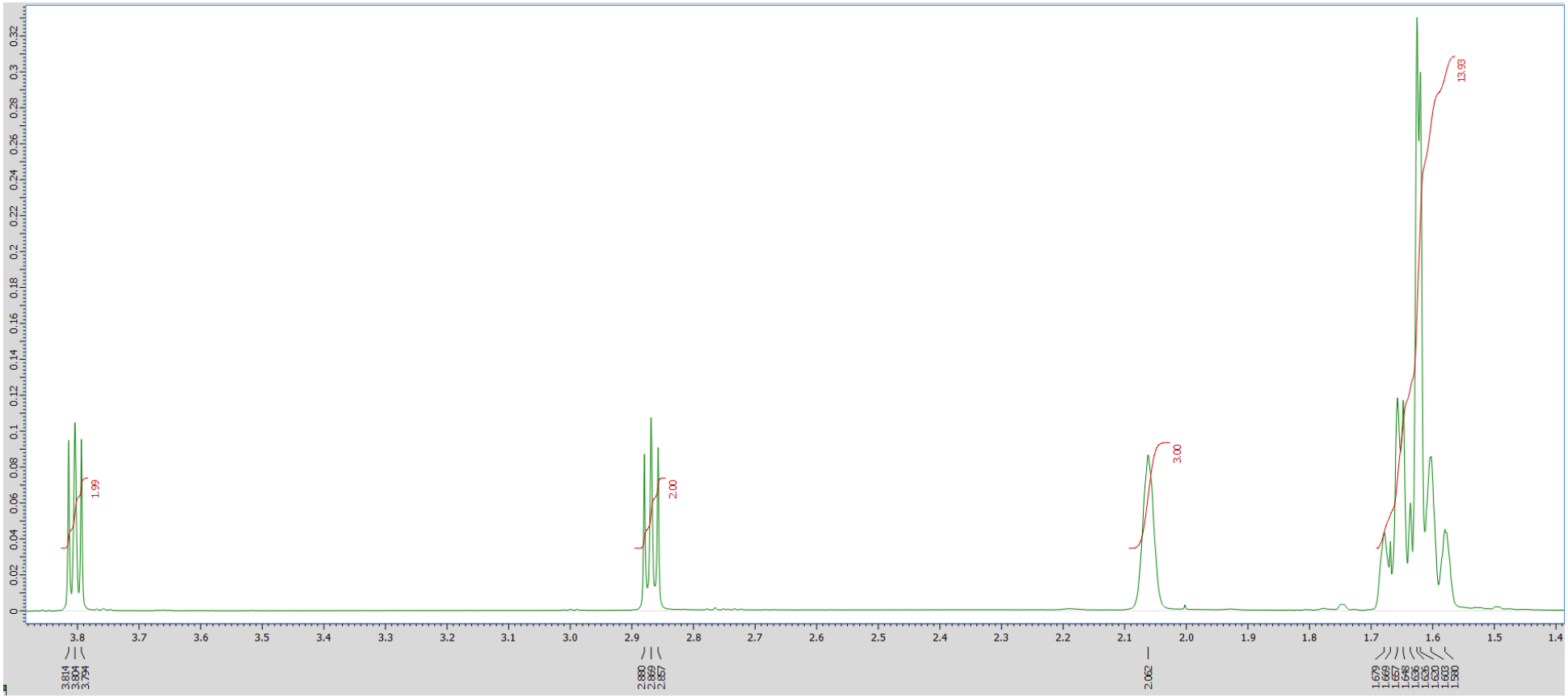

Figure S30- 3-(adamantylamino)propan-1-ol, [**AdAPr**]H, COSY

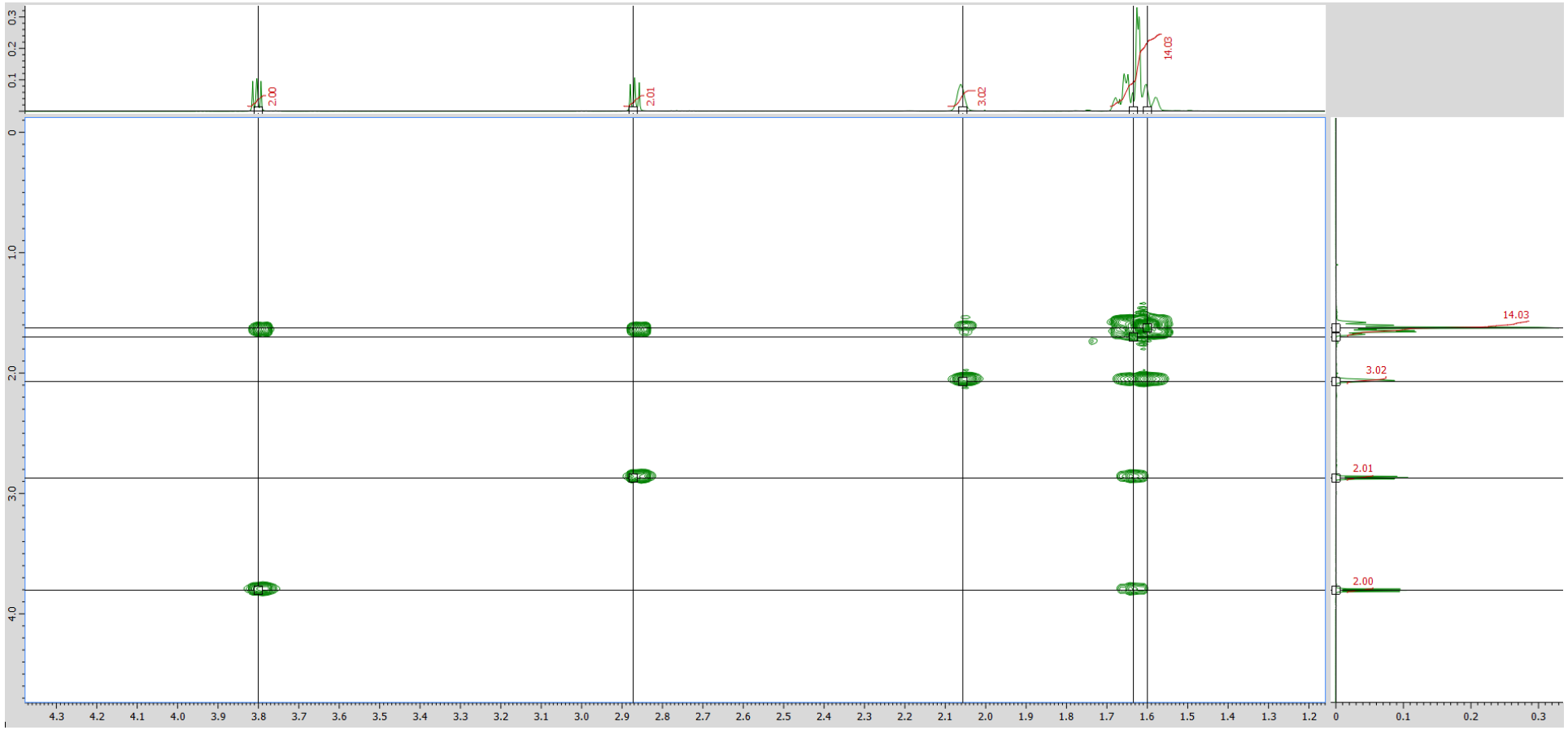

Figure S31- 3-(adamantylamino)propan-1-ol, [**AdAPr**]H, ^{13}C NMR

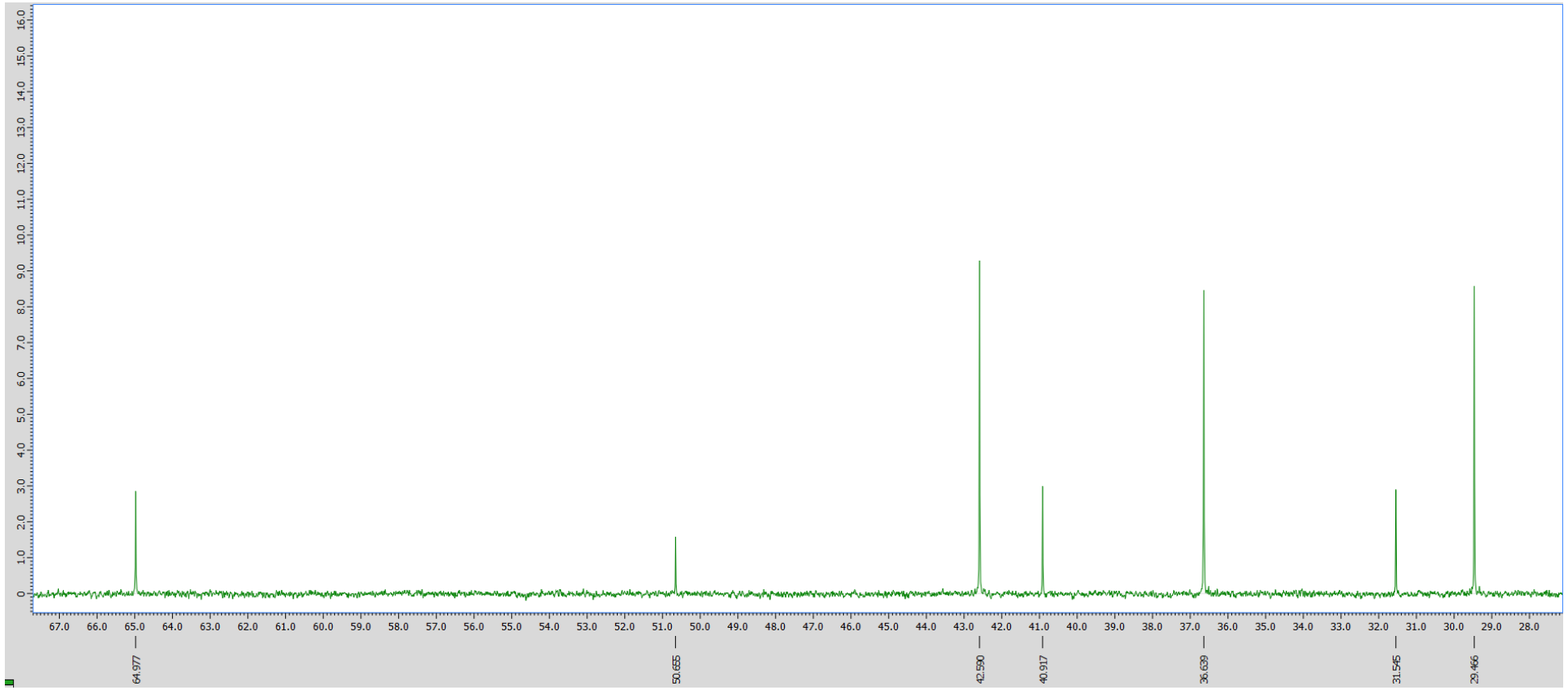

Figure S32- 3-(adamantylamino)propan-1-ol, [**AdAPr**]H, HMQC

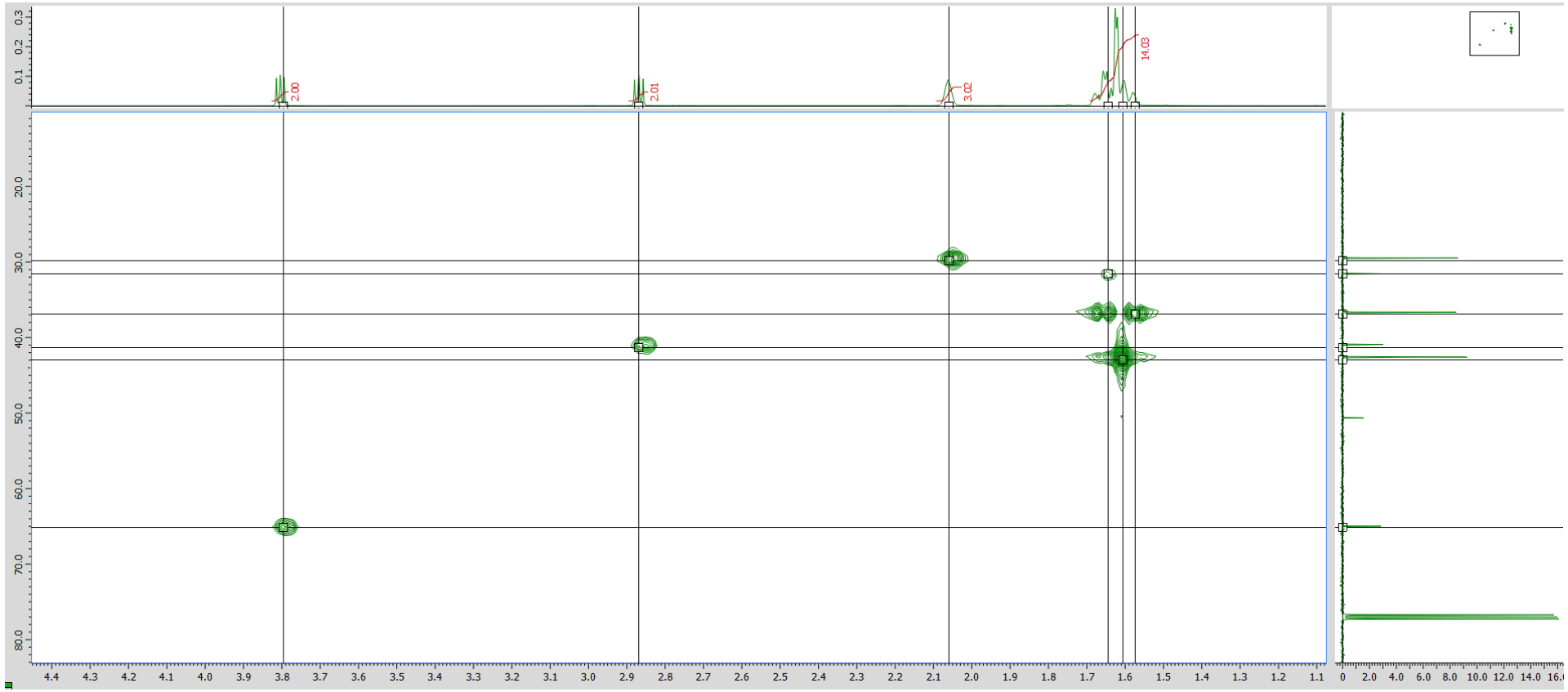

Figure S33- N-methyldiethanolamine, [**MDEA**]H_2, ^{1}H NMR

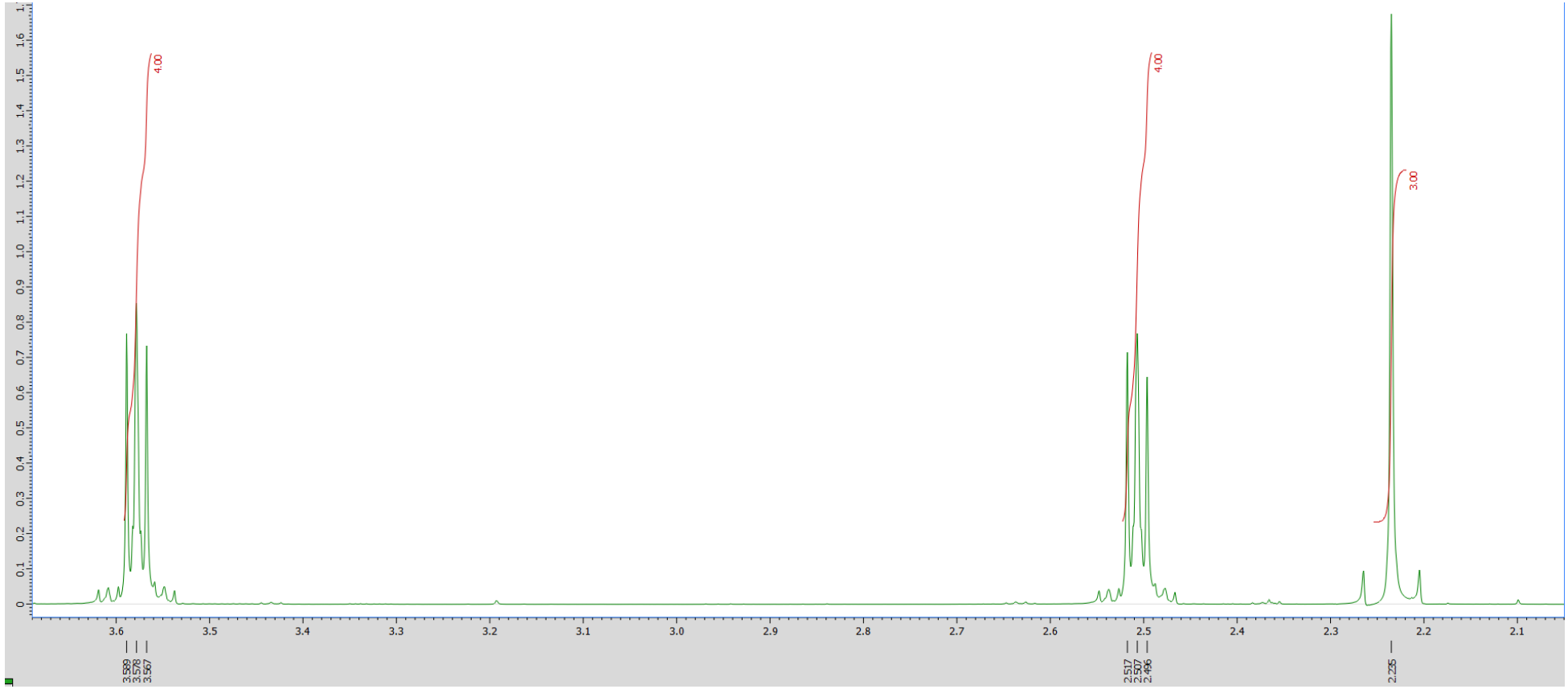

Figure S34- N-methyldiethanolamine, [**MDEA**]H_2, COSY

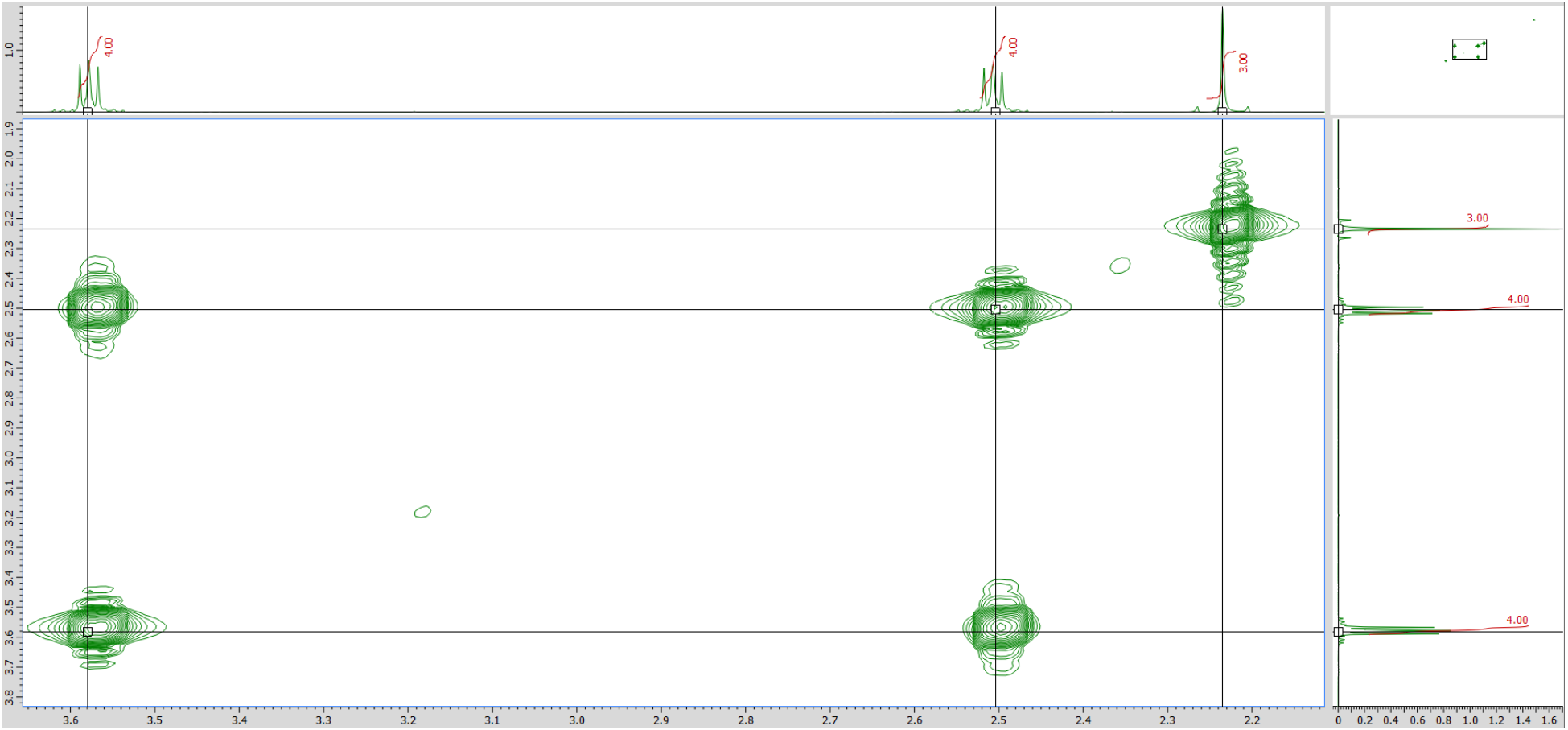

Figure S35- N-methyldiethanolamine, [**MDEA**]H_2, ^{13}C NMR

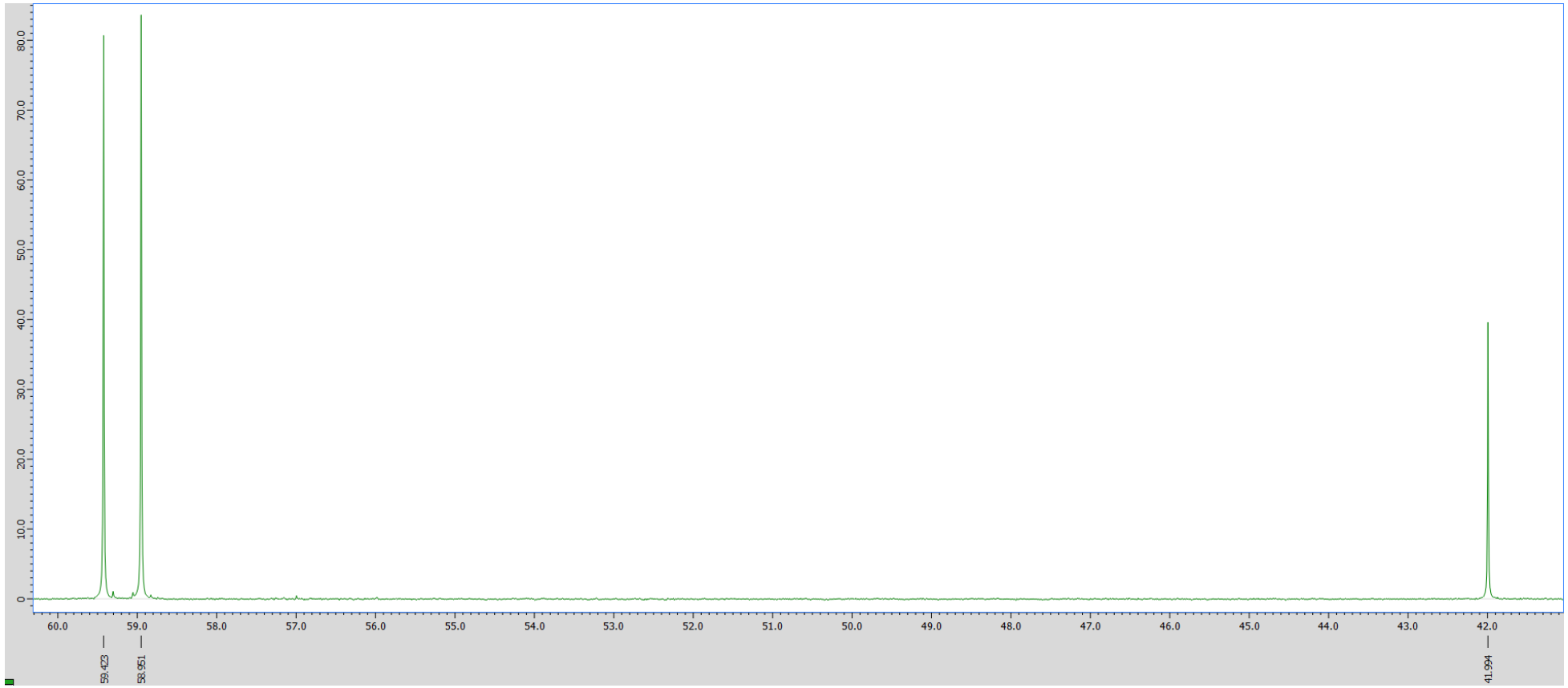

Figure S36- N-methyldiethanolamine, [**MDEA**]H_2, HMQC

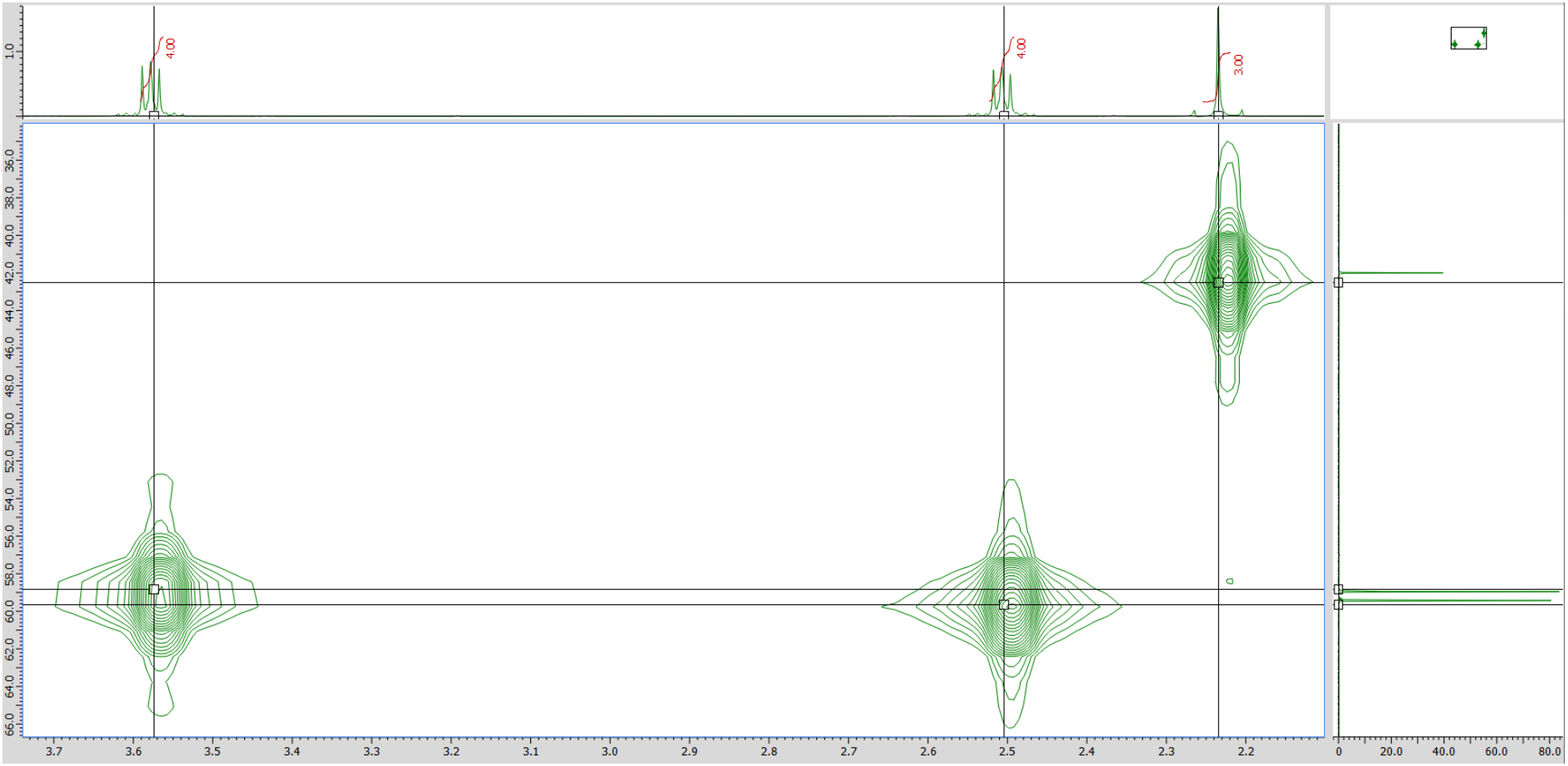

Figure S37- N-ethyldiethanolamine, [**EDEA**]H_2, ^{1}H NMR

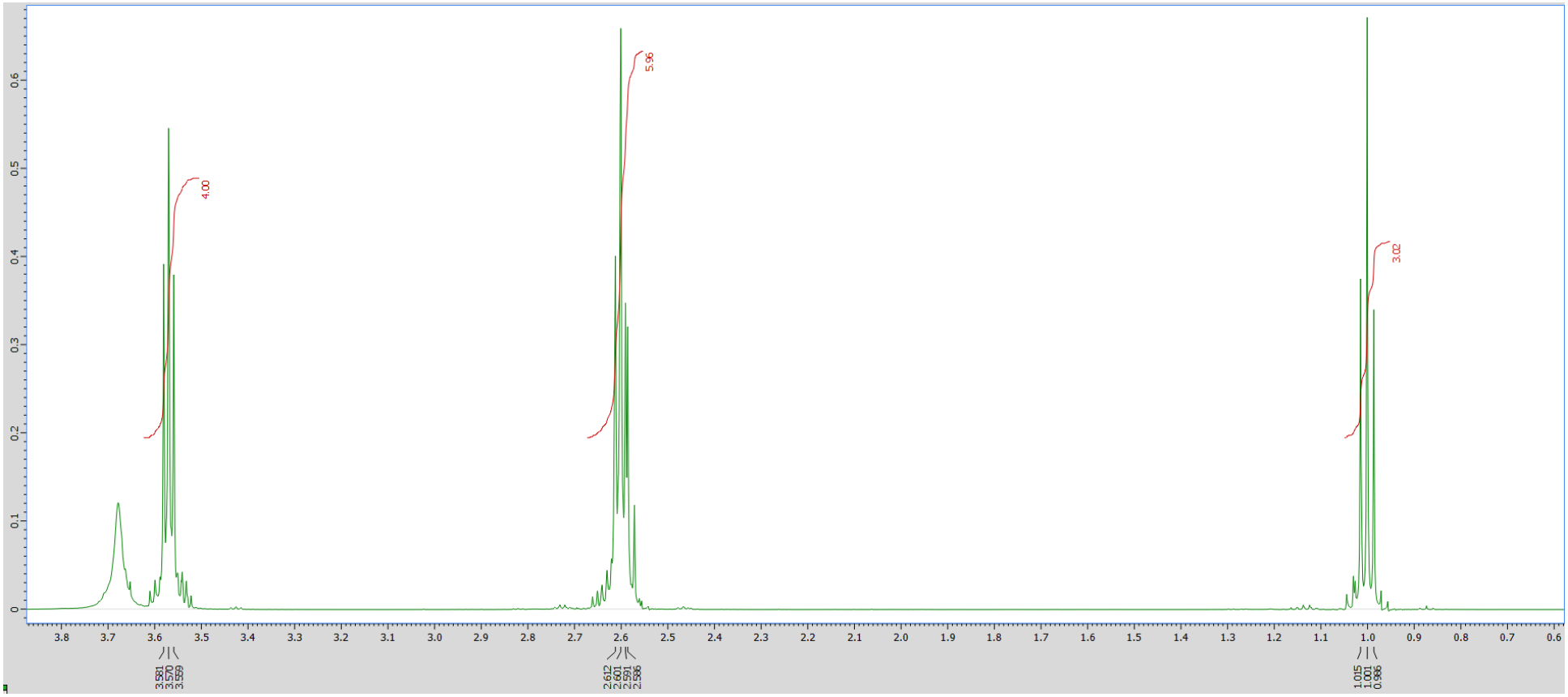

Figure S38- N-ethyldiethanolamine, [**EDEA**]H_2, COSY

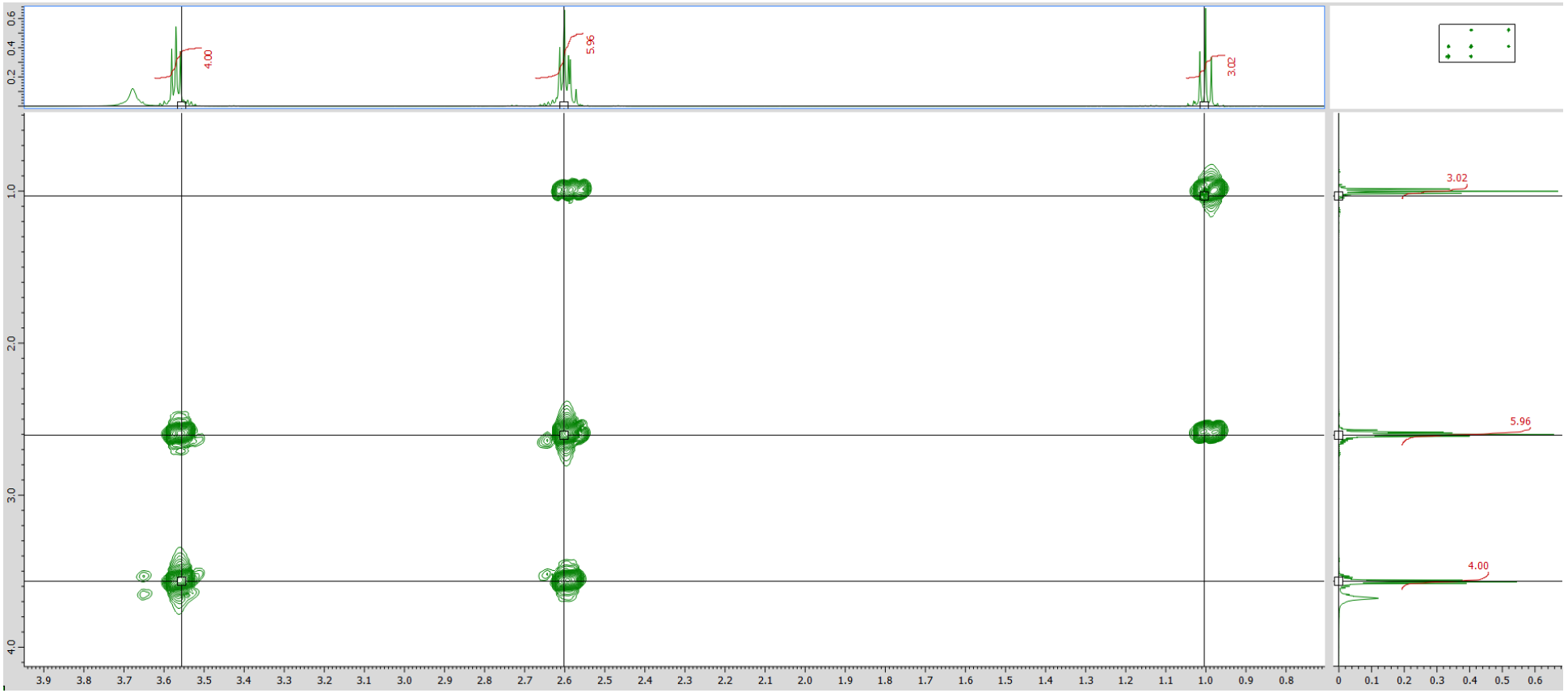

Figure S39- N-ethyldiethanolamine, [**EDEA**]H_2, ^{13}C NMR

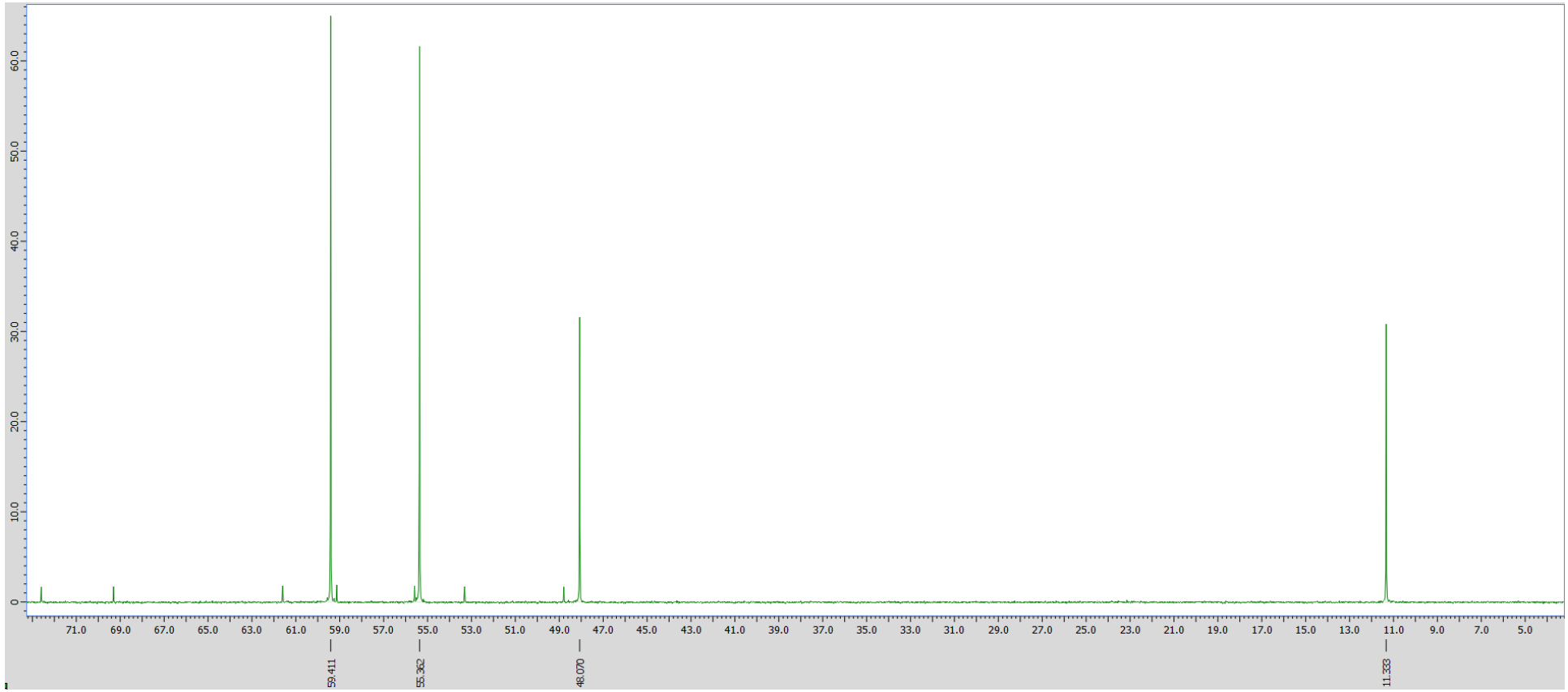

Figure S40- N-ethyldiethanolamine, [**EDEA**]H_2, HMQC

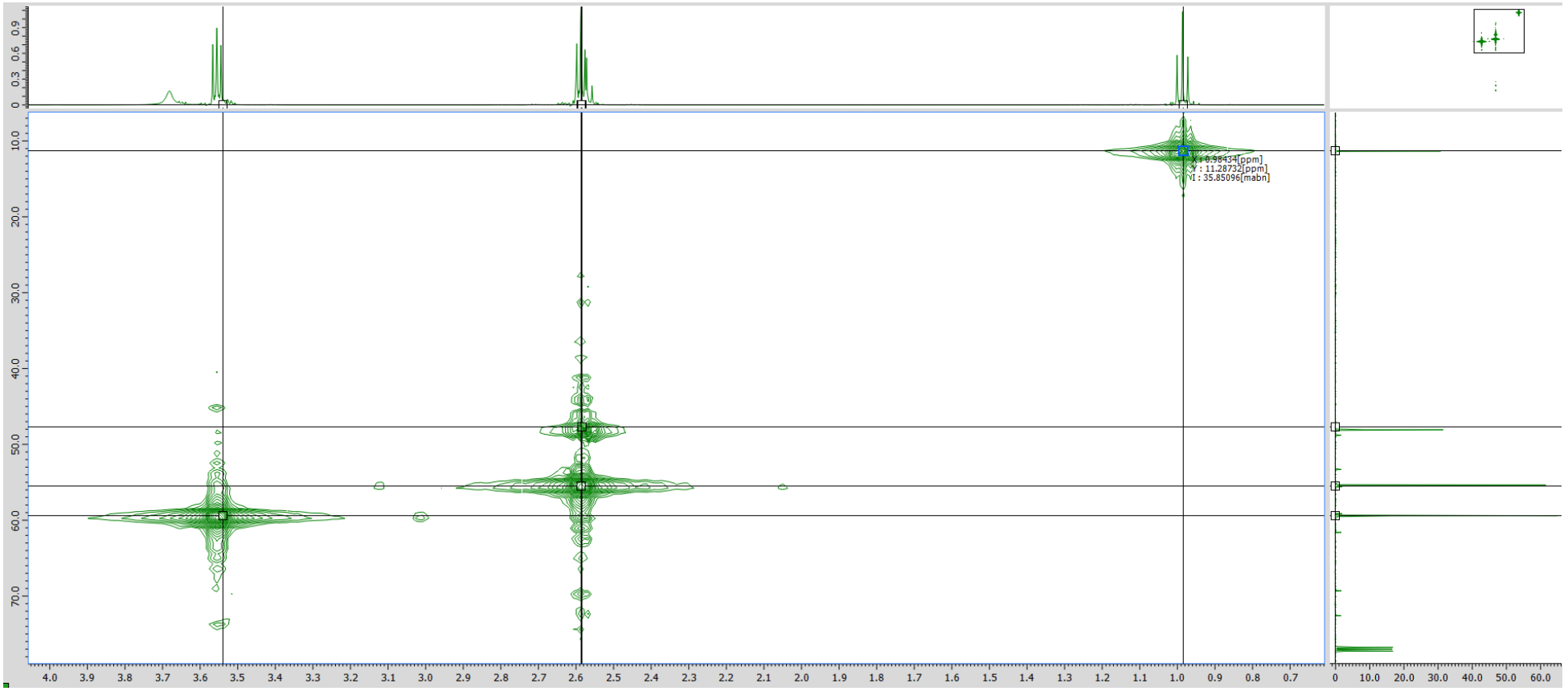

Figure S41- N-isopropyldiethanolamine, [^{i}**PrDEA**]H_2, ^{1}H NMR

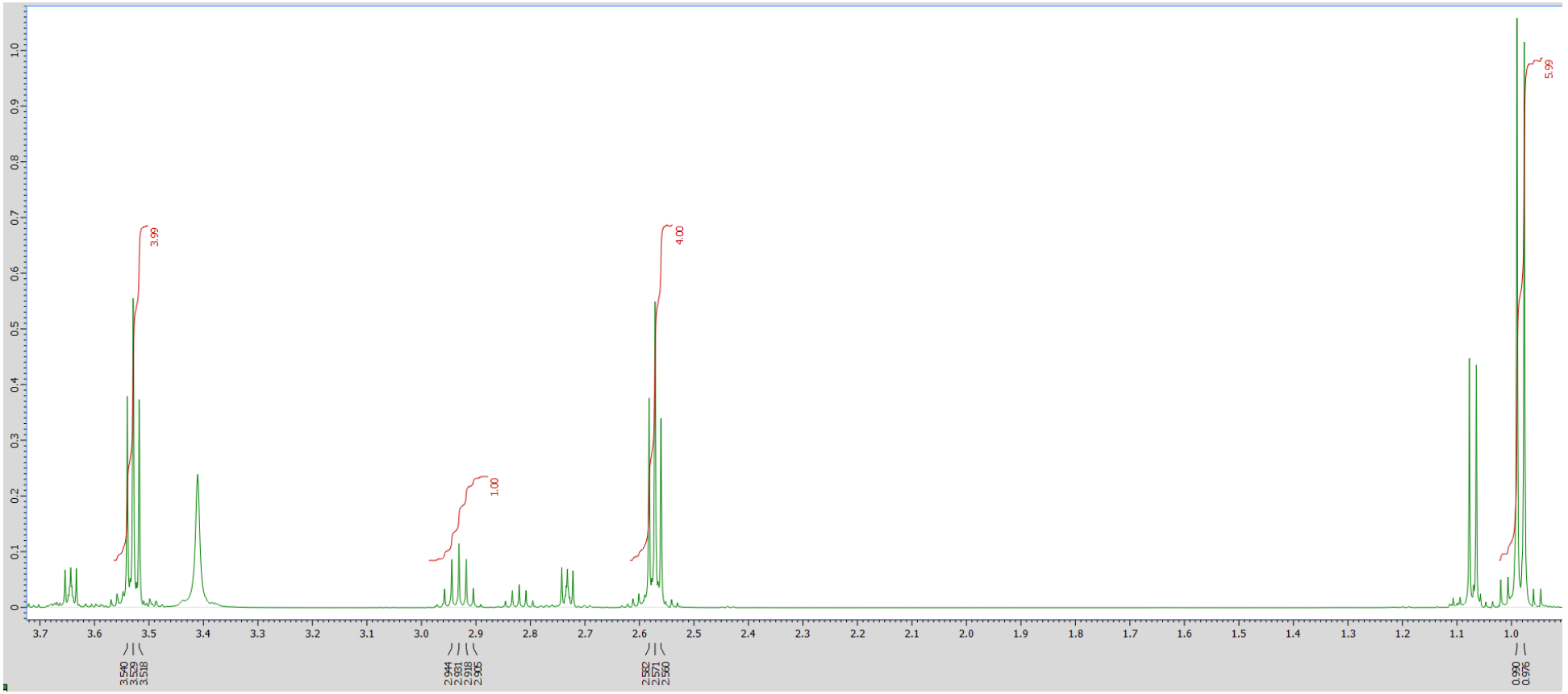

Figure S42- N-isopropyldiethanolamine, [^{i}**PrDEA**]H_2, COSY

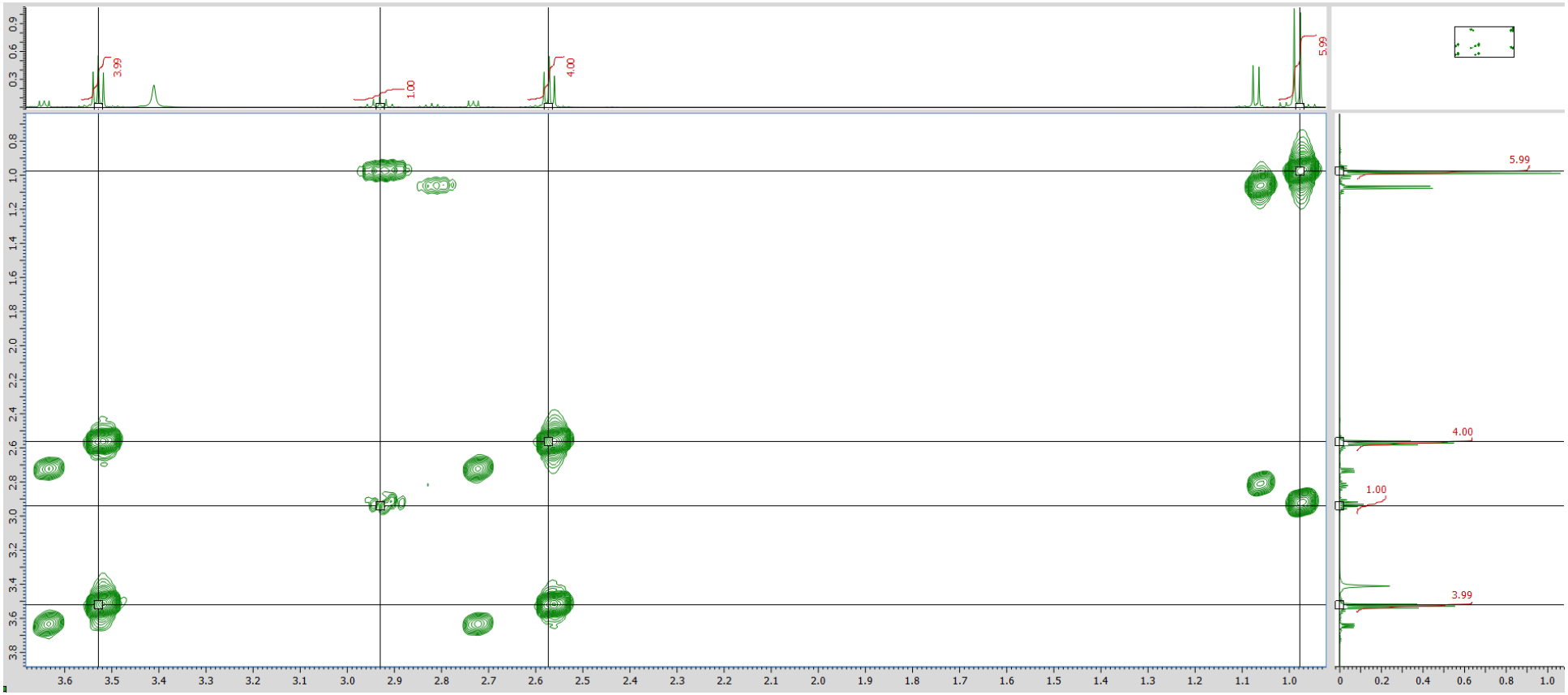

Figure S43- N-isopropyldiethanolamine, [^{i}**PrDEA**]H_2, ^{13}C NMR

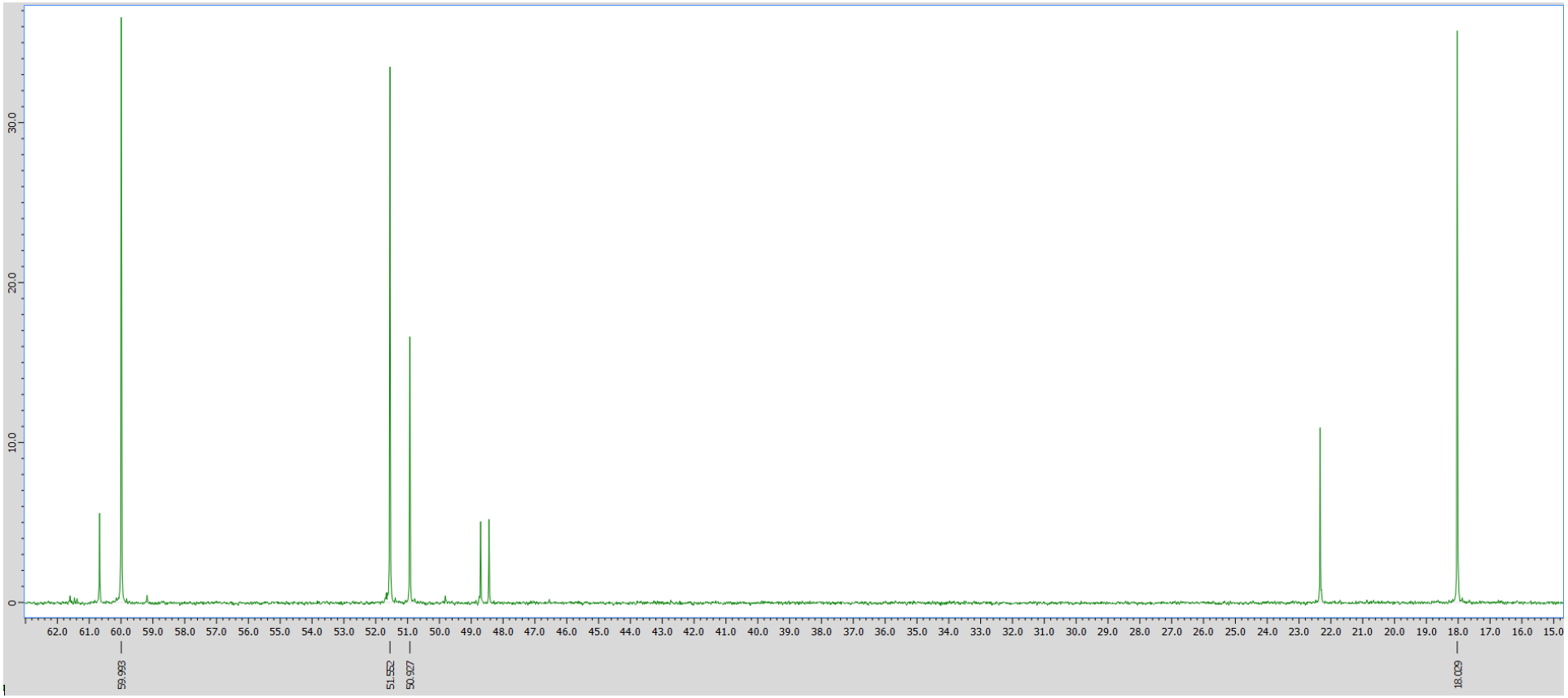

Figure S44- N-isopropyldiethanolamine, [^{i}**PrDEA**]H_2, HMQC

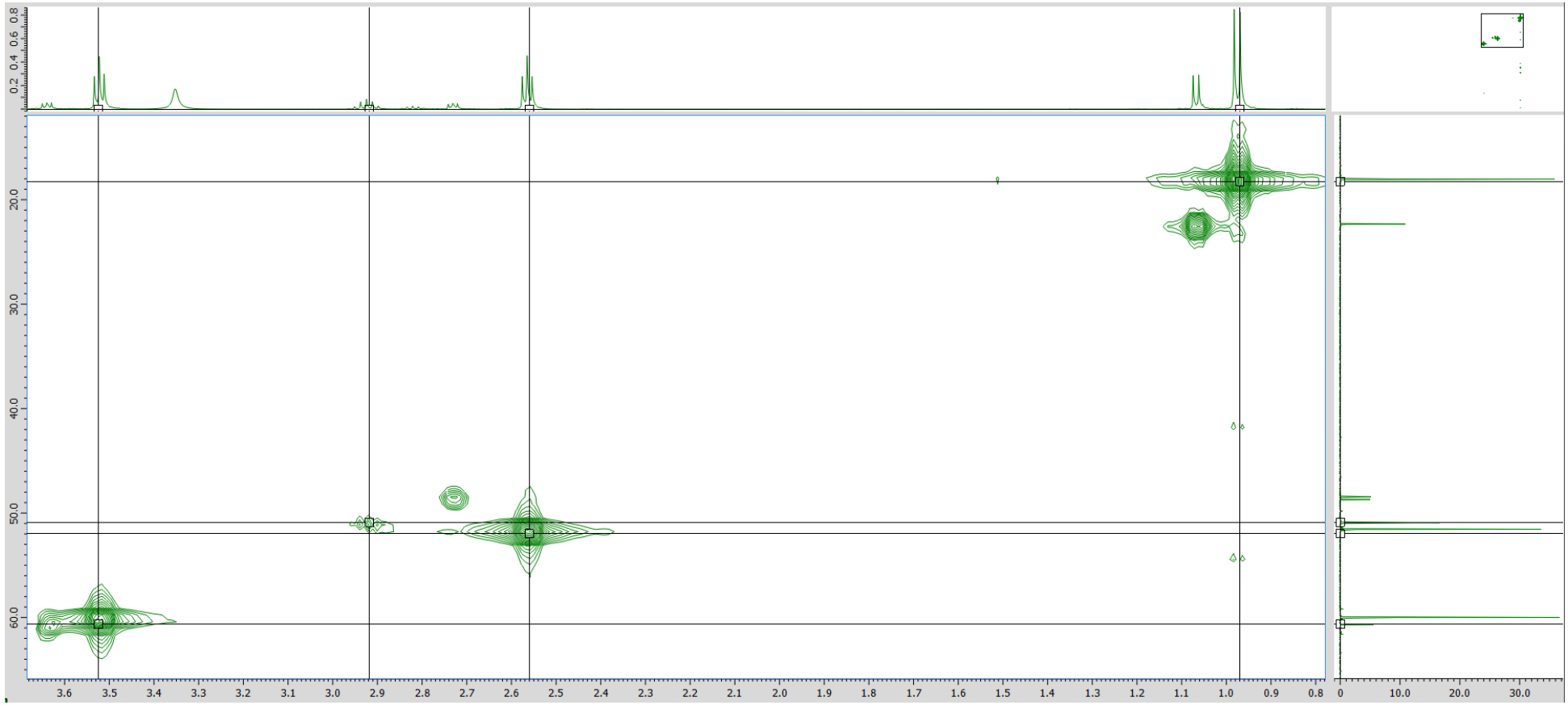

Figure S45- N-n-butyldiethanolamine, [^{n}**BuDEA**]H_2, ^{1}H NMR

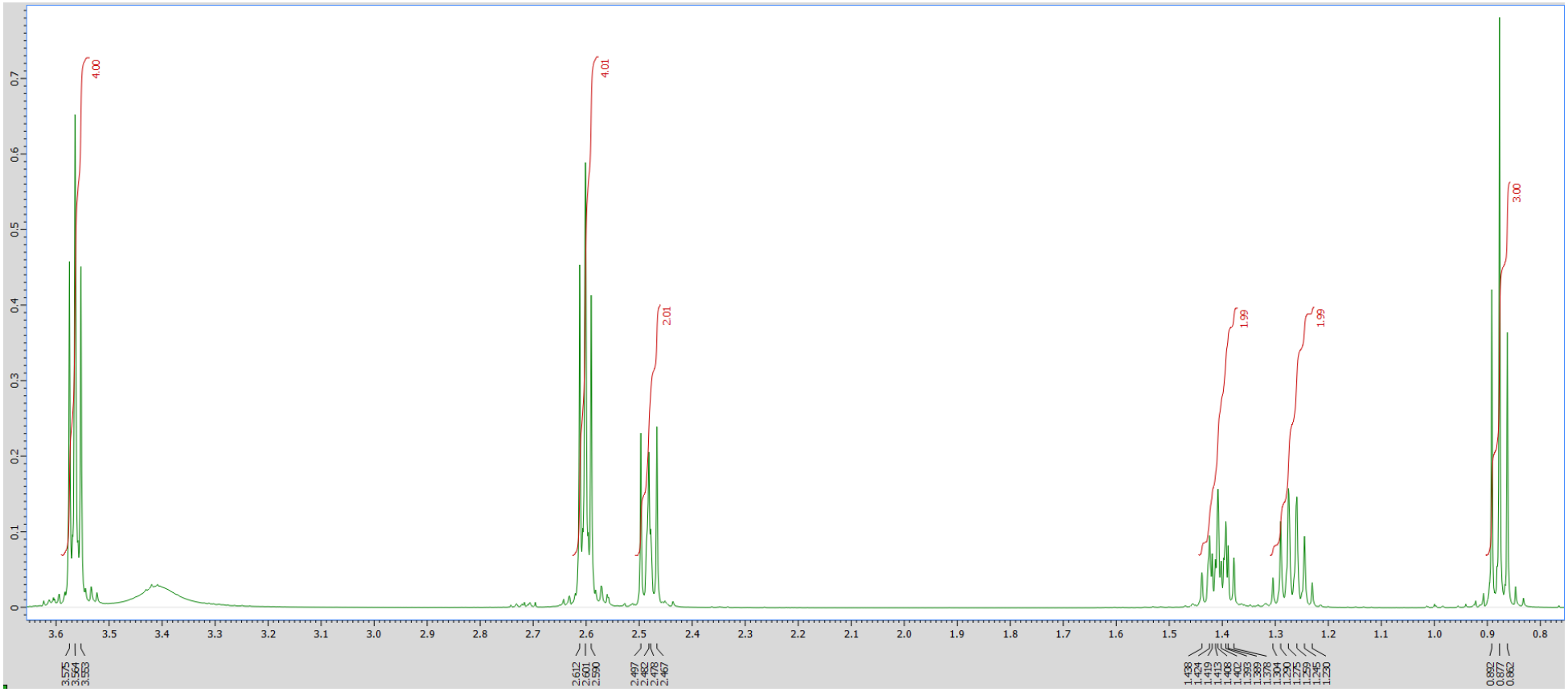

Figure S46- N-n-butyldiethanolamine, [^{n}**BuDEA**]H_2, COSY

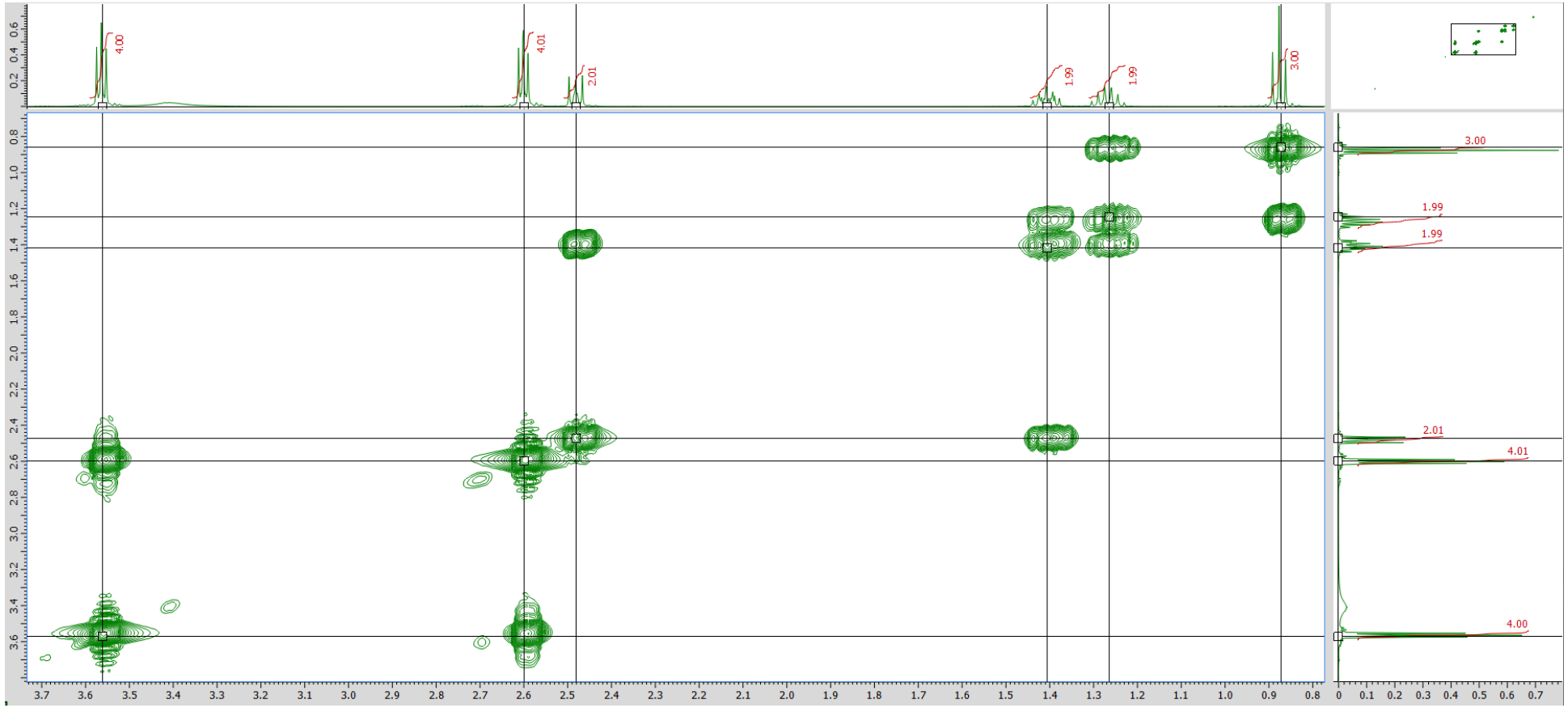

Figure S47- N-n-butyldiethanolamine, [^{n}**BuDEA**]H_2, ^{13}C NMR

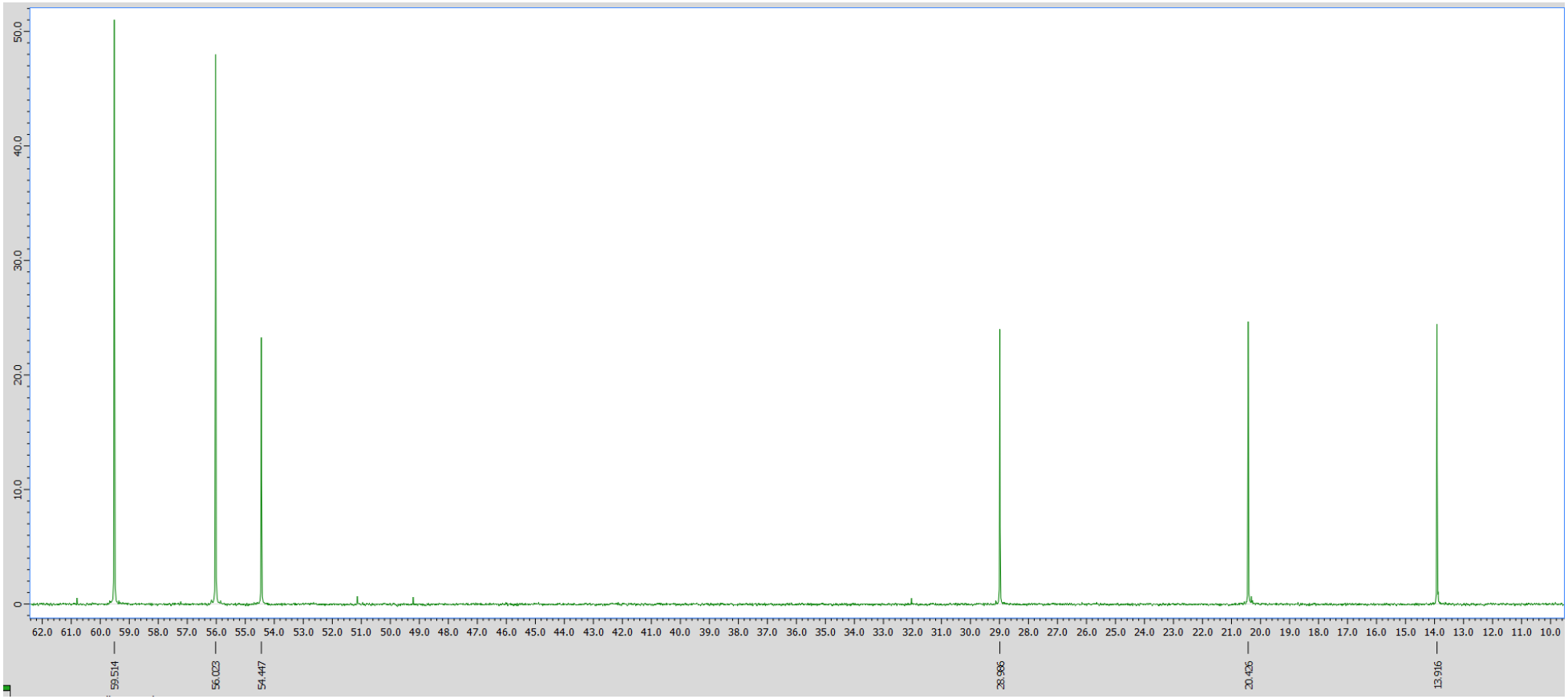

Figure S48- N-n-butyldiethanolamine, [^{n}**BuDEA**]H_2, HMQC

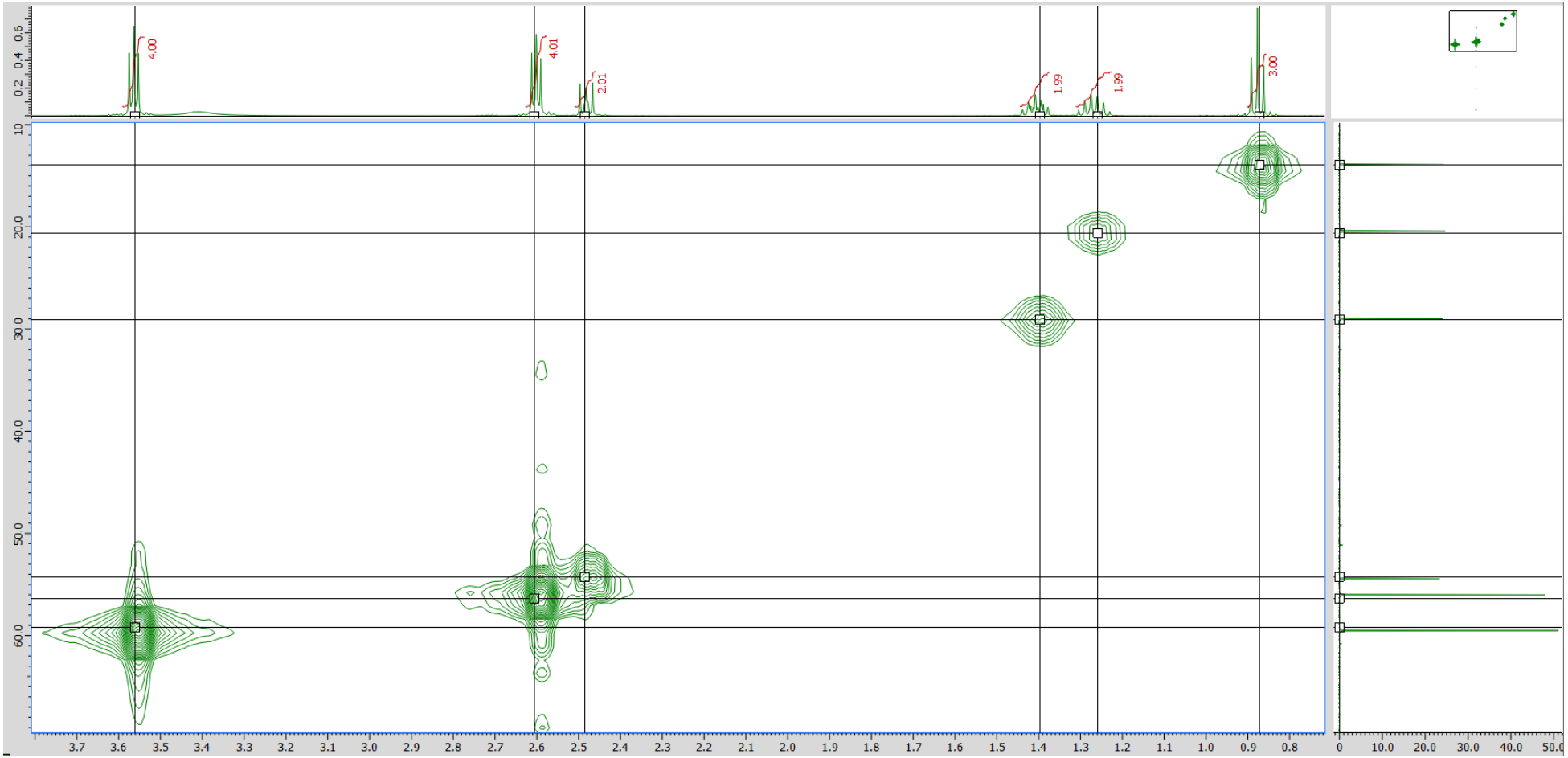

Figure S49- N-phenyldiethanolamine, [**PhDEA**]H_2, ^{1}H NMR

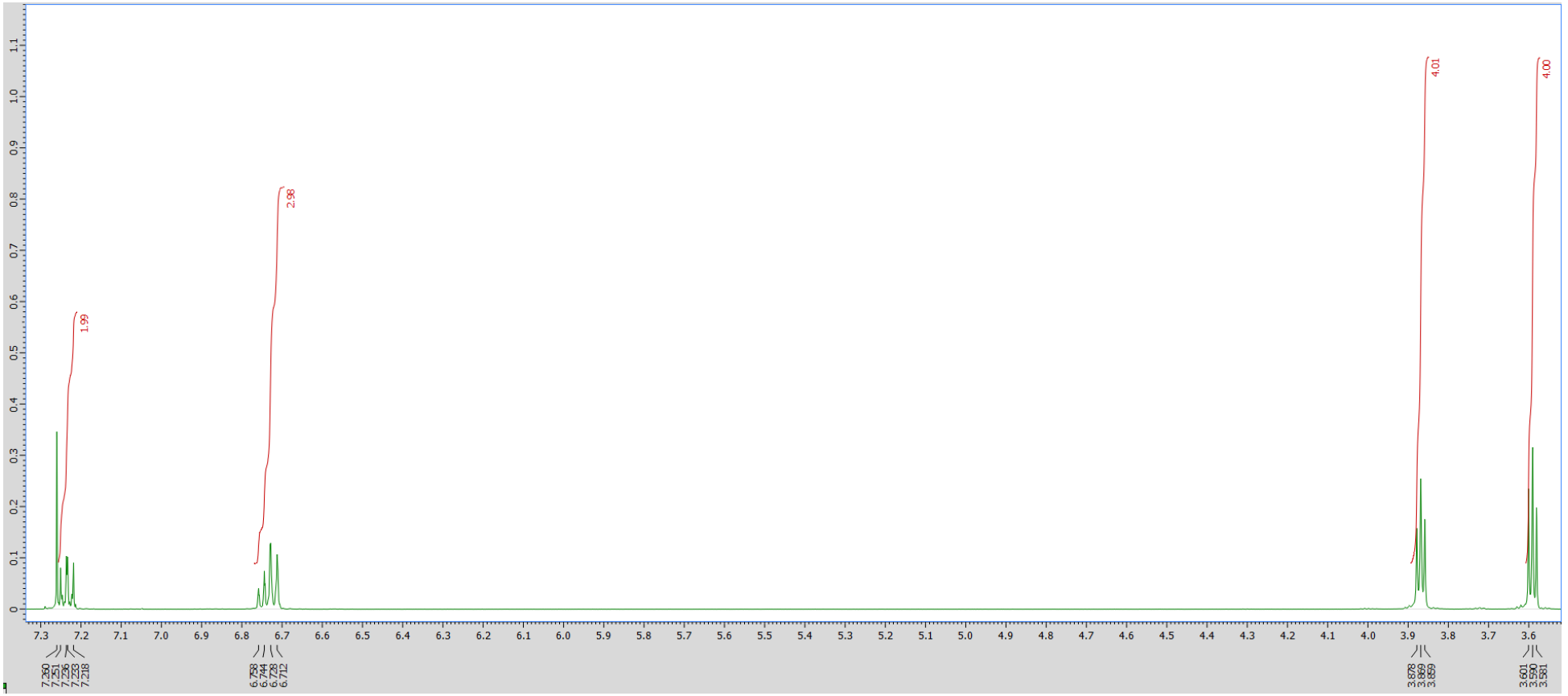

Figure S50- N-phenyldiethanolamine, [**PhDEA**]H_2, COSY

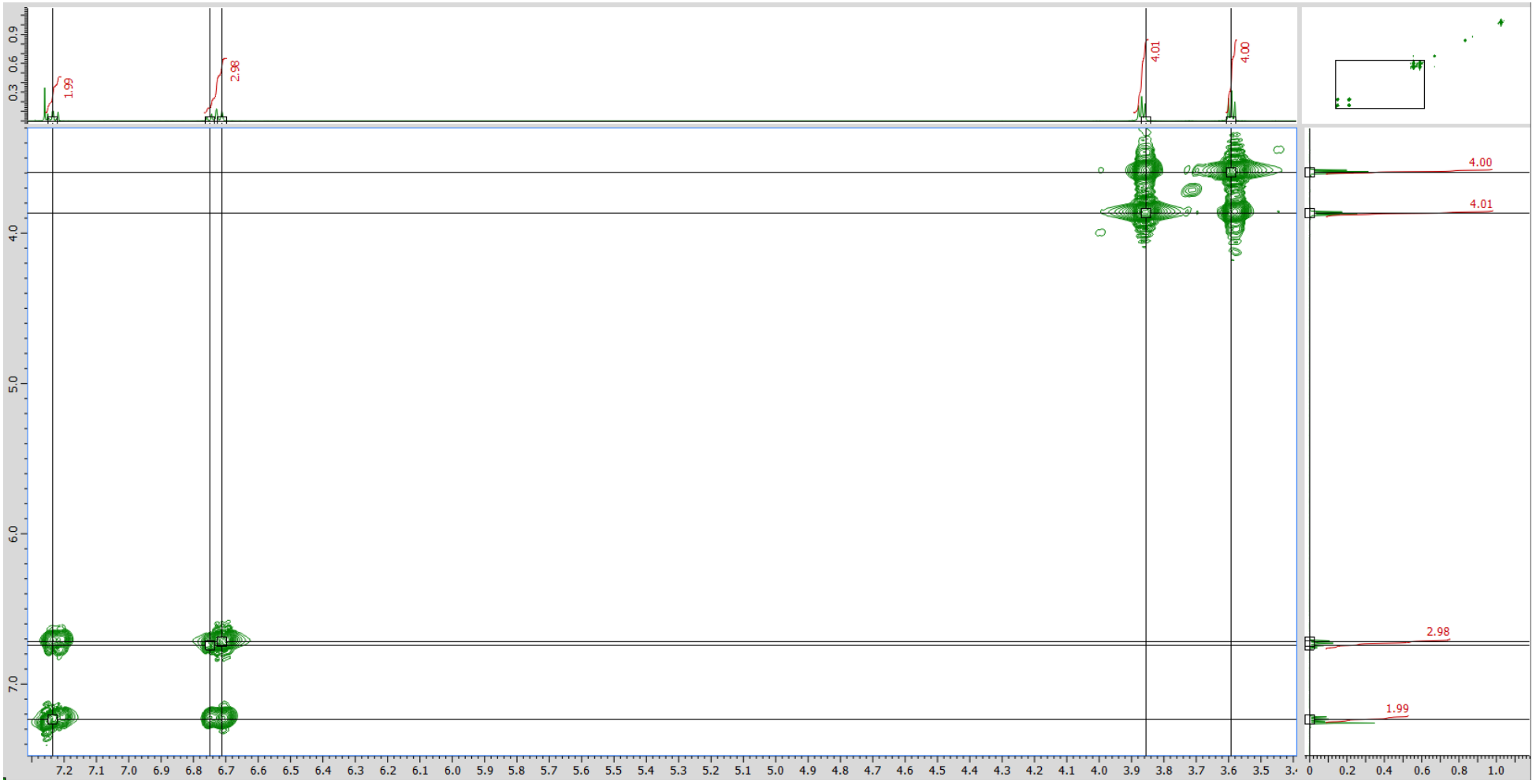

Figure S51- N-phenyldiethanolamine, [**PhDEA**]H_2, ^{13}C NMR

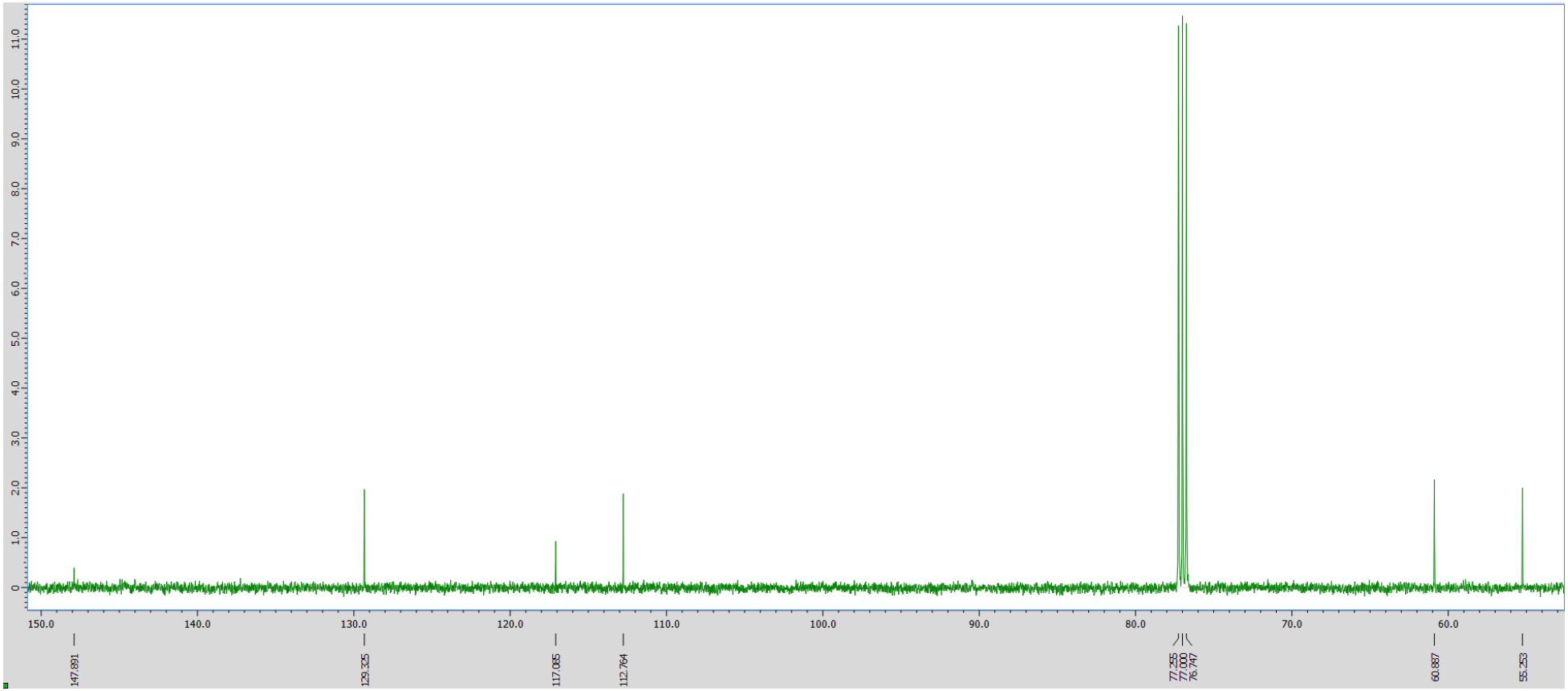

Figure S52- N-phenyldiethanolamine, [**PhDEA**]H_2, HMQC

Figure S53- Triethanolamine, [**TEA**]H_3, ^{1}H NMR

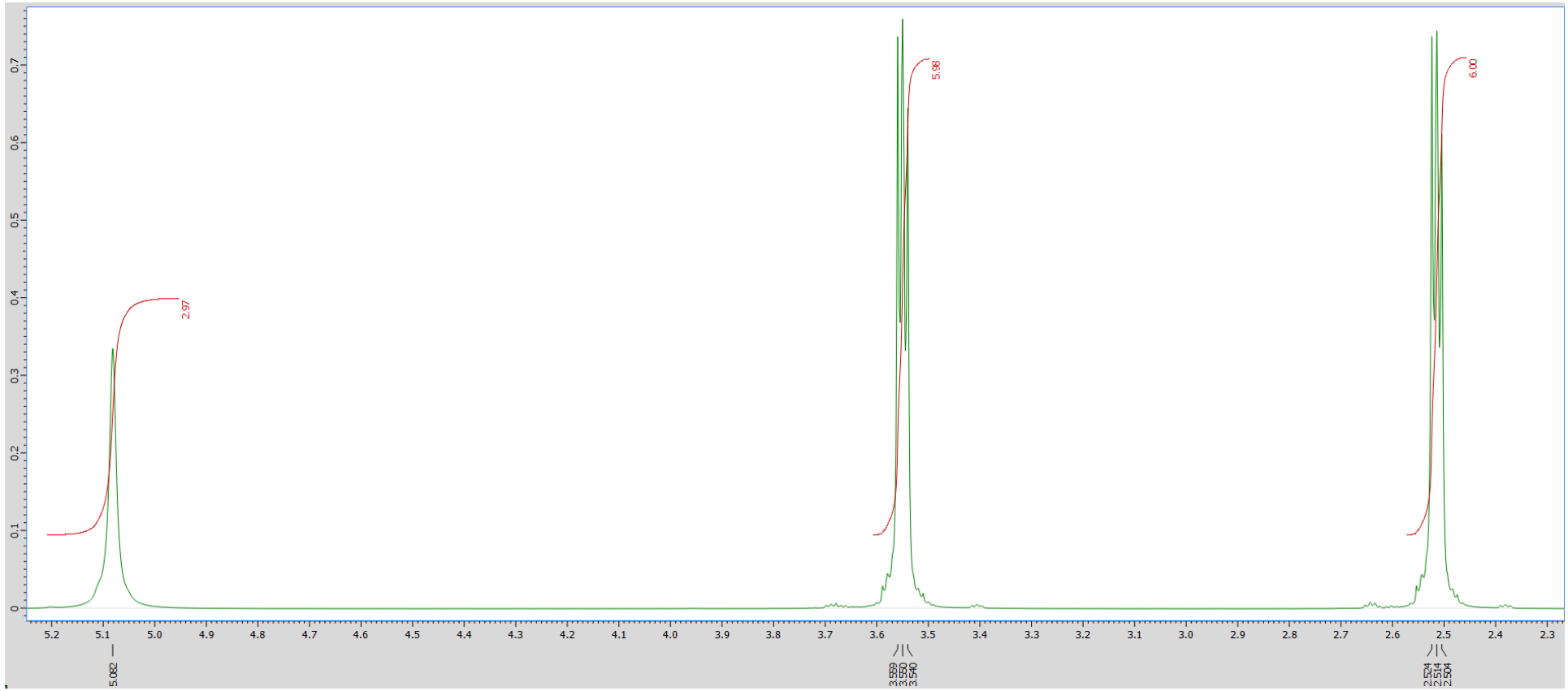

Figure S54- Triethanolamine, [**TEA**]H_3, COSY

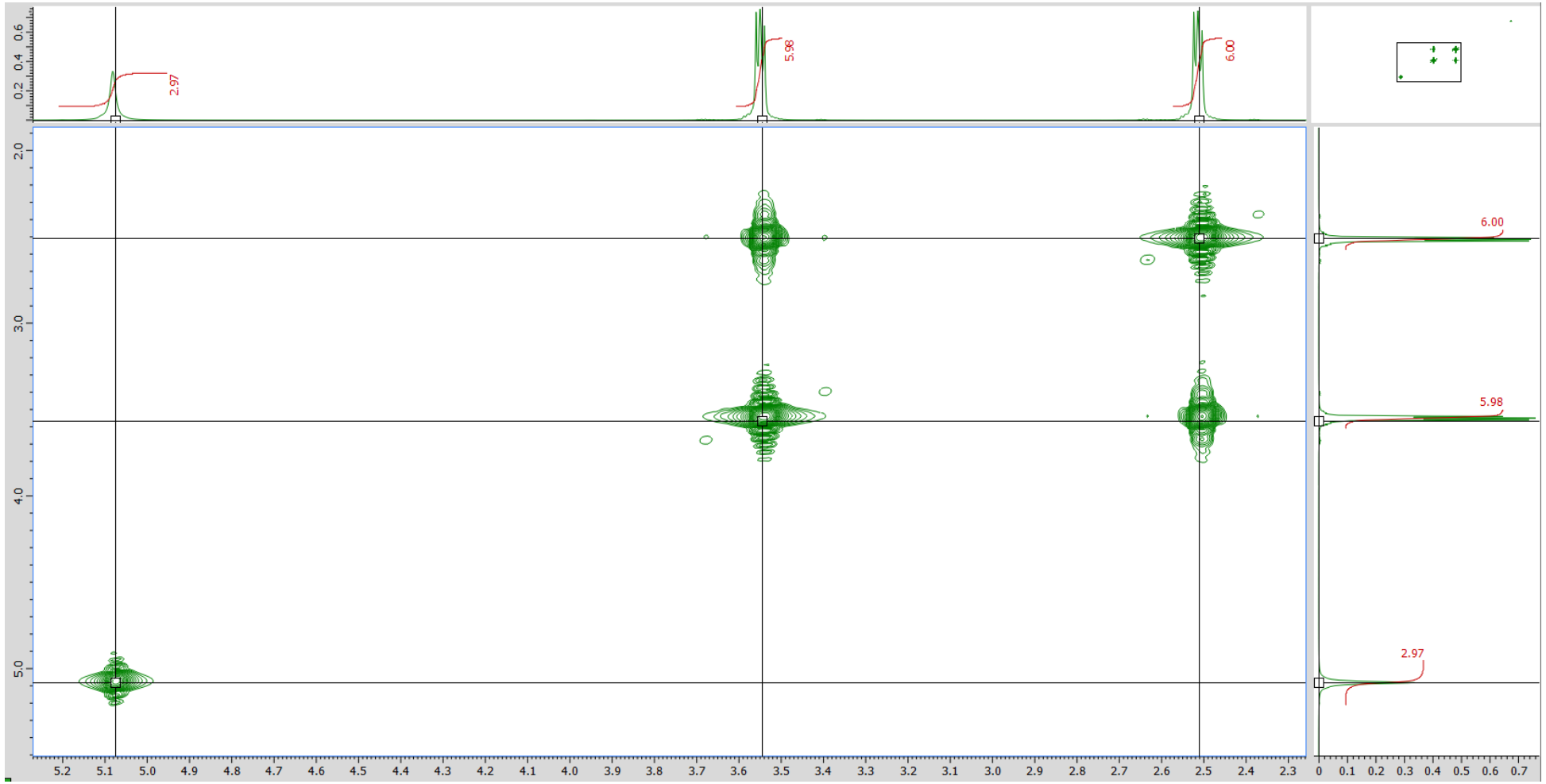

Figure S55- Triethanolamine, [**TEA**]H_3, ^{13}C NMR

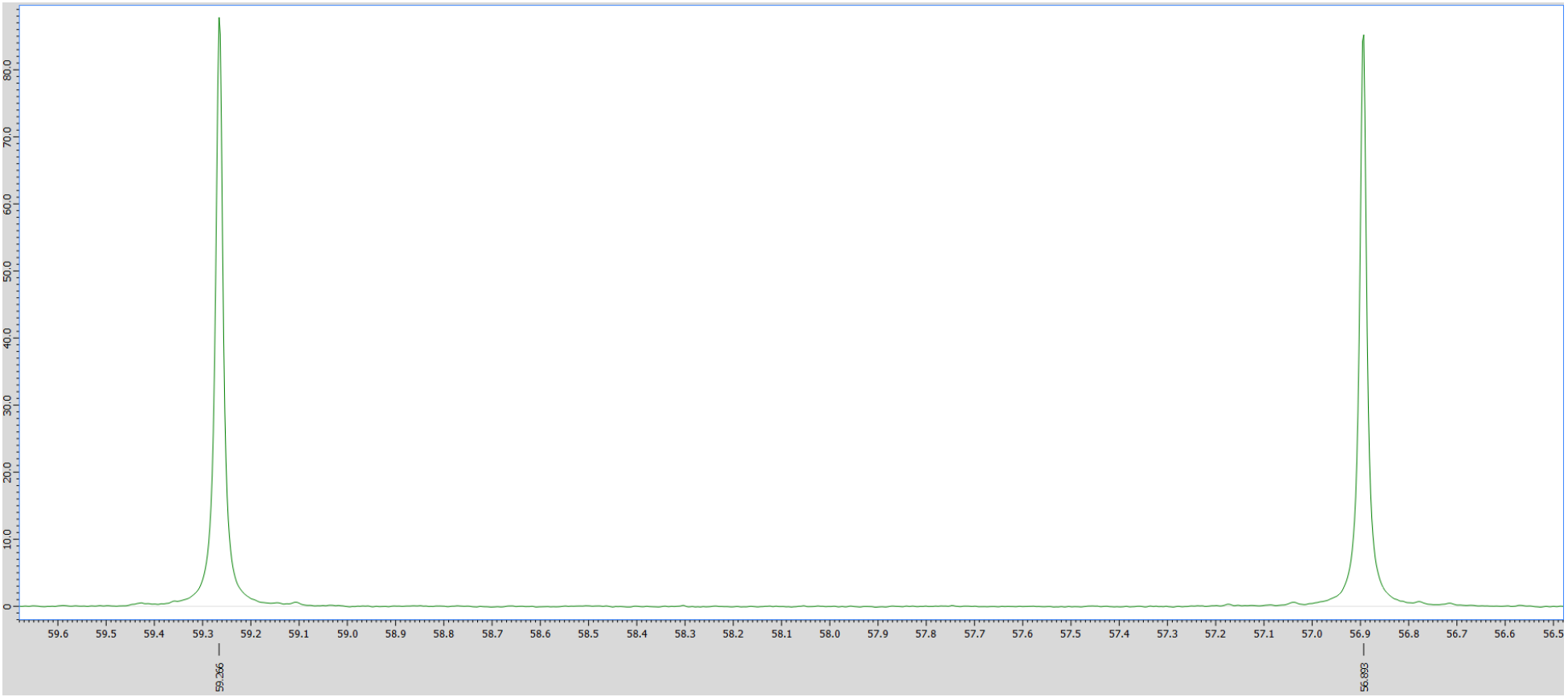

Figure S56- Triethanolamine, [**TEA**]H_3, HMQC

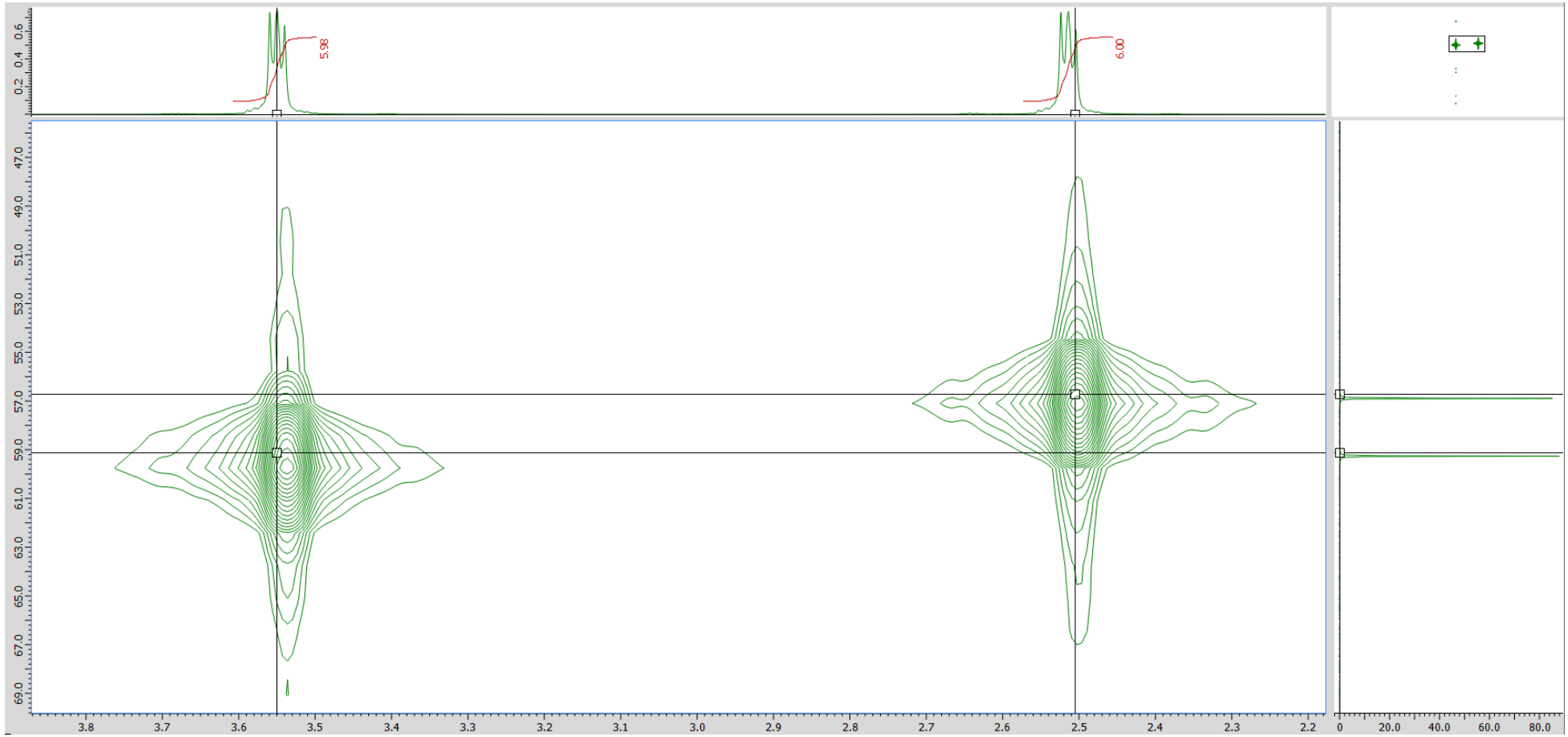

Figure S57- 3-[(2-hydroxyethyl)(methyl)amino]propan-1-ol, [**HMAP**]H_2, ^{1}H NMR

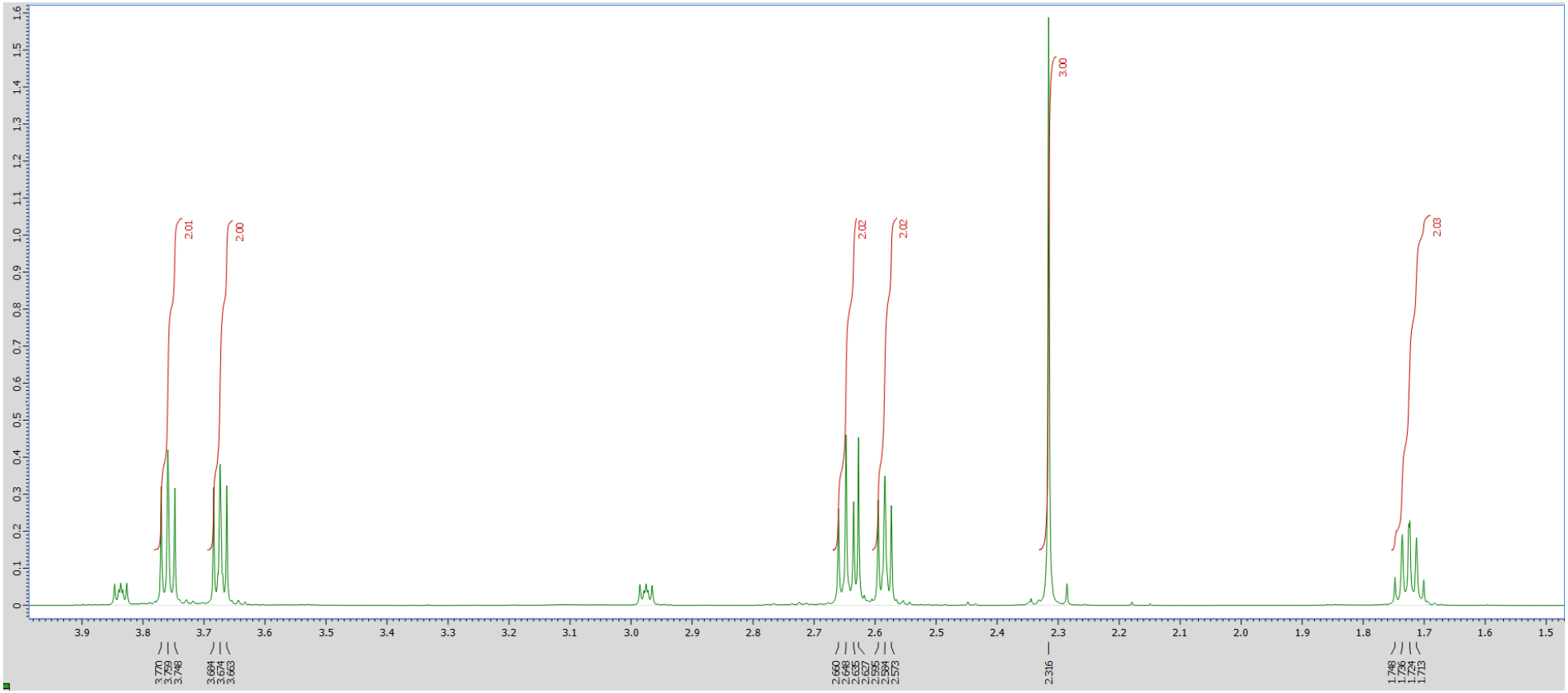

Figure S58- 3-[(2-hydroxyethyl)(methyl)amino]propan-1-ol, [**HMAP**]H_2, COSY

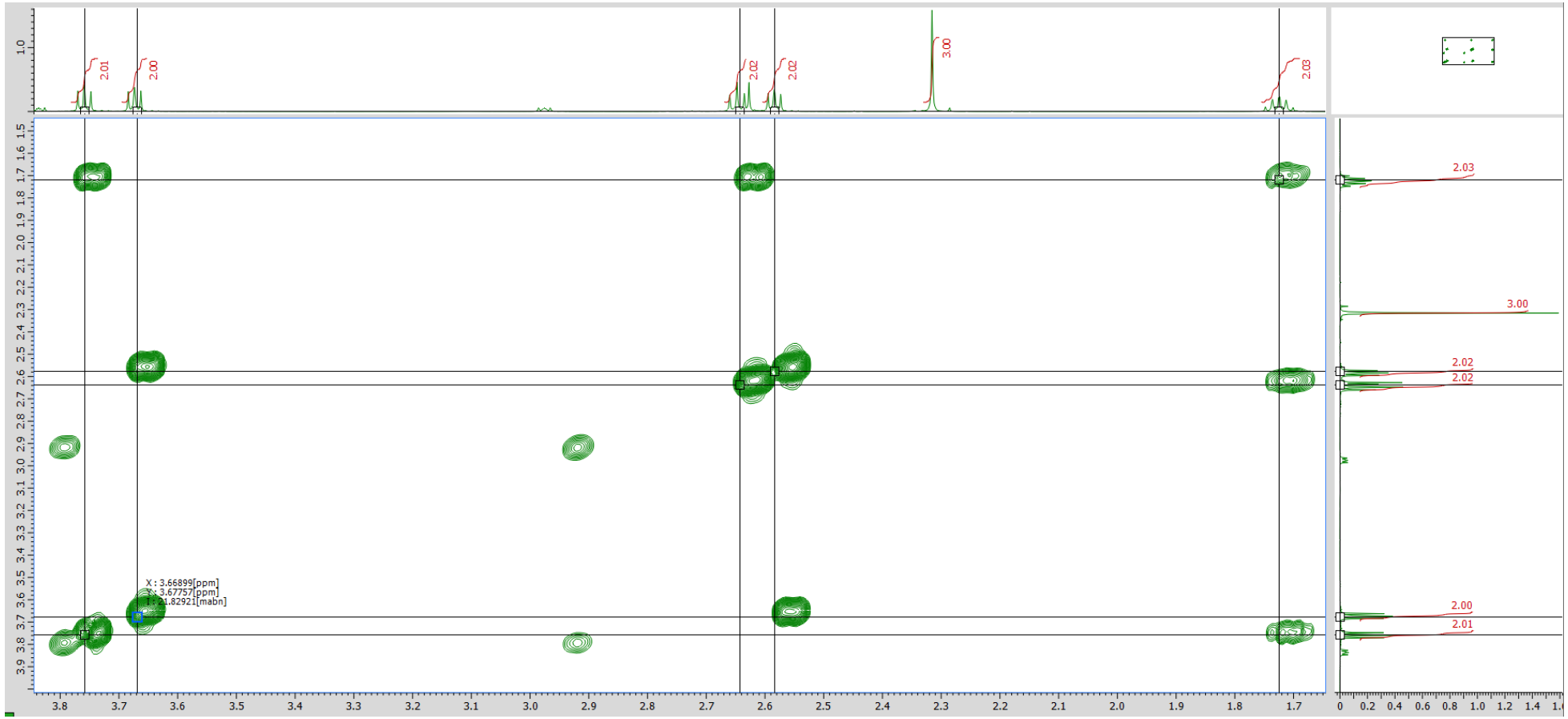

Figure S59- 3-[(2-hydroxyethyl)(methyl)amino]propan-1-ol, [**HMAP**]H_2, ^{13}C NMR

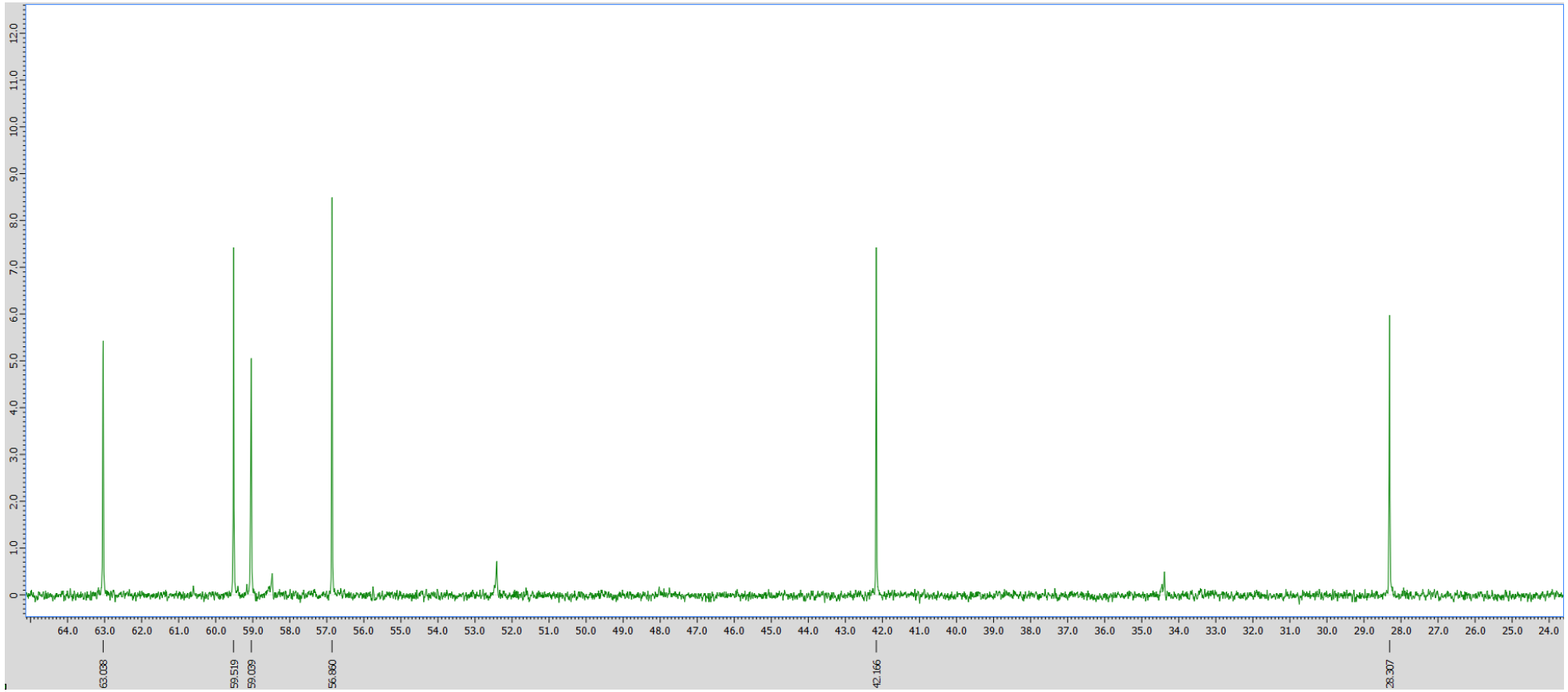

Figure S60- 3-[(2-hydroxyethyl)(methyl)amino]propan-1-ol, [**HMAP**]H_2, HMQC

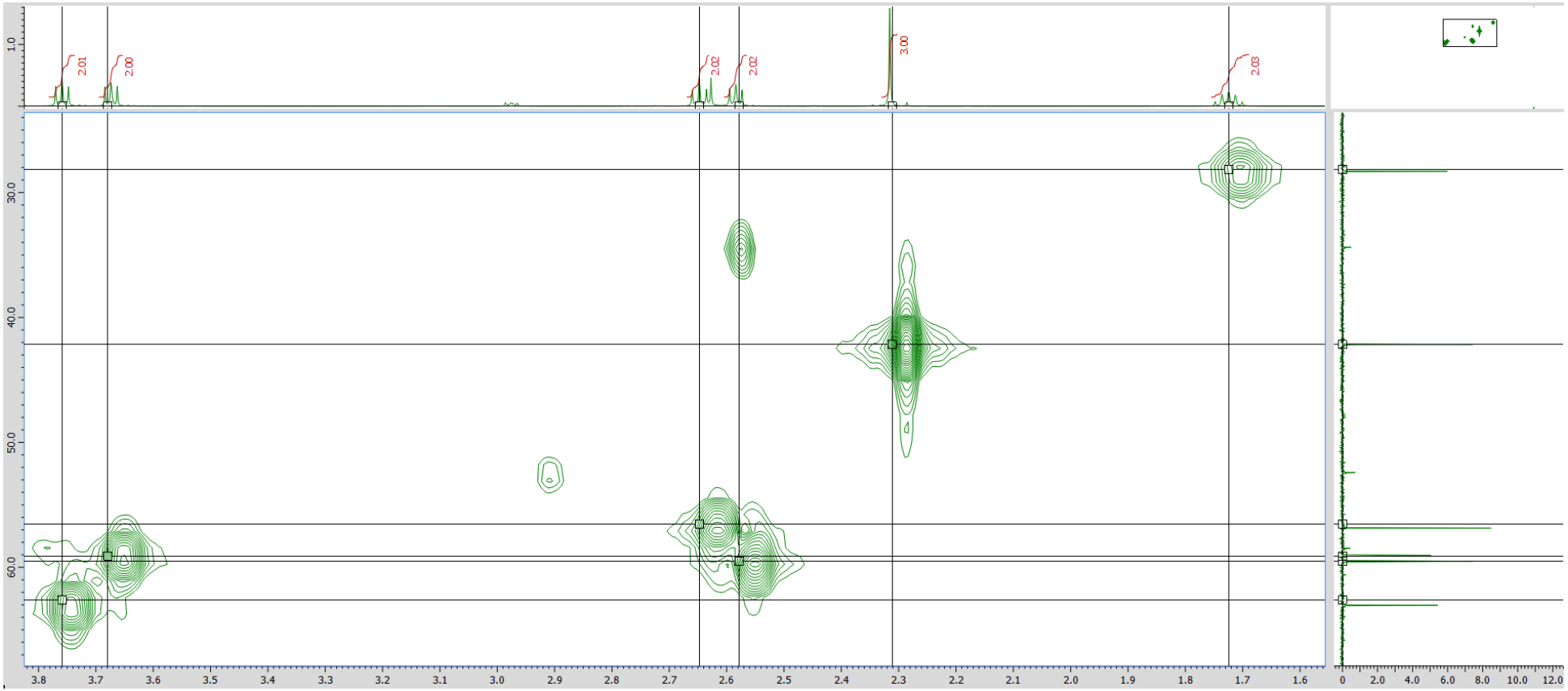

Figure S61- 3-[(2-hydroxyethyl)(ethyl)amino]propan-1-ol, [**HEAP**]H_2, ^{1}H NMR

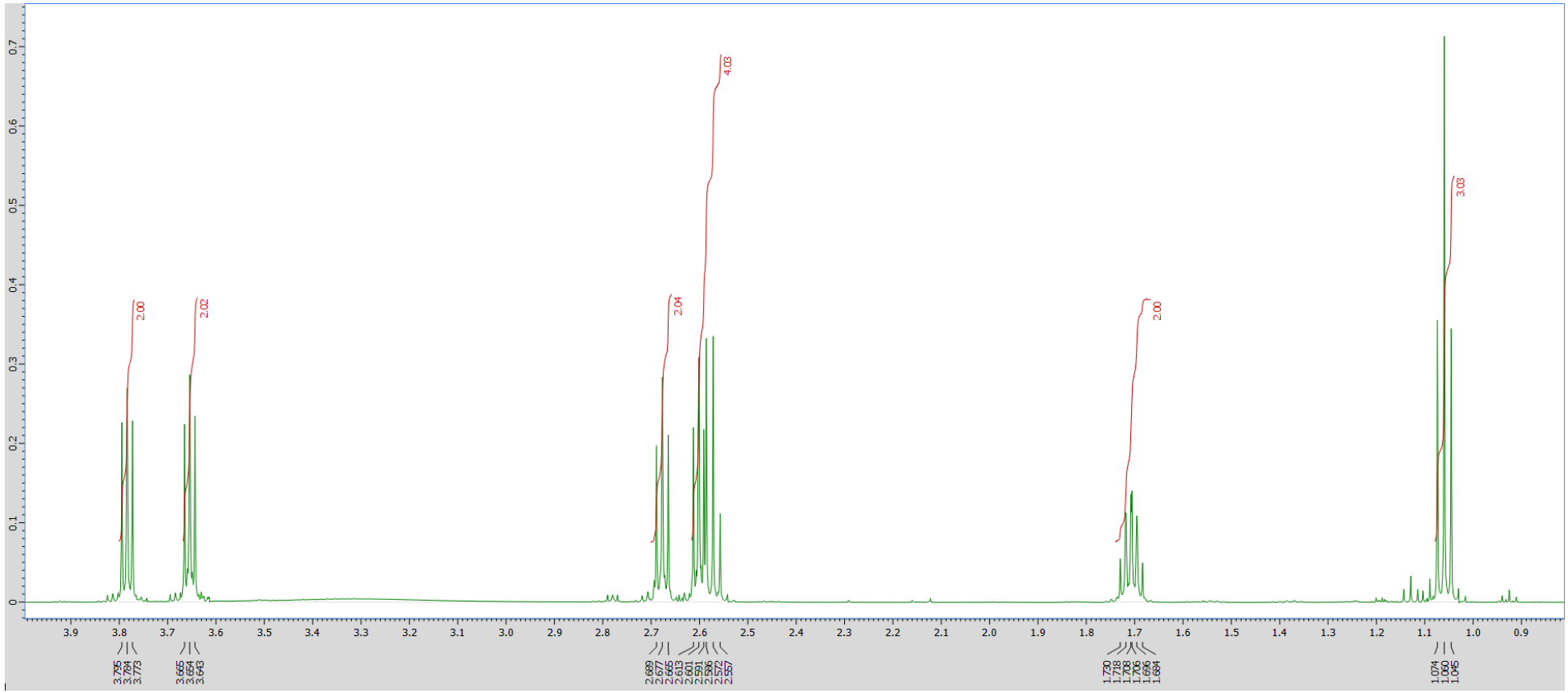

Figure S62- 3-[(2-hydroxyethyl)(ethyl)amino]propan-1-ol, [**HEAP**]H_2, COSY

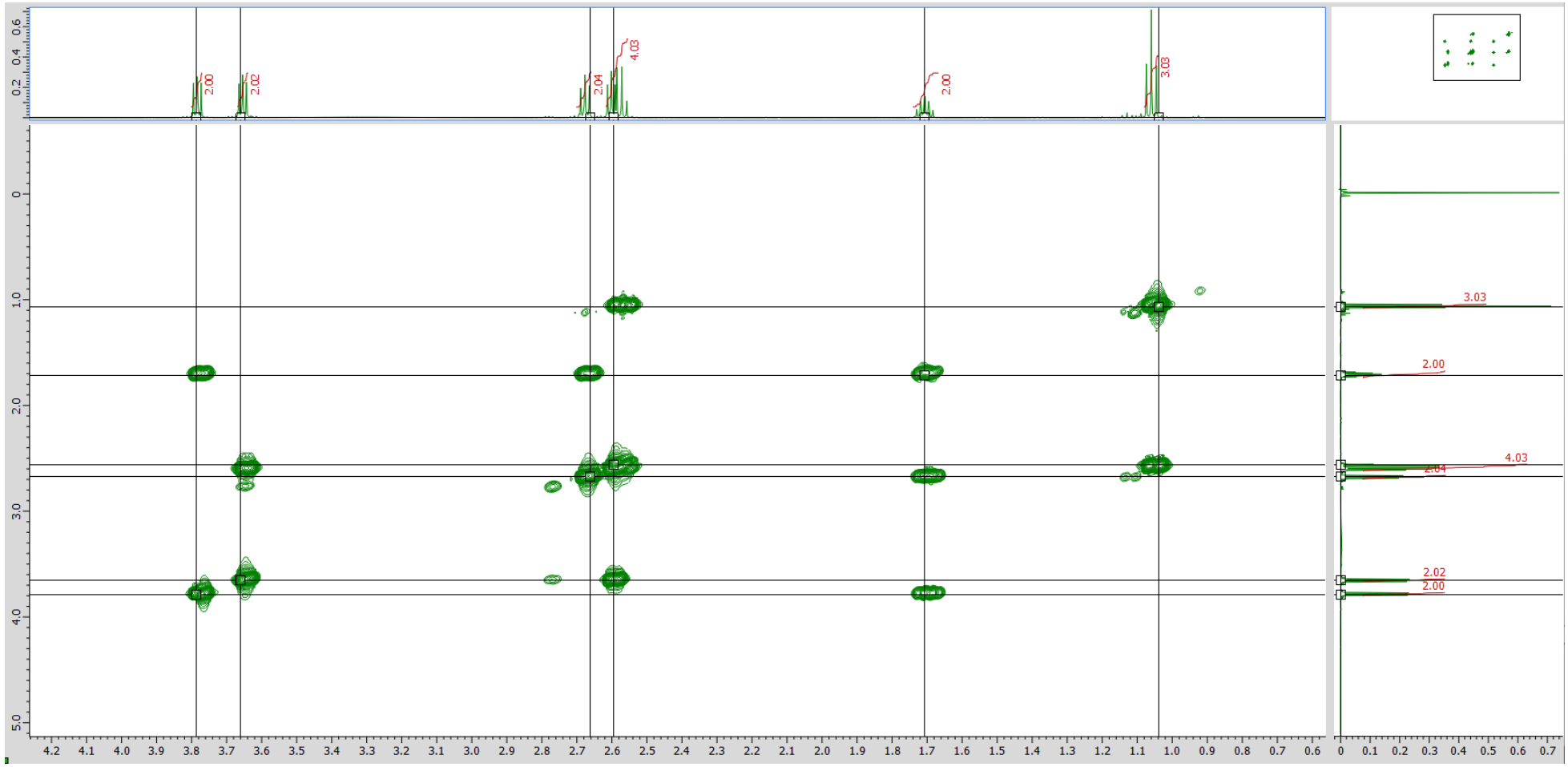

Figure S63- 3-[(2-hydroxyethyl)(ethyl)amino]propan-1-ol, [**HEAP**]H_2, ^{13}C NMR

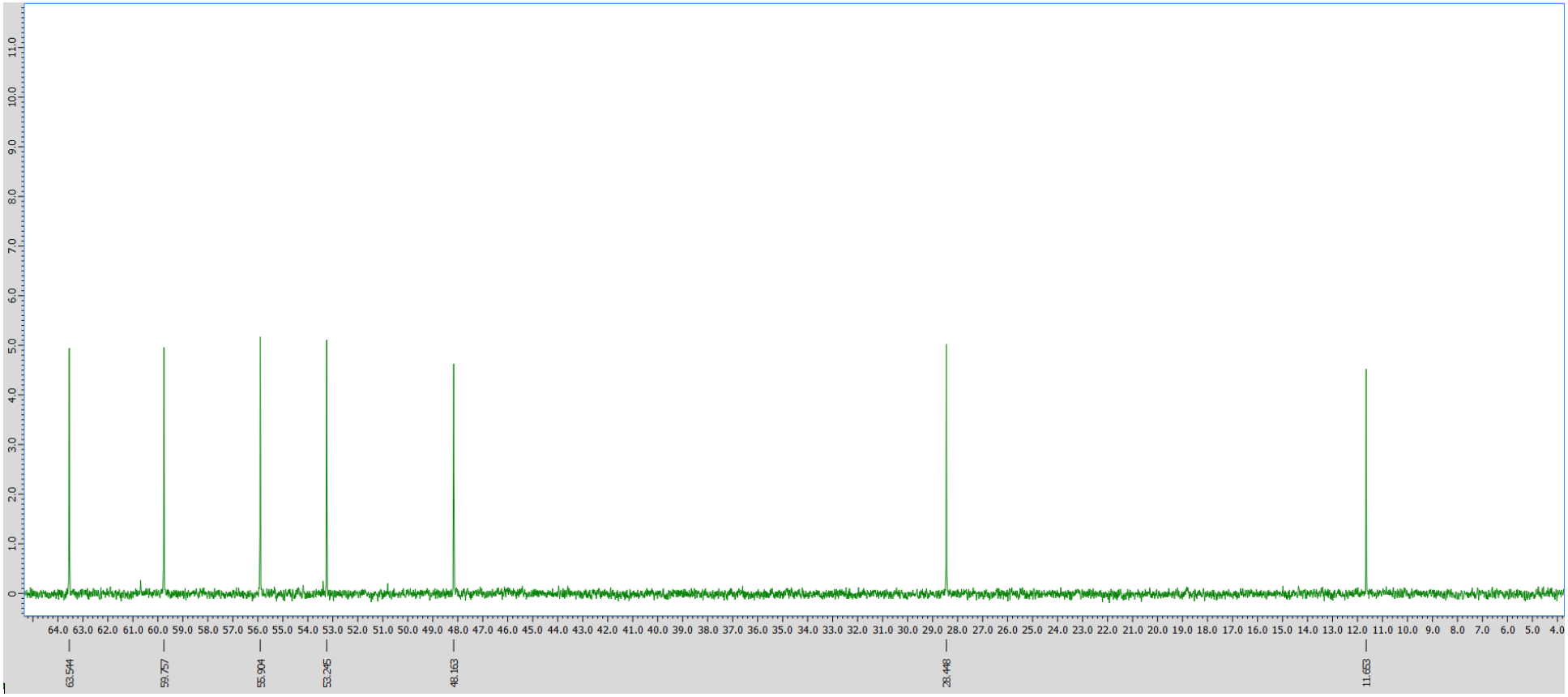

Figure S64- 3-[(2-hydroxyethyl)(ethyl)amino]propan-1-ol, [**HEAP**]H_2, HMQC

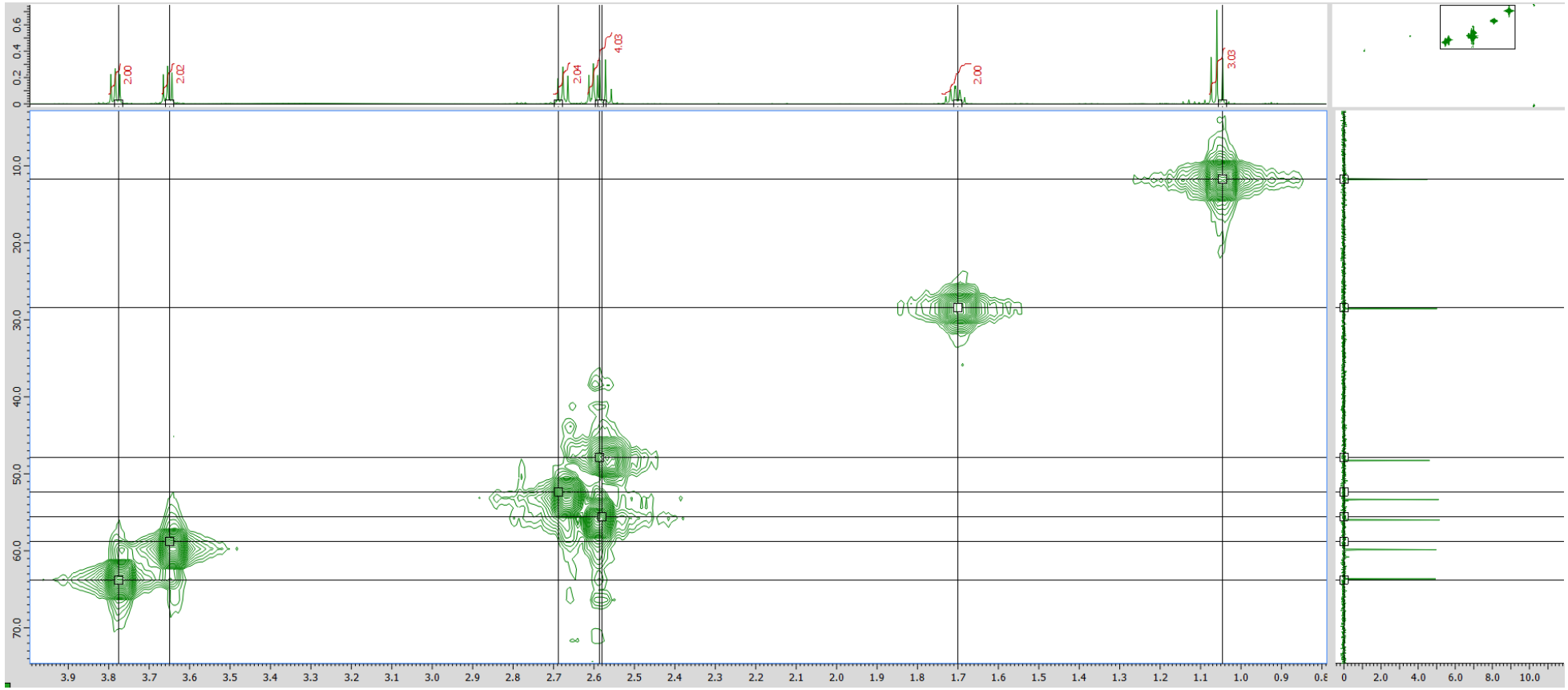

Figure S65- 3-[(2-hydroxyethyl)(iso-propyl)amino]propan-1-ol, [**H^{i}PrAP**]H_2, ^{1}H NMR

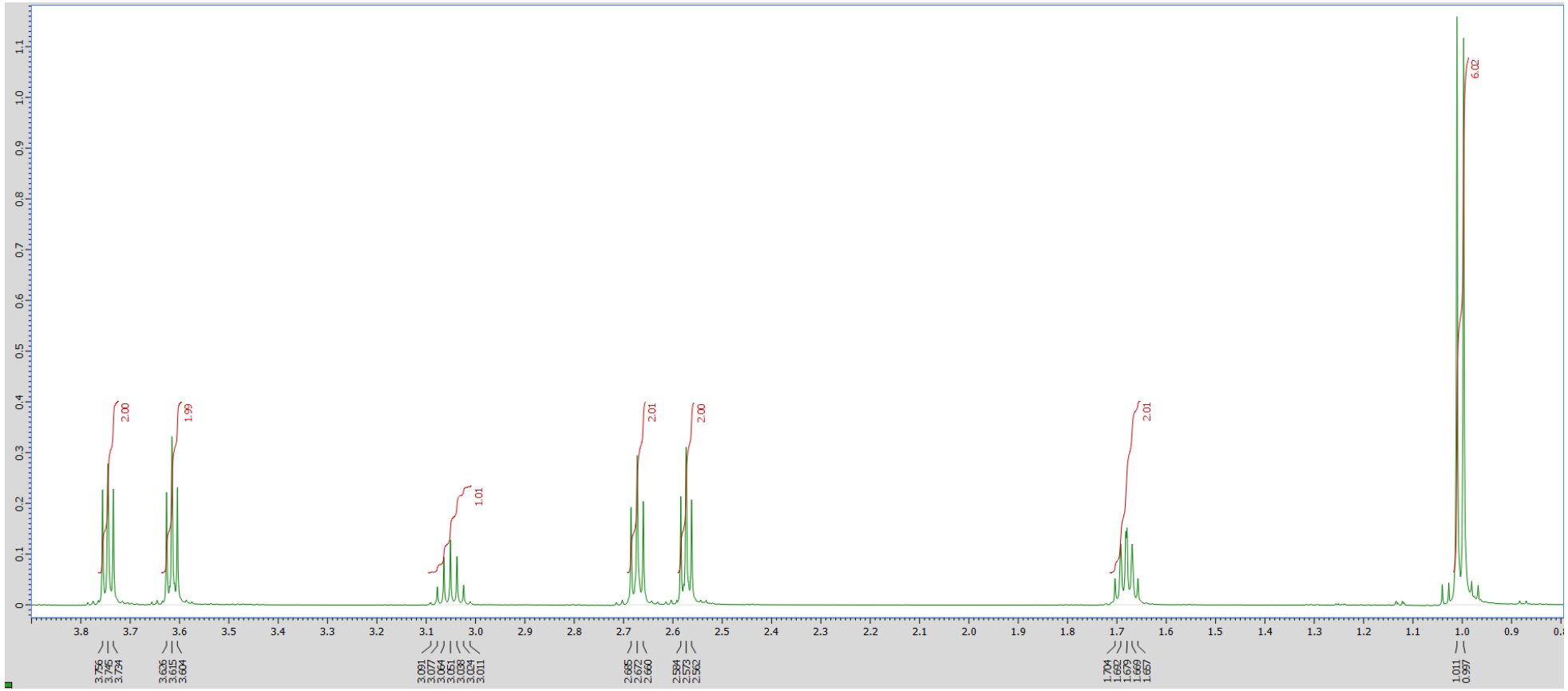

Figure S66- 3-[(2-hydroxyethyl)(iso-propyl)amino]propan-1-ol, [**H^{i}PrAP**]H_2, COSY

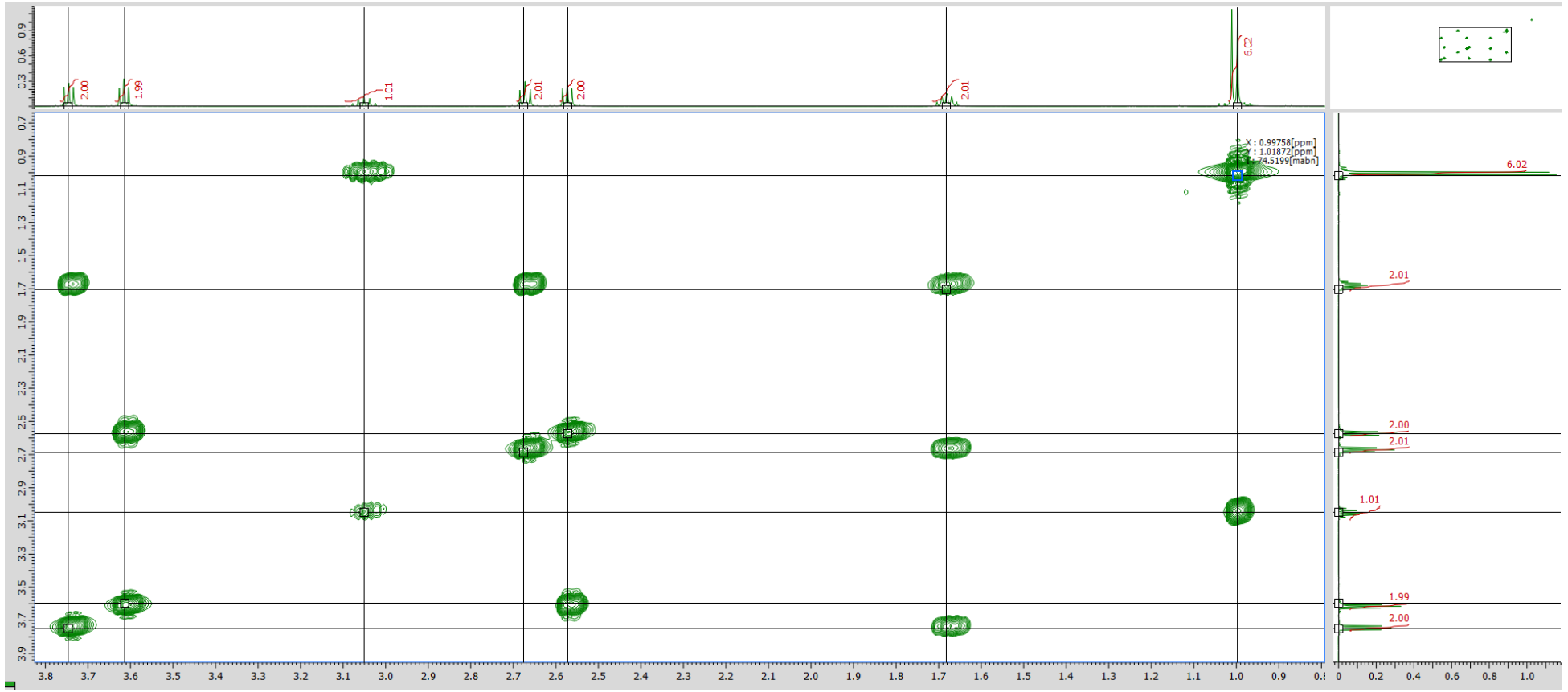

Figure S67- 3-[(2-hydroxyethyl)(iso-propyl)amino]propan-1-ol, [**H^{i}PrAP**]H_2, ^{13}C NMR

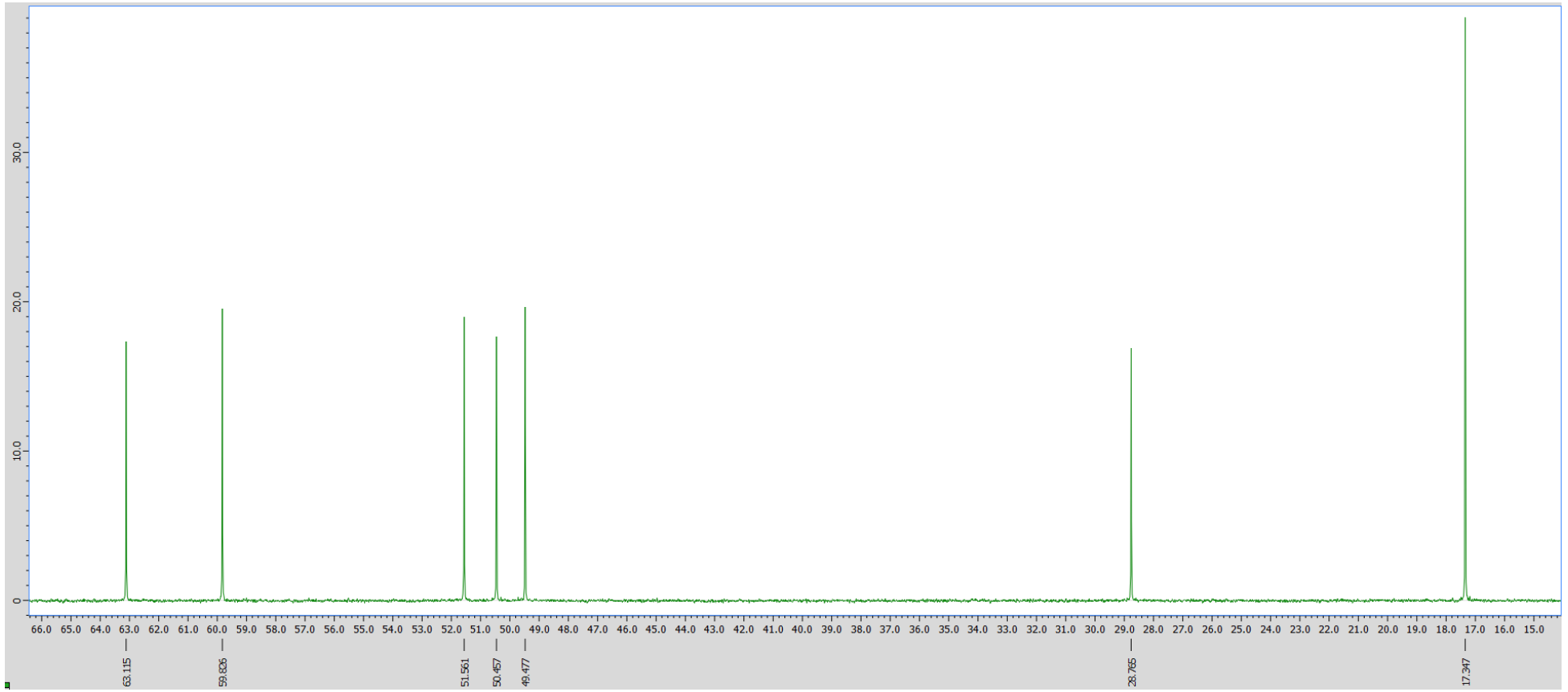

Figure S68- 3-[(2-hydroxyethyl)(iso-propyl)amino]propan-1-ol, [**H^{i}PrAP**]H_2, HMQC

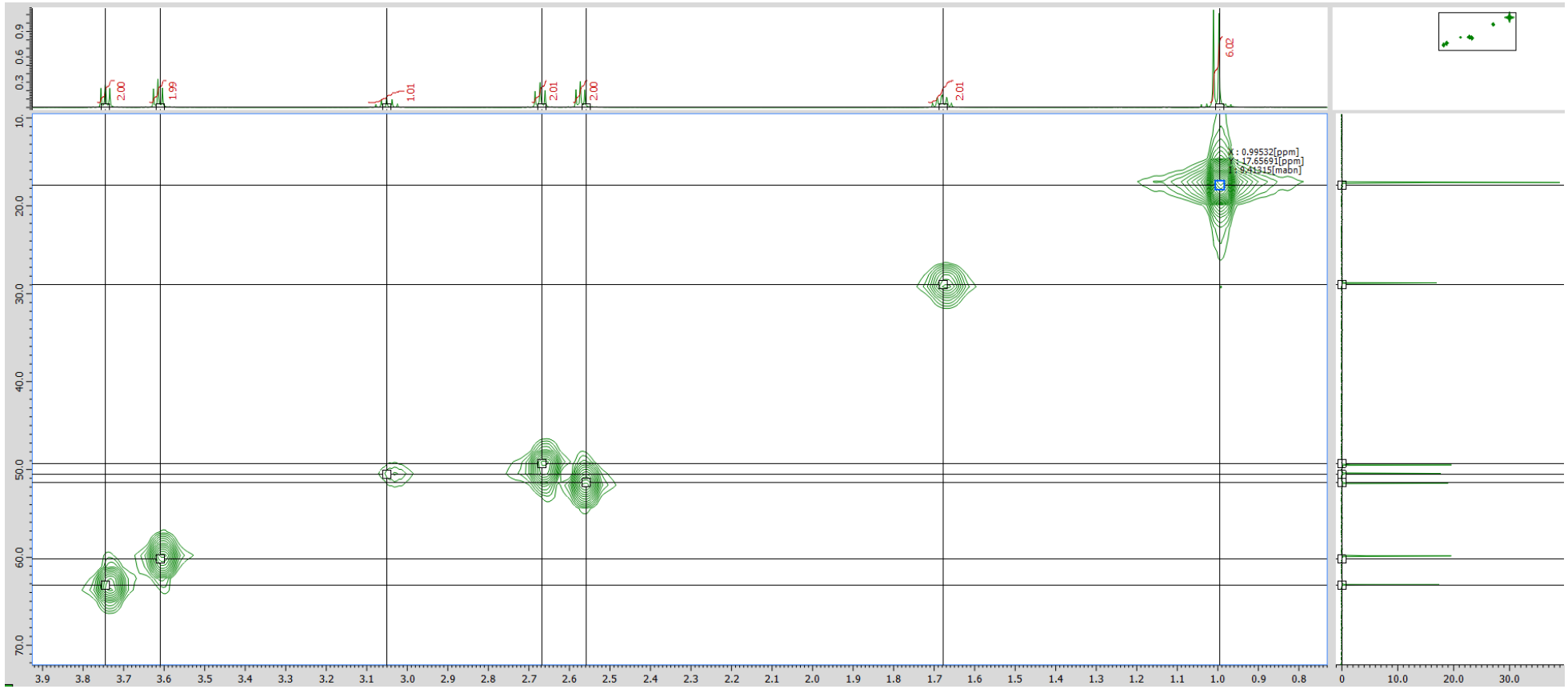

Figure S69- 3-[(2-hydroxyethyl)(phenyl)amino]propan-1-ol, [**HPhAP**]H_2, ^{1}H NMR

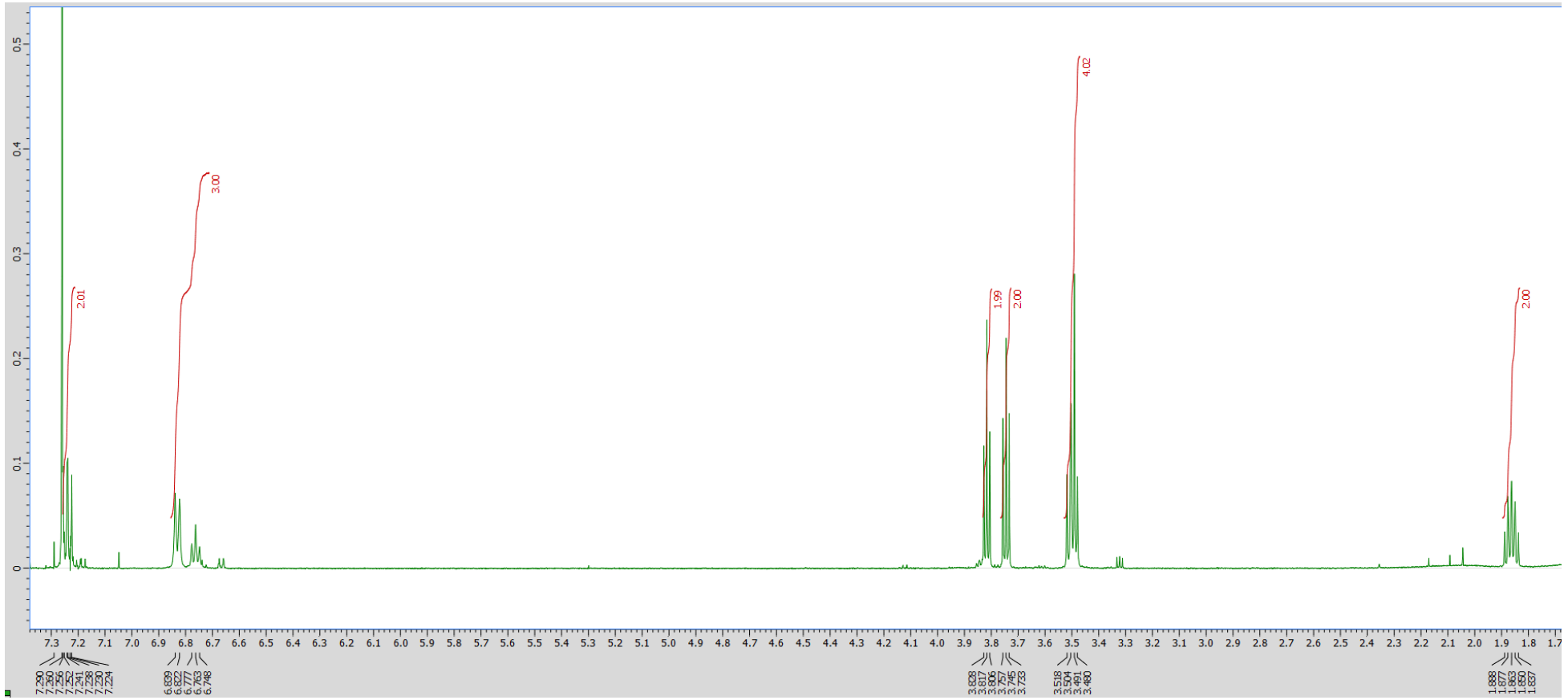

Figure S70- 3-[(2-hydroxyethyl)(phenyl)amino]propan-1-ol, [**HPhAP**]H_2, COSY

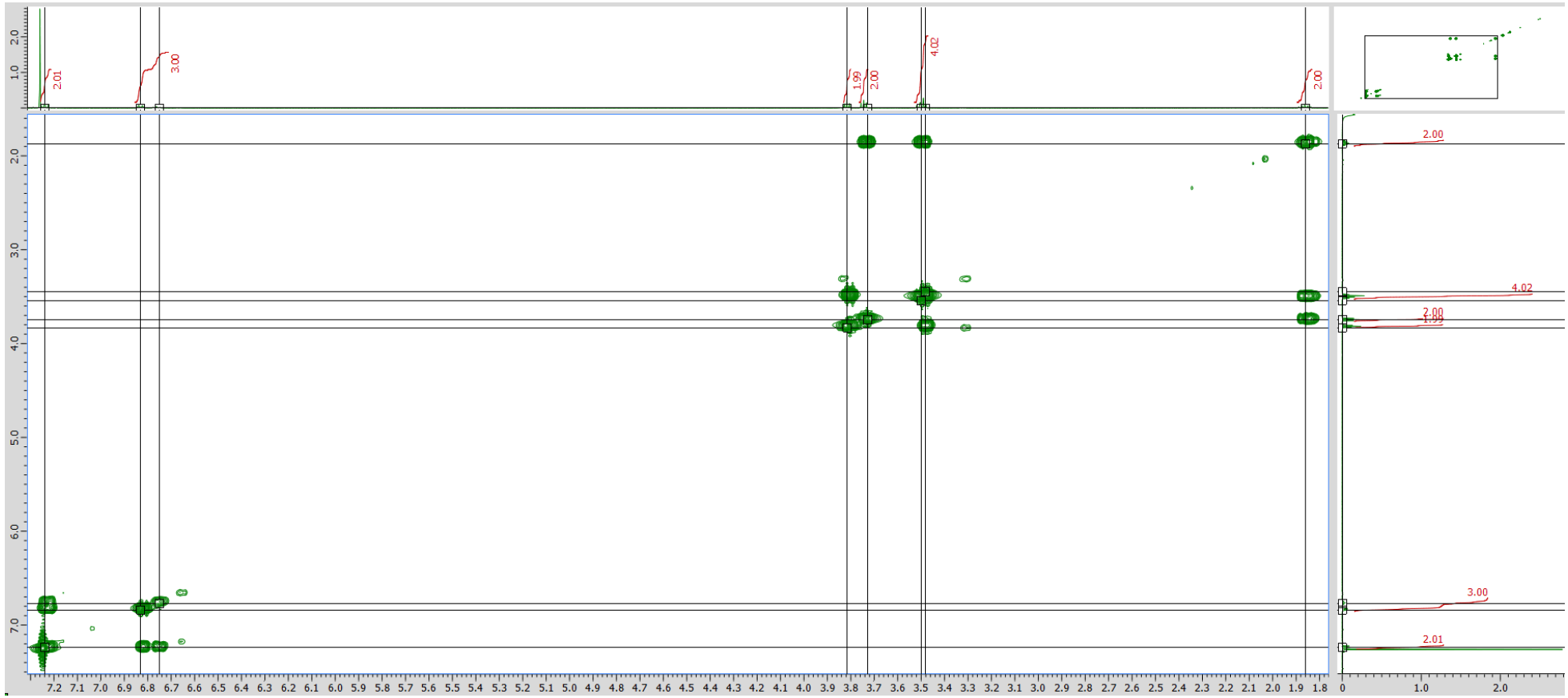

Figure S71- 3-[(2-hydroxyethyl)(phenyl)amino]propan-1-ol, [**HPhAP**]H_2, HMQC

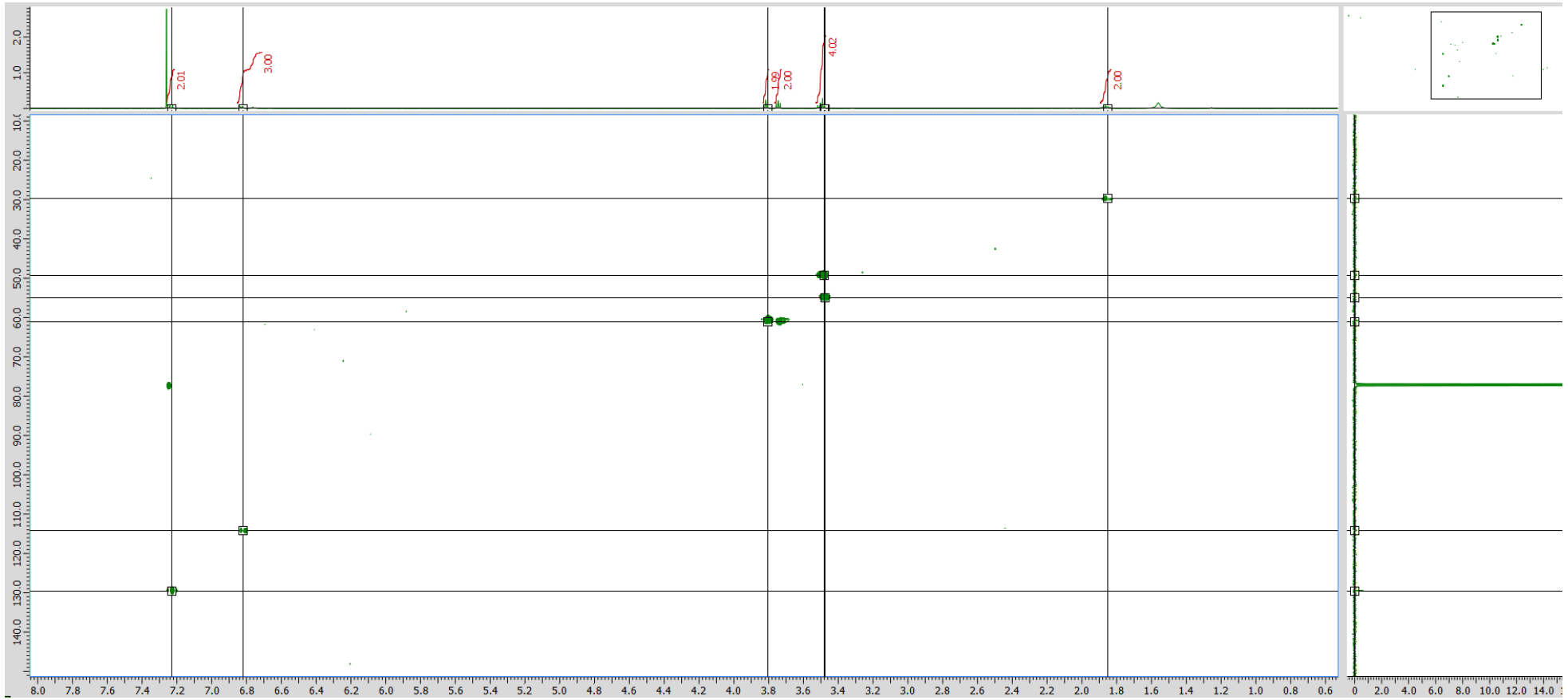

Appendix D – Infrared Spectroscopy

Synthesised organic compounds were characterised by IR spectroscopy with data collected on a Thermo Electron Corporation Nicolet 380 FT-IR with a Smart iTR™ Attenuated Total Reflectance (ATR) Sampling Accessory. Spectra were collected typically within the range of 4000-650 cm^{-1} (Wavenumbers).

IR processing was carried out making use of Omnic version 8.3.

IR signals were allocated according to values tabulated by Nakamoto, Fleming and Williams where reasonably modern data was not available.[263, 264]

Figure S72 -2-(methylamino)ethan-1-ol, [**MAE**]H, FT-IR

Figure S73- 2-(ethylamino)ethan-1-ol, [**EAE**]H, FT-IR

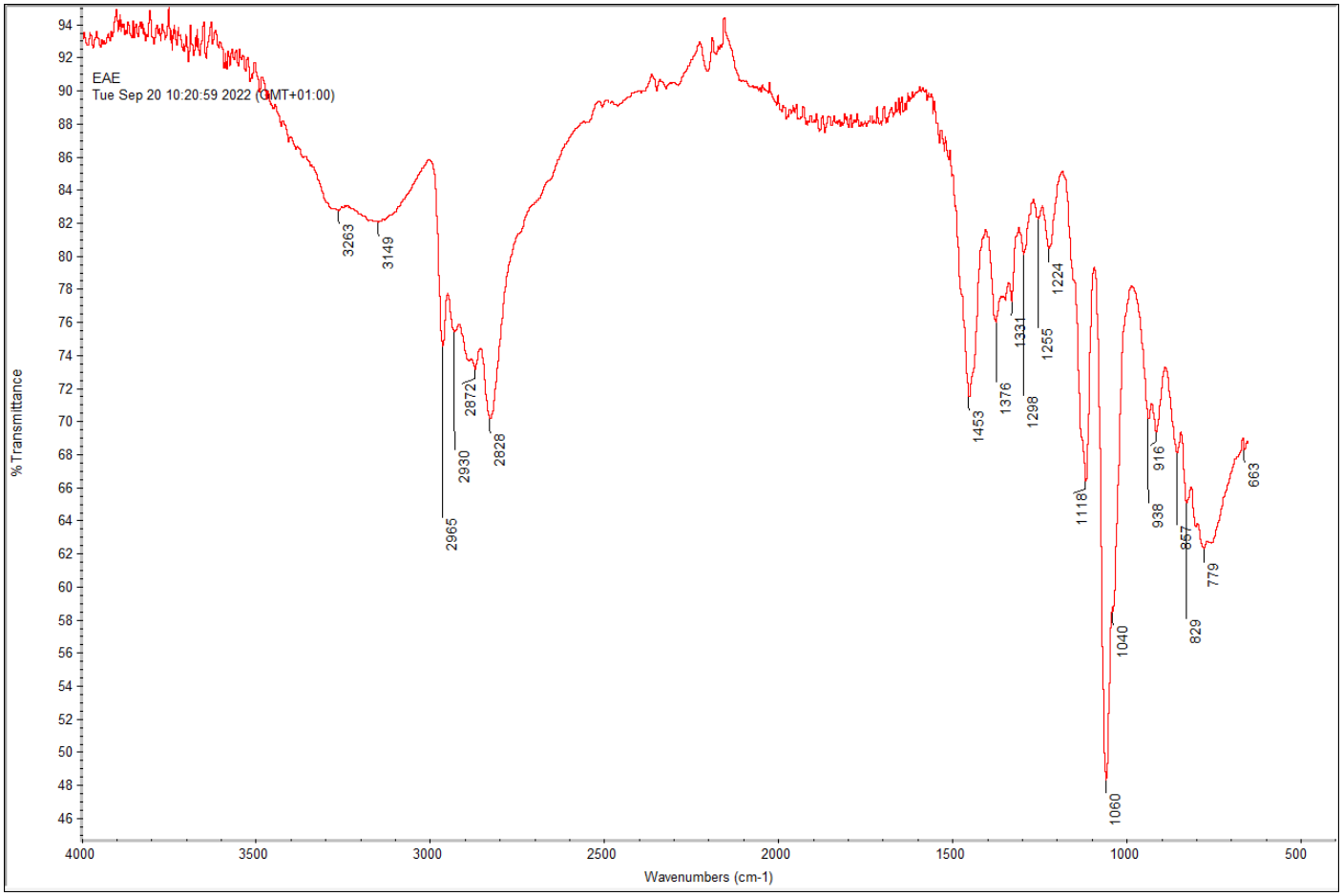

Figure S74- 2-(isopropylamino)ethan-1-ol, [^{i}**PrAE**]H, FT-IR

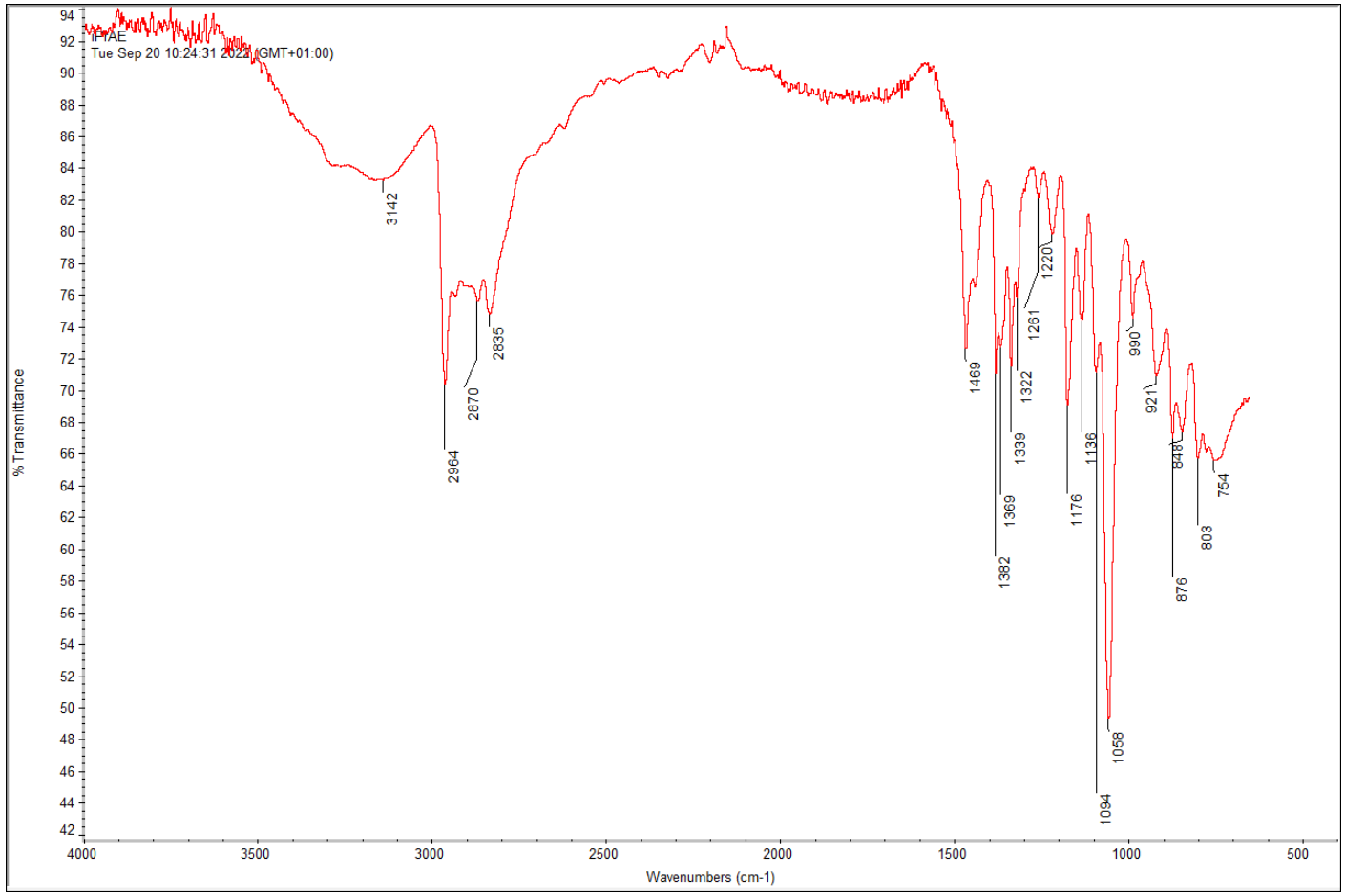

Figure S75- 2-(tertbutylamino)ethan-1-ol, [^{t}**BuAE**]H, FT-IR

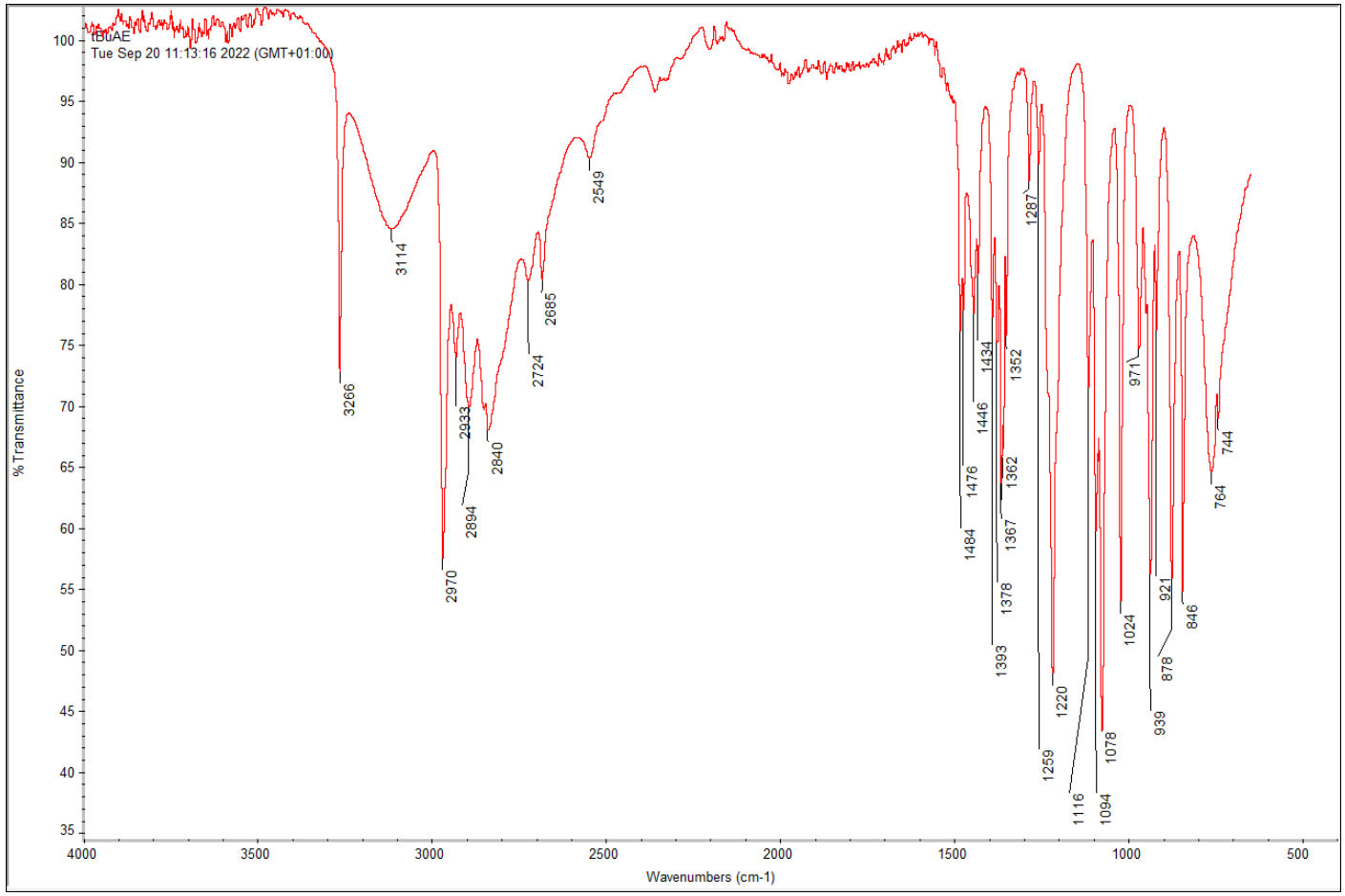

Figure S76- 2-(phenylamino)ethan-1-ol, [**PhAE**]H, FT-IR

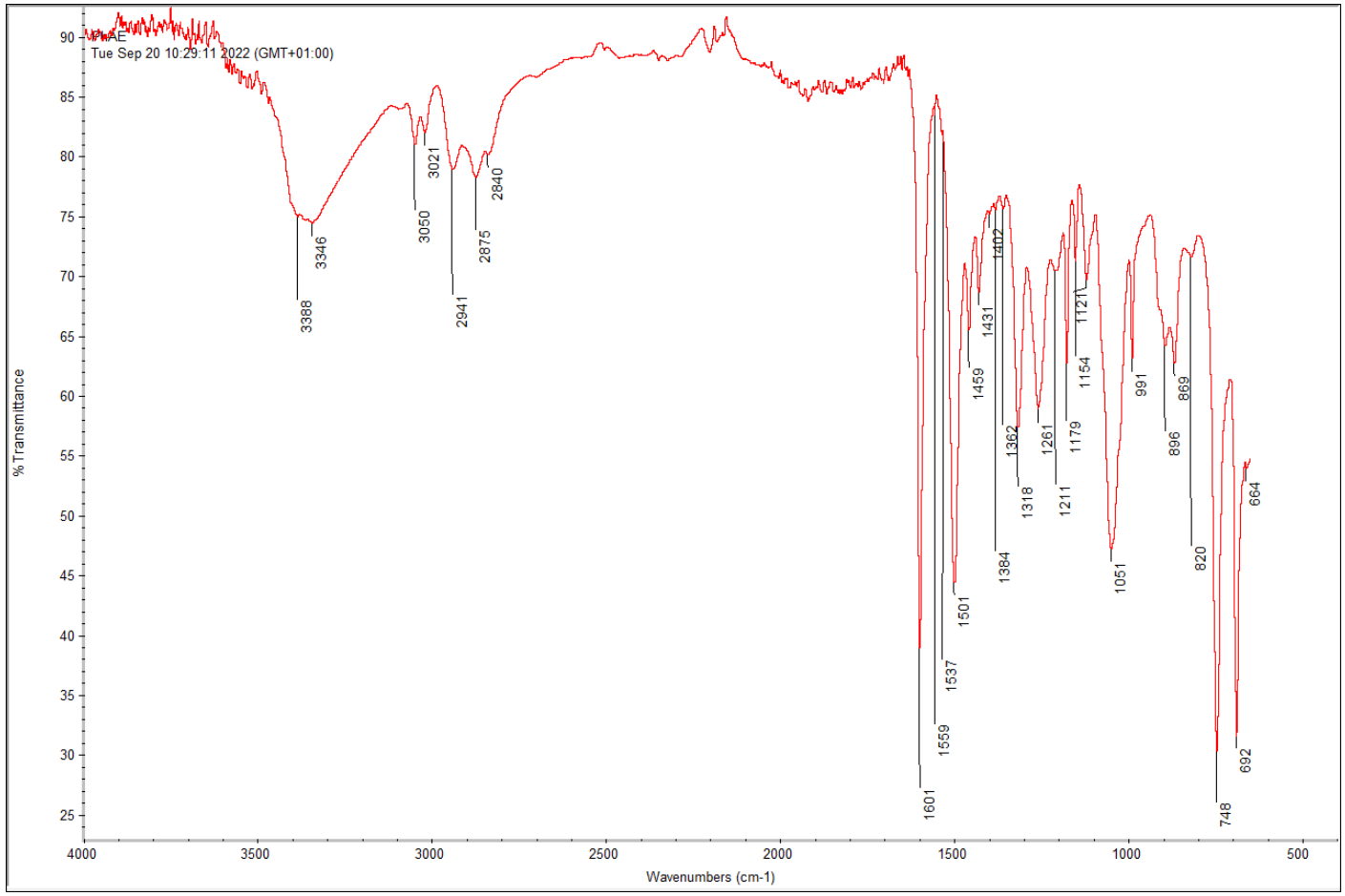

Figure S77- 2-(adamantylamino)ethan-1-ol, [**AdAE**]H, FT-IR

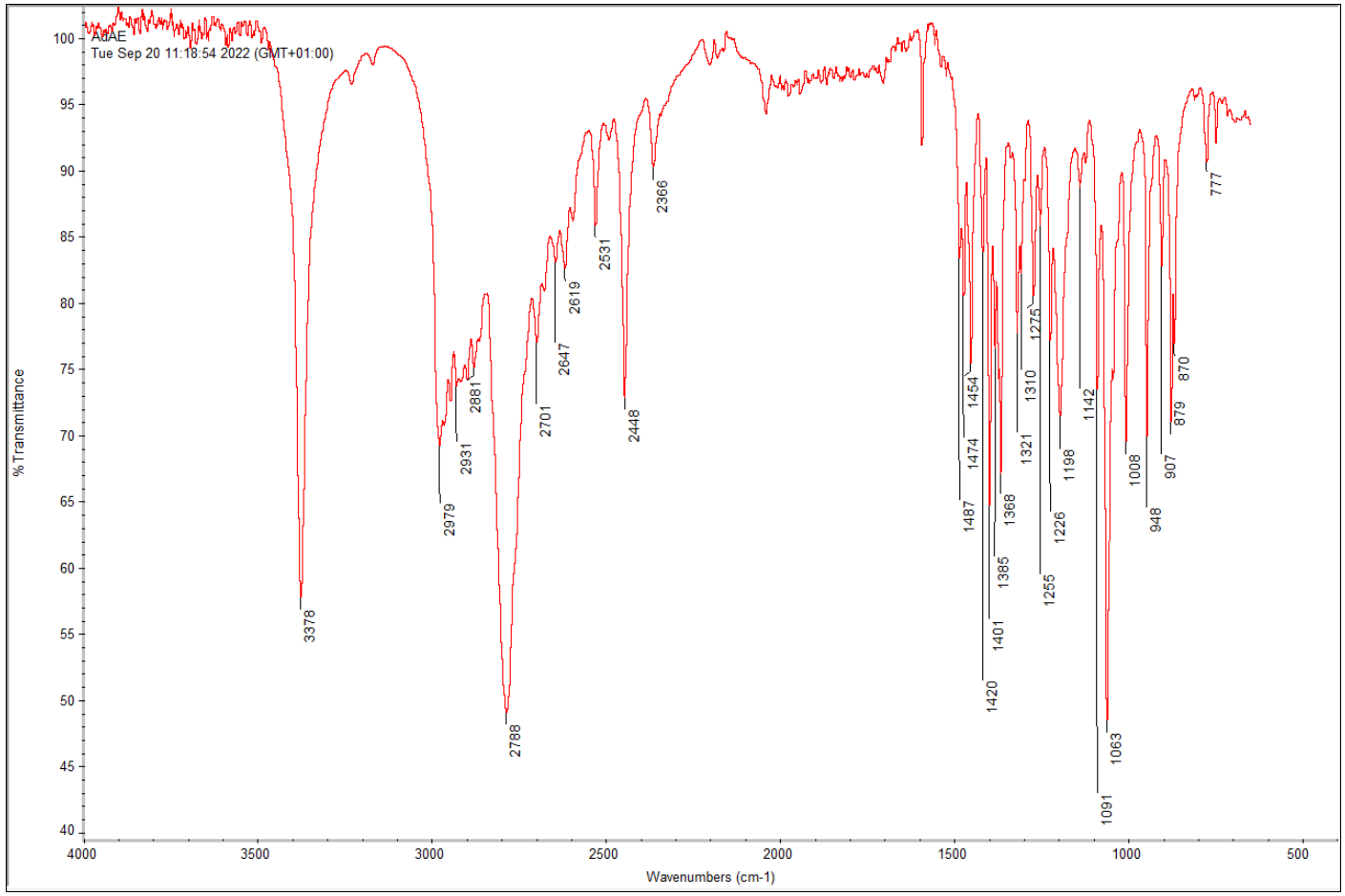

Figure S78- 3-(tertbutylamino)propan-1-ol, [^{t}**BuAPr**]H, FT-IR

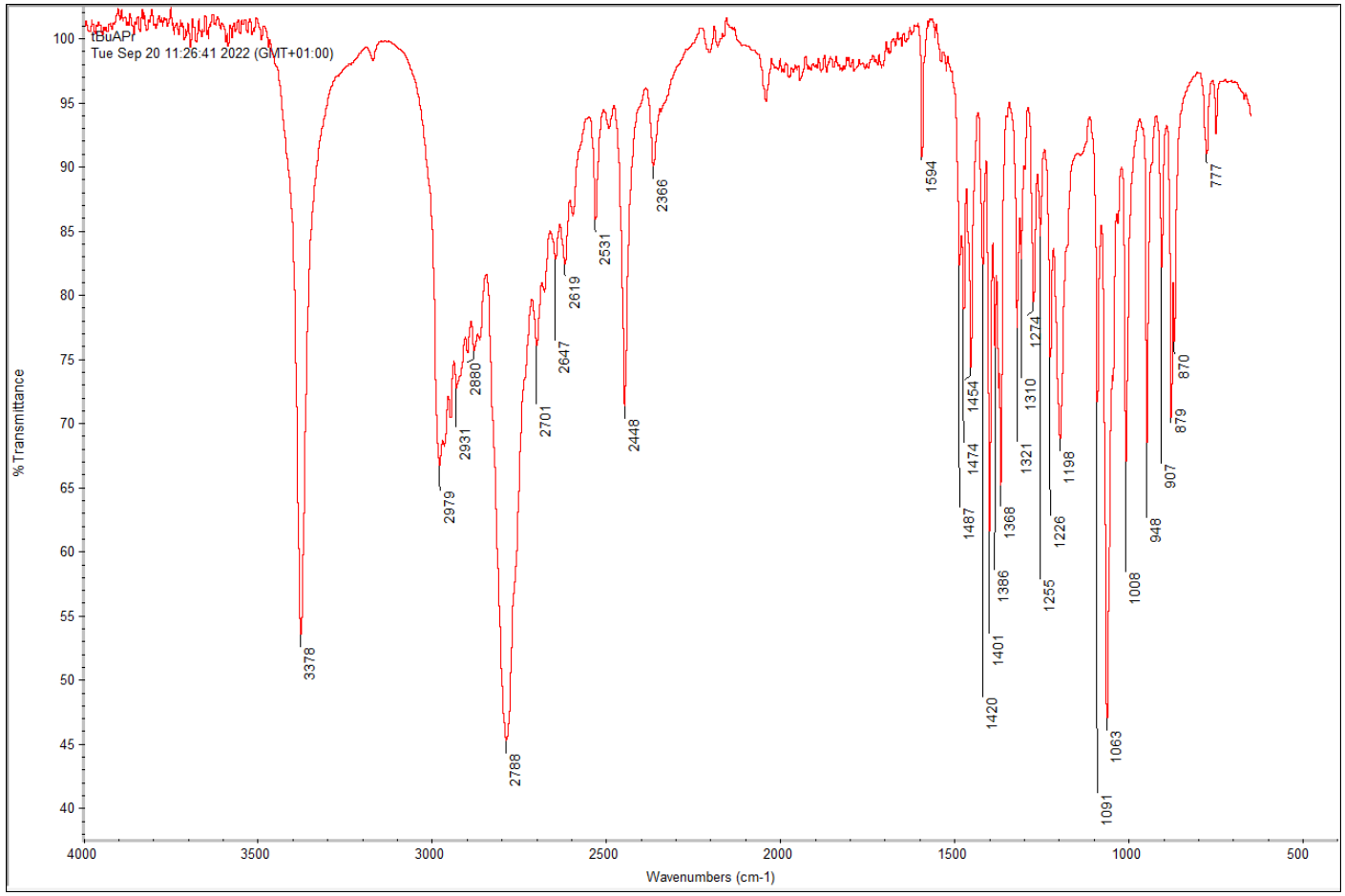

Figure S79- 3-(adamantylamino)propan-1-ol, [**AdAPr**]H, FT-IR

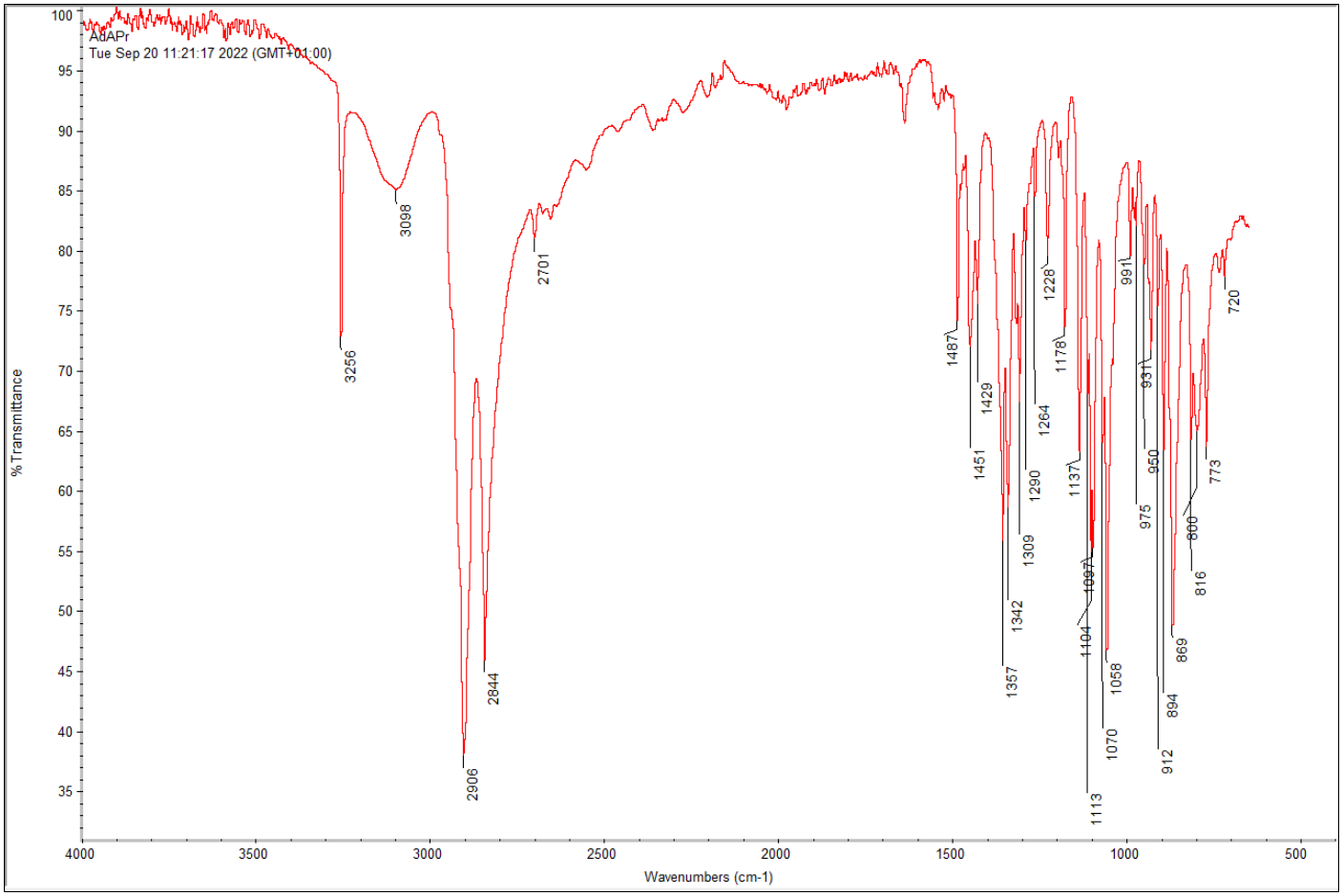

Figure S80- N-methyldiethanolamine, [**MDEA**]H_2, FT-IR

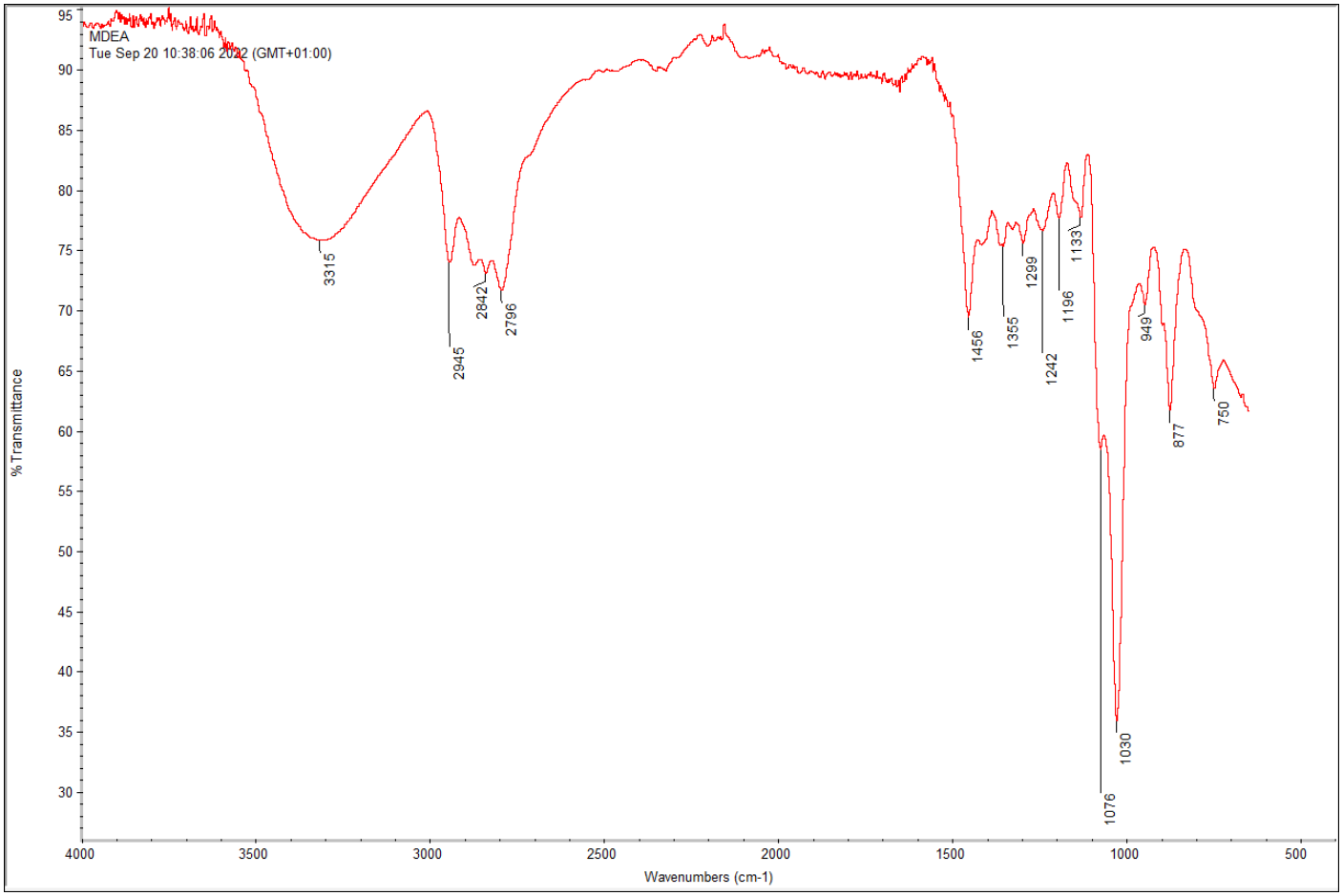

Figure S81- N-ethyldiethanolamine, [**EDEA**]H_2, FT-IR

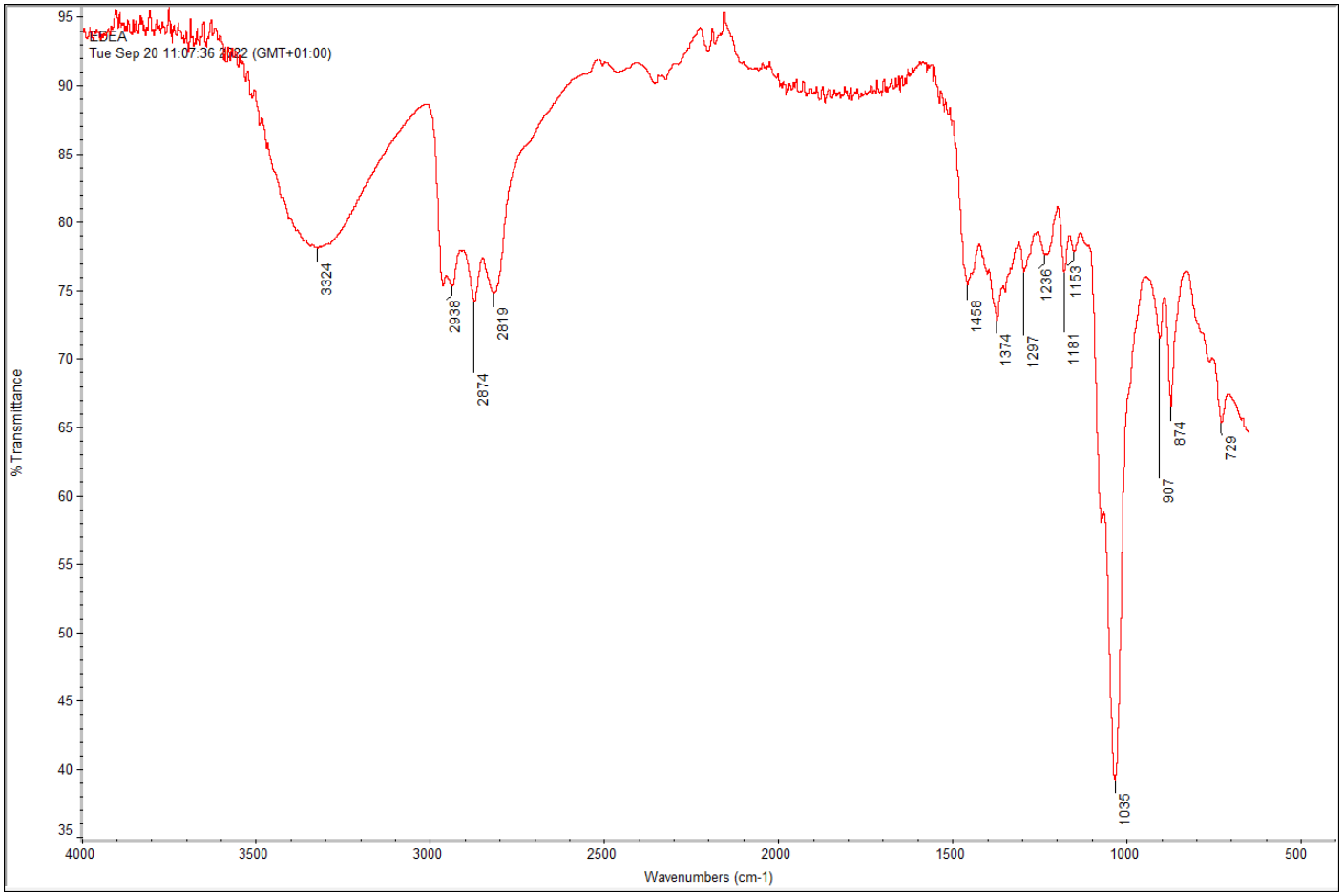

Figure S82- N-isopropyldiethanolamine, [^{i}**PrDEA**]H_2, FT-IR

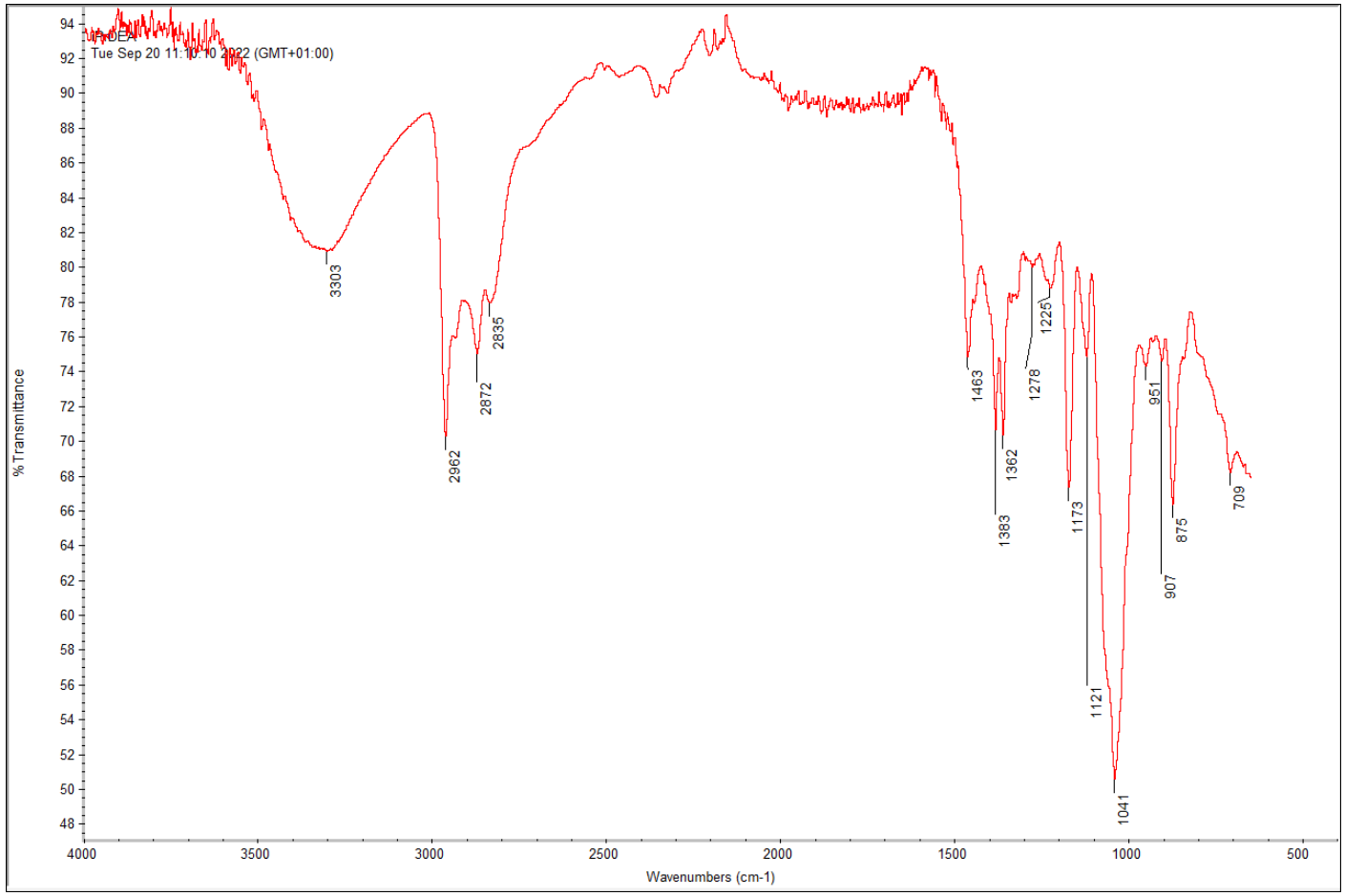

Figure S83- N-n- butyldiethanolamine, [^{n}**BuDEA**]H_2, FT-IR

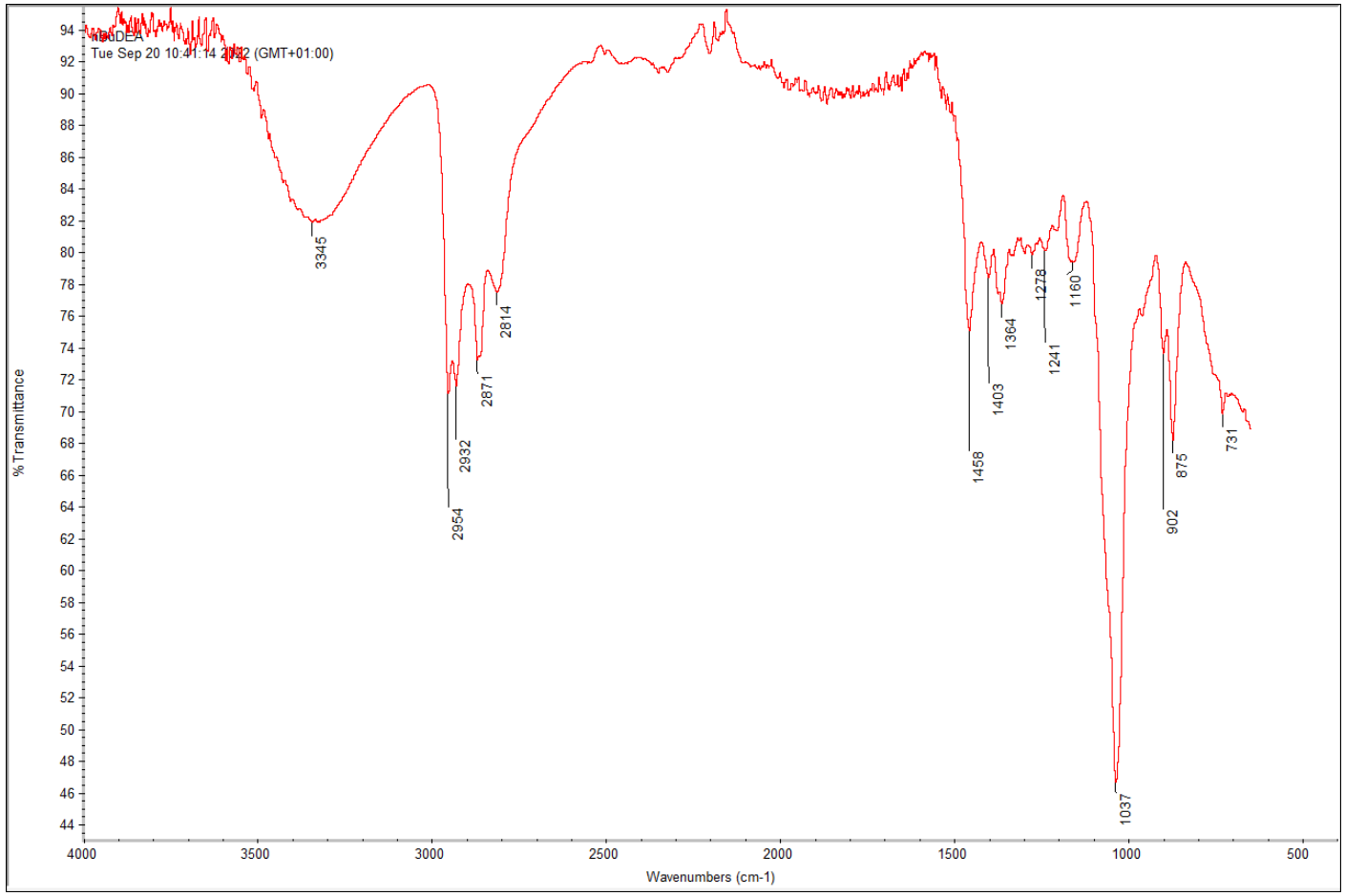

Figure S84- N-phenyldiethanolamine, [**PhDEA**]H_2, FT-IR

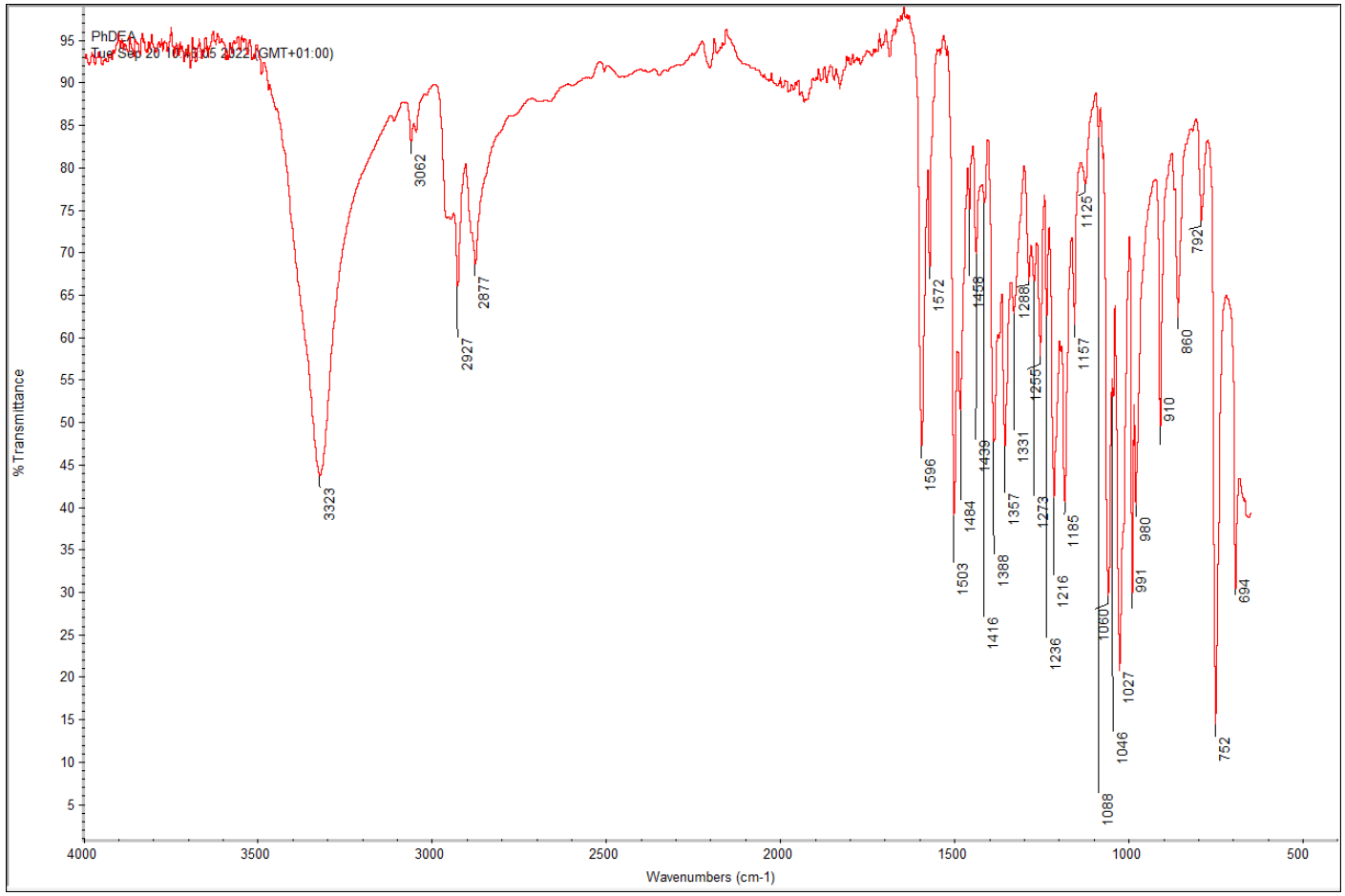

Figure S85- Triethanolamine, [**TEA**]H_3, FT-IR

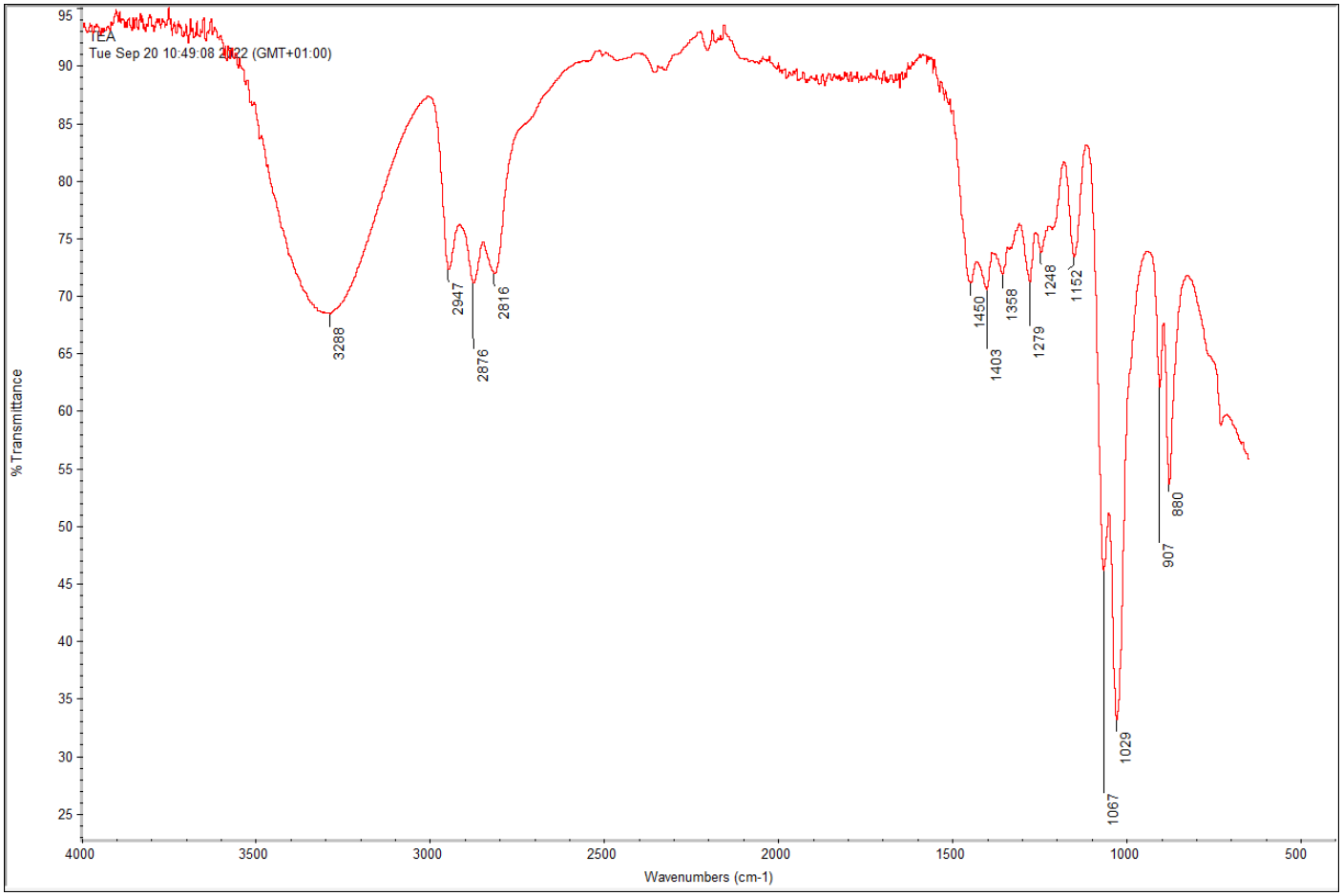

Figure S86- 3-[(2-hydroxyethyl)(methyl)amino]propan-1-ol, [**HMAP**]H_2, FT-IR

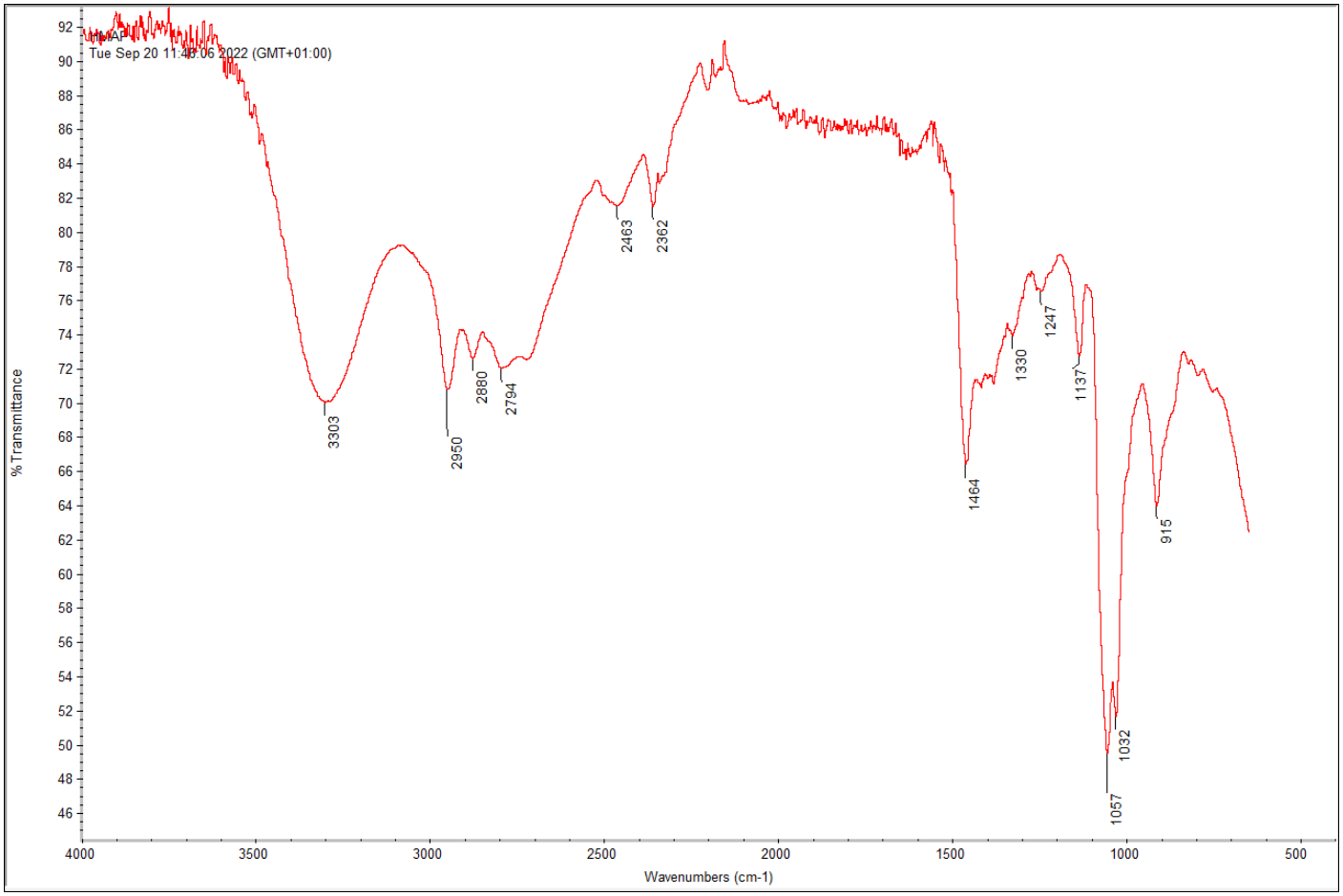

Figure S87- 3-[(2-hydroxyethyl)(ethyl)amino]propan-1-ol, [**HEAP**]H_2, FT-IR

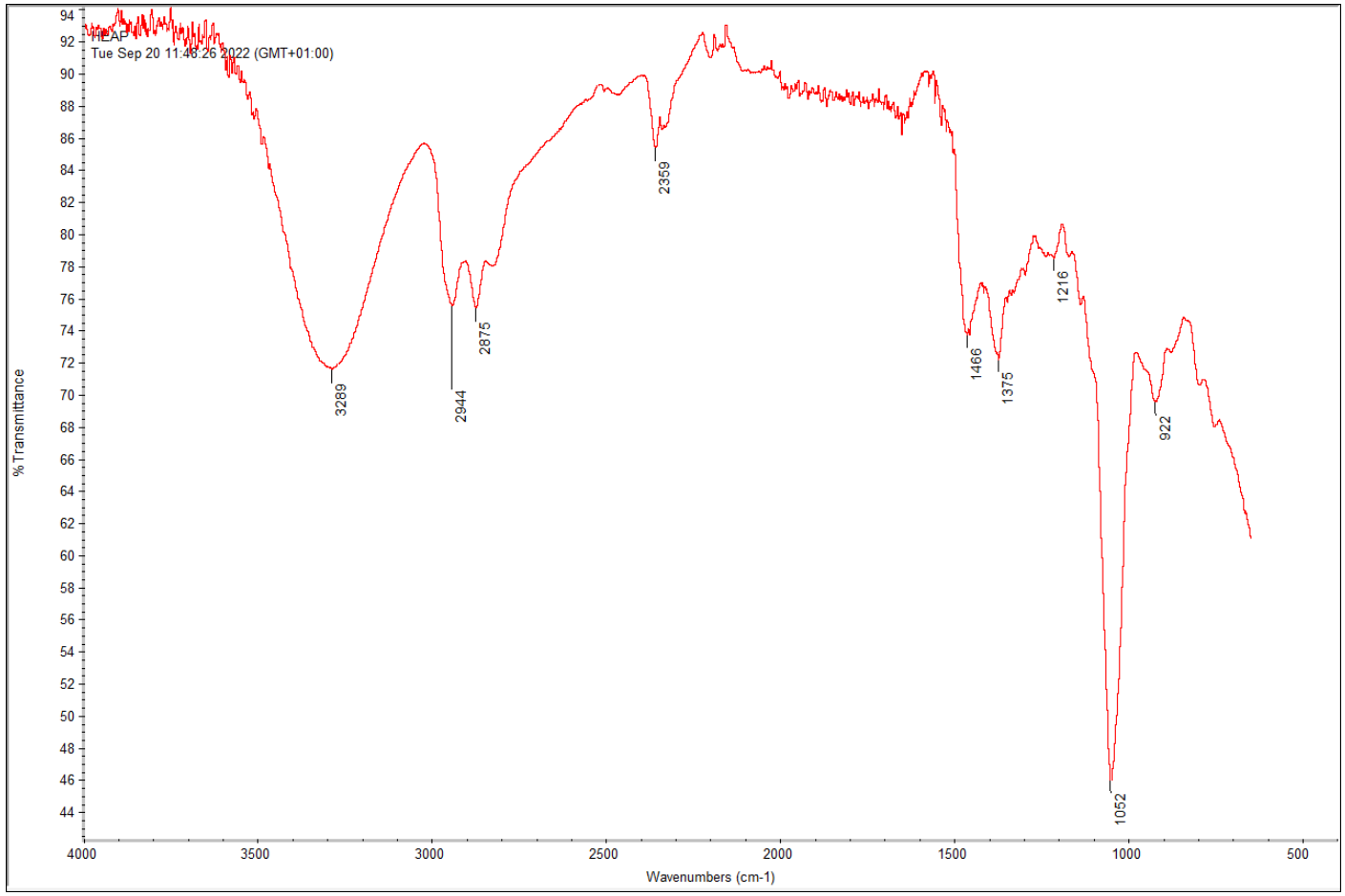

Figure S88- 3-[(2-hydroxyethyl)(iso-propyl)amino]propan-1-ol, [**H^{i}PrAP**H_2, FT-IR

Figure S89- 3-[(2-hydroxyethyl)(phenyl)amino]propan-1-ol, [**HPhAP**]H_2, FT-IR

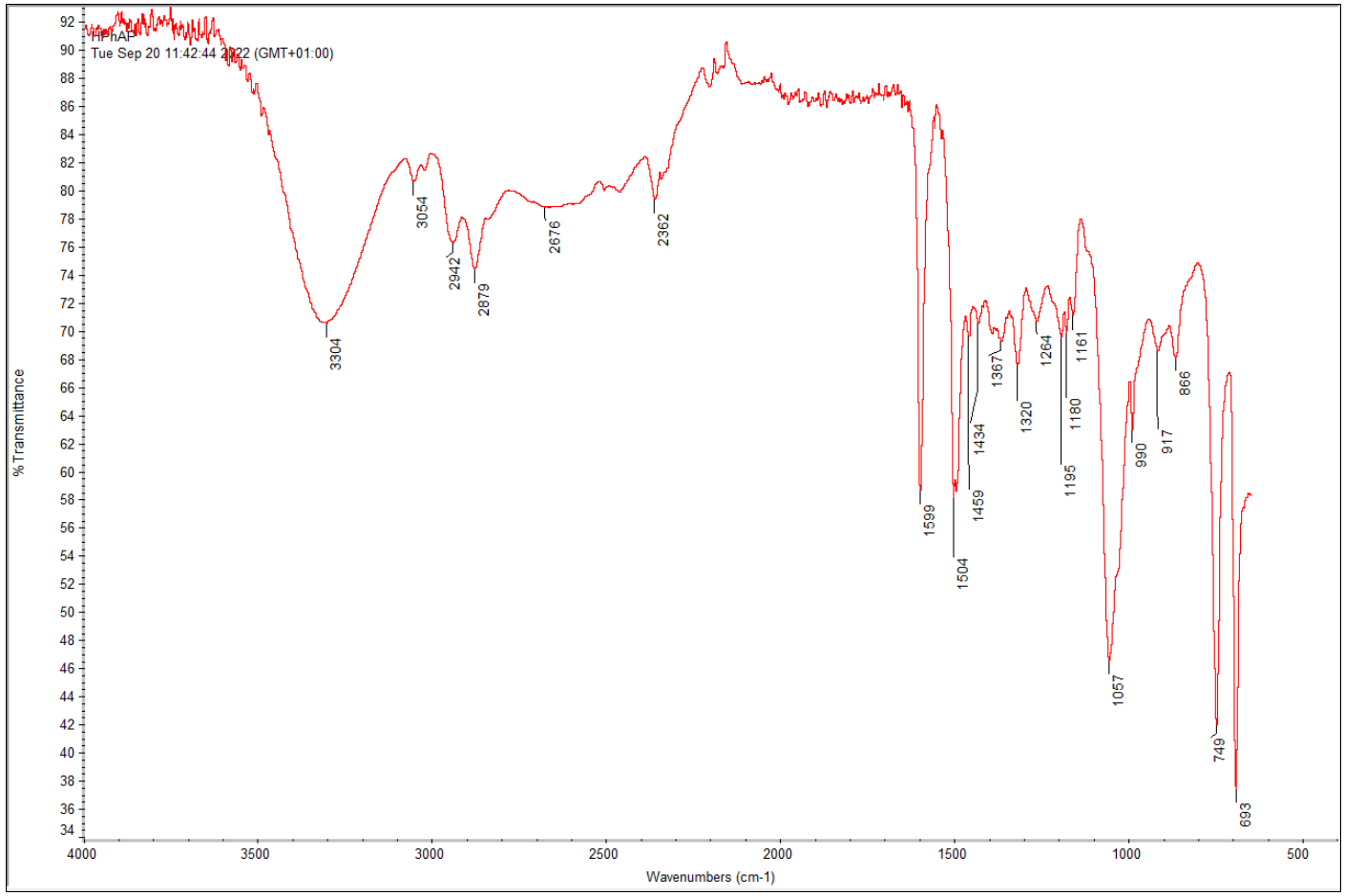

Appendix E – Mass Spectrometry

Mass spectrometry was performed using an Agilent technologies 6540 UHD Accurate-Mass Q-TOF LC/MS system. As and when required, LC separation was performed on an Agilent technologies 1260 infinity series LC system.

Figure S90- 2-(methylamino)ethan-1-ol, [**MAE**]H, MS

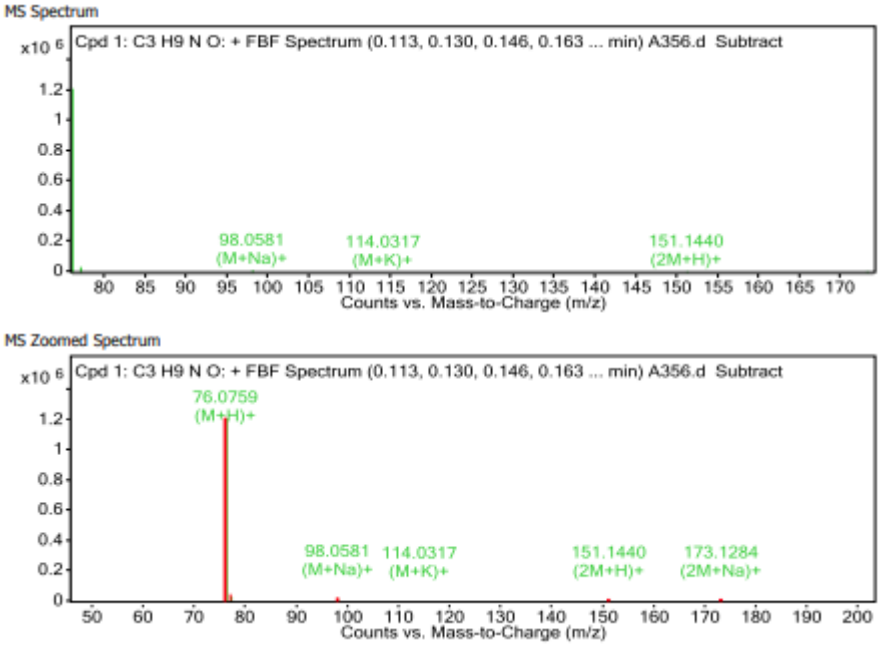

Figure S91- 2-(ethylamino)ethan-1-ol, [**EAE**]H, MS

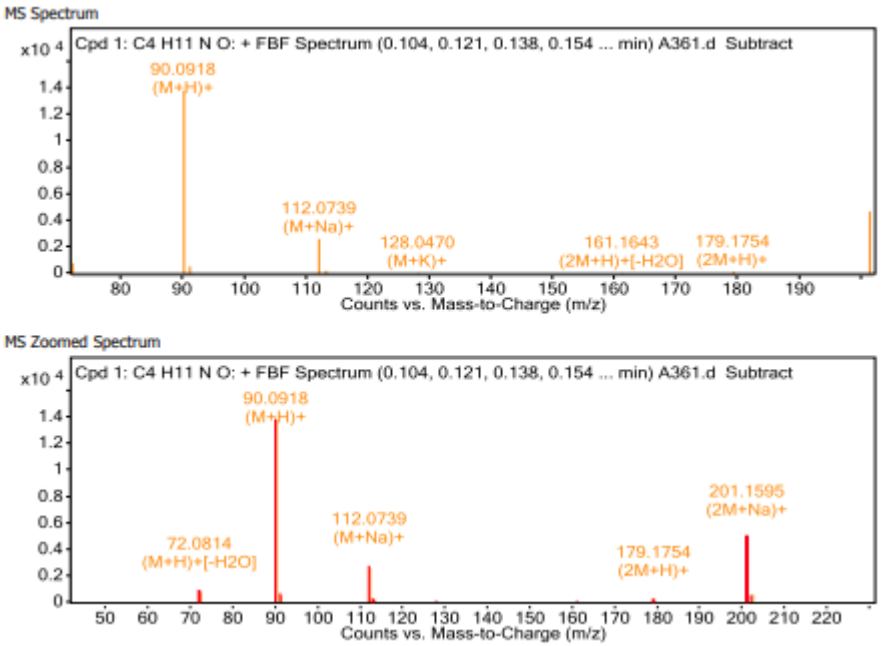

Figure S92- 2-(isopropylamino)ethan-1-ol, [^{i}**PrAE**]H, MS

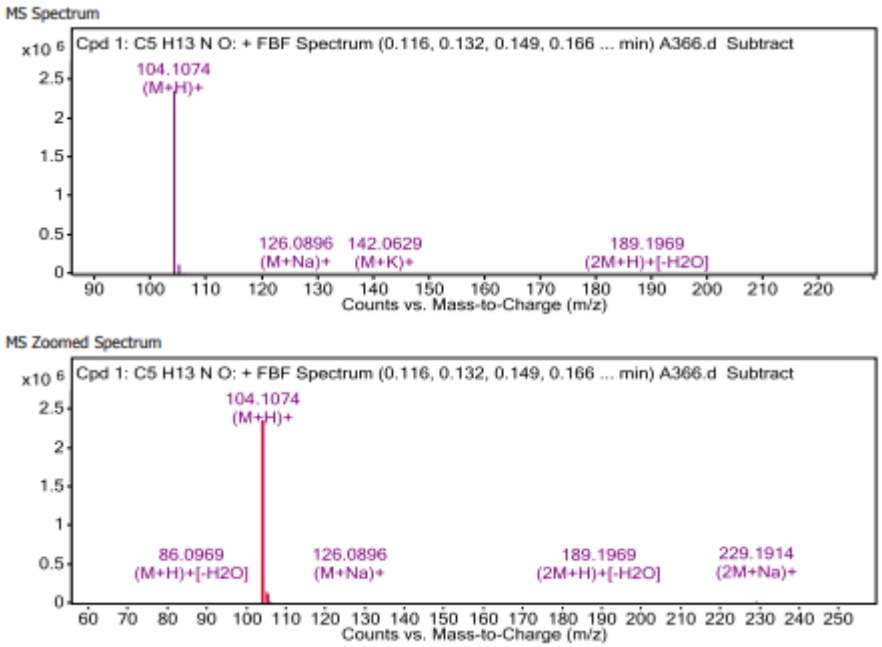

Figure S93- 2-(tertbutylamino)ethan-1-ol, [^{t}**BuAE**]H, MS

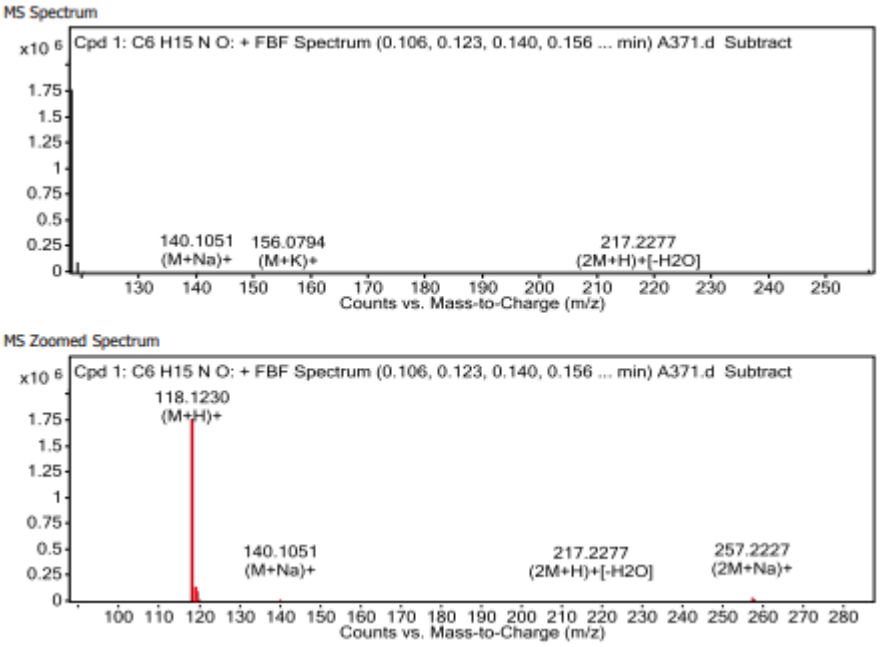

Figure S94- 2-(phenylamino)ethan-1-ol, [**PhAE**]H, MS

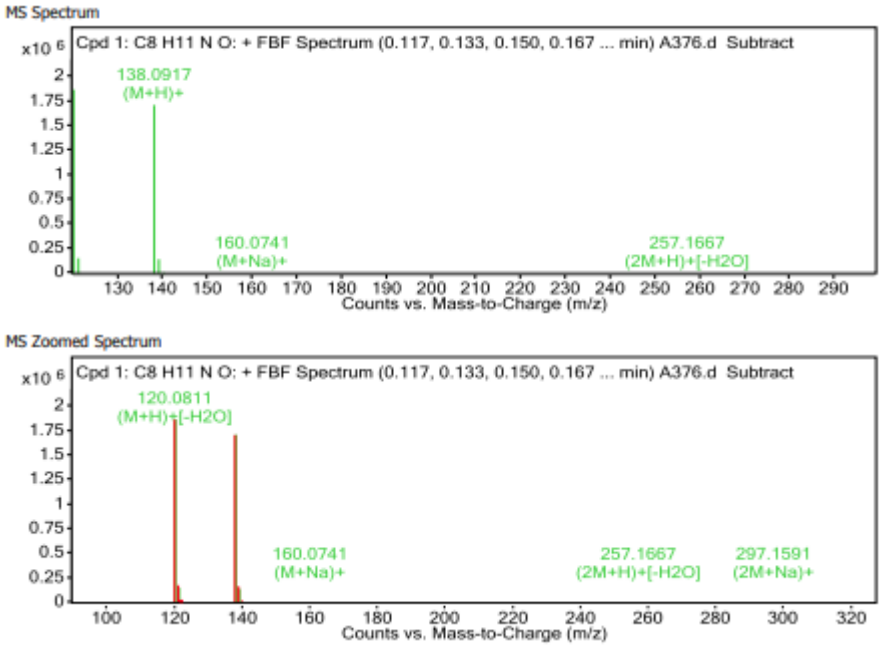

Figure S95- 2-(adamantylamino)ethan-1-ol, [**AdAE**]H, MS

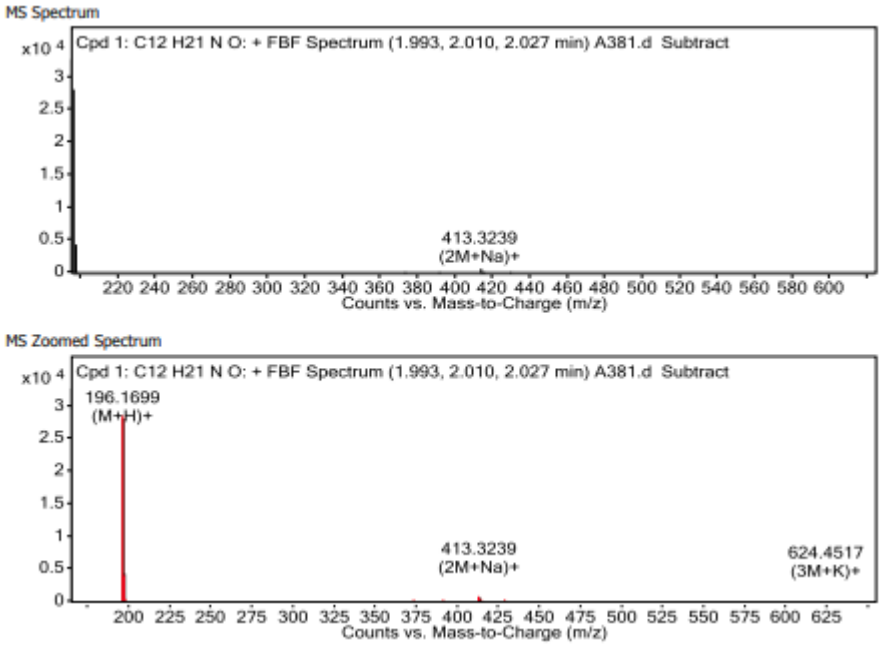

Figure S96- 3-(tertbutylamino)propan-1-ol, [^{t}**BuAPr**]H, MS

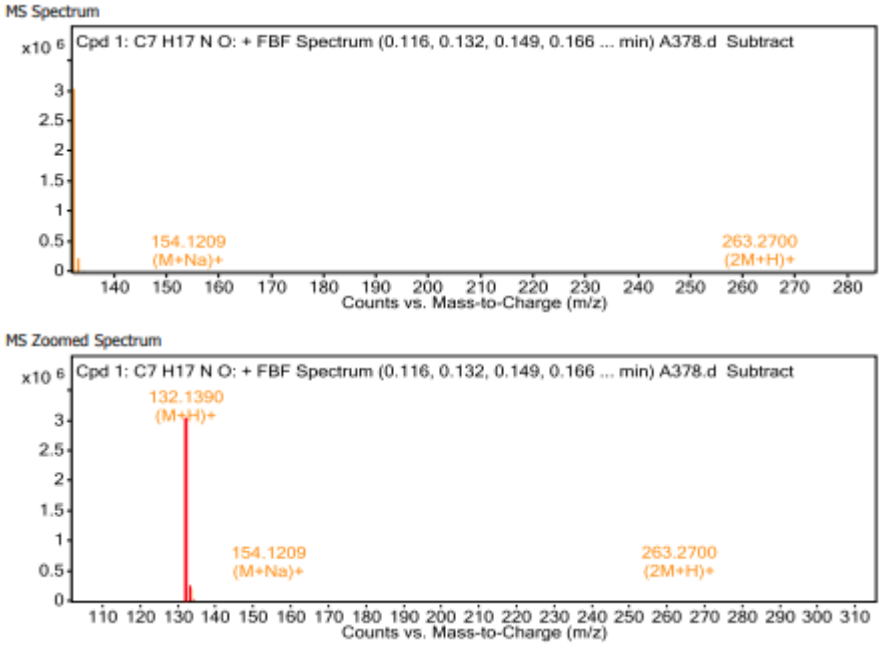

Figure S97- 3-(adamantylamino)propan-1-ol, [**AdAPr**]H, MS

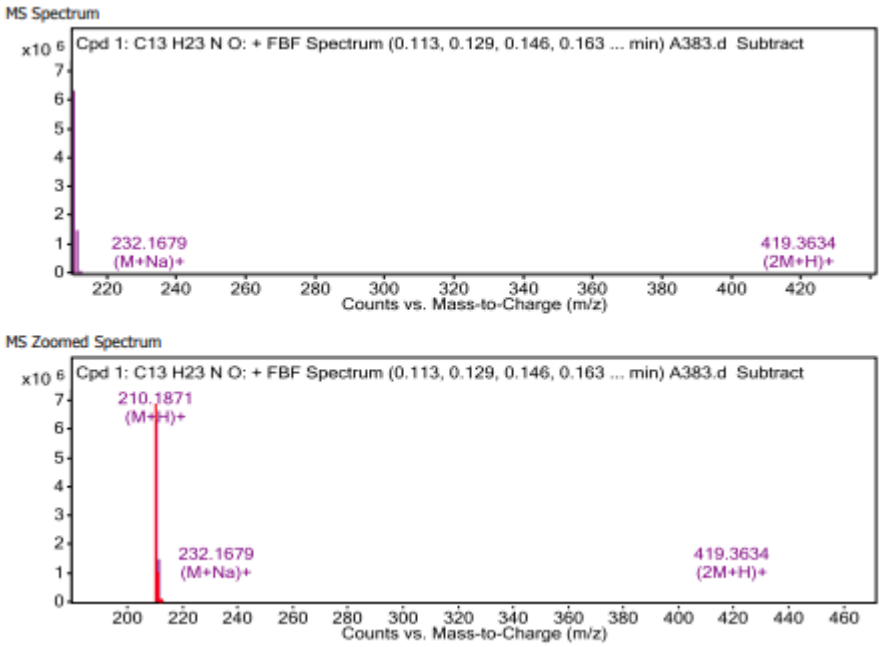

Figure S98- N-methyldiethanolamine, [**MDEA**]H_2, MS

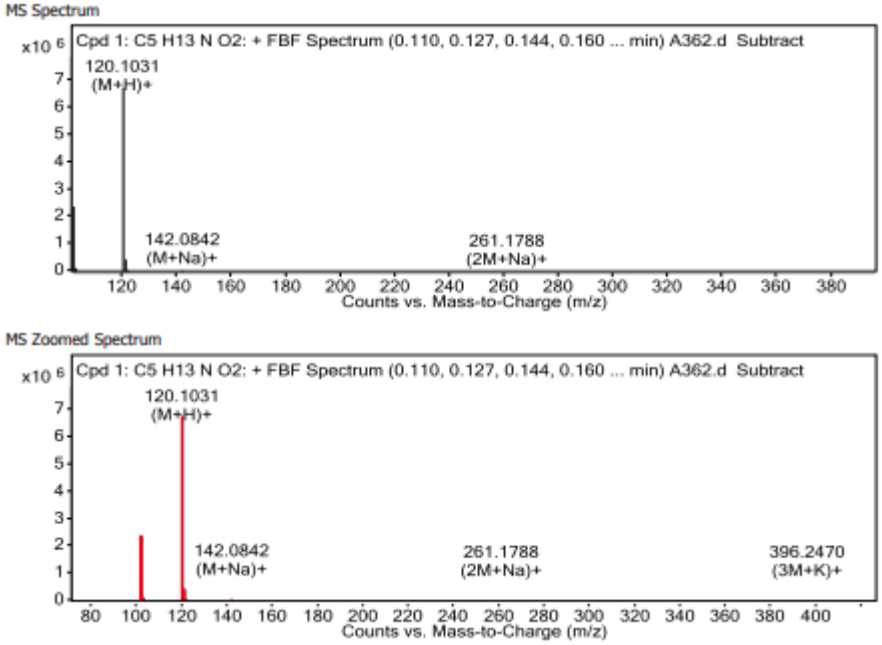

Figure S99- N-ethyldiethanolamine, [**EDEA**]H_2, MS

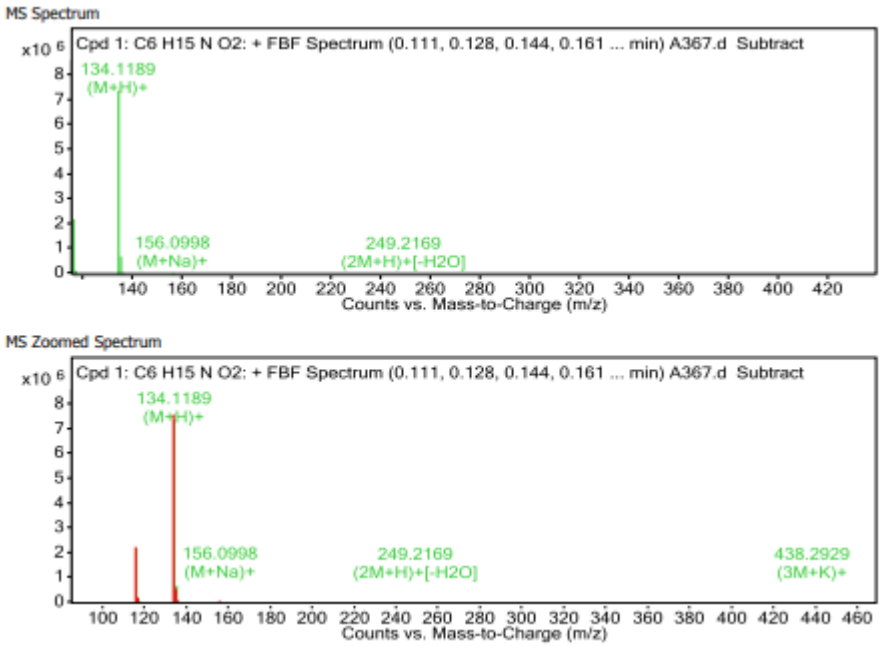

Figure S100- N-isopropyldiethanolamine, [^{i}**PrDEA**]H_2, MS

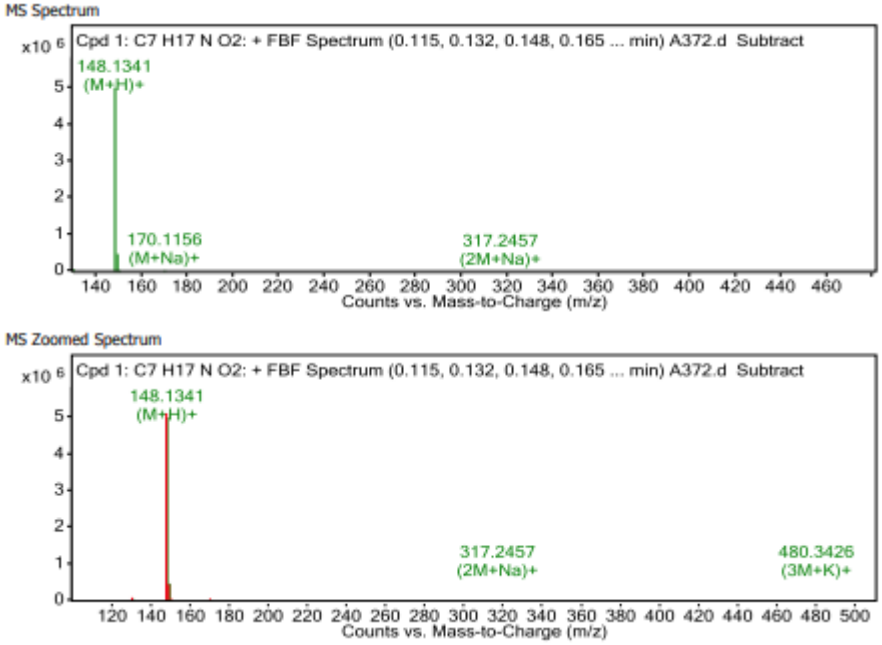

Figure S101- N-n- butyldiethanolamine, [^{n}**BuDEA**]H_2, MS

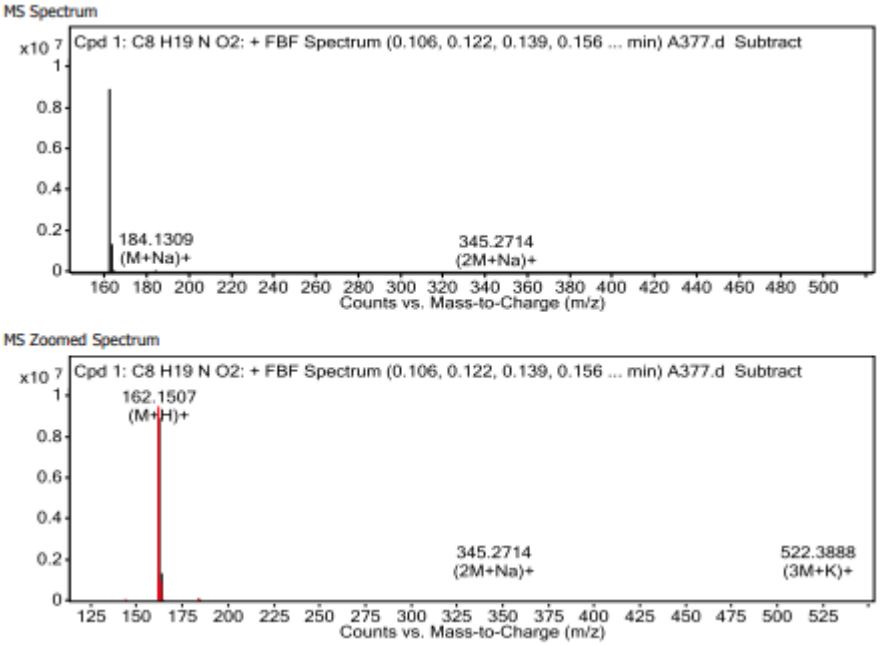

Figure S102- N-phenyldiethanolamine, [**PhDEA**]H_2, MS

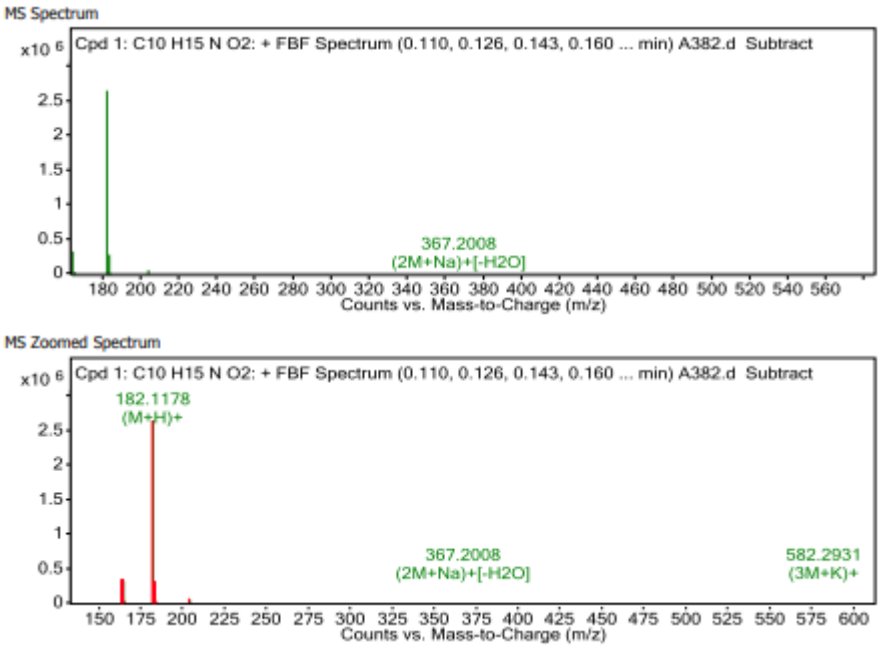

Figure S103- Triethanolamine, [**TEA**]H_3, MS

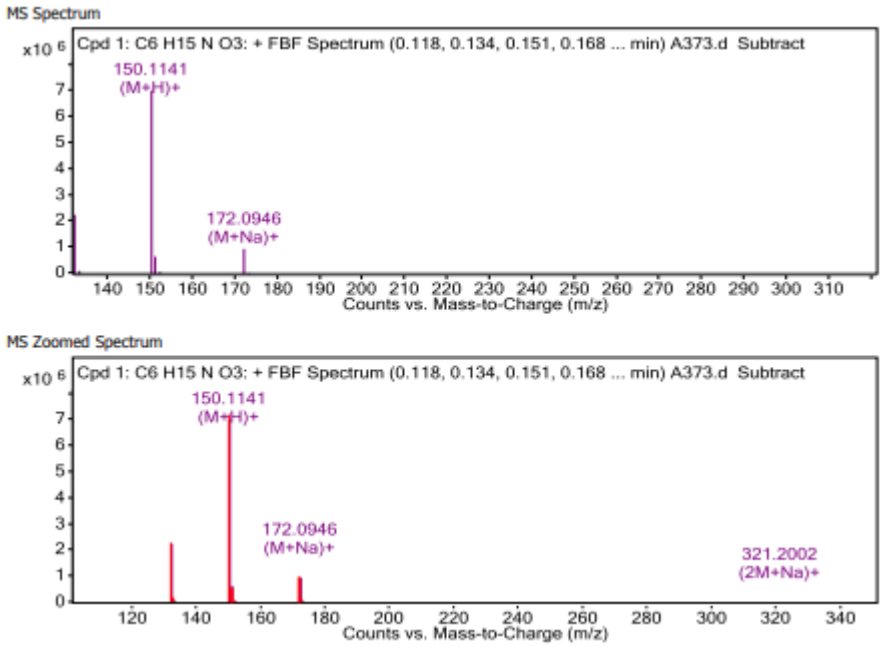

Figure S104- N-tert butyldiethanolamine, [^{t}**BuDEA**]H_2, MS

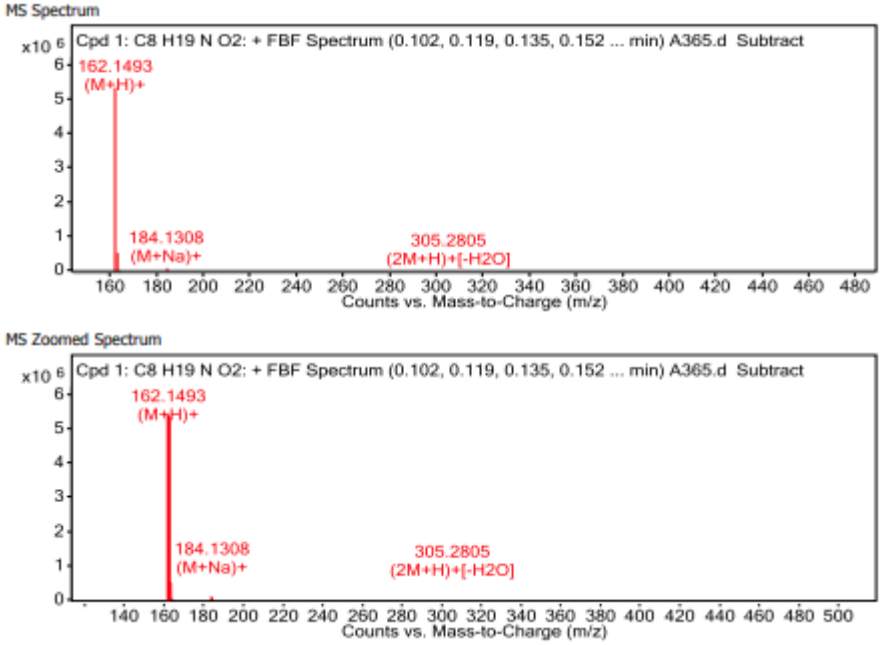

Figure S105- N-adamantyldiethanolamine, [**AdDEA**]H_2, MS

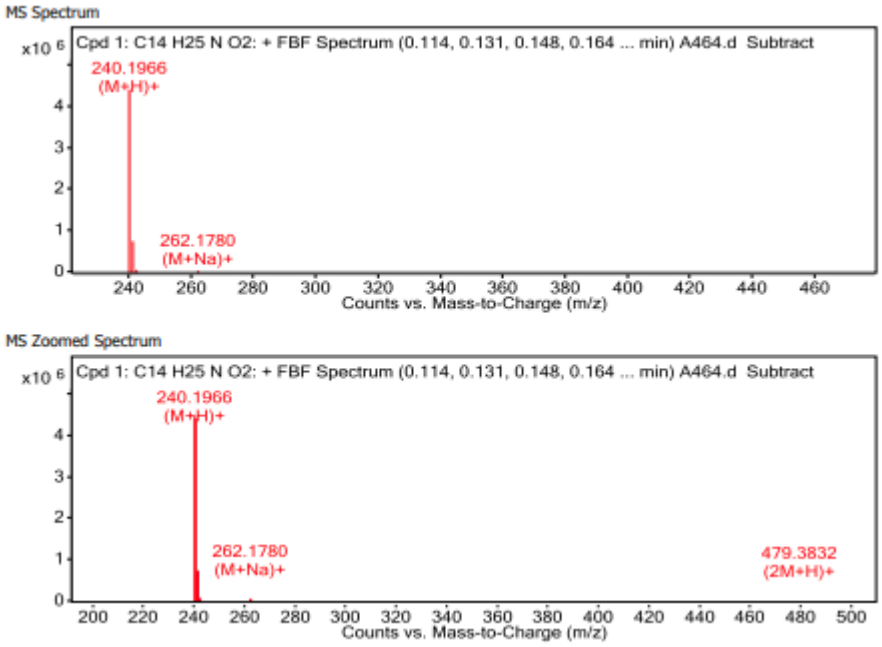

Figure S106- 3-[(2-hydroxyethyl)(methyl)amino]propan-1-ol, [**HMAP**]H_2, MS

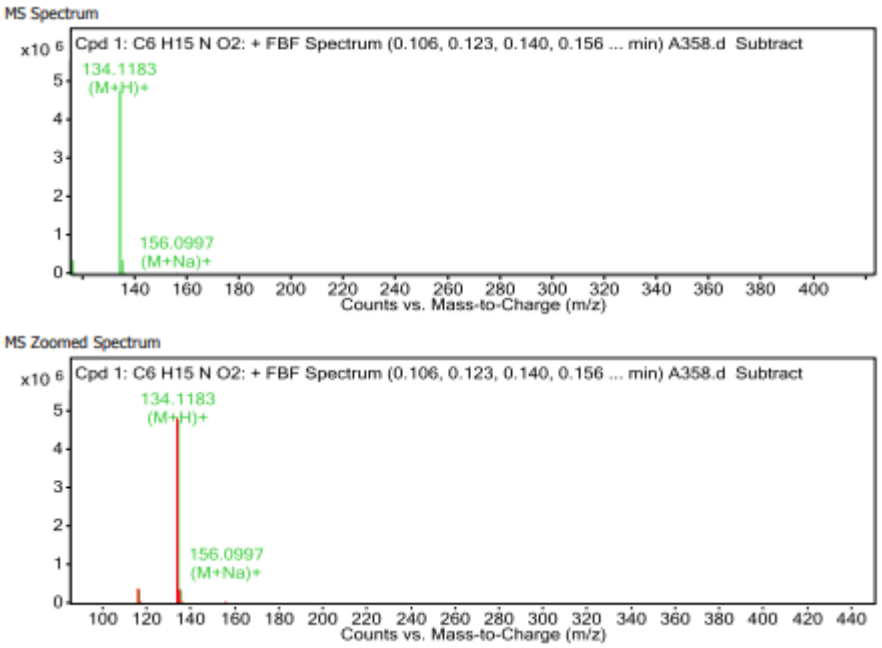

Figure S107- 3-[(2-hydroxyethyl)(ethyl)amino]propan-1-ol, [**HEAP**]H_2, MS

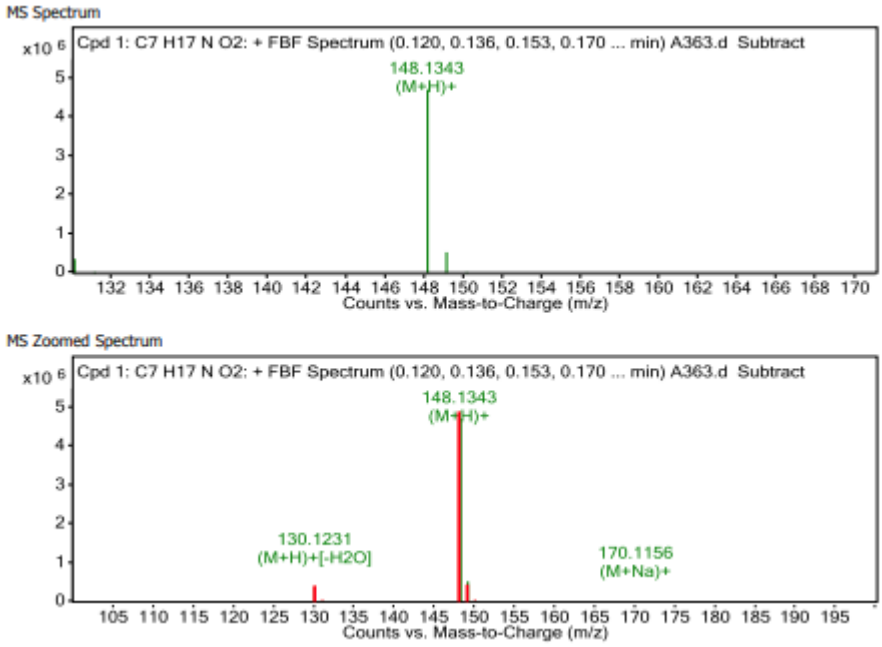

Figure S108- 3-[(2-hydroxyethyl)(iso-propyl)amino]propan-1-ol, [**H^{i}PrAP**]H_2, MS

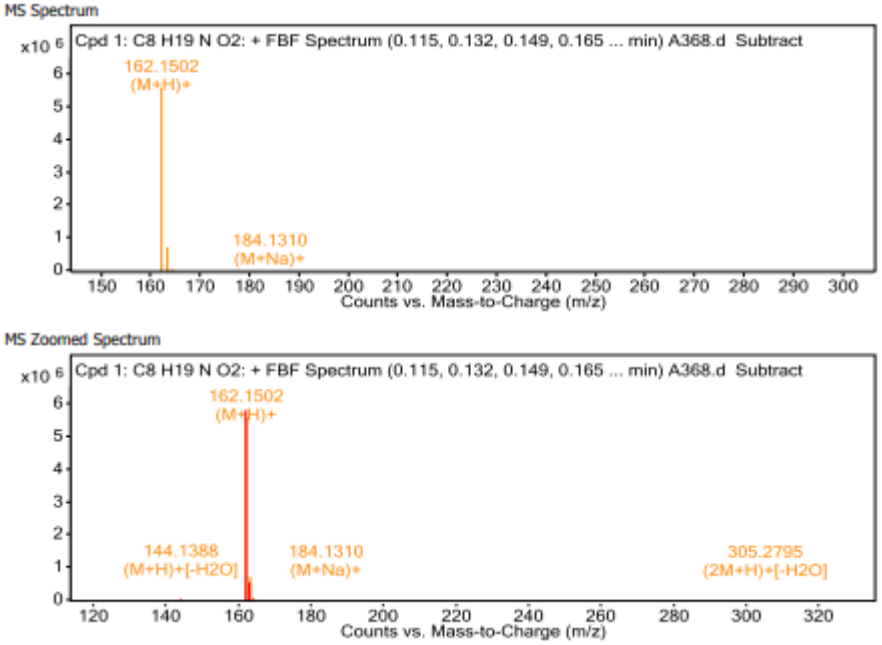

Figure S109- 3-[(2-hydroxyethyl)(phenyl)amino]propan-1-ol, [**HPhAP**]H_2, MS

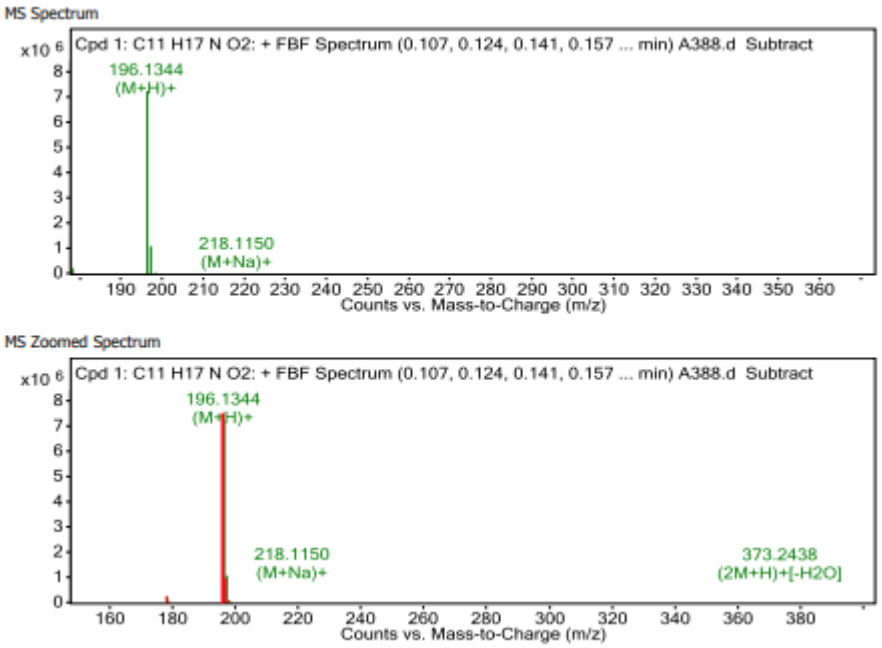

Figure S110- 3-[(2-hydroxyethyl)(phenyl)amino]propan-1-ol, [**HtBuAP**]H_2, MS

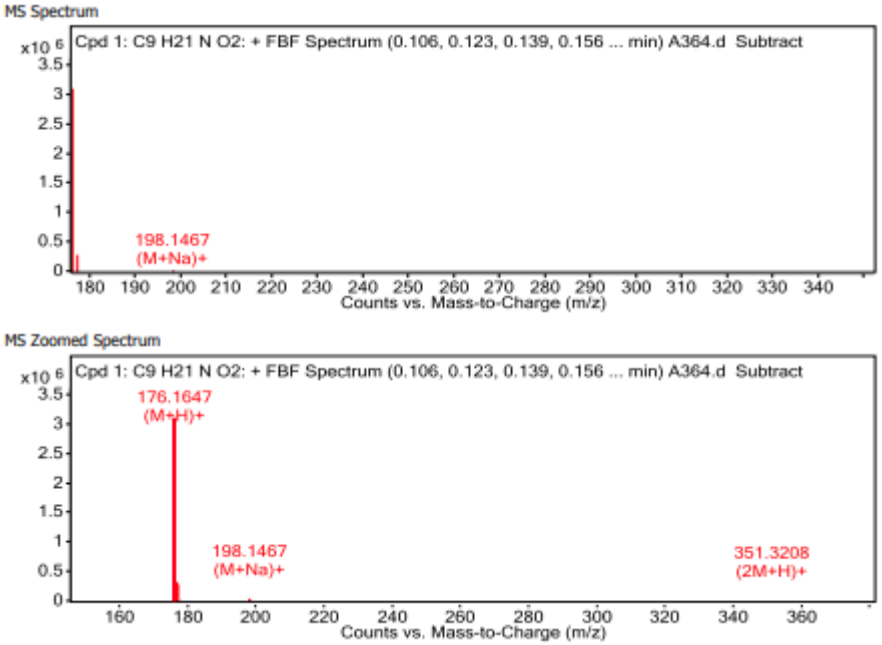

Figure S111- 3-[(2-hydroxyethyl)(phenyl)amino]propan-1-ol, [**HAdAP**]H_2, MS

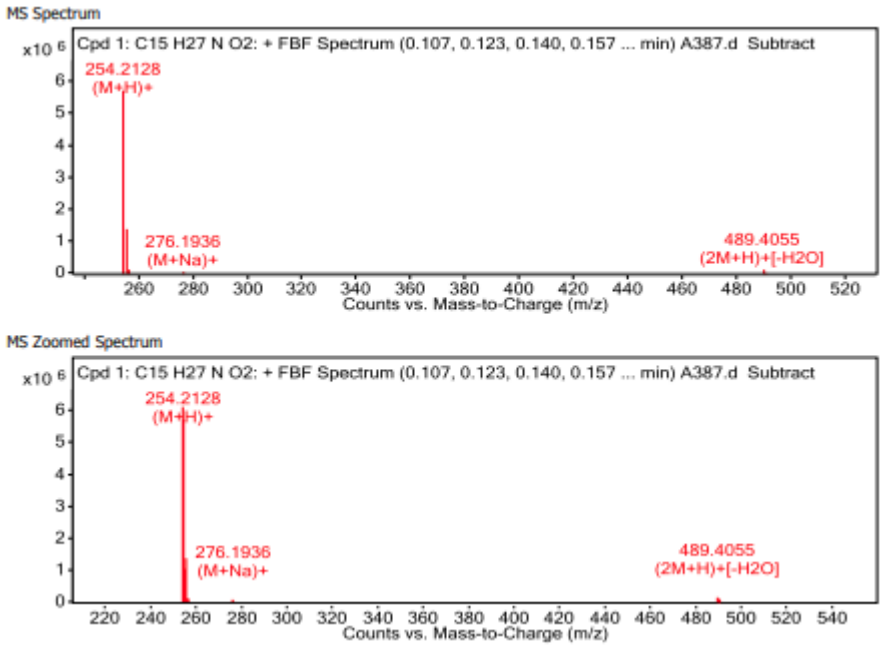

Figure S112- 2,2'-[(3-hydroxypropyl)imino] bis-ethanol, [^{n}**Pr'DEA**]H_3, MS

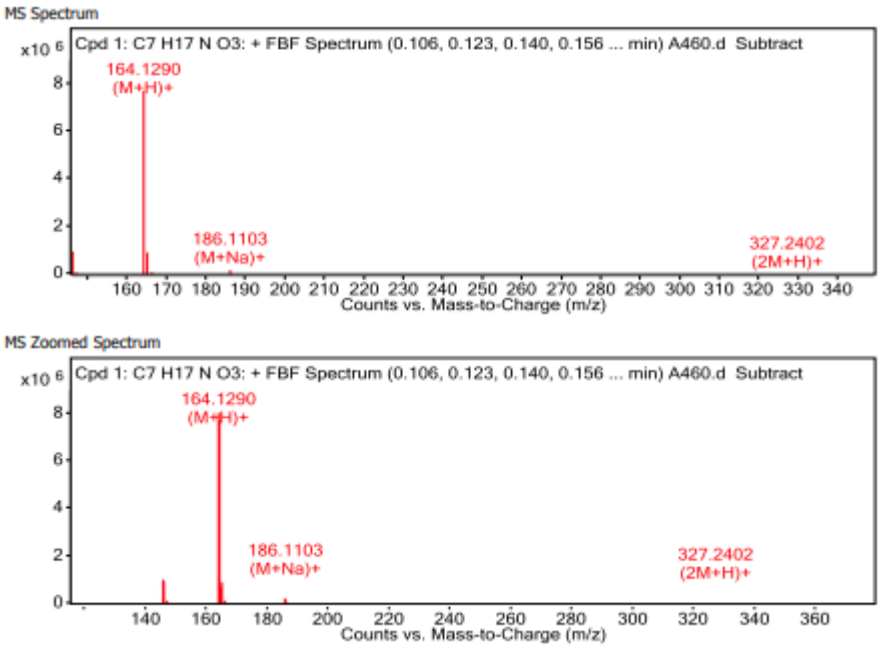

Appendix F – Magnetism

The magnetic susceptibility measurements for compounds **C8** and **C12-17** were carried out at the University of Melbourne on a Quantum Design SQUID magnetometer MPMS3-VSM operating between 1.8 and 300 K for dc-applied fields ranging from -5 to 5 T. The remaining magnetic susceptibility measurements, for samples **C21-23** and **C26-28**, were carried out on a Quantum Design SQUID magnetometer MPMS-XL 7 operating between 1.8 and 300 K for dc-applied fields ranging from 0–5 T. Microcrystalline samples were dispersed in Vaseline® in order to avoid torqueing of the crystallites. The sample mulls were contained in a calibrated gelatine capsule held at the centre of a drinking straw that was fixed at the end of the sample rod. Alternating current (ac) susceptibilities were carried out under an oscillating ac field of 3.5 Oe and frequencies ranging from 0.1 to 1500 Hz.

Magnetic data processing was carried out making use of Microsoft Excel. Further values were extrapolated using CC-Fit.[245]

Figure S113- Argand plot, **C15**

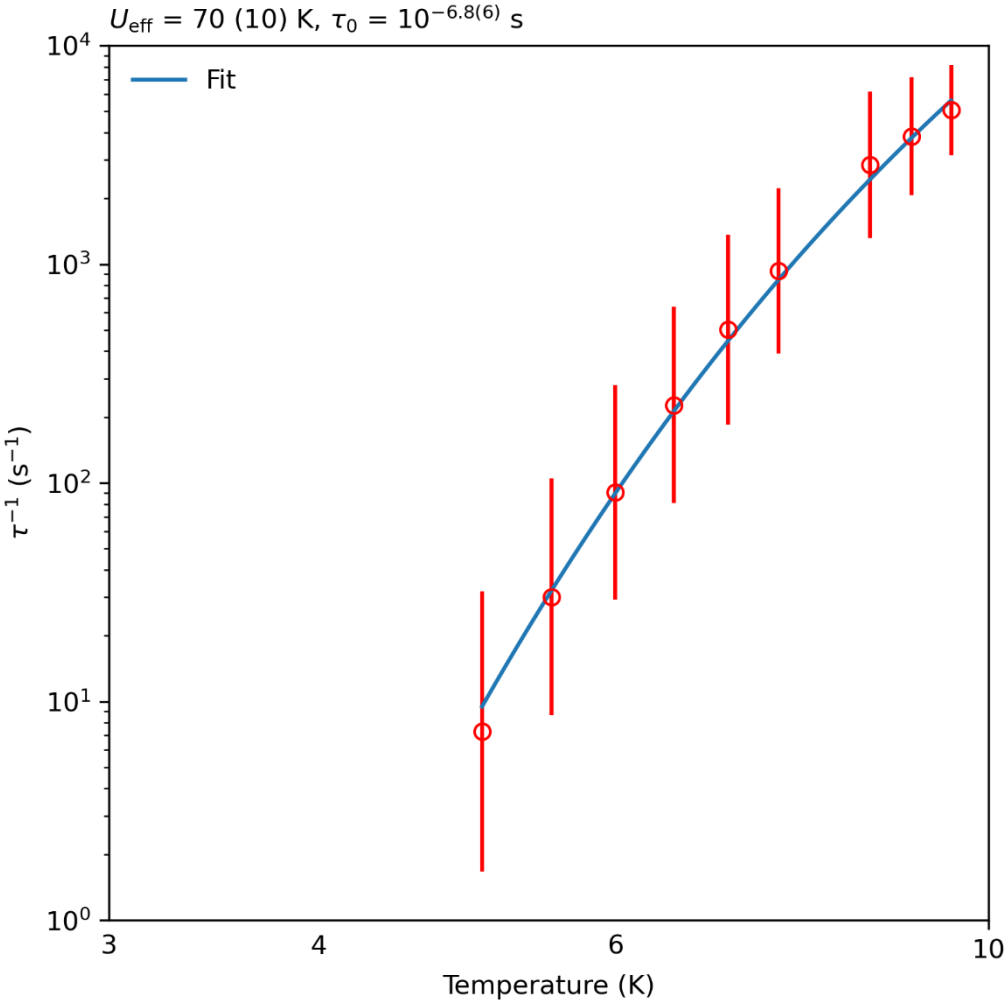

Figure S114- Argand plot, **C16**

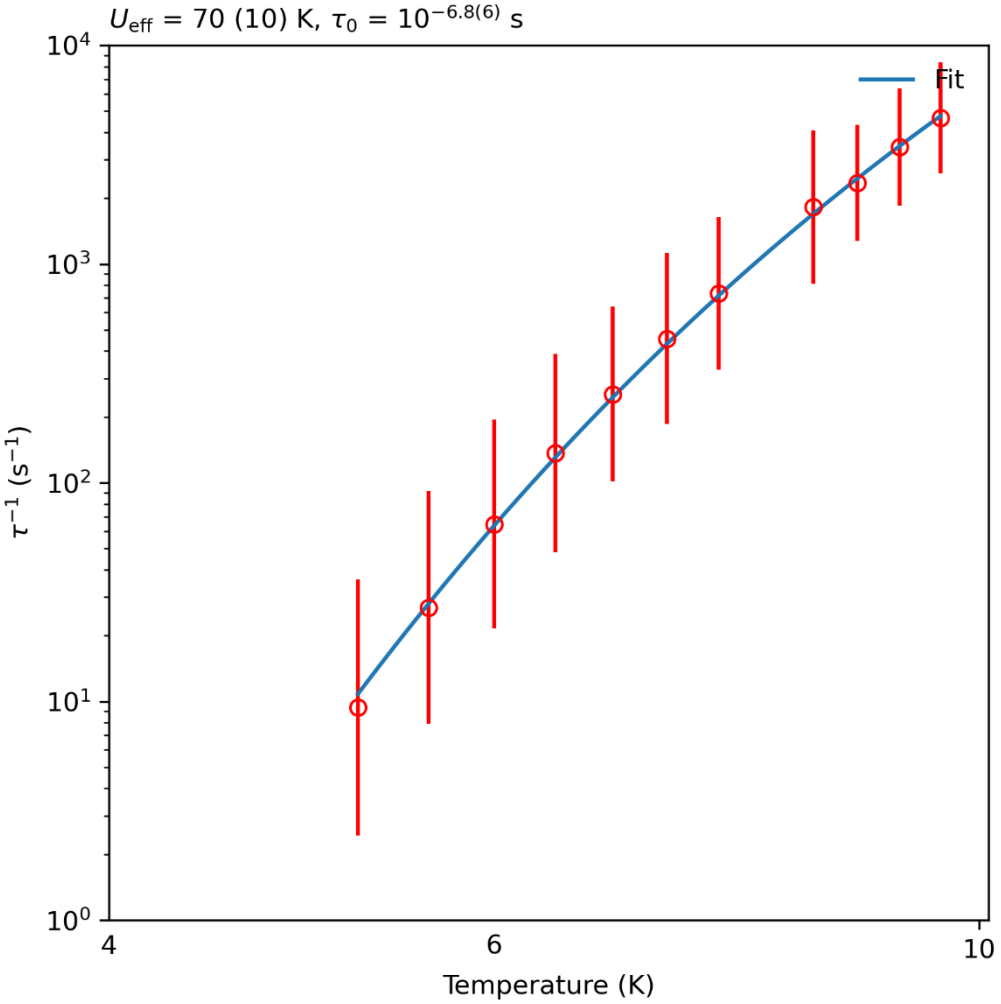

Direct current (dc) magnetic susceptibility analysis, **C21**

Figure S115- $\chi_M T$ vs Temperature

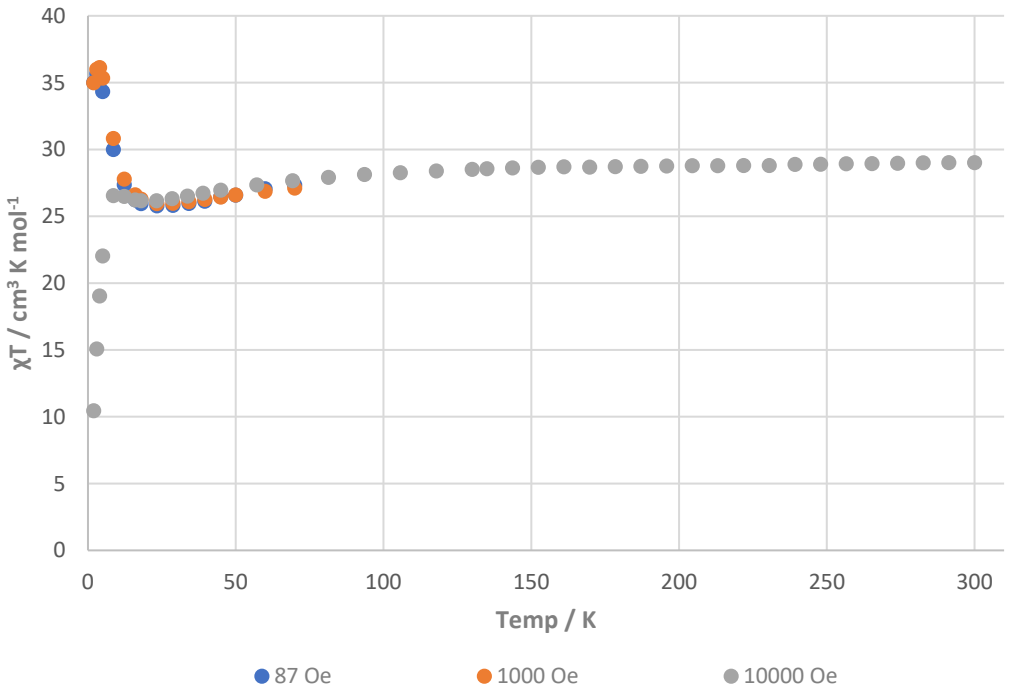

Figure S116- M vs H

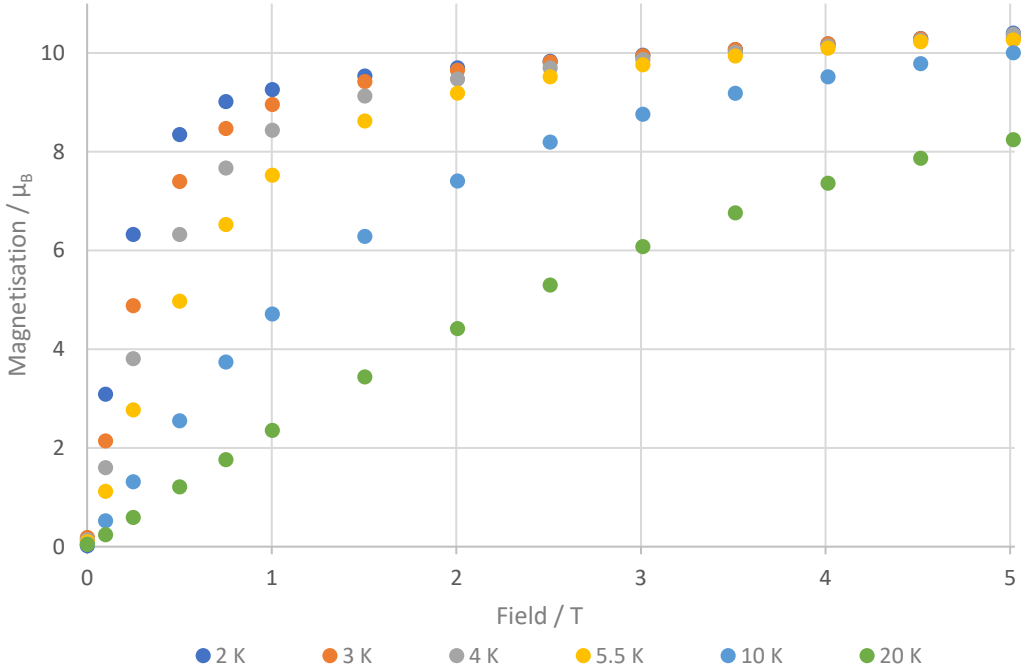

...

Alternating current (ac) magnetic susceptibility analysis, **C21**

Figure S117- χ_M" vs Frequency

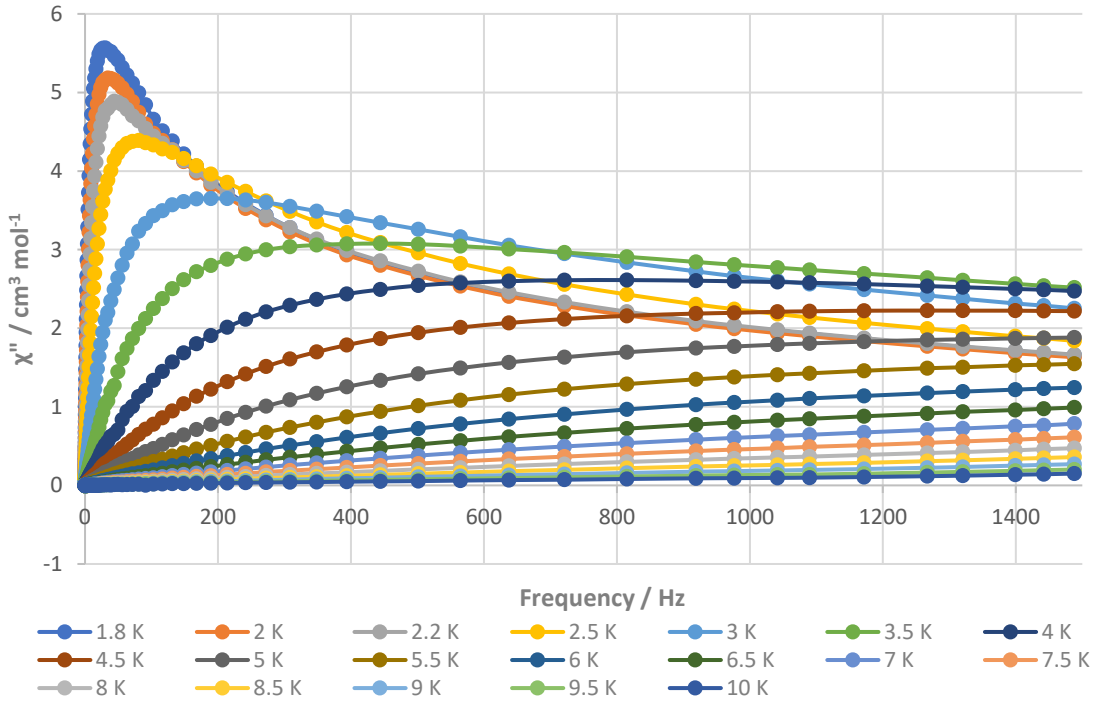

Figure S118- χ_M" vs Temperature

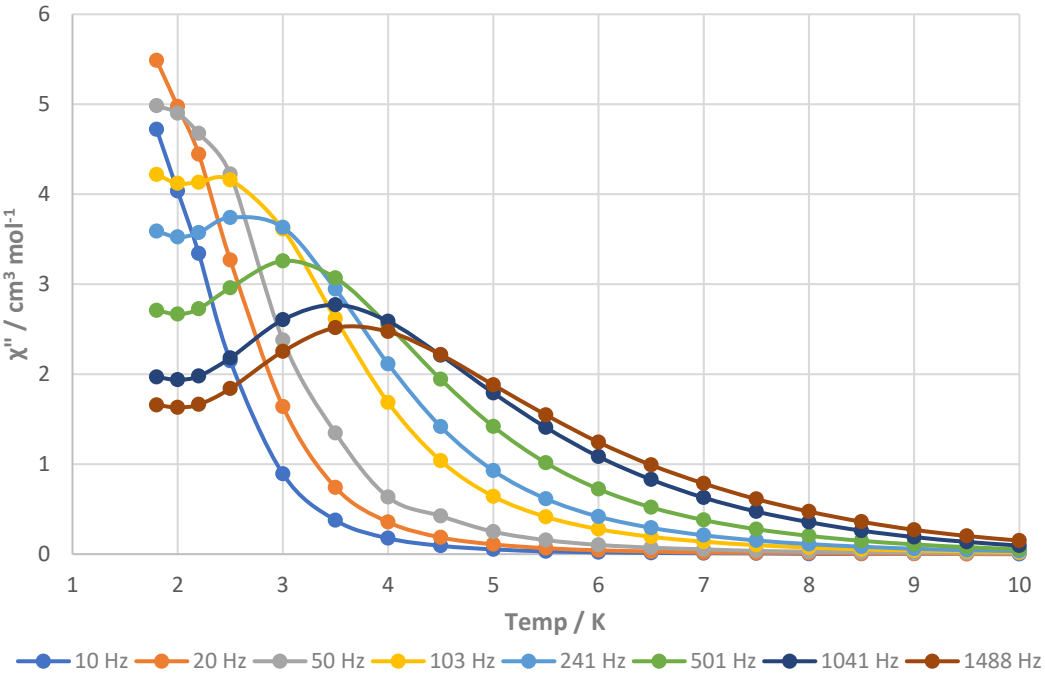

Figure S119- Argand plot, **C21**

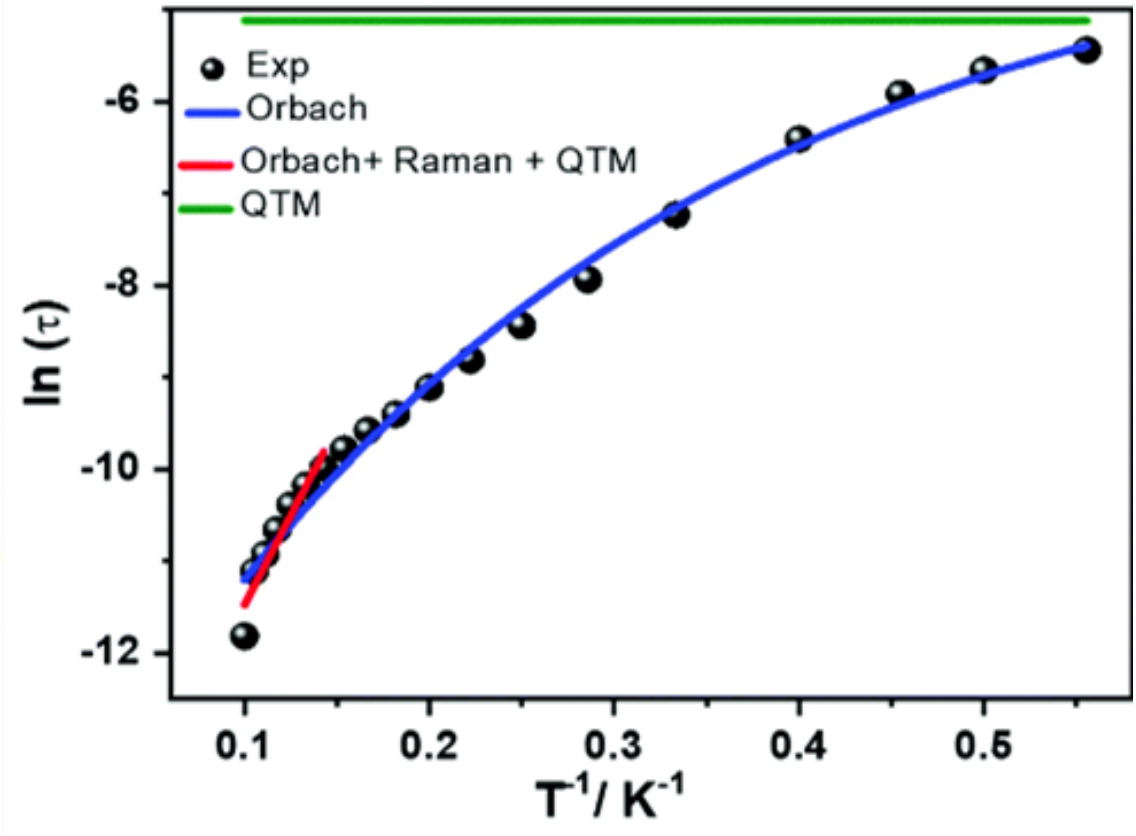

Figure S120- Argand plot, **C26**

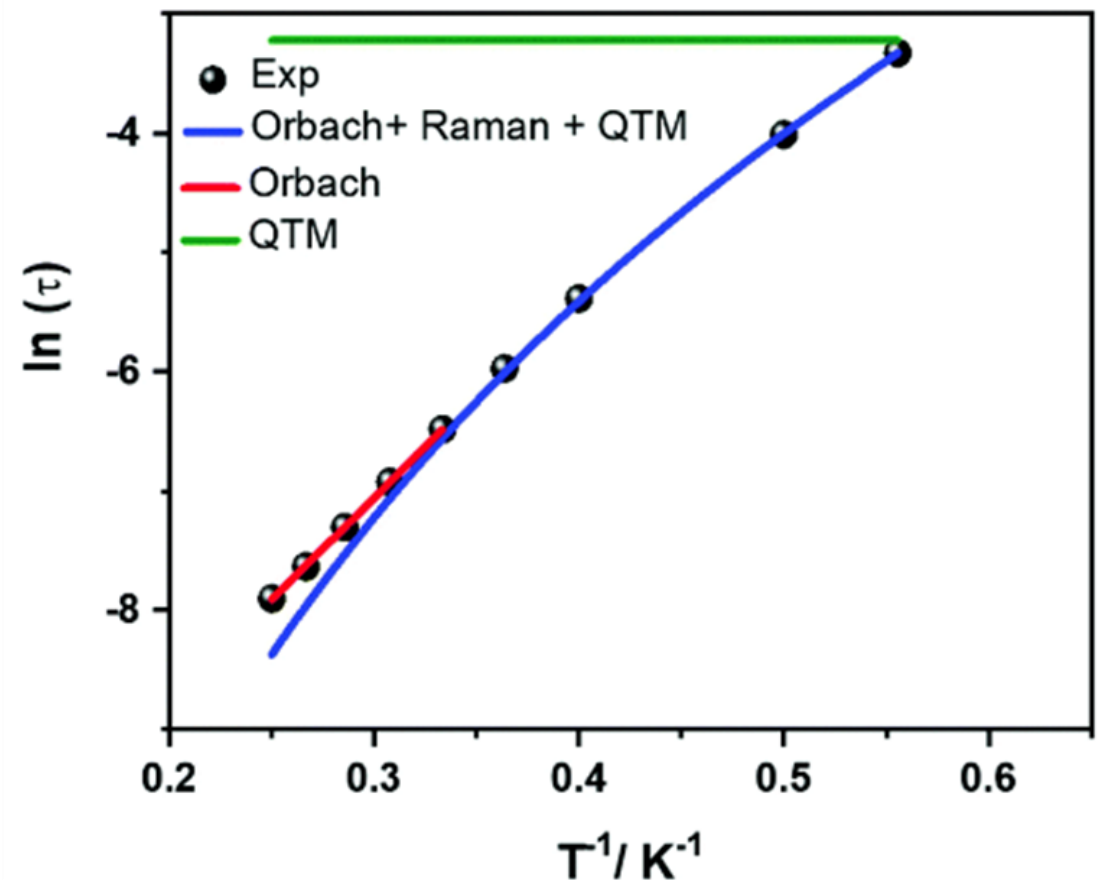

Appendix G – Papers